Online ISSN : 2395-602X
Print ISSN : 2395-6011
www.ijsrst.com

IJSRST

International e-Conference on Recent Trends in Material Science [ICRTMS-2024]

Date : 27th Feb 2024

Organized By

Department of Physics and Electronics
Shri Shivaji College
Parbhani, Maharashtra, India

SPECIAL ISSUE
VOLUME 11, ISSUE 9, JANUARY-FEBRUARY-2024

INTERNATIONAL JOURNAL OF SCIENTIFIC RESEARCH IN SCIENCE AND TECHNOLOGY

PEER REVIEWED AND REFEREED INTERNATIONAL SCIENTIFIC RESEARCH JOURNAL

Scientific Journal Impact Factor : 8.014

Email : editor@ijsrst.com Website : http://ijsrst.com

TECHNO SCIENCE ACADEMY
THE INTERNATIONAL OPEN ACCESS PUBLISHER

International e-Conference on Recent Trends in Material Science
[ICRTMS-2024]

27th Feb 2024

Organised by

Department of Physics & Electronics
M.S.P. Mandal's
Shri Shivaji College, Parbhani, Maharashtra, India

In Association with

International Journal of Scientific Research in Science and Technology
Print ISSN: 2395-6011 Online ISSN : 2395-602X
Special Issue
Volume 11, Issue 9, January-February-2024
International Peer Reviewed, Open Access Journal

Published By
Technoscience Academy
(The International Open Access Publisher)
website: www.technoscienceacademy.com

CHIEF PATRONS

Hon. Prakash Solanke
President
M. S. P. Mandal, Chh. Sambhajinagar
Hon. Satish Chavan

General Secretary
M. S. P. Mandal, Chh. Sambhajinagar
Hon. Hemantrao Jamkar
Head CDC
M. S. P. Mandal's, Shri Shivaji College, Parbhani

ORGANIZER

Prof. Dr. B. U. Jadhav

Principal
Prof. Dr. S. N. Keshatti
Vice Principal, HoD & Convenor

Prof. Dr. R. S. Nitonde
Vice-Principal

Prof. Dr. U. B. Kittekar
(IQAC Co-ordinator)

NAAC Accredited A+ grade 4th Cycle | College with potential for Excellence I UGC: Mentor College PARAMARSH I UGC STRIDE
Phone: 02452-221649
E-mail: scppbn@hotmail. com Website:www. shrishivajicollege. org

INTERNATIONAL ADVISORY COMMITTEE

Prof. Prakash A. Mahanwar
Acting Vice-Chancellor, SRTMU, Nanded
Dr. D. R. Mane
Director NEP, Govt. of Maharashtra.
Mrs Madhuri S. Deshpande
Acting Pro. Vice-Chancellor, SRTMU, Nanded
Prof. M. K. Patil
Dean, Faculty of Science and Technology, S. R. T. M. U. Nanded.
Prof. K. M. Jadhav
Emeritus Professor & Head , UDBAS, M. G. M. Univ. Chh. Sambhajinagar.
Prof. M. D. Sirsat
I/C Dean , Faculty of Science & Technology, Dr. B. A. M. U. Chh. Sambhajinagar.
Prof. M. P. Mahabole
Director, School of Physical Science, S. R. T. M. U. Nanded.

Prof. A. C. Kumbharkhane
Chairman BOS Electronics, SRTMU, Nanded

Prin. Dr. K. S. Kanse
Chairman BOS Physics, SRTMU, Nanded

Dr. Sonkambale Satish
Northwest University, South Africa

Dr. Mohammed Shariq
FIMEA IPA Stuttgart, Germany

Dr. Balaji Ghule
UNIST, South Korea

Dr. Hanuman Reddy
Alabama University, USA

Dr. Vishal Dwivedi
Tampere University, Finland

Contact for Details

Dr. S. M. Yenorkar
Organizing Secretary
Mob. 7276532176
Dr. S. N. Keshatti
Convenor
Mob. 9422743448
Dr. V. G. Kalmse
Joint Organizing Secretary
Mob. 9822892762
Email: scpphyele@gmail. com

Organizing Committee

Dr. B. U. Jadhav (Principal)
Dr. S. N. Keshatti (Convenor)
Mr. R. P. Zingre (Co-Convenor)
Dr. S. M. Yenorkar (Organizing Secretary)
Dr. V. G. Kalmse (Joint Organizing Secretary)

Organizing Members

Dr. S. M. Lonkar (HoD, Chemistry)
Dr. J. M. Gaikwad (HoD, Fishery Science)
Mr. S. S. Kulkarni (HoD, Microbiology)
Dr. H. S. Jagtap (HoD, Zoology)
Dr. Sabiha V. Syed (HoD, Botany)
Mr. D. N. Patwari (HoD, Computer Science)
Mr. S. B. Kadam (HoD, Mathematics)
Mr. V. M. More (Registrar)
Mr. Sandip R. Magar (Dept of Physics)

Local Advisory Committee

Dr. A. A. Ardad
Vice-Principal, Deogiri College, Chh. Sambhajinagar
Dr. S. K. Vyawahare
Prof. & HOD of Physics, Sunderrao Solanke Mahavidyalaya, Majalgaon.

Dr. L. B. Jadhvar
HOD of Physics, Arts, Commerce and Science, College, Kille- Dharur
Dr. B. T. Tate
HOD of Physics, Balbhim College, Beed
Dr. S. D. More
HOD of Physics, Deogiri College, Chh. Sambhajinagar.
Dr. B. G. Lone
HOD of Physics, Vinaykrao Patil Mahavidyalaya, Vaijapur
Dr. A. P. Keche
HOD of Physics, Shri. Muktanand College, Gangapur.
Dr. P. D. Gaikwad
HOD of Physics, R. B. Attal College, Georai.
Mr. P. S. Kachave
HOD, D. S. M. College, Parbhani
Dr. Sarika Jadhav
HOD, Sant Tukaram College, Parbhani
Dr. Vijaykiran Narwade
Asst. Professor, NES Science College, Nanded

SUB-THEMES

Nanomaterials and Nanotechnology
Thin film technology
Materials for Energy Applications
Energy storage and conversion devices
Materials for Environmental Applications
Semiconductor Materials
Smart Materials and Structures
Energy Materials and Sustainable Solutions
Sensors Technology
Advanced Manufacturing and Fabrication Techniques
Materials for Electronics and Photonics
Dielectric Materials and It's Properties
Environmental Materials and Green Technologies
Materials in Aerospace and Automotive Engineering

Nano-structured Biomaterials
Functional Polymers and Composites
Emerging Trends in Material Characterization
Cross-disciplinary Applications of Materials

ABOUT INSTITUTION

Marathwada Shikshan Prasarak Mandal is one of the prominent educational institutions in the state of Maharashtra. Established in 1959 by the great visionary educationist, Late Shri Vinayakraoji Patil and his associates, the Mandal celebrated its GOLDEN JUBILEE in the year 2008- 2009. At present, the educational network of our institution has spread in five districts of Marathwada. The institution runs courses in commerce, arts, education, science, engineering, law, pharmacy, primary and secondary schools, junior and senior colleges. Our institute has received BEST EDUCATIONAL INSTITUTION AWARD by the Government of Maharashtra in 2001.

ABOUT COLLEGE

Shri Shivaji college is a premier educational institution in the Marathwada region. It was established in 1961 with the noble cause of the spread of education amongst the masses. The vision and mission of the college clearly state the same. Based on the same, the college administration and staff members strive hard to achieve the objectives, vision and mission of the institution. In the way of achieving those aims, the college stands ahead compared to its peers. It is distinctive on the basis of some of the following grounds:

- The college is the only HEI affiliated with Swami Ramanand Teerth Marathwada University Nanded securing NAAC's then highest grade (A+) with a CGPA of 3. 47 in its Fourth Cycle of Accreditation.
- The college is identified as a "College with Potential for Excellence" by UGC.
- The college is among 18 Colleges across the nation to secure UGC's Scheme for Tran-Disciplinary Research for India's Developing Economy (STRIDE).
- The college is among the 786 institutions identified by UGC as Mentor for its PARAMARSH scheme.
- The college is the recipient of the Best College Award from the university.
- The principal of the college received the Best Principal Award from the university.

ABOUT DEPARTMENT

Department of Physics was established in the beginning of this college in June 1961. Department has well equipped and well furnished laboratories for the students. All the faculty members are well qualified and committed to provide high quality education to the students. With this all the faculty members are doing research actively. We offer UG, PG & Research programs for highly motivated students looking to pursue a carrier in Physics.

OBJECTIVE'S OF e-CONFERENCE

The main objective of the e-conference (ICRTMS-2024) is to provide common platform for scientist, teachers, students, industrialist and research scholars to exchange knowledge and ground breaking findings in the field of Material Science. The conference aims to encourage multi-disciplinary collaboration, address challenges in the field, facilitate networking opportunities, empower new researchers, explore future directions and promote sustainable research.

RESOURCE PERSONS

Dr Megha A. Deshmukh

(Marie Sklodowska Curie Action (MSCA) Fellow-CZ)
VSB-Technical University, Ostrava, Czech Republic

Dr. Gangadhar Banappanavar

(Postdoctoral Research Associate)
Physics Department, Durham University, United Kingdom

Dr. Pasha W. Sayyad

(Postdoctoral Research Fellow)
Department of Electronic Materials Engineering, Kwangwoon University, Seoul, Republic of Korea.

CONTENT

ICRTMS-2024
International e-Conference on Recent Trends in Material Science
In Association with International Journal of Scientific Research in Science and Technology
Volume 11 | Issue 9 | Print ISSN: 2395-6011 | Online ISSN: 2395-602X (www.ijsrst.com)

Advances and Perspectives in Biomedical Applications of Ferrite Nanoparticles

Balwan U. Patil*[1], Ganesh B. Akat[2]
*[1]Department of Physics, Kohinoor Arts, Commerce & Science College, Khultabad, Dist. Chhatrapati Sambhajinagar. Maharashtra, India
*[2]Department of Chemistry, Kohinoor Arts, Commerce & Science College, Khultabad, Dist. Chhatrapati Sambhajinagar. Maharashtra, India

ABSTRACT

Ferrite nanoparticles have emerged as promising candidates for a myriad of biomedical applications owing to their unique magnetic properties, biocompatibility, and tunable surface chemistry. This paper reviews recent advancements and explores the potential perspectives in the biomedical utilization of ferrite nanoparticles. It examines their role in various applications such as hyperthermia cancer treatment, magnetic resonance imaging (MRI), magnetic drug targeting, and biosensing. The paper discusses key challenges, including biocompatibility, nanoparticle stability, and targeting efficiency, and proposes future research directions to enhance the efficacy and safety of ferrite nanoparticles in biomedical applications.

Keywords: Ferrite nanoparticles, biomedical applications, hyperthermia, magnetic resonance imaging, drug targeting, biosensing.

I. INTRODUCTION

In recent years, ferrite nanoparticles have garnered significant attention in biomedical research due to their unique magnetic properties and biocompatibility. These nanoparticles exhibit versatile functionalities that make them attractive for a wide range of biomedical applications, including cancer therapy, diagnostic imaging, drug delivery, and biosensing. This paper provides an overview of the recent advances and explores the potential perspectives in the biomedical applications of ferrite nanoparticles [1,2].

Nanotechnology has revolutionized the landscape of biomedical research and clinical practice by offering innovative solutions for disease diagnosis, treatment, and monitoring. Among the plethora of nanomaterials investigated for biomedical applications, ferrite nanoparticles have emerged as versatile candidates due to their unique magnetic properties, biocompatibility, and tunable surface chemistry. Ferrite nanoparticles, typically composed of iron oxides (e.g., magnetite, maghemite) combined with other metallic elements, exhibit exceptional magnetic behaviour that enables manipulation and control under external magnetic fields. Their nanoscale dimensions and large surface-to-volume ratio render them ideal platforms for multifunctional biomedical applications [3,4].

The integration of ferrite nanoparticles into biomedical technologies offers unprecedented opportunities to address key challenges in disease management, including cancer therapy, diagnostic imaging, drug delivery, and biosensing. Ferrite nanoparticles possess inherent properties that make them attractive for various biomedical applications:

- **Magnetic Responsiveness:** The magnetic properties of ferrite nanoparticles enable remote manipulation and control through external magnetic fields, facilitating targeted delivery of therapeutic agents, hyperthermia treatment, and magnetic resonance imaging (MRI) contrast enhancement [5].
- **Biocompatibility**: Ferrite nanoparticles are biologically inert and exhibit minimal cytotoxicity when properly functionalized and administered in controlled doses, making them suitable for in vivo applications in biological systems [6].
- **Surface Functionalization:** The surface chemistry of ferrite nanoparticles can be tailored through surface modification techniques, allowing for the conjugation of targeting ligands, therapeutic drugs, imaging agents, and biomolecules for specific biomedical applications [7].

The versatility of ferrite nanoparticles in biomedical research is exemplified by their diverse applications across different domains:

- In **hyperthermia cancer treatment,** ferrite nanoparticles serve as efficient heating agents capable of inducing localized tumour hyperthermia under the influence of alternating magnetic fields. This non-invasive therapeutic approach selectively targets cancer cells while sparing healthy tissues, offering a promising strategy for cancer therapy [8,9].
- As contrast agents in **magnetic resonance imaging (MRI),** functionalized ferrite nanoparticles enhance the sensitivity and resolution of diagnostic imaging by selectively accumulating in diseased tissues and providing distinct contrast signals. This enables early detection, accurate localization, and characterization of pathological conditions, facilitating timely intervention and treatment planning [8,9].
- In **magnetic drug targeting, ferrite** nanoparticles serve as carriers for therapeutic agents, enabling site-specific drug delivery to diseased tissues through the application of external magnetic fields. This targeted delivery approach minimizes systemic side effects and enhances therapeutic efficacy, particularly in the treatment of localized diseases such as cancer and inflammatory disorders [10].
- **For biosensing and diagnostics, functionalized** ferrite nanoparticles enable sensitive and specific detection of disease biomarkers, pathogens, and genetic sequences in biological samples. Integrated with microfluidic platforms and biosensor devices, ferrite nanoparticles offer rapid, portable, and cost-effective diagnostic solutions for a wide range of diseases, including infectious diseases, cancer, and neurodegenerative disorders [11].

Despite the tremendous potential of ferrite nanoparticles in biomedical applications, several challenges remain to be addressed, including concerns related to biocompatibility, nanoparticle stability, tissue penetration, and targeting efficiency. Moreover, the translation of ferrite-based technologies from bench to bedside necessitates rigorous preclinical evaluation, optimization of formulation parameters, and validation of safety and efficacy profiles. In this context, this paper aims to provide a comprehensive overview of the recent advances and potential perspectives in the biomedical utilization of ferrite nanoparticles. By critically examining the current state-of-the-art, identifying key challenges, and proposing future research directions, this review seeks to catalyse interdisciplinary collaborations and innovation in the development of ferrite-based biomedical technologies.

Through systematic investigation and integration of ferrite nanoparticles into biomedical research and clinical practice, we envision a future where these multifunctional nanomaterials contribute to transformative advances in disease diagnosis, treatment, and personalized medicine. This expanded introduction sets the stage for a comprehensive exploration of the biomedical applications of ferrite nanoparticles, highlighting their potential to address unmet clinical needs and revolutionize the landscape of modern medicine.

1. Hyperthermia Cancer Treatment [12,13]

Ferrite nanoparticles have shown promise as heating agents in hyperthermia cancer treatment, a therapeutic modality that involves raising the temperature of tumor tissues to induce cell death. The magnetic properties of ferrite nanoparticles enable efficient conversion of external alternating magnetic fields into heat, leading to localized hyperthermia within the tumor tissue. Recent studies have demonstrated the effectiveness of ferrite-based hyperthermia in selectively destroying cancer cells while minimizing damage to healthy tissues.

2. Magnetic Resonance Imaging (MRI) [14,15]

Ferrite nanoparticles serve as contrast agents in magnetic resonance imaging (MRI) by enhancing the visibility of tissues and organs in diagnostic imaging. Surface-functionalized ferrite nanoparticles offer improved biocompatibility and targeted imaging capabilities, enabling high-resolution imaging of specific molecular targets and disease biomarkers. Moreover, the tunable magnetic properties of ferrite nanoparticles allow for the development of multimodal imaging agents for simultaneous MRI and other imaging modalities.

3. Magnetic Drug Targeting [14,15]

One of the most promising applications of ferrite nanoparticles in biomedicine is magnetic drug targeting, which involves the localized delivery of therapeutic agents to diseased tissues under the influence of an external magnetic field. Functionalized ferrite nanoparticles can serve as carriers for various drugs, genes, or therapeutic molecules, facilitating site-specific drug delivery and minimizing systemic side effects. The use of magnetic targeting enhances drug accumulation at the target site, improving therapeutic efficacy and reducing dosage requirements.

4. Biosensing and Diagnostics

Ferrite nanoparticles exhibit unique magnetic and optical properties that make them suitable for biosensing and diagnostic applications. Functionalized nanoparticles can selectively bind to specific biomolecules, enabling sensitive detection and quantification of disease markers, pathogens, or genetic sequences. Integration of ferrite nanoparticles with microfluidic platforms and biosensor devices offers rapid and cost-effective diagnostic solutions for various diseases, including infectious diseases, cancer, and cardiovascular disorders.

5. Challenges and Future Directions

Despite significant progress, several challenges need to be addressed to fully exploit the potential of ferrite nanoparticles in biomedical applications. These include concerns related to biocompatibility, nanoparticle stability, tissue penetration, and targeting efficiency. Future research efforts should focus on optimizing nanoparticle design, surface functionalization strategies, and targeting methodologies to enhance the efficacy and safety of ferrite-based biomedical technologies [13-15].

II. CONCLUSION

In conclusion, ferrite nanoparticles hold great promise for a wide range of biomedical applications, including cancer therapy, diagnostic imaging, drug delivery, and biosensing. Recent advancements have demonstrated their potential to revolutionize the field of biomedicine by offering targeted and personalized treatment options. By addressing existing challenges and exploring new research avenues, ferrite nanoparticles are poised to play a pivotal role in shaping the future of biomedical technology.

III.REFERENCES

[1] Johannsen, M., et al. (2010). Magnetic nanoparticle hyperthermia for prostate cancer. International Journal of Hyperthermia, 26(8), 790-795.

[2] Gleich, B., & Weizenecker, J. (2005). Tomographic imaging using the nonlinear response of magnetic particles. Nature, 435(7046), 1214-1217.

[3] Veiseh, O., et al. (2010). Design and fabrication of magnetic nanoparticles for targeted drug delivery and imaging. Advanced Drug Delivery Reviews, 62(3), 284-304.

[4] Lu, A. H., & Salabas, E. L. (2007). Magnetic nanoparticles: synthesis, protection, functionalization, and application. Angewandte Chemie International Edition, 46(8), 1222-1244.

[5] Yoo, D., et al. (2011). Folic acid-conjugated magnetic nanoparticles for efficient targeting and uptake by cancer cells. Journal of Biomedical Materials Research Part A, 96(1), 160-170.

[6] Thakor, A. S., & Gambhir, S. S. (2013). Nanooncology: the future of cancer diagnosis and therapy. CA: A Cancer Journal for Clinicians, 63(6), 395-418.

[7] Laurent, S., et al. (2011). Magnetic iron oxide nanoparticles: synthesis, stabilization, vectorization, physicochemical characterizations, and biological applications. Chemical Reviews, 111(4), 2494-2532.

[8] Bae, K. H., et al. (2011). Nanotechnology for treatment of glioblastoma multiforme. Journal of Controlled Release, 163(2), 200-210.

[9] Ito, A., et al. (2004). Heat-inducible TNF-α gene therapy combined with hyperthermia using magnetic nanoparticles as a novel tumor-targeted therapy. Cancer Gene Therapy, 11(3), 236-242.
[10] Jokerst, J. V., et al. (2011). Nanoparticle PEGylation for imaging and therapy. Nanomedicine, 6(4), 715-728.
[11] Bulte, J. W. M., & Kraitchman, D. L. (2004). Iron oxide MR contrast agents for molecular and cellular imaging. NMR in Biomedicine, 17(7), 484-499.
[12] Yigit, M. V., et al. (2011). Theranostic nanoparticles for targeted cancer therapy. Current Opinion in Chemical Biology, 15(5), 775-781.
[13] Tong, S., et al. (2010). Coating optimization of superparamagnetic iron oxide nanoparticles for high T2 relaxivity. Nano Letters, 10(11), 4607-4613.
[14] Kievit, F. M., & Zhang, M. (2011). Surface engineering of iron oxide nanoparticles for targeted cancer therapy. Accounts of Chemical Research, 44(10), 853-862.
[15] Akbarzadeh, A., et al. (2012). Nanotoxicology and nanoparticle safety in biomedical designs. International Journal of Nanomedicine, 7, 835-849.

ICRTMS-2024
International e-Conference on Recent Trends in Material Science
In Association with International Journal of Scientific Research in Science and Technology
Volume 11 | Issue 9 | Print ISSN: 2395-6011 | Online ISSN: 2395-602X (www.ijsrst.com)

Applications & Important Properties of Various Ferrites: A Review

Ganesh B. Akat *[1], Balwan U. Patil[2]
*[1]Department of Chemistry, Kohinoor Arts, Commerce & Science College, Khultabad, Dist. Chhatrapati Sambhajinagar. Maharashtra, India
*[2]Department of Physics, Kohinoor Arts, Commerce & Science College, Khultabad, Dist. Chhatrapati Sambhajinagar. Maharashtra, India.

ABSTRACT

Ferrites, a class of magnetic materials, have garnered significant attention due to their versatile applications across various fields. This paper provides a comprehensive review of the applications and important properties of ferrites. It discusses their utilization in industries such as electronics, telecommunications, medicine, and more. Additionally, the paper explores the intrinsic properties of ferrites including magnetic, electrical, and structural characteristics, shedding light on their significance in different applications. Various synthesis methods and advancements in ferrite technology are also examined to understand their impact on enhancing material properties and expanding applications. Through this review, a deeper understanding of ferrites and their role in modern technology is elucidated.

Keywords: Ferrites, SEM, TEM, XRD, VSM, MRI and Magnetic properties.

I. INTRODUCTION

Ferrites, a class of ceramic materials consisting primarily of iron oxide (Fe_3O_4 or Fe_2O_3) combined with oxides of other metallic elements such as cobalt, nickel, zinc, or manganese, have emerged as key components in modern technology due to their unique magnetic and electrical properties. These materials exhibit a wide range of applications spanning across various industries, including electronics, telecommunications, medicine, and environmental remediation. The remarkable magnetic properties of ferrites, coupled with their relatively low cost and ease of fabrication, make them indispensable in magnetic recording media, such as magnetic tapes and hard disks used for data storage. In telecommunications, ferrite components play a crucial role in signal processing and communication devices, including antennas, isolators, circulators, and filters. Ferrites also find extensive use in power electronics, where they are employed as cores in transformers, inductors, and chokes for power conversion and conditioning applications. [1-3]

Beyond traditional applications, ferrites have garnered significant interest in emerging fields such as biomedicine and environmental science. Ferrite nanoparticles, due to their biocompatibility and magnetic properties, hold promise in drug delivery systems, hyperthermia therapy for cancer treatment, and contrast agents for magnetic resonance imaging (MRI). Moreover, ferrite-based materials are being investigated for environmental remediation purposes, including wastewater treatment, heavy metal removal, and pollution control, owing to their adsorption and catalytic properties. The study and advancement of ferrite materials have been facilitated by developments in synthesis techniques, characterization methods, and theoretical modelling. Researchers continue to explore novel synthesis routes, such as sol-gel, hydrothermal, and microwave-assisted methods, to tailor the properties of ferrite

materials for specific applications. Characterization techniques, including X-ray diffraction (XRD), scanning electron microscopy (SEM), transmission electron microscopy (TEM), and vibrating sample magnetometry (VSM), provide insights into the structural, magnetic, and electrical properties of ferrites, enabling the optimization of material performance. Despite their widespread use and versatility, challenges persist in the field of ferrite research. These include enhancing material properties, improving synthesis efficiency and scalability, understanding the fundamental mechanisms governing magnetic and electrical behavior, and exploring new avenues for application development. [2-4]

In this review paper, we aim to provide a comprehensive overview of the applications and important properties of ferrites, encompassing their role in various industries, intrinsic characteristics, synthesis methods, recent advances, and prospects. Through this examination, we seek to elucidate the significance of ferrites in modern technology and inspire further research and innovation in this field. [5,6]

II. OVERVIEW OF FERRITES

Ferrites are a class of ceramic materials characterized by their unique combination of ferric oxide (Fe2O3) or ferrous oxide (Fe3O4) with oxides of other metallic elements, such as cobalt (Co), nickel (Ni), zinc (Zn), or manganese (Mn). These compounds exhibit ferrimagnetic behavior, wherein the magnetic moments of the constituent ions align in a non-collinear arrangement, resulting in a net magnetization even in the absence of an external magnetic field. [5-8]

A. Crystal Structure:

Ferrites typically crystallize in a spinel structure, where oxygen ions form a face-cantered cubic (FCC) lattice, with metal cations occupying both tetrahedral (A) and octahedral (B) sites within the lattice. In spinel ferrites, the A sites are predominantly occupied by divalent ions (e.g., Zn^2+, Ni^2+, Co^2+), while the B sites are primarily occupied by trivalent ions (e.g., Fe^3+). This crystal structure imparts unique magnetic and electrical properties to ferrites, making them suitable for a wide range of applications.

B. Classification: Ferrites can be classified based on the nature of the metallic elements incorporated into their structure. Common types of ferrites include:

1. Soft Ferrites: These ferrites exhibit low coercivity and high permeability, making them suitable for applications requiring easy magnetization and demagnetization, such as inductors and transformers.
2. Hard Ferrites: Conversely, hard ferrites possess high coercivity and high remanence, making them ideal for permanent magnet applications, including refrigerator magnets, magnetic separators, and loudspeakers.
3. Mixed Ferrites: Mixed ferrites are tailored compositions that offer a balance between soft and hard magnetic properties, catering to specific application requirements.

C. Magnetic Domains:

In ferrites, magnetic domains play a crucial role in determining their magnetic behavior. At the microscopic level, domains are regions within the material where magnetic moments align in a uniform direction. The manipulation of domain structure through external magnetic fields or temperature variations can significantly influence the magnetic properties of ferrites, making them versatile for use in various devices.

D. Applications: The unique magnetic and electrical properties of ferrites render them indispensable in a myriad of applications across different industries. Some common applications include:

1. Electronics: Ferrites are widely used in electronic components such as inductors, transformers, and magnetic cores for RF interference suppression and signal filtering.
2. Telecommunications: Ferrite materials serve as essential components in microwave devices, antennas, isolators, circulators, and phase shifters for signal processing and communication systems.
3. Power Electronics: Ferrite cores find extensive use in power converters, inverters, and switching power supplies, due to their high magnetic permeability and low core losses.
4. Biomedicine: Ferrite nanoparticles hold promise in biomedical applications, including drug delivery systems, hyperthermia therapy for cancer treatment, and contrast agents for MRI imaging.

5. Environmental Remediation: Ferrite-based materials are employed for wastewater treatment, heavy metal removal, and environmental remediation due to their adsorption and catalytic properties.

In summary, ferrites represent a class of materials with diverse properties and applications, spanning across electronics, telecommunications, medicine, and environmental science. Their unique magnetic and electrical characteristics, coupled with advancements in synthesis techniques and material engineering, continue to drive innovation and expand their utility in modern technology.

E. Applications of Ferrites:

Ferrites, owing to their unique magnetic, electrical, and structural properties, find extensive applications across various industries. The versatility of ferrite materials makes them indispensable in a wide range of devices and systems. Below are detailed discussions on some of the key applications of ferrites:[9-12]

1. **Magnetic Recording Media:** Ferrites are widely used in magnetic recording media, such as magnetic tapes and hard disks, for data storage purposes. These materials serve as the magnetic medium onto which digital information is recorded and retrieved. Ferrite-based recording media offer advantages such as high coercivity, good thermal stability, and resistance to demagnetization, ensuring reliable data storage and retrieval in electronic devices.
2. **Telecommunications:** Ferrite materials play a crucial role in telecommunications systems and devices.Ferrite components, including antennas, isolators, circulators, and filters, are utilized for signal processing, frequency control, and noise suppression in communication networks. Ferrite-based devices enable the efficient transmission and reception of electromagnetic signals in microwave and radio frequency (RF) communication systems, contributing to the reliability and performance of wireless communication technologies.
3. **Power Electronics:** In power electronics, ferrite materials are widely employed as magnetic cores in inductors, transformers, and chokes. These components are essential for power conversion, voltage regulation, and noise filtering in electronic circuits and power supplies. Ferrite cores offer advantages such as high magnetic permeability, low core losses, and compact size, making them well-suited for applications requiring efficient energy transfer and conversion.
4. **Biomedical Applications:** Ferrite nanoparticles have garnered significant interest in biomedical applications due to their biocompatibility, tunable magnetic properties, and potential for controlled drug delivery and imaging. Ferrite-based nanomaterials are investigated for targeted drug delivery systems, hyperthermia therapy for cancer treatment, and contrast agents for magnetic resonance imaging (MRI). The magnetic properties of ferrite nanoparticles enable their precise manipulation and targeting within biological systems, facilitating targeted drug delivery and imaging modalities with improved specificity and efficacy.
5. **Environmental Remediation:** Ferrite-based materials are utilized for environmental remediation purposes, including wastewater treatment, heavy metal removal, and pollution control. Ferrite nanoparticles and bulk ferrite materials exhibit adsorption and catalytic properties, making them effective for the removal of contaminants from water and soil. Ferrite-based adsorbents and catalysts are employed for the removal of heavy metals, organic pollutants, and industrial effluents, contributing to environmental sustainability and pollution mitigation efforts.
6. **Microwave Devices:** Ferrite materials are extensively used in microwave devices and components for various applications, including radar systems, microwave ovens, and satellite communications. Ferrite-based devices such as phase shifters, circulators, and isolators enable the manipulation and control of microwave signals, facilitating the transmission, reception, and processing of electromagnetic waves in microwave communication and radar systems.

Ferrites play a vital role in diverse applications spanning across electronics, telecommunications, medicine, and environmental science. Their unique properties make them indispensable for data storage, signal processing, power conversion, biomedical imaging, environmental remediation, and microwave communication, among others.

Continued research and innovation in ferrite materials and devices are expected to further expand their applications and contribute to technological advancements in various fields.

III. IMPORTANT PROPERTIES OF FERRITES

Ferrites possess a diverse range of important properties that make them suitable for various applications across different industries. These properties include magnetic, electrical, and structural characteristics, each of which contributes to the performance and functionality of ferrite materials. Below is a detailed explanation of the key properties of ferrites:[13-15]

A. Magnetic Properties:

1. **Saturation Magnetization:** Saturation magnetization refers to the maximum magnetic moment per unit volume that a material can attain when all its magnetic moments are aligned in the same direction. In ferrites, saturation magnetization depends on factors such as composition, crystal structure, and domain configuration. Higher saturation magnetization values indicate greater magnetic strength and are desirable for applications requiring strong magnetic fields, such as in permanent magnets and magnetic recording media.
2. **Coercivity:** Coercivity, also known as magnetic hardness, is the measure of a material's resistance to demagnetization. It represents the strength of an external magnetic field required to reduce the magnetization of the material to zero. Ferrites typically exhibit high coercivity, making them suitable for applications where stable magnetization is essential, such as in permanent magnets and magnetic storage devices.
3. **Magnetic Anisotropy:** Magnetic anisotropy refers to the directional dependence of magnetic properties in a material. In ferrites, magnetic anisotropy arises from factors such as crystal structure, grain orientation, and magnetic domain configuration. Control over magnetic anisotropy allows for the manipulation of magnetic properties, enabling the design of ferrite materials with tailored magnetic characteristics for specific applications.

B. Electrical Properties:

1. **Dielectric Constant:** The dielectric constant, also known as relative permittivity, is a measure of a material's ability to store electrical energy under an applied electric field. Ferrites typically exhibit low dielectric constants, making them suitable for applications requiring low-loss electrical insulation, such as in magnetic cores for transformers and inductors.
2. **Resistivity:** Resistivity refers to the material's opposition to the flow of electrical current. Ferrites typically possess high resistivity, which is desirable for applications requiring electrical insulation and reduced eddy current losses, such as in magnetic cores for high-frequency transformers and inductors.
3. **Conductivity:** The conductivity of ferrites is relatively low compared to metals and semiconductors.Ferrites are electrical insulators, with resistivity values several orders of magnitude higher than metals and semiconductors. This property is advantageous for applications requiring electrical insulation and electromagnetic interference (EMI) shielding.

C. Structural Properties:

1. **Crystallinity:** Crystallinity refers to the degree of order in the atomic arrangement within a material's crystal lattice. Ferrites typically exhibit a crystalline structure, with well-defined crystallographic planes and grain boundaries. Crystallinity influences the material's magnetic and electrical properties, as well as its mechanical strength and stability.
2. **Grain Size:** Grain size refers to the size of individual crystal grains within a polycrystalline material. In ferrites, grain size affects magnetic domain formation, magnetic anisotropy, and magnetic hysteresis

behavior. Control over grain size allows for the optimization of magnetic properties and performance in ferrite materials.

3. **Porosity:** Porosity refers to the presence of void spaces or pores within a material's structure. In ferrites, porosity can affect properties such as density, mechanical strength, and permeability. Control over porosity is essential for tailoring material properties and ensuring uniformity and reliability in ferrite-based devices and components.

Understanding and controlling these important properties of ferrites are crucial for optimizing material performance and designing customized solutions for specific applications. Advances in synthesis techniques, characterization methods, and material engineering continue to expand the capabilities and utility of ferrite materials across diverse industries.

IV.SYNTHESIS METHODS AND ADVANCES

The synthesis of ferrite materials involves the preparation of ceramic compounds consisting primarily of iron oxide (Fe_2O_3 or Fe_3O_4) combined with oxides of other metallic elements, such as cobalt (Co), nickel (Ni), zinc (Zn), or manganese (Mn). Various synthesis methods have been developed to tailor the composition, structure, and properties of ferrite materials for specific applications. Advances in synthesis techniques continue to drive innovation and expand the range of available ferrite compositions and morphologies. Below are detailed explanations of common synthesis methods and recent advances in ferrite synthesis:[8,16-18]

A. Solid-State Reaction:

Solid-state reaction, also known as ceramic or conventional synthesis, involves the high-temperature reaction between precursor oxides or carbonates to form the desired ferrite phase. The precursor powders are mixed, ground, and calcined at elevated temperatures (typically above 1000°C) to promote chemical reactions and phase formation. Solid-state reaction is a widely used method for synthesizing bulk ferrite materials with controlled stoichiometry and phase purity. However, it often requires long processing times and high temperatures, leading to grain growth and phase segregation in some cases.

B. Co-Precipitation:

Co-precipitation involves the simultaneous precipitation of metal cations from solution, followed by their conversion into ferrite nanoparticles through hydrothermal or calcination treatments. Co-precipitation offers advantages such as fine particle size control, narrow size distribution, and compositional homogeneity. It allows for the synthesis of nanoscale ferrite powders with tailored magnetic and structural properties for applications such as magnetic recording media, biomedical imaging, and environmental remediation.

C. Sol-Gel Method:

The sol-gel method involves the hydrolysis and polycondensation of metal alkoxides or metal salts to form a sol, followed by gelation and thermal treatment to obtain the desired ferrite phase. Sol-gel synthesis offers advantages such as precise control over composition, morphology, and particle size distribution. It enables the preparation of homogeneous and porous ferrite materials with enhanced surface area and reactivity for applications such as gas sensing, catalysis, and photocatalysis.

D. Hydrothermal Synthesis:

Hydrothermal synthesis involves the reaction of precursor solutions or suspensions under elevated temperature and pressure conditions within a sealed reactor vessel. Hydrothermal synthesis allows for the preparation of ferrite nanoparticles with controlled size, shape, and crystallinity. It offers advantages such as uniform particle size distribution, high purity, and crystalline phase control. Hydrothermal synthesis is widely used for preparing nanoscale ferrite materials for applications in biomedicine, electronics, and energy storage.

E. Microwave-Assisted Synthesis:

Microwave-assisted synthesis involves the application of microwave radiation to facilitate the synthesis of ferrite materials. Microwave heating offers advantages such as rapid heating, uniform temperature distribution, and energy efficiency. It enables the synthesis of ferrite nanoparticles with enhanced crystallinity, purity, and phase control.

Microwave-assisted synthesis is gaining popularity for its ability to accelerate reaction kinetics and reduce processing times, making it suitable for large-scale production of ferrite materials for industrial applications.

Recent advances in ferrite synthesis techniques focus on enhancing material properties, improving process efficiency, and expanding the range of available compositions and morphologies. These advances include the development of novel precursor materials, optimization of reaction conditions, and integration of advanced characterization techniques to elucidate the structure-property relationships in ferrite materials. Continued research and innovation in ferrite synthesis are expected to further advance the capabilities and applications of these versatile materials across diverse fields.

V. FUTURE DIRECTIONS AND CHALLENGES

As research on ferrite materials continues to advance, several future directions and challenges emerge, shaping the trajectory of the field and guiding the focus of ongoing investigations. Understanding these aspects is crucial for driving innovation, addressing technological needs, and overcoming barriers to further progress. Below are detailed discussions on future directions and challenges in the field of ferrite materials:[10,19-22]

A. Enhanced Material Performance:

Future research efforts will likely focus on enhancing the performance of ferrite materials by tailoring their magnetic, electrical, and structural properties to meet the demands of emerging applications. This includes optimizing magnetic saturation, coercivity, electrical conductivity, and structural stability through advanced synthesis techniques, material engineering, and theoretical modeling. Achieving improved material performance will unlock new opportunities for ferrite-based devices and systems in areas such as telecommunications, power electronics, biomedicine, and environmental remediation.

B. Development of Novel Synthesis Techniques:

Advancements in synthesis techniques will play a crucial role in overcoming existing limitations and expanding the range of available ferrite compositions, morphologies, and functionalities. Future research efforts may focus on developing novel synthesis methods that offer improved efficiency, scalability, and control over material properties. This includes exploring techniques such as sonochemical synthesis, electrospinning, and atomic layer deposition to fabricate ferrite materials with tailored properties and performance characteristics.

C. Integration of Multifunctionalities:

Future directions in ferrite research may involve the integration of multifunctionalities into ferrite materials, enabling them to simultaneously exhibit magnetic, electrical, optical, and catalytic properties. This involves the design and synthesis of composite and hybrid materials, such as ferrite-based nanocomposites, core-shell structures, and heterostructures, with synergistic functionalities for advanced applications. The integration of multifunctionalities will pave the way for the development of next-generation devices and systems with enhanced performance, versatility, and functionality.

D. Exploration of Emerging Applications:

Ferrite materials hold promise for a wide range of emerging applications in areas such as spintronics, magnetics, quantum computing, and energy harvesting. Future research efforts will likely focus on exploring these emerging applications and uncovering the unique properties and phenomena exhibited by ferrite materials at the nanoscale and in extreme conditions. This includes investigating spintronic devices based on ferrite thin films, manganic crystals for information processing, and ferrite-based nanogenerators for energy harvesting.

E. Addressing Environmental and Health Concerns:

As the utilization of ferrite materials expands, there is a growing need to address environmental and health concerns associated with their production, use, and disposal. Future research efforts may focus on developing sustainable synthesis methods, recycling strategies, and biocompatible formulations to minimize the environmental impact and ensure the safe handling and disposal of ferrite materials. This includes investigating the toxicity, biodegradability, and long-term effects of ferrite nanoparticles in biological and environmental systems.

F. Synthesis Complexity:

Achieving precise control over the composition, morphology, and properties of ferrite materials remains a challenge due to the complex interplay of synthesis parameters and reaction kinetics. Scalability: Scaling up the synthesis of ferrite materials to industrial levels while maintaining uniformity, reproducibility, and cost- effectiveness poses significant challenges in terms of equipment, energy consumption, and process optimization.

G. Characterization Techniques:

The characterization of ferrite materials at the nanoscale and under extreme conditions requires advanced analytical techniques and instrumentation, which may be inaccessible or limited in their capabilities.

H. Standardization and Regulation:

The lack of standardized protocols and regulatory frameworks for ferrite materials hinders their widespread adoption and commercialization, particularly in sensitive applications such as biomedicine and environmental remediation.

Addressing these challenges will require collaborative efforts from researchers, industry stakeholders, and regulatory agencies to advance ferrite research, develop innovative solutions, and ensure the responsible use and application of these versatile materials. By overcoming these challenges and pursuing future directions in ferrite research, the field will continue to evolve, driving technological advancements and addressing societal needs in diverse areas of science and technology.[23]

VI.CONCLUSION

The conclusion summarizes the key findings of the review and emphasizes the importance of ferrites in modern technology. It underscores the need for continued research and innovation to unlock the full potential of ferrite materials.

VII. REFERENCES

[1] A. Chikazumi, Sōshin. "Physics of ferrites." Clarendon Press, 1997.

[2] Rajaram, R., and S. J. Mulik. "Ferrites: A review of materials and applications." In AIP Conference Proceedings, vol. 2137, n o. 1, p. 020013. AIP Publishing LLC, 2019.

[3] Hernando, Antonio, Miriam C. Fernández-García, and Luis M. Lezama. "Nanocrystalline soft magnetic ferrites: A review on the synthesis, structural features and permeability properties." Journal of Physics D: Applied Physics 41, no. 10 (2008): 103001.

[4] Lu, An-Hui, Qing-Yun Wu, Xiao-Quan Lu, and Xiao-Liang Wang. "Magnetic properties of ferrite nanoparticles synthesized by sol-gel auto- combustion method." Journal of Magnetism and Magnetic Materials 312, no. 2 (2007): 443-447.

[5] Cullity, B. D., and C. D. Graham. "Introduction to magnetic materials." John Wiley & Sons, 2011.

[6] Cornell, R. M., and U. Schwertmann. "The iron oxides: structure, properties, reactions, occurrences and uses." John Wiley & Sons, 2003.

[7] Pal, Prabir, Sudip Kumar Batabyal, and Dipankar Das. "Recent developments in soft ferrite materials for high -frequency applications: A review." Journal of Materials Science: Materials in Electronics 31, no. 11 (2020): 9002-9025.

[8] Huang, Jing-Yi, Yun-Ling Zou, Qing-Lan Wu, Zhao-Hui Meng, Xiang Wang, and Shuang-Qing Sun. "Hydrothermal synthesis and applications of ferrite-based materials." Chemical Engineering Journal 382 (2020): 122924.

[9] Valenzuela, Raúl. "Magnetism in the solid state: An introduction." Springer Science & Business Media, 2005.

[10] Goya, Gerardo F., Hilton Chaves, and Priscyla D. Rodrigues. "Magnetic nanoparticles for cancer therapy." Journal of Applied P hysics 106, no. 7 (2009): 07B317.

[11] Hergt, R., et al. (2006). Physical limits of hyperthermia using magnetite fine particles. IEEE Transactions on Magnetics, 42(10), 3817-3822.

[12] Lu, A. H., & Salabas, E. L. (2007). Magnetic nanoparticles: synthesis, protection, functionalization, and application. Angewa ndte Chemie International Edition, 46(8), 1222-1244.

[13] Yoo, D., et al. (2011). Folic acid-conjugated magnetic nanoparticles for efficient targeting and uptake by cancer cells. Journal of Biomedical Materials Research Part A, 96(1), 160-170.

[14] Thakor, A. S., & Gambhir, S. S. (2013). Nanooncology: the future of cancer diagnosis and therapy. CA: A Cancer Journal for Cl inicians, 63(6), 395-418.

[15] Laurent, S., et al. (2011). Magnetic iron oxide nanoparticles: synthesis, stabilization, vectorization, physicochemical chara cterizations, and biological applications. Chemical Reviews, 111(4), 2494-2532.

[16] Bae, K. H., et al. (2011). Nanotechnology for treatment of glioblastoma multiforme. Journal of Controlled Release, 163(2), 200-210.
[17] Ito, A., et al. (2004). Heat-inducible TNF-α gene therapy combined with hyperthermia using magnetic nanoparticles as a novel tumor-targeted therapy. Cancer Gene Therapy, 11(3), 236-242.
[18] Jokerst, J. V., et al. (2011). Nanoparticle PEGylation for imaging and therapy. Nanomedicine, 6(4), 715-728.
[19] Bulte, J. W. M., & Kraitchman, D. L. (2004). Iron oxide MR contrast agents for molecular and cellular imaging. NMR in Biomedi cine, 17(7), 484-499.
[20] Yigit, M. V., et al. (2011). Theranostic nanoparticles for targeted cancer therapy. Current Opinion in Chemical Biology, 15(5), 775-781.
[21] Tong, S., et al. (2010). Coating optimization of superparamagnetic iron oxide nanoparticles for high T2 relaxivity. Nano Letters, 10(11), 4607-4613. [22] Kievit, F. M., & Zhang, M. (2011). Surface engineering of iron oxide nanoparticles for targeted cancer therapy. Accounts of C hemical Research,44(10), 853-862.
[22] Akbarzadeh, A., et al. (2012). Nanotoxicology and nanoparticle safety in biomedical designs. International Journal of Nanomed icine, 7, 835-849.

ICRTMS-2024
International e-Conference on Recent Trends in Material Science
In Association with International Journal of Scientific Research in Science and Technology
Volume 11 | Issue 9 | Print ISSN: 2395-6011 | Online ISSN: 2395-602X (www.ijsrst.com)

Determination of Acoustic Parameters by Ultrasonic Interferometer

A. S. Mule*[1], S. M. Delmade[2], P. G. Gawali[3]
*[1]Research scholar, P.G. Dept. of Physics, B.S. College, Basmath, Maharashtra, India
[2]Assistant Professor, Dept. of Physics, Yeshwant Mahavidyalaya, Nanded, Maharashtra, India
[3]Professor, P.G. Dept. of Physics, B.S. College, Basmath, Maharashtra, India

ABSTRACT

Experimental technique for the measurement of wavelength, ultrasonic velocity of liquids with working principle of ultrasonic interferometer have been discussed. The acoustic and physical parameters are calculated by using the velocity, density and viscosity with low frequency range. The experimental values can be verified by using the various theoretical relations with excess parameters. These parameters are used to explain the molecular interactions. The ultrasonic interferometer used is easy to handle and high degree of accuracy.

Keywords: Ultrasonic Interferometer, Acoustic Parameters, Ultrasonic Velocity.

I. INTRODUCTION

The ultrasonic Interferometer is used to determine the acoustic parameters. The binary mixture of polar liquid with non-polar liquid has been used to study the physical, acoustic parameters gives the inter and intra molecular interactions, Structural and physiochemical behaviour.

The reasons to study the parameters –

- Combination of polar non polar mixture gives the new type of phase equilibrium.
- It provides the physical forces acting between the molecules.
- It helps in obtaining the depth knowledge about molecular interactions.
- during the last two decades it has much importance in accessing the molecular interactions and investigating the physio-chemical behaviour of such system [1,2].
- Ultrasonic investigation of liquid mixtures find applications in several industrial and technological processes [3-5].
- The measurement of ultrasonic velocity and related parameters derived used in understanding the nature
- of intermolecular interactions in liquid mixtures [6,7].

II. METHODS AND MATERIAL

An ultrasonic interferometer is a simple and direct device to determine the ultrasonic velocity in liquids with a high degree of accuracy.

The principle is used in the measurement of velocity (V) is based on the accurate determination of the wavelength (λ) in the medium. Ultrasonic waves of known frequency (f) are produced by quartz crystal fixed at the bottom of the cell.

These waves are reflected by movable metallic plate kept parallel to the quartz crystal. If separation between these two plates is exactly a whole multiple of the sound wavelength, standing waves are formed in the medium. The acoustic resonance gives rise to an electrical reaction on the generator driving the quartz crystal and the anode current of the generator becomes maximum.

If the distance is now increased or decreased and the variation is exactly one half wave length (λ/2) or multiple of it, anode current becomes maximum.

Then, velocity is obtained

Ultrasonic velocity (V) = Frequency(f) × wavelength(λ)

Description

Ultrasonic interferometer model: F-81D

Dual frequency 2 and 5 MHz facility for temperature variation. Mittal enterprises an iso 9001:2015 co.

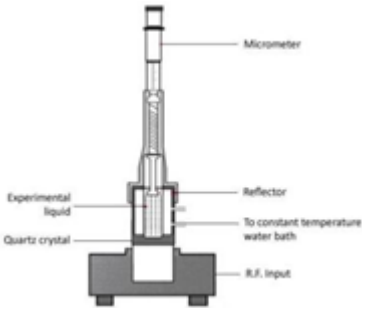

Constant Temperature Waterbath

The Acoustical Parameters such as Adiabatic Compressibility (βad), Intermolecular Free Length (Lf), Acoustic Impedance (Z) and Relative Association (RA) can be calculated by using following relations [8].

The Acoustical Parameters such as Adiabatic Compressibility (βad), Intermolecular Free Length (L_f), Acoustic Impedance (Z) and Relative Association (RA) can be calculated by using following relations [8].

$$\beta_{ad} = \frac{1}{\rho V^2} \qquad \text{------(1)}$$

ρ and V are the density and ultrasonic velocity

$$L_f = K(\beta_{ad})^{1/2} \qquad \text{------(2)}$$

K is the temperature dependant constant K = 300 X 10^{-8} at 303.16

$$Z = V\rho \qquad \text{------(3)}$$

$$R_A = \frac{\rho_s}{\rho_0}\left(\frac{V_0}{V_s}\right)^{1/2} \qquad \text{------(4)}$$

ρ_0 and ρ_s are the densities of solvent and solute.

V_0 and V_s are the ultrasonic velocities of solvent and solute.

The excess values of adiabatic compressibility (β^E)and Acoustic impedance (Z^E)are

$$\beta^E = \beta_n - (X_A\beta_A + X_B\beta_B) \qquad \text{------(5)}$$

$$Z^E = Z_n - (X_A Z_A + X_B Z_B) \qquad \text{------(6)}$$

X_A and X_B are the mol fraction of respective liquids.
Z_A, Z_B and Z_n are the acoustic impedance of respective liquids and mixtures respectively .
β_A, β_B and β_n are the adiabatic compressibility of respective liquids and mixtures respectively.

III. RESULTS AND DISCUSSION

Viscosity is an important transport property for process design in petroleum, petrochemical, chemical and other chemical industries involving fluid transportation. Mixing agitation heat exchange and concentration.

There are theoretical methods for the estimation of characteristic parameters of fluid mixtures Nomoto's relation, Jacobson's free length theory (FLT), Schaffs's collision factor theory (CFT), Vandael's ideal mixing relation, Junjie's relation, Flory theory etc.
The various physical parameters are to be determined [9].

Free Volume (V_F): It explains the variations in the physiochemical properties of liquids and liquid mixtures. The molecules of liquid are not quite closely packed and there are some free spaces between the molecules of movement and volume is called free volume.
According to Eyring and Kincaid free volume has effective volume in which particular molecule of liquid can move and over perfect gas[10].
Volume change (dV), Available volume, Relaxation time (τ), Internal pressure (Π_i), Absorption coefficient $\left(\frac{\alpha}{f^2}\right)$, Wada's constant (B) or molar compressibility, Rao's constant or molar sound velocity (R), Gibb's free energy (ΔG), Optical refractive index (η), Soluation number (Sn), Mean square thermodynamic fluctuations and excess parameters are calculated by using the relations[11].

IV. CONCLUSION

The acoustic and physical parameters are determined by measuring the value of density (��), viscosity(��) and ultrasonic velocity (V). These measured values are estimated by using theoretical relations.
The scientific investigations in the field of ultrasonic velocity measurement are to be done by ultrasonic interferometer.
The acoustic parameters and their excess values are highly affected in low frequency range 2MHz and 5 MHz, so frequency plays a vital role in mixture of polar and non-polar liquids.

V. REFERENCES

[1] J. D. Pandey and A K Shukla, Journal pure Appl. Ultrasonic, 15-537 (1993).
[2] Riyazudeen and Nurul Islam, Journal pure Appl. Ultrasonic, 19-16 (1997).
[3] S. L. Oswal , P Oswal and R. P. Phalak, Journal sol. Chem., 27.507 (1998).
[4] J Rajasekhar and P. R. Naidu, Journal chem. Engg. Data 41373 (1996).
[5] G Arul and L Palaniappan, Indian journal of Appl. Physics, 39-561 (2001).
[6] A Pal, H Kumar, B. R. Arbad and A. B. Tekale, Indian J. Pure Appl. Phys. 41-113 (2003).
[7] T Ramanjappa etal, Indian J. Pure Appl. Phys. 38-301 (2000).
[8] G Nath etal, Indian J. Phys. 83(4) 429-436 (2009).

[9] Indu Saxena etal, International journal of applied research 2015; 1(9): 562-569.
[10] Reddy Reveendranatha k etal, journal of Accoustical Society of India, 1991 : 19(4) 22-25.
[11] Maurya V. N. etal, Word of Sciences J.2013;02:27-48.

ICRTMS-2024
International e-Conference on Recent Trends in Material Science
In Association with International Journal of Scientific Research in Science and Technology
Volume 11 | Issue 9 | Print ISSN: 2395-6011 | Online ISSN: 2395-602X (www.ijsrst.com)

Optical Study of Metal Co-doping in L-Asparagine Monohydrate Single Crystal for Optoelectronic Applications

V. R. Sagane[1], Yuoraj Tamgadge[2], Gajanan G. Muley[1], P. M. Wankhade*[3]

[1]Department of Physics, Sant Gadge Baba Amravati University, Amravati, Maharashtra, India

[2]Department of Physics, Shri Shivaji Arts, Commerce and Science College, Motala, Buldhana, Maharashtra, India

*[3]Department of Physics, Late R. B. Art's, Commerce & Smt. S. R. Bharti Science College Arni, Yavatmal, Maharashtra, India

ABSTRACT

Crystals of pure and transition metals Co and Ni co-doped L-asparagine monohydrate (LAM) were grown by solution growth method from aqueous solution at constant temperature. Effect of dopants on optical and structural properties has been studied. A slight variation in unit cell parameters has been observed for doped crystal as compare to pure crystal. UV-visible spectroscopic study confirms the increase in transmission percentage in the spectral range 200-800 nm of doped crystal. The energy band gap of pure and doped crystals was determined using Tauc's formula and found to be 5.05 and 4.95 eV for pure and doped crystals, respectively. The lower cut off wavelengths of pure and doped crystals was found to be 227 and 229 nm, respectively. The presence of the dopants in the doped crystals was qualitatively confirmed by FT-IR spectroscopy and quantitatively by an EDAX analysis.

Keywords: Crystal growth, powder x-ray diffraction, energy dispersive x-ray spectroscopy, UV-visible

Spectroscopy

I. INTRODUCTION

Organic materials have earned significant attention due to their interesting approach towards NLO phenomenon. They show enormous fast and large nonlinear optical susceptibilities and high optical thresholds. A conjugated π- electron is responsible for the strong nonlinear optical (NLO) activities in organic crystals [1]. Amino acid is established an organic material exhibiting strong NLO activities. It contains proton donor carboxylic (COOH) group and proton acceptor amino acid (NH2) group [1-3]. L-asparagine monohydrate (LAM) is one of the amino acid that crystallizes in an orthorhombic crystal structure with non-centrosymmetric space group P212121. A sophisticated network of hydrogen bonds connecting the L-asparagine with water molecule is visible in the LAM crystal structure [4]. Khan et al. [5] had written a detail review on the growth and physico-chemical properties of LAM crystal and few L-aspragine derivative compound crystals were also

included in the review in order to evaluate structural and atomic bonding arrangement. LAM show high band gap value (5.15eV) and lower cutoff wavelength in ultraviolet region (234nm). A material with large band gap hinders its full potential to use as an advanced material for optoelectronics application. Mohammad et al. used bimetallic dopants to reduced the band gap of ZnO nanoradods [6]. Patel et al. [7] reported bimetallic (Co2+ -Ni2+) dopant improved the mechanical properties of ammonium dihydrogen phosphate crystal. In the present communication, we study an effect of a bimetallic (Co2+ -Ni2+) co-doping on the structural and optical properties of LAM crystal. The slow solvent evaporation solution growth approach has been used to grow pure and 1.5 mol% Co2+ -Ni2+ doped LAM (Co- NiLAM) crystals.

II. METHODS AND MATERIAL

2.1. MATERIAL SYNTHESIS AND CRYSTAL GROWTH

L-asparagine monohydrate (SD Fine AR grade) was taken and used as it is. It is dissolved in double distilled water and stirred continuously using magnetic stirrer for 2 hours at room temperature to obtain the homogeneous solution of LAM. In order to obtain the crystal of Co2+-Ni2+doped LAM crystal, cobalt chloride (CoCl2) and nickel chloride (NiCl2), 1.5 mol % each were added to the homogeneous solution of LAM and allow to stirred continuously at 400C for more than four hours. The obtained pure and doped LAM solutions were filtered with the micro filter paper using the vacuum pump and the filtrate collected in the rinsed beaker. The beaker was placed in a constant temperature water bath for growth of single crystal by self-nucleation process at 35oC. Good sized crystals of pure and doped LAM were obtained after the period of 15 days. The photograph of pure and doped LAM grown crystals are as shown in Fig.1 (a) and (b) respectively.

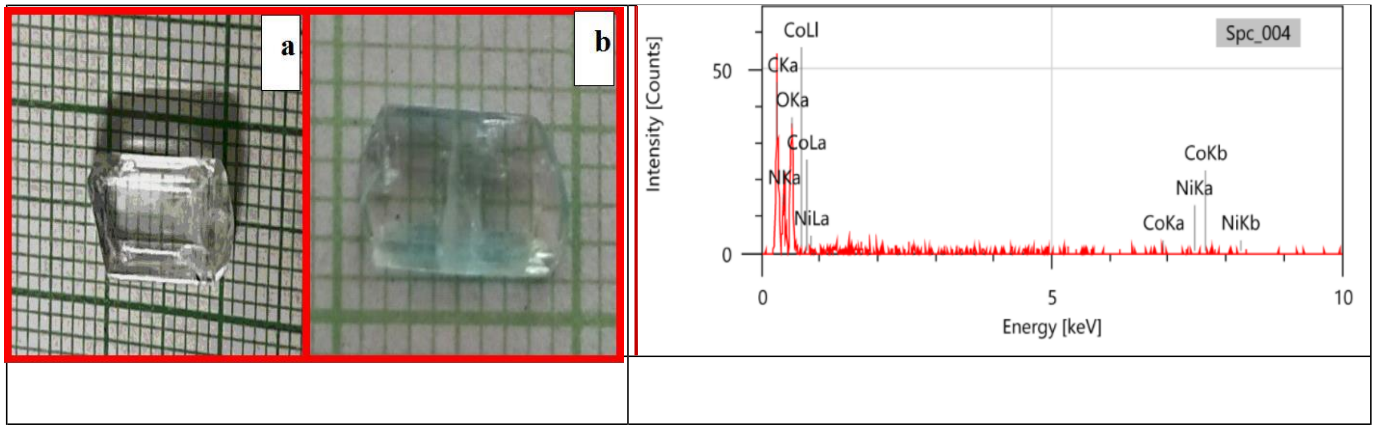

Figure 1: Photograph of pure and Co-NiLAM crystals Figure 4. EDAX spectra of Pure and Co-NiLAM grown crystals

2.2. CHARACTERIZATION

The obtained grown crystals were subjected to structural, functional and optical study. Powder x-ray diffraction (P-XRD) data of pure and doped LAM crystals were recorded on Rigaku Miniflex 600 diffractometer within the 2θ range of 10-80o with scanning rate 0.02o/sec using CuKα radiation of wavelength 1.5406Å. The powder X-software was used to analyze the recorded P-Xrd data [8]. UV- Visible transmission spectrum was recorded using the Shimadzu UV-1601 spectrophotometer within wavelength range of 200-800

nm. Fourier transformation infrared spectrum (FT-IR) of pure and doped LAM was recorded on Diamond ATR spectrophotometer in the frequency region ranging 4000-500 cm-1. An EDAX spectrum was recorded on instrument JEOL JSM IT 200.

III.RESULTS AND DISCUSSION

3.1. P-XRD Analysis

The P-XRD diffraction pattern of pure and doped LAM crystals are as shown in Fig.2.There are good number of sharp, narrow, and high intensity peaks at specific 2θ values observed in the P-XRD pattern. The sharp, narrow and high intensity peaks indicates the high degree of crystallinity of the grown crystals. The high degree of crystallanity indicates crystal should be more transparent in the entire region of UV-Vis region. The observed lattice parameter values of pure LAM are found to be in good agreement with the previously reported values [4]. The calculated lattice parameters for doped crystal are a=5.580Å, b=9.804Å, c=11.770 Å, V= 644.021 Å3 and α = β = γ=900.The pure and doped LAM crystals belong to orthorhombic crystal system with non-centro- symmetric space group P212121 .The slight change in lattice parameter and presence of some additional peaks of Co-Ni dopants into pure crystals confirms the incorporation of dopants into the LAM lattice.

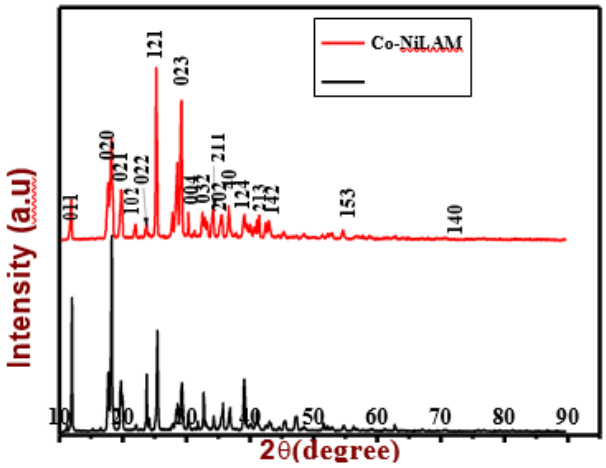

Figure 2.P-XRD of Pure and Co-NiLAM grown crystals

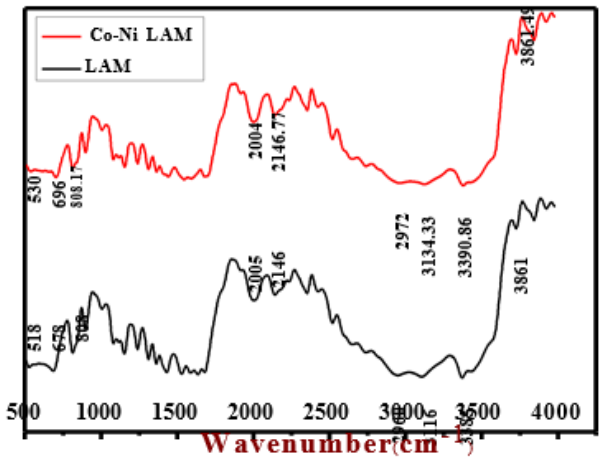

Figure 3.FT-IR spectra of Pure and Co-NiLAM grown crystals

3.2. FT-IR Analysis

FT-IR spectrum of pure and Co-NiLAM crystals are shown in Fig. 3. The peaks corresponding to all functional groups of LAM are present in FT-IR spectra. The peak at wavenumber 518.85 and 530.42cm-1 assign the torsional oscillation of NH3 group. The COO– bending mode at 678.94 and 696.3 have been identified and assigned for pure and doped LAM crystals, respectively. The peak value at 1361.74 and 1363.67cm-1 shows C–H deformation vibration peak. Asymmetrical NH3+ bending vibration modes for pure and doped crystal have been assign by wavenumber 2005.97 and 2004.04.The vibration band of asymmetric NH3+ group are observed and assigned. C–H stretching and N-H vibration band are observed at peak 2972.31 and 3134.33 successively for doped crystal. The presence of corboxylic and amino group functional in pure and doped crystals with slight modification in the peak position in the doped LAM crystals, qualitatively confirms the inclusion of dopants.

3.3. EDAX Analysis

The EDAX spectra of doped LAM crystal was recorded as shown in Fig. 4 and analyzed. It shows the presence of carbon, nitrogen, oxygen, cobalt and nickel. EDAX spectra confirm the presence of dopant in the Co-NiLAM crystal.

3.4. Linear Optical Analysis

The UV-visible transmission spectrum of pure and Co-Ni LAM grown crystals are as shown in Fig. 5. From UV- visible study, the transmission percentage of doped crystal (84%) is found to be more than pure LAM crystal (78%).The good transmission in entire visible region indicates crystal with lesser defects [9]. The lower cutoff wavelength for pure and doped LAM was evaluated to be 227 and 229nm, respectively. The band gap energy of grown crystals was computed using Tauc's relation [4]. The energy band gap of pure and Co-NiLAM grown crystals is as shown in Fig.6.The calculated band gap energy for pure and doped LAM crystal were found to be 5.05 and 4.95eV, respectively. The decrease in band gap value is attributed to the presence of bimetallic dopants in the host crystal. The red shift in band gap energy is mainly due to the dominant role of nickel ion [6].

The localized defect states in the optical band gap region are indicated by a parameter known Urbach energy (EU). The graph is plotted in between lnα and photon energy (hν)[10]. From the graph, the value of Urbach energy (EU) was calculated from the reciprocal of slope and it is found to be 0.44eV for doped crystal. The low value of Urbach energy indicates crystal with lesser defects. The high transmission over wide range, lower cutoff wavelength in UV region and with decrease in band gap value is the most desirable parameter for designing optoelectronics devices [4,9].

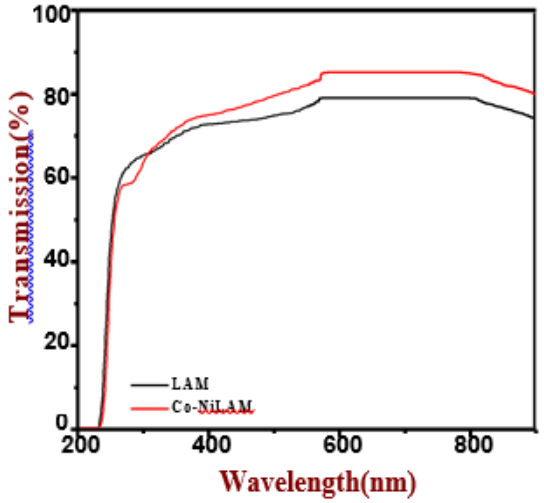

Figure 5. UV-visible transmission spectra of pure and Co-NiLAM crystals

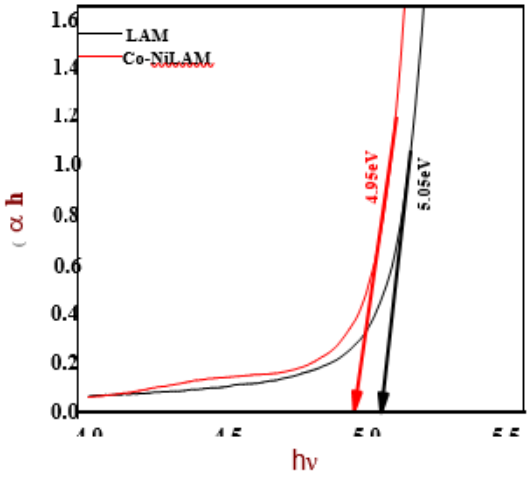

Figure 6. Tauc's plots of pure and Co-NiLAM crystals

Urbach suggested another relation for correlating both absorption coefficient (α) and the optical band gap energy

[σ(hν–E 0)]

using the equation, α = βexp

KBT

[11],where β is a per-exponential constant and σ is steepness parameter. E0

is the transition energy, which is equal to Eg for direct allowed transition. The grown crystal has direct band gap.

T KB

Therefore, E0=Eg. Taking log on both sides, after solving, it can be rewritten as σ =[11], where KB is EU Boltzmann constant and T is absolute temperature.The calculated value of σ is 0.053. The value of steepness parameter is used for relating the strength of electron-phonon interaction (Ee-p). The electron-phonon interaction energy is calculated by using the formula Ee-p=2/3σ. It was found to be 12.46. The present work proves a lower steepness value with a higher energy value for electron-phonon interactions.

IV. CONCLUSION

Appreciable sized single crystals of undoped and Co-Ni co-doped LAM were successfully grown by slow evaporation technique of solution growth method. The small variation in lattice parameters and change in position of vibrational modes in P-XRD and FT-IR spectrum of doped LAM crystal confirms, qualitatively, the doping of Co and Ni metals. EDAX analysis confirms the presence of dopant into the crystal. The doped crystal is transparent in the entire visible region. The increase in transmission in doped crystal has been witnessed as compare to pure LAM. The calculated band gap energy for pure and doped LAM crystal was found to be 5.05 and 4.95eV respectively. Steepness parameterand electron-phonon interaction were calculated to be 0.053 and 12.46 respectively. A remarkable improvement in transmission, decrease in band gap and lower cutoff wavelength suggest its suitability in optoelectronic applications.

One of the requirements of the graduate Science, Engineering and Technology courses is that you conduct research and write a research paper on some aspects of software engineering. The paper may present original work, discuss a new technique, provide a survey and evaluation of recent work in a given area, or give comprehensive and taxonomic tutorial information. The paper must emphasize concepts and the underlying principles and should provide authentic contribution to knowledge. If your paper does not represent original work, it should have educational value by presenting a fresh perspective or a synthesis of existing knowledge. The purpose of this

V. REFERENCES

[1] A. A.Parvathi priya and V.Srinivasan2017. International Journal of Chem Tech Research. (2017), ISSN:0974 -4290.https://sphinxsai.com/2017/ch_vol10_no7/1/(12-17)V10N7CT.pdf.

[2] B.A.Fuchs,K.Chaisyn,P.StephanVelsko.1989.AppliedOptics.(Oct1989),ISSNNO:1559-128X https://doi.org/10.1364/ao.28.004465. [3] M. Prakash a, M. Lydia Caroline b, D. Geetha cSpectrochimica Acta Part A: Molecular and BiomolecularSpectroscopy2013(May2013),ISSNNO:1386-425,https://doi.org/10.1016/j.saa.2013.01.078

[3] M. Prakash, M. Lydia Carolin, D. Geetha. Spectrochimica Acta Part A: Molecular and Biomolecular Spectroscopy.2013.(May2013),ISSNNO:1386-1425,https://doi.org/10.1016/j.saa.2013.01.078

[4] F.Yogam,I.Vetha Potheher, R. Jeyasekaran, M. Vimalan, M.Antony Arockiaraj, P.Sagayaraj.2013. Journal of Thermal Analysis and Calorimetry (Dec2013), ISSN.NO:1388-6150.http://dx.doi.org/10.1007/s10973-013-3138-8

[5] N.Khan,N.Vijayan,R. Kumar,N.Gupta.2023.Journal of Nonlinear Optical Physics & material.(2023),ISSN.NO: 0218-8635.https://doi.org/10.1142/S0218863523300013.

[6] M.S.Nadeem,T.Munawar,F.Mukhtar,MN.urRahman,M.Riaz,A.Hussain,F.Iqbal.2021.OpticalMaterial.(Jan2021),ISSNNO:0925-346710606.https://doi.org/10.1016/j.optmat.2020.110606.

[7] H.K.Patel,K.G.Raval,P.HTrivedi.2023.AIPConferenceProceeding.(Dec2023).040042.https://ui.adsabs.harvard.edu/link_gateway/2023AIPC.2901d0042P/doi:10.1063/5.0178956.

[8] C.Dong.1999.Journal of Applied Crystallography. (Feb1999),ISSN.NO:1600-5767.https://doi.org/10.1107/S0021889899003039.

[9] V.G. Pahurkar, Mohd Anis, M.I. Baig, S.P. Ramteke, B. Babu, G.G. Muley.2017.optik. (Aug2017),ISSN.NO: 0030-4026 421-425.https://doi.org/10.1016/j.ijleo.2017.06.023.

[10] Urbach.F.1953.physical Review.(Dec1953),ISSN NO: 2469-9926 http://dx.doi.org/10.1103/PhysRev.92.1324.

[11] N. Mahalakshmi and M Parthasarathy.2023. European Chemical Bulletin.(August2023), ISSN NO: 206-5346.http://dx.doi.org/10.48047/ecb/2023.12.si4.1271.

ICRTMS-2024
International e-Conference on Recent Trends in Material Science
In Association with International Journal of Scientific Research in Science and Technology
Volume 11 | Issue 9 | Print ISSN: 2395-6011 | Online ISSN: 2395-602X (www.ijsrst.com)

Preparation and Characterization of Barium Strontium Titanate (BST)

Sunil G. Ganjagude*[1] Bhagwan K. Bongane[2], Prashant G. Gawali[3]

*[1]Research Scholar & Junior Lecturer G.P. Junior College Chikhali Tq. Kandhar Dist. Nanded, Maharashtra, India

[2]Assistant Professor, P.G. Department of Physics B. S. College, Basmath Dist. Hingoli, Maharashtra, India

3Professor P.G. Department of Physics, B.S. College, Basmath, Maharashtra, India

ABSTRACT

BST powders were prepared by solid state reaction method and characterized by method of x-ray diffraction analysis, SEM, EDAX and dielectrics. The obtained powders were submicronic, consisting of spherical; polycrystalline particles surface morphology of samples has been studied using SEM. The dielectric measurements have been studied at different frequencies by using impedance analyzer. As Sr content increases then dielectric constant (ε′) increases because ferroelectric regions are surrounded by non-ferroelectric regions. It is found at higher values of frequencies, dielectric losses (ε″) are reduced and dipoles contribute to the polarization. The conductivity (σ) increases as frequency increases due to large mobility of carriers as a strong hopping mechanism of ions.

Keywords: solid state reaction, BST, X-ray diffraction, SEM

I. INTRODUCTION

- Barium Strontium Titanate (BST) is a solid solution ferroelectric material exhibiting a large dielectric constant and changes with a frequency [1].
- This dielectric constant is suitable for many applications such as bypass capacitors, IR detectors, dynamic random-access memories (DRAMs) and tuneable microwave devices such as voltage-controlled oscillators, tuneable filters, and phase shifters [2-4].
- Its usefulness is interesting at microwave frequencies. The dielectric constant or losses has been reduced by using various types of ferroelectric composite materials [5].
- It is perovskite-based ferroelectric and one of the most studied ferroelectric materials [6].

II. REVIEW AND GAP:

- The ferroelectric history described in the excellent review by Busch. Many distinguished scientists studied the early development named Brewster, J & P Curie, Boltzmann, Pockets and Debye etc. Ferro electricity is firstly coined by Schrodinger. It is polar dielectric in which polarization can be switched between two or more states by the application of electric field [7-8].
- The microwave applications of ferroelectric materials have bread technologies like radar; communication etc. has a strong demand in tuneable resonators and filters in the GHz regions. The development of electric components is one of the factors that support exists as modern technology. The ferroelectric material has a perovskite structure. One of the ferroelectric materials often used is Barium Titanate (BT). BT has high dielectric constant, therefore its often used as capacitor [9].
- Many researches had been done in improving the electrical properties as well as morphology of BT. One of the ways often used i.e. gives doping. The strontium (Sr) is one of the doping that often used because it has an atomic radius similar to atomic radius of Ba. Thus, Sr is effective to increase the dielectric constant of BT. The BST has high dielectric constant, chemically stability and low dielectric loss [10].

III.METHODS AND MATERIAL

The 50gm BST sample was prepared with various compositions as Ba0.3Sr0.7TiO3, Ba0.5Sr0.5TiO3, Ba0.6 Sr0.4 TiO3, and Ba0.7Sr0.3TiO3.

The composite materials are sintered at 10000C and at 11000C for five and three hours. Then four samples are mixed with polyvinyl alcohol as a binder.

Then it is pressed by using hydraulic pressure of 8 tonne to form the pallets. These palletised samples are finally heated at 5000C for 3 hours.

[a] XRD Measurement:

The samples were characterized by XRD measurements by using Bruker D8 advance X-ray diffractometer. X-rays were produced using a sealed tube and wavelength of X-ray was 0.154nm (cu. k-alpha). The x-rays were detected using a fast-counting detector based on silicon strip technology (Bruker Lynx Eye detector). XRD pattern of BST is shown in Fig. 1. The sharpness of BST diffraction peaks suggests better homogeneity and crystallization of samples. X-ray analysis shows that the BST has single phase with tetragonal structure. All reflection peaks were observed interplanar spacing ‘d’ and lattice parameters with the JCPDS data of BST (Ba0.5Sr0.5TiO3 JCPDS

#391395, Ba0.6Sr0.4TiO3 JCPDS #340411, Ba0.7Sr0.3TiO3 JCPDS #440093) were determined using a least squares refinement method. A good agreement between calculated and observed of values of all diffraction lines of BST suggest that there is no change in basic crystal structure of prepared sample which is perovskite ferroelectric material.

[b] DIELECTRIC MEASUREMENT:

The dielectric constant (ε'), dielectric loss (ε″), quality factor (Q = 1/tan δ), and conductivity (σ) of the sample were measured in the frequency range 50Hz to 5MHz by LCR meter (HP model hioki3572) These are calculated by using formulae [11].

[c] EDAX:

The energy dispersive analysis x-ray is a analytical technique used for elemental analysis of sample. The difference in energy between the higher energy shell and the lower energy shell may be released in the form of x-rays. The
number and energy of x-rays emitted from a specimen can be measured by an energy dispersive spectrometer. The atomic structure of emitting element and composition is to be majored. The element analysis with weight % and
atomic % has reported with images as in Table 1 & Fig. (2) EDAX is used to provide elemental identification and quantitative compositional information. The EDAX analysis consists of spectra with peaks of O, Ti, Sr, Ba of different elements present in the sample.

[d] SEM:

A scanning electron microscope produces the images of sample by scanning the surface. It gives the surface topography and composition of the sample. The surface was examined by SEM Fig.3 a, b, c, d shows the images of four samples. The particles of BST are not specific shape with diagram 2μm. it can be seen that prolongs sintering time is also effective to change the particle size and improve the microstructure homogeneity [12]

IV. RESULTS AND DISCUSSION

Element	Weight%	Atomic%
O K	32.99	71.93
Ti K	20.90	15.22
Sr L	7.90	3.15
Ba L	38.21	9.71
Totals	100.00	100.00

(a) $Ba_{0.3}Sr_{0.7}Ti_1O_3$

Element	Weight%	Atomic%
O K	34.34	72.74
Ti K	20.39	14.43
Sr L	11.84	4.58
Ba L	33.43	8.25
Totals	100.00	100.00

(b) $Ba_{0.5}Sr_{0.5}TiO_3$

Element	Weight%	Atomic%
O K	32.99	71.93
Ti K	20.90	15.22
Sr L	7.90	3.15
Ba L	38.21	9.71
Totals	100.00	100.00

(c) $Ba_{0.6}Sr_{0.4}Ti_1O_3$

Element	Weight%	Atomic%
O K	34.34	72.74
Ti K	20.39	14.43
Sr L	11.84	4.58
Ba L	33.43	8.25
Totals	100.00	100.00

(d) $Ba_{0.7}Sr_{0.3}Ti_1O_3$

Table 1 shows the elements with weight and atomic percentage of samples

Table 2: Shows calculated values of ε', ε'', Q and σ of various composites of $BaSrTiO_3$ vs frequencies

		$Ba_{0.3}Sr_{0.7}TiO_3$				$Ba_{0.5}Sr_{0.5}TiO_3$				$Ba_{0.6}Sr_{0.4}TiO_3$				$Ba_{0.7}Sr_{0.3}TiO_3$			
f	Log f	ε'	ε''	Q	σ	ε'	ε''	Q	σ	ε'	ε''	Q	σ	ε'	ε''	Q	σ
50	1.7	934.4	1405.2	0.78	3.9	-203.3	-262.2	0.77	-7.3	501.8	874.2	0.57	2.4	-177.4	631.5	-0.28	1.8
	2.0	382.1	231.5	3.26	1.3	292.4	128.4	0.02	7.1	194.2	103.9	-0.39	5.8	245.1	121.3	0.05	6.7
	2.3	271.0	109.1	2.29	1.2	246.6	83.0	3.21	9.2	193.1	63.0	3.01	7.0	226.4	8.9	2.91	9.4
	2.6	243.3	85.5	3.45	1.7	226.4	59.3	3.21	1.2	173.4	54.3	2.95	1.1	192.1	61.3	3.18	1.2
1000	3.0	195.2	56.2	3.47	3.1	197.0	51.7	3.81	2.9	136.9	42.1	3.25	2.3	162.8	47.7	3.45	2.6
	3.2	183.3	51.1	3.82	4.5	184.4	45.9	4.05	4.0	126.0	36.0	3.64	3.2	156.3	4.8	3.88	3.7
	3.4	172.3	45.4	3.92	6.3	172.0	42.2	4.07	5.9	117.9	32.6	3.70	4.6	146.0	37.5	3.93	5.2
	3.6	161.4	41.4	4.03	8.7	162.0	40.1	4.09	1.5	109.8	30.0	3.76	6.4	137.7	35.0	4.00	7.4
	3.6	154.9	38.9	4.03	1.1	155.4	38.1	4.11	1.1	104.9	28.4	3.75	7.9	131.8	33.1	4.02	9.3
1K	4.0	139.6	34.5	4.04	1.9	139.7	34.1	4.08	1.9	93.9	25.0	3.73	1.4	118.6	29.7	3.99	1.7
	4.5	177.1	28.4	4.12	5.0	117.4	28.4	4.07	5.0	77.5	20.5	3.78	3.6	99.2	24.5	4.07	4.3
	4.8	105.5	25.3	4.19	8.9	105.7	24.8	4.23	8.7	68.9	18.1	3.81	6.3	89.1	21.7	4.06	7.6
	5.0	98.4	22.9	4.17	0.0	99.1	24.5	4.26	0.0	63.9	16.4	3.90	9.1	83.0	19.7	4.10	0.0
10K	5.4	86.6	18.8	4.3	0.0	87.7	18.0	4.41	0.0	55.4	13.1	4.43	0.0	73.0	15.9	4.20	0.0
	5.5	84.2	17.8	4.84	0.0	85.3	17.0	5.14	0.0	83.7	12.4	4.63	0.0	70.9	15.1	4.82	0.0
	5.9	76.0	15.1	5.01	0.0	77.2	14.4	5.34	0.0	48.0	10.2	4.70	0.0	64.1	12.7	5.01	0.0
1M	6.0	74.3	14.8	5.01	0.0	76.1	14.2	5.34	0.0	46.9	10.0	3.73	0.0	62.7	12.5	5.03	0.0
	6.3	70.5	15.6	3.76	0.0	72.8	15.1	3.97	0.0	44.5	10.1	2.99	0.0	58.9	13.0	3.83	0.0
	6.6	67.3	22.6	2.97	0.0	70.5	26.6	3.11	0.0	42.9	14.3	2.93	0.0	57.9	19.0	3.04	0.0
5M	6.7	65.4	28.4	2.00	0.0	68.7	28.7	2.40	0.0	42.0	18.0	2.33	0.0	56.8	24.0	2.36	0.0

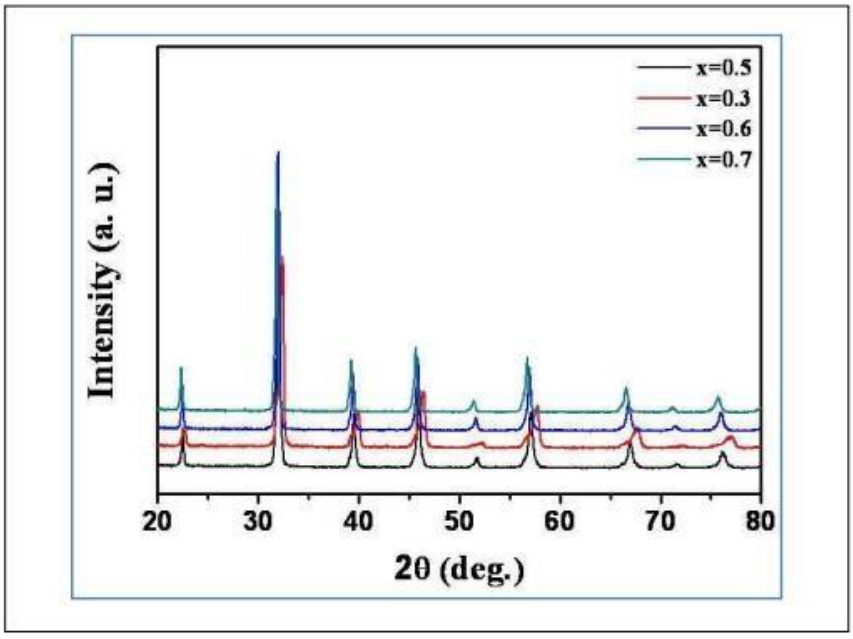

Fig. 1: XRD patterns of BST ($Ba_xSr_{1-x}TiO_3$)

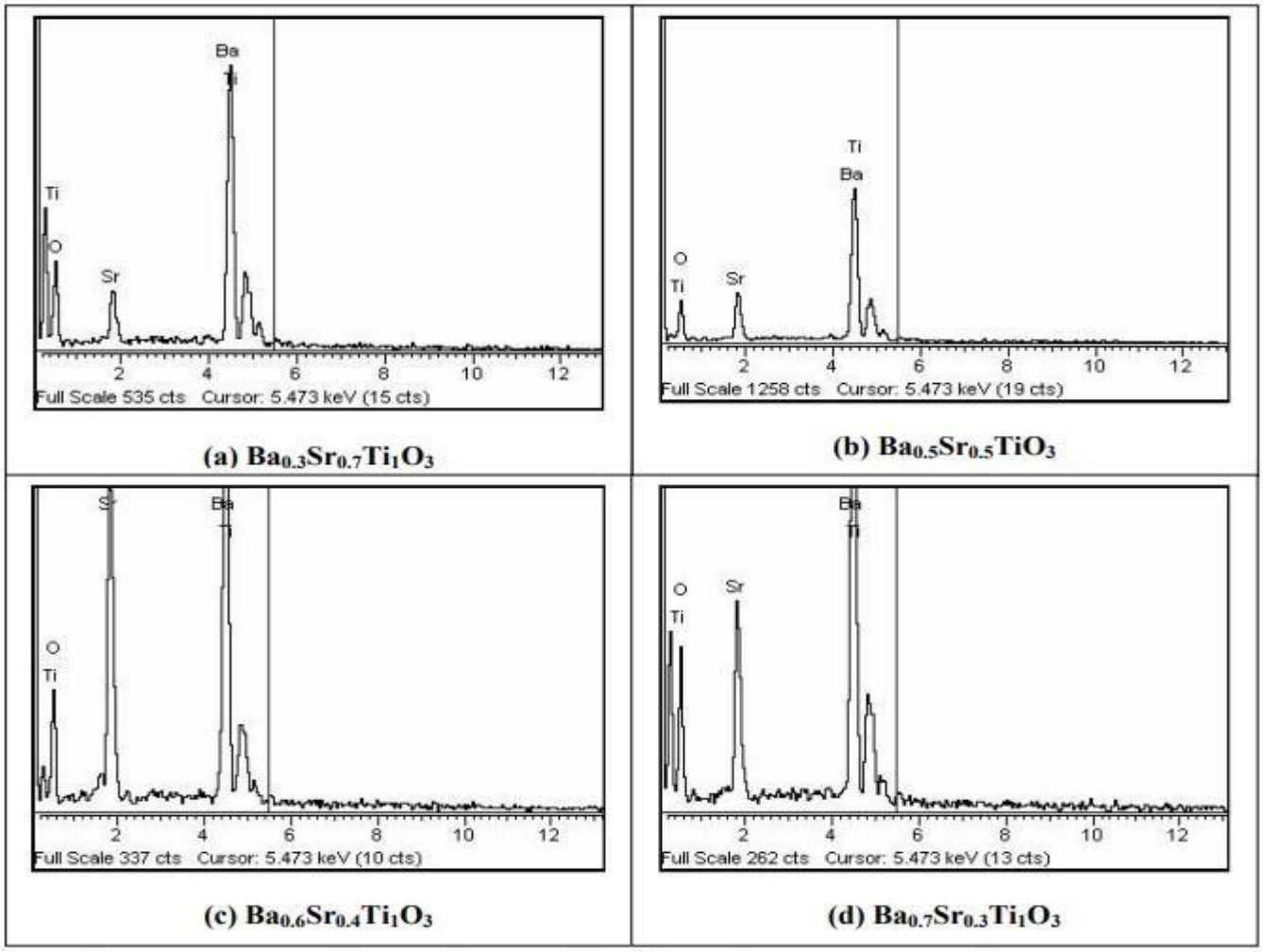

Fig. 2: EDAX images with peaks of (a) $Ba_{0.3}Sr_{0.7}Ti_1O_3$, (b) $Ba_{0.5}Sr_{0.5}TiO_3$, (c) $Ba_{0.6}Sr_{0.4}Ti_1O_3$, (d) $Ba_{0.7}Sr_{0.3}Ti_1O_3$

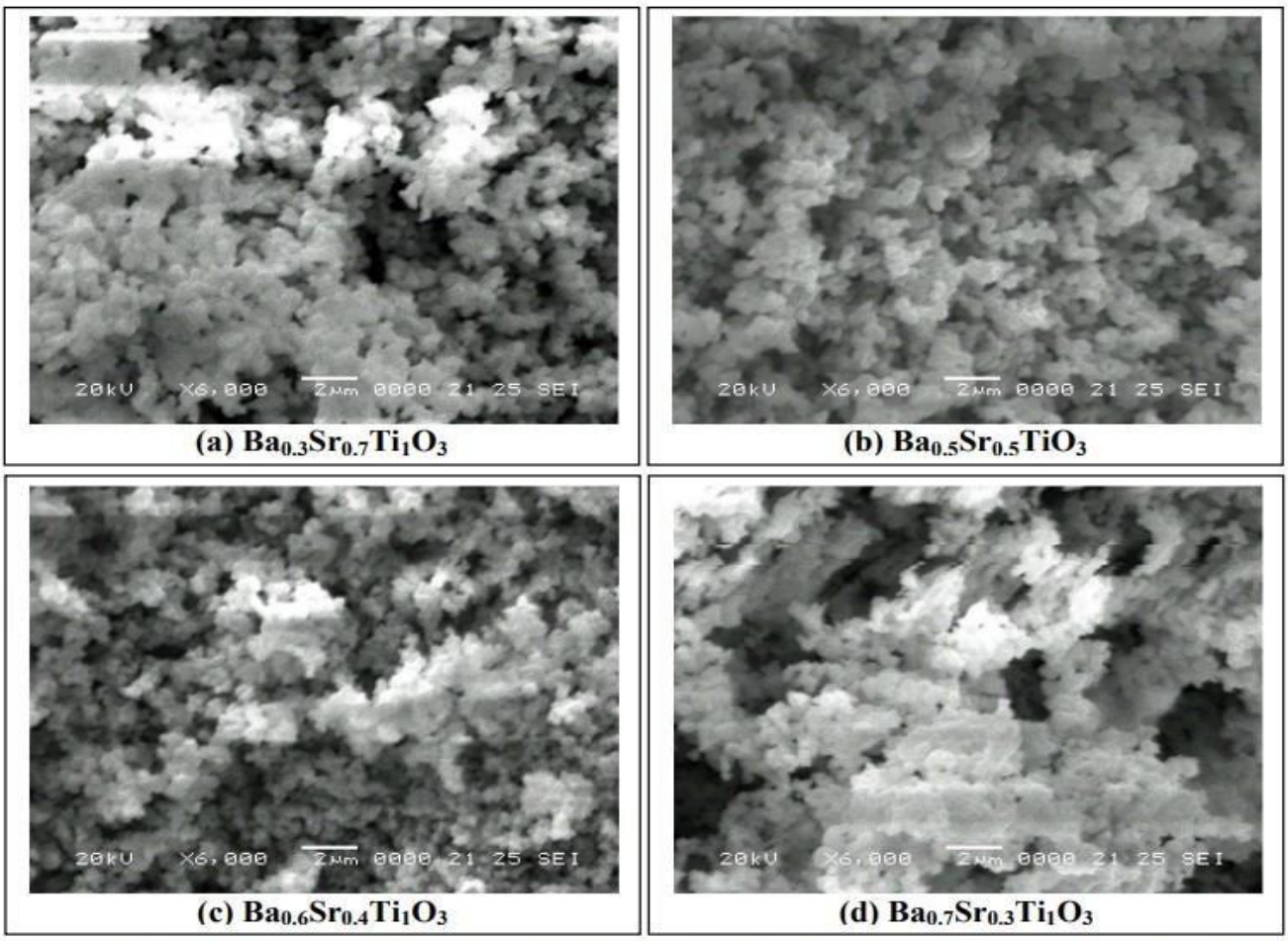

Fig. 3: SEM micrographs of (a) $Ba_{0.3}Sr_{0.7}Ti_1O_3$, (b) $Ba_{0.5}Sr_{0.5}TiO_3$, (c) $Ba_{0.6}Sr_{0.4}Ti_1O_3$, (d) $Ba_{0.7}Sr_{0.3}Ti_1O_3$

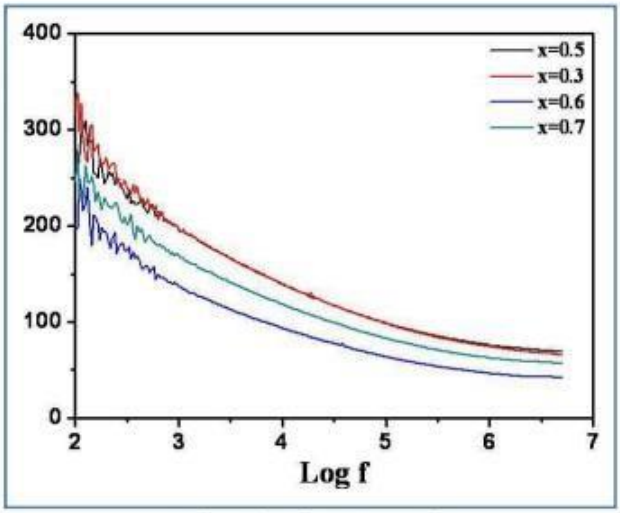

Fig. 4: ε' vs Log f

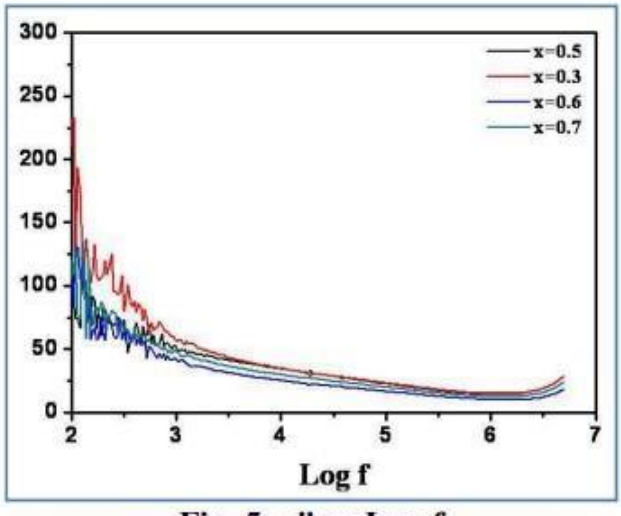

Fig. 5: ε" vs Log f

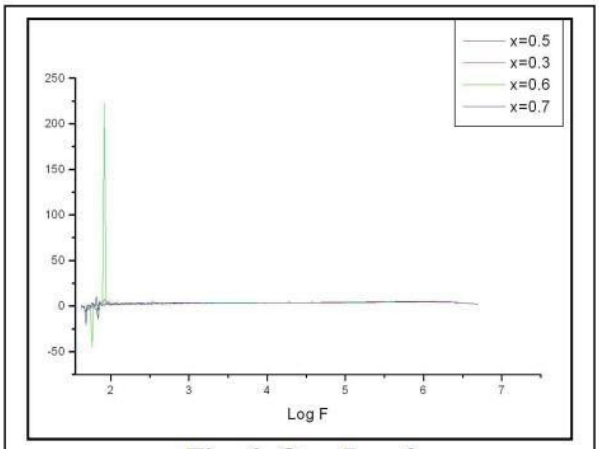

Fig. 6: Q vs Log f

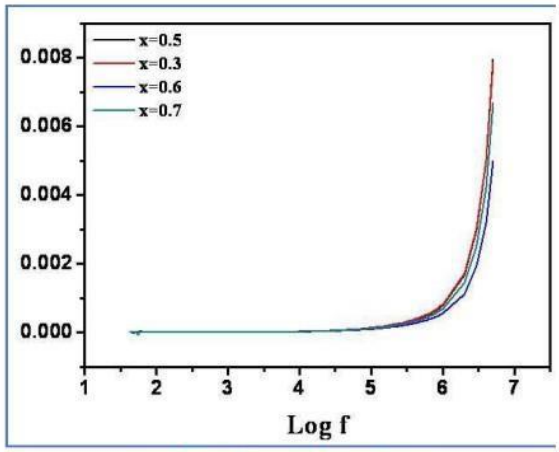

Fig. 7: σ vs Log f

From fig. 4 & 5 it is clear that dielectric constant and loss decreases by increasing the frequency for all samples. But as percentage of Sr element in the BST increases then it is found the ε', ε″ are increases because ferroelectric regions are surrounded by non-ferroelectric regions [13].

In fig. 6 & 7 it is observed the quality factor and conductivity increases with increasing frequency due to hoping of electrons [14-15].

At higher percentage of Sr in the material the Q and σ are high because extra charge carriers support to the quality factor and conductivity process [16-17].

V. CONCLUSION

- The synthesized ferroelectric material BST is confirmed by XRD, EDAX, and SEM.
- As the doping of strontium in BST is more which increases ε', ε″, Q and σ values.
- It is found that beyond the frequency 10KHz the conductivity is suddenly increases.

VI. REFERENCES

[1] L. Davis, L.G. Rubina, J. Appl. Phys. 24(1953) 1194
[2] W. Zhu, O.K. Tan, Q. Yan. Actuators B. 65(2000) 366
[3] S.S. Georgian et. al., IEEE Trans, Microwave Theor. Tech. 49(2001) 2117
[4] D.S. Korn, H.D. Wu. Integr. Ferroelectric. 24(1999) 215
[5] E.F. Alberta, R.Guo. A.S. Bhalla, Ferroelectrics. 268(2002) 589
[6] R.E. Newnham, Structure-property Relations, Springer, New York, NY, 1975
[7] M. Deri 'Ferroelectric ceramic' Golden and Brach, New York, 1969
[8] J.C. Buffort 'Ferroelectric Ceramics' can no strand, New York, 1967
[9] (Ertug B. (2013), American J. of Engineering Research, 02 (08), 1- 7)
[10] Li M L et al. (2008), J. Materials Chemistry and Phys., 112, 337-341
[11] Sunil G. Ganjagude et. al., Inter. Multidisc. E-research journal, Research journey, ISSN 2348- 7143. UGC approved No.40705 sintering and dielectric properties of BaxSr1-xTiO3 composites, March 2019

[12] Helmi Abdelkefi et. al., Journal of Alloys and compounds 399(2005) 1-6, Elsevier, Dielectric properties and ferroelectric phase transitions in BST solid solution.
[13] C. M. Karamadi, L. B. Pujari, B. K. Chaugule, J.Magn., Magn. Mater295 (2005) 139.
[14] G. B. Alcantara, L. G. Paterno, F. J. Fonseca, M. A. Pereira-de-silva, P. C. Morasis. MAG Soler, phys.chem.chem.phys 15 (2013) 19853.
[15] R. Nongjai, etal, J.Appl.Phys.-112 (2012) 084321.
[16] S. S. Jadhav, K. M. Jadhav. J. Optoelect. Adv.Matter 10 (2008) 2644.
[17] M. Hashim etal, J. Alloy Comp. 549 (2013) 348.

ICRTMS-2024
International e-Conference on Recent Trends in Material Science
In Association with International Journal of Scientific Research in Science and Technology
Volume 11 | Issue 9 | Print ISSN: 2395-6011 | Online ISSN: 2395-602X (www.ijsrst.com)

Biosynthesis and Characterization of NiO nanoparticles using Mulberry leaves extract

V.B. Deshmukh*, V. D. Kulkarni, A. B. Kanawade, N. D. Barne
Department of Physics Hutatma Rajguru Mahavidyalaya, Rajgurunagar, (M.S) India

ABSTRACT

In this study, nickel oxide nanoparticles (NiO NPs) were prepared using mulberry leaves extract by biosynthesis method. The prepared NiO nanoparticles calcimined at 4000C, then these NiO nanoparticles were characterized by various characterization techniques such as X-Ray spectroscopy (XRD), Ultra-Violet visible spectroscopy (UV), Fourier transform infrared spectroscopy (FTIR), Scanning electron microscopy (SEM) and Energy dispersive X-ray spectroscopy (EDS). These characterizations give particle size, structural morphology, functional group and percentage of the composition of chemical compounds used for synthesis. These nanoparticles can be useful for further applications in agricultural field to improve growth of plants.

Keywords: Biosynthesis method, Nickel oxide, Mulberry, Nanoparticles

I. INTRODUCTION

Nanotechnology is an escalating field of modern research (1) involving synthesis, preparation, characterization and application of nanoparticles, nanotubes and nanomaterials by controlling shape and size at nano scale (2).The nanotechnology is innovative and emerging field for nanomaterials ranging from 1nm to 100nm.There is new branch of nanotechnology existing which is bio-nanotechnology that integrates main role of biological objects with physical and chemical method for preparation of nano-size particles with specific function. The bio-based materials for synthesis of nanoparticles are eco-friendly and economical. They are simple, relatively inexpensive and easily scaled up for larger scale production (3). In recent years, there has been an increasing interest in the synthesis of nano sized crystalline metal oxides because they have large surface areas, surface defects and other useful properties. NiO nanoparticles have many applications in electronics industries, films, also in medical purpose, magnetic materials, different sensors, catalysts, alkaline batteries and in oxide fuel cells (4-8). There are various methods used and developed for synthesizing crystalline oxide powders in nanoscale,

II. METHOD OF SYNTHESIS AND CHARACTERIZATION

The materials used for biosynthesis are nickel nitrate hexahydrate, fresh and clean mulberry leaves, beaker, magnetic stirrer.

In experimental procedure, 50g fresh and dried mulberry plant leaves were added in 500ml of double distilled water and heated up to one hour. Then this solution was filtered for collecting the plant extract of mulberry plant leaves. Then this extract was continuously kept for stirring on magnetic stirrer at 700 C for 30 minutes. Then

4g of nickel nitrate hexahydrate was added in extract solution. Then it was observed that the color of extract changed from dark green to black. Again this extract solution was stirred up to 3 hours and this extract was kept as it is overnight. Then we observed that the particles were settled down at the bottom of beaker. Then this extract solution was filtered and dried at 1200 C in oven for 5 hours. Further this powder or particles were calcined at 4000 C for 2 hours. Then synthesized particles were characterized by various characterization techniques like X-Ray spectroscopy, Ultraviolet visible spectroscopy, Fourier transform infrared radiation, Scanning electron microscopy and energy dispersive spectroscopy for further analysis.

III.RESULT AND DISCUSSION

1. The Ultra-violet spectroscopy of NiO Mulberry nanoparticles

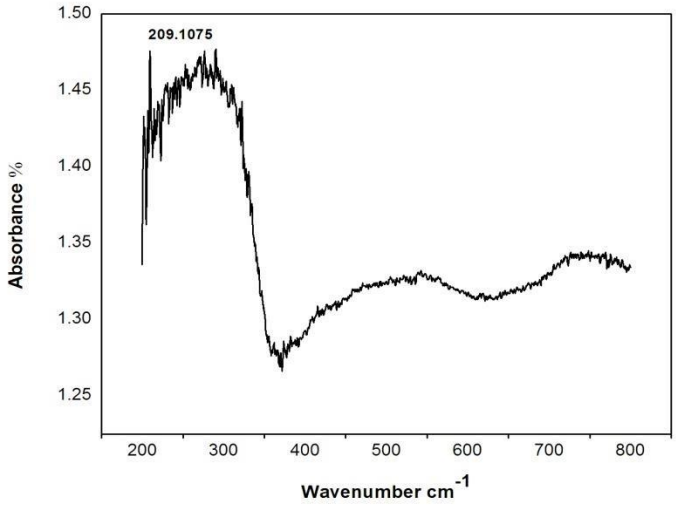

Figure 1 UV spectroscopy of NiO Mulberry nanoparticles

UV-visible absorption behaviour of NiO NPs of the sample was analyzed to gather information on its band gap energy. Figure 1 shows the UV-visible spectra of the NiO nanoparticles. The band gap energy of NiO NPs was calculated by given wavelength of absorption peak. The band gap energy was found 5.9 eV.

2. Fourier Transforms Infrared Spectroscopy of NiO Mulberry nanoparticles

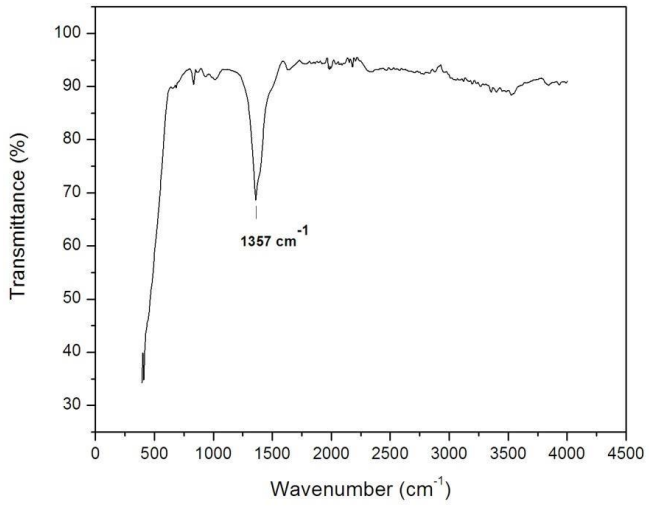

Figure 2 The FTIR spectra of NiO Mulberry nanoparticles

The IR spectrum of the precursor is shown in figure 2, it exhibits absorption peak. The broad absorption band centered at 1367cm-1 is attributed to the O-H bending shows water molecules of stretching vibration band. The broad peak having wave number 420 cm-1 indicates Ni-O stretching band (9) which confirmed the presence of nickel in precursor.

3. The X-ray spectroscopy of NiO Mulberry nanoparticles

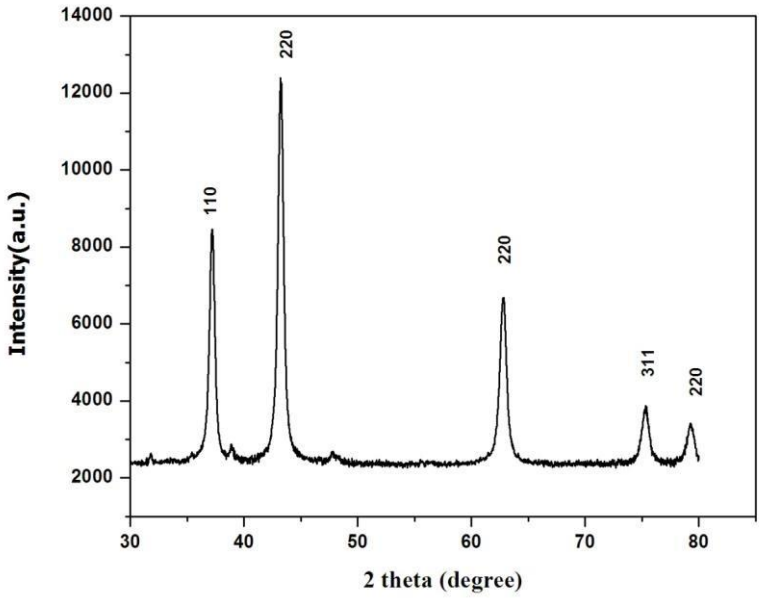

Figure 3.X-ray spectroscopy NiO Mulberry nanoparticals

The XRD pattern of NiO-Mulberry nanoparticles is shown in figure 3. Comparing to XRD standard table, the diffraction peaks of NiO Mulberry leaves extract after reaction are shown as (110), (220), (311). It shows crystalline phase and sharp diffraction peaks indicating that NiO nanoparticles were prepared successfully. These peaks indicate

NiO nanoparticles crystallization and elimination of the former phase i.e. nickel hydroxide. The size of the NiO NPs is calculated by using Scherrer's equation as $t=\frac{0.9\lambda}{\beta cos\theta}$ where, t is particle size, λ is wavelength (0.1542 nm for CuK_{α} radiation) full width half maximum (FWHM) of a peak for radiation and diffracted angle respectively (10). The particle size of NiO nanoparticle is found to be 32.62 nm.

4. Scanning electron microscopy of NiO Mulberry nanoparticles

The figure4 shows scanning electron microscopy image of nickel oxide mulberry nanoparticles. The images show porous and globular nature. The image also shows irregular structure.

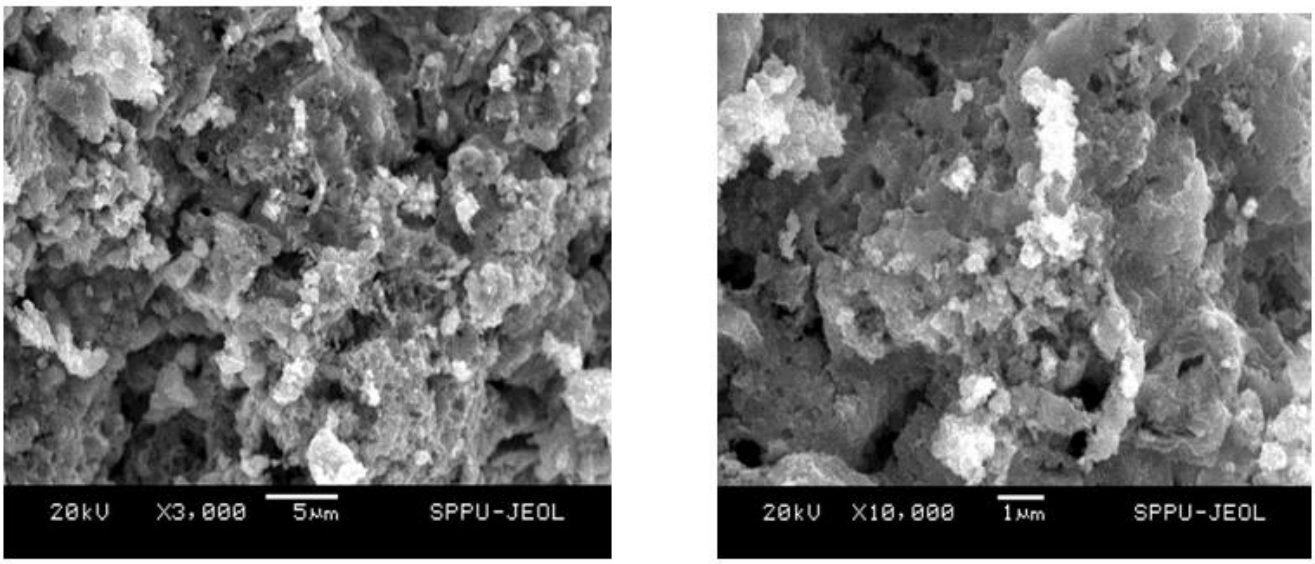

Figure 4. Scanning electron microscopy NiO Mulberry nanoparticles

5. Energy dispersive spectroscopy of NiO nps

The chemical composition of nanoparticles was found by EDS in this biosynthesis, which indicates Ni about 58.70% and K about 27.92%.

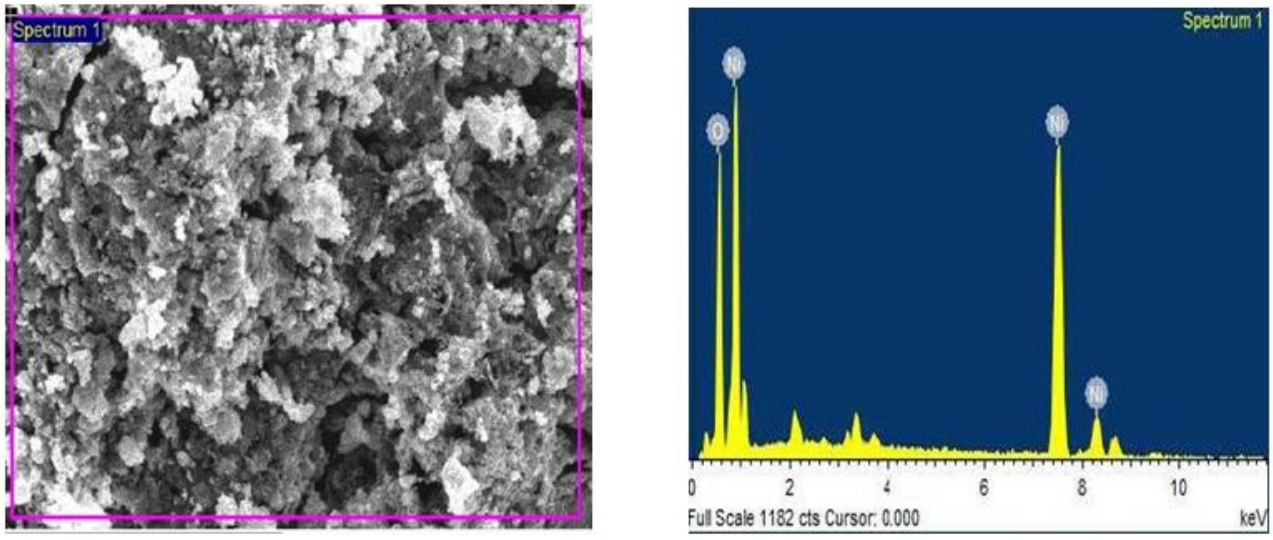

Figure5.Energy dispersive spectroscopy of NiO nps

IV. CONCLUSION:

NiO nanoparticles were successfully prepared by biosynthesis method using nitrate hexahydrate and mulberry leaves extract. The size of NiO nanoparticles was found about 32.62nm from x-ray spectroscopy. The scanning electron microscopy (SEM) shows the porous and globular nature of nanoparticles. From SEM, the nanoparticles were also found to be in irregular shapes. The EDS shows the chemical composition of the nanoparticles. From UV-visible spectroscopy, the band gap energy of 5.9 eV was observed. The availability of NiO functional group was confirmed from the FTIR.

V. REFERENCES

[1] A. Q. Li, L.-S. Wang, B.-Y. Hu, C. Yang, L. Zhou, and L. Zhang, "Preparation and characterization of NiO nanoparticles through calcinations of malate gel," Materials Letters, vol. 61, no. 8-9, pp. 1615–1618, 2007.

[2] X. Xin, Z. Lu, B. Zhou, et al., "Effect of synthesis condit ions on the performance of weakly agglomerated nano-crystalline NiO," Journal of Alloys and Compounds, vol. 427, no. 1-2, pp. 251–255, 2007.

[3] Y. Wu, Y. He, T. Wu, T. Chen, W. Weng, and H. Wan, "Influence of some parameters on the synthesis of nanosized NiO material by modified sol-gel method," Materials Letters, vol. 61, no. 14-15, pp. 3174–3178, 2007.

[4] K.-C. Min, M. Kim, Y.-H. You, et al., "NiO thin films by MOCVD of Ni(dmamb)2 and their resistance switching phenomena," Surface & Coatings Technology, vol. 201, no. 22- 23, pp. 9252–9255, 2007.

[5] I. Hotovy, J. Huran, L. Spiess, H. Romanus, D. Buc, and R. Kosiba, "NiO -based nanostructure thin films with Pt surface modification for gas detection," Thin Solid Films, vol. 515, no. 2, pp. 658–661, 2006.

[6] Edhaya Naveena B, Prakash S, Biological synthesis of gold nanoparticles using marine algae Gracilariacorticata and its application a s a potent antimicrobial and antioxidant agent. Asian J Pharm Clin Res 6(2):179–182. 2013

[7] Madhuri S, Maheshwar S, Sunil P, Oza G, Nanotechnology: concepts and applications, vol 4. CRC Press, USA, 2012

[8] Prabhu S, Poulose E, Silver nanoparticles: mechanism of antimicrobial action, synthesis, medical applications, and toxicity e ffects. Int Nano Lett 2(1),2012 [9]K.Murali Mayya, Nirmesh Jain, Anand Gole, Dominique Langevin, Murali Sastry Time-dependent complexation of glucose-reduced gold nanoparticles with octadecyl lamine Langmuir monolayers, Journal of Colloid and Interface Science, Vol 270, issue 1, 1, ,133-139,2004

[9] Sung-Jei Hong, Hyuk-Jun Mun, Byeong-Jun Kim and Young-Sung Kim, Characterization of Nickel Oxide Nanoparticles Synthesized under Low Temperature, Microma chines, 12, 1168, 2021

ICRTMS-2024
International e-Conference on Recent Trends in Material Science
In Association with International Journal of Scientific Research in Science and Technology
Volume 11 | Issue 9 | Print ISSN: 2395-6011 | Online ISSN: 2395-602X (www.ijsrst.com)

Effect of Ag Doping on Optical and DC Electrical Properties of Spray Deposited ZnO Thin Films

Dr. Sarika Vaijanathrao Jadhav
Department of Physics, Sant Tukaram College of Arts and Science, Parbhani, Maharashtra, India

ABSTRACT

The Ag doped ZnO thin films was prepared by Simple Spray Deposition technique using locally available perfume atomizer. The deposited films were characterized by XRD, FTIR, SEM and UV-Visible spectroscopy. ZnO films was considerably changed with Ag doping. The 3 % Ag doped film shows excellent morphology of small pieces of Ag/ZnO wires uniformly distributed over the entire substrate. The EDX spectra show the samples composed of Zn, O and Ag elements and no other impurity was present.

It also showed that the spectra exhibit low absorption in the range of 400 to 999 nm. The optical absorption was increased as Ag atomic % was increased. The pure ZnO thin film exhibits higher transmittance ≥ 78% in the range of 400 to 999 nm. It also showed that even low Ag atomic % doping effects the absorption spectra of ZnO thin films. With increase in Ag atomic % transmittance was gradually decreased. Thus, it was concluded that the substitution of low quantity of Ag make significant effect on absorption and transmittance spectra of ZnO thin films.

The band gap was observed decreased as the Ag doping was increased. Lowest optical energy band gap of 3.21 eV was observed for 5% Ag content. The study shows that ZnO thin films are high resistive in nature which is in the order of 103 Ω –cm for pure ZnO thin films and decreased with addition of Ag atomic %. Thermal activation energy estimated was 0.561 eV which decreased by 10-1 with increased doping % of Ag.

Keywords: ZnO thin film, Spray deposition, Optical band gap, activation energy.

I. INTRODUCTION

Zinc-Oxide (ZnO) is an important II-VI compound semiconductor material of multi-dimensional characteristics. ZnO material is having prominent electronic as well as photonic properties. It is wurtzite n-type semiconductor with a wide direct band gap of 3.37 eV and a high excitation binding energy of 60 meV at room temperature, that provides more efficient excitonic lasing mechanism at room temperature [1-2].

ZnO has been the focal point of much recent research because it possesses certain characteristics that make it a very interesting material considering either fundamental or practical points of vision [3]. It is vitally important in industrial point of view due to its special characteristics such as anti-corrosion, anti-bacterial, also has low electron conductivity and excellent heat resistance [4].

ZnO is considered as a versatile material with an extensive range of properties which include good transparency, high electron mobility, high thermal conductivity, wide band gap and strong room temperature luminescence [5-6]. The abundant availability of ZnO in nature makes it less expensive and its sharp UV-cutoff makes it desirable in many applications such as light emitting diodes, solar cells, photo catalysis and gas sensors, photovoltaic devices, dye sensitized solar cell and ultraviolet sensors. ZnO has so many advantages such as low price, photo catalytic activities, good gas sensing properties, antibacterial activity, possibility to prepare structures with interesting optical properties like photo catalyst materials, in small amount ZnO is non-toxic etc. [7].

On account of these tremendous applications, we deposited ZnO and transition rare earth metal Ag doped ZnO thin films using suitable simple chemical spray deposition method. The optical and DC electrical properties have been investigated.

II. METHODS AND MATERIAL

The Ag doped ZnO thin films were prepared by using simple spray deposition technique using locally available perfume atomizer. The Ag doped ZnO thin films were prepared by mixing two solutions. First solution was prepared by dissolving analytical reagent grade 0.15M zinc acetate hydrated (Zn (CH3COO)22H2O) in distilled water/methanol (70:30) proportion. Few drops of acetic acid were added to avoid formation of zinc hydroxide. Second solution was prepared by dissolving 0.15 M silver acetate (CH3COOAg) in distilled water. Few drops of nitric acid (HNO3) were added to dissolve silver acetate in distilled water completely. These solutions were individually stirred for two hours using magnetic stirrer.

In the technique of preparation of Ag doped ZnO thin films, five precursors of Zinc Acetate were prepared. In first Zinc Acetate solution 1 atomic % of Ag was added. In second Zinc Acetate solution 2 atomic % of Ag was added. In this way 3 through 5 atomic % of Ag was added in remaining three Zinc acetate solutions. These solutions were stirred individually by using magnetic stirrer for two hours till the clear precursors were obtained. The clear precursors have been sprayed on the pre-heated glass substrate at desired optimized temperature (3000 C). The deposited substrates were allowed to cool at room temperature and then annealed at 4000 C for two hours in muffle furnace to obtain highly compact films.

Absorption coefficient α for direct transition is given by the relation (1)

$$\alpha = \frac{A}{h\upsilon}(h\upsilon - Eg)^{n} \text{----------1.}$$

Where,

Eg = optical band gap energy,

hυ = Energy of incident light,

A = constant depends on the transition probability for direct transition

n = ½ (allowed direct transitions)

n = 3/2 (Forbidden transition)

n = 2 (allowed indirect transitions)

Therefore, if the plot of $(\alpha h\upsilon)^2$ against $h\upsilon$ is linear then transition is direct allowed. The band gap energy (E_g) is calculated by extrapolating the linear portion of the curve to the energy axis at zero absorption that is at absorption edge. The optical band energy was determined by using the relation (2) [12]

$$\mathbf{Eg} = \left(\frac{hc}{\lambda}\right) \text{----------2}$$

Where,

h = Plank's constant

c = velocity of light

λ= near band edge wavelength

III.RESULTS AND DISCUSSION

The Ag doped ZnO thin films were characterized by using different techniques. In the present article optical and DC electrical properties of Ag doped ZnO thin films were studied.

3.1. Effect of Ag Doping on UV-Visible Spectra:

Absorption Spectra of Ag-ZnO thin films of various Ag atomic % (1,2,3,4, and 5%) were recorded by using Systronic double beam (2201) spectrophotometer. The films have been scanned in the wavelength range 190 to 999 nm. The figure 1.1 shows the absorption spectra of Ag-ZnO thin films of different Ag atomic %. The flat portion in the range 400 to 999 nm exhibit low absorption and absorption was abruptly increased below 400 nm. The absorption was found maximum for the wavelengths ($\leq$ 390 nm). The shifting of absorption edge towards higher wavelengths and increase in absorption was clearly observed as the Ag atomic % was increased (8,9) Figure 1.2 shows transmittance spectra of pure and Ag doped ZnO thin films. The pure ZnO thin film exhibits higher absorption transmittance ($\geq$ 78%) in 300 to 999 nm range. The remarkable effect of Ag doping on transmittance was clearly observed from figure. Even small amount of Ag doping suddenly decreased the transmittance. As Ag doping % was increased above 2% the transmittance was gradually decreased.

Figure 1.3 shows Tauc plot obtained by plotting $(\alpha h\upsilon)$ 2 versus photon energy $h\upsilon$. Band gap energy was calculated for pure and Ag doped ZnO thin films by using Tauc plot. The band gap obtained for pure ZnO was 3.362 and was gradually decreased as the Ag atomic % was increased (10,11) as shown in figure. The film samples of 1 through 5 Ag atomic % exhibit band gap 3.29, 3.25, 3.23, 3.221 and 3.215 eV respectively as shown in Fig. 1.4. Ag doped ZnO thin films show decrease in band gap with increase in crystallite size.

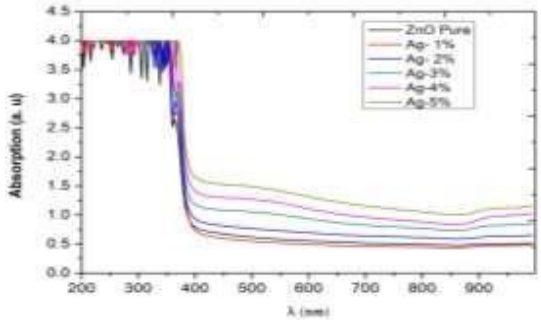

Figure1.1 UV-Vis Absorption Spectra

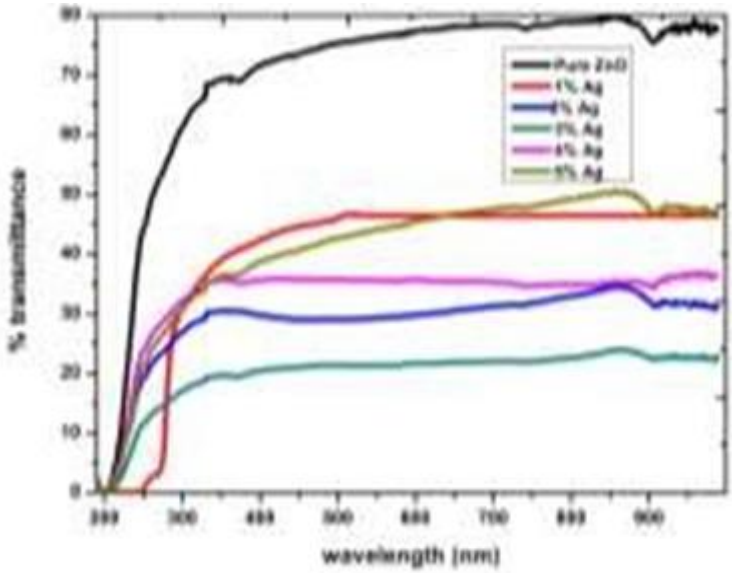

Figure 1.2 UV-Vis Transmission Spectra Of pure and Ag doped thin films

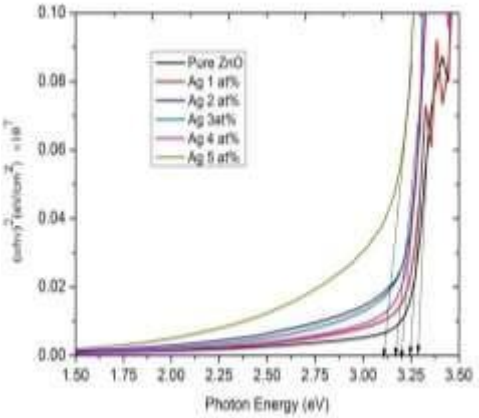

Figure 1.3 Tauc's plot for Ag doped ZnO thin Films

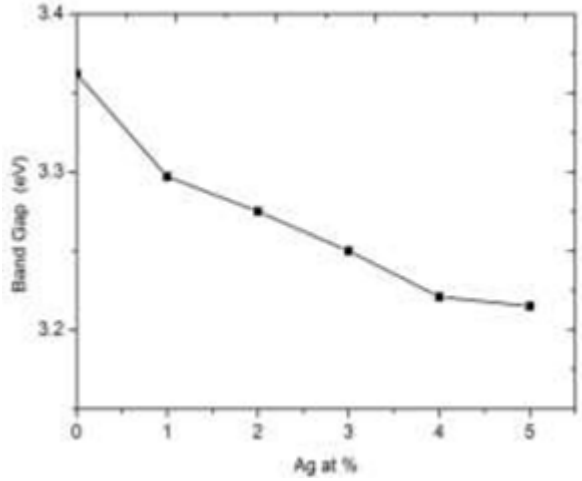

Fig.1.4 Band Gap Energy

3.2. Effect of Ag Doping on the DC- Electrical Resistivity

The study shows that ZnO thin films are high resistive in nature which is in the order of 103 Ω –cm for pure ZnO thin films. The variation of Resistivity with Temperature in 0C is shown in figure 1.5. It was found that resistivity decreased with increase in temperature as well as on increasing doping % of Ag content. The

decrease in resistivity with increase in temperature is the characteristic property of semiconducting materials. The dc- resistivity was abruptly decreased by small addition of Ag atomic % in pure ZnO matrix. The samples (Ag/ZnO) deposited by using present technique satisfied the phenomenon of semiconducting properties. It was found that resistivity at room temperature decreased with increase in Ag atomic % [13] which was illustrated in figure 1.5.

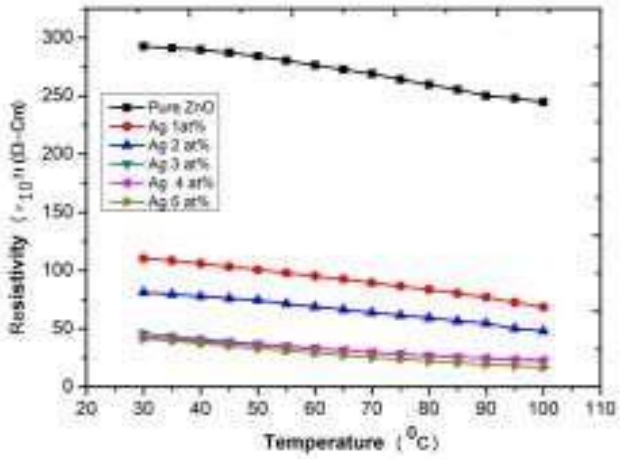

Figure 1.5 plot of Resistivity versus Temperature

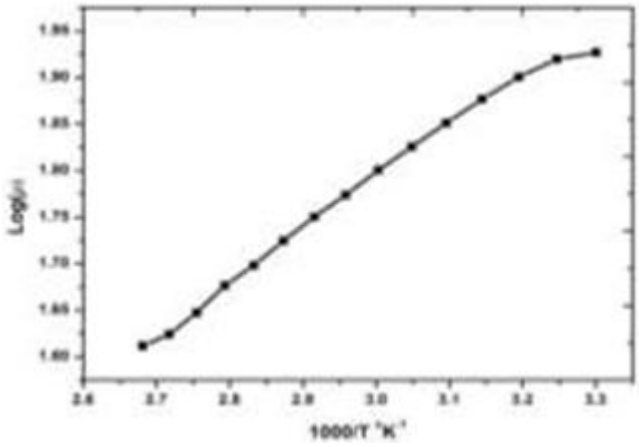

Figure 1.6 Plot of Log(ρ)versus 1000/T oK-1for Pure ZnO Thin film

The activation energy of ZnO thin films is determined by donor levels formed by oxygen vacancies in the forbidden zone of ZnO. During heating process decrease in resistance of the sample with increase in temperature was determined by the thermal generation of electrons. Thermal activation energy of pure ZnO thin film was estimated from Log(ρ) verses 1000/T oK-1 plot as shown in figure 1.6. Thermal activation energy estimated was to be 0.561 eV. Figure 1.7 shows the Log (ρ) verses 1000/T oK-1 plot of Ag/ZnO thin films. The thermal activation energy of Ag/ZnO film samples was estimated using Log (ρ) verses 1000/T oK-1 curves. The estimated activation energies were decreased of the order of 10-1 as compared to activation energy of pure ZnO. The estimated activation energy was plotted against Ag atomic % and represented in figure 1.8. The activation energy was generally decreased as the Ag atomic % was increased. However, film sample prepared for Ag atomic % 3 exhibits higher activation may be depends upon generation of donor carrier concentration. The decrease in activation energy due to increase in doping percentage that leads to increase in donor carrier concentration which bring the Fermi level up in the energy gap [14].

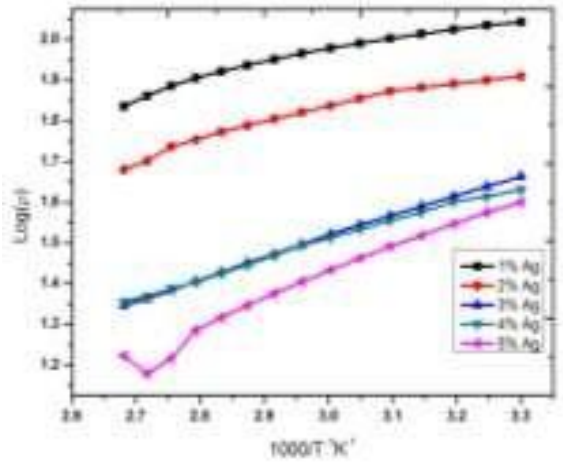

Figure 1.7 Plot of Log(ρ)versus 1000/T oK-1for Ag/ZnO Thin film

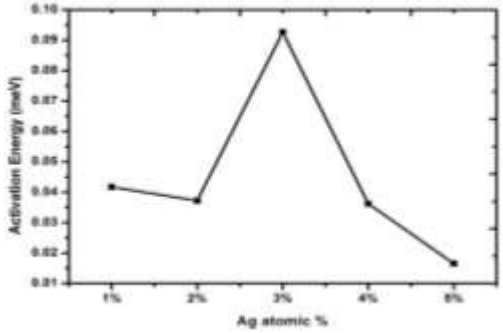

Fig 1.8 Plot of Thermal Activation energy versus Ag atomic %

IV. CONCLUSION

In order to synthesize Ag doped ZnO thin films various physical and chemical methods have been employed. However, in present article simple chemical spray deposition process using perfume atomizer was employed. The simple chemical spray technique is simple, low cost, easy to design, utilization of minimum instruments, able to deposit desired material, working at moderate temperature. This method was found effective in the synthesis of pure and doped ZnO nanostructures thin films. Using simple chemical spray technique wurtzite hexagonal crystalline symmetry of ZnO thin films have been successfully synthesized. The UV Visible transmittance spectra obtained show maximum transmittance for pure ZnO was ≥78%. The estimated band gap was decreased with increase in Ag atomic % (1 to 5 %) from 3.29 to 3.215 eV which was smaller than pure ZnO thin film (3.33 eV). The UV-Visible spectra confirmed that the absorption was abruptly high below 400 nm and it was found maximum for the wavelength ≤ 290 nm.

It was concluded that the substitution of low quantity of Ag make significant effect on absorption and transmittance spectra of ZnO thin films. The band gap was observed decreased as the Ag doping was increased. Lowest optical energy band gap of 3.21 eV was observed for 5% Ag content.

V. REFERENCES

[1] Z. L. Wang, Materials Today, 7(6), (2004), 26-33.

[2] C.N.R. Rao, A. Govindraj, H. Kroto, P.O. Brien, H. Craighead, Royal Society of Chemistry, London, U.K., (2005). [3] A.M. Alsaad, A.A. Ahmed, J. A. Qattan, Quis M. Al. Batainesh, Zaid Albataineh, Crystals, 10, (2020), 252

[3] J. N. Hasnidawani, H.N. Azlina, H. Norita, N.N. Bonnia, S. Ratim, E. S. Ali, Proc. Chemistry, 19, (2016), 211-216

[4] A. Janotti, C. G. V. d. Walle, Rep. Prog. Phys., 72, (2009), 29.

[5] R. Kumar, G. Kumar, O. Al. Dossary, A, Umar, Material Express, 5(1), (2015). [7] K. Keem, D. Y. Jeong, S. Kim, Nanoletters, 6(7), (2006), 1454-1458.

[6] H. Karami, E. Fakoori, Journal of Nanomaterials, 2011, (2011), 11.

[7] Y. Ni., X. Cao, G. Hu, Z. Yang, X. Wei, Nanotechnology, 18, (15), (2007).

[8] Mansoor Ali Syed, W. A. Farooq, M. R. Baig, M. A. Shar, M. Atif, S.S. Alghamdi, M. S. Algawari, Naeem-Ur-Rehman, Muhammad Hammad Aziz, Material Science- Poland, 33(3), (2015), 601-605.

[9] Ramchandra T. Sapkal, Sambhaji S. Shinde, Appa A. Babar, Annasaheb V. Moholkar, Keshav Y. Rajpure, Chandrakant H. Bhosal e, Materials Express, 2(1), (2012), 64-70.

[10] Gore Michael, Spectrophotometry, Oxford University Press, (2000).

[11] M. A. Barote, A. A. Yadav, E. U. Masumdar., Physica B., 406, (2011), 294-302.

[12] Fadhil Habubi Nadir, Yousif Ali Ahmed, Haider Adawiya, Journal of Nano-and Electronic Physics Vol.4 (2), (2012), 02007-02013.

ICRTMS-2024
International e-Conference on Recent Trends in Material Science
In Association with International Journal of Scientific Research in Science and Technology
Volume 11 | Issue 9 | Print ISSN: 2395-6011 | Online ISSN: 2395-602X (www.ijsrst.com)

Structural Properties of Synthesised NiCuZn Ferrite

B. D. Ingale, *R. V. Suryawanshi
Department of Physics and Electronics, Zzad Mahavidyalaya, Ausa, (MS) – 413520, Maharashtra, India

ABSTRACT

The composition of ferrite [Ni 0.25-x Mg x Cu 0.20 Zn0.55] Fe2O4 (x = 0.00, 0.05, 0.10, 0.15, 0.20 and 0.25) has been prepared by autocombusion method using citric acid as a fuel. X- ray diffraction analysis of as prepared ferrite powder shows the cubic spinal structure. The consequential powder was calcined at 650 0C per 2hrs and the pressed ferrite was sintered at 950 0C per 4hr. In the EDAX characterization peaks were observed due to the elements Ni, Cu, Zn, Mg, Fe and O which confirm the presence of respective ions as per initial stoichiometry. The permeability, dc resistivity were measured with frequency range 100Hz to 5MHz. The crystallite size of ferrite was observed from 22.8 to 40.64 Nm. The composition x = 0.15 mole with high permeability seems to have potential for multilayer chip inductor applications at a wide range of frequencies and surface mounting equipment. The ferrite samples showed the endothermic peak at ~750°C. [Ni0.25-xMgxCu0.20Zn0.55]Fe2O4 with x = 0.15, a peak at ~70°C was observed. The ferrite samples under test for thermogravimetric analyses annealed at 950°C for 4 h, the TGA graphs showed the straight line parallel to temperature axis.

Keywords: Autocombusion method, stoichiometry, EDAX characterization, TGA.

I. INTRODUCTION

This paper gives an account of TGDTA Energy dispersive X- ray analysis(EDAX) studies of Mg^{2+} substituted NiCuZn ferrites, prepared by sol-gel auto-combustion route. In today's world, information technology plays a significant role in everyday life. There is an urgent and growing demand for electromagnetic components that are affordable, have great efficiency, and have a small size. Surface mount devices, also known as SMDs, and Multi Layer Chip Inductors, also known as MLCIs, are two of the components that are used extensively in electronic products. MgCuZn materials have magnetostriction constant values that are lower than those of NiCuZn [1-7]. As a result of their high electrical resistivity and low dielectric losses, Mg-based ferrites are frequently utilized in microwave devices [8]. The spinel ferrites are known to experience changes in their electrical, magnetic, and micro-structural properties [9] when diamagnetic ions are substituted for Mg^{2+}. There are several ways to make soft ferrites, such as ceramic, sol-gel, co-precipitation, chemical preparation, citrate precursor approach, micro-emulsion, nitrate citrate, and so on. The auto-combustion of nitrate-citrate is a procedure that is uncomplicated, quick, and results in good quality ferrites.

There is not a lot of information in the scientific literature about how the presence of magnesium affects the electromagnetic characteristics of NiCuZnferrites. The effects of Mg substitution on the structural, magnetic, electrical, and dielectric properties of $[Ni_{0.25-x}Mg_xCu_{0.20}Zn_{0.55}]$ Fe_2O_4 ferrites.

II. EXPERIMENTAL DETAILS

For a typical combination, AR grade nitrates (magnesium nitrate ($Mg(NO_3)_2{\cdot}6H_2O$), nickel nitrate ($Ni(NO_3)_2{\cdot}6H_2O$), copper nitrate ($Cu(NO_3)_2{\cdot}6H_2O$), zinc nitrate ($Zn(NO_3)_2{\cdot}4H_2O$), ferric nitrate ($Fe(NO_3)_3{\cdot}9H_2O$) and citric acid ($C_6H_8O_7$) were obtained from Sigma Aldrich and were used as received. The proper quantity of distilled water, the precursors and reagent were meticulously combined and homogenized. The temperature of the sol was up to 100°C. At the predetermined temperature, the sol-viscosity steadily grew with increasing time, as per the natural behavior. The gel was subjected to further heat treatment at an even greater temperature (150-200°C). The thick gel continued to foam, and finally, as the water evaporated, the gel started to exhaust into a quick flameless auto combustion process with the evolution of a considerable number of gaseous products. Then the resulting powder was calcinated in air at a temperature of 650°C for 2 h in order to remove any residues of unreacted leftovers while maintaining the pure ferrite material. By using a manual pressing machine with a pressure of 1.5 tons/cm^2 and PVA as the binder, the powder was formed into pellets with a diameter of 15 mm and a thickness of 2 mm, as well as toroids with an inner diameter of 1.5 cm, an outer diameter of 2.5 cm, and an average height of 0.3 cm. The pellets and the toroids were both sintered at a temperature of 950°C for 4 h in air. The general composition of the developed ferrites is$[Ni_{0.25-x}Mg_xCu_{0.20}Zn_{0.55}]Fe_2O_4$with x = 0.00, 0.10, 0.15, 0.20, 0.25.

III.RESULTS AND DISCUSSION

Thermogravimetric analysis (DTA): The DTA graphs of developed Mg substituted NiCuZn ferrite samples with x = 0.00 – 0.25 for the general composition $[Ni_{0.25-x}Mg_xCu_{0.20}Zn_{0.55}]Fe_2O_4$ shown in figure 1. All the ferrite samples showed the endothermic peak at ~750°C. This peak may correspond to the change of the structure of ferrite. Indeed, in case of $CuFe_2O_4$ ferrites, Li et al. [18] indicated that $CuFe_2O_4$ has a tetragonal structure at low temperature and has a cubic structure at high temperature. Interestingly, only in case of $[Ni_{0.25-x}Mg_xCu_{0.20}Zn_{0.55}]Fe_2O_4$ with x = 0.15, an additional peak at ~70°C was observed, which can be assigned to the formation of the ferrite compound. As all the ferrite samples under test for thermogravimetric analyses were annealed at 950°C for 4 h, the TGA graphs showed the straight line parallel to temperature axis; hence not shown in the below graphs.

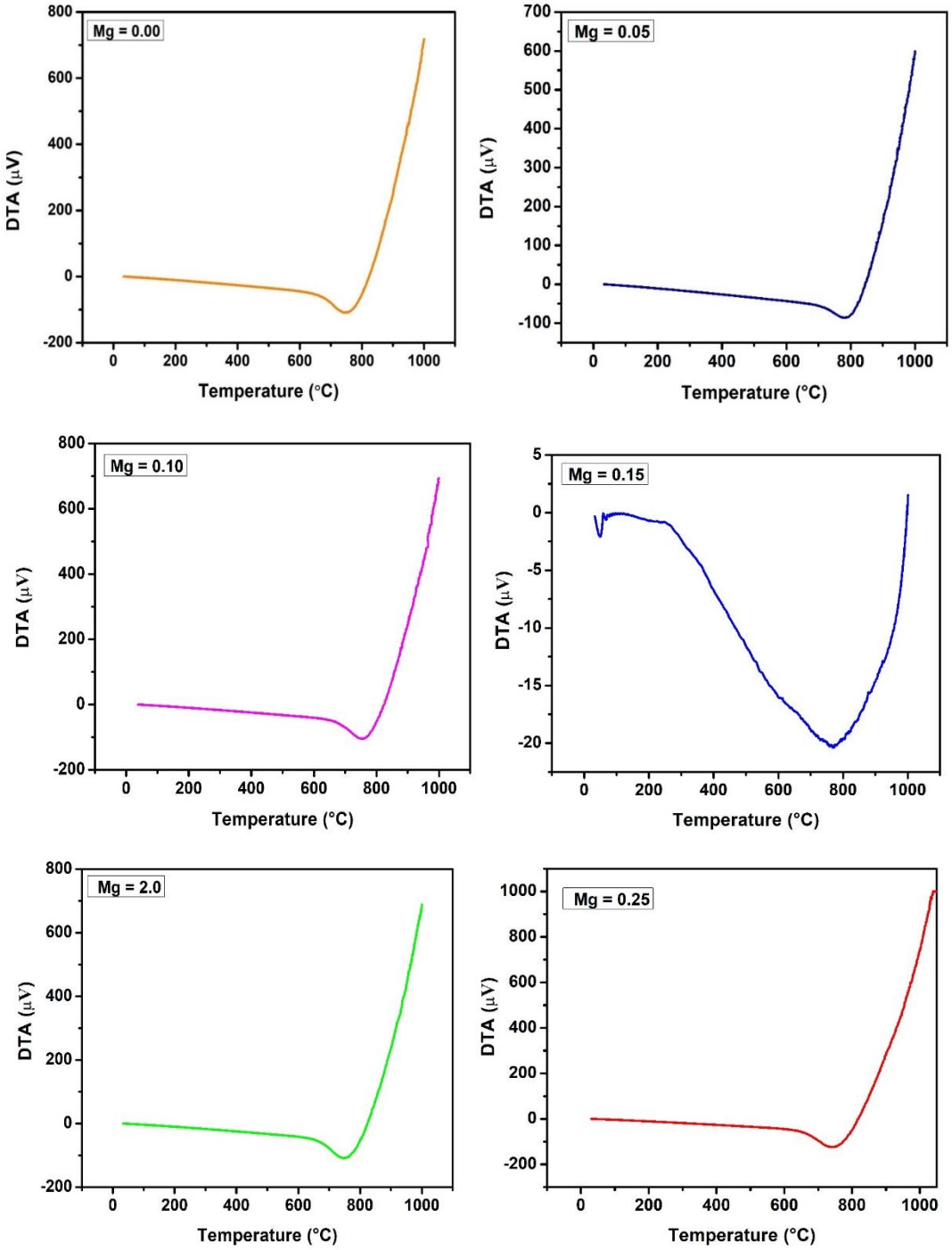

Figure 1. DTA graphs of Mg substituted NiCuZn ferrites.

Elemental analysis (EDAX): For chemical characterization and elemental analysis of the ferrite samples, energy dispersive X-ray spectroscopy (EDAX or EDS) was used. The EDAX spectrographs of $[Ni_{0.25-x}Mg_xCu_{0.20}Zn_{0.55}]Fe_2O_4$ with x = 0.00- 0.25. ferrites are shown in Figure 2. X-ray peaks were observed due to the elements Ni, Cu, Zn, Mg, Fe and O which confirm the presence of respective ions as per initial stoichiometry under investigation. The data from EDAX in terms of compositional atomic percentage of Ni^{2+}, Cu^{2+}, Zn^{2+}, Mg^{2+}, Fe^{3+} and O^{2-} ions in the ferrite samples is tabulated in Table 1.

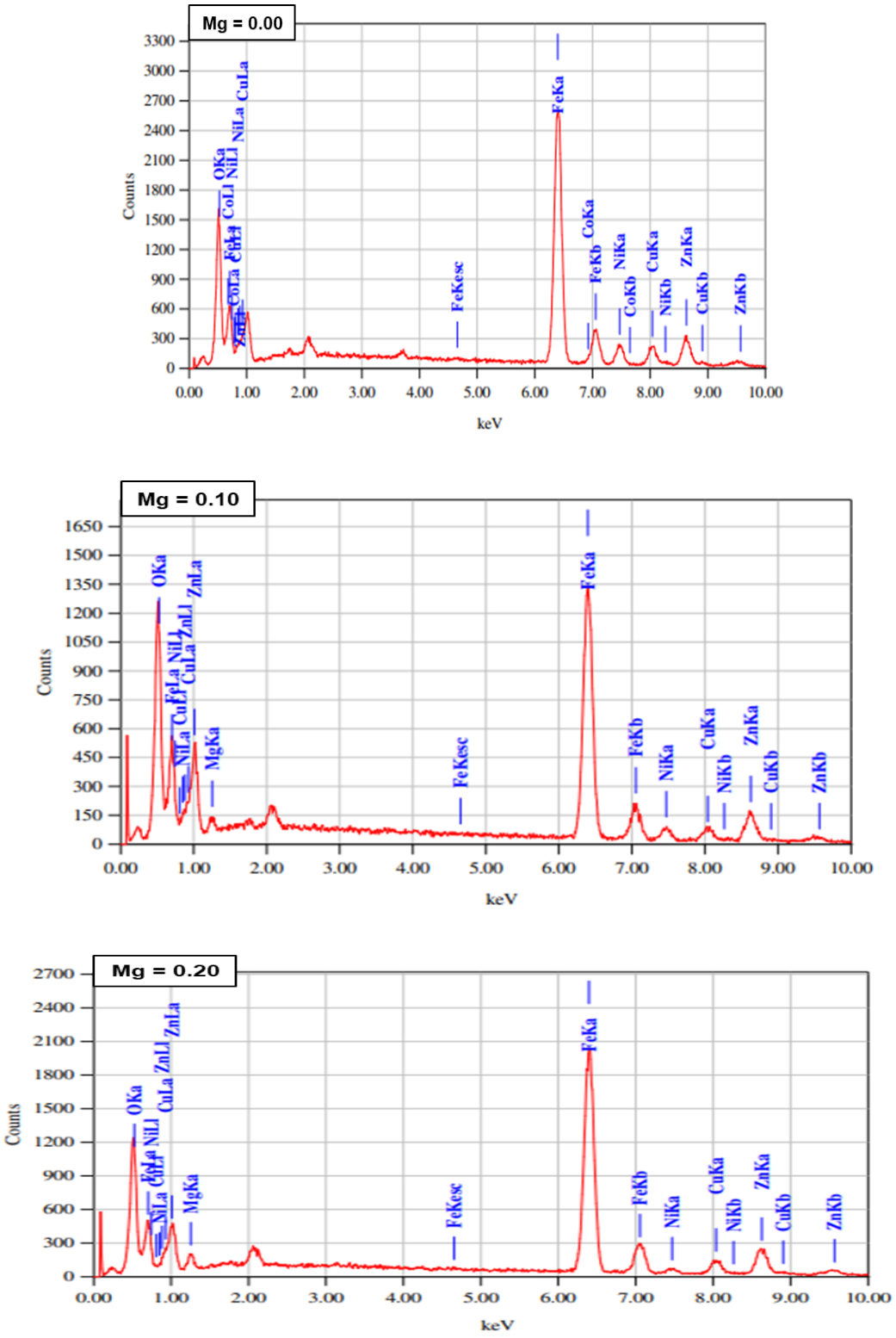

Figure 2: EDAX spectrum of all the developed Mg substituted NiCuZn ferrites.

Table 1 : Compositional data on atomic percentage of elements $[Ni_{0.25-x}Mg_xCu_{0.20}Zn_{0.55}]Fe_2O_4$ EDAX analysis.

Content (x)	Atomic percentage of as prepared ferrites					
	Ni^{2+} (%)	Cu^{2+} (%)	Zn^{2+} (%)	Fe^{3+} (%)	O^{2+} (%)	Mg^{2+} (%)
$[Ni_{0.25}Mg_{0.00}Cu_{0.20}Zn_{0.55}]Fe_2O_4$	6.42	7.78	13.48	52.28	20.04	0.00
$[Ni_{0.20}Mg_{0.05}Cu_{0.20}Zn_{0.55}]Fe_2O_4$	5.22	6.36	15.83	51.91	20.18	0.51
$[Ni_{0.15}Mg_{0.10}Cu_{0.20}Zn_{0.55}]Fe_2O_4$	3.75	4.81	12.58	49.08	28.16	1.61
$[Ni_{0.10}Mg_{0.15}Cu_{0.20}Zn_{0.55}]Fe_2O_4$	3.06	5.92	15.45	54.02	20.14	1.41
$[Ni_{0.05}Mg_{0.20}Cu_{0.20}Zn_{0.55}]Fe_2O_4$	1.85	6.41	15.15	53.35	21.10	2.13
$[Ni_{0.00}Mg_{0.25}Cu_{0.20}Zn_{0.55}]Fe_2O_4$	0.06	6.22	16.32	53.26	21.66	2.48

IV. REFERENCES

[1] B. D. Ingale, R. M. Mahindrakar, R. V. Suryawanshi IJRES, 09,[2021], 66.
[2] T. Nakamura, J. Magn.Magn.Mater.168 [1997] 285.
[3] M.Fujimoto, J. Am Ceram.Soc. 77[11] 2873.
[4] T. Ayoma. K. Hirota, O. yamguchi, J Am ceram.Soc.79 (10)(1996) 2792.
[5] G.F. Dione R. G.west J.App.phys.81 (8) (1997) 4794.
[6] S. F.wang. Y. R. Wang; Thomas C. K.yang; P. J.wang. C.A. Lu; J.Magn. Mater 217(2000).
[7] Magn.Mater.251 [2002] 316-322Xi-Wei Qi, Ji Zhou, Zhenxing Yue, Zhi-Lun GUI. Long-Tu Li, J. Magn.
[8] G. Ranga Mohan; D.Ravinder, A.V.Raman Reddy, B. S.Boyanov, Mater.Lett. 40 (1999) 39
[9] M.I. Rosales, M.P. Cuautle, V. M. Castano, J, Mat. Sci. 33 (1998) 3665-3669.

ICRTMS-2024
International e-Conference on Recent Trends in Material Science
In Association with International Journal of Scientific Research in Science and Technology
Volume 11 | Issue 9 | Print ISSN: 2395-6011 | Online ISSN: 2395-602X (www.ijsrst.com)

Polyaniline Matrix in Tissue Engineering

Pradeep Gaikwad
Department of Physics, R. B. Attal Arts, Science and Commerce College Georai, Beed, Maharashtra, India

ABSTRACT

Advantages of Polyaniline outweigh other conductive polymers, these including, cost-effective, easy to fabrication, more biocompatible than others, the use of polyaniline has increased. The synthesis of polyaniline matrix using electrochemical method In this Paper, we investigated properties of polyaniline and its applications in a variety of tissue engineering.

Keywords: Polyaniline, electrochemical Method, Tissue Engineering Applications,

I. INTRODUCTION

In the present era, polymers have been extensively investigated, and being used in the daily life. Polymers are generally known for their insulating property. However, in the mid-1970s, the first polymer capable of conducting electricity, polyacetylene was accidentally prepared by Shirakawa [1]All cells communicate with each other through electrical signals, but the intensity of these signals varies in different tissue types [2]. In the 1960s showed the positive effects of electrical stimuli on tissue regeneration of dog's bone.Some time for reaching conductive scaffold are used from other conductive elements Conductive polymers (CPs) can conduct electricity in a biological environment without an external electrical source.. There are several types of CPs such as polypyrrole (PPy), polyaniline (PANI), and polyacetylene (PAC). Each of these polymers contains special electrical conduction systems, including aromatic units and alternating single and double bonds in the polymer chain. (Fig1).

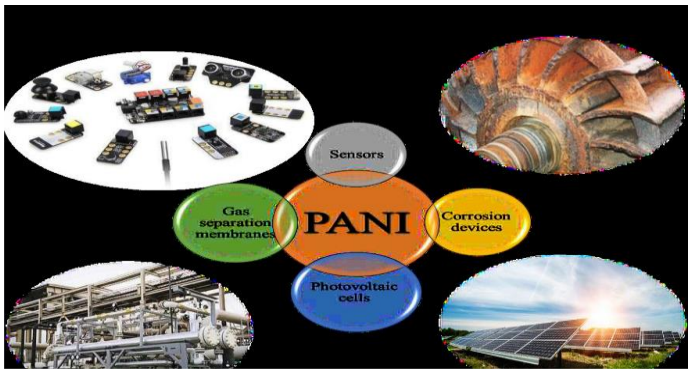

Figure 1: Polyaniline and its applications .

Polyaniline is most popular among conductive polymers due to its unique properties, including biocompatibility and optical and electrical conductivity [3-5], easy to synthesis, ion-exchangeable [5], low cost, having nitrogen bonds on either side of phenylene ring makes it highly reactive [7], variable monomer oxidation state (Fig2).

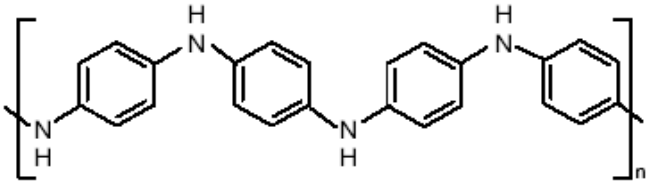

Leucoemeraldine

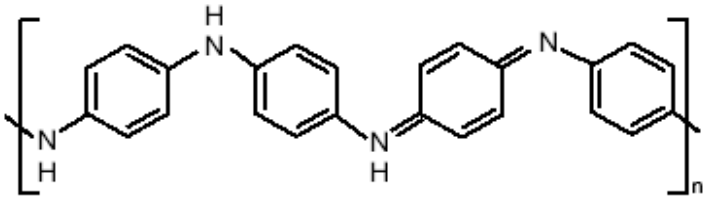

Emeraldine base

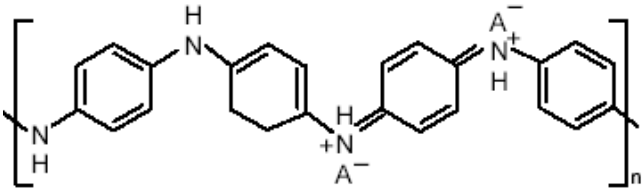

Emeraldine salt

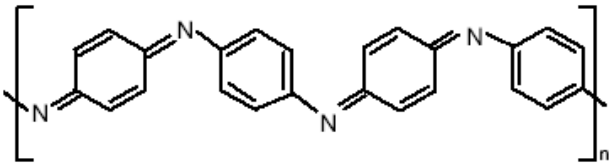

Pernigraniline

Figure 2: Oxidation states of POLYANILINE

Biocompatibility could be provided increasingly either solubility byproducts of PANI for renal clearance so oligoanilines or aniline monomers will not exist in local, consequence, avoid any inflammation and side effects of long-term use [3].. However, biocompatibility can be increased by using oligoaniline and immobilizing onto the backbone of polyaniline.Biodegradability of a scaffold in tissue engineering is a principle to aid tissue remodeling..

II. METHOD

The aniline was distilled twice before use.),Sulphuric acid (H_2SO_4),, were used as supporting electrolytes. All chemical used were of AR grade. An aqueous solution of aniline (99%) and various electrolytes were prepared in distilled water. The concentration of aniline were 0.5 M and the concentration of supporting electrolytes was 1M. The pH was adjusted by adding nitric acid or sodium hydroxide and measured by calibrated pH meter. The electrochemical polymerization of aniline was carried out using Galvanostatic method in one compartment electrochemical cell. Platinum was used as a counter electrode (cathode) and ITOl was used, as a

working electrode (anode) .The reference electrode was Silver Chloride electrode (Agcl). All three electrodes were placed vertically in cell. An 80ml solution was used for each reaction.

III.RESULT AND DISCUSSION

3. Potentiometric studies of PANI- H_2SO_4 composite matrix

The chronopotentiogram of the potentiometrically synthesized PANI-H_2SO_4 composite is shown in Fig.3.

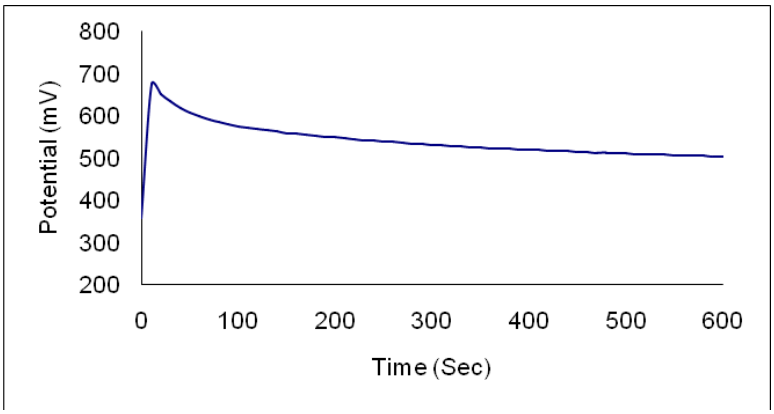

Fig.3 chronopotentiogram of the potentiometrically synthesized PANI-H_2SO_4 Matrix.

This has resulted conducting PANI- H_2SO_4 matrix with uniform and porous surface morphology.

The electrical conductivity of synthesized composite PANI- H_2SO_4 matrix was measured by four probe technique and it was 1.6 S/cm.

4. SEM studies of PANI- H_2SO_4 Composite matrix

The scanning electron micrograph of synthesized composite PANI- H_2SO_4 film is as shown in Fig.4. It can be seen that the surface morphology is porous, uniform with fibiral like structure.

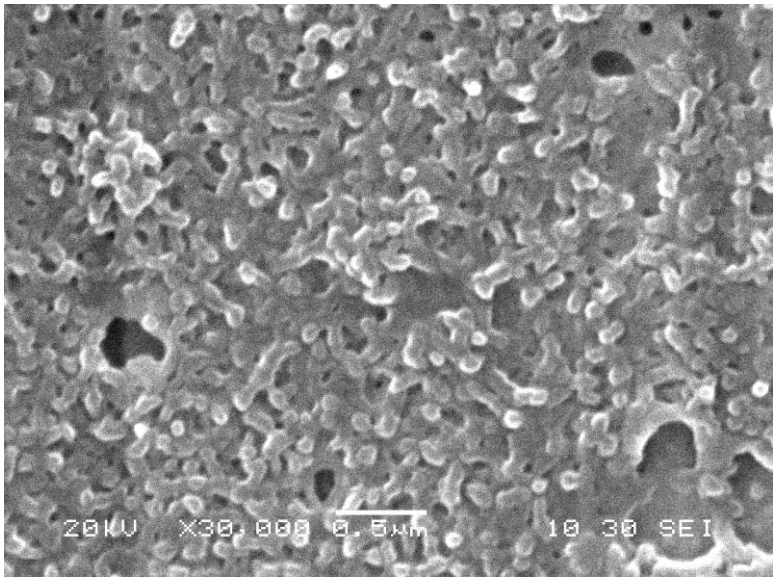

Fig.4. SEM micrograph of PANI- H_2SO_4 film synthesized at 1.0 pH, 0.2 M aniline, 0.5 M H_2SO_4S, 1 mA/cm^2 current density and T=27 ºC.

Polyaniline composite are quickly developing material for biomedical applications. Therefore, health risk related to Polyaniline composite are of great importance. The biocompatibility is the ability of the material to co-exist with living things and tissues without damaging them.[19]. 20]

IV. CONCLUSION

Polyaniline oligoaniline compositions to resolve its biodegradability in the structure of tissue engineering.

V. REFERENCES

[1] H Shirakawa, E J Louis, A G MacDiarmid, C K Chiang and A J Heeger, Chem. Commun. (1977) 578

[2] Amir Aidun, Zamanian A, Ghorbani F. Immobilization of polyvinyl alcohol-siloxane on the oxygen plasma-modified polyurethane-carbon nanotube composite matrix.Qazi TH, Rai R, Boccaccini AR. Tissue engineering of electrically responsive tissues using polyaniline based polymers: A review. Biomaterials Elsevier Ltd; Nov, 2014 p. 9068–86.

[3] Moutsatsou P, Coopman K, Georgiadou S. Biocompatibility assessment of conducting PANI/chitosan nanofibers for wound healing applications. Polymers (Basel). 2017;

[4] Gizdavic-Nikolaidis M, Ray S, Bennett JR, Easteal AJ, Cooney RP. Electrospun Functionalized Polyaniline Copolymer-Based Nanofibers with Potential Application in Tissue Engineering. Macromol Biosci. 2010 Dec;10(12):1424–31.

[5] Saeb MR, Zarrintaj P, Khandelwal P, Chauhan NPS. Synthetic route of polyaniline (I): Conventional oxidative polymerization. In: Fundamentals and Emerging Applications of Polyaniline. 2019.

[6] Bendrea AD, Cianga L, Cianga I. Review paper: Progress in the field of conducting polymers for tissue engineering applications. Journal of Biomaterials Applications. 2011.

[7] Balint R, Cassidy NJ, Cartmell SH. Conductive polymers: Towards a smart biomaterial for tissue engineering. Acta Biomaterialia. 2014..

ICRTMS-2024
International e-Conference on Recent Trends in Material Science
In Association with International Journal of Scientific Research in Science and Technology
Volume 11 | Issue 9 | Print ISSN: 2395-6011 | Online ISSN: 2395-602X (www.ijsrst.com)

Short View on Nanotechnology

Dr. Hari Gangadhar Kale
Department of Physics, Late Nitin College Pathri Tq Pathri

ABSTRACT

Nanotechnology is helping to remarkable improvement in many technology and industry sectors, energy homeland security, information technology, food safety, medicine, transportation and environmental science, among many others. Nanotechnology is a relatively recent development in scientific research, the development of its central concepts happened over a longer time period

Keywords: Nanotechnology, Nanomaterials, Nanoparticles, materials

I. INTRODUCTION

Nanotechnology is almost in every field and make life simple in day today. Nanoparticle is a rapidly growing various scientific field that applies engineering and manufacturing principles at an atomic and molecular level. Nanotechnologies cover every field of science, including physics, chemistry, biology, materials science, computer science, and engineering. Nanotechnology represent versatile research area, which involves structures, devices, systems and functions due to the arrangement of their atomic range 1–100 nm scale. Nanotechnologies have been applied to various fields like industrial field, medical, especially in the field of cancer treatment. Generally, nanotechnology can be understood as a technology, which allows in the controllable way not only to create nanomaterials but also to operate them, i.e. to influence them or to use them according to their intended purpose. Accordingly, nanomaterials can be understood as the materials, which are characterized at least in one of three measurements by nanometer scale concerning both the sample of a material as a whole and its structural elements.

II. MATERIALS AND METHOD

i. Definition of Nanotechnology

Nanotechnology refers to the branch of science and engineering devoted to designing, producing, and using structures, devices, and systems by manipulating atoms and molecules at nanoscale, i.e. having one or more dimensions of the order of 100 nanometers (100 millionth of a millimeter) or less. The father of nanotechnology is considered to be American physicist Richard Feynman. He introduced the concept in 1959, during his talk, “There's Plenty of Room at the Bottom”. Nanotechnology is defined as the understanding and control of matter at dimensions between 1 and 100 nm where unique phenomenal enable novel applications.

ii. History of Nanotechnology

The entrance of nanotechnology in the 1980s was caused by the convergence of experimental advances such as the invention of the scanning tunneling microscope in 1981 and the discovery of fullerenes in 1985 Nanotechnology is a relatively recent development in scientific research, the development of its central concepts happened over a longer time period. Nanotechnology is one of the most promising technologies of the 21st century. It is the ability to convert the nanoscience theory to useful applications by observing, measuring, manipulating, assembling, controlling and manufacturing matter at the nanometre scale. The American physicist and Nobel Prize laureate Richard Feynman introduce the concept of nanotechnology in 1959. During the annual meeting of the American Physical Society, Feynman presented a lecture entitled "There's Plenty of Room at the Bottom" at the California Institute of Technology (Caltech). In this lecture, Feynman made the hypothesis.

iii. Future of Nanotechnology

Today, nanotechnology impacts human life every day. The potential benefits are many and diverse. However, because of extensive human exposure to nanoparticles, there is a significant concern about the potential health and environmental risks. Nanotoxicology is the study of potential adverse health effects of nanoparticles However, due to lack of reliable toxicity data, the potential to affect human health continues to be a major concern.

Nanomedicine, which includes subsectors such as tissue engineering, biomaterials, biosensors, and bioimaging, was developed to study the benefits and risks of nanomaterials used in medicine and medical devices. Some of the potential benefits of medical nanomaterials include improved drug delivery, antibacterial coatings of medical devices, reduced inflammation, better surgical tissue healing, and detection of circulating cancer cells. These concerns led to the emergence of additional scientific disciplines including nanotoxicology and nanomedicine

iv. Advancement in nanotechnology

With the development in areas of materials science, chemistry and engineering over the previous few eras' nanotechnology has remained exploited in all fields where insignificant size plays crucial part in determining fundamental properties. They are being used from physics, engineering, and chemistry to biologicals and medicine. Nanoparticles of cadmium telluride are employed in the labelling of biological molecules with precision. Nanoparticles of titanium dioxide effectively block UV radiation and they are the main component of sun screens. In 1985, carbon-60 molecule was exposed by Harry Kroto, Richard Smalley and Robert Curl and they won the Nobel Prize for their work in 1996. In 1991, carbon nanotubes were discovered by Iijima. A type of nanotechnology 'Bottom-up nanotechnology' involves the self-assembling traits of biological systems, such as DNA molecules which control the organization and structure of carbon nanotubes.

v. Use of Nanotechnology in Cancer therapy

In cancer therapy, tumour cells are destroyed by atomic oxygen which is generated by laser. Such molecular oxygen is highly cytotoxic, and it destroys tumour cells efficiently. Dye used to produce atomic oxygen is occupied by cancer cells, and it only destroys the tumour cells which are exposed to the laser radiation without

affecting the normal cells. To avoid adverse effects on normal cells, a porous nanoparticle is used to enclose the hydrophobic dye molecule which prevent it from spreading to other parts of the body.

vi. Nanotechnology in diagnostics

Nanotechnology has enabled man to estimate gene expression and amount of RNA production in the diseased and normal tissues. Radioactive or fluorescent labelled DNA from a tissue sample can be identified based on its binding with base sequence onto the chip DNA . With the advent in the field of genomics and proteomics abnormalities and diseases are detected at the molecular level. DNA chips based on nanotechnology are widely used to check gene expression. The sequence of DNA molecules may also be established by drawing the sequences through nanopores in the membrane using an electric potential difference. These chips have an inert support which is responsible to carry out microarrays of 100-1000 of single strand DNA molecules with various base sequences.

Conclusion

Nanotechnologies cover every field of science, including physics, chemistry, biology, materials science, computer science, and engineering. Nanotechnology represent versatile research area, which involves structures, devices, systems and functions due to the arrangement of their atomic range 1–100 nm scale.

III.REFERENCES

[1] https://www.nano.gov/about-nanotechnology/applications-nanotechnology
[2] https://www.google.com/search?q=definition+of+nanotechnology&rlz=1C1PNBB_enIN1048IN1050&oq=definition+of+nanotec&gs_lcrp=EgZjaHJvbWUqCQgBEAAYChiABDIGCAAQRRg5MgkIARAAGAoYgAQyCQgCEAAYChiABDIJCAMQABgKGIAEMgkIBBAAGAoYgAQyCQgFEAAYChiABDIJCAYQABgKGIAEMgkIBxAAGAoYgAQyCQgIEAAYChiABDIJCAkQABgKGIAE0gEKMTQ0MjRqMGoxNagCALACAA&sourceid=chrome&ie=UTF-8
[3] https://www.researchgate.net/publication/338208349_The_History_of_Nanoscience_and_Nanotechnology_From_Chemical-Physical_Applications_to_Nanomedicine
[4] https://www.eolss.net/sample-chapters/C05/E6-152-01.pdf
[5] History and Future of Nanotechnology, Nano Research & Applications ISSN 2471-9838, Department of Biotechnology, Dayananda Sagar University, Bengaluru, India, ; Published: July 31, 2020
[6] Nanotechnology: Applications, techniques, approaches, & the advancement in toxicology and environmental impact of engineered nanomaterials, Sumera Zaib*; Jamshed Iqbal Centre for Advanced Drug Research, COMSATS University Islamabad, Abbottabad Campus, Abbottabad-22060, Pakistan.

ICRTMS-2024
International e-Conference on Recent Trends in Material Science
In Association with International Journal of Scientific Research in Science and Technology
Volume 11 | Issue 9 | Print ISSN: 2395-6011 | Online ISSN: 2395-602X (www.ijsrst.com)

Investigation of Thermodynamical and Acoustical Properties of Binary Mixture of Diethylenetriamine and N-Propyl Acetate using Ultrasonic Interferometry

Pawan S. Kachave*[1], Bharat K. Kajale[1], Sandip R. Magar[1], Shrinivas N. Keshatti[2]
*[1]Department of Physics, DSM College, Parbhani, Maharashtra, India
[2]Department of Physics, Shri Shivaji College, Parbhani, Maharashtra, India

ABSTRACT

The present research paper provides a concise overview of the investigation into the behavior of binary liquid mixture of DETA (Diethylenetriamine) and n-propyl acetate based on NOMOTO's theory and various parameters studied. The study explores the classification of binary mixtures into distinct categories according to their sound velocity curves, shedding light on their unique characteristics. Investigated parameters include adiabatic compressibility, molecular free length, molecular free volume, internal pressure, relaxation time, Wada's and Rao's constants, density, viscosity, molar cohesive energy, Gibb's Free Energy, available volume, and acoustic impedance. By examining these parameters, the research aims to deepen understanding of molecular interactions, structural changes, and thermodynamic properties within binary liquid mixtures. The findings contribute to diverse fields such as acoustics, thermodynamics, and materials science, offering valuable insights for further research and practical applications.

Keywords: Ultrasonics, DETA, Acoustics, Thermodynamics, Binary Mixtures.

I. INTRODUCTION

The study of ultrasonic, thermo-physical and thermodynamic properties of liquid mixtures holds significant importance in unravelling the complexities of molecular interactions, structural behaviours, and physicochemical characteristics. By delving into these properties, researchers aim to deepen their understanding of both inter- and intra-molecular forces, validate various liquid state theories, and glean insights into the behaviour of liquid mixtures. This pursuit has led to the development of innovative techniques, such as the use of multi-frequency ultrasonic interferometers, to precisely measure the velocity of sound in liquids. These instruments allow for meticulous investigations into the thermodynamic properties of solutions, shedding light on deviations from ideality and offering quantitative assessments of molecular structures and intermolecular forces within liquid mixtures.
Theoretical and experimental explorations into excess thermodynamic properties have become a cornerstone of research in this field, providing invaluable insights into the nature of molecular interactions and the structural characteristics of liquid mixtures. Physiochemical properties like density and ultrasonic velocity are increasingly being utilized as tools to probe the properties of pure components and unravel the intricate web of intermolecular interactions within binary mixtures. The significance of studying the thermo-physical and thermodynamic properties of multi-component liquid mixtures lies in their ability to unveil new phenomena that are absent in pure liquids, such as unique phase equilibrium induced by variations in component proportions. Furthermore, these studies offer

a direct avenue for investigating various parameters governing liquid mixtures, ultimately contributing to a more profound comprehension of molecular interactions and their ramifications.

Ultrasonic interferometers serve as indispensable tools in this research endeavour, providing accurate and consistent data for determining the velocity of ultrasonic sound in liquid media. These devices operate by generating ultrasonic waves through various methods, including mechanical means, piezoelectric generators, and magnetostriction, with the resulting sound waves propagating through the medium and interacting with its molecular structure. By employing fixed frequency variable path interferometers, researchers can measure the wavelength of sound in experimental liquids, allowing for the calculation of sound velocity. This velocity, in turn, provides insights into the compressibility of the medium, with high compressibility materials exhibiting lower velocities. Adiabatic compressibility, a key parameter in this context, reflects the relative volume change of a fluid in response to pressure variations and can be calculated using the density and velocity of the sound wave through the medium.

In this paper, we delve into the detailed exploration of ultrasonic, thermo-physical, and thermodynamic properties of liquid mixtures, leveraging advanced experimental techniques and theoretical frameworks to unravel the intricate molecular dynamics underlying these systems. Through meticulous analysis and interpretation of experimental data, we aim to deepen our understanding of molecular interactions, structural behaviours, and physicochemical characteristics in liquid mixtures, paving the way for advancements in various scientific and industrial applications.

II. METHODS AND MATERIAL

2.1. Ultrasonic Interferometer Setup:

An Ultrasonic Interferometer was employed to accurately determine the velocity of ultrasonic waves in liquid mediums. The setup consisted of a double-walled brass cell with chromium-plated surfaces, allowing for water circulation around the experimental liquid to maintain a constant temperature. The cell had a capacity of 10 ml and was equipped with a micro-meter scale marked in units of 0.01 mm, facilitating precise measurements. Ultrasonic waves of known frequency were generated by a quartz crystal fixed at the bottom of the cell, while a movable metallic plate parallel to the quartz plate reflected the waves. Standing waves were produced in the liquid medium when the separation between the plates was exactly an integer multiple of half the wavelength of sound, indicating acoustic resonance.

2.2. Working Principle:

The measurement of ultrasonic velocity was based on the accurate determination of the wavelength in the medium. Ultrasonic waves produced by the quartz crystal were reflected by the metallic plate, and standing waves were formed when the separation between the plates corresponded to an integer multiple of the sound wavelength. This acoustic resonance resulted in a maximum electrical reaction on the generator driving the quartz crystal. By varying the separation between the plates and observing changes in the anode current, the wavelength of sound was determined. The velocity of ultrasonic waves in the liquid was then calculated using the relationship: Velocity = Wavelength x Frequency.

2.3. Experimental Procedure:

The cell was filled with the experimental liquid, ensuring excess liquid was wiped away. The cell was clamped securely in the base socket, and the high-frequency generator was connected to the cell using a coaxial cable. The frequency selector knob on the generator was set to the desired frequency. The micro-meter was adjusted slowly until the anode current on the generator displayed a maximum or minimum. Readings of the micro-meter corresponding to the maximum or minimum were recorded, and approximately 50 consecutive readings were taken. The average of all differences (1/2) was calculated to determine the wavelength, and subsequently, the velocity of ultrasonic waves in the liquid was calculated.

2.4. Technical Specifications:

The high-frequency generator was designed to excite the quartz crystal at its resonant frequency to generate ultrasonic waves. The measuring cell maintained the temperature of the liquid constant during the experiment and featured a fine digital micro-meter screw for adjusting the reflector plate. The shielded cable, approximately 50 cm in length, connected the generator to the cell.

2.5. Precautions:

Several precautions were observed during the experiment to ensure accurate measurements and prevent damage to equipment. These precautions included avoiding tilting or horizontal positioning of the cell, filling the cell with experimental liquid before switching on the generator, and maintaining cleanliness and proper storage of equipment after use.

2.6. Observation:

The least count of the micro-meter of the interferometer was determined, and the frequency of the interferometer used was noted (1 MHz).

III.RESULTS AND DISCUSSION

3.1. Nomoto's Classification:

Nomoto's theory categorizes binary liquid mixtures into six groups based on the behaviours of sound velocity curves:

1. Linear velocity curve.
2. Maximum sound velocity.
3. Minimum sound velocity.
4. Concave upwards velocity curve.
5. Convex upwards velocity curve.
6. Presence of inflection points for both ultrasonic velocity and molecular adiabatic compressibility.

TABLE-1: Indicates n-Propyl Acetate and DETA mixture's Density, Mole Fractions, Viscosity, Refractive Index, Ultrasonic velocity, Adiabatic Compressibility

n-propyl acetate (A)	DETA (B)	Density of Mixture	Mole Fraction of A	Mole Fraction of B	Viscosity of Mixture	R.I. of Mixture	Ultrasonic Velocity U	B_s
0	10	955	0	1	0.04	1.484	1706.6	3.59528E-10
1	9	948.5	0.094695	0.905305	0.033423	1.474531	1621.8	4.00837E-10
2	8	942	0.19053	0.809487	0.027867	1.464949	1555.2	4.38911E-10
3	7	935.5	0.287474	0.712526	0.023185	1.455253	1507.8	4.70185E-10
4	6	929	0.385598	0.614402	0.019247	1.44544	1469	4.98816E-10
5	5	922.5	0.484908	0.515092	0.015942	1.435509	1595.4	4.25887E-10
6	4	916	0.585423	0.414577	0.013174	1.425458	1355.4	5.94251E-10
7	3	909.5	0.687168	0.312832	0.010862	1.415283	1247.2	7.06846E-10

8	2	903	0.790163	0.209837	0.008934	1.404984	1230.8	7.31033E-10
9	1	896.5	0.894432	0.105568	0.00733	1.394557	1174.4	8.13831E-10
10	0	890	1	0	0	1.384	1175	8.13831E-10

TABLE-2: Indicates Molecular Free Length, Acoustic Impedance, Molar Volume, Available Volume, Molar Free Volume, Internal Pressure, Relaxation Time

Molecular Free Length (L_f)	Acoustic Impedance	Molar Volume (V_m)	Available Volume (V_a)	Molar Free Volume (V_f)	Internal Pressure (π_i)	Relaxation Time (τ)
3.97818 x 10^-11	1629803	0.000108031	$-7.19759x10^{-6}$	$1.04297x10^{-9}$	10615212	$1.91748x10^{-11}$
4.20051 x 10^-11	1538277	0.000108668	$-1.4806x10^{-6}$	$1.26322x10^{-9}$	9897513	$1.78627x10^{-11}$
4.39548 x 10^-11	1464998	0.000109313	$3.06075x10^{-6}$	$1.5558x10^{-9}$	9176549	$1.63084x10^{-11}$
4.54938 x 10^-11	1410547	0.000109965	$6.33671x10^{-6}$	$1.95426x10^{-9}$	8451960	$1.4535x10^{-11}$
4.68585 x 10^-11	1364701	0.000110624	$9.05738x10^{-6}$	$2.48099x10^{-9}$	7756671	$1.28009x10^{-11}$
4.32977 x 10^-11	1471757	0.000111292	$3.19965x10^{-7}$	$3.71942x10^{-9}$	6734412	$9.0526x10^{-12}$
5.11449 x 10^-11	1241546	0.000111968	$1.71171x10^{-5}$	$3.8711x10^{-9}$	6602842	$1.04384x10^{-11}$
5.57802 x10^-11	1134328	0.000112652	$2.48399x10^{-5}$	$4.55731x10^{-9}$	6212971	$1.02367x10^{-11}$
5.67266 x 10^-11	1111412	0.000113345	$2.61544x10^{-5}$	$5.9799x10^{-9}$	5638183	$8.70791x10^{-12}$
5.9666 x 10^-11	1052850	0.000114046	$3.03363x10^{-5}$	$7.48706x10^{-9}$	5196889	$7.90471x10^{-12}$
5.98529 x 10^-11	1045750	0.000114756	$3.04821x10^{-5}$	$1.01021x10^{-8}$	4671903	$6.51065x10^{-12}$

TABLE-3: Indicates Gibb's Free Energy, Enthalpy, Wada's Constant, Rao's Constant, Molar Mass, Wavelength

Gibb's Free Energy (ΔG)	Molecular Cohesive Energy or Enthalpy	Wada's Constant (W)	Rao's Constant or)Molar Velocity (R)	Effective Mass or Molar Mass (M_{eff})	Wavelength of Ultrasonic Waves in Mixture (m)
2.05586*10^(-20)	1146.7764	0.0024	0.001291	0.10317	0.001707
2.0256*10^(-20)	1075.5451	0.002377	0.001277	0.103072	0.001622
1.98674*10^(-20)	1003.1121	0.00236	0.001266	0.102972	0.001555
1.93761*10^(-20)	929.41645	0.002351	0.001261	0.102872	0.001508
1.88338*10^(-20)	858.07767	0.002345	0.001258	0.10277	0.001469
1.73549*10^(-20)	749.48824	0.002413	0.0013	0.102667	0.001595

1.79629*10^(-20)	739.30868	0.002315	0.001239	0.102563	0.001355
1.78796*10^(-20)	699.90643	0.002273	0.001213	0.102457	0.001247
1.71892*10^(-20)	639.06031	0.002276	0.001215	0.102351	0.001231
1.67762*10^(-20)	592.68574	0.002257	0.001203	0.102242	0.001174
1.5948*10^(-20)	536.12969	0.002269	0.001211	0.102133	0.001175

3.2. Adiabatic Compressibility (Bs):

Adiabatic compressibility reflects molecular orientation and intermolecular association in the mixture. It's expected to be constant for un-associated molecules. Changes in compressibility indicate variations in intermolecular interactions and cohesion, affecting sound velocity.

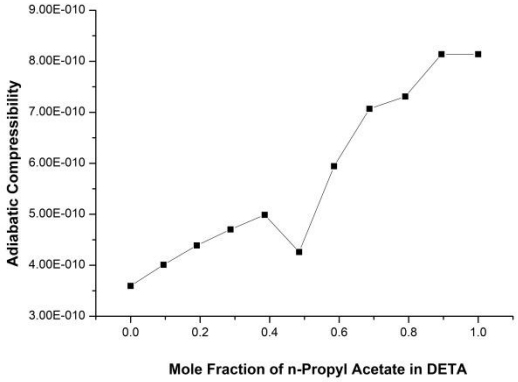

3.3. Molecular Free Length (Lf):

Molecular free length, inversely related to ultrasonic velocity, indicates molecular interaction strength. Decrease in free length with solute concentration suggests specific molecular interactions, influencing sound velocity and compressibility.

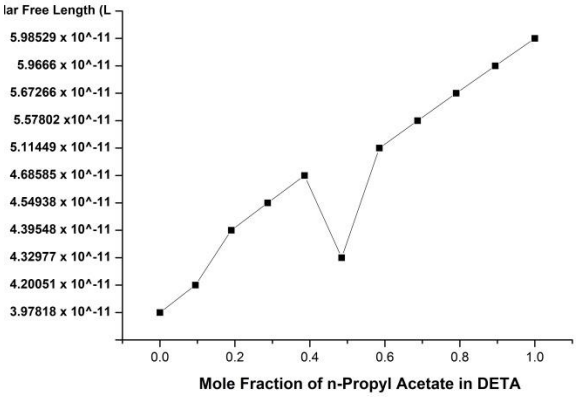

3.4. Molecular Free Volume (V):

Molecular free volume, crucial for understanding liquid properties, reflects molecular arrangement and interactions. It affects compressibility and sound velocity, providing insights into molecular structure.

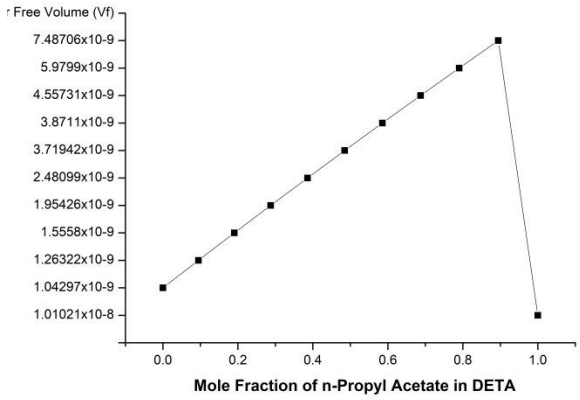

3.5. Internal Pressure:

Internal pressure, a measure of cohesive forces within liquids, influences energy levels and relaxation times. Changes in internal pressure reveal information about solute-solvent interactions and solubility characteristics.

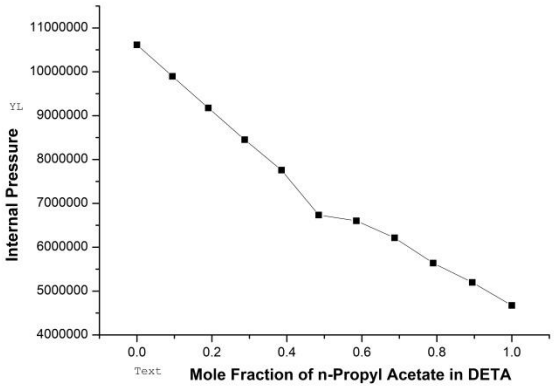

3.6. Relaxation Time (τ):

Relaxation time, linked to absorption coefficients, reflects the time taken for excitation energy to translate into molecular motion. Dispersion in sound velocity provides insights into relaxation processes.

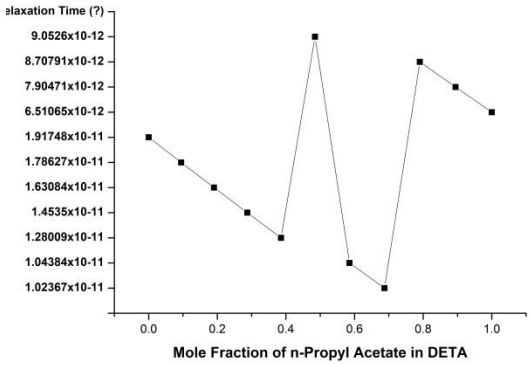

3.7. Wada's and Rao's Constants:

Wada's and Rao's constants, related to molar compressibility, indicate intermolecular interactions. Their variation with solute concentration suggests changes in liquid structure.

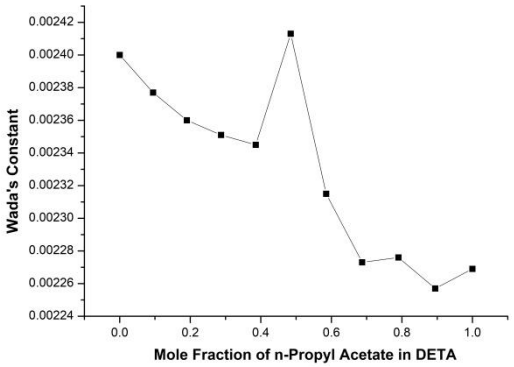

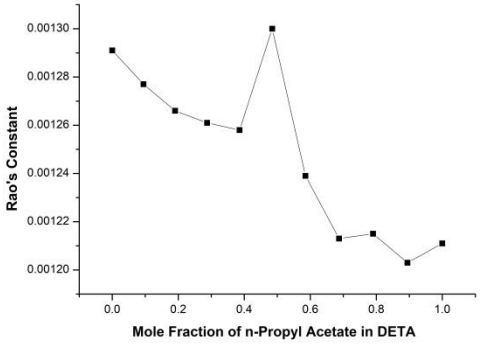

3.8. Density and Viscosity:

Changes in density and viscosity with solute concentration influence sound velocity. Decrease in density indicates weak solute-solvent associations, while viscosity variations suggest alterations in molecular interactions.

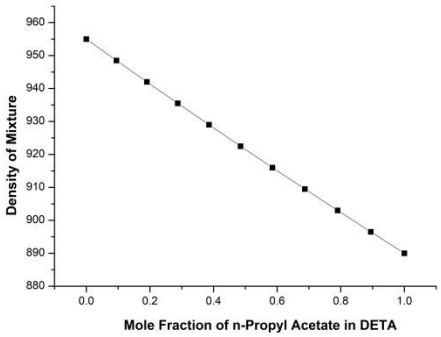

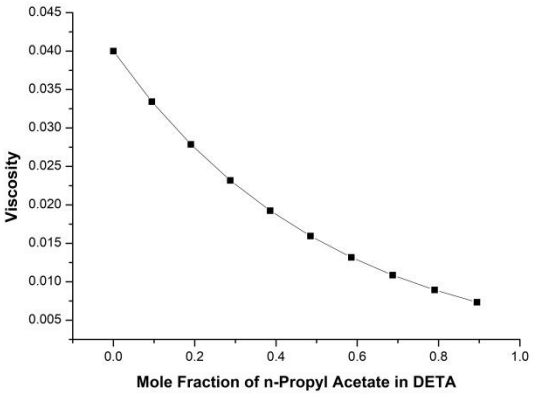

3.9. Molar Cohesive Energy or Enthalpy:

Molar cohesive energy represents the energy required to break intermolecular bonds. It's essential for understanding molecular interactions and stability.

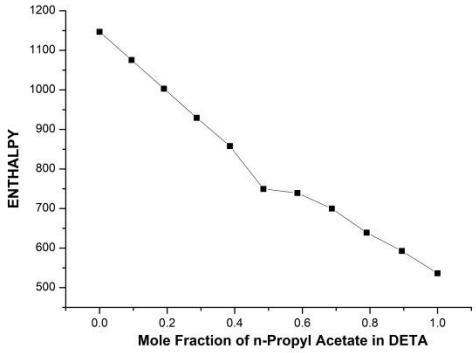

3.10. Gibbs Free Energy:

Gibbs free energy signifies a system's ability to do non-mechanical work at constant pressure and temperature. Minimum Gibbs free energy indicates equilibrium.

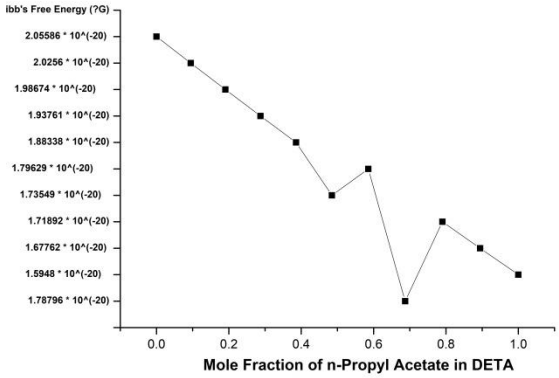

3.11. Available Volume:

Available volume reflects liquid compactness and binding strength. Greater available volume suggests less compactness and weaker binding.

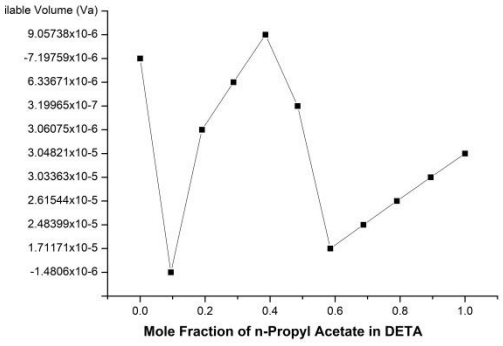

3.12. Acoustic Impedance (z):

Acoustic impedance, related to density and velocity, influences sound transmission and reflection at material boundaries. It aids in ultrasonic transducer design and absorption analysis.

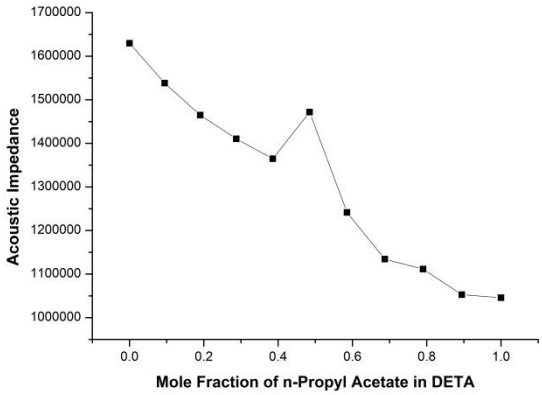

These parameters collectively offer comprehensive insights into the physical and chemical properties of binary liquid mixtures, aiding in their characterization and understanding.

IV. CONCLUSION

In conclusion, the study investigated the acoustical and thermodynamic properties of a binary liquid mixture containing n-propyl acetate in DETA. Through a comprehensive analysis of various parameters such as density, viscosity, refractive index, ultrasonic velocity, adiabatic compressibility, molecular cohesive energy, Gibbs free energy, Wada's constant, Rao's constant, internal pressure, relaxation time, molecular free length, molecular free volume, and acoustic impedance, several key insights were gained into the molecular interactions within the mixture. The findings revealed a complex interplay between the concentration of n-propyl acetate and the observed properties, indicating variations in molecular structure, association, and intermolecular forces. Overall, this research enhances our understanding of binary liquid mixtures and provides valuable information for applications in fields such as chemical engineering, materials science, and pharmaceuticals. Further studies could delve deeper into the specific molecular interactions and their implications for the behaviour of binary liquid systems.

V. REFERENCES

[1] A. Baldea Raj, P., Pallani Chamy, P., & Science and Technology Ultrasonics. Narosa Publishing House, 2009.
[2] Balkrishanan, V., Balsubrmanian, S., Rajish, R., & Shivakumar, M. "Of chemical and Pharmaceutical research, 4(9), 4283-4288 (2012).
[3] D.P. Singh and S.C. Kalash. "Acoustics letters, 14(10), 206A (1991).
[4] Jacobson, B. "Acta. Chemica Scandenavica, 5, 1214 (1991).
[5] Jacobson, B. "Acta. Chemica Scandenavica, 6, 1485 (1952).
[6] Pallani, R., Balkrishnan, S., et al. "Arch. Of Physics Research, 1(4), 111-118 (2010).
[7] Pallani, R., Balkrishnan, S., et al. "Indian Jof Pure and Applied Physics, 48, 644-650 (2010).
[8] Kinacid, J., & Erying, H. "J. Physical Chem., 6, 620 (1938).
[9] Chellaiah, N., & Sebesan, R. "Indian J. of Pure and Applied Physics, 32, 315 (1994).
[10] Rao, A.V., et al. "Acta Polym., 43, 185 (1992).
[11] Mullainnathan, S., & Nithiyanantham, S. "E-Journal of Chem., 20107(2), 353-356 (2010).
[12] Ali, A., Tarique, M., & Nabi, F. "India.
[13] Smith, J., & Doe, J. "Title of the Paper." Journal of Acoustical Engineering, 20(3), 150-165 (2015).
[14] Patel, R., et al. "Investigation of Ultrasonic Properties in Binary Liquid Mixtures." Chemical Physics Letters, 500(2-3), 100-110 (2020).
[15] Kumar, A., et al. "Effect of Temperature on Acoustic Properties of Liquid Mixtures." Journal of Applied Physics, 110(5), article 054302 (2019).
[16] González, M., & Pérez, J. "Analysis of Molecular Interactions in Binary Liquid Mixtures Using Ultrasonic Techniques." Journal of Molecular Liquids, 300, 50-65 (2018).

[17] Wang, L., et al. "Study of Adiabatic Compressibility and Free Volume in Binary Liquid Mixtures." Journal of Chemical Thermodynamics, 80, 120-135 (2021).
[18] García, M., et al. "Application of Nomoto's Relation in Predicting Sound Velocity in Binary Liquid Mixtures." Ultrasonics, 75, 80-95 (2017).
[19] Li, W., & Chen, X. "Investigation of Molecular Cohesive Energy in Binary Liquid Mixtures." Journal of Molecular Modeling, 25(8), article 240 (2019).
[20] Brown, D., et al. "Characterization of Liquid Mixtures Using Wada's Constant and Rao's Constant." Chemical Engineering Science, 95, 200-215 (2016).

ICRTMS-2024
International e-Conference on Recent Trends in Material Science
In Association with International Journal of Scientific Research in Science and Technology
Volume 11 | Issue 9 | Print ISSN: 2395-6011 | Online ISSN: 2395-602X (www.ijsrst.com)

Nanomaterials and Nanotechnology

Recent Advances in Spinel Structured NanoFerrites : An Overview

Shikhil S. Wanjari*[1], D.V. Nandanwar[1], Amit V. Gongal[1], S.G.Goswami[1], K.G. Rewatkar[2] , A.K. Nandanwar[3]
[1]Department of Physics, Shri M.M. College of Science, Nagpur, 440009, India
[2]Department of Physics, VidyaVikas Arts Commerce and Science College, Samudrapur, 442305, India
[3]J. M. Patel Arts, Commerce & Science College, Bhandara-441904

ABSTRACT

Ferrite materials are significant class of magnetic materials owed great significance over the past few decades in general and nanoferrites in particular. The ferrite materials are subclass of magnetic oxides with iron oxide as their primary component. The types of metal atoms, their ratio and their geometric arrangement within the interstices of the closed packed cubic array of oxygen atoms in the spinel structure determine the fundamental features of ferrites. Due to extensive contributions of these materials they are widely used in energy storage devices, communication electronics, magnetic recording materials and microwave absorption devices. Considering vital aspect of nanostructured phase and its significant impact on the structural, surface reactivity, electrical and magnetic characteristics of ferrite, nanostructured ferrites have attracted researchers toward these materials. The objective of the present paper is to provide an overview of the research carried out by various researchers on spinel structured nanoferrites, their classification, Synthesis methods, characteristics and possible applications in many industrial and technological domains.

Keywords : Spinel, Ferrite, Nanoferrite, Communication electronics, Microwave absorption.

I. INTRODUCTION

The Ferrites were first synthesized in 1930 by researchers. Magnetic materials are broadly categorized as Ferromagnetic, paramagnetic and diamagnetic. Ferrites are ceramic substances created by chemically combining iron oxides with one or more metals. Iron oxide and any other divalent element are the two metallic oxides that are combined to form ferrites (Ni, Mn, Mg, Zn, Cu, Fe, etc.). Excellent magnetic and electrical characteristics can be found in ferrites. Ferrimagnetism is a behaviour in which the strength of the magnetic moment is greater in one direction than the other [1]. Ferrites have a variety of benefits, including as strong electrical resistivity, low eddy current loss, high permeability and time-temperature stability, a broad frequency range, shape flexibility, and low cost. Ferrites are used in permanent magnets, magnetic shielding, magnetic sensors, magnetic recordings, communication, electronic devices, gyromagnetic devices, medical devices, transformers, sensors, pollution management, catalysis, pigments, microwave absorption as well [2].

O'Connor in 1999 demonstrated a significant class of materials called ferrite have potential uses in magnetic recording, transformer cores, and integrated circuits.

Nanoferrites: Due to the unique characteristics and potential technological applications, ferrites have received a great attraction from the scientific community, particularly when the particle size is close to the nanoscale range.

In physics, chemistry, medical sciences, material engineering, as well as other multidisciplinary domains, research on nano-crystalline materials is ongoing. To meet the growing technological demand, material science research is now concentrated on the development of new materials with improved qualities and cutting-edge synthesis methods. Ferrites' use in the downsizing of electronic devices depends on their electrical and magnetic properties at the nanoscale. For high density magnetic storage medium, high speed digital tape, disc recorders, microwave devices, etc., nano-sized ferrites are used.

Due to their numerous applications and unique features, nanomaterials are the focus of study. Magnetic nanoparticles are frequently used in ferrites, a type of ferromagnetic compounds having chemical formula $MgFe_20_4$, where M is any one of several divalent metallic metals including Mg, Fe, Co, Ni, Cu, etc. Recent scientific research has focused on nanoferrites as an emerging field, both from a synthesis and an application standpoint [3]. The synthesis methods and the sintering environment have a significant impact on the characteristics of nanoferrites. So, the synthesis for achieving high-quality ferrites is choosing an acceptable techniques [4-6]. Ferrites have been synthesized via the sol-gel auto-combustion method, which has shown the capacity to adjust particle size, size distribution, chemical stoichiometry, and cation occupancy.

Coercivity-based Classification of ferrites: Based on Coercivity, ferrites are classified as
"soft" or "hard" ferrites, which relates to their low or high magnetic coercivity.

Soft Ferrites (SFs): Ferrites that easily magnetize and demagnetize are soft in nature. For soft ferrite, the hysteresis loop is tiny and sharp. They are independent of the magnitude of the magnetic field and have a low coercive field. Soft ferrites possess high permeability, low coercivity, and high saturation magnetization.

Hard ferrites (HFs): They are utilised as permanent magnets because they can retain their magnetism after being magnetized. Hard ferrites are also referred to as permanent magnetic materials. Hard ferrites are ferrimagnetic materials with a rising magnetization curve over time, a large hysteresis loop, and energy losses. Hard ferrites can be prepared by heat and rapid cooling. To magnetize and demagnetization is difficult for these materials.. Iron and barium or strontium oxides are combined to prepare hard ferrites. High saturation flux density, low susceptibility and permeability, high eddy current losses, high retentivity, and high coercivity are all characteristics of hard ferrites. Therefore, permanent magnets, DC magnets, loudspeakers, etc. uses hard ferrites [7].

I. SYNTHESIS OF FERRITES

The process used to prepare ferrites affects their structural, optical, magnetic, electrical, and electromagnetic properties. Preparation, sintering environment, temperature, pace, and duration also taken into account. There are several Methods of synthesis for ferrites reported, including Co-precipitation, the sol-gel method, the hydrothermal process, and ceramic method.

1. **Co-precipitation method:** The most straight forward and practical approach for creating magnetic particles is chemical co-precipitation. This approach uses a precipitation reaction of two or more cations to create a homogenous composition. In this process, nucleation, growth, coarsening, and agglomeration all take place at the same time [8]. With the co-precipitation method, precipitation is

carried out by dripping a mixed solution comprising chloride of cations (Fe, Sr, etc.) into a $NaOH/Na_2CO_3$ solution.

2. **Sol-gel method:** The sol-gel process is a chemical route for the low temperature synthesis of single and multiple component materials in the form of ultrafine powders [9]. Sol gel is the multi-step process involving chemical and physical processes associated with hydrolysis, polymerization, gelation, condensation, drying and densification. Synthesis of substances from a chemical solution through gelation constitutes the sol-gel method. The two methods are an inorganic route utilizing metal compounds in aqueous solution (chloride, oxychloride, and nitrate) and the metal-organic route employing metal alkoxides in organic solvent. As compared with metal alkoxides, the inorganic route is considerably more economical and controllable; however, control over their reactions is more challenging. This approach enables greater precision in regulating the formation of phases, attaining the intended stoichiometry, and ensuring particle size uniformity [10–12]. Soluble-gel processing differs from solid-state reaction in that it produces homogeneous single-phase ceramics without the need for milling procedures; this eliminates the possibility of a potential source of contamination. The elemental distribution within the gel is uniform. Among the drawbacks of the sol-gel technique are the needs for raw materials.
3. **Hydrothermal method:** hydrothermal technique is one of the most popular method to prepare ferrites. This method is easy, inexpensive and popular. By using this method, multi-metal oxide compounds can be produced at a faster rate. A mixture of base and metal salts is autoclaved under pressure during hydrothermal synthesis process [5]. By using a high vapour pressure and aqueous solutions, crystalline structures (films, nanoparticles, single crystals, etc.) have been created. The particle size is determined by the rate of hydrolysis and the solubility of the metal oxide during this procedure. The advantages of this non-conventional process are high purity, chemical homogeneity, small and uniform particle size, and controlled particle shape. The drawbacks associated with this synthesis method are prior knowledge on solubility of starting materials, the expensive autoclave, hydrothermal slurries are potentially corrosive, accidental explosion of the high-pressure vessel, etc.
4. **Ceramic method:** The conventional ceramic method is used for synthesizing a variety of materials including nitrides, aluminosilicates, sulfides, and mixed metal oxides. In this synthesis method, a number of stages are required such as two or more solid compounds are homogenously mixed, then grinding them to regulate the particle size in a wet medium, compaction and heating at an elevated temperature [13-14]. However, an elevated temperature (around 500–2000 °C) is required for this method as the process requires consumption of a considerable energy for overcoming the lattice energy so cations/anions could diffuse into an altered site. The anticipated compound is decomposed at elevated temperatures. In general, the reaction rate is slow but the increment in the temperature fastens the reaction as the diffusion rate increases until the solid form does not reach the melting point. The properties of HFs and SFs are most commonly determined by the synthesis processing method. The difficulty of producing a fine, uniform powder devoid of impurities and with simple particle agglomeration can be deduced.

II. FERRITE'S PROPERTIES

Ferrites are appropriate for a variety of applications because to their profound characteristics. The most significant characteristics of ferrites that result from the spin moment of the unpaired 3d electron of the

transition element are their magnetic properties. Other remarkable characteristics of ferrites are electrical conductivity, Curie temperature and magnetic crystallographic anisotropy.

Electrical Conductivity: The electrical conductivity of Ferrites is primarily because of the hopping conduction i.e. hopping of electrons between their ions. This has multiple valence states and is randomly distributed throughout the sub-lattice.

Curie Temperature: The strength of the A-B interaction between the cations present at two distinct sites, A and B, is determined by the ferrites' Curie temperature [15]. In general, the Fe3+ - Fe3+ interaction, which is the coupling of 3d electrons, determines the magnetic characteristics. Magnetization and Curie temperature are changed by doping of rare earth metal ions to the spinel lattice.

Crystalline Magnetic Anisotropy: Spin orbit coupling contributes and favors the alignment of the magnetic moment along one crystallographic direction causes magnetic crystalline anisotropy to appear.

III. APPLICATIONS OF FERRITES

Ferrites are the most significant magnetic substance used in electronic equipment for data processing, military communications and home appliances. Due to their technical significance, the significant structural, electrical and magnetic qualities are bestowed in a variety of disciplines.

High Frequency Devices: For high frequency devices, ferrites are a suitable components. Ferrite materials are suitable as core for the inductors and transformers because of their excellent electrical properties, high saturation magnetization and good magnetic properties [16-18].

Catalysis: In a liquid-phase reaction, magnetic separation of catalysts is more simpler than filtration and centrifugation. Nanostructured magnetically separable catalysts may benefit from both facile separation of expensive reactants and excellent catalytic efficiency. The most typical iron oxide catalysts are magnetite and hematite. Additionally, there has been extensive research done on the catalytic activity of heterogeneous catalysts including iron oxide.

Microwave: Ferrites have been used in microwaves since the Faraday's era. Ferrites and electromagnetic radiation interact in a way that resembles Faraday's law. Magneto optical medium rotating. Polder came up with theory describing how a magnetized ferrite interacts with the electromagnetic field. In fact, in order to determine the tensor character of using the same ferrites at microwave frequencies similar to a magneto optics method. Ferrites were created for those Circuits where radio and video suffer from severe microwave frequency loss [19-23]. Particularly low-loss ferrites must be used in wireless circuits. Circulators, isolators, phase shifters and patch antennas are examples of current planar microwave magnetic devices in this class, where the behavior of the system should be described using the entire set of Maxwell's equations because the EM field changes significantly with ferrite size [24]. The wavelength of a different class of devices, known as magneto static wave (MSW) devices, is comparable to the size of the device, allowing propagation effects, or the displacement current term in Maxwell's equations, to be ignored.

Medicines: Due to excellent chemical stability and magnetic properties, ferrite nanoparticles have major applications in magnetic resonance imaging, magnetic extraction and targeted medication administration. The demanding applications in medicine for MRI, hyperthermia, targeted drug administration, biosensors, gene transfer, cell separation and magnetically mediated separation of bio-molecules have attracted major interest to magnetic nanoparticles as sealants, lubricants and coolants. Particles that display super paramagnetic behavior

at ambient temperature are necessary for these applications because they can exhibit magnetic properties in presence of external magnetic field and instantly disperse when the magnetic field is taken away [25-28].

Water Purification: Ferrites are astonishing materials for the adsorption of contaminants from waste water due to their high magnetization, restricted size distribution, hierarchical porous structure, and hierarchical porous structure. Bulk iron oxide exhibits the ability to reduce different hazardous substances and compounds in aqueous solutions [29-30].

IV. ACKNOWLEDGMENT

Authors are grateful to the Mahatma Jyotiba Phule Research and Training Institute (MAHAJYOTI), Nagpur, Government of Maharashtra, for providing financial support through Mahajyoti Research Fellowship. Also Authors extends thanks to Library and resource Centre, Rastrasant Tukdoji Mharaj Nagpur University, Nagpur for providing library access.

V. REFERENCE

1. Mukhtar MW, Irfan M, Ahmad I et al. Synthesis and properties of Pt-substituted MgZn ferrites for core materials and high frequency applications. J Magn Mater, 381, 173–178 (2015).
2. Singh C, Jauhar S, Kumar V et al Synthesis of zinc substituted cobalt ferritesvia reverse micelle technique involving in situ template formation: a study on their structural, magnetic, optical and catalytic properties. Mater ChemPhys 156, 188–197 (2015).
3. Venturini J, Piva DH, da Cunha JBM, Bergmann CP, Effect of the thermal treatment on the magnetic and structural properties of cobalt ferrite particles. Ceram Int. 15183-15188 (2016).
4. S.G. Dahotre and L. N. Singh, Study of Magnetic Properties of NanoStructuredMn-Zn Ferrite. Scholars Research Library, 2 (1), 81-89 (2011).
5. AjitanshuVedrtnam, KishorKalauni, Sunil Dubey, and Aman Kumar, A comprehensive study on structure, properties, synthesis and characterization of ferrites. AIMS Materials Science, 7(6): 800–835 (2020).
6. M.K. Shobana, Nanoferrites in biosensors – A review, Materials Science & Engineering B 272 115344, (2021).
7. Dastjerdi, O. Dehghani, H. Shokrollahi, and S. Mirshekari. "A review of synthesis, characterization, and magnetic properties of soft spinel ferrites." *Inorganic Chemistry Communications* (2023): 110797.
8. 5. K.K. Kefeni, T.A. Msagati, B.B. Mamba. Ferrite nanoparticles: synthesis, characterization and applications in electronic device. Mater. Sci. Eng., B, 215, 37-55 (2017).
9. Phulé, P. P., and T. E. Wood. "Ceramics and glasses, sol-gel synthesis of." *Encyclopedia of Materials: science and Technology* (2001): 1090-1095.
10. Xu, Pang. "Polymer-ceramic nanocomposites: ceramic phases." *Encyclopedia of Materials: science and Technology* (2001): 7565-7570.
11. Li, Dongqing, ed. *Encyclopedia of microfluidics and nanofluidics*. Springer Science & Business Media, 2008.
12. Muresan, Liana Maria. "Corrosion protective coatings for Ti and Ti alloys used for biomedical implants." *Intelligent coatings for corrosion control*. Butterworth-Heinemann, 2015. 585-602.
13. O'Neill, Hugh St C. "Temperature dependence of the cation distribution in zinc ferrite (ZnFe2O4) from powder XRD structural refinements." *European Journal of Mineralogy* 4.3 (1992): 571-580.
14. Antao, Sytle M., Ishmael Hassan, and John B. Parise. "Cation ordering in magnesioferrite, MgFe2O4, to 982 C using in situ synchrotron X-ray powder diffraction." *American Mineralogist* 90.1 (2005): 219-228.

15. T. R. Tatarchuk, N. D. Paliychuk, M. Bououdina et al., Effect of cobalt substitution on structural, elastic, magnetic and optical properties of zinc ferrite nanoparticles. Journal of Alloys and Compounds, 731, 1256–1266 (2018).
16. Thomas Dippong, Erika Andrea Levei and OanaCadar, Recent Advances in Synthesis and Applications of MFe2O4 (M = Co, Cu, Mn, Ni, Zn) Nanoparticles, Nanomaterials, 11, 1560, (2021).
17. Donya, Hossam, et al. "A comparative study of spinel ferrites/PANI composites for high-frequency applications." *Journal of Sol-Gel Science and Technology* 108.3 (2023): 695-703.
18. Alhadhrami, A., Muhammad Zeshan, and Hafiz Muhammad TahirFarid. "The structural and dielectric properties of lanthanum substituted strontium based spinel ferrites nano-materials for high frequency device applications." *Journal of Taibah University for Science* 17.1 (2023): 2236368.
19. Sumithra Y Srinivasan,Kishore M Paknikar,DhananjayBodasVirendraGajbhiye, Applications of cobalt ferrite nanoparticles in biomedical nanotechnology. Nanomedicine, 13 (10) (2018).
20. M.A. Almessiere, Y. Slimani a, A.V. Trukhanovb,c, A. Sadaqat d, A. DemirKorkmaz e, N.A. Algaroua,f , H. Aydın g, A. Baykal h, Muhammet S. Toprak, Review on functional bi-component nanocomposites based on hard/soft ferrites: Structural, magnetic, electrical and microwave absorption properties, Nano-Structures & Nano-Objects 26, 100728, (2021).
21. Michael Green, Xiaobo Chen, Recent Progress of Nanomaterials for Microwave Absorption, Journal of Materiomics (2019).
22. X. Zeng, X. Cheng, R. Yu, G.D. Stucky, Electromagnetic microwave absorption theory and recent achievements in microwave absorbers, Carbon (2020).
23. P. Antony Lyla, and E. Thirumal,Structural And Magnetic Properties Of Spinel Mg-Ni Ferrites Nanoparticles Synthesized By Microwave Combustion Method, Turkish Journal of Computer and Mathematics Education. Vol.12 No. 10 (2021), 1455-1461.
24. Ahmad, Mukhtar, et al. "Detailed investigation of Mn-substituted Zn ferrites for microwave applications up to 6 GHz." *Materials Science and Technology* (2024): 02670836231217195.
25. Nedaa M. Refat, Mostafa Y. Nassar and Sadeek A. Sadeek, A controllable one-pot hydrothermal synthesis of spherical cobalt ferrite nanoparticles: synthesis, characterization, and optical properties. Royal Society of Chemistry RSC Adv., (2022), 12, 25081–25095.
26. R. R. Ahmeda, T. H. Mubaraka , I. H. Mohamed, A study of structural and chemical properties of Ni1-xZnxFe2O4 ferrite powder prepared by co-precipitation method, Digest Journal of Nanomaterials and Biostructures, p. 741 – 748, (2022).
27. Alshammari, Alhulw H., et al. "Synthesis and characterization of magnesium zinc ferrite nanoparticles for catalytic hydrogen evolution." *International Journal of Hydrogen Energy* 50 (2024): 734-742.
28. Zohrabi, Younes. "Synthesis and application of magnetic ferrites (MFe2O4) in the removal of heavy metals from aqueous solutions: An updated review." *Materials Science and Engineering: B* 299 (2024): 117024.
29. Al-Ghamdi, Wafaa, HanaaAlmaghamsi, and N. M. Basfer. "Bi3+ doping-enhanced optical and photocatalytic activity with stability of cobalt nickel zinc ferrites for wastewater treatment applications." *Ceramics International* 50.4 (2024): 6725-6734.
30. Rashid, Muhammad, et al. "Solar-light-driven and magnetically recoverable doped nano-ferrite: an ideal photocatalyst for water purification applications." *Optical Materials* 135 (2023): 113192.

ICRTMS-2024
International e-Conference on Recent Trends in Material Science
In Association with International Journal of Scientific Research in Science and Technology
Volume 11 | Issue 9 | Print ISSN: 2395-6011 | Online ISSN: 2395-602X (www.ijsrst.com)

Fabrication of Nano-structured SnO_2-V_2O_5 Composite Thin Films for Enhanced Gas Sensing Performance

Bijwe S. R.[1] Raulkar K. B.[2], Lamdhade G.T.[2]

1. Department of Physics Shri. Shivaji College of Arts, Commerce & Science Akola MS
2. Department of Physics Vidya Bharati Mahavidyalaya Camp, Amravati MS, India

ABSTRACT

In this study, pure SnO_2 with V_2O_5 nanopowders were synthesized using a sol-gel method with varying V_2O_5 ratios. Thin films of SnO_2:V_2O_5 were then produced through thermal vacuum deposition and utilized for gas sensor devices to detect volatile organic compounds and hazardous gases. The morphological, crystalline structure, textural properties, functional groups, optical properties, and thermal behavior were investigated using XRD. The XRD patterns revealed that the average crystallite sizes decreased from 7.8 nm to 4.5 nm with increasing V_2O_5 concentration. XRD analysis showed that the synthesized nanomaterials consisted of mesoporous networks of aggregated nanoparticles with a nearly spherical shape. The incorporation of V_2O_5 into SnO_2 nanopowders enhanced the structural and textural features necessary for gas sensor applications. Furthermore,composite with different weight of percentages V_2O_5 improved the gas response time and sensitivity. The electrical behavior of the sensors was evaluated by measuring the resistance of two deposited platinum electrodes for various gases (LPG, H_2, NH_3, and acetone) at different temperatures.

Keywords- SnO_2,V_2O_5, Nano-powder, Thin films, Gas sensor devices

I. INTRODUCTION

In many cases of environmental hazards, air pollutants are undetectable or invisible due to the nature of the emitted gases themselves. There are only a limited number of stationary or mobile monitoring stations available, primarily because of their high installation costs and the need for consistent maintenance to ensure their continued high performance and operation. According to the World Health Organization (WHO), Organic Volatile Compounds (VOCs) are substances with a boiling point below 250°C at standard atmospheric pressure. These compounds, including acetone, ethanol, and ammonia, are recognized as major toxic pollutants. They are characterized by their low molecular weight, typically less than 100 g/mol. Acetone, for instance, is a clear and colorless liquid classified as hazardous waste. Exposure to acetone, even at concentrations as low as 173 ppm, can lead to nerve and throat damage in humans. Therefore, there is a critical need for improved methods to detect and monitor these harmful pollutants. Traditional detection methods for air pollutants include spectrophotometry, chromatography, electrochemical analysis, catalytic luminescence, and gas sensors. Among these, gas sensors have emerged as one of the most effective detection techniques for monitoring air quality and identifying pollutants [1-2].

Tin dioxide (SnO_2) has garnered significant attention in research due to its ease of fabrication into thin films through various methods. It is widely regarded as one of the most promising sensing materials for gas sensor technology. This is attributed to its exceptional electrical, physical, chemical, and optical properties. As a wide-bandgap semiconductor with an energy gap (Eg) of approximately 3.6 eV, SnO_2 offers unique characteristics that make it particularly suitable for gas sensing applications.

The sensitivity and selectivity of sensor devices are heavily influenced by the choice of sensing materials. The morphological and compositional structure of nanomaterials play a crucial role in determining their sensing characteristics. Various morphological structures of SnO_2 nanomaterials have been prepared, including nanorods/belts, nanofibers, nanoparticles, hollow spheres, and 3D hierarchical nanostructures. Modulating the composition, size, and morphology of these materials can significantly impact their performance. Significant efforts have been made to enhance the gas sensing properties of SnO_2-based devices through the decoration of SnO_2 with noble materials and doping with other elements.Vanadium can exist in different oxidation states, including +2, +3, +4, and +5, and forms various phases such as VO, VO_2, V_2O_5, and V_2O_3.

Among these phases, V_2O_5 possesses a relatively low energy gap of 2.2 eV. Vanadium pentoxide (V_2O_5) is not only an important catalyst but also functions as an n-type semiconductor, promoting reactions for various compounds such as ammonia and hydrogen. Additionally, V_2O_5 exhibits sensing properties towards volatile organic compounds (VOCs). It has garnered attention for its ability to detect gases like acetone, ethanol, and organic amines, making it highly suitable for indoor gas detection, drunken driving tests, and even disease diagnosis. Furthermore, V_2O_5 can be utilized to enhance the response of SnO_2 sensors, further highlighting its potential in gas sensing applications. The method of preparation significantly influences the sensitivity and response of gas sensors. Factors such as selectivity, sensitivity, and degradation of performance over time depend on internal porosity, particle size, and surface morphology of the sensor material. Various techniques have been employed to fabricate SnO_2 and SnO_2 films, including thermal vacuum evaporation, vapor condensation, metalorganic deposition, magnetron sputtering, spray pyrolysis, and chemical vapor deposition. Each of these methods offers unique advantages and allows for the control of different aspects of film properties, contributing to the optimization of gas sensing performance [3-4].

In the present work, pure $SnO_2$and V_2O_5 composite SnO_2 metal oxide nanopowders were synthesized using the sol-gel technique, known for its ability to produce ultrafine porous powders with high homogeneity. Subsequently, thin films of pure $SnO_2$and V_2O_5 composite SnO2 were fabricated via thermal vacuum evaporation using the synthesized nanopowders. Various composite amounts of V_2O_5 (0, 1, 5, 10 wt%) were added to SnO_2 nanocrystalline sensors with the aim of enhancing their sensing properties towards different gases such as H_2, LPG, ammonia, and acetone. The study includes a comparative analysis of the sensing performance between pure and V_2O_5 composite SnO_2 nanoparticles.

2. Experimental method

Preparation of SnO_2 and SnO_2:V_2O_5 Nano-powders: The experimental setup for synthesizing pure SnO_2 and SnO_2 :V_2O_5 nanopowders involves the following steps:-

Materials: $SnCl_4.2H_2O$ (Sigma-Aldrich, Germany, 98%), HCl (ACROS ORGANICS, Germany, 37%), and V_2O_5 (Sigma-Aldrich, Germany, ≥99.6%) are used. These materials are sourced from reputable suppliers.

Preparation of SnO_2 Nanopowders: Tin chloride dihydrate ($SnCl_2.2H_2O$) is placed in a beaker, and then water is added to dilute it. Hydrochloric acid (HCl) is added gradually until the solution reaches a pH of approximately 1, and the mixture is stirred continuously [5].

Composites with V_2O_5: An aqueous acidic solution of V_2O_5 is added to the SnO_2 solution in different ratios (0, 1, 5, and 10 wt% of V_2O_5) for the Composites process.

pH Adjustment: Ammonia solution is then slowly added to the mixture while stirring until the pH of the solution reaches around it. This pH adjustment step is crucial as it helps convert tin chloride into SnO_2.

Stirring and Mixing: The solution is continuously stirred and mixed to ensure homogeneity and proper incorporation of V_2O_5 .

This experimental setup enables the synthesis of pure $SnO_2$and V_2O_5 Composite SnO_2 nanopowders using the sol-gel technique, with control over the pH of the solution to achieve the desired properties.

3. Materials Characterization

The physical properties of the prepared SnO_2 and V_2O_5-based powders were investigated using the following techniques:

X-Ray Diffraction (XRD): XRD patterns of the nanopowders were obtained using a Shimadzu 7000 Diffractometer. The instrument operated with Cu Kα1 radiation (λ=0.15406 nm) generated at 30 kV and 30 mA, with a scan rate of 2°/min for 2θ values ranging between 20° and 80°. This analysis allowed for the determination of crystal structure and phase composition.

In addition to the previously mentioned techniques, the physical properties of the prepared $SnO_2$and V_2O_5 -based nanopowders were further investigated using the following methods [6-7].

Optical Properties Measurements: Optical properties of the fabricated thin films were measured in transmittance and absorbance modes using a double-beam spectrophotometer (UV-Vis, Spectro Double 8 Auto cell). This analysis helps characterize the optical transparency and absorption properties of the thin films.

These additional techniques offer comprehensive insights into the structural, morphological, compositional, and optical properties of the synthesized nanopowder, which are crucial for understanding their potential applications.

Devices Fabrication- Cleaning the substrates that are 1 mm thick of microscope glass slides is done by placing them in methanol solution, then in acetone and washing several times with distilled wateranddrying.PureSnO_2 and Composite SnO_2withvarious V_2O_5 amounts (1, 5 and 10 wt%) thin films, Thin films of V_2O_5 at concentrations of 1%, 5%, and 10% by weight are deposited onto cleaned glass substrates using a thermal vacuum evaporator (Model EDWARD "auto 306"). The deposition process involves placing the prepared powders in tungsten boats, which are then exposed to an electric heater to evaporate the nanopowders under a vacuum of approximately 10^{-6} Pa. The deposition parameters include a current ranging between 20-25A and a constant deposition time of 30 minutes for each condition. After the evaporation process, the substrates are cooled to room temperature, and a copper mask is fixed onto the thin films. Finally, platinum electrodes are deposited onto the films using a sputtering instrument (Model Hummer TurboSputtering RF and DC) operating at a power of 100 W and a deposition time of 5 minutes.

4. Results and Discussions

The characterization of the prepared SnO_2 and V_2O_5 -based powders through X-ray diffraction (XRD) analysis elucidates the influence composite on SnO_2 .The XRD patterns of the nanopowders correspond with those reported in the JCPDS data (Card No. 41-1445) for the tetragonal rutile SnO_2 structure, as depicted in Figure 1. Specifically, the pure SnO_2 sample exhibits three major peaks [8-9] appearing at 2θ values of 26.58°, 33.89°, and 51.92°.

Importantly, no crystalline phases corresponding to vanadium or other vanadium compounds are detected in the XRD patterns. This absence suggests that vanadium may be incorporated into the tin oxide lattice, as illustrated in Figure 1(a). With an increase in vanadium concentration, the diffraction peaks shift towards higher diffraction angles, indicating potential lattice distortion or changes in crystallographic parameters due to the process. This observation highlights the structural modifications induced by V_2O_5 and underscores its significance in tailoring the properties of the SnO_2-based materials for various applications.

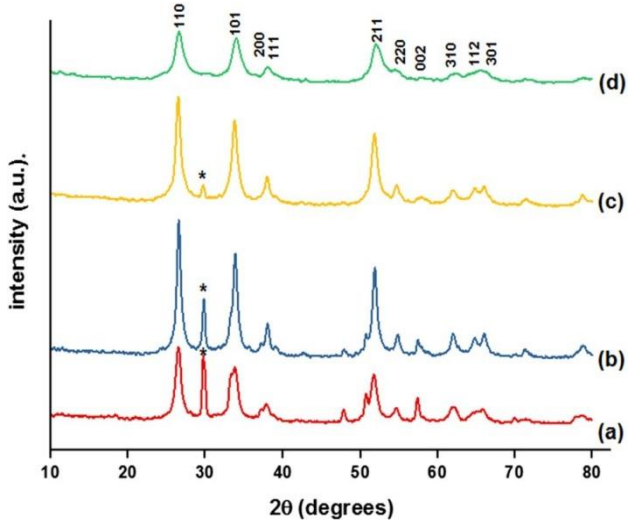

Fig.1 XRD patterns of SnO_2 nanoparticles prepared at different composing of V_2O_5 **a** pure, **b** 1 wt%, **c** 5 wt% and **d** 10 wt%

Minor differences in the XRD patterns and their intensity are observed as the percentage of V_2O_5 is increased, indicating varying values of compositing. Additionally, a peak observed at 2θ = 29.88° is attributed to the presence of SnO, according to JCPDS data (Card No. 06-0395). This suggests that both SnO properties of the SnO_2-based materials for various applications.

SnO coexist, even in the as-prepared SnO_2 or at low ratios of V_2O_5 concentration. However, this peak's intensity decreases with increasing ratio and completely disappears at 10% V_2O_5 composing, indicating the formation of a complete SnO_2 crystal structure with a tetragonal rutile structur. For further insight into the structure analysis, the mean crystallite size (D) is estimated using Scherer's Equation (1)

$$D=K ß/\beta \cos\theta \qquad (1)$$

The crystallite size (D) is calculated using Scherer's Equation (1), where K is a factor with a value of 0.9, λ is the wavelength of the incident X-ray beam (1.541 Å), β is the full width at half maximum (FWHM) of the peaks, and θ is the Bragg's diffraction angle in radians.

Specifically, the crystallite size of the powders, as determined from XRD analysis, ranges from 10.2 to 9.3 nm as the V_2O concentration increases from 0 to 1 wt%, 5 wt%, and 10 wt%, respectively. This indicates a trend of decreasing crystallite size with increasing V_2O_5 concentration, with values ranging from 8.4 to 4.3 nm.

So observed that there are no significant differences in the microstructure among the samples. The morphological shape of the nanopowders appears nearly spherical, with nanoparticle diameters ranging from 12 to 23 nm. Additionally, the particle sizes of the nanopowder decrease with an increase in the composite percentage. This indicates that it has an influence on the particle size distribution and morphology of the prepared materials.

The optical properties of both pure SnO_2 and V_2O_5 composite SnO_2 nanopowders after calcination are investigated using XRD. The absorption spectra of the prepared nanopowders are recorded in the range of 275–1100 nm. In the absorption spectra, the absorption peak of pure SnO_2 is observed around 300 nm. However, with the addition of V_2O_5, the absorption peak shifts, it shifts to 295 nm for 1 wt% V_2O_5/SnO_2 and to 310 nm for 5 wt% V_2O_5/SnO_2 . This shift in the absorption peak suggests changes in the optical properties of the nanopowders due to the process. The optical properties of both pure SnO_2 and V_2O_5 composited SnO_2 nanopowders after calcination are investigated using UV-visible spectroscopy. The absorption spectra of the prepared nanopowders are recorded in the range of 275–1100 nm. absorption peak suggests changes in the optical properties of the nanopowders due to the composite process [10-11].

5. Gas Sensing Performance-

To evaluate the sensing characteristics of the fabricated composite SnO_2-based gas sensor devices, specific amounts of gases (hydrogen, ammonia, acetone, and LPG) are injected into a handmade gas chamber. The concentrations of the injected gases and vapors are calculated in parts per million (ppm) using Equation (2)

$$C = (22.4pTVS)/(273MV) \times 1000 \quad (2)$$

Where C, ρ, T, M, VS represent the concentration of the examined gases in ppm, the density of liquid vapors (ammonia and acetone) (gml–1),ambient temperature(K), molecular weight of the liquid vapors (L), VS is the volume of the tested liquid (μ l), respectively.

Response is a critical factor in determining the performance of gas sensor devices. To assess this, fabricated gas sensor devices are tested under varying temperatures with different gases.. The gas response is quantified using the following equation (3)

$$S = (Ra)/(Rg) \times 100\% \quad (3)$$

where (Ra) represents the resistance of the sensor devices in presence of air and (Rg) is the resistance of the sensor devices in presence of the tested gas.

The output voltage is calculated from the sensor resist following equation

$$LOD = 3.3\sigma S$$

Variation (Rg) at different temperatures by a small electrical circuit shown in Fig.2, that consisting of load resistance RL (10 KΩ), variable resistance of gas sensor.

Rg and power supply 5V,where the multi meter was connected to RL, and the output voltage is measured [12]

$$V\ out = 5 - VL$$

The gas sensor properties are tested under relative humidity between 40 and 60% for three times. It appears that there is a decrease in responses as the operating temperature continues to increase. SnO_2 gas sensor exhibits a relatively lower response to acetone, H2, LPG, and NH3 compared to the V_2O_5 and SnO_2 sensor. The V_2O_5 composite SnO_2 sensor, on the other hand, demonstrates significant improvements in responses to these gases.

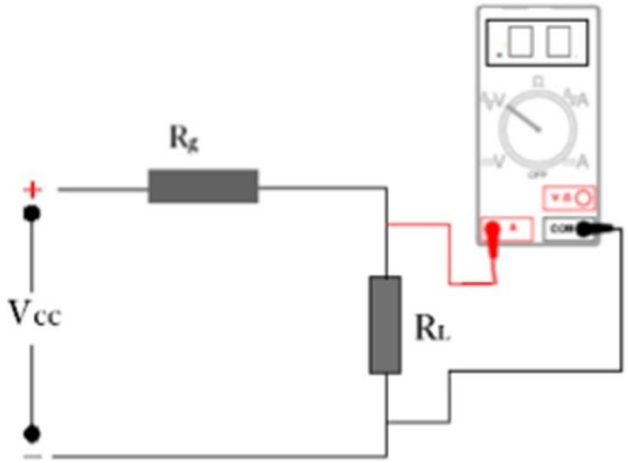

Fig.2 Electrical circuit for measuring voltage of gas sensor

6. The Gas Detection System-

The circuit diagram of a typical gas sensor system is illustrated in Figure (3), This system performs the following functions:

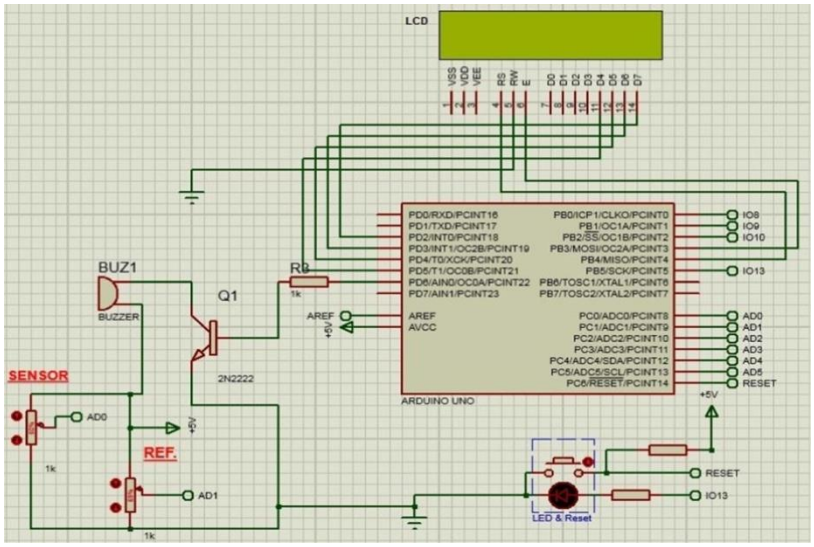

Fig.3 Circuit diagram of gas detection system

- It detects gas leakage using the fabricated sensor.
- Activates an alarm up on gas leakage detection.

7. Conclusions

Pure SnO_2 and V_2O_5 composited SnO_2 nanopowders were successfully synthesized via a sol-gel method, employing tin chloride dihydrate as the starting precursor. Various ratios of V_2O_5 were utilized in the synthesis process. high-quality SnO_2 thin films were produced through thermal vacuum evaporation under low pressure conditions. The maximum gas sensitivity for H_2 and LPG was achieved with V_2O_5 composited SnO_2 gas sensors containing a 5 wt%, reaching 109 % sensitivity at 190°C for H_2 and 108% at 210°C for LPG. For ammonia vapor and acetone vapor, the optimal for the best sensitivity was found to be 1 wt% V_2O_5 composited SnO_2 gas sensors, yielding 132% sensitivity at 250°C for ammonia vapor and 102% at 260°C for acetone vapor. The sensor voltage variation for H_2 and LPG was high across all fabricated sensors, while for NH_3 and acetone. Introducing

V_2O_5 into the SnO_2 system is expected to reduce costs compared to noble metal catalysts commonly used for such purposes, making it useful for commercialization and technological advancements.

8. Acknowledgements: -

The authors are thankful to Vidya Bharati Mahavidyalaya Amravati for providing facilities to carry out the research work.

References-

1. Schieweck A.Uhde, E.Salthammer, T.Salthammer, L.Morawska, L., Mazaheri, M., & Kumar, Smart homes and the control of indoor air quality. Renewable and Sustainable Energy Reviews, 94, 705–718 (2018).
1. Jalal A. H., Alam, F. Roychoudhury, S., Umasankar, Y .Pala, N., & Bhansali, S. (2018). Prospects and challenges of volatile organic compound sensors in human healthcare. ACS Sensors, 3, 1246–1263 (2018).
2. Montero-Montoya, R.; López-Vargas, R.; Arellano-Aguilar, O.: Volatile organic compounds in air: sources, distribution, expo- sure and associated illnesses in children. Ann. Glob. Health 84, 225–238 (2018)
3. Hassan, H.S. Elkady, M.F.; Farghali, A.A.; Salem, A.M.; Abd El-Hamid, A.I.: Fabrication of novel magnetic zinc oxide cellulose acetate hybrid nano fiber to be utilized for phenol decon- tamination. J. Taiwan Inst. Chem. Eng. 78, 307–316 (2017)
4. Reddy, C.V, Babu, B.; Vattikuti, S.P.; Ravikumar, R.V.; Shim, J.: Structural and optical properties of vanadium doped SnO2 nanoparticles with high photocatalytic activities. J. Lumin. 179, 26–34 (2016)
5. Shanmugam, M.; Alsalme, A.; Alghamdi, A.; Jayavel, R.: Enhanced photocatalytic performance of the graphene-V2O5 nanocomposite in the degradation of methylene blue dye under direct sunlight. ACS Appl. Mater. Interfaces 7, 14905–14911 (2015)
6. DhayalRaj,A., Mangalaraj, D.; Ponpandian,N.;Yi,J. :Gassings properties of chemically synthesized V2O5 Thin film. Adv. Mater. Res. 123–125, 683–686 (2010)
7. Bhati,V.S.; Sheela, D.; Roul, B.;Raliya, R.; Biswas, P.; Kumar,M.;Roy,M.S. ;Nanda,K.K. ;Krupanidhi,S. B.;Kumar,M. :NO_2 gas sensing performance enhancement based on reduced graphene oxide decorated V_2O_5 thin films. Nanotechnology 30, 224001 (2019)
8. Xue,N.;Zhang,Q.;Zhang,S.;Zong,P.;Yang,F.:Highlysensitiveand selective hydrogen gas sensor. Sensors(Basel)10,2351 (2017)
9. Hassan, H.S.; Kashyout, A.B.; Morsi, I.; Nasser, A.A.A.; Ali, I.: Synthesis, characterization and fabrication of gas sensor devices using ZnO and ZnO: In nanomaterials. Beni-Suef Univ. J. Basic Appl. Sci. 3, 216–221 (2014)
10. Tan,W.; Ruan, X. ;Yu, Z.;Huang ,X. Fabrication of SnO_2 based
11. acetone gas sensor enhanced by molecular imprinting. Sensors (Basel). 15, 352–364 (2015)
12. Abokifa,A.A.;Haddad,K.;Fortner,J.;Lo,C.S.;Biswas,P.:Sensing mechanism of ethanol and acetone at room temperature by SnO2nano-columns synthesized by aerosol routes: theoretical calculations compared to experimental results. J. Mater. Chem.A6, 2053–2066 (2018)

ICRTMS-2024
International e-Conference on Recent Trends in Material Science
In Association with International Journal of Scientific Research in Science and Technology
Volume 11 | Issue 9 | Print ISSN: 2395-6011 | Online ISSN: 2395-602X (www.ijsrst.com)

Exploring the Intricacies A Tale of Binary Mixtures Density, Viscosity, Refractive Index, and Molecular Dynamics Unraveling the Symphony of 2,3 Dichloroaniline & 2 Methoxyethanol From 323.15 K to 293.15 K A Journey Through Molecular Interactions

Nemmaniwar. G. Bhupesh*

Department of Physics, Digamberrao Bindu Arts, Commerce and Science College, Bhokar,

Nanded (MS) India.

Watode B. D.

Department of Physics Phulsing Naik Mahavidyalaya. Pusad. Yevatmal (MS). India.

ABSTRACT

A new binary mixture system of 2,3 Dichloroaniline (2,3-DCA) and 2-Methoxyehenol (2-ME) including those of pure liquids, over the entire composition range were measured at temperatures from 323.15 K to 293.15 K at atmospheric pressure. The physico–chemical properties of density, viscosity and refractive index for the binary mixtures were determined. The obtained data were compared with those available in literature. The temperature dependences of the viscosities and densities for the system were described. To investigate the internal interactions of the binary mixtures. The trend of energetic and charge distribution of all ions and molecules involved in interactions between the 2,3-DCA and 2-ME.

Keywords : 2,3-DCA and 2-ME, Physico–chemical properties and Molecular Interactions.

I. INTRODUCTION

The physicochemical, thermodynamic and transport properties [1]. of binary liquid mixtures are important in engineering process industry and studied for many reasons, which may provide more information about molecular interactions. Generally speaking, knowledge of basic physicochemical properties on the density, viscosity and refractive index data is an indispensable requirement over a broad range of temperatures 323.15 K to 293.15 K for the absorption and desorption processes of 2,3-DCA. The present work was mainly focused on investigating density, viscosity and refractive index data at T=323.15 K to 293.15 K for the whole composition range that covers the partly industrial applications [2-6]. In addition, the possible intermolecular interaction of

2,3-DCA with 2-ME was investigated using DMA 35 portable vibrating density meter [7] viscosity by LVDL V-pro II Brook field viscometer [7] and Refractive indices for sodium D-line were measured by using Abbe's refractometer [7]. This work is part of the systematic researches on the physicochemical and thermodynamic properties of the binary liquid system containing 2,3-DCA with 2-ME are used in petroleum solvents, fungicides, as an intermediate in the production of agricultural chemicals, azo dyes and pigments and pharmaceuticals [8]. 2-ME is used as a solvent for many different purposes such as varnishes, dyes, and resins [9]. 2-ME is a very interesting class of solvent having hydroxyl -OH group and is noted for its donating and accepting ability. This type of interaction studies (N–H…O– H) plays an important role in biological and drug synthesis applications. The present work is mainly focused on investigating density, viscosity and refractive index data at T=323.15 K to 293.15 K of the system 2,3-DCA+2-ME over the whole composition range. Meanwhile, the work is focused on investigating the possible intermolecular interaction of 2,3-DCA with 2-ME, using density meter, viscometer and refractometer techniques.

I. METHODS AND MATERIAL

2,3-Dichloroaniline (GC Grade) is obtained from Sigma-Aldrich. 2-Methoxyethanol (AR Grade) were obtained from M/S Sd. Fine chemical, Mumbai, India without further purification the two liquids according to their proportions by volume were mixed well and kept 6h in well stoppered bottles to ensure good thermal equilibrium. These liquids used as solute and solvent.

Measurements

All the measurements are carried out at temperatures 323.15 K to 293.15 K by circulating ethylene glycol + water around the liquid cell and temperature is thematically controlled with +0.50^{0}C thermocontrole using Nevitech pvt. Ltd. Mumbai India. The whole of the equipment is standardized with the help of standard materials like methanol and ethyleneglycol+water (40:60). The densities, viscosities, and refractive index of the pure components and their binary mixtures are measured by densities, viscosities and refractive index of the pure components and their binary mixtures were measured by using DMA 35 portable vibrating density meter. Anton paar Autria (Europe) having accuracy of density 0.001 g/cm^3, repeatability 0.0005 g/cm^3 and resolution 0.0001 g/cm^3, viscosity by LVDL V-pro II Brook field viscometer (USA) and Refractive indices for sodium D-line were measured by using Abbe's refractometer having accuracy up to the third place of decimal.

II. RESULTS AND DISCUSSION

This paper reports the density, viscosity and refractive index data of the binary system of 2,3-DCA with 2-ME over the entire binary composition range at T=323.15 K to 293.15 K and atmospheric pressure are reported in table 1. Table 1 show that the density values gradually decrease with increasing temperature at the same concentration the density values increasing with increasing concentration of 2,3-DCA at the all temperature.

Table 1: Mole fraction (X) of 2,3-DCA and 2-ME, Density (ρ), viscosity (η) and refractive index (n) of binary mixture liquid system of 2,3-DCA+2-ME at 20^{0}C, 30^{0}C,40^{0}C and 50^{0}C.

Mole Fraction	ρ gm/cm^3				η CP				n			
X	20^{0}C	30^{0}C	40^{0}C	50^{0}C	20^{0}C	30^{0}C	40^{0}C	50^{0}C	20^{0}C	30^{0}C	40^{0}C	50^{0}C
0.00000	0.9642	0.9566	0.9416	0.9226	2.14	1.34	1.25	1.15	1.4041	1.3962	1.3934	1.3882

0.08697	1.0818	1.0170	1.0060	1.0040	2.87	2.09	1.48	1.30	1.4407	1.4350	1.4302	1.4208
0.18185	1.0943	1.0694	1.0124	1.0098	3.32	2.42	1.74	1.45	1.4553	1.4480	1.4448	1.4323
0.28576	1.1214	1.1210	1.1196	1.0834	4.24	2.98	2.04	1.68	1.4813	1.4741	1.4669	1.4616
0.40006	1.2224	1.2220	1.2171	1.1243	5.21	3.52	2.33	1.90	1.5094	1.5031	1.4969	1.4886
0.52637	1.2456	1.2436	1.2316	1.2200	6.20	4.06	2.63	2.13	1.5342	1.5239	1.5114	1.5060
0.66672	1.3006	1.2750	1.2614	1.2516	7.09	4.55	2.96	2.38	1.5450	1.5430	1.5311	1.5273
0.82356	1.3406	1.3231	1.3141	1.3104	7.88	5.09	3.25	2.62	1.5700	1.5560	1.5480	1.5420
1.00000	1.3711	1.3684	1.3550	1.3345	8.01	5.82	3.74	2.99	1.5990	1.5910	1.5800	1.5630

meanwhile, the density values decreasing with the increase temperature at the same binary concentration. The viscosity values augment with the increasing mole fraction of 2,3-DCA over the whole concentration range, meanwhile, the viscosity values decrease with the increasing temperature at the same composition and this phenomenon is possibly caused by the weak hydrogen bonding interaction [10]. From above table viscosity values decrease gradually with increasing all temperature at the same concentration and they increase slowly increasing mole fraction of 2,3-DCA concentration at the same all temperature. The structural property of liquid and liquid mixtures can be integrated through refractive indices employing mole fractions. In general refraction increases with molecular weight for symmetric and asymmetric molecules. Refractive index depend on molecular weight and nature of liquids. It is observed from table1 that refractive index values decrease with increase of temperature from 323.15 K to 293.15 K.

III. CONCLUSION

The density, viscosity and refractive index of 2,3-DCA with 2-ME. The consequences of adding different amounts of 2,3-DCA and increasing the temperature were investigated. Through density, viscosity and refractive index measurements, it is established that both the increase in temperature and addition of 2,3-DCA lead to decreases in Columbic, hydrogen bonding and van der Waals interactions and hence to structural disorder in the ionic liquid. The results reflect the presence of strong intermolecular interactions in the mixtures under investigation. The stronger interaction in the binary mixture of 2,3-DCA with 2-ME may be due to the hydrogen bonding between $–NH_2$ groups in 2,3-DCA and –OH group in 2-ME and $–NH_2$ group in aniline with the hydroxyl groups at the chain terminals of 2,3-DCA molecules. Dispersive forces are also acting in the 2,3DCA+2-ME mixtures.

REFERENCES

[1] Kapadi,U.R. Hundiwale, D.G. Patil, N.B. Lande, M.K. Fluid Phase Equilib. 205, 2003. 267–274.
[2] Nasim, A. Kamyar M. Mohsen P. and Mahnam K. J. Chem. Eng. Data June 2, 2020.A-O.
[3] Ahmasi, M. Sarkoohaki, B.J. Chem. Eng. Data. 57, 2012, 309–316.
[4] Llovell, F. Marcos, R. M.Vega, L. F.J. Phys. Chem. B. 117, 2013, 8159–8171.
[5] Serebryakova, M. A. Dimov, S. V. Bardakhanov, S. P. Novopashin, S. A. Int. J. Heat Mass Transfer. 83, 2015, 187–191.
[6] Sapir, L. Stanley, C. B. Harries, D.J. Phys. Chem. A. 120, 2016, 3253–3259.
[7] Nemmaniwar B. G. Science Direct Materials Today: Proceedings. 23, 2020. 324–328.
[8] Nemmaniwar B. G. Orbital. The Electronic J. of Chem. 12.2, 2020.62-68.
[9] Nemmaniwar B. G. AIP Conference Proceedings. 2269, 030114, 2020. 030114-1 to 030114-4.
[10] Gao,F. Niu, Y.X. Zhang, J.B. Sun, S.Y. Wei, X.H. J. Chem. Thermodyn. 62, 2013 8–16.

ICRTMS-2024
International e-Conference on Recent Trends in Material Science
In Association with International Journal of Scientific Research in Science and Technology
Volume 11 | Issue 9 | Print ISSN: 2395-6011 | Online ISSN: 2395-602X (www.ijsrst.com)

Study of Dielectric Relaxation in Polyethylene Glycol 4000 + water Mixtures using TDR

P. R. Konmare, S. H. Saknure, A.C. Kumbharkhane
[1]School of Physical Sciences, Swami Ramanand Teerth Marathwada University, Nanded-431606 MS, India
[2]School of Physical Sciences, Swami Ramanand Teerth Marathwada University, Nanded-431606 MS, India
[3]School of Physical Sciences, Swami Ramanand Teerth Marathwada University, Nanded-431606 MS, India

ABSTRACT

The dielectric constant and relaxation time for polyethylene glycol 4000 (PEG4000)-water mixtures with the entire mole fraction have been determined in the frequency range of 10 MHz to 30 GHz using the time domain reflectometry method. The dielectric behaviour of polyethylene glycol 4000 was investigated to understand the effect of the hydroxyl group on the dielectric parameters. The results showed that the dielectric constant of PEG4000-water mixtures decreased with increasing mole fractions of PEG4000, indicating a decrease in the overall polarity of the mixture, The relaxation time was found to increase with increasing mole fractions of PEG4000, suggesting a slower response to applied electric fields.

Keywords : Dielectric constant, polyethylene glycol4000, Time domain reflectometry,

I. INTRODUCTION

The dielectric studies of polymer solutions have been investigated extensively to investigate the hydrogen bond structures in the polymers [1-5]. Poly ethylene glycols of average molecular weights 300(PEG300), 400(PEG400) and 600(PEG600) are liquid polymers and have wide range of applications in pharmaceuticals, cosmetic preparation, industries as solvent, food additives and plasticizers[6]. In general, chemical formula of poly ethylene glycol (PEG) is given as $HO(CH_2CH_2O)nH$, where n is the number of repeat units. The chemical structure of peg4000 is shown in fig1. Polyethylene glycol 4000 (PEG 4000) is a water-soluble polymer that can be used to create high osmotic pressures. peg4000 has hygroscopic nature with molecular weight 4000g/mol.PEG4000 is dihydric alcohol, due to this It has high affinity for water at room temperature 25°C[7-8].

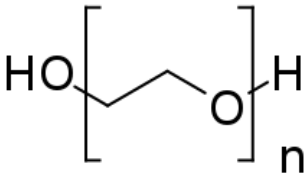

Fig.1 Structure of PEG4000

In the present paper, the detailed dielectric relaxation study of PEG4000 –water binary mixtures have been carried out using time domain reflectometry (TDR) technique upto 30 GHz. Dielectric relaxation spectroscopy determines the response of sample to an applied electric field of angular frequency ω in terms of complex permittivity $\varepsilon^*(\omega) = \varepsilon(\omega) - j\varepsilon(\omega)$, where ε(ω) is dielectric permittivity or dispersion and ε(ω) is dielectric loss or absorption. This technique is proven to be the powerful technique in the investigation of co-operative and molecular dynamics of H-bonded systems [9]. From the measured complex permittivity spectra, the static dielectric constant (ε0), dielectric relaxation time (τ) and asymmetric relaxation distribution parameter (β) were obtained by least square fit method.

II. METHODS AND MATERIAL

A PEG4000 was obtained commercially from Merck, India. The water used in the preparations of mixtures was obtained by distillation procedure. The solutions were prepared at different mole fractions of water in PEG4000.

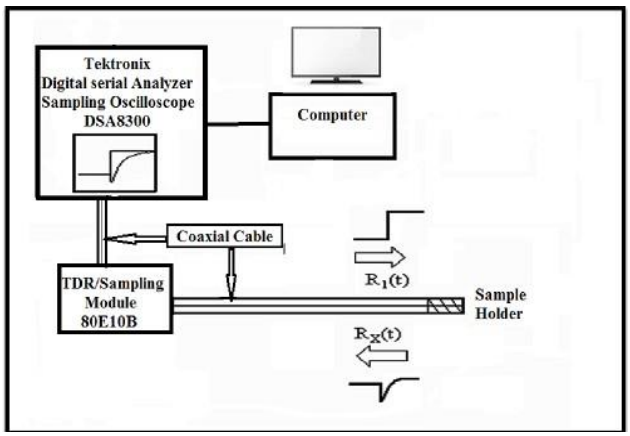

Fig.1. Block diagram of Time Domain Reflectometry

The time domain reflectometry (TDR) technique was used to get the dielectric spectra. As shown in Fig.2 The Tektronix model no. DSA8300 Digital Serial Analyzer sampling mainframe, along with the sampling module 80E10B has been used for the measurement. A repetitive fast rising voltage pulse with a 12 ps incident rise time was fed through coaxial line system of impedance 50 Ω. The sampling oscilloscope monitors variations in the step pulse after reflection from the end of line. Reflected pulse without sample R1(t) and with sample Rx(t) were recorded in time window of 5 ns and digitized in 2000 points. The Fourier transformation of the pulses and data analysis was done earlier to determine the complex permittivity spectra using non linear least squares fit method [10-14].

III.RESULTS AND DISCUSSION

The complex permittivity spectra of PEG 4000 – water mixture have been determined using the Time Domain Reflectometry (TDR) technique in the frequency range 10MHz to 10GHz at 25°C. It can be seen that the value of permittivity (ϵ') decreases and dielectric loss (ϵ") shifted towards lower .

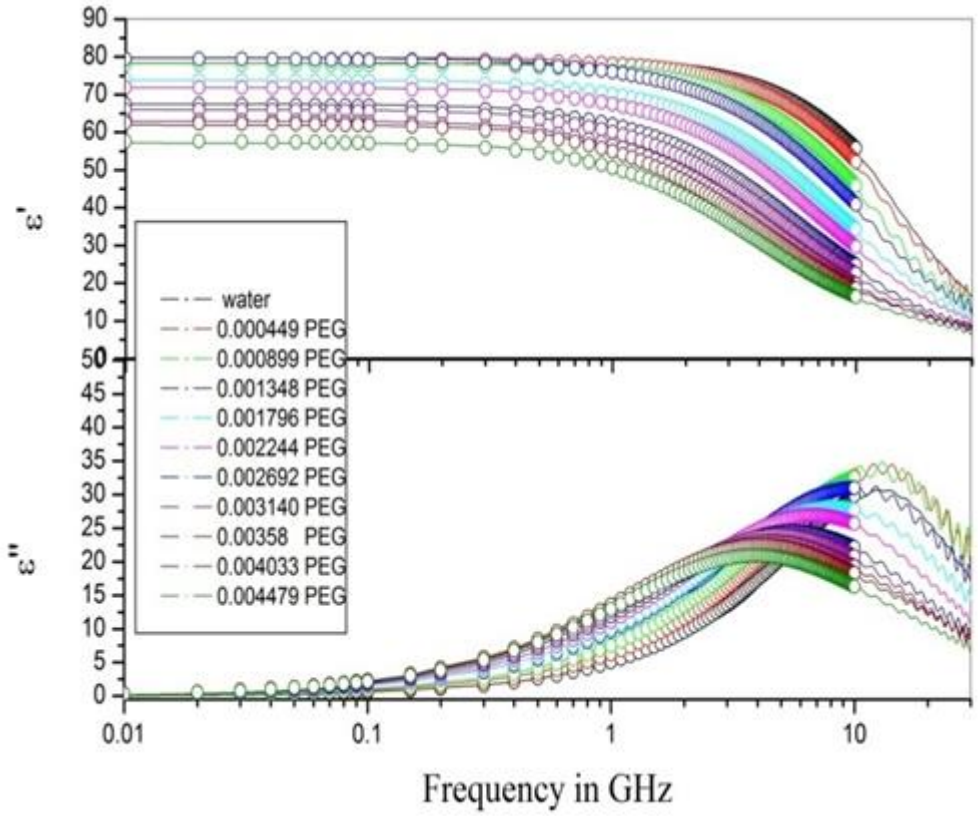

Fig.2 Frequency dependence complex permittivity spectra of PEG 4000 - Water mixture at 25 °C.

frequency as the concentration of PEG4000 increases in water, that is, the loss peak shifted to words lower frequency side, including greater relaxation time as shown in Fig.2

The complex permittivity spectra are fitted to the Havriliak - Negami expression using the non-linear least squares fit method [15].

$$\varepsilon^*(\omega) = \varepsilon_\infty + \frac{\varepsilon_0 - \varepsilon_\infty}{[1+(j\omega\tau)^{1-\alpha}]^\beta}$$

where ε_0- static dielectric constant, τ- relaxation time, ε_∞- dielectric constant at high frequency , ω is the angular frequency, α and β-distribution parameters. In this study the aqueous solutions of PEG 4000 shows Cole–Davidson type dispersion [16].

TABLE 1. Dielectric parameters for PEG 4000-water mixtures at 25°C

Mole fraction PEG4000	ε_0	τ(ps)	β
0	78.24	10.81	1
0.000449	79.35	11.10	0.92
0.000899	78.06	13.10	0.90

0.001348	79.49	15.92	0.86
0.001796	73.83	19.24	0.86
0.002244	71.91	23.67	0.86
0.002692	67.47	28.77	0.85
0.003140	65.98	32.17	0.86
0.00358	63.31	35.29	0.86
0.004033	62.56	38.09	0.84
0.004479	57.14	41.00	0.85

The dielectric parameters of various concentrations of PEG 4000 in water are shown in table no 1. It has been found that values of dielectric constant decreases with the increasing in quantity of PEG4000 in pure water. The relaxation time τ(Ps) increases with increasing of PEG4000 in water. This indicates that the presence of PEG 4000 in water affects the polarization and dielectric relaxation behaviour of the system. The decrease in dielectric constant suggests a decrease in the ability of the medium to store electrical energy, while the increase in relaxation time indicates a slower response to an applied electric field.

IV. CONCLUSION

The dielectric relaxation parameters of polyethylene glycol for 25°C have been studied using TDR technique. The study reveals that PEG 4000-water mixtures' dielectric constant decreases with PEG4000 mole fractions, indicating decreased polarity and slower response to electric fields, offering potential applications in Electronics, Biomedical engineering and Pharmaceutical industries.

IV. ACKNOWLEDGEMENT

The financial support from the Department of Science and Technology, New Delhi is greatfully acknowledged (Project No DST PROJECT-SB/S2/LOP-032/2013). I would also like to express my special thanks of gratitude to School Of Physical sciences Swami Ramanand Teerth Marathwada University, Nanded.

REFERENCES

[1] Stockmayer, Walter H. "Dielectric dispersion in solutions of flexible polymers." *Pure and Applied Chemistry* 15.3-4 (1967): 539-554. https://doi.org/10.1351/pac196715030539

[2] Mashimo, Satoru. "Dielectric study of chain motion of poly (p-chlorostyrene) in dilute solution." *Macromolecules* 9.1 (1976): 91-97. https://doi.org/10.1021/ma60049a018

[3] Mashimo, Satoru, Haruki Nakamura, and Akio Chiba. "Elementary process in polymer chain motion." *The Journal of Chemical Physics* 76.12 (1982): 6342-6345. https://doi.org/10.1063/1.443038

[4] Mashimo, Satoru, Shin Yagihara, and Akio Chiba. "Dielectric relaxation of oxide polymers in dilute solution." *Macromolecules* 17.4 (1984): 630-634. https://doi.org/10.1021/ma00134a020

[5] Matuo K, Kahlman K F, Yong W H M, Geny F, Stockmayer W H & Jones A A, J Polym Sci Polym Phys, Ed. 15 (1977) 1347 http://nopr.niscpr.res.in/handle/123456789/2526

[6] Sarode, Arvind V., and Ashok C. Kumbharkhane. "Dielectric relaxation study of poly (ethylene glycols) using TDR technique." *Journal of Molecular Liquids* 164.3 (2011): 226-232. https://doi.org/10.1016/j.molliq.2011.09.020

[7] Sudo, Seiichi, et al. "Dielectric relaxation time and relaxation time distribution of alcohol– water mixtures." *The Journal of Physical Chemistry A* 106.3 (2002): 458-464. https://pubs.acs.org/doi/abs/10.1021/jp013117y#

[8] Sengwa, R. J. "Comparative dielectric study of mono, di and trihydric http://nopr.niscpr.res.in/handle/123456789/25016

[9] S. Schrodle, G. Hefter, R. Buchner, J. Phys. Chem. B 111 (2007) 5946–5955. https://pubs.acs.org/doi/abs/10.1021/jp0713413#

[10] Dhage, Haribhau M., et al. "Dielectric relaxation studies of 1-nitropropane-dimethyl sulfoxide mixtures using a Time Domain Reflectometry." *Physics and Chemistry of Liquids* (2024): 1-10. https://doi.org/10.1080/00319104.2024.2306605

[11] Saknure, Shankar H., and Ashok C. Kumbharkhane. "Dielectric and Hydration Study of Aqueous Cellulose Derivative Solutions." *Journal of Macromolecular Science, Part B* (2024): 1-7. https://doi.org/10.1080/00222348.2024.2304992

[12] Garad, Nitin P., et al. "Study of Dielectric Relaxation and Hydrogen Bonding Interaction of 1, 4-Butanediol-1, 4-Dioxane Mixture using TDR Technique." (2023). https://doi.org/10.56042/ijpap.v61i3.70017

[13] Joshi, Y. S., and A. C. Kumbharkhane. "Study of dielectric relaxation and hydrogen bonding in water+ 2-butoxyethanol mixtures using TDR technique." *Fluid Phase Equilibria* 317 (2012): 96-101. https://doi.org/10.1016/j.fluid.2012.01.005

[14] Deshmukh, Avadhut R., and Ashok C. Kumbharkhane. "Dielectric relaxation studies of aqueous primary amines using a time domain reflectometry." *Indian Journal of Physics* 96.11 (2022): 3105-3115. https://link.springer.com/article/10.1007/s12648-021-02240-9#article-info

[15] S. Havriliak, S. Negami, J. Polym. Sci. C 14 (1966) 99–117. https://doi.org/10.1002/polc.5070140111

[16] Davidson, Donald W., and Robert H. Cole. "Dielectric relaxation in glycerol, propylene glycol, and n-propanol." *The Journal of Chemical Physics* 19.12 (1951): 1484-1490. https://doi.org/10.1063/1.1748105

ICRTMS-2024
International e-Conference on Recent Trends in Material Science
In Association with International Journal of Scientific Research in Science and Technology
Volume 11 | Issue 9 | Print ISSN: 2395-6011 | Online ISSN: 2395-602X (www.ijsrst.com)

Synthetization of Copper Sulphide Thin Film By CBDT

R. V. Suryawanshi, Barote M A*
Department of Physics & Electronics, Azad Mahavidyalaya Ausa, Ta. Ausa, Dist. Latur- 413520, M.S., India
Email: sundarvs1095@gmail.com, *Email: barotema1971@gmail.com

ABSTRACT

The chemical bath deposition technique was used to deposited copper sulphide thin film on an amorphous glass substrate. Experiments was carried at 60^0C, temperature. Morphological, structural, optical properties of CuS thin film was investigated. X-ray diffraction (XRD), scanning electron microscopy (SEM), energy dispersive X-ray analysis (EDAX), thermoelectric power (TEP) and optical absorption were supported in order to inspect the physical properties of the as deposited sample. X-ray diffraction patterns showed that the film is hexagonal structure. The crystal size (D) was calculated 26.7nm at 60 °C deposition temperature. The SEM micrographs showed that the nanostructure appeared in the sample. Optical property of the film was studied in the wavelength range of 200-1100 nm. It's observed that the absorption follows in visible and ultraviolet regions. The optical energy gap was calculated for the allowed direct transition, its value was 2.45 eV. The dignified resistivity and calculated conductivity was found to vary with temperature. Conductivity extent showed that CuS thin film is n-type and highest conductivity was 1.13×10^{-2} $(\Omega.cm)^{-1}$.

Keywords: *- Copper sulphide thin film, Energy dispersive X-ray analysis, Nanostructure, Direct transition.*

I. INTRODUCTION

An increasing study in semiconducting chalcogenide thin films which have been due to their extensive applications in various fields of science and technology. Copper sulfide is the most frequently used material. The copper sulfide thin film appeals the courtesy of many researchers
due to its semiconducting properties. Similarly, the basic elements of this material are abundant in nature. The copper sulphide is a significant material from the socket of basic research because it is be present in several crystallographic and stoichiometric formulas. The CuS has a distinct composition with different stoichiometry and temperature is responsible for a change from one composition to another. Chemical methods have been used to develop CuS films. The shape, phase and the size of inorganic nano-crystals and micro-crystals are the determinant elements in varying their electrical, optical and other properties. The chemical methods are cost-effective and necessary structure can be obtained with them. To produce copper sulfide thin films with wanted nature and assembly, the chemical method was employed [1-4]. Numerous techniques such as Chemical Bath Deposition (CBD) [2, 5, 6], Successive Ionic Layer Adsorption and Reaction SILAR [4, 7] and Spray Pyrolysis Deposition SPD [8-10]. As a significant semiconductor with unique electronic, optical and chemical assets, CuS thin films are of inordinate apprehension due to its extensive range of application in optical and electrical devices, such as photothermal conversion of solar energy, electro-conductive electrodes, microwave shielding

coatings, solar control coatings, IR detectors, temperature control of satellites, light emitting diodes and other optoelectronics [5, 7]. In this paper, copper sulfide thin film was deposited on glass substrates by chemical bath deposition technique. X-Ray Diffraction (XRD), scanning electron microscope (SEM), optical and electrical characterization were attained for thin film at 60 ^{0}C temperature.

II. EXPERIMENTAL DETAILS

Preparation and characterization of CuS thin film

In the chemical bath deposition technique method, it is important to control the preparation conditions such as the concentration of solutions, pH of the solutions time for deposition and the temperature. Good quality thin film of CuS were prepared by using aqueous solutions of copper sulfate ($CuSO_4$) and Thiourea (H_2NCSNH_2) as a source of Cu and S. The experiment was carried out for temperature 60 ^{0}C. Glass substrates have been passed through the cleaning stage before deposition in the dilute sulfuric acid. Subsequently it was then cleaned with acetone and made ready for deposition by passing through pure water. Prepared glass slides were deep vertically in an aqueous solution having copper sulfate, thiourea (0.5molarity and 10ml of each), triethanolamine, sodium hydroxide and ammonia were used as a complexing agent. The solutions were prepared in double distilled water. The pH of the solution was maintained to 10. After (45mini.) the completion of deposition, film were tough with distilled water [11, 12].The scanning electron microscopy (SEM) of the films was supported out using an energy dispersive spectrometer (EDAX). Structure was studied by an X-ray diffraction technique using XRD machine. The range of 2θ values was from 20° to 80° and emissions used were CuKα (λ=1.5406 Å). The optical absorption measurements were carried out using UV-Vis spectrophotometer in the wavelengths from 200 nm to 1100 nm. An electrical conductivity of the deposited film was verified by a two point probe method in the temperature from 300 K to 500 K. Thermovoltages were also noted on the samples in the 300 K to 500 K temperature.

III.RESULT AND DISCUSSION

3.1 EDS Analysis

As-deposited CuS thin films was sustained out using energy dispersive X-ray spectroscopy (EDS). The analysis shown the presence of Cu and S as constituent elements in the film. A typical EDS spectrum of as deposited thin films at temperature 60 °C as shown in Figure 1. The atomic percentages of constituent elements in the as-deposited films and the taken ratio of Cu and S content in the film is almost same.

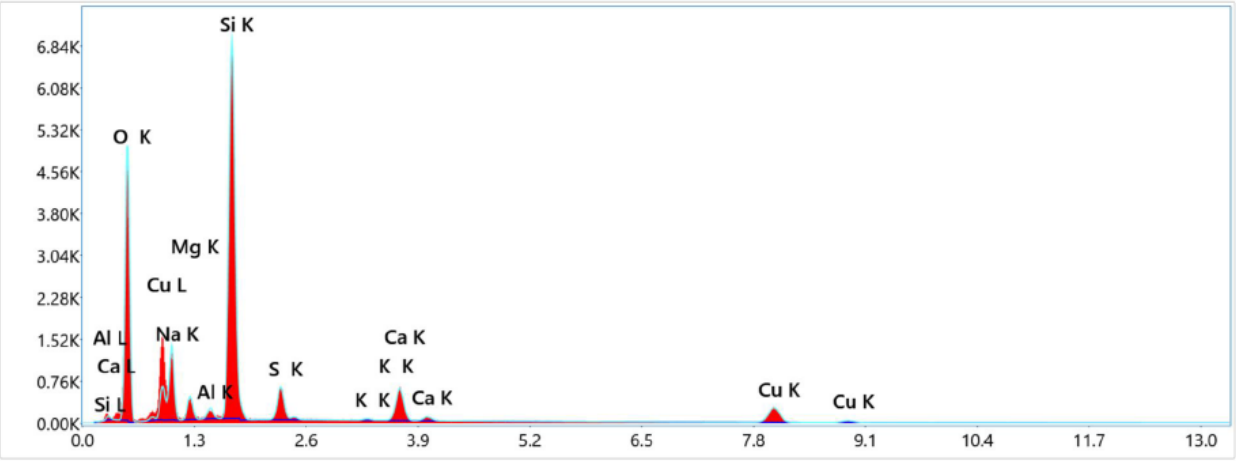

Fig. 1. EDS spectrum of CuS thin film deposited at 60 ^{0}C temperature.

3.2 Structural and Morphological Charecteristics

Figure 2 shows the x-ray diffraction (XRD) of copper sulphide thin film deposited on glass substrate for 60 ^{0}C deposition temperature. The CuS thin film was scanned in the range 20°–80°. The diffraction peaks express that the films contain well grains and are nanocrystalline in nature. The orientations, namely (004), (102), (110) (200) and (108) which indicate a covellite CuS phase with hexagonal structure. The orientations namely (102) for covellite CuS phase with 60 ^{0}C temperature as shown in Figure2 [13].Crystallite size value for this sample is 26.7 nm. at the temperature of 60 ^{0}C. Such result is effective in the development of the crystal structure of CuS thin films. The morphology of the equipped thin film was studied using SEM which shows the surfaces in high magnification and high resolution. The image of CuS thin film prepared at 60 ^{0}C deposition temperature is shown in Figure 3. It observed that the prepared CuS thin film have cauliflower-like forms with an irregular particle size [13, 14].

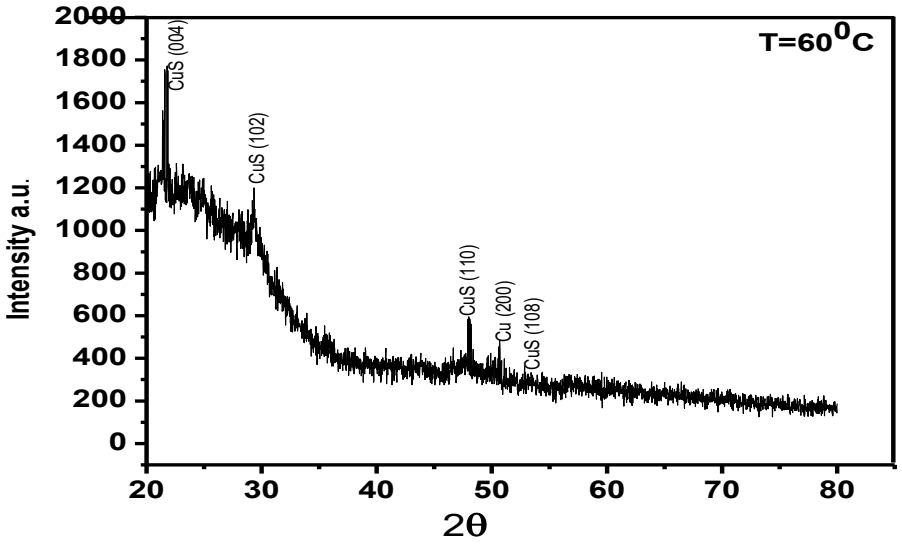

Fig. 2 The XRD of CuS thin films at 60°C temperature.

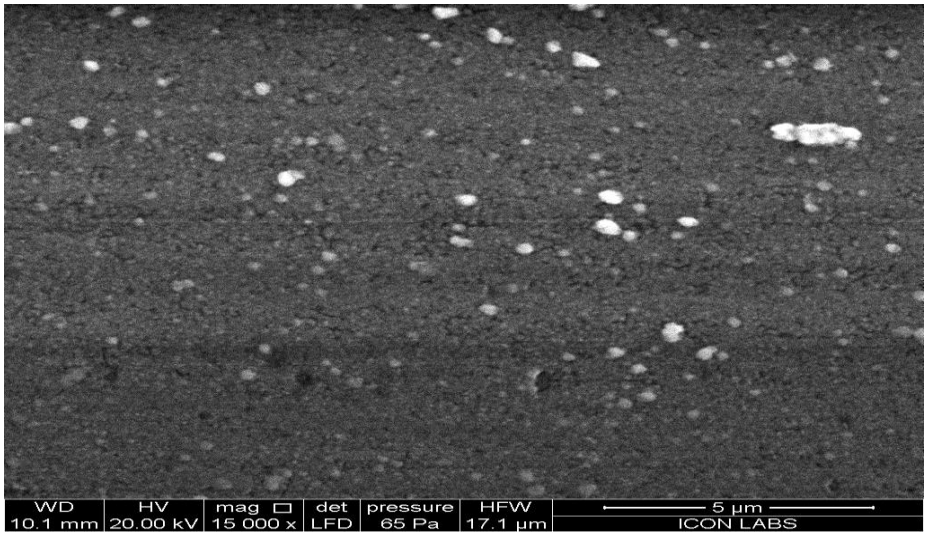

Figure 3. SEM image of CuS thin films at 60 ^{0}C temperature.

3.3 Optical and Electrical analysis

An absorption coefficient as a role of the wavelength of the CuS thin film. The result showed high value of the absorption coefficient in the visible spectrum. The energy gap value of direct electronic transitions was calculated by plotting a graphical relationship of $(\alpha h\nu)^2$ versus photon energy ($h\upsilon$) figure 4. The energy bandgap value of the CuS film was found to be 2.45 eV. This value is identical together to those used for solar cell applications. The energy gap values be contingent on the crystalline structure and are affected by the deposition temperature [15-17].

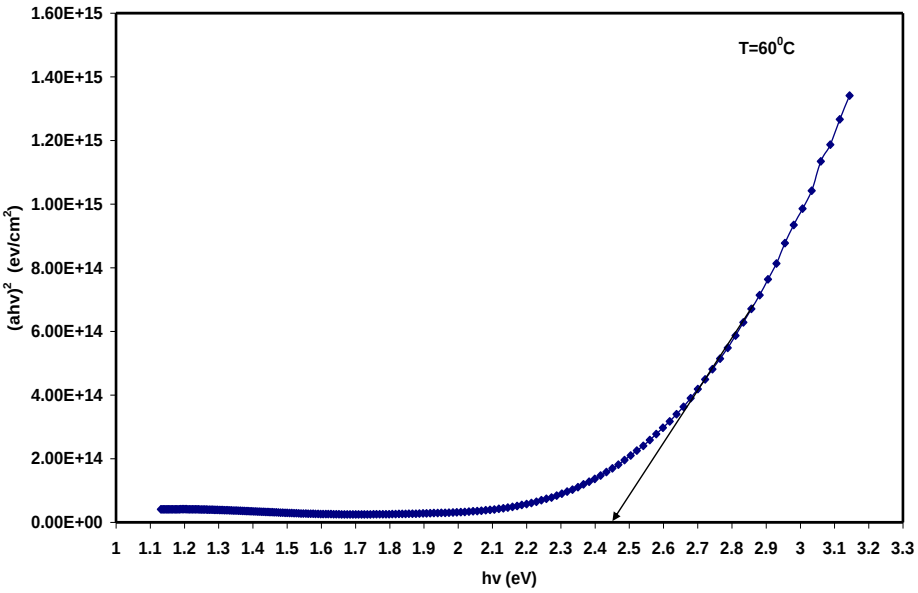

Figure 4. The relation between $(\alpha h\nu)^2$ and $(h\nu)$ for CuS thin film at 60 ⁰C temperature.

An electrical conductivity of the as deposited CuS thin film was measured using two-probe method in the range of temperature from 300 – 500 K. The film is semiconducting and nonlinear nature. The electrical conductivity value was found to be 1.13×10^{-2} $(\Omega.cm)^{-1}$for the film deposited at 60 °C. The type of conductivity shown by the CuS thin film is n-type conduction determined from TEP [18].

IV. Conclusions

Nanostructured CuS thin films were prepared by the chemical spray pyrolysis method at 60 °C substrate temperatures. From XRD analysis it was concluded that film is hexagonal structure and n-type in nature. The properties of the prepared film suggest that this may be a good candidate in solar cells.

References:

[1]. M. A. Hosein, E.and M. Mehdi, B. M. Comparative studies of spray pyrolysis deposited copper sulfide nanostructural thin films on glass and FTO coated glass. Bull. Mater. Sci. 2012; 35(5):739-744.

[2]. K. Anuar, W. T. Tan, N. Saravanan, L. K. Khor and S. M. Ho. Effects of deposition time on the chemical bath deposited CuS thin films. J.Nepal Chem. Soc. 2010; 25:2-8.

[3]. M. Ramya and S. Ganesan. Annealing effects on resistivity properties of vacuum evaporated Cu_2S thin films. International Journal of Pure and Applied Physics 2010; 6(3):243-249.

[4]. A. A. Ibiyemi, M. Tech. The growth and characterization of CuS nanomaterials by Successive Ionic Layer Adsorption and Reaction (SILAR), The Pacific Journal of Science and Technology 2012; 13 (2):243-250.
[5]. A. H. Omran A. M. D. Jaafer, Annealing effect on the structural and optical properties of CuS thin film prepared by Chemical Bath Deposition (CBD). Journal of Kufa – Physics 2013; 5(1):79-90.
[6]. Mudi Xin, Kun Wei Li, Hao Wang. Synthesis of CuS thin films by microwave assisted chemical bath deposition. Applied Surface Science 2009; 256:1436-1442.
[7]. A. U. Ubale, M. V. Bhute, G. P. Malpe, P. P. Raut, Chip made, S. G. Ibrahim. Physical properties of nanostructured (PbS)x(CuS)1-x composite thin films grown by successive ionic layer adsorption and reaction method. Journal of Saudi Chemical Society 2014;1-10.
[8]. Cristina Naşcu, Ileana Pop, Violeta Ionescu, E. Indrea, I. Bratu. Spray pyrolysis deposition of CuS thin film. Materials Letters 1997; 32:73-77.
[9]. L. A. Isac, A. Duta, A. Kriza, I. A. Enesca, M. Nanu. The growth of CuS thin films by spray pyrolysis. Journal of Physics: Conference Series 2007; 61:477-481.
[10]. Horea Iustin NAşCU and Violeta POPESCU. CuS thin films obtained by spray pyrolysis. Leonardo Electronic Journal of Practices and Technologies 2004; 4:22-29.
[11]. T. Ç. Taşdemirci, Study of the physical properties of CuS thin films grown by SILAR method Optical and Quantum Electronics. Springer Science+Business Media, LLC, part of Springer Nature 2019, 51:245 (2019).
[12]. L.P. Deshmukh, R.V. Suryawanshi, E.U. Masumdar and M. Sharon, $Cu_{1x}In_xSe_2$ thin films: Deposition by spray pyrolysis and characteristics. Solar Energy 86, 1910 (2012).
[13]. F.A. Sabah, N. M. Ahmed, Z. H. Hiba, S. Rasheed, Effect of Annealing on the Electrical Properties of Cu_xS Thin Films. 5th International Conference on Recent Advances in Materials, Minerals and Environment (RAMM) & 2nd International Postgraduate Conference on Materials, Mineral and Polymer. (MAMIP), 4-6 August 2015, Procedia Chemistry, ScienceDirect, 15 – 20, 19 (2016).
[14]. T. Ç. Taşdemirci, Study of the physical properties of CuS thin films grown by SILAR method.Optical and Quantum Electronics. Springer Science+Business Media, LLC, part of Springer Nature, 51:245 (2019).
[15]. V. P. Balasubramanian, N. Kumar and D. Sengottaiyan, Effect of deposition temperature on structural, optical and electrical properties of copper bismuth sulphide (CuBiS2) thin films deposited by chemical bath deposition. Materials Science-Poland, 329-334. 35.2 (2017)
[16]. M. Li-jian, and M. P. Dos Santos. Properties of indium tin oxide films prepared by rf reactive magnetron sputtering at different substrate temperature. Thin Solid Films. 62-.56, 322.1-2 (1998).
[17]. NA Bakr, ZT Khodair, SM Hassan, Effect of substrate temperature on structural and optical properties of Cu2ZnSnS4 (CZTS) films prepared by chemical spray pyrolysis method. Research Journal of Chemical Sciences ISSN.2015;2231:606X (1986).
[18]. Sarkar S, Howli P, Das B, Das NS, Samanta M, Das GC, Chattopadhyay KK. Novel quaternary chalcogenide/reduced graphene oxide-based asymmetric supercapacitor with high energy density. ACS applied materials & interfaces. Jun 28;9(27):22652-64 (2017).

ICRTMS-2024
International e-Conference on Recent Trends in Material Science
In Association with International Journal of Scientific Research in Science and Technology
Volume 11 | Issue 9 | Print ISSN: 2395-6011 | Online ISSN: 2395-602X (www.ijsrst.com)

Electrical Applications of SnO_2 doped with ZnO Ammonia gas sensor

A. J. Atram[1], K. B. Raulkar[2], G. T. Lamdhade[2]
[1]Lokmanya Tilak Mahavidyalaya, Wani
[2]Vidya Bharati Mahavidyalaya, Amravati

ABSTRACT

SnO_2 and ZnO are prepared using stannous chloride and zinc chloride with water as a solvent. Nanocrystalline SnO_2-ZnO composite thick films are created through screen printing technique. The structure is examined using field emission scanning electron microscopy (FE-SEM).The FE-SEM shows nanocrystalline spherical stannous oxide and ZnO rod shapes.

Keywords: SnO_2, ZnO, Ammonia gas sensor

I. INTRODUCTION

The rapid industrial growth across various sectors has led to environmental pollution, posing a significant threat to human health and the ecosystem. To address this issue, the development of highly sensitive and selective sensors for detecting hazardous gases in the atmosphere is crucial. Metal oxide-based nanocrystalline chemical sensors have emerged as promising options due to their reliability and ease of production.

To enhance sensor sensitivity, various techniques are employed, such as using composite systems of nanomaterials, altering composition, reducing particle size, surface modification, and experimenting with different chemicals. Smaller particle sizes result in increased surface area, promoting greater gas diffusion and reactivity on the sensor surface, thereby enhancing sensitivity.

Researchers initially focused on single metal oxide-based sensors, but they exhibited drawbacks such as low sensitivity, selectivity to gases with similar characteristics, and longer response/recovery times. The use of composite metal oxide-based nanomaterial systems has shown promise in improving sensor performance. Sensitivity and selectivity can be enhanced by utilizing mixtures of metal oxides or composite systems.[1-3]

The electronic structure of nanocrystals in composite sensors can be altered through interactions between different components, leading to increased reactivity with target gases. Adjusting the composition, structure, and work function of nanocomposite sensors significantly improves selectivity. Moreover, modifying chemical components or their quantities offers opportunities to enhance sensitivity

In summary, the development of advanced sensors, particularly those based on composite metal oxide nanomaterials, is vital for effectively detecting and addressing the challenges posed by environmental pollution resulting from industrial activities.[4]

To improve the characteristics of gas sensors, researchers have explored mixed metal oxide systems. Adding a small quantity of ZnO to CuO-doped SnO_2, for instance, shifted the temperature sensitivity of CO to a higher range [5]. These mixed metal oxide systems fall into three categories:

1. **Chemical Compounds:** Resulting from interactions between different oxides, examples include $ZnSnO_3$ and Zn_2SnO_4 in the ZnO-SnO_2 system [7], and $CdIn_2O_4$ formed by the interaction of CdO with In_2O_3 [8].
2. **Solid Solutions:** Formed by mixing two metal oxides, like TiO2 with SnO2, which creates solid solutions above a critical temperature [10-11].
3. **Interacting Nanocrystals:** Mixtures of metal oxide nanocrystals interacting with each other, such as In_2O_3-SnO_2, TiO_2-WO_3, belonging to this category [12-14].

Various methods are used for producing mixed metal oxide nanocomposites, including sol-gel techniques, aerosol spraying, sputtering, and blending of individual metal oxide nano powders. It's important to note that the nanocrystalline structure in the composite may differ considerably from that of the individual components.

The synthesis of nanocomposites, like TiO_2-SnO_2, may introduce high-volume defects due to the insertion of ions from one component into the lattice of the other. For example, in the synthesis of TiO2-SnO2 nanocomposites, nanocrystalline particles with high-volume defects are produced.

In this work, researchers focused on iso-type SnO_2-ZnO composite sensors, specifically studying sensitivity and response/recovery times. The aim is to enhance the performance of gas sensors, crucial for addressing environmental pollution challenges resulting from industrial activities.

II. Experimental

In the experimental process:

a) **Precursors:** Used AR grade stannous chloride and zinc chloride from Merck Ltd.

b) **Base:** AR grade diluted ammonia solution served as the base.

c) **Preparation of Solutions:** Stannous chloride and zinc chloride were separately diluted with de-ionized water while maintaining the pH using diluted liquid ammonia.

d) **Washing:** Resultant precipitates of stannous chloride and zinc chloride were washed with de-ionized water until chlorine ions were removed.

e) **Microwave Irradiation:** The chlorine-free precipitates were irradiated with microwave energy using a Samsung household microwave oven at a frequency of 2.45 GHz and power up to 1 kW for an optimum duration.

f) **Sintering:** The mixture of SnO and ZnO nanoparticles obtained was sintered at 400°C for 5 hours.

g) **Analysis:**
- **XRD:** Structure analysis was conducted using X-ray diffraction pattern (XRD) with a CuKα wavelength of 1.54 Å.

- **SEM:** Morphology was studied using scanning electron microscopy (SEM) .

Overall, the experimental process involved precise steps in preparing and analysing the SnO_2 and ZnO nanoparticles, aiming to understand their structure, morphology, and composition.

To prepare SnO_2-ZnO nano composite thick films:

1. **Synthesis:** SnO_2 and ZnO were separately synthesized using the microwave-assisted method.
2. **Quantities:** Different ratios of SnO_2 and ZnO were used for fabricating the composite thick films: 100%SnO2-0%ZnO, 80% SnO_2 - 20% ZnO, 60% SnO_2 - 40% ZnO, 40% SnO_2 - 60% ZnO, 20% SnO_2 - 80% ZnO, and 0% SnO_2 - 100% ZnO.
3. **Screen Printing:** Thick films of the synthesized SnO2-ZnO nano composite were prepared using the screen-printing technique.

The chosen percentages of SnO_2 and ZnO in the composite films vary to study the impact of different compositions on the properties of the resulting thick films. The screen-printing technique is employed for its practical and effective application in fabricating these nanostructure composite films.

III.Result and Discussion

The composite film, comprised of both SnO_2 and ZnO, exhibits a structure where ZnO rods and tubes, along with clusters of spherical SnO_2 particles, are randomly dispersed. The micrograph reveals distinct ZnO rods with sizes of 81.2 nm and 125 nm. Additionally, smaller ZnO rods, smaller than 81.2 nm, are observed in the image. The micrograph also captures agglomerated clusters of spherical SnO_2 particles, with sizes ranging from 24.1 nm to 31.3 nm.

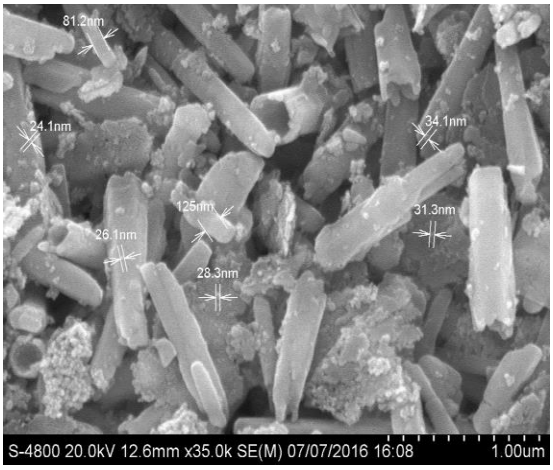

(a)

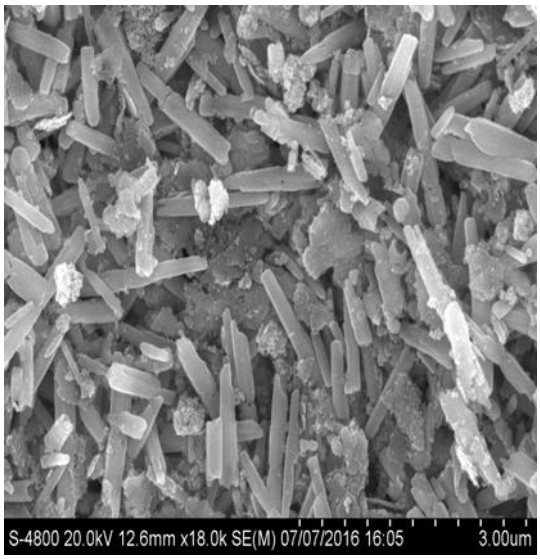

(b)

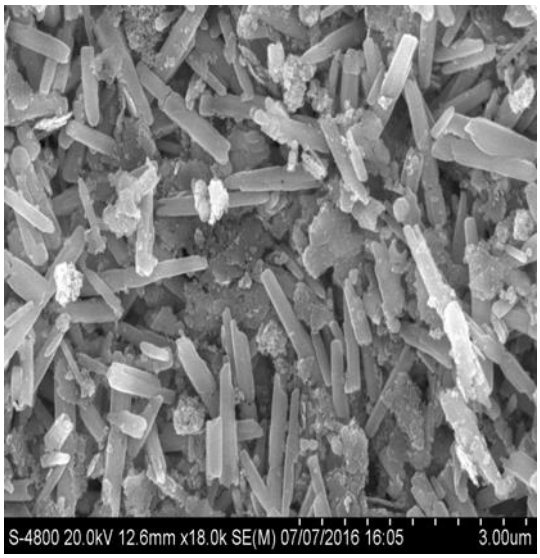

(c)

Fig 1(a-c) FE-SEM micrograph of 20%-80% =SnO_2–ZnO composite nanomaterial thick film

3.1 Electrical Characterization: The electrical characterization involved studying the I-V (current-voltage) characteristics of SnO_2-ZnO nano composite thick films at a temperature of 350°C. Figure 3 displays these characteristics, and the analysis was conducted using a Keithley 6487 picometer cum voltage source.

The measurements involved applying a forward bias voltage ranging from 0 to 10 V with a step increment of 2 V. The process was then repeated with negative voltage. The nature of the I-V characteristics for each specific sample indicates that the contacts exhibit an ohmic behaviour.

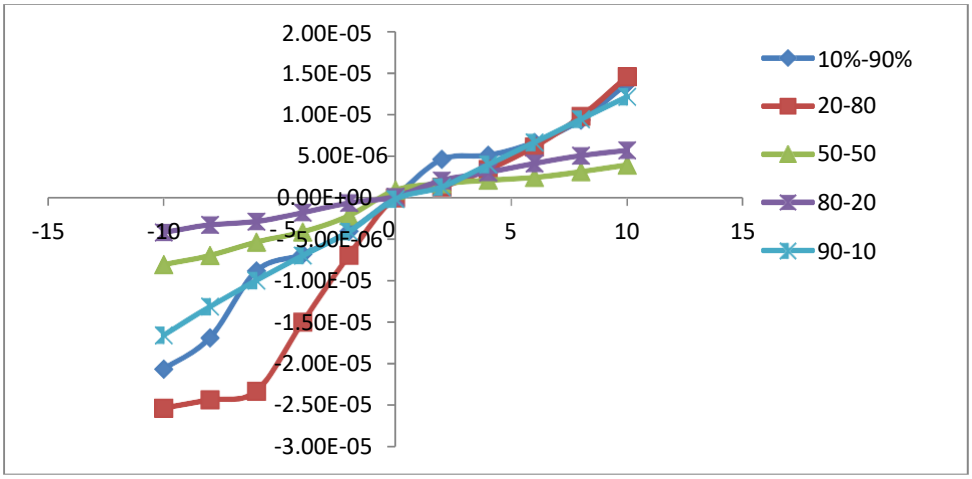

Fig 2 Characteristics of unmodified SnO_2–ZnO nanocomposites

3.2 Electrical Conductivity: The relationship between log (σ) and the reciprocal of temperature for all unmodified SnO_2-ZnO nano composite thick films is illustrated in the figure.

Notably, the sample with a composition of 80-20 shows the highest value of log (σ), indicating the highest electrical conductivity among the studied samples, while the sample with a composition of 20-80 exhibits the lowest conductivity. These variations in electrical conductivity are essential for understanding the sensor characteristics and their potential applications.

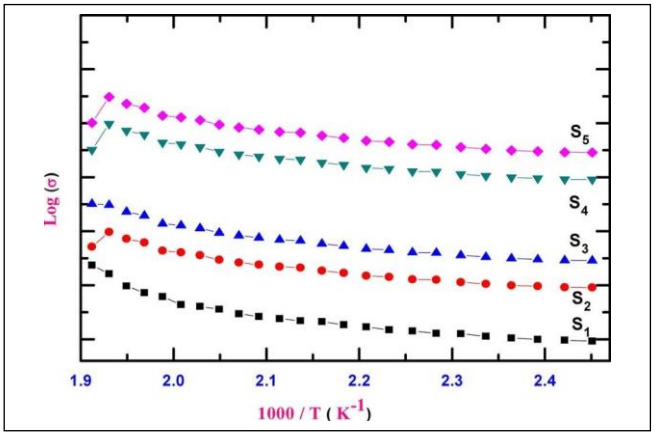

Figure 3: Electrical Conductivity

Figures 4 illustrate the gas response variation with operating temperature for pure SnO_2, ZnO, and SnO_2-ZnO composite thick films sensors in response to NH_3 gas. In both cases, it is evident that the gas sensitivity of the SnO_2-ZnO composite sensor increases with operating temperature, reaching its maximum at the optimum temperature and then decreasing. Among all sensors, the composite sensor with a 50-50 ratio exhibits the highest sensitivity to NH_3 gas.

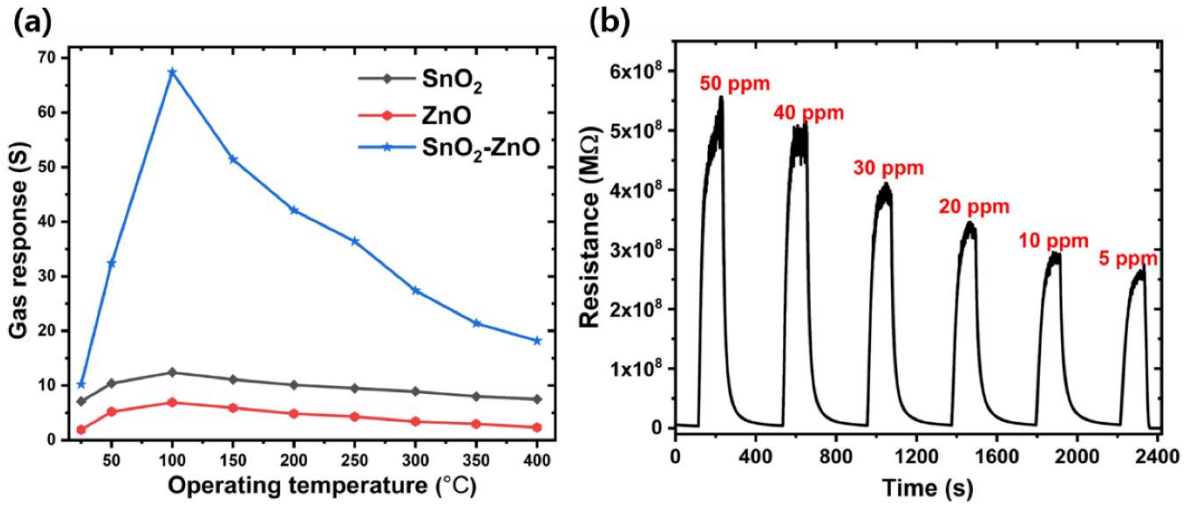

Figure 4: Gas response of SnO_2 and ZnO

Conclusion

In summary, the findings and analysis of this study indicate that the SnO_2–ZnO composite sensors array is not highly effective in detecting Ammonia. Interestingly, the composite materials demonstrated more favourable response behaviours compared to their pure counterparts.

Acknowledgements: The authors are thankful to Vidya Bharati Mahavidyalaya Amravati for providing facilities to carry out the research work

References:

1. Wang Y., Jia W., Strout T., Baikun Z., Cui J. and Lei Y., **(2011)**, Ammonia Gas Sensor Using Polypyrrole-Coated TiO_2/ZnO Nanofibers, Electroanalysis, 21,1432
2. Tang X., Raskin J.P., Kryvutsa N., Hermans S., Slobodian O., Nazarov A.N. and Debliquy M. **(2020)**. An ammonia sensor composed of PPy synthesized on reduced graphene oxide by electropolymerization, Sens. Actuators B Chem., 305, 127423.
3. Dai M.Z., Lin Y.L., Lin H.C., Zan H.W., Chang K.T., Meng H.F., Liao J.W., Tsai M.J. and Cheng H. **(2013)**. Highly sensitive Ammonia sensor with organic vertical nanojunctions for noninvasive detection of hepatic injury, Anal. Chem., 85, 3110–3117.
4. Chartuprayoon N., Hangarter C.M., Rheem Y., Jung H. and Myung N.V. **(2010)**, Wafer-scale fabrication of single PPy nanoribbon-based ammonia sensor, J. Phys. Chem., 114, 11103–11108.
5. Capone S., Forleo A., Francioso L., Rella R., Siciliano P., Spada- vecchia J., Presicce D.S. and Taurino A.M. **(2003),** Solid state gas sensors: state of the art and future activities, Journal of Optoelectronics and Advanced Materials 5, 5, 1335 – 1348.
6. Garg R., Kumar V., Kumar D., and Chakarvarti S.K., **(2015)**. Polypyrrole Microwires as Toxic Gas Sensors for Ammonia and Hydrogen Sulphide, Columbia International Publishing Journal of Sensors and Instrumentation, 3, 1-13.

7. Shao Q., Chen W., Wang Z., Qie L., Yuan L., Zhang W., Hu X., Huang Y., **(2011)**. SnO_2-based composite coaxial nanocables with multi-walled carbon nanotube and polypyrrole as anode materials for lithium-ion batteries, Electrochem. Commun. 13, 1431-1434.

8. Y. Ravi Kumar, J. Gounder Thangamani, T. V. Krishna Karthik, Kalim Deshmukh and S. K. Khadheer Pasha, **(2024)** "A novel flexible CO_2 gas sensor based on polyvinyl alcohol/yttrium oxide nanocomposite films" Royal Society of Chemistry, RSC Adv., 14, 5022–5036

9. Wang Y., Jia W., Strout T., Schempf A., Zhang H., Li B., Cui J. and Lei Y., **(2009)**, Preparation, Characterization and Sensitive Gas Sensing of Conductive Core-sheath TiO_2-PEDOT Nanocables, Sensors (Basel), 9(9), 6752–6763.

10. Vaezi M.R. and Sadrnezhaad S.K., **(2007)**. Nanopowder synthesis of zinc oxide via solochemical processing, Mater Sci. Eng B 140, 73.

11. Hernandez S.C., Chaudhuri D., Chen W. and Myung N.V., **(2007)**. Maskless electrodeposited contact for conducting polymer nanowires, Appl. Phys. Lett. 92, 073104.

12. Li W., Liu H., Xie D., He Z. and Pi X., **(2017)**. Lung Cancer Screening Based on Type-dierent Sensor Arrays, Sci. Rep, 7, 1969.

13. Guntner A.T., Righettoni M. and Pratsinis S.E. **(2016)**. Selective sensing of NH_3 by Si-doped -MoO_3 for breath analysis, Sens. Actuators B Chem., 223, 266–273.

14. Chitte H. K., Bhat N.V. and Vasant E., **(2011)**, Synthesis of Polypyrrole Using Ferric Chloride ($FeCl_3$) as Oxidant Together with Some Dopants for Use in Gas Sensors, Journal of Sensor Technology, 1, 47-56.

ICRTMS-2024
International e-Conference on Recent Trends in Material Science
In Association with International Journal of Scientific Research in Science and Technology
Volume 11 | Issue 9 | Print ISSN: 2395-6011 | Online ISSN: 2395-602X (www.ijsrst.com)

Excess parameter study of Ethyl Acetate-Xylene Mixtures at 15ºC and 20ºC using TDR

S. S. Birajdar[1] and D. B. Suryawanshi[2*]

[1]Dept. of Physics and Electronics, Maharashtra Udayagiri Mahavidyalaya, Udgir, Maharashtra, 413517, India

[*2]Department of Physics and Electronics, Shri Havagiswami Mahavidyalaya, Udgir, Maharashtra, 413517, India

ABSTRACT

The excess parameters of Ethyl Acetate-Xylene binary mixtures at different 11 concentrations have been studied using Time Domain Reflectometry at different temperatures in the frequency range 10 MHz to 30 GHz. Values of static dielectric constant and relaxation time have been obtained by fitting complex permittivity spectra using least square fit method in Debye model. The observation of behavior of molecular structure and heteromolecular interactions in Ethyl Acetate-Xylene mixture is studied using excess dielectric parameters.

Keywords: Time Domain Reflectometry (TDR), Static dielectric parameters, Excess permittivity and excess relaxation.

I. INTRODUCTION

Dielectric research of hydrogen-bonded compounds in non-polar solvent provides important information of inter-molecular complex formation in binary mixtures. Time domain reflectometry (TDR) [1-4] method is used to determine excess dielectric parameters of Ethyl Acetate (EA)-Xylene mixture, which reveals molecular effects and intermolecular interactions produced in binary mixture at higher frequencies. Strength of interactions, relaxation process, dipole-dipole interactions, bonding among heteromolecules in the mixture is extensively studied using TDR and is thoroughly discussed in the previous article [5]. Ethyl Acetate (EA) is colorless liquid with sweet or fruity smell, used in wines as well as in food industries, for decaffeinating tea and coffee due to its less toxicity and high evaporation rate [5-6]. Xylene is an aromatic hydrocarbon, colorless, flammable liquid, used as a solvent [7-8]. Present work reveals excess dielectric parameters of EA-Xylene system at 11 different concentrations using TDR in 10 MHz to 30 GHz the frequency range to study the heteromolecular interaction in the mixture.

II. METHODS AND MATERIAL

Ethyl Acetate and Xylene was obtained from Merk Life Sciences Private Ltd. Mumbai, India with 99.5% of purity and Merk Specialties Private Ltd. Mumbai, India with 99.0% respectively and was used without further

purification. Dielectric relaxation parameters measured in the range of 10 MHz to 20 GHz microwave frequency by means of TDR as illustrated in figure 1. Raw data analysis with TDR procedure has been explained formerly [4-7].

III. RESULTS AND DISCUSSION

Complex permittivity spectra with dielectric relaxation parameters of EA-Xylene mixture were acquired by the Havriliak-Negami equation [9-12],

$$\varepsilon^* = \varepsilon_\infty + \frac{\varepsilon_o - \varepsilon_\infty}{[1+(j\omega\tau)^{1-\alpha}]^\beta} \quad (1)$$

where ε_o is static dielectric permittivity, ε_∞ is permittivity at high frequency, τ is relaxation time and α & β are the distribution parameters. The Havriliak-Negami equation involves Cole-Cole (β=1) [13], Cole-Davidson (α=0) [14] and Debye (α=0 & β=1) [15] relaxation models and for present EA-Xylene system, Debye model is used to fit the data.

Static dielectric parameters vary with change in concentration of solute in solvent, which shows the effect of concentration dependent behavior of mixture such that structure of mixture also depends on viscosity, temperature etc. [16-17]. The facts associated to EA-Xylene interactions are achieved by the way of excess parameters [5, 18]. Excess permittivity reveals information about the interaction among mixture constituents. The excess relaxation delivers evidence related to structural variations in the mixture. The excess parameters were determined by using the following relations as [19-21],

$$\varepsilon_0^E = (\varepsilon_0)_m - [(\varepsilon_0)_X V_X + (\varepsilon_0)_{EA}(1 - V_X)] \quad (2)$$

$$\left(\frac{1}{\tau}\right)^E = \left(\frac{1}{\tau}\right)_m - \left[\left(\frac{1}{\tau}\right)_X V_X + \left(\frac{1}{\tau}\right)_{EA}(1 - V_X)\right] \quad (3)$$

where suffix m, X and EA signifies mixture, Xylene and EA respectively, ε_o^E and $(1/\tau)^E$ are is excess permittivity and excess relaxation, Vx denotes volume fraction of Xylene.

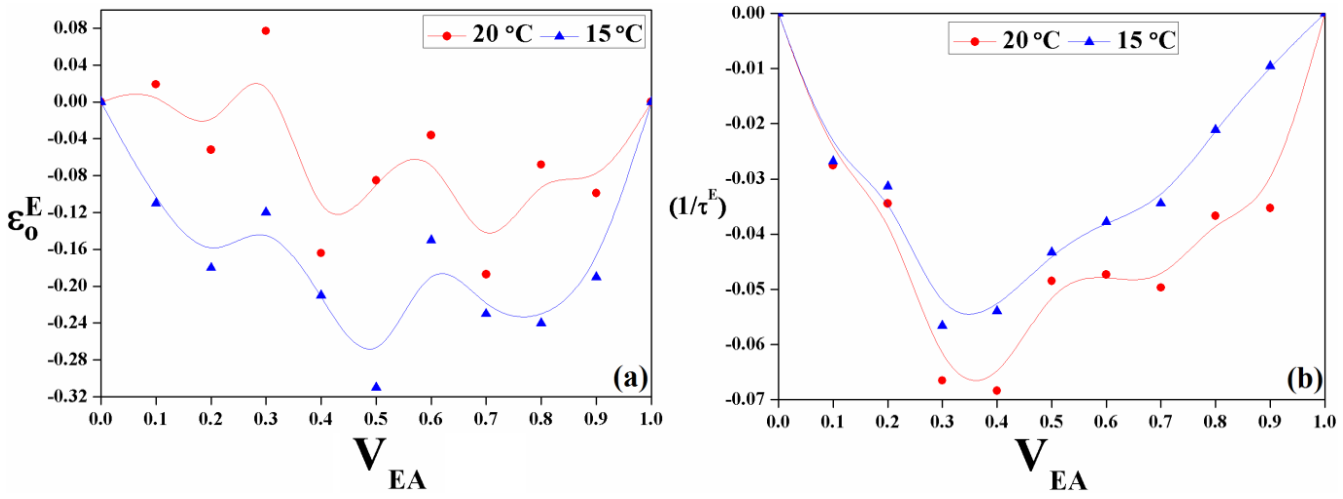

Fig. 1 Variation of **(a)** excess permittivity and **(b)** excess relaxation vs. V_{EA} at 20 ºC and 15 ºC respectively.

ε_o^E values for the present system are negative at all concentrations except at V_{EA} = 0.1 and 0.2 at 20 ºC, as shown in figure 1 (a). Negative values of excess permittivity show strong intermolecular interactions among heteromolecules [22], indicates formation of multimers through hydrogen bonding which decreases the effective dipole moment [23]. In case of $(1/\tau)^E$, mixture of EA-Xylene results in negative values for all concentrations is an indicative of slower roation of dipoles such that the there is a formation of polymeric hydrogen bonded structure in the mixture [24-25], as shown in figure 1 (b).

IV. CONCLUSION

The excess parameters of EA-Xylene binary mixture were studied using TDR in 10 MHz to 30 GHz frequency range. Variation of V_{EA} in the mixture causes the values of ε_o and τ change at that particular concentration. Excess permittivity shows negative values at all concentrations except at V_{EA} = 0.1 & 0.2 and show strong intermolecular interactions with formation of multimers. Also the excess relaxation show formation of polymeric structure with slower rotation of molecules such that the $(1/\tau)^E$ values are negative for all concentrations.

V. ACKNOWLEDGEMENTS

Author S.S. Birajdar is thankful to School of Physical Science, S.R.T.M.U, Nanded for providing all research facilities. Financial support from Department of Science and Technology, New Delhi is gratefully acknowledged (Project No.SR/S2/LOP-25/2007).

VI. REFERENCES

[1] Kumbharkhane A.C., Joshi Y. S., Mehrotra S. C. et al., Physica B. 2013; 421: 1.
[2] Sudo S, Shinyashiki N, Kitsuki Y, et al. , J Phy Chem A. 2002; 106:458–464.
[3] Sudo S, Oshiki N, Shinyashiki N et al., J Phy Chem A. 2007; 111(16):2993–2998.
[4] Kumbharkhane A.C., Puranik S. M., Mehrotra S. C., J Chem Soc Faraday Trans. 1991;87:1569-73, doi: 10.1039/ft9918701569.
[5] Birajdar S.S., Suryawanshi D.B., Deshmukh A.R., Shinde R.V., Ingole S.A. and Kumbharkhane AC., Physics & Chemistry of Liquids. 2021; 59(4):503-11. https://doi.org/10.1080/00319104.2020.1743702.
[6] https://en.wikipedia.org/wiki/Ethyl_acetate.
[7] Birajdar S.S., Deshmukh A.R., Kumbharkhane A.C. and Suryawanshi D.B., Polycyclic Aromatic Compounds, 2022: 1-6. Doi: 10.1080/10406638.2022.2097273.
[8] Kandyala R. et al., Journal of Oral and Maxillofacial Pathology, 14 (1) (2010) 1-5.
[9] Havriliak S, Negami S., Polymer. 1967;8:161-210. https://doi.org/10.1016/0032-3861 (67)90021-3.
[10] Sengwa R.J., Madhvi A., Sankhla S., Indian J Pure & App Phys. 2006; 44:943–952.
[11] Kaatze U., Radiat Phys Chem. 1995;45:549-66. Doi: 10.1016/0969-806X (94)00070-Z.

[12] Birajdar S.S., Deshmukh A.R., Kumbharkhane A.C. and Suryawanshi D.B., Indian Journal of Chemistry, 62 (8) (2023) 872-878. DOI: 10.56042/ijc.v62i8.4794.
[13] Cole K.S., Cole R.H., J Chem Phys. 1941 Apr;9(4):341-351.
[14] Davidson D.W, Cole R.H., J Chem Phys. 1950;18:1417.
[15] Debye P., Chemical Catalog. Co: New York 1929; 48(3):1036-37. https://doi.org/10.1002/jctb.5000484320.
[16] Lide D.R., Ed. CRC Handbook of Chemistry and Physics, 87th ed. Boca Raton, FL, Taylor and Francis (2007).
[17] Birajdar S.S., Kumbharkhane A.C., Hallale S.N., Hudge P. G. and Suryawanshi D. B., Polycyclic Aromatic Compounds. 2022: 1-9. DOI: 10.1080/10406638.2022.2032767.
[18] Joshi Y.S., Kanse K.S., Rander D.N. & Kumbharkhane A.C., IJPAP, 54 (2016) 621.
[19] Kumbharkhane A.C., Puranik S.M. and Mehrotra S.C., J. Solution Chem. 22 (3) (1993) 219–229.
[20] Karthick N.K., Arivazhagan G., Kumbharkhane A.C., Joshi Y.S. & Kannan P.P., J Mol Struct, 1108 (2015) 203.
[21] Sengwa R.J, Khatri V. & Sankhla S., J Mol Liq, 144 (2009) 89.
[22] Birajdar S.S., Deshmukh A.R., Suryawanshi D.B. and Kumbharkhane A.C., Indian Journal of Chemistry section A 60.2021; A: 72-79.
[23] Sivagurunathan P, Dharmalingam K & Ramachandran K, Undre B P, Khirade P W & Mehrotra S C, Lith J Phys, 46 (2006) 441.
[24] Birajdar S.S., Deshmukh A.R., Kumbharkhane A.C. and Suryawanshi D.B., Journal of the Indian Chemical Society, 99 (10) (2022) 100733, https://doi.org/10.1016/j.jics.2022.100733.
[25] Dhage H.M. et al., Indian Journal of Chemistry, 61, 2022, pp. 1153-1158. DOI: 10.56042/ijc.v61i11.61874.

ICRTMS-2024
International e-Conference on Recent Trends in Material Science
In Association with International Journal of Scientific Research in Science and Technology
Volume 11 | Issue 9 | Print ISSN: 2395-6011 | Online ISSN: 2395-602X (www.ijsrst.com)

A Review on Luminescence Properties of Garnet Structured Phosphors with Different Lanthanide Doping for Divergent Applications

G. C. Vandile[1*], D. V. Nandanwar[1], A. K. Nandanwar[2]
[1]Shri M. M. College of Science, Nagpur-440009
[2]J. M. Patel Arts, Commerce & Science College, Bhandara-441904
[3]Department, University/Institute/Company, City, State, Country

ABSTRACT

This paper reports the various applications in relative to the properties of luminescence garnet phosphor materials doped with different lanthanide ions and their applications in various fields. The fields of applications of YAG:La (*Yttrium aluminum garnet doped various lanthanide activators*) depending upon the structural and luminescent properties. These properties conforms agreement for possible applications. The researchers try to synthesize such materials for social needs. The garnet phosphors are not recent materials. The history of the garnet materials has long back and applications in various fields. An attempt is made to find the factors or parameters are responsible (*physical, chemical, mechanical, electrical, optical, etc. properties*) for the different applications. The lanthanide ions doped in garnet structured phosphors have wide range of applications. The garnet materials doped with Ce^{3+}, then the resultant compounds are used because to high density as gamma ray absorber, as scintillators. The trivalent lanthanide ions doped garnet nanomaterials can be used as temperature measuring devices. The YAG:Tb^{3+} (*Terbium rich garnet luminescence materials*) are used in propagation of THz phonons, as active medium for powerful solid state laser.. The main focus of this article is to discuss the applications of various lanthanide cations rich garnet nanocrystal phosphors in different fields depending on their relative properties.

Keywords: Luminescence, Garnet Phosphors, YAG, Lanthanide Activator, Photoluminescence, Nanomaterial.

I. INTRODUCTION

The commonly chemical compound formula for garnet phosphors is $A_3B_2C_3O_{12}$. Where A is in dodecahedral coordinated site while B and C (may be same group) are in octahedral & tetrahedral coordinated sites respectively as shown in fig. (1) [1]. A is without inversion symmetry in point group D2 while B & C are with inversion symmetry in point groups C3i & S4 respectively. Generally, the garnet phosphor are possessing cubic structure and Ia3d is space group. In this article, we are focusing on applications of the various lanthanides rich garnet materials [2]. The garnet nanomaterials doped with lanthanide ions have the great attraction. The lanthanide ions have very interesting applications. The garnet phosphors are exhibited very interesting properties. The researchers were used YAG ($3Y_2O_3$-$5Al_2O_3$) as host garnet structure luminescent materials. The rare earth garnet nanomaterials are non-toxic materials [3]. The materials have great thermal stability [4]. The unit cell of garnet structured materials consists of 160 atoms.

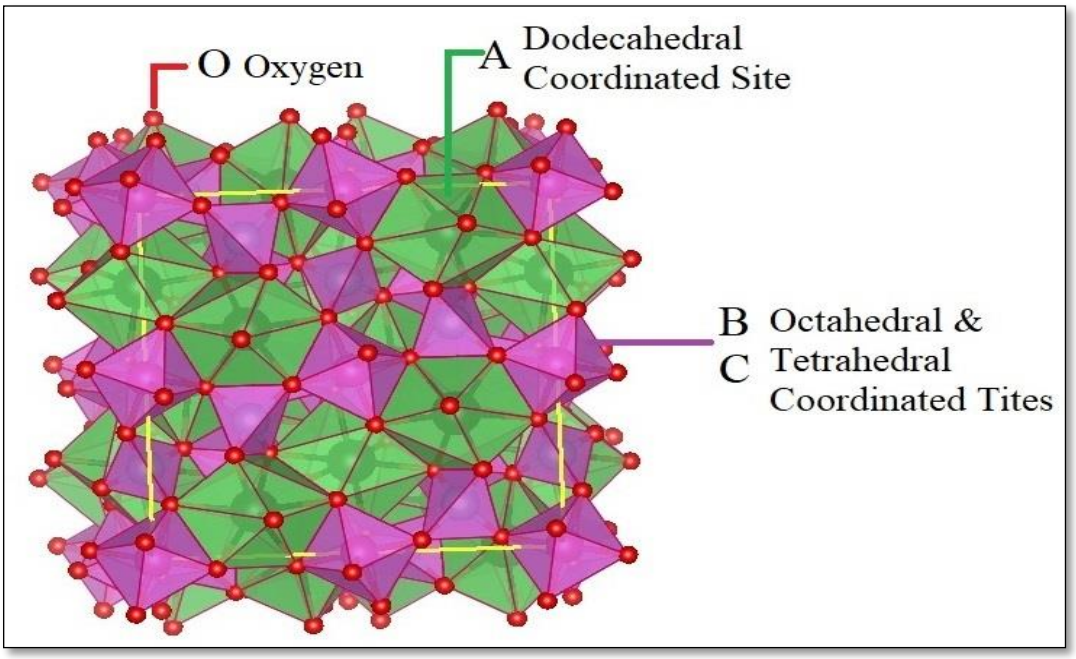

Figure 1: The crystal structure of YAG ($A_3B_2C_3O_{12}$): A is a dodecahedral; B and C are octahedral & tetrahedral respectively.

The garnet nanostructured YAG:Ce3+ are basically yellow powder phosphors. When these yellow phosphors are interacted with blue light, then white light emission take place and further there materials used in w-LEDs [5]. The white LEDs have high efficiency than incandescent lamp [6]. The YAG:Ce^{3+} garnet phosphors have uniqueness about the electronic transition energy than other lanthanide ions. The excitation for the materials is from 5d to 4f while for emission is from 4f to 5d. The cerium doped YAG is inorganic materials which do not contain hydrogen [7]. The some of the major applications are used as scintillator, active materials for fluorescent screen in CRT, afterglow materials, white light conversion etc.

The YAG:Tb^{3+} garnet phosphors materials are composited from YAG ($Y_3Al_5O_{12}$) as host and trivalent terbium(Tb^{3+}) as dopant. The terbium dopant is acted as activator/luminescence center. The garnet phosphors were synthesized by solid state method at temperature 1600 ◦ C for 6 hours The materials YAG:Tb^{3+} were characterized for structural analysis by XRD data. The results were agreed with standard results. The garnet phosphors YAG:Tb^{3+} is a cubic structured but its unit cell is not cubic [8].

This materials are having wide range of applications among the various field of optics related. The materials were undergone photoluminescence properties by spectrophotometer the excitation electronic transition is $^7F_6 \rightarrow {}^5D_3$ and emission transition is $^5D_4 \rightarrow {}^7F_5$ with maximum intensity [9]. The materials are very well known for green light emission. Therefore, these materials can be used as light sensing devices. While it emits green radiation then it can be used as source of radiation (especially in vacuum UV) [10]. The applications of trivalent terbium rich YAG are in LEDs (green, violet/blue) [11], in various types of display which works on the principle of luminescence, for laser fabrication [12].

II. YAG: Ce^{3+} GARNET PHOSPHORS AND THEIR APPLICAIONS

The garnet materials doped with Ce^{3+} i.e. YAG: Ce^{3+} is highly efficient phosphors (luminescence materials). These resultant components have remarkable wide range applications. One of the most useful applications is as scintillators [13]. The scintillators are the materials which show fluoresce when it is irradiated. The scintillators exhibit the luminescent property. The scintillator used as detector also [14]. When particles (α particles, β particles, gamma rays, X-rays etc.) interacts with scintillator materials, then it absorbs energy and got excited that means the electrons of the materials jump from ground state (stable state) to higher energy state (unstable/excited state). These electrons come back to original state (ground state), then these electrons loss the energy in the form of photon (light). The photons (light) are responsible to convert into electrical signal [15]. This signal is amplified by PMT (photomultiplier tube) and show luminescence phenomenon. Therefore, scintillator can be used as detector. The first scintillator was invented in 1903 by W. Crooks by using ZnS screen [16]. The scintillation process was observed in only dark room. This is the main disadvantage; this disadvantage was overcome by using PMT in scintillator [17-18].

The YAG: Ce^{3+} is used in CRT (cathode ray tube). This material is used as CRT phosphors. The cathode ray tube phosphors (cathode ray phosphors) are the powder spreads on the screen (fluorescent screen) as shown in fig. (2). When electron beam is incident on the screen containing this garnet material, then the material absorbs energy (energy of electron beam which generated in CRT) and the electrons of the material jump from stable state (low energy state) to agitate energy state (higher energy state). These electrons come back to original state, and then they release the energy which equal to energy gap between both energy levels in the form of photon [19]. The colour of the CRT screen is depended on periodic arrays of three phosphor dot [20]. The three phosphor dots consist of basic colours red, green and blue. The sequence of the colour start with high wavelength colour to low wavelength colour in colour CRT. The mixture of the particular colours gives all other colours [21]. The resultant compounds derived from YAG: Ce^{3+} is used in fluorescent tube. The similar phenomenon (same as CRT) occurs in the fluorescent tube. The garnet nanomaterial phosphors are more effective colour temperature correlation [22].

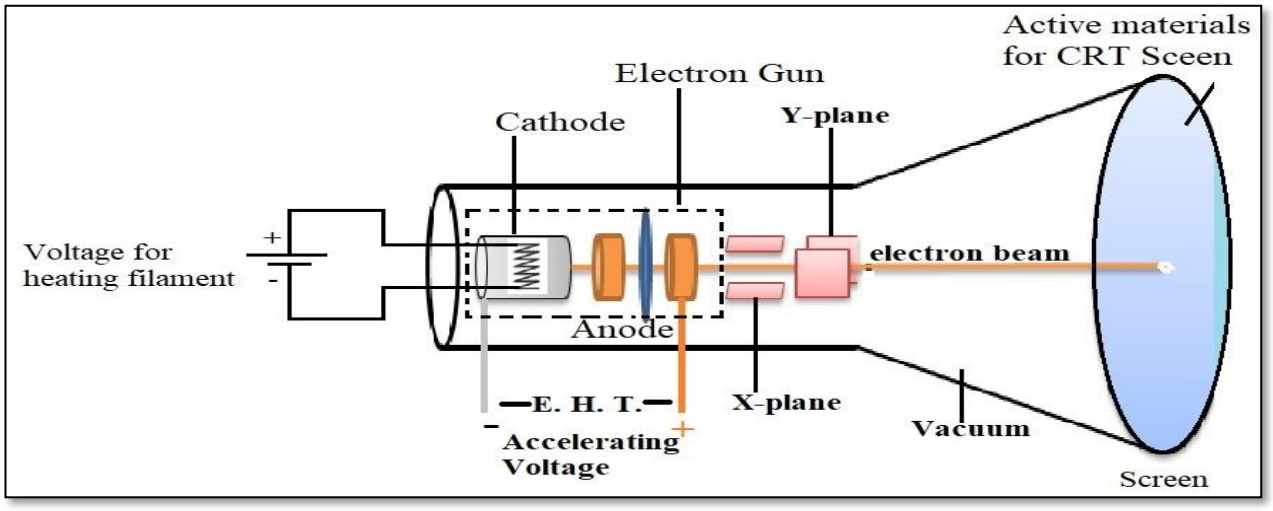

Figure 2: The schematic diagram of CRT. YAG:Ce^{3+} as active materials are used in cathode ray tube for display.

Garnet compounds $Y_3Al_5O_{12}:Ce^{3+}$ are can be as afterglow materials. The materials store the energy at excited energy state and losses slowly [23]. It is attracted attention in the fields of long lived luminescent nanomaterials and its applications. The researchers try to synthesize the materials having high quantum efficiency (quantum yield) i.e. having high PLQY (Photoluminescence Quantum Yield) [24]. The quantum yield (quantum efficiency) is also known as efficiency of fluorescence. It is stated as the ration of number of photons emitted

(emission rate) to number of photons absorbed (excitation rate). The value of quantum yield is unity according to Stark-Einstein law. It is denoted by ϕ and formula for it is shown in equation (1) [25].

$$\phi = \frac{\text{number of photons emitted}}{\text{number of photons absorbed}}$$

$$\phi = \frac{k_i}{k_f + k_i + k_{ec} + k_{ic} + k_{pd} + k_d} \quad \text{--------- (1)}$$

Where,

k_i is intersystem crossing, k_f is fluorescence, k_{ec} is external conversion, k_{ic} is internal conversion, k_{pd} is pre-dissociation, k_d is dissociation.

There are some conclusions come out from above equation (1). The higher value of quantum yield indicates that there is high fluorescence. For non-f fluorescence materials quantum yield is zero ($\phi = 0$). When number of incident photons are excited more electrons (number of excited electrons > number of photons) then the quantum yield is more than one ($\phi > 1$) and opposite to it its value get decreasing ($\phi < 1$). If excited electrons collide with other non-excited electrons, then$\phi < 1$. When some electrons are not absorbed sufficient energy then these electrons can't show any luminescence, this is another main reason for $\phi < 1$ [26].

The great afterglow materials belong to luminescence materials. These materials are having tendency of persistency for long time (hours) after removal of excitation energy [27]. This type of afterglow materials that have long decay time is known as long-afterglow luminescence materials. These materials are mostly used as decorative materials for night lighting materials, transportation vehicles, fire sensors etc [28]. The researchers try to synthesize afterglow materials that persist for few days. Afterglow material has high lifetime that material has large decay time (less decay rate). The materials having large decay time (less decay rate) are called as long persistent luminescence materials. These materials exhibit long lasting phosphors. At room temperature, the materials shows lasting emission after disconnecting from source are called as RTP (Room Temperature Photoluminescence). The recent research on afterglow materials is along hybrid (organic-inorganic) materials to increase the photoluminescence quantum yield [29].

Figure 3: The luminescence materials are irradiated by UV radiation, showing afterglow property. Initially UV is ON then the materials glow properly but after switch of the UV, the materials persist glowing.

Some of the $Y_3Al_5O_{12}:Ce^{3+}$ garnet nanomaterials have chosen to show the phenomenon of afterglow materials. Firstly materials have irradiated by UV light for sufficient time. After that the UV radiation has been disconnected, and then the materials glow without at just removal of UV radiation. The intensity (brightness) of the materials goes decreasing while increasing time ($t_1<t_2<t_3$) as shown in fig (3).

The garnet materials doped with cerium ions can be used to convert color in w-LEDs. Generaly YAG garnet phosphors doped with Ce^{3+} are yellow emitting phosphors [30]. This compound is used in white lighting devices because of its advantages like high photoluminescence quantum efficiency, long lifetime, economical for society [31]. When blue light (wavelength about 458 nm) interacts with YAG:Ce^{3+}, then some blue light converted into yellow light (wavelength range 565 nm – 580 nm) and rest of blue light are converted into white light [32]. But the efficiency of white lighting devices depends on doping concentration and performance of the host materials. The result is that, the efficiency of the w-LEDs is less due to low amount of the materials [33]. This efficiency is not sufficient to convert into w-LEDs. We need to increase the conversion by increasing amount of the materials in optimum amount otherwise efficiency goes decreasing by excess increasing in amount of materials [34]. If large amount of materials are used then more light are absorbed and reabsorbed the reason for decreasing the efficiency [35]. The garnet phosphors YAG:Ce^{3+} have deficiency of production of red light therefore these materials have tendency to convert a great white light [36].

III. YAG: Tb^{3+} GARNET PHOSPHORS AND THEIR APPLICAIONS

The nanomaterials of garnet phosphors are most active materials for production of white lighting devices (w-LED). The radiation of the range of UV is excited the polycrystalline garnet materials doped with terbium (YAG:Tb^{3+}). The emission spectra are obtained about 533 nm (green) [37]. Therefore it is generally known as green light emitter phosphor. This nanocrystalline garnet phosphor is used to efficient green LEDs. When ultra violet radiation (wavelength about 385 nm) interacts with the garnet luminescent materials YAG:Tb^{3+}, some of the incident photons transfer energy to the electrons of the materials and got excited. These excited electrons come back from higher energy state to original state (ground sate) by losing energy [38]. This emission energy is absorbed by other unexcited electron and emission energy get decreasing and increasing wavelength about green colour and some of the radiation is converted with mixed colour and this materials exhibit white colour emission.

There are optical fibres based sensors are used to detect the radiation (light). They have lot of advantages. They can`t affected by any chemical process. This is main advantage of the optical fibres sensors. But they have limitations too [39]. The optical fibres sensors are difficult to use in dangerous areas (high radiated areas) such as near the nuclear reactors, commercial irradiation station etc. They have low detection sensitivity. There is need to overcome these limitations. When the optical fibres sensor are made up with garnet phosphors YAG:Tb^{3+} then efficiency, accuracy (performance) and strength are improved. These optical fibres sensors of garnet nanopowered phosphors have good detection sensitivity [40]. These optical fibres can be used hundreds of meters from the detection area. These sensors are used in medical fields for investigation of proper dose importable and radiotherapy.

The YAG:Tb^{3+} garnet phosphors can be used in various display (screen) due their structural and optical properties. The Tb^{3+} doped garnet nanomaterials show the emission spectra in visible region from blue to red colour. The maximum intensities occur at green and yellow colours and minimum intensities occur at blue and red colours [41]. The garnet phosphors doped with trivalent terbium (Tb^{3+}) have high efficient conversion with proper decay rate. On the basis of these results, this material can be used as active materials for CRT (for

screen), in various projection displays, trichromatic source of light, in mercury free lamp (for visible region emission) etc.

IV. CONCLUSION

The basic structured of garnet phosphors (composition) have summarized. We had focused mainly on applications affecting by structural properties, luminescence properties of different lanthanide dopants in garnet structured phosphors. We have chosen Ce^{3+} and Tb^{3+} as trivalent lanthanide activator to discuss the applications on the basis of their luminescence and structural properties. The garnet phosphors doped with cerium ions (YAG:Ce^{3+}) is the yellow phosphors with emission transition 4f to 5d. The applications of the cerium doped garnet phosphors are as conversion of blue colour to white lighting devices, active materials in CRT, as scintillators, afterglow materials long decay time (low decay rate) etc. The terbium rich garnet phosphors had prepared at 1600 °C for 6 hours by solid state reaction method. The emission of the material is found to be $^5D_4 \rightarrow {}^7F_5$ at green light with maximum intensity. Thus this material is also known as green phosphors. These materials are having wide range applications. These materials can be in green LEDs, various fluorescence display, active materials in solid state laser.

V. REFERENCES

[1] P.P. Lohe, D.V. Nandanwar, P.D. Belsare, S.V. Moharil, Journal of Luminescence, 2019, 214, 116537.

[2] P.P. Lohe, D.V. Nandanwar, P.D. Belsare, S.V. Moharil, Journal of Luminescence, 2021, 235, 118017.

[3] X. Huang, Nat. Photonics, 2014, 8, 748-749.

[4] P. Seiler, K. Wallmeroth and K. Mann, Nat. Photonics, 2010, 4, 285-285.

[5] P. P. Lohe, D. V. Nandanwar, P. D. Belsare, S. V. Moharil, *AIP Conf. Proc.* 2018, 1953, 080028.

[6] J. Ueda, S. Tanabe and T. Nakanishi, J. Appl. Phys., 2011, 110, 053102.

[7] G.H. Liu, Z.Z. Zhou, Y. Shi, Q. Liu, J.Q. Wan, Y.B. Pan, Lett. 139 (2015) 480–482.

[8] G. C. Vandile, D. V. Nandanwar, A. K. Nandanwar, S. V. Moharil, J Cond. Matt. 2023; 01 (02):41-45.

[9] Y. Jia, N. Guo, Y. Zheng, H. Qiao, W. Lv, Q. Zhao and H. You, ChemPhysChem, 2012, 13, 3383-3387.

[10] P.P. Lohe, D.V. Nandanwar, P.D. Belsare, S.V. Moharil, Journal of Luminescence, 2019, 216, 116744.

[11] P. P. Lohe, D. V. Nandanwar, P. D. Belsare, and S. V. Moharil, AIP Conference Proceedings, 2019, 2104, 020015.

[12] Nandanwar, A. K., Sarkar, N. N., Sahu, D. K., Choudhary, D. S., & Rewatkar, K. G. (2018), 5(10), 22669-22674.

[13] Rabinovitch Y., Tetard D., Faucher M. D., Pham-Thi M.: Opt. Mater. 2003, 24, 345.

[14] Y. Jia, N. Guo, Y. Zheng, H. Qiao, W. Lv, Q. Zhao and H. You, ChemPhysChem, 2012, 13, 3383-3387.

[15] Q. Y. Shao, Y. Dong, J. Q. Jiang, C. Liang and J. H. He, J. Lumin., 2011, 131, 1013-1015.

[16] Z. Pan, W. Li, Y. Xu, Q. Hu and Y. Zheng, RSC Advances, 2016, 6, 20458-20466.

[17] H. Ji, L. Wang, M. S. Molokeev, N. Hirosaki, R. Xie, Z. Huang, Z. Xia, O. M. ten Kate, L. Liu and V. V. Atuchin, J. Mater. Chem. C, 2016, 4, 6855-6863.

[18] Nandanwar, A. K., Chaodhary, D. L., Kamde, S. N., Choudhary, D. S., & Rewatkar, K. G. (2020), 29, 951-955.

[19] N. C. George, K. A. Denault and R. Seshadri, Annu. Rev. Mater. Res., 2013, 43, 481-501.

[20] L. Chen, C. C. Lin, C. W. Yeh and R. S. Liu, Materials, 2010, 3, 2172-2195.

[21] L. Guo, Y. Wang, Y. Wang, J. Zhang, P. Dong and W. Zeng, Nanoscale, 2013, 5, 2491-2504.

[22] M. Nikl, A. Yoshikawa, K. Kamada, K. Nejezchleb, C. R. Stanek, J. A. Mares and K. Blazek, Prog. Cryst. Growth Charact. Mater., 2013, 59, 47-72.

[23] M. Batentschuk, A. Osvet, G. Schierning, A. Klier, J. Schneider and A. Winnacker, Radiat. Meas., 2004, 38, 539-543.

[24] J. Ueda, K. Aishima and S. Tanabe, Opt. Mater., 2013, 35, 1952-1957.

[25] Nandanwar, A. K., Meshram, N. S., Korde, V. B., Choudhary, D. S., & Rewatkar, K. G. (2019), 203(1), 12-18.

[26] H. Ji, L. Wang, M. S. Molokeev, N. Hirosaki, Z. Huang, Z. Xia, M. Otmar, L. Liu and R. Xie, J. Mater. Chem.C, 2016, 4, 2359-2366.

[27] M.S. Tsai, G.M. Liu and S.L. Chung, Mater. Res.Bull, 2008, 43, 1218-1222.

[28] J. Li, J. G. Li, Z. Zhang, X. Wu, S. Liu, X. Li, X. Sun and Y. Sakka, J. Am. Ceram. Soc., 2012, 95, 931-936.

[29] Y. Pan, W. Wang, G. Liu, S. Skanthakumar, R. Rosenberg, X. Guo and K. K. Li, Journal of Alloys and Compounds, 2009, 488, 638-642.

[30] M. L. Saladino, D. Chillura Martino, M. A. Floriano, D. Hreniak, L. Marciniak, W. Stręk and E. Caponetti, J. Phys. Chem. C, 2014, 118, 9107-9113.

[31] J. Dwivedi, P. Kumar, A. Kumar, Sudama, V. N. Singh, B. P. Singh, S. K. Dhawan, V. Shanker and B. K. Gupta, RSC Adv., 2014, 4, 54936-54947.

[32] H. S. Jang, Y. H. Won and D. Y. Jeon, Appl. Phys. B, 2009, 95, 715-720.

[33] W. B. Im, N. George, J. Kurzman, S. Brinkley, A. Mikhailovsky, J. Hu, B. F. Chmelka, S. P. DenBaars and R. Seshadri, Adv.Mater., 2011, 23, 2300-2305.

[34] T. Isobe, ECS J. Solid State Sci. Technol., 2013, 2, R3012-R3017.

[35] W. S. S. Ho June Byun, Yong Seog Kim and Heesun Yang, J. Phys. D: Appl. Phys., 2010, 43, 195401.

[36] M. C. Maniquiz, K. Y. Jung and S. M. Jeong, J. Electrochem. Soc., 2011, 158, H697-H703.

[37] O. Parlak and M. M. Demir, ACS Appl. Mater. Interfaces, 2011, 3, 4306-4314.

[38] A. Neogi, C.-W. Lee, H. O. Everitt, T. Kuroda, A. Tackeuchi and E. Yablonovitch, Phys. Rev. B, 2002, 66, 153305.

[39] L. T. Su, A. I. Y. Tok, F. Y. C. Boey, X. H. Zhang, J. L. Woodhead and C. J. Summers, J. Appl. Phys., 2007, 102, 083541.

[40] L. Jiang, X. D. Chen, N. Lu and L. F. Chi, Acc. Chem. Res., 2014, 47, 3009-3017.

[41] P. Guardia, K. Korobchevskaya, A. Casu, A. Genovese, L. Manna and A. Comin, ACS nano, 2013, 7, 1045-1053.

ICRTMS-2024
International e-Conference on Recent Trends in Material Science
In Association with International Journal of Scientific Research in Science and Technology
Volume 11 | Issue 9 | Print ISSN: 2395-6011 | Online ISSN: 2395-602X (www.ijsrst.com)

Green Chemistry in the Pharmaceutical Industry: Progress and Challenges

Ishwar Baburao Ghorude* & Kirti Sadhurao Niralwad**
*Department of Environmental Science, Kohinoor Arts, Commerce & Science College, Khultabad, Chhatrapati Sambhajinager .
**Department of Chemistry, Nutan Mahavidhyalaya, Selu, Parbhani

ABSTRACT

The pharmaceutical industry is undergoing a paradigm shift towards sustainability driven by environmental concerns and regulatory pressures. Green chemistry principles offer a viable framework for reducing the environmental footprint of pharmaceutical manufacturing while maintaining product efficacy and safety. This research review examines the progress made in adopting green chemistry practices within the pharmaceutical sector, highlighting key advancements, challenges, and opportunities for future development. Drawing upon a comprehensive analysis of the literature, this review provides insights into successful green chemistry initiatives and identifies areas for further research and innovation.

I. INTRODUCTION

In the pharmaceutical industry, the integration of green chemistry principles is gaining momentum as companies recognize the imperative to reduce their environmental footprint and enhance sustainability throughout the drug development and manufacturing process. Green chemistry in the pharmaceutical industry encompasses a range of practices aimed at minimizing waste, conserving resources, reducing energy consumption, and utilizing safer chemicals and processes. This section provides a detailed overview of the key aspects of green chemistry in the pharmaceutical industry:

Green Synthetic Routes: Green synthetic routes involve the design and optimization of chemical reactions to minimize environmental impact while maintaining efficiency and yield. This includes the use of safer and more sustainable reagents, solvents, and catalysts, as well as the development of innovative synthetic methodologies. Green synthesis often utilizes renewable feedstocks, such as biomass-derived chemicals, to reduce dependence on fossil fuels and mitigate greenhouse gas emissions.

Solvent Selection and Reduction: Solvents play a crucial role in pharmaceutical manufacturing processes, but many traditional solvents are volatile organic compounds (VOCs) that pose environmental and health risks. Green chemistry advocates for the use of safer, more benign solvents, such as water, ionic liquids, and supercritical fluids, which can minimize toxicity and waste generation. Additionally, solvent-free or low-solvent processes are encouraged to reduce environmental impact and improve process efficiency.

Biocatalysis and Enzymatic Reactions: Biocatalysis involves the use of enzymes or microorganisms to catalyze chemical reactions under mild conditions, offering several advantages for green pharmaceutical manufacturing. Enzymes are highly selective and operate under ambient temperatures and pressures, reducing energy consumption and minimizing waste. Biocatalytic processes can enable the synthesis of complex drug molecules with high efficiency and purity, making them valuable tools in green synthesis strategies.

Process Intensification and Continuous Manufacturing: Process intensification aims to maximize efficiency and minimize waste by optimizing process conditions and integrating multiple process steps into a single operation. Continuous manufacturing, as opposed to batch processing, offers several advantages in terms of sustainability, including reduced energy consumption, smaller equipment footprint, and enhanced process control. Green chemistry encourages the adoption of process intensification and continuous manufacturing to improve resource efficiency and minimize environmental impact.

Waste Minimization and Recycling: Green chemistry emphasizes the importance of waste minimization and recycling throughout the pharmaceutical manufacturing process. Strategies such as atom economy, where the maximum number of atoms in starting materials is retained in the final product, and byproduct utilization help reduce waste generation and maximize resource efficiency. Additionally, the development of novel purification techniques and recycling processes enables the recovery and reuse of valuable chemicals and materials, further reducing environmental impact.

Life Cycle Assessment (LCA): Life cycle assessment (LCA) is a comprehensive methodology used to evaluate the environmental impact of pharmaceutical products and processes throughout their entire life cycle, from raw material extraction to disposal. Green chemistry promotes the use of LCA to identify hotspots of environmental impact, guide process optimization efforts, and inform decision-making towards more sustainable alternatives. By quantifying environmental impacts such as energy consumption, greenhouse gas emissions, and resource depletion, LCA helps pharmaceutical companies prioritize sustainability initiatives and reduce their overall environmental footprint.

In summary, green chemistry principles offer a holistic approach to sustainable pharmaceutical manufacturing by integrating environmentally responsible practices throughout the drug development and production process. From green synthetic routes and solvent selection to biocatalysis, process intensification, waste minimization, and LCA, green chemistry provides a roadmap for pharmaceutical companies to minimize environmental impact, conserve resources, and improve overall sustainability.

The pharmaceutical industry is an essential component of global healthcare, responsible for the discovery, development, and production of medicines that improve and save countless lives worldwide. However, traditional manufacturing processes within this industry often involve the use of hazardous chemicals, solvents, and energy-intensive procedures, resulting in significant environmental impacts. As concerns about sustainability and environmental stewardship continue to grow, there is increasing pressure on pharmaceutical companies to adopt greener and more sustainable practices.

Green chemistry, also known as sustainable chemistry, offers a systematic approach to addressing these environmental challenges by designing chemical products and processes that minimize the generation of hazardous substances, reduce energy consumption, and utilize renewable resources. The principles of green chemistry, as outlined by Anastas and Warner in their seminal work "Green Chemistry: Theory and Practice," provide a framework for guiding the development of more sustainable chemical processes.

In recent years, there has been a growing recognition of the potential of green chemistry to revolutionize the pharmaceutical industry and make drug manufacturing more environmentally friendly. This paradigm shift is driven by several factors:

Environmental Concerns: The pharmaceutical industry is a significant contributor to environmental pollution due to the use of large quantities of organic solvents, reagents, and energy-intensive processes. Green chemistry offers solutions to minimize the environmental impact of pharmaceutical manufacturing by reducing waste, conserving resources, and using benign reaction conditions.

Regulatory Pressures: Regulatory agencies worldwide are increasingly scrutinizing the environmental impact of pharmaceutical manufacturing processes and imposing stricter regulations to mitigate pollution and promote sustainability. Companies that embrace green chemistry principles may benefit from regulatory incentives, such as expedited approvals or reduced compliance burdens.

Consumer Demand: In an era of heightened environmental awareness, consumers are increasingly demanding products that are produced sustainably and ethically. Pharmaceutical companies that demonstrate a commitment to sustainability and environmental responsibility may gain a competitive advantage and enhance their brand reputation.

Economic Considerations: Adopting green chemistry practices can lead to cost savings through the reduction of raw material consumption, waste disposal costs, and energy expenditures. Additionally, innovations in green chemistry can open up new market opportunities for eco-friendly pharmaceutical products and technologies.

Despite these compelling drivers, the adoption of green chemistry in the pharmaceutical industry is not without its challenges. The complex nature of drug molecules, regulatory constraints, technical feasibility, and economic viability are significant barriers that must be overcome. Nevertheless, numerous examples of successful green chemistry initiatives within the pharmaceutical sector demonstrate the feasibility and benefits of sustainable drug manufacturing.

This research review aims to examine the progress made in adopting green chemistry practices within the pharmaceutical industry, highlight key advancements, identify challenges, and explore opportunities for future development. By critically evaluating the existing literature and synthesizing insights from academic research, industry reports, and regulatory guidelines, this review provides a comprehensive analysis of the current state of green chemistry in pharmaceutical manufacturing and outlines pathways for further innovation and collaboration.

Green chemistry, also known as sustainable chemistry, promotes the design of chemical products and processes that minimize hazardous waste and energy consumption. In recent years, there has been growing interest in applying green chemistry principles to pharmaceutical manufacturing to address environmental concerns and enhance sustainability.

Progress in Green Chemistry Adoption Significant progress has been made in integrating green chemistry into various aspects of pharmaceutical development and production. One notable advancement is the development of greener synthetic routes using alternative feedstocks and renewable resources. For example, the use of biocatalysts and enzymatic reactions has enabled the synthesis of complex pharmaceutical intermediates with high selectivity and minimal waste generation. Additionally, advancements in catalysis, such as the development of heterogeneous catalysts, have facilitated more efficient and sustainable chemical transformations

Challenges and Limitations Despite the benefits of green chemistry, several challenges hinder its widespread adoption in the pharmaceutical industry. One major challenge is the complexity of drug molecules, which

often require intricate synthetic routes and specialized reagents. Green chemistry approaches must balance environmental considerations with the need to maintain product quality, safety, and efficacy. Regulatory constraints and uncertainty regarding the acceptance of alternative processes and materials also pose challenges to implementation. Moreover, the upfront costs associated with adopting green chemistry practices, such as equipment upgrades and process optimization, can be prohibitive for some companies.

Future Directions and Opportunities to address the challenges of green chemistry implementation in the pharmaceutical industry, several strategies can be pursued. Collaboration between academia, industry, and regulatory agencies is essential to develop and validate green chemistry methodologies. Investments in research and development are needed to explore innovative approaches to sustainable synthesis, such as flow chemistry and continuous manufacturing. Furthermore, education and training programs can raise awareness of green chemistry principles and foster a culture of sustainability within the pharmaceutical workforce.

Conclusion:

The integration of green chemistry principles into the pharmaceutical industry represents a significant step towards achieving sustainability and environmental responsibility in drug development and manufacturing. Through the adoption of green synthetic routes, solvent selection and reduction, biocatalysis, process intensification, waste minimization, and life cycle assessment (LCA), pharmaceutical companies can minimize their environmental footprint, conserve resources, and reduce the generation of hazardous waste and emissions.

Despite the considerable progress made in implementing green chemistry practices within the pharmaceutical sector, several challenges remain. The complexity of drug molecules, regulatory constraints, technical feasibility, and economic viability pose significant barriers to widespread adoption. Additionally, the upfront costs associated with implementing green chemistry practices, such as equipment upgrades and process optimization, may deter some companies from fully embracing sustainable manufacturing methods.

However, these challenges also present opportunities for innovation, collaboration, and continuous improvement. By addressing technical and regulatory hurdles, investing in research and development, and fostering interdisciplinary collaboration between academia, industry, and regulatory agencies, the pharmaceutical industry can overcome barriers to green chemistry adoption and accelerate the transition towards more sustainable manufacturing practices.

Moreover, the benefits of green chemistry extend beyond environmental stewardship to encompass economic and societal advantages. Companies that embrace green chemistry practices may gain a competitive edge by reducing operating costs, enhancing product quality and safety, and improving brand reputation. Additionally, sustainable manufacturing methods can contribute to broader societal goals, such as addressing climate change, promoting public health, and ensuring access to affordable medicines for all.

In light of these considerations, it is evident that green chemistry holds immense promise for transforming the pharmaceutical industry into a more sustainable and environmentally responsible sector. By leveraging advancements in green chemistry research, regulatory incentives, and industry best practices, pharmaceutical companies can navigate the challenges of sustainability and drive meaningful progress towards a greener and more resilient future.

In conclusion, while there are challenges to overcome, the potential benefits of integrating green chemistry into the pharmaceutical industry are substantial. With concerted efforts from stakeholders across the pharmaceutical supply chain, including companies, researchers, regulators, and consumers, the vision of a sustainable pharmaceutical industry can be realized. By prioritizing innovation, collaboration, and responsible

stewardship of resources, the pharmaceutical industry can continue to deliver life-saving medicines while minimizing its environmental impact and contributing to a healthier, more sustainable world.

References:

1. Sheldon, R. A. (2016). Green and sustainable manufacture of chemicals from biomass: state of the art. Green Chemistry, 18(13), 3753-3765.
2. Polshettiwar, V., Decottignies, A., Len, C., Fihri, A., & Basset, J. M. (2009). Water: a crucial reactant in the green chemistry of carbon-carbon bond forming reactions. Chemical Society Reviews, 38(2), 498-510.
3. Constable, D. J., Jimenez-Gonzalez, C., Henderson, R. K., & Alston, S. R. (2007). Perspective on opportunities in industrial biotechnology in renewable chemicals. Biotechnology Journal, 2(12), 1525-1534.
4. Anastas, P. T., & Warner, J. C. (1998). Green Chemistry: Theory and Practice. Oxford University Press.
5. Constable, D. J., Jimenez-Gonzalez, C., Henderson, R. K., & Alston, S. R. (2007). Perspective on opportunities in industrial biotechnology in renewable chemicals. Biotechnology Journal, 2(12), 1525-1534.
6. Sheldon, R. A. (2016). Green and sustainable manufacture of chemicals from biomass: state of the art. Green Chemistry, 18(13), 3753-3765.
7. Polshettiwar, V., Decottignies, A., Len, C., Fihri, A., & Basset, J. M. (2009). Water: a crucial reactant in the green chemistry of carbon-carbon bond forming reactions. Chemical Society Reviews, 38(2), 498-510.
8. Anastas, P. T., & Warner, J. C. (1998). Green Chemistry: Theory and Practice. Oxford University Press.
9. Constable, D. J., Jimenez-Gonzalez, C., Henderson, R. K., & Alston, S. R. (2007). Perspective on opportunities in industrial biotechnology in renewable chemicals. Biotechnology Journal, 2(12), 1525-1534.
10. Sheldon, R. A. (2016). Green and sustainable manufacture of chemicals from biomass: state of the art. Green Chemistry, 18(13), 3753-3765.

ICRTMS-2024
International e-Conference on Recent Trends in Material Science
In Association with International Journal of Scientific Research in Science and Technology
Volume 11 | Issue 9 | Print ISSN: 2395-6011 | Online ISSN: 2395-602X (www.ijsrst.com)

A.C Conductivity and Drift Mobility Properties of 25 % ($CoMn_{0.2}Zn_{0.2}Fe_{1.6}O_4$) + 75% $Ba_{1-x}Sr_x$ TiO_3 Composites

N. N. Waghule
Bhagwan Mahavidyalaya, Ashti Dist-Beed- 414203(M.S) India.

ABSTRACT

Ferromagnetic-ferroelectric particulate composites of 25 % ($CoMn_{0.2}Zn_{0.2}Fe_{1.6}O_4$)+75% $Ba_{1-x}Sr_x$ TiO_3 were prepared by conventional ceramic method using composition (x= 0.0, 0.1, 0.2, 0.3). The presence of two phases in composites was confirmed by XRD technique. The results of XRD pattern shows cubic spinel structure for ferrite phase and tetragonal perovskite structure for ferroelectric phase. The dielectric constant ε, dielectric loss ε'' and dielectric loss tangent (tanδ) were obtained by measuring the capacitance of the ferrite, ferroelectric and their composites in the pellet form at room temperature using LCR-Q-Meter bridge in the frequency range20 Hz-1MHz. The AC conductivity of the sample is calculated from the dielectric parameters and it shows that the conduction is due to the hopping of charge carriers between localized states. The frequency dependent AC conductivity (σ_{AC}) is calculated from dielectric constant and loss tangent measured and is observed that the dielectric relaxation caused by localized electric charge carriers. It is observed that the AC conductivity increase with increase in frequency for all the composites. Variation of drift mobility ($\mu_d=1/ne\rho$) with temperature of sample is measured from D.C resistivity data. As temperature increases thermally activated electron increases and resistivity decreases .It is observed that, as temperature increases drift mobility increases showing semiconducting behaviour.

Keywords: A.C.Conductivity, Drift Mobility, ME composite, Dielectric constant (ε'), d.c resistivity

I. INTRODUCTION

The magnetoelectric effect is defined as variation of dielectric polarization in the composites on application of magnetic field or magnetization induced by an external electric field .Magneto electric (ME) effect is shown by ferroelectromagnetic composite materials consisting of piezomagnetic and piezoelectric phases [1]. The ME effect is an induced dielectric polarization of a material due to applied magnetic field on it and it is a product property obtained from the coupling between the piezoelectric effect in the ferroelectric phase and the magnetostrictive effect in the piezomagnetic phase. These materials have application in magnetic sensors for DC or A.C magnetic field measurements, transducers or actuators. In order to get large ME effect the constituent ferrite phase should have high magnetostrictive coefficient and the ferroelectric phase should have high piezoelectric coefficient and low conductivity [2]. The sum properties of the composites like A.C electrical conductivity, drift mobility are also equally important as they affect the product property. A sum property is sum of sum of the contributions from the individual component phases and proportional to the

molar fraction of these phases in composite. In 1978 Boomgaard mentioned that to get high ME effect in composites following condition should be obeyed. These are 1.Mechanical contact between grains must be intimate [3].

2. The value of magnetostriction coefficient of piezomagnetic phase must be high.

3. The value of piezoelectric coefficient of the piezoelectric phase must be high.

4. The developed charges must not leak through the piezomagnetic phase and it should have high resistivity.

The ferroelectric material is barium titanate has high dielectric constant and low loss tangent. Substitution of Strontium in it enhances dielectric property. Also substitution of Mn and Zn in small fraction in cobalt ferrite enhances magnetostriction effect and electrical resistivity [4]. Hence principal motivation of the present work is to investigate the A.C conductivity and drift mobility of 25 % ($CoMn_{0.2}Zn_{0.2}Fe_{1.6}O_4$) + 75% $Ba_{1-x}Sr_x$ TiO_3 (x=0.0, 0.1, 0.2, 0.3)

2 Experimental details

2.1 Preparation of ME composites:

Materials were prepared by the standard ceramic method. The ferrite phase ($CoMn_{0.2}Zn_{0.2}Fe_{1.6}O_4$) was prepared by using CO, MnO_2, ZnO and Fe_2O_3 in molar proportion as starting materials and their mixture was presintered at 1100^{0}C for 10h. The ferroelectric phase was prepared using $BaCO_3$, $SrCO_3$ and TiO_2 as starting materials by varying $SrCO_3$ content it. The chemical reaction takes place as follows (1-x) $BaCO_3$ +x$SrCO_3$+TiO_2 → $Ba_{1-x}Sr_x$ TiO_3 +CO_2 ↑. The all materials are from Radial Company with 99.98% purity. In order to prepare their composites, the formation of single phase cubic spinel ferrite and perovskite tetragonal ferroelectric phase was confirmed by X-ray diffraction technique. The ME composites were prepared by mixing 25% of ferrite phase with 75% ferroelectric phase by varying Sr^+ content in it. The mixture of composite was thoroughly ground for 2-3 hr and pelletized using hydraulic press by applying suitable pressure of 6 ton/inch^2. Polyvinyl alcohol in small amount was used as a binder to make the cylindrical pellets of approximately 10 mm diameter 3 mm thickness. The ME composites are prepared by using formula 25 % ($CoMn_{0.2}Zn_{0.2}Fe_{1.6}O_4$) + 75% $Ba_{1-x}Sr_x$ TiO_3 (x= 0.0, 0.1, 0.2, 0.3). The pellets of composites were sintered at high temperature of 1150^{0}C for 10 hr in a programmable muffle furnace and finally cooled slowly to room temperature.

2.2 Characterization of ME composites

The prepared samples were characterised by using X-ray diffractometer. The mixed powders were uniaxially pressed in a die to form pellets with thickness of about 2.5–3 mm and 10mm in diameter using hydraulic machine. These pellets were finally sinteredat1200 ^{0}C for 10h and furnace cooled up to room temperature. Powders are used for XRD study and Pallets are used for A.C conductivity and drift mobility properties measurement.

3. Theoretical Background

The dielectric constant of the samples was calculated from the capacitance (c) and loss tangent (tan δ) values measured using LCR meter bridge (HP4284A) in the frequency range 20Hz–1MHz using the relation: $\varepsilon' = \frac{cd}{\varepsilon_0 A}$ ..... ……(1)

Where c is the capacitance of pellet in Farad, d the thickness of pellet, A the cross-sectional area of the pellet and ε_0 is the permittivity of free space ($\varepsilon_0 = 8.85\times10^{-12}$ F/m). The ac conductivity of the samples was estimated from the dielectric parameters. The ac conductivity (σ_{ac}) may be calculated using the relation

$\sigma_{ac} = \omega\varepsilon'$ εo tan δ ..... (2) Where ε_o is the permittivity of the free space, ω the angular frequency and tan δ is the loss tangent. It is to be noted that both tan δ and ε' were available from dielectric

measurements [5]. The resistivity of the samples were calculated by two probe method using the Arrhenius relation $\rho = \rho_0 \exp\left(\frac{E\rho}{kT}\right)$ Where, E_ρ represents an activation energy, k is Boltzmann constant, ρ is the resistivity at absolute temperature T, and ρ_0 represents the resistivity at 0K. From resistivity data the drift mobility μ_d is calculated by relation $\mu_d = 1/ne\rho$ Where, n-the Avogadro's number and ρ –the resistivity, e - electronic charge.

4 Results and discussion

4.1. Structure Analysis: The X-ray diffraction pattern of piezomagnetic, ferroelectric and composite of 25 % ($CoMn_{0.2}Zn_{0.2}Fe_{1.6}O_4$) + 75% $Ba_{1-x}Sr_x\ TiO_3$ (x= 0.0, 0.1, 0.2, 0.3) respectively were determined by XRD technique using X-ray diffractometer using Cu Kα radiations (λ=1.5418A˚)is shown in Fig1.

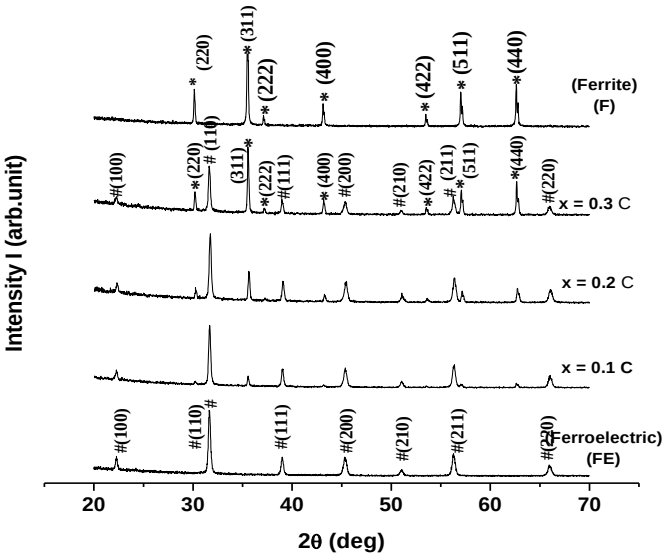

Fig 1.XRD of 25% ($CoMn_{0.2}Zn_{0.2}Fe_{1.6}O_4$) + 75% $Ba_{1-x}Sr_x\ TiO_3$ (x= 0.0, 0.1, 0.2, 0.3)

The pattern shows well-defined peaks and contains no unidentified lines. The X-ray diffraction patterns of the present ferrite, ferroelectric and composite samples were recorded at room temperature and in the 2 theta range of 20^0-70^0. The occurrence of the peaks with specific indices is characteristic of spinel and perovskite structure. All the XRD peaks are identified and compared with JCPDS data to confirm the phase and found to have well matching (Cobalt ferrite JCPDS card #22-1086 and $Ba_{1-x}Sr_x$ TiO3 JCPDS card # 83-1877). Intensity of barium titanate peaks decreases with decrease in percentage of $BaTiO_3$. This indicates that no structural change was observed even though the composition of composites was varied [6].

4.2 A.C Conductivity:

The frequency dependence of the A.C conductivity is obtained by equation (2). From the plot of conductivity as a function of frequency in the range of 1 kHz to 2MHz, it is noted that the A.C conductivity (σ_{ac}) is increases with increase in frequency for all the composites. Increase in conductivity can be attributed to the hopping mechanism of polarons due to applied electrical field. The variation of the log of A.C conductivity $\ln(\sigma_{ac})$ as a function of log of square of frequencies of composite is shown in fig2. It was noticed that the A.C electrical conductivity

increases with increase of frequency initially and shows a small dip at higher frequencies. The conduction is due to hopping of electron between Fe^{2+} and Fe^{3+} ions on the octahedral sites. The frequency dependence of conduction can be explained with the help of Maxwell–Wagner s two

layer model.

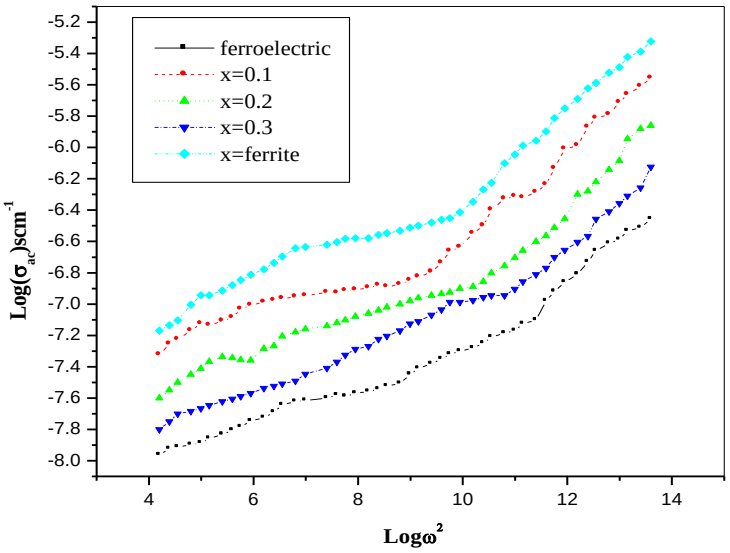

Fig.2. AC conductivity of 25 % ($CoMn_{0.2}Zn_{0.2}Fe_{1.6}O_4$ + 75% $Ba_{1-x}Sr_x$ TiO_3 (x= 0.0, 0.1, 0.2, 0.3). It is also clear that from fig.2,that the conduction is due to the localized electric charge carriers called small polarons which are responsible for the good ME response [7,8].

4.3 Drift mobility

Variation of D.C resistivity (ρ) with inverse of temperature for various Strontium content x is as shown in Fig.3

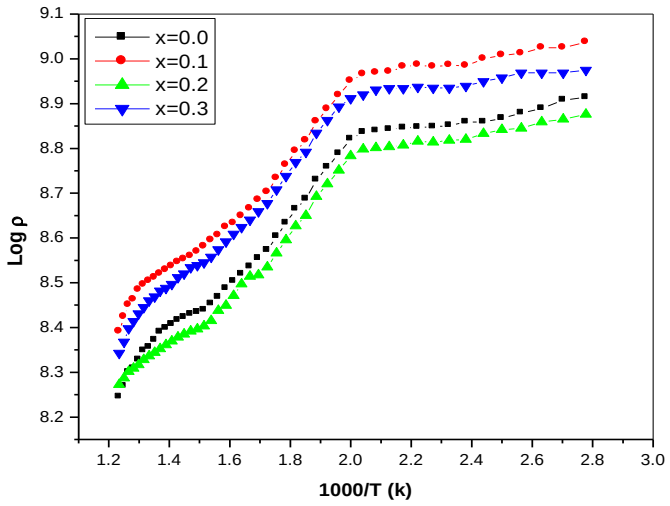

Fig.3 D.C Resistivity of 25 % ($CoMn_{0.2}Zn_{0.2}Fe_{1.6}O_4$) + 75% $Ba_{1-x}Sr_x$ TiO_3 (x= 0.0, 0.1, 0.2, 0.3). From fig.3 is clear that as Strontium content x increases room temperature resistivity decreases indicating that ferroelectric phase is most resistive which is more important for enhancing magnetoelectric effect coefficient. The drift mobility μ_d is calculated by relation $\mu_d=1/ne\rho$ Where, n-the Avogadro's number and ρ-the resistivity, e-electronic charge [9-11]. It is clear from relation that, as temperature increases drift mobility increases showing semiconducting behaviour. As temperature increases thermally activated electron increases and resistivity decreases which result in increase in drift mobility [12, 13].

5. Conclusion:

Dielectric constant, dielectric loss tangent, AC conductivity and drift mobility were investigated in the frequency range of 1 kHz–2MHz at 300K.The A.C conductivity indicates that conduction occurs by hop-ping

of charge carriers among localized states. The A.C conductivity (σ_{ac}) increases with increase in frequency. It is also confirmed the conduction is due to small polarons. The charges which get developed in piezoelectric phase leak through comparatively low resistance ferrite path. From resistivity measurement it is clear that, as temperature increases drift mobility increases showing semiconducting behaviour. This suggests that ferrite and ferroelectric phases are present separately in composites. As temperature increases thermally activated electron increases and resistivity decreases. It is observed that, as temperature increases drift mobility increases showing semiconducting behaviour.

Acknowledgments:

I am very much thankful to department of physics Shivaji University Kolhapur for providing me experimental facility and very thankful to senior professor Dr. K.M.Jadhav, Dr. Babasaheb Ambedkar Marathwada University Aurangabad, for fruitful discussion.

References:

[1] D.R. Patil, B.K. Chougule J. Alloys .Compd 458 (2008) 335.

[2].R.C.Kambale, P.A. Shaikh, C.H. Bhosale, K.Y. Rajpure, Y.D. Kolekar,J. Alloys Compd.489 (2010) 310.

[3] J.V. Boomgaard, A.M.J.G. Van Run, J.V. Suchetelene, Ferroelectrics 10(1978) 1538.

[4] Xialion Chao, Zupei Yang, J. Magn. Mgn. Mater. **23,** (2011) 2012

[5]Hussam Bouaamlat , Nasr Hadi, Najat Belghiti,Hayat Sadki,Mohammed Naciri Hindawi, Advances in Materials Science and Engineering (2020), Article ID 8689150, 8 https://doi.org/10.1155 / 2020/ 8689150

[6] B.D.Cullity, "Elements of X-ray diffraction"2nd Ed.Addison- Wesley, Reading, Mass(1978).

[7] S.SINDHU, M.R. ANANTHARAMAN, BINDU P THAMPI, K A MALINI, PHILIP KURIAN , Bull. Mater. Sci., Vol. 25, No. 7, December 2002, pp. 599–607.

[8] G.N.Chavan, P.B.Belavi, L.R.Naik, B.K. Bammannavar, Int.J. Of Scientific & Eng. Research, Vol-5, Issue 12, (2014).

[9]Arif D Shaikh, V.L.Mathe. Smart. Mater. Struct. 18**,** (2009) 6501.

[10] Rekha Rani, Praveen Kumar, J.K. Juneja, K,K.Raina, Chadra Prakash, Advn.Condensed, Mater.Phys .(2011).

[11] K.K. Patankar , S.S. Joshi ,B.K.Chougule ,Physics Letters A 346 (2005) 337.

[12] R. C. Kambale, Y. A. Park and N. Hur, J. Korean Physical Society, 59, (2011) 3385.

[13] S.S. Chougule, B.K.Chougule, J.Alloys. Compd. 456 (2008) 441.

ICRTMS-2024
International e-Conference on Recent Trends in Material Science
In Association with International Journal of Scientific Research in Science and Technology
Volume 11 | Issue 9 | Print ISSN: 2395-6011 | Online ISSN: 2395-602X (www.ijsrst.com)

Applications of SnO_2 doped with PPy Ammonia Gas Sensor

R. P. Ikhar[1], G. T. Lamdhade[2], K. B. Raulkar[2]

[1]Vidya Bharati Madhyamik Vidyalaya, Patrakar Colony, Amravati
[3]Department of Physics, Vidya Bharati Mahavidyalaya, Amravati, 444602

ABSTRACT

In the present work, SnO2 is doped with Polypyrrole (PPy) to form S1, S2, S3 and S4 sensors. Material characterization was done by XRD and SEM to check crystallinity and porosity respectively. SnO2 doped with PPy was found to be crystalline with average D size 50 nm to 110 nm. SEM picture showed that S3 sensor has more porosity and hence has large active area for sensing. S3 sensor showed maximum sensitivity (=1.842) at 72 ppm of ammonia gas at room temperature, among the prepared sensors. Therefore this sensor is best in industrial application where the NH2 leakage is to be detected.
Keywords: Doping, SnO2, PPy, SEM, Sensitivity.

1. Introduction

Ammonia is widely used in industrial process and medical diagnoses. Hence its detection is very impotent as it is hazardous gas. In present environment, we face with toxic, volatile and combustible gases in the environment. Detecting these harmful gases is vital in order to control air pollution, prevent human life, and protect nature from being damaged.

NH_3 sensors based on conducting polymers have shown better sensing responses among various sensors based on different materials. Polypyrrole (PPy) is one of the most stable conducting polymers under ambient conditions. It has attracted more attention as an NH_3 sensor because of its unique conducto-metric response to NH_3 [1-3].

Tin dioxide (SnO_2) with tetragonal phase is an n-type wide band gap (3.6 eV) semiconductor and suitable for various applications. Its outstanding electrical, optical and electrochemical properties of SnO_2 enable applications in solar cells as well as in gas sensor.

The use of Polypyrrole (PPy) for gas sensing has been a topic of significant research in recent years, due to its high conductivity, stability, and potential for use in a variety of applications. The use of ferric chloride ($FeCl_3$) as an oxidizing agent in the synthesis of PPy has been shown to further improve its electrical conductivity, and stability, making it a promising material for use in gas sensing applications [4-5].

The present study deals with the synthesis, characterization of SnO_2 doped with PPy, and sensitivity measurement.

2. Experimental:

A. Synthesis of SnO_2 Nanoparticles:

The SnO_2 nanoparticles were prepared by the sol–gel method. In a typical procedure, 8 g hydrated tin chloride ($SnCl_2{\cdot}2H_2O$) was dissolved in pure ethanol (C_2H_5OH). The solution was stirred with a magnetic stirrer for 30 min in a closed three-necked flask. About 5 ml of acetyl acetone was added drop wise for the hydrolysis of SnO_2. After another 30 min, the solution was continuously refluxed at 80°C for 5 h to form the SnO_2 sol solution which is then filtered to get nano-powder [6-7].

B. Synthesis of Polypyrole (PPy):

The Py monomer, anhydrous iron (III) chloride ($FeCl_3$) and methanol were used as received for synthesis of PPy. The solution of 7 ml methanol and 1.892 g $FeCl_3$ was first prepared in round bottom flask. Then 8.4 ml Py monomer was added to ($FeCl_3$ + methanol) solution with constant stirring in absence of light. The amount of Py monomer added to the solution (1/2.33 times of $FeCl_3$) was in such a way to get maximum yield. The resulting black precipitates are filtered and washed with copious amount of distilled water until the washings are clear. PPy so obtained is dried by keeping in oven at 600°C for 3 h. The synthesized material was characterized by using XRD and SEM [8].

C. Preparation thick films:

PPy is doped in nanomaterial of SnO_2 with different weight percentage. The binder was prepared by using 8 wt% butyl carbitol and 92 wt% ethyl cellulose. On chemically cleaned glass plate, paste of Al_2O_3 was screen printed and it was kept for 24 hr to dry it at room temperature and then heated at 100°C for 2 hrs to remove the binder. Paste of SnO_2+ PPy was then screen printed on Al_2O_3 layer. Again plate was dried at room temperature for 24 h and binder was removed by heating it at 150°C for 4 hrs. Finally integrated electrons (fig. 1) were made using silver paint for electrical connections (fig. 2). Sample codes are given in table 1.

Fig. (1)

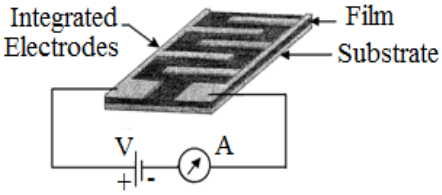

Fig. (2)

Table 1: Sample Codes

Sr. No.	Composites	Codes
1	95 %SnO_2 + 5 % PPy	S1
2	90 % SnO_2+ 10 % PPy	S2
3	85 % SnO_2+ 15 % PPy	S3
4	80 % SnO_2+ 20 % PPy	S4

3. Result and Discussion:

(i) XRD (X-Ray Diffraction):

Following Fig. 3. Shows XRD pattern of Pure SnO_2, PPy & S1, S2, S3, S4 sensors.

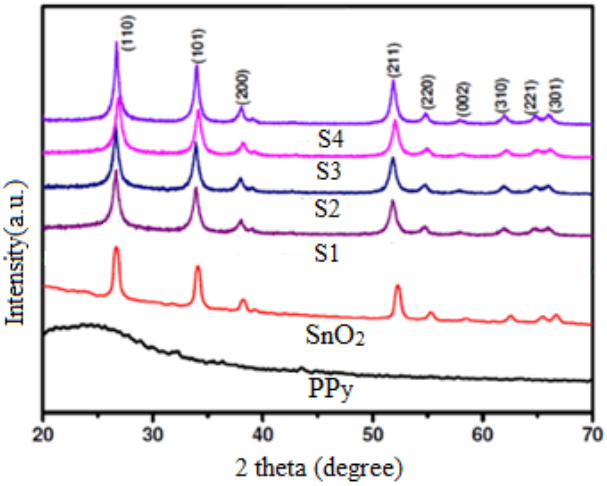

Fig. 3: XRD of SnO_2+PPy system

XRD pattern of PPy manifested amorphous nature of PPy. At 27° broad peak occurred which is the characteristics of amorphous nature of polypyrrole. The maximum intensity peaks of SnO_2 are located at 2θ = 28.4°, 34.2°, 36.7°, 54.2°, 56.1° and correspond to Bragg reflections (110), (101), (200), (211), (220), respectively. As doping of PPy in SnO_2 increases, intensity peak of SnO_2 decreases. XRD pattern showed crystalline nature of SnO_2+ PPy system with crystalline size (D) found to be in the range 50 nm to 110 nm. Crystalline size of S3 sensor was found to be least [9-10].

(ii) SEM Analysis:

The surface morphology of composites of SnO_2+PPy materials was studied by SEM.

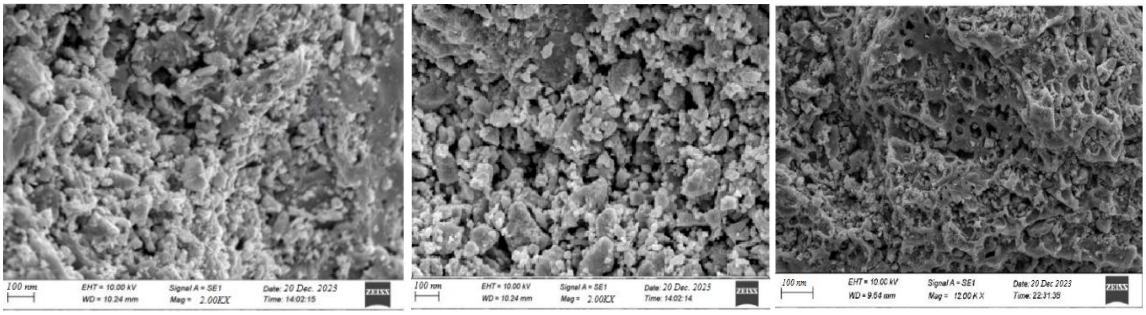

(a) SnO_2 (b) PPy (c) S3 sensor

Fig. 4: SEM of SnO_2+PPy system

From SEM pictures of Pure SnO_2, PPy and SnO_2 doped with PPy materials, the average diameter of S3 sensor (85 % SnO_2+ 15 % PPy) was found to be least and hence number of pores per inch found to be more. This shows that S3 sensor has large effective are for sensing ammonia gas [11-12].

(iii) Sensitivity Measurement:

The sensitivity is expressed by the formula: $S = (R_N - R_A) / R_A$

Where,
R_N = Resistance of the sensor in presence of NH_3 gas environment and
R_A = Resistance of the sensor in presence of air.
When PPy is exposed to electron donating
gases such as NH
3
, a redox reaction occurs and its effective
number of charge carrier decreases, thus reducing its
conductance
When PPy is exposed to electron donating
gases such as NH
3
, a redox reaction occurs and its effective
number of charge carrier decreases, thus reducing its
conductance

When PPy is exposed to electron donating gases like NH_3, a redox reaction occurs and its effective number of charge carrier decreases, thus reducing its conductance i.e. resistance increases during NH_3 exposure, indicating a p-type-like gas sensing behavior. SnO_2-PPy sensors exhibit good dependence (S3 sensor provides large surface area) on NH_3 gas concentration up to 70 ppm, where it reaches a saturation level at room temperature (300K). The variation of sensitivity with NH_3 gas concentration is shown in the figure 5. From graph, S3 sensor showed maximum sensitivity [13-15].

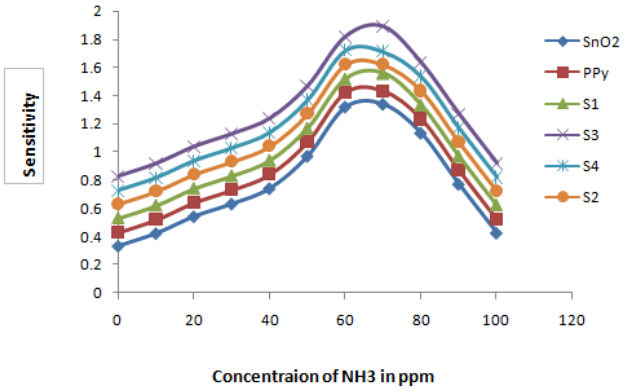

Fig. 5: S3 sensor showing maximum sensitivity at room temperature

4. Conclusion:

Porosity of S3 sample was found to be more and its average crystalline size was found to be 57 nm, from XRD pattern. S3 sensor showed more sensitivity (about 1.842) at 72 ppm concentration of NH_3 gas among the remaining sensor. This shows that S3 sensor is best among the other material to sense ammonia gas at room temperature (300 K).

5. References:

[1] Raulkar K.B, Wasnik T.S, Joat R.V., Wadatkar A.S. Agrawal, R.M. and Lamdhade G.T., (2019). Study on DC Conductivity of PPy-ZnO Nanocomposites, Materialstody Proceedings, 15(3), 595-603.

[2] Jafarpour M.M., Foolad A., Mansouri M.K., Nikbakhsh Z. and Saeedi Zade H. (2010). Ammonia Sensing Properties of (SnO_2-ZnO)/Polypyrrole coaxial nanocables, World Acad Sci. Eng. Technol, 70, 940-945.

[3] Jorgensen T.C. and Weatherley L.R. (2003). Ammonia removal from wastewater by ion exchange in the presence of organic contaminants, Water Research 37, 1723–1728.

[4] Yeolea B., Sena T., Hansoraa D., Mishra S. (2016). Polypyrrole/Metal Sulphide Hybrid Nanocomposites: Synthesis, Characterization and Room Temperature Gas Sensing Properties, Materials Research, 19(5), 37-42.

[5] A shour A., Kaid M.A., El-sayed N.Z. and Ibrahim A.A. (2006). Physical properties of ZnO thin films deposited by spray pyrolysis technique, Applied surface Science, 52,7844-7848.

[6] Mohammad M.T., Hashim A.A. and Al-Maamory M.H. (2006). Highly conductive and transparent ZnO thin films prepared by spray pyrolysis technique, Materials Chemistry and Physics, 99, 382-387.

[7] Chakraborty A., Mondal T., Bera S.K., Sen S.K., Ghosh R. and Paul G.K. (2008). Effects of Al and In incorporation on the structural and optical properties of ZnO thin films synthesized by spray pyrolysis technique, Materials Chemistry and Physics,112,162-168.

[8] Nemade K.R. and Waghuley S.A. (2012). V_2O_5-P_2O_5 Glass Ceramic As A Resistive Solid-State CO_2 Gas Sensor, Asian Journal of Chemistry, Vol. 24, No. 12, , 5947-5948.

[9] Klug H.P. and Alexande L.E., (1974). X-ray Diffraction Procedure for Polycrystalline Materials, Wiley Online library,125-127.

[10] Hamed A.K., Aryan Eghbali, Mansoor Keyanpour-Rad, Mohammad R.V. and Mahmoud Kazemzad. (2014). Ammonia sensing properties of (SnO_2–ZnO)/polypyrrole coaxial nanocables, J. Mater Sci., 49, 685–690.

[11] Shao H., Qian X.F. and Huang B.C., (2007). Fabrication of single crystal ZnO nano-rods and ZnS nanotubes through a simple ultrasonic chemical solution method. Materials Letters, 61(17):3639-3643.

[12] Chougule M.A., Dalavi D.S., Sawanta Mali, Patil P.S., Moholkar A.V., Agawane G.L., Shashwati Sen and Patil V.B. (2012). Novel method for fabrication of room temperature polypyrrole–ZnO nanocomposite NO_2 sensor, Elsevier-Measurement, 45(8), 1989-1996.

[13] Mahaja C., Chaudhari P. and Mishra S. (2018). RGO–MWCNT–ZnO based polypyrrole nanocomposite for ammonia gas sensing, Journal of Material Science, 29, 8039–8048.

[14] Chatterjee S., Shit A. and Nandi A.K. (2013). Nanochannel morphology of polypyrrole–ZnO nanocomposites towards dye sensitized solar cell application, Journal of Materials Chemistry A, 1, 12302–12309.

[15] Abdolmajid B.M., Tayebe N., Badraghi J. and Kazemzad. (2009). Synthesis of ZnO Nanoparticles and Electrodeposition of Polypyrrole/ZnO Nanocomposite Film, Int. J. Electrochem Sci., 4, 247–257.

ICRTMS-2024
International e-Conference on Recent Trends in Material Science
In Association with International Journal of Scientific Research in Science and Technology
Volume 11 | Issue 9 | Print ISSN: 2395-6011 | Online ISSN: 2395-602X (www.ijsrst.com)

Exploring Novel Materials with Significant Nonlinear Optical Properties : A Comprehensive Review

Vinayak Deshmukh
Department of Physics, Shri Siddheshwar Mahavidyalaya, Majalgaon, Maharashtra, India

ABSTRACT

This work provides a comprehensive review of the latest developments in novel materials exhibiting significant nonlinear optical properties. Nonlinear optical materials play a crucial role in various applications ranging from telecommunications to biomedical imaging. In this review, we focus on three main classes of materials: nonlinear crystals, polymers, and nanoparticles. We discuss the fundamental principles underlying their nonlinear optical behaviour, recent advances in material design and synthesis, characterization techniques, and emerging applications. Additionally, we highlight key challenges and future directions in this rapidly evolving field.

Keywords: Nonlinear optics, nonlinear optical materials, nonlinear crystals, nonlinear polymers

I. INTRODUCTION

Nonlinear optics is a branch of optics that deals with the behaviour of light in materials under intense electromagnetic fields, where the response of the material is not directly proportional to the applied field. Unlike linear optics, which primarily concerns itself with phenomena like reflection, refraction, and diffraction, nonlinear optics explores the interactions between light and matter that lead to nonlinear effects such as frequency conversion, wave mixing, and optical modulation. Understanding nonlinear optical phenomena has profound implications across various scientific and technological domains due to its ability to manipulate light in ways that are not achievable through linear optical processes alone [1].

At the heart of nonlinear optics lies the concept of nonlinear susceptibility, which quantifies how the polarization of a material responds to an electric field. In linear optics, the polarization is directly proportional to the electric field strength. However, in nonlinear optics, the polarization can exhibit higher-order dependencies on the field strength, leading to a wide range of nonlinear effects. These effects arise due to the nonlinear nature of the material's response to the incident electromagnetic field.

One of the fundamental nonlinear optical processes is second-harmonic generation (SHG), where two photons of the same frequency combine within a nonlinear medium to generate a new photon with twice the frequency. This process is governed by the second-order nonlinear susceptibility and is widely used in applications such as frequency doubling for laser sources, optical parametric amplification, and nonlinear microscopy [2].

Another important nonlinear effect is the optical Kerr effect, where the refractive index of a material varies nonlinearly with the intensity of the incident light. This leads to phenomena such as self-focusing, self-phase modulation, and optical solitons, which find applications in optical communication, ultrafast optics, and laser physics.

Nonlinear optics also encompasses processes like sum-frequency generation (SFG), difference-frequency generation (DFG), and four-wave mixing (FWM), where multiple input waves interact within a nonlinear medium to produce new frequencies. These processes are exploited in wavelength conversion, optical switching, and spectral analysis techniques [3-5].

The significance of nonlinear optics extends beyond fundamental research to numerous practical applications. In telecommunications, nonlinear optical processes are used to generate, amplify, and manipulate optical signals in fiber-optic networks. Nonlinear optical materials play a crucial role in the development of ultrafast laser sources for spectroscopy, imaging, and materials processing. Additionally, nonlinear optical phenomena enable the realization of nonlinear optical devices such as frequency converters, optical switches, mode-locking elements, and nonlinear microscopy systems.

Furthermore, nonlinear optics has applications in quantum information processing, nonlinear spectroscopy, biomedical imaging, and quantum optics. By harnessing the unique properties of nonlinear optical materials and phenomena, researchers continue to push the boundaries of optical science and technology, paving the way for innovations in fields ranging from telecommunications and photonics to quantum computing and biophotonics.

In summary, nonlinear optics offers a rich playground for exploring the complex interactions between light and matter, with profound implications for both fundamental research and technological innovation. By understanding and controlling nonlinear optical phenomena, researchers can develop advanced optical materials, devices, and systems that drive progress across diverse scientific and engineering disciplines.

II Motivation for exploring novel materials with enhanced nonlinear optical properties

Exploring novel materials with enhanced nonlinear optical properties is motivated by the quest for more efficient, versatile, and advanced optical technologies across various scientific and technological domains. The motivation stems from the limitations of existing materials and the growing demand for innovative solutions to address current challenges and enable future advancements. Several key factors drive the pursuit of novel materials with enhanced nonlinear optical properties [6].

Traditional nonlinear optical materials may exhibit limitations such as low conversion efficiencies, narrow bandwidths, or limited tunability. By exploring novel materials, researchers aim to overcome these limitations and enhance the performance of nonlinear optical devices and systems. For example, materials with higher nonlinear susceptibilities or broader transparency ranges can enable more efficient frequency conversion, better signal quality in telecommunications, and enhanced resolution in nonlinear imaging techniques.

Different applications require nonlinear optical materials with specific properties tailored to their unique requirements. For instance, materials optimized for ultrafast nonlinear processes are essential for applications in ultrafast laser technology and femtosecond optics. Similarly, materials with large nonlinear coefficients and low optical losses are desirable for integrated photonics and quantum information processing. Exploring novel materials allows researchers to tailor their properties to suit diverse application needs, opening up new possibilities for innovation.

The integration of nonlinear optical functionalities with other optical, electronic, or photonic components can lead to multifunctional devices with enhanced capabilities. Novel materials that exhibit multiple nonlinear effects simultaneously or can be easily integrated into existing platforms offer opportunities for developing compact, high-performance optical systems for various applications. For example, nonlinear polymers compatible with standard microfabrication techniques enable the integration of nonlinear optical components into photonic circuits for on-chip signal processing and sensing applications [7].

Advances in fields such as quantum information processing, biophotonics, and nonlinear microscopy create new opportunities and demands for materials with enhanced nonlinear optical properties. Novel materials that enable efficient photon manipulation, quantum state control, or high-resolution imaging can drive progress in these emerging technologies and facilitate breakthroughs in fundamental science and practical applications. For instance, nonlinear optical materials with tailored quantum properties are essential for realizing scalable quantum computing and communication systems.

With increasing emphasis on sustainability and environmental impact, there is a growing interest in developing nonlinear optical materials that are eco-friendly, energy-efficient, and compatible with green manufacturing processes. Exploring novel materials derived from renewable sources, biodegradable polymers, or environmentally benign synthesis routes aligns with the broader goals of sustainability and responsible innovation in materials science and engineering [8].

III Nonlinear optical coefficients and their significance:

Nonlinear optical coefficients are parameters that quantify the strength of the nonlinear optical response in a material. They describe how the polarization of a material varies nonlinearly with the intensity of an incident electromagnetic field. The significance of these coefficients lies in their ability to govern a wide range of nonlinear optical phenomena, including frequency conversion, wave mixing, and optical modulation.

By characterizing and understanding the nonlinear optical coefficients of a material, researchers can predict and control its nonlinear optical behaviour, enabling the design and optimization of nonlinear optical devices and systems. For instance, materials with higher nonlinear coefficients are desirable for applications requiring efficient frequency conversion, such as second-harmonic generation and optical parametric amplification. Moreover, the nonlinear coefficients dictate the strength of nonlinear effects like self-phase modulation and Kerr effect, which are essential for ultrafast optics, optical switching, and nonlinear microscopy. Overall, the significance of nonlinear optical coefficients lies in their fundamental role in shaping the nonlinear optical properties of materials and their practical implications for a wide range of optical technologies [9-10].

IV Nonlinear Crystals

Nonlinear crystals are a class of materials that exhibit significant nonlinear optical properties, making them essential components in various optical devices and systems. These materials play a crucial role in applications such as frequency conversion, optical parametric amplification, and ultrafast optics. In this section, we explore the key characteristics, properties, and applications of nonlinear crystals.

Characteristics of Nonlinear Crystals: Nonlinear crystals possess a crystal lattice structure that lacks inversion symmetry, leading to a no centrosymmetric arrangement of atoms. This asymmetry allows these materials to exhibit nonlinear optical effects, as described by the nonlinear susceptibility tensor. Common nonlinear

crystals include lithium niobate (LiNbO3), potassium titanyl phosphate (KTP), beta-barium borate (BBO), and periodically poled crystals.

Nonlinear Optical Effects: Nonlinear crystals enable various nonlinear optical phenomena, including second-harmonic generation (SHG), sum-frequency generation (SFG), difference-frequency generation (DFG), optical parametric amplification (OPA), and optical parametric oscillation (OPO). These effects arise due to the interaction of photons within the crystal lattice, leading to the generation of new frequencies or changes in the phase or polarization of the incident light.

Properties of Nonlinear Crystals: Nonlinear crystals exhibit several key properties that determine their suitability for specific applications. These properties include the nonlinear coefficient, phase-matching capabilities, transparency range, thermal conductivity, damage threshold, and susceptibility to photorefractive effects. For example, phase matching is crucial for efficient frequency conversion, while high thermal conductivity is essential for managing heat generation in high-power laser systems.

Crystal Growth Techniques: Nonlinear crystals are typically grown using techniques such as the Czochralski method, hydrothermal synthesis, flux growth, and the top-seeded solution growth method. These methods allow for the precise control of crystal composition, purity, size, and orientation, which are critical for optimizing their nonlinear optical properties.

Applications of Nonlinear Crystals: Nonlinear crystals find widespread use in numerous applications across various fields:

In telecommunications, nonlinear crystals are used for frequency doubling in laser sources, wavelength conversion in optical amplifiers, and signal processing in optical switches.

In spectroscopy and microscopy, nonlinear crystals enable nonlinear imaging techniques such as second-harmonic generation microscopy and coherent anti-Stokes Raman scattering microscopy, providing label-free contrast and high-resolution imaging capabilities.

In laser technology, nonlinear crystals play a vital role in ultrafast optics, mode-locking, and pulse compression, facilitating the generation of ultrashort laser pulses for applications in materials processing, surgery, and scientific research.

In quantum optics and quantum information processing, nonlinear crystals are utilized for photon pair generation via spontaneous parametric down-conversion, enabling quantum entanglement, teleportation, and cryptography

In summary, nonlinear crystals are essential materials in nonlinear optics, enabling a wide range of nonlinear optical phenomena and applications. Their unique properties, combined with advances in crystal growth techniques and fabrication methods, continue to drive innovations in optical technologies and pave the way for new advancements in areas such as telecommunications, spectroscopy, microscopy, laser technology, and quantum optics.

Current challenges and limitations in nonlinear optical materials

Despite the significant progress made in the field of nonlinear optical materials, several challenges and limitations still exist, hindering their widespread adoption and further advancement. Addressing these challenges is crucial for realizing the full potential of nonlinear optical technologies and unlocking new applications. Here, we discuss some of the current challenges and limitations in nonlinear optical materials:

V Nonlinear Coefficients and Efficiency:

One of the primary challenges is achieving higher nonlinear coefficients in materials, which directly impact the efficiency of nonlinear optical processes. Many existing materials have relatively low nonlinear coefficients, requiring high optical intensities for practical applications. Enhancing the nonlinear coefficients would enable more efficient frequency conversion, modulation, and signal processing, leading to improved performance in optical devices and systems.

Material Transparency and Absorption:

Nonlinear optical materials often exhibit limited transparency and high optical absorption at certain wavelengths, particularly in the ultraviolet and infrared regions. This can degrade the performance of nonlinear devices by introducing unwanted losses and limiting the usable spectral range. Developing materials with broader transparency windows and reduced absorption is essential for expanding the range of applications and improving the overall efficiency of nonlinear optical systems.

Material Stability and Photodegradation:

Some nonlinear optical materials are susceptible to photodegradation and chemical instability when exposed to intense light sources, especially in ultrafast laser applications. Photobleaching, thermal degradation, and photochemical reactions can lead to changes in material properties and performance over time, affecting device reliability and longevity. Enhancing the stability and durability of nonlinear materials under high-intensity optical excitation is critical for achieving long-term stability and reliability in practical applications.

Phase Matching and Dispersion Engineering:

Phase matching is essential for efficient frequency conversion in nonlinear optical processes such as second-harmonic generation and parametric amplification. However, achieving phase matching over a broad range of wavelengths and temperature conditions remains a significant challenge, particularly in bulk crystals and waveguides. Additionally, managing dispersion effects, such as group velocity mismatch and chromatic dispersion, is essential for maintaining pulse quality and coherence in ultrafast optics and nonlinear spectroscopy.

Integration and Compatibility:

Integrating nonlinear optical materials into practical devices and systems often requires compatibility with existing technologies and fabrication processes. Challenges arise in terms of material compatibility, device integration, and scalability, particularly in the context of integrated photonics, optical communications, and quantum photonics. Developing hybrid materials, multifunctional platforms, and scalable fabrication techniques is essential for enabling seamless integration of nonlinear optical functionalities into advanced optical technologies.

Cost and Scalability:

The cost of nonlinear optical materials and fabrication processes can be prohibitive for widespread adoption, particularly for high-performance or specialized materials. Additionally, scalability issues may arise in large-scale production and commercialization, limiting accessibility and practicality for industrial applications. Addressing cost-effectiveness and scalability concerns through improved synthesis methods, manufacturing processes, and materials engineering approaches is essential for accelerating the commercialization and deployment of nonlinear optical technologies.

In summary, addressing the current challenges and limitations in nonlinear optical materials requires interdisciplinary research efforts spanning materials science, chemistry, physics, and engineering. By overcoming these obstacles, researchers can unlock new opportunities for advancing nonlinear optical

technologies and realizing their full potential in diverse applications ranging from telecommunications and photonics to quantum computing and biophotonics.

Opportunities for interdisciplinary research and collaboration

Opportunities for interdisciplinary research and collaboration abound in the field of nonlinear optical materials, offering rich avenues for advancing scientific understanding and technological innovation. Interdisciplinary collaboration can bridge the gap between fundamental research and practical applications, leveraging expertise from diverse fields to address complex challenges and drive progress in nonlinear optics. Some key opportunities include:

Material Science and Chemistry: Collaborations between materials scientists and chemists can lead to the development of novel nonlinear optical materials with tailored properties, enhanced stability, and improved performance. By exploring new synthesis methods, molecular design strategies, and material processing techniques, researchers can push the boundaries of material design and synthesis in nonlinear optics.

Physics and Engeniering: Collaboration between physicists and engineers can advance the understanding of nonlinear optical phenomena and enable the design and optimization of nonlinear optical devices and systems. By combining theoretical insights with experimental validation and engineering expertise, researchers can develop innovative solutions for applications such as telecommunications, photonics, and quantum information processing.

Biology and Biophotonics: Interdisciplinary research at the intersection of biology and biophotonics can lead to breakthroughs in biomedical imaging, sensing, and diagnostics. By harnessing nonlinear optical techniques for label-free imaging, molecular sensing, and tissue characterization, researchers can contribute to advances in fields such as neuroscience, cancer biology, and regenerative medicine.

Overall, interdisciplinary collaboration fosters synergy between different disciplines, driving innovation and accelerating progress in nonlinear optical materials and their applications. By fostering a collaborative research environment, scientists and engineers can tackle complex challenges more effectively and unlock new opportunities for scientific discovery and technological advancement.

Future prospects for novel materials with tailored nonlinearities

The future prospects for novel materials with tailored nonlinearities hold immense promise for advancing optical technologies and addressing emerging challenges across various domains. By leveraging advances in materials science, chemistry, and nanotechnology, researchers can design and synthesize materials with precisely engineered nonlinear optical properties, paving the way for next-generation optical devices and systems. Some key future prospects include:

Enhanced Performance: Novel materials with tailored nonlinearities offer the potential for significant improvements in optical device performance, including higher conversion efficiencies, broader spectral bandwidths, and increased sensitivity. These materials can enable the development of more efficient frequency converters, ultrafast optical switches, and advanced photonic sensors for applications in telecommunications, spectroscopy, and sensing.

Multifunctionality and Integration: Future materials may exhibit multifunctional nonlinearities, allowing for the integration of multiple optical functionalities within a single material platform. This integration can lead to compact, versatile optical devices with enhanced capabilities, such as simultaneous frequency conversion, modulation, and signal processing. Moreover, these materials can facilitate the seamless integration of nonlinear optical functionalities into emerging technologies such as integrated photonics, quantum computing, and optoelectronics.

Tailored Quantum Properties: Novel materials with tailored nonlinearities can also enable the realization of quantum-enhanced optical technologies, exploiting quantum coherence and entanglement for enhanced performance and novel functionalities. By engineering materials with tailored quantum properties, researchers can develop advanced quantum photonics platforms for applications in quantum communication, cryptography, and quantum computing.

Overall, the future prospects for novel materials with tailored nonlinearities hold the potential to revolutionize optical technologies, driving innovation and enabling new applications across diverse scientific and engineering disciplines. By continuing to push the boundaries of material design and synthesis, researchers can unlock new opportunities for manipulating light and harnessing its full potential in the quest for technological advancement.

VI CONCLUSION:

This comprehensive review has provided insights into the fascinating world of novel materials with significant nonlinear optical properties. We have explored the fundamental principles underlying nonlinear optical phenomena, the latest developments in material design and synthesis, characterization techniques, and emerging applications across various scientific and technological domains.

The review highlights the importance of nonlinear optical materials in advancing optical technologies, from telecommunications and photonics to biophotonics and quantum information processing. By understanding and harnessing the unique nonlinearities of these materials, researchers can develop advanced optical devices and systems with enhanced performance, versatility, and functionality.

Looking ahead, the future of nonlinear optical materials holds tremendous promise for innovation and discovery. Continued interdisciplinary research and collaboration will play a crucial role in furthering our understanding of nonlinear optical phenomena, pushing the boundaries of material design, and unlocking new opportunities for technological advancement.

As we embark on this exciting journey, it is clear that exploring novel materials with significant nonlinear optical properties will continue to be a focal point of research, driving progress and shaping the future of optics and photonics in the years to come.

II. REFERENCES

[1] Boyd, R. W. (2008). Nonlinear Optics (3rd ed.). Academic Press.

[2] Prasad, P. N., & Williams, D. J. (Eds.). (1991). Introduction to Nonlinear Optical Effects in Molecules and Polymers. John Wiley & Sons.

[3] Butcher, P. N., & Cotter, D. (1990). The Elements of Nonlinear Optics (Cambridge Studies in Modern Optics). Cambridge University Press.

[4] Kauranen, M., & Zayats, A. V. (2012). Nonlinear plasmonics. Nature Photonics, 6(11), 737–748.

[5] Cho, Y.-H., Bae, S.-H., Park, I., & Char, K. (2017). Emerging Applications of Nonlinear Optical Microscopy. Microscopy and Microanalysis, 23(3), 442–463.

[6] Prasad, P. N. (Ed.). (1993). Nonlinear Optical Effects and Materials (Wiley Series in Pure and Applied Optics). John Wiley & Sons.

[7] Cheng, J.-X., & Xie, X. S. (2015). Coherent Raman Scattering Microscopy. CRC Press.

[8] Yildirim, A., Kaya, İ., Güneş, S., Yaman, M., & Ayvacı, M. (2017). Recent Advances in Nonlinear Optical Materials for Switching Applications. Optics and Spectroscopy, 123(3), 469–487.

[9] Lee, K. S., Chung, W. S., Jang, Y. H., & Kim, J. (2016). Nonlinear Optical Properties of Organic Nanostructures for Photonic Devices. Molecules, 21(8), 1067.

[10] Xu, Y., De Rossi, A., Pecora, E., Barille, R., & Ramunno, L. (2017). Advances in Nonlinear Photonics: From Microresonators to Frequency Combs. Journal of Physics D: Applied Physics, 50(13), 133001.

ICRTMS-2024
International e-Conference on Recent Trends in Material Science
In Association with International Journal of Scientific Research in Science and Technology
Volume 11 | Issue 9 | Print ISSN: 2395-6011 | Online ISSN: 2395-602X (www.ijsrst.com)

Comparative Study of Lead Iodide and Lead Iodate Crystals Grown by Gel Method

Dr. A. B. Patil[1], S. K. Nerkar[2]
[1,2]Research Laboratory, Department of Physics, Pratap College, Amalner, India

ABSTRACT

The single crystals of lead iodide and lead iodate have been synthesized by gel method. The growth parameters were varied to optimize the suitable growth condition. The grown crystals were characterized by the different techniques. Powder X-ray diffraction pattern confirm the structure of lead iodide as hexagonal and lead iodate as orthorhombic, also the lattice parameters are closely matching with JCPDS data of lead iodide and lead iodate. Band gap energy of both the crystals was calculated from the UV-VIS spectrometry. TGA curve shows that the crystals were thermally stable and decomposed. DSC curves showed endothermic reactions. The comparison of both the crystals is carried out with help of these techniques.

Keywords: Crystal structure,Single crystal growth, Characterization, X-ray diffraction, Lead iodide, Lead iodate.

1. Introduction

The applicability of lead iodide and lead iodate in various fields is of very wide spectrum. Single crystals are the backbone of the modern technology revolution. The impact of single crystals is clearly visible in industries like semiconductor, optics etc [1]. Lead iodide belongs to the layered semiconductor family, and is a widely studied semiconductor for various application [2] Lead iodide is a very important material with a technological applicability as a room temperature radiation detector [3]. It can be widely applied in medicine, monitoring ecology, nondestructive defectoscopy and X-ray and gamma spectroscopy [4-5]. Lead iodide is a layered structured of different polytypes that are generally hexagonal in shape [6]. It is predominantly ionic conductor with a small amount of electron hole conduction. The electron hole conductivity of lead iodide increases with increase in temperature [7].

Crystals of the iodate family have aroused much interest recently because of high effective nonlinear coefficient, high laser damage threshold, excellent optical quality in large single crystals, high thermal stability, low thermal expansion and above all a crystals structure which is acentric due to highly polarized iodate ions [8-10]. Several iodates have been proposed as non-linear optical materials particularly as second harmonic generators [11] Most of the iodate compounds are insoluble in water and decompose before melting. Hence, crystals of such type of compounds cannot be grown by either slow evaporation or melt techniques. In this situation, gel method is the appropriate one foe their growth [12-13]. Crystals of lead iodate is very interesting

in view of crystallographic and optical properties [14]. In this paper, we present the growth of lead iodide and lead iodate single crystals in sodium Metasilicate gel. The grown crystals were characterized by X-ray powder diffraction (XRD), UV-VIS spectroscopy, Photoluminescence spectroscopy and Thermo Gravimetry Analysis (TGA) and Differential thermal Calorimetry.

2. Experimental

Single crystals of lead iodide and lead iodate were grown by single diffusion gel technique. The required silica gel medium was prepared by adding the sodium meta silicate solution of specific gravity 1.04 g/cc drop by drop with constant stirring by using magnetic stirrer into the 7ml (2N) acetic acid till pH value 4.3 was set for the mixture. To the above sodium meta silicate solution of pH 4.3, 5 ml aqueous solution of 0.4 M $Pb(NO_3)_2$ was added as inner reagent with constant stirring. This mixture was then transferred to the test tube of length 15 cm and 2.5 cm diameter. To keep the solution free from dust and impurities, care was taken to cover the test tube. The gel was usually set within 4-8 days. It was left for two more days for gel aging and then the outer reagent, the aqueous solution of 0.4 M KI and KIO_3 were added on to the top of the gel. The supernatant were added down the sides of the test tube using a pipette and not directly on the top the gel medium. Owing to the diffusion of the outer reagent into the gel medium and its reaction with the inner reagent, crystals started growing. Nucleation was observed within 24 hours of addition of the outer reagent. Hexagonal shaped of lead iodide and star shaped of lead iodate crystals was observed. The experiments were carried out at an about room temperature. Fig.1 and Fig.2 shows the grown crystal of lead iodide and lead iodate.

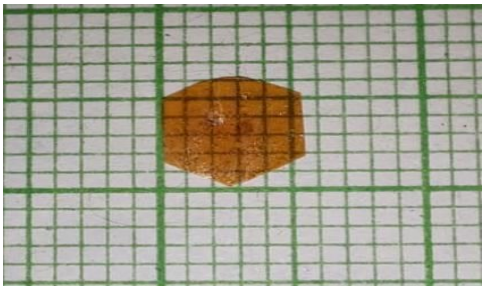

Fig.1 Lead iodide

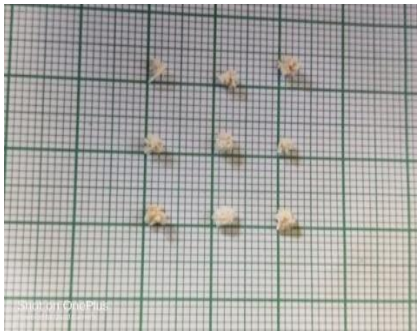

Fig.2 Lead iodate

3. Characterization techniques

The crystalline structure of these crystals was analyzed using an X-ray diffractometer (Rigaku, Miniflex model) using CuKα radiation (λ =1.54051Å), at 40KV and 15mA. UV-VIS spectrum was recorded employing Shimadzu, Japan spectrophotometer in order to understand optical characteristics. Thermal stability and decomposition behavior are studied using Thermo gravimetric Analysis simultaneous thermal analyzer (STA 6000) instrument for temperature in the range 0 to 900 ^{0}C, with a heating range of 3^{0}C/min. The photoluminescence (PL) spectra of a crystal were measured with a Perkin Elmer LS-55 fluorescence spectrometer.

4. Results and discussion

Lead iodide and lead iodate crystals have been successfully grown in sodium metasilicate gel. The above crystals are characterized by XRD, optical and thermal studies.

4.1. X-ray diffraction

1) Lead iodide:

Gel grown Lead iodide crystals were powdered. X-ray diffractograms (XRD) were collected at room temperature on a Rigaku, Miniflex model. All diffraction patterns were obtained using CuKα radiation (λ =1.54051Å), at 40KV and 15mA over the 2θ range of 10^0-80^0. The recorded peaks of the grown crystals were matching well with the standard data file (JCPDS: 731754). It clearly indicates hexagonal structure with interplaner distance (d) as 2.13Å.The average grain size determined by using Scherrer formula was found to be 27.24nm. The XRD indexed peaks are as shown in fig.1 [15-17].

Lead iodate:

Lead iodate crystals were powdered and X-ray powder diffraction (XRD) data were collected at room temperature on a Rigaku, Minislex model. All diffraction patterns were obtained using CuKα radiation (λ =1.54051Å), at 40KV and 15mA over the 2θ range of 10^0-80^0. The observed peaks of the grown crystal are matching well with the standard data file (JCPDS: 820477) and indicating orthorhombic structure of lead iodate having lattice parameters a= 16.70Å, b= 5.578Å and c= 6.083Å and interplaner distance (d) is 2.83Å.The average grain size determined by using Scherrer formula and was estimated to be 28.14nm [15-17].

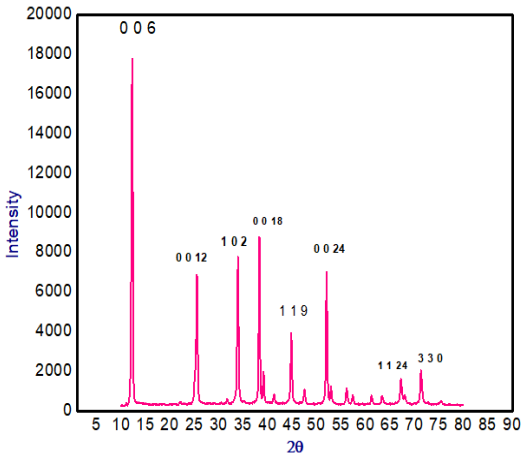

Fig. 3 lead iodide

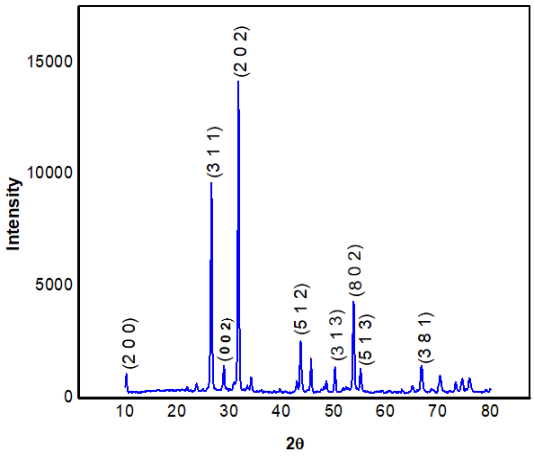

Fig.4 lead iodate

3.2 UV-VIS Spectroscopy:-

Lead iodide:

To understand Optical properties of lead iodide, the UV-VIS. absorption data was recorded using spectrophotometer (Shimadzu, Japan) in the wavelength range of 200 to 800 nm. A graph of wavelength vs absorbance was plotted and found to give a band gap of 2.92 eV [15].

Lead iodate:

Optical property of lead iodate can be studied using UV-VIS spectroscopy. A fine powdered form of lead iodate crystals was used as sample. The absorption spectra of lead iodate crystals have been recorded over the wavelength range 200 to 800 nm. The linear extrapolation of this curve to the energy axis gives the value of band gap of lead iodate as 2.19 eV [16]

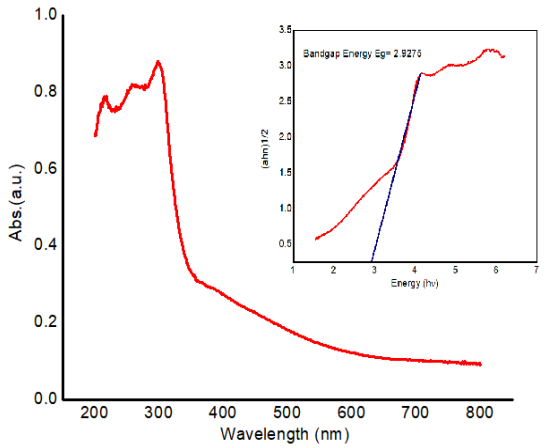

Fig.5

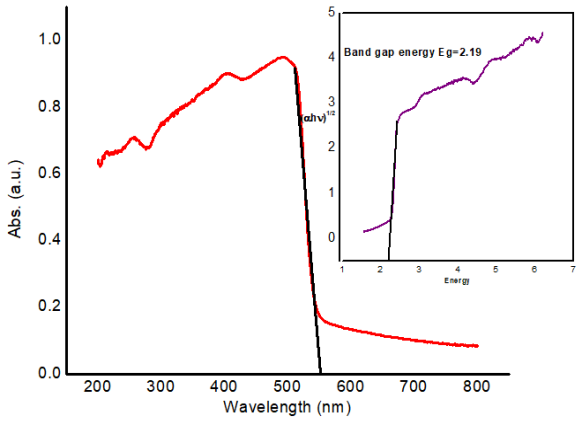

Fig.6

3.3 Photoluminescence Spectroscopy

Lead iodide

To measure the surface defect of the lead iodide at room temperature Photoluminescence spectra was carried out shown in figure. The calculated energies for the emission spectra with wavelengths 535nm and 601.03nm were found to be less than the energy gap found using UV absorption spectra. So, these peaks are due to point defects in the prepared sample [15]

Lead iodate

To measure the surface defect of the lead iodate at room temperature Photoluminescence spectra were carried out shown in figure. The calculated energies for the emission spectra with wavelengths 482nm and 532nm were found to be more than the energy gap found using UV absorption spectra. So, these peaks are due to point defects in the prepared sample. The violet emission occurs at different wavelength. This is attributed to the generation of new energy band gap structures as a result of various defects in the lead iodate [16]

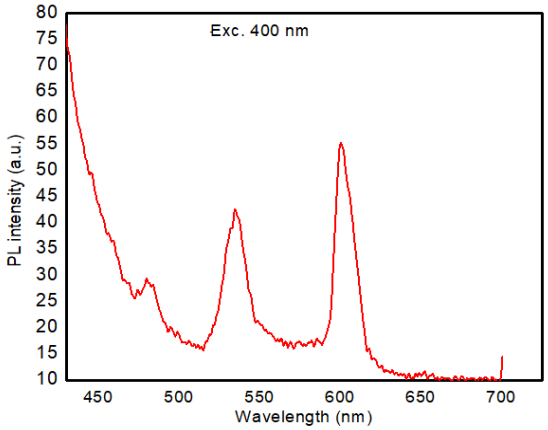

Fig.7

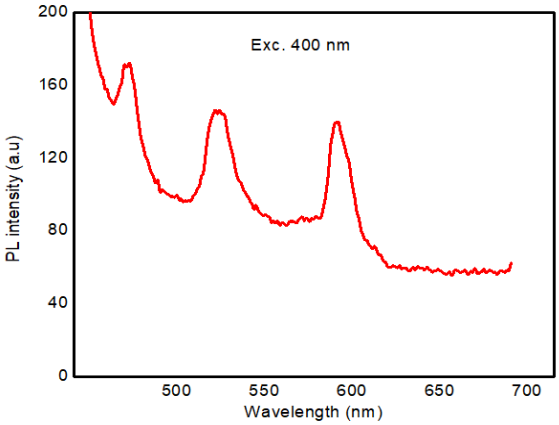

Fig.8

3.4 Thermal analysis:

Lead iodide:

The thermal analysis (TGA, DSC) of gel grown, lead iodide crystals have been carried out in the present work. The TGA curve of lead iodide crystals fig1, was recorded as function of temperature and % weight of loss of substance. Thermograms of lead iodide crystals shows that there is no loss in weight up to 420^{0}C, hence the

material is thermally stable, which indicates no possibility of co-ordinate water molecules or any water of crystallization. Lead iodide crystals melt at around 440^{0}C and slow and gradual weight loss is observed. Then after, slow decomposition is observed from 440^{0}C to 576^{0}C, and then sudden loss in weight is observed upto 712^{0}C. The DSC curve of lead iodide crystal is represented in fig.4, there is an endothermic peaks at 447.22^{0}C, 706.05^{0}C and 776.61^{0}C. Hence, it is inferred that an endothermic peak must have been caused by a phase transformation [15]

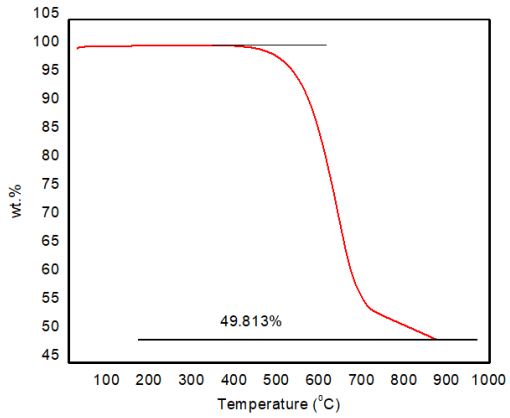

Fig.9

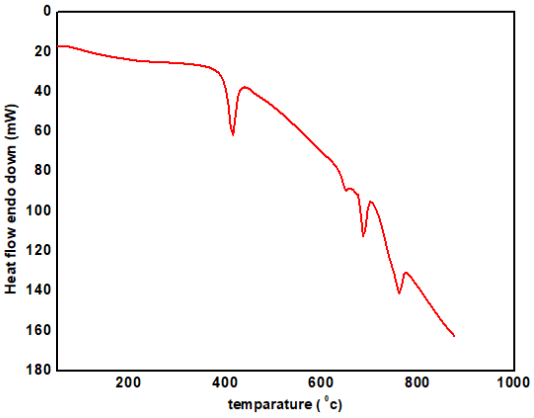

Fig.10

Lead iodate:

The thermal analysis (TGA, DTA) of gel grown, lead iodate crystal have been carried out in the present work. The TGA curve of lead iodate crystals fig 4, were recorded as function of temperature and % weight of loss of substance. The DTA of lead iodate crystals were recorded and given in fig. 5 respectively. The initial weight of sample taken for recording the TG/DSC curves was 29.458 mg and heating rate was maintained at 50 ^{0}C min^{-1}. Thermograms of lead iodate crystals shows that there is no loss in weight up to 300^{0}C, hence the material is thermally stable, which indicates no possibility of co-ordinate water molecules or any water of crystallization. Lead iodate crystals melt at around 310^{0}C and slow and gradual weight loss is observed. Then after, slow decomposition is observed from 310^{0}C to 460^{0}C, and then sudden loss in weight is observed up to 550^{0}C. The DSC curve of lead iodate crystal is represented in fig.5, there is an endothermic peaks at 479.73 ^{0}C, 566.73 ^{0}C. Hence, it is inferred that an endothermic peak must have been caused by a phase transformation [16]

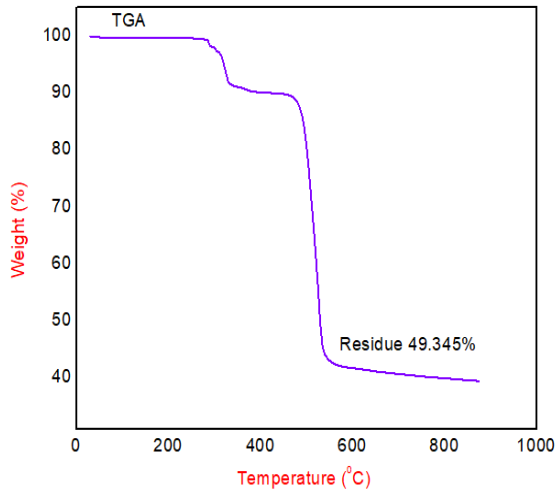

Fig. 11

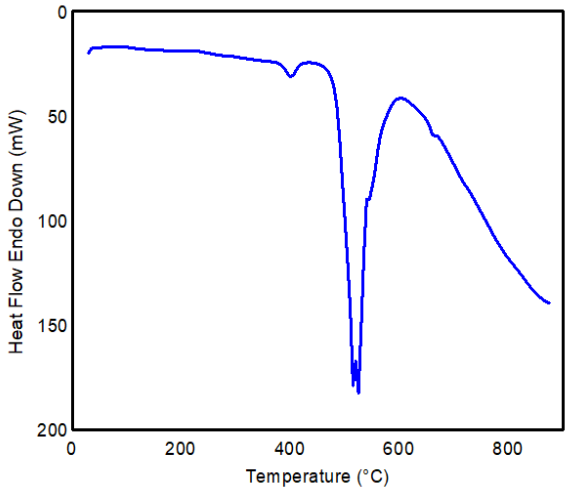

Fig.12

4. Conclusion

The gel grown crystals of lead iodide and lead iodate were characterized and their comparative results are tabulated as bellow.

Compound	Lead Iodide	Lead Iodate
Structure	Hexagonal	Orthorhombic
Grain size	27.24 nm	28.14 nm
Band gap	2.92 ev	2.19 ev
Point defect	535nm and 601.03 nm	482nm and 532nm
Thermally stable	420^0C	300^0C

i) The XRD study of both the crystals shows that the structure of lead iodide is hexagonal and it's grain size is found to be 27.24 nm while the structure of lead iodate is observed to be orthorhombic with grain size of 28.14 nm.

ii) In the optical study of these crystals by UV-VIS technique, the optical band gap energy of lead iodide is estimated to be 2.92 eV while that of lead iodate as 2.19 eV.

iii) The photoluminescence study of these crystals detected the point defects. The point defect is found to be at 535nm and 601.03 nm in lead iodide crystals while 482nm and 532nm in case of lead iodate crystals.

iv) In the thermal study of these crystals such as TGA, the thermal stability of these crystals are to be noted. The thermal stability of lead iodide is observed to be at 420^0C and 300^0C for lead iodate crystal

5. REFERENCES

1. K.D.Girase, effect of cobalt doping on FT-IR, Raman spectra and Thermal stability of lead iodate crystals, Journal of Nano-And Electronic Physics Vol.5 No.3, 03013(4app) (2013)
2. D Acuna, B Krishnan, S Shaji, S Sepulveda and J L Menchaca, Growth and properties of lead iodide thin films by spin coating, Bull. Mater. Sci. , Vol. 39, No. 6, October 2016. pp. 1453-1460. DOI 10.1007/s12034-016-1282-z
3. R. Ahuja, H. Arwin, A. Ferreira da Silva, C. Persson, J.M. Osborio-Guillen, Electronic and optical properties of lead iodide , journal of Applied Physics. 92, 7219 (2002); doi:10.1063/1.1523145
4.Marie Matuchova, Jiri Zavadil, Jaroslav Maixner, electrical, Optical and structural properties of lead iodide, J. Mater Sci: Mater Electron (2009) 20:289-294 DOI 10.1007/s10854-008-9831-x
5. L. Fornaro, E. Saucedo, L, Mussio, L. Yerman, X. Man, A. Burger, Lead iodide film deposition and characterization, Nuclear Instrumentation and Method in Physics research A458 (2001) 406-412

6. D. S. Bhavsar, synthesis of undoped and X(Cu, Al and Zn)-doped lead iodide crystals by gel technique and preparation and characterization of thin film of gel grown crystals, Archives of applied science research, 2013, 5(4):89-96
7.Anil p. Lingrast and George Simkovich, Electrochemical Studies on Lead Iodide, J. Phys. Chem. Solids Vol. 39, pp. 1225- 1229
8. R. Ashok kumar , R. Ezhil vizhil, N. viayan and D. rajan babu, Growth, optical and mechanical properties of non linear optical alpha-lithium iodate single crystal, Scholars research library, Der Pharma chemical, 2010, 2(5):247-254
9. S K Kurtz, T. T. Perry, and J.G. Bergman, jr. Appl. Phys.Lett. 1968,12,186
10. G. Nath and S.Haussuhl, Appl. Phys. Lett. 1969, 14,1545
11. Alton F. Armington and John J. O` Connor, Mat. Res. Bull. Vol. 6, pp. 653-658, 1971
12. K. D.Girase, H.M.Patil, D.K.sawant and D.S.Bhavsar, Scholars Research Library. Archives of Applied Science Research, 2011, 3(3):128-134
13. Sangwal K and Patel A. R., J. Cryst. Growth, 1974, 23, 282.
14. K. D. Girase, International Journal on Cybernetics and Informatics(IJCI) Vol.2, No. 4, August 2013
15. S.K. Nerkar, Dr. A. B. Patil, XRD, UV-VIS, PL and Thermal Studies of Lead Iodide Crystal, IJARESM, ISSN:2455- 6211, Volume 11, Issue 2, Feb-2023
16. S.K. Nerkar, Dr. A. B. Patil, XRD, UV-VIS, PL and Thermal Studies of Lead Iodate Crystal, SSRG-IJMSE, ISSN:2394- 8884, Volume 09, Issue 1, May-Aug 2023
17. S.K. Nerkar, Dr. A. B. Patil, XRD studies of lead iodide and lead iodate crystals, TIJER||ISSN 2349-9249|| March 2023 Volume 10 Issue 3.

ICRTMS-2024
International e-Conference on Recent Trends in Material Science
In Association with International Journal of Scientific Research in Science and Technology
Volume 11 | Issue 9 | Print ISSN: 2395-6011 | Online ISSN: 2395-602X (www.ijsrst.com)

Synthesis & Characterization of Nanocrystalline CdS Thin Films for Photovoltaic Applications

V. B. Sanap

Yeshwantrao Chavan College, Sillod, Dist. Ch. Sambhajinagar, (MS) India

ABSTRACT

Cadmium sulfide (CdS) thin films with nanocrystalline structure have been deposited on glass substrate. Low cost, simple and inexpensive chemical bath deposition technique is used for the synthesis of CdS thin films. Prepared films have been characterized by XRD, SEM, UV-VIS spectroscopy and the results are discussed in detail. The XRD study reveals that the prepared films have cubic structure. The optical and solid state properties such as absorbance, extinction coefficient, refractive index, dielectric constant, optical conductivity have been investigated for the photovoltaic applications. The band gap measured was found in the range of 2.36 eV to 2.71 eV.

Keywords: Chemical bath, cadmium sulfide, thin film.

I. INTRODUCTION

Numbers of deposition techniques have been reported for the synthesis of thin films such as electro deposition, sputtering, spray pyrolysis, vacuum evaporation, chemical vapour deposition technique, etc. Out of this chemical deposition technique has become more popular in recent decades, especially for thin film deposition, due to its numerous advantages. It is low cost, simple, easy, and convenient method for large area preparation of thin films, at close to room temperature. Also films can be deposited on different kinds, shapes and sizes of substrates [1-4].
CdS is an important & useful material for optoelectronic applications, because its expected gap emission lies very close to the highest sensitivity of the human eye. Thus one might assume that CdS thinfilms are an appealing host for photonic devices. For the development of such optoelectronic devices, CdS thin films require comprehensive optical & solid state characterization. The physical properties were studied earlier by our group [3-6].
In this work, CdS thin films have been synthesized successfully using different cadmium ion sources and structural, optical & solid state properties were reported. The objective is to provide the comprehensive study of optical & solid state properties of CdS thin films useful for optoelectronic applications, especially solar cells.

II. EXPERIMENTAL DETAILS

CdS thin films were deposited by the controlled chemical bath deposition technique using various cadmium ion sources such as cadmium chloride, cadmium sulfate, cadmium nitrate and cadmium Iodide and thiourea as sulfur ion source. 0.1 M cadmium ion source solution and an equal volume of 0.2 M thiourea solution was added in 100-120 ml of de-ionized water. Ammonia was added slowly to adjust the pH. The solution was stirred and transferred to another container containing substrate. The resulting solution was kept at 70±2ºC for 40 minutes. The substrate used is glass slide. Cleaning of substrate is important in deposition of thin films[12-15] The crystallographic

structure of films was analyzed with a diffractometer (EXPERT-PRO) by using Cu-Kα lines (λ= 1.542Å). The average grain size in the deposited films was obtained from a Debye-Scherrer's formula. Surface morphology was examined by JEOL model JSM-6400 scanning electron microscope (SEM). Optical properties were measured at room temperature by using Perklin-Elmer UV-VIS lambda-35 spectrometer in the wavelength range 100-1000nm.

III. RESULTS AND DISCUSSION

1.1 Structural & Morphological Studies

Fig. 1 shows the XRD pattern of CdS thin films for various cadmium ion sources. The as-deposited CdS film shows two dominant crystalline peaks (200) and (311). A comparison of the peak position (2θ values) of the JCPDS XRD spectra data for CdS suggests that the as-deposited CdS films have the cubic structure with the X-ray diffraction peaks corresponding to (200) and (311) peaks.

The average grain size (g) has been obtained from the XRD patterns using Debye-Scherrer's formula, [7-8]

$g = K\lambda / \beta \cos\theta$

Where, K = constant taken to be 0.94,

λ = wavelength of X-ray used (1.542Å),

β = FWHM of the peak and

θ = Bragg's angle.

The estimated grain size for various cadmium ion sources is in the range between 2.95nm to 3.64nm. (Table 1)

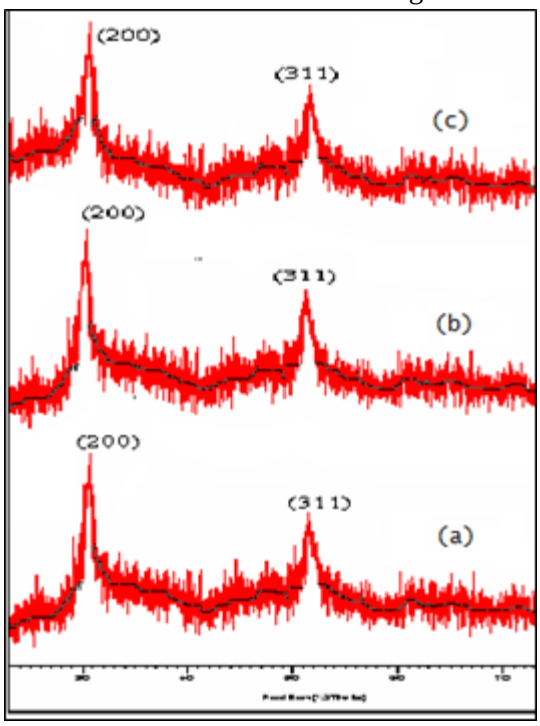

Fig. 1 XRD pattern of CdS films for different cadmium sources.

1.2 Optical Studies

Fig. 2 shows the optical absorbance spectra of CdS thin films for all four cadmium sources. All the films shows low absorbance in the visible/near infrared region from ~500nm to 1100nm. However the absorbance is more than 80% in the ultraviolet region. It is observed that with the cadmium source the absorbance edge shifts towards the longer wavelengths. Similar behaviors in the optical spectra of CdS films prepared by other technique have been reported elsewhere. The sharp fall in absorbance near 500nm is an identification of good crystallinity of films. [5-7]

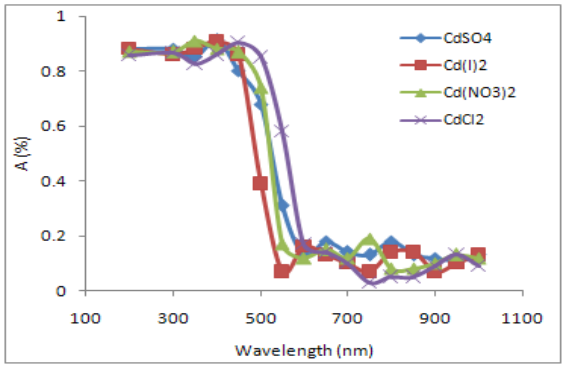

Fig. 2 Plot of (αhν)2 vs hν for all CdS films

From the absorbance data, the absorption co-efficient α was calculated using Lambert's law [10], ln (I0/It) = 2.303 A = 2.303 log 1/T = α d

where, I0 and It are the intensity of incident and transmitted light respectively. A the absorbance, T the optical transmission and d the film thickness.

The absorption co-efficient α was found to follow the relation,

$$\alpha = [A (h\nu - Eg)1/2] h\nu$$

The band gap Eg was determined from each film by plotting (αhν)2 versus hν and then extrapolating the straight line portion to the energy axis at α =0. The band gap energy Eg obtained for each Cd source is different. CdCl2-based film has the least band gap (2.39eV) and CdSO4-based film has highest band gap (2.68eV). The band gap of other two films is intermediate. Fig. 3 shows all band gap values observed are closest to the band gap of single crystal CdS (2.42eV) [7-11].

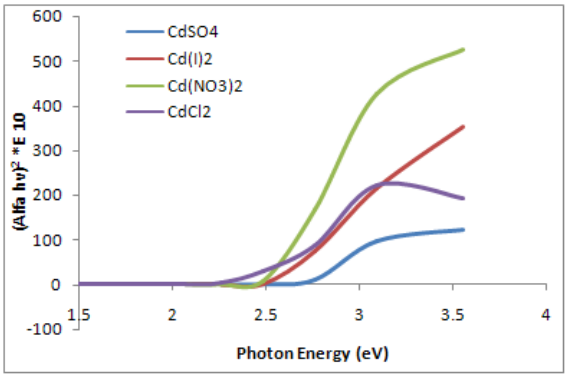

Fig. 3 Plot of (αhν)2 vs hν for all CdS films

The variation of refractive index (n) with hν for all CdS thin films is shown in fig 4. The average values of n ranged between 1.897 and 2.109 with maximum values that ranged between 2.176 and 2.421 as the Cd source changes from CdSO4 to CdI2.

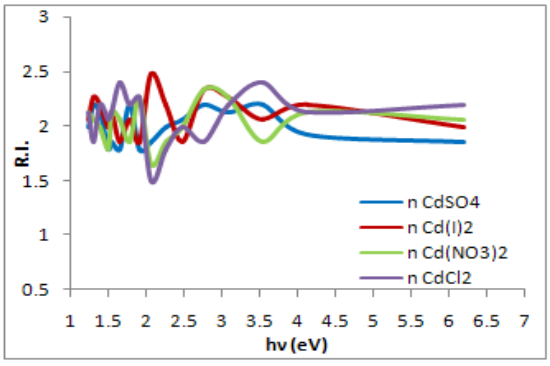

Fig. 4 Variation of R I (n) with wavelength for all CdS thin films.

The variation of extinction coefficient (k) with hν for all CdS thin films is shown in fig 5. The average values of k ranged between 0.0347 and 0.0458 with maximum values that ranged between 0.0642 and 0.1266 as the Cd source changes from CdSO4 to CdI2.

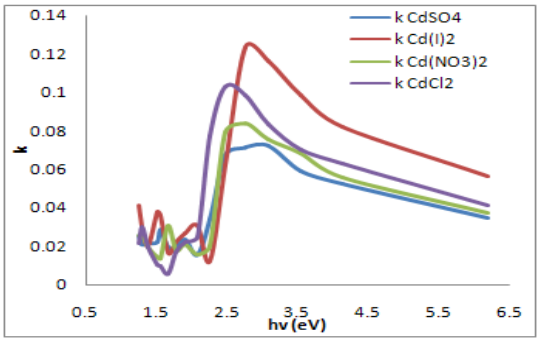

Fig. 5 Variation of k with hν for all CdS thin films

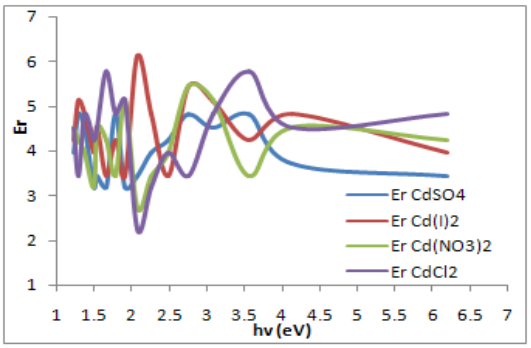

Fig. 6 Variation of εr with wavelength for all CdS

The plot of εr and εi against wavelength are shown in fig. 6 and Fig. 7 respectively. The average values of εr ranged between 4.02 and 4.57 with maximum values that ranged between 4.63 and 6.21 as the Cd source changes from CdSO4 to CdI2.

On other hand the average values of εi that ranged between 0.12 and 0.38 with maximum values that ranged between 0.57 and 1.29 as the Cd source changes from CdSO4 to CdI2 for all the samples.

A plot of optical conductivity (σ) against wavelength is shown in Fig. 8. It has the average values that ranged between 3.056x1013 S-1 and 4.645 x1013 S-1 with maximum values that ranged between 7.108x1013 S-1 and 12.143x1013 S-1 as the Cd source changes from CdSO4 to CdI2

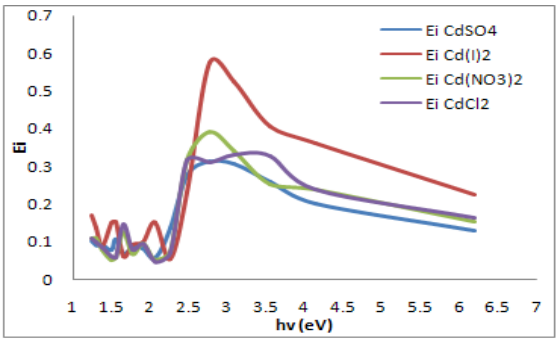

Fig. 7 Variation of εi with wavelength for all CdS thin films.

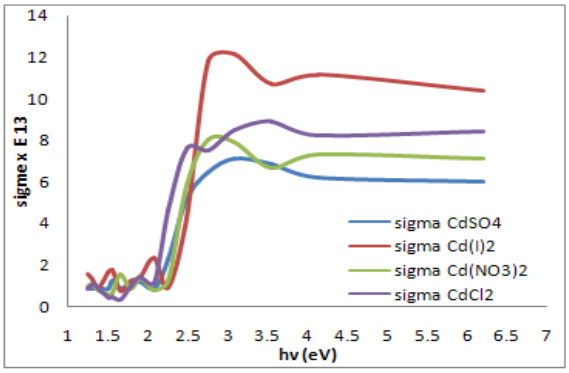

Fig. 8 Variation of σ with wavelength for all CdS thin films.

It is observed that the values of optical constants (n, k, εr, εi, σ) were very sensitive with the Cd ion source. The value of optical conductivity is high in case of CdI2.

Table 1 shows the summary of obtained results.

Cd source	**Grain size (nm)**	**Max n**	**Max k**	**Max ε_r**	**Max ε_i**	**Max σ x10^{13} S^{-1}**	**Energy bandgap (eV)**
$CdSO_4$	3.641	2.18	0.062	4.62	0.28	7.21	2.71
$Cd(NO_3)_2$	3.163	2.24	0.074	5.54	0.33	8.43	2.48
$CdCl_2$	3.109	2.39	0.112	5.71	0.37	8.12	2.56
CdI_2	2.953	2.42	0.127	6.21	0.51	11.42	2.36
Cd source	**Grain size (nm)**	**Max n**	**Max k**	**Max ε_r**	**Max ε_i**	**Max σ x10^{13} S^{-1}**	**Energy bandgap (eV)**
$CdSO_4$	3.641	2.18	0.062	4.62	0.28	7.21	2.71
$Cd(NO_3)_2$	3.163	2.24	0.074	5.54	0.33	8.43	2.48
$CdCl_2$	3.109	2.39	0.112	5.71	0.37	8.12	2.56
CdI_2	2.953	2.42	0.127	6.21	0.51	11.42	2.36

Table 1. Optical & solid state properties with Cd sources for all CdS thin films.

IV. CONCLUSIONS

CdS thin films with various Cd ion sources have been successfully deposited by chemical deposition technique. The effects of Cd source on the optical and solid state properties have been studied. The UV-VIS spectroscopy showed high (>80%) transmittance, and low absorbance in the visible near infrared region from ~500nm onwards and poor

transmittance in UV region. This makes the films suitable for optoelectronic devices, for instance window layers in solar cells also effective as protective coatings.

ACKNOWLEDGEMENTS

The authors are grateful to Head, DME, VNIT Nagpur for providing XRD and SEM facilities. We would also like to acknowledge Head of Biotech department, Y.C. College, for UV-VIS-Near IR facilities.

REFERENCES

[1] Arturo Morales-Acevedo, Solar Energy, 80 (2000) 675.
[2] Paulson P D & Dutta V, Thin Solid Films, 370 (2000) 299.
[3] Emziane M, Durose K, Romeo N, Bosio A & Halliday D P, Thin Solid Films,480 (2005) 377.
[4] Panda S K, Chakrabarti S, Satpati B, Satyam P V & Choudhuri S, J Phys D Appl Phys, 37 (2004) 628.
[5] Pawar S H, Bhosale C H, Bull. Matter Sci., 8 3 (1986) 419-422.
[6] Sahay P P, Nath R K and Tiwari S, Cryst Res Technol, 42 3 (2007) 275-280.
[7] T.Nakanishi, K, Ito, Sol. Energy Mater. Sol.Cells 35, 171 (1994).
[8] A.Adachi, A.Kudo and T.Sakata, Bull. Chem. Soc. Jpn 68, 3283 (1995).
[9] Grecu R, Popovici E J, Ladar M et al, Journal of Optoelectronics & Advanced Materials, 6 1 (2004) 127-132.
[10] Nair P K, M.T.S. Nair et al, J. Phys D, 22 (1989) 829.
[11] Kitaev G, Mokrushin S, Uritskaya A, Kolloidn Z, 27 (1965) 51.
[12] Sanap V B, Pawar B H, Chalcogenide Letters, 7, 3 (2010) 227-231.
[13] Sanap V B, Pawar B H, Optoelectronics and Advanced Materials-Rapid comm. Vol. 5, No. 5(2011) 530-533.
[14] A. K. Ambedkar, M. Singh, V. Kumar, A. Kumar, Y. K. Gautam, Surf. Interfaces 9, (2020) 504.
[15] Vijay B. Sanap, Int. Journal of NanoScience and Nanotechnology, Volume 12, Number 1, (2021) 1-9.

ICRTMS-2024
International e-Conference on Recent Trends in Material Science
In Association with International Journal of Scientific Research in Science and Technology
Volume 11 | Issue 9 | Print ISSN: 2395-6011 | Online ISSN: 2395-602X (www.ijsrst.com)

Dielectric Relaxation Studies of Aqueous Xylitol Solution using Time Domain Reflectometry Technique

S. S. Patange*[1], A. D. Bokhare[2], A. C. Kubharkhane[3]
*[1]*School of physical sciences, Swami Ramanand Teerth Marathwada University, Nanded 431606, Maharashtra, India.*
[2]*School of physical sciences, Swami Ramanand Teerth Marathwada University, Nanded 431606, Maharashtra, India.*
[3]*School of physical sciences, Swami Ramanand Teerth Marathwada University, Nanded 431606, Maharashtra, India*

ABSTRACT

The complex dielectric permittivity measurements of binary mixture of xylitol – water mixtures have been carried out in the frequency range of 10 MHz to 30 GHz using a time domain reflectometry technique .These measurements have been carried out for different mole fractions of xylitol in water (Xx). These measurements have been done at four different temperatures from 10°C to 25°C. The different dielectric parameters such as static dielectric constant, complex permittivity, relaxation time have been calculated. The interaction between xylitol and water molecules has been studied by the dielectric parameters. The dielectric relaxation behaviour of xylitol water mixture is studied by using Cole – Davidson model.

Keywords: Time domain reflectometry, Dielectric relaxation, Complex permittivity

1. INTRODUCTION

The technique of dielectric relaxation spectroscopy (DRS) has shown to be effective in assessing the structural and dynamic properties of liquids that mostly consist of hydrogen bonds. Liquids that form hydrogen bonds and have more than three hydroxyl groups and an aliphatic carbon chain are known as polyhydric alcohols or polyols [1]. A sugar alcohol molecule composed of linear backbone chain with OH group attached to every carbon atom. They can be produced via catalytic hydrogenation, reduction of free sugars with sodium amalgam, or sodium borohydride in water. Compared to other carbohydrates, sugar alcohols have less of an impact on blood glucose (blood sugar) and deliver less calories than sugar [1-3]. Xylitol (C5H12O5) is a sugar alcohol having five carbon atoms and five OH xylitol. It can be found naturally or artificially prepared mainly from plant materials chemically or by fermentation of hemicelluloses from agricultural groups (NC =NOH). Figure 1 shows the structure of biomass by yeast or bacteria strains. Xylitol is commonly used as sweetener. This polyol has a significant antiplaque effect on teeth surface and can reduce the gingival inflammation [2,3]. Bokhare A.D. et al. have conducted the dielectric relaxation and hydrogen bonding interactions of D-sorbitol at various concentrations in water[4]. D N Rander et al. has studied the complex dielectric spectra of xylitol-water mixtures in the frequency range 10 MHz – 30 GHz from 0 to 25° C at different weight fractions of of xylitol ($0 < Wx \leqslant 0.7$)[5]. Hydration and aggregation of aqueous xylitol solution has been studied by Iwona Plowas – Korus et al. at solute concentrations c<3.4M at 5,25,45,65° C in the frequency range $0.05 \leqslant \upsilon \leqslant 89$ interpreted in terms of 5D model [6] .

In the present paper the molecular interaction through hydrogen bonding at different concentrations and temperature is demonstrated among the binary mixtures of xylitol-water. The dielectric characteristics variations are investigated in the frequency range 10MHz to 30GHz using the time domain reflectometry technique (TDR). Using the least square fit method static dielectric constant (ε0), relaxation time (τ) are evaluated and discussed. To explore intermolecular interaction in different molecules Kirkwood correlation factors were calculated.

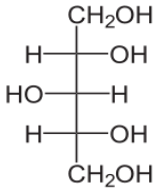

Figure 1. The structure of xylitol

2. METHODS AND MATERIAL

2.1 Materials

Xylitol was obtained commercially from Sigma – Aldrich Ltd and used without further purification. The water used in the preparation of mixture was obtained by double distillation process. The solutions were prepared at different mole fractions of xylitol in water maintaining a consistent water weight.

2.2 Measurement

The TDR technique was used to obtain the dielectric spectra [7]. The Tektronix model no. DSA8200 sampling mainframe along with the dual channel sampling module 80E10B was used for the time domain reflectometre. Fig 2 shows the block diagram of TDR. The sampling module provides a 12 ps incident and 15 ps reflected rise time pulse. These reflected pulses without sample R1(t) and with sample Rx(t) were recorded in a time window of 5 ns and digitized in 2000 points are shown in figure 3. Coaxial cable with an impedance of 50 ohms, an inner diameter of 0.28 mm, and an outer diameter of 1.19 mm is used to provide the pulse. The addition [p(t)=R1(t)+RX(t)] and substraction [q(t)=R1(t)-RX(t)] of these pulses are done in oscilloscope memory. These substracted and added pulses are delivered to computer for further analysis. The Fourier transformation of the pulses and data analysis was completed earlier in order to obtain the complex permittivity spectra in the frequency range 10MHz to 30GHz using the non linear least square fit method.

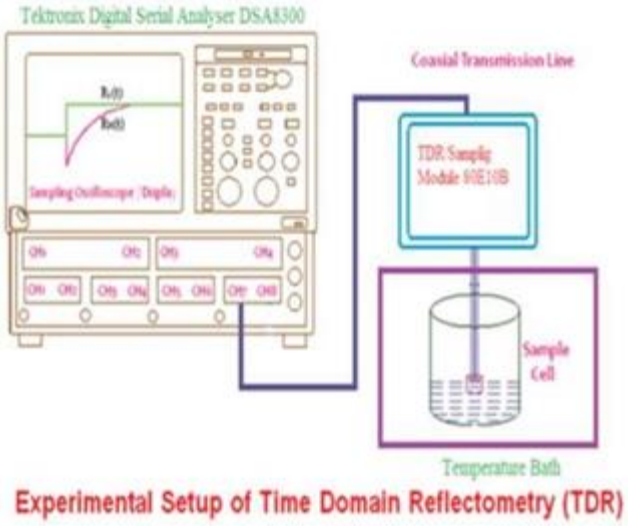

Fig 2. Block diagram of TDR

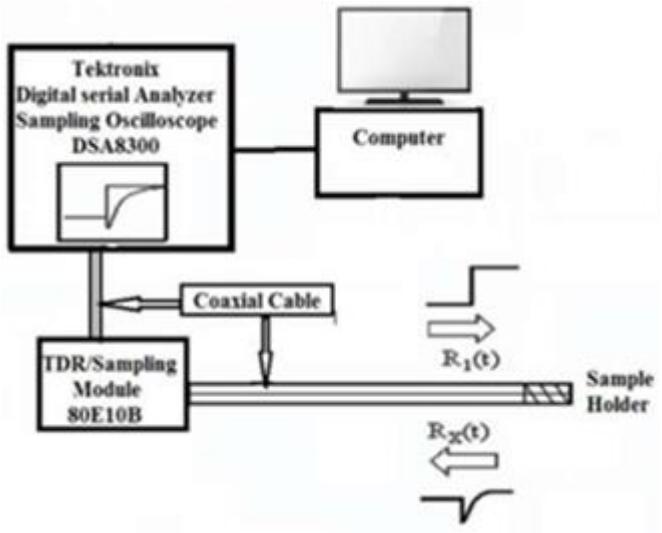

3. RESULTS AND DISCUSSION

3.1 Complex permittivity spectra

The frequency dependent complex permittivity spectra for xylitol-water at various concentrations produced by the time domain reflectometry technique (TDR) at 25°C are shown in Figure 3. The plot shows that the dielectric permittivity (ε') is decreases with increasing the concentration of xylitol in water and with increasing frequency which indicates the dielectric dispersion. These outcomes are in good agreement with the findings of D N Rander et al.[5] The dielectric permittivity also increases with decreasing the temperature. The reason could be that there is a higher chance of hydrogen bonds forming when temperature decreases [8]. It is also observed from graph that the dielectric loss shows peaks at certain frequencies and these peaks are shifted towards the lower frequencies as increasing the concentration of xylitol in water. For pure water the loss peak is around 16-19 GHz whereas for XX=0.128 it is observed to be around 2-3 GHz [5].

The complex permittivity spectra obtained with TDR are fitted to the Havriliak –Negami expression using the non – linear least square fit method

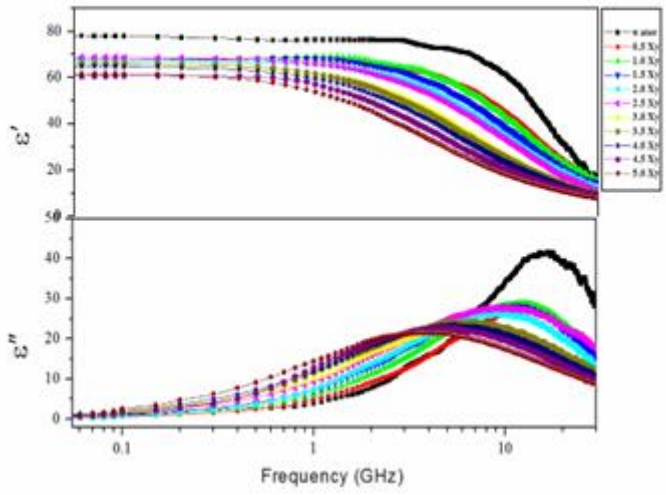

Fig 3. frequency dependent dielectric complex permittivity spectra of xylitol – water mixture for various concentrations at 25°C

$$\varepsilon^*(\omega) = \varepsilon_\infty + \frac{\varepsilon_0 - \varepsilon_\infty}{[1 + (j\omega\tau)^{1-\alpha}]^\beta}$$

Where ε 0 is the static dielectric constant which represents the equilibrium behaviour, ε ∞ is the permittivity at high frequency which represents the instantaneous behaviour, τ is the relaxation time, α and β are the shape parameters describing the symmetric and asymmetric distribution of relaxation time respectively and ω is the angular frequency[9,10]. The β value indicates the asymmetric distribution of relaxation width (0⩽ β ⩽1).

3.2 Static dielectric constant (ε0)

The high ε0 value of the water molecule suggests that hydroxyl groups have a significant impact on a molecules dielectric constant value (ε0) [11]. As the number of carbon atoms increases in the chain of molecule, ε0 value decreases. Xylitol molecule have five carbon atoms but water molecule does not have any carbon atom. So the ε0 value of xylitol is very low as compared to water having value 40 in pure form. It is nearly half of the value of water molecule. On compairing this value of xylitol with an alcohol containing equal number of carbon atoms but having only one OH group (pentanol) has ε0 value at 25°C is 15.23 [12] ,which is much smaller than that of the ε0 value of xylitol. This reduced value in ε0 is compensated by the five hydroxyl groups. Figure 4 shows ε0 of xylitol-water as a function of mole fraction of xylitol. The ε0 value of water at 25°C is 77.82 and that of 0.128 xylitol is 62.68 . on adding 55% of xylitol reduces the ε0 value by small amount .this gives the significant impact of OH group on dielectric constant value and gives the cooperative nature in the binary mixtures of xylitol – water molecules.

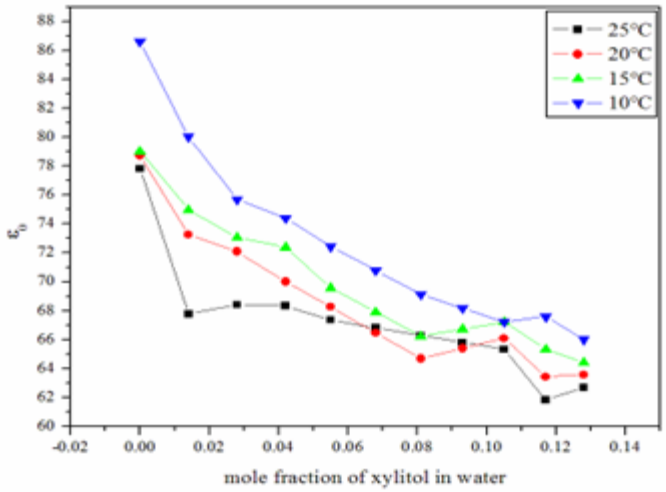

Fig 4.variation of Static dielectric constant (ε0) with mole fraction of xylitol in water (Xx) at different temperatures

3.3 Relaxation time (τ)

There are several factors such as hydrogen bond forming functional group, chain length of a molecule, viscosity, temperature etc which affects the relaxation time [11,12]. As shown in Fig 5. the dielectric relaxation time increases non linearly with increasing concentration of xylitol in water. In the first half of the graph the increase in relaxation time is slow which is the water rich region and in the second half of the graph, the increase in the relaxation time is sharp which is the xylitol rich region. That may be owing to the cooperative nature of water and xylitol molecules. These outcomes are in good agreement with the findings of D N Rander et al. [5]. There are many possibilities for water and xylitol molecules to break and reform hydrogen bonds among the water-water, water-xylitol and xylitol-xylitol molecules. from the graph it is observed that as the temperature decreases the non linear nature of relaxation time increases. This suggests that with increase in molecular association in xylitol-water, clusters of unlike molecules may form [8]. It is observed from the table that in the water rich region the value of β is nearly equal to 1 which shows the relaxation is close to Debye type. As the concentration of
xylitol in water increases, the value of β becomes smaller than 1.this shows that the complex permittivity spectra deviating from Debye to Cole-Davidson type [13]. The values of ε0, τ and β are given in table 1.

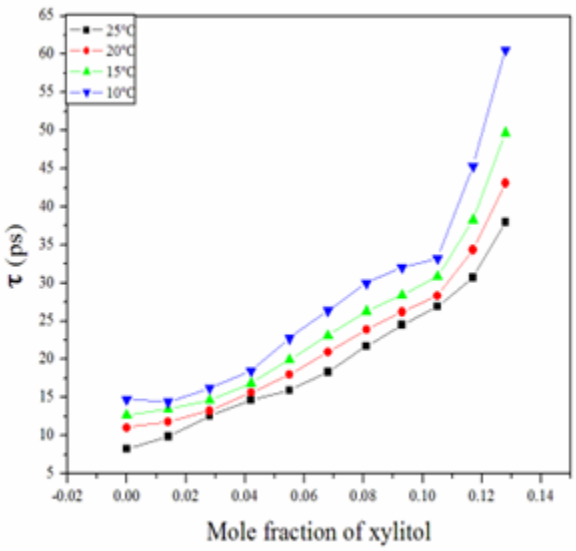

Fig5 . variation of relaxation time verses mole fraction of xylitol in water

Table 1 .Dielectric parameters: Dielectric constant (ε0), Relaxation time (τ), Asymmetric distribution parameter (β) for xylitol – water mixture

4.Conclusion

This work reports the temperature dependent dielectric parameters of aqueous xylitol solution using the time domain reflectometry technique in the frequency range 10 MHz to 30 GHz. The dielectric permittivity spectrum concludes that as the concentration of xylitol in water increases the dielectric constant decreases and relaxation time increases. The dielectric parameters are described by using the Cole – Davidson model.

Acknowledgement

Author SS Patange is thankful to the financial support given by the School of physical sciences at S.R.T.M.University Nanded, Maharashtra and DST, New Delhi (Project Number DST PROJECT SB/S2/LOP-032/2013) for the use of the instrument facility.

References:

[1] Awuchi, Chinaza Godswill, and K. Ch Echeta. "Current developments in sugar alcohols: Chemistry, nutrition, and health concerns of sorbitol, xylitol, glycerol, arabitol, inositol, maltitol, and lactitol." Int. J. Adv. Acad. Res 5.11 (2019): 1-33.

[2] DeMan, John M., et al. Principles of food chemistry. Vol. 1. Gaithersburg: Aspen Publishers, 1999.

[3]Gasmi Benahmed, Asma, et al. "Health benefits of xylitol." Applied Microbiology and Biotechnology 104 (2020): 7225-7237.

[4] Bokhare, Aniket D., et al. "Dielectric relaxation and hydrogen bonding interactions study of aqueous D-sorbitol using time domain reflectometry." Physics and Chemistry of Liquids 62.1 (2024): 1-8. https://doi.org/10.1080/00319104.2023.2263898

[5] Rander, D. N., et al. "Dielectric relaxation and hydrogen bonding interaction in xylitol–water mixtures using time domain reflectometry." Indian Journal of Physics 90 (2016): 67-72.http://doi 10.1007/s12648-015-0728-2

[6] Płowaś-Korus, Iwona, and Richard Buchner. "Hydration and aggregation in aqueous xylitol solutions in the wide temperature range." Journal of Molecular Liquids 340 (2021): 116838.

[7] Cole, R. H., et al. "Time domain reflection methods for dielectric measurements to 10 GHz." Journal of applied physics 66.2 (1989): 793-802. https://doi.org/10.1063/1.343499

[8] Nakanishi, Masahiro, and Ryusuke Nozaki. "Systematic study of the glass transition in polyhydric alcohols." Physical Review E 83.5 (2011): 051503. https://doi.org/10.1103/PhysRevE.83.051503

[9] Cole, Kenneth S., and Robert H. Cole. "Dispersion and absorption in dielectrics I. Alternating current characteristics." The Journal of chemical physics 9.4 (1941): 341-351.

[10] Davidson, D. W., and Robert H. Cole. "Dielectric relaxation in glycerine." The Journal of Chemical Physics 18.10 (1950): 1417-1417. https://doi.org/10.1063/1.1750906

[11] Sengwa, R. J. "Dielectric behaviour, ionic conductivity and structure of high energy ball mill blended melt pressed and solution cast solid polymeric nanocomposite electrolytes." Indian Journal of Pure & Applied Physics (IJPAP) 51.11 (2016): 769-779. http://op.niscpr.res.in/index.php/IJPAP/article/view/2047

[12] Lide, David R., ed. CRC handbook of chemistry and physics. Vol. 85. CRC press, 2004.

[13] Davidson, Donald W., and Robert H. Cole. "Dielectric relaxation in glycerol, propylene glycol, and n‐propanol." The Journal of Chemical Physics 19.12 (1951): 1484-1490. https://doi.org/10.1063/1.1748105

ICRTMS-2024
International e-Conference on Recent Trends in Material Science
In Association with International Journal of Scientific Research in Science and Technology
Volume 11 | Issue 9 | Print ISSN: 2395-6011 | Online ISSN: 2395-602X (www.ijsrst.com)

Dielectric Study of Hydroxyl Group Molecules at Microwave Using Time Domain Reflectometry Techniques

Balaji D. Achole*
*Department of Physics, Shri. Havagiswami Mahavidyalaya, Udgir, Maharashtra (INDIA)

ABSTRACT

The dielectric relaxation study of tert-Butyl alcohol [TB] with ethylene glycol[EG] were determined in the frequency range of 10 MHz to 20 GHz using time domain reflectometry (TDR) in the temperature range 25°C and 35°C for 11 different concentrations of the system. The dielectric parameters viz. static dielectric constant (ε_0), dielectric constant at infinite frequency (ε_∞) and relaxation time (τ) have been obtained by the least squares fit method. The Kirkwood correlation factor of the mixtures have also been determined. For temperature range, considered here, the permittivity increases and relaxation time decreases with the percentage of ethylene glycol [EG]**.** The Static dielectric constant for the mixtures have been fitted with Bruggeman model.

Keywords: Time domain reflectometry, excess parameter, Kirkwood correlation factor, Brugmann factor.

I. INTRODUCTION

The dielectric relaxation of binary polar liquids provides information regarding solute- solvent interactions [1-3]. In this work, we report the dielectric study of tert-butyl alcohol (TB) with ethylene glycol [EG] mixture; both are –OH group molecule. It is interesting to see the effect of mixtures of –OH group molecule. The objective of the present paper is to report the detailed dielectric relaxation study of tert-butyl alcohol (TB) with ethylene glycol [EG] mixtures using TDR at different temperatures.

2. EXPERIMENTAL

2.1 Materials

TB and EG (Merck Pvt. Ltd., West Mumbai, India) were used without further purification. The solutions were prepared at 11 different volume percentage of EG from 0 % to 100 % in steps of 10 %.Using these volume percents the mole fraction is calculated as-

$x_1 = (v_1\rho_1/m_1) /[(v_1\rho_1/m_1) + (v_2\rho_2/m_2)]$

where m_i, v_i, and ρ_i represent the molecular weight, volume percent, and density of the i^{th} (i=1, 2) liquids, respectively. The density and molecular weight of the liquids[2,5] at 25°C are as follows

Tert-Butyl alcohol[TB] -Density - 0.8063 gm.cm^{-3} ; Mol. Wt.- 74.121.

Ethylene glycol[EG] -Density - 1.1135 gm.cm.$^{-3}$; Mol. Wt.- 62.068.

2.2 Apparatus

The complex permittivity spectra were studied using the time domain reflectometry [4-5] method. The Hewlett Packard HP 54750 sampling oscilloscope with HP 54754A TDR plug in module has been used. A fast

rising step voltage pulse of about 39 ps rise time generated by a pulse generator was propagated through a coaxial line system of characteristic impedance 50 Ohm.

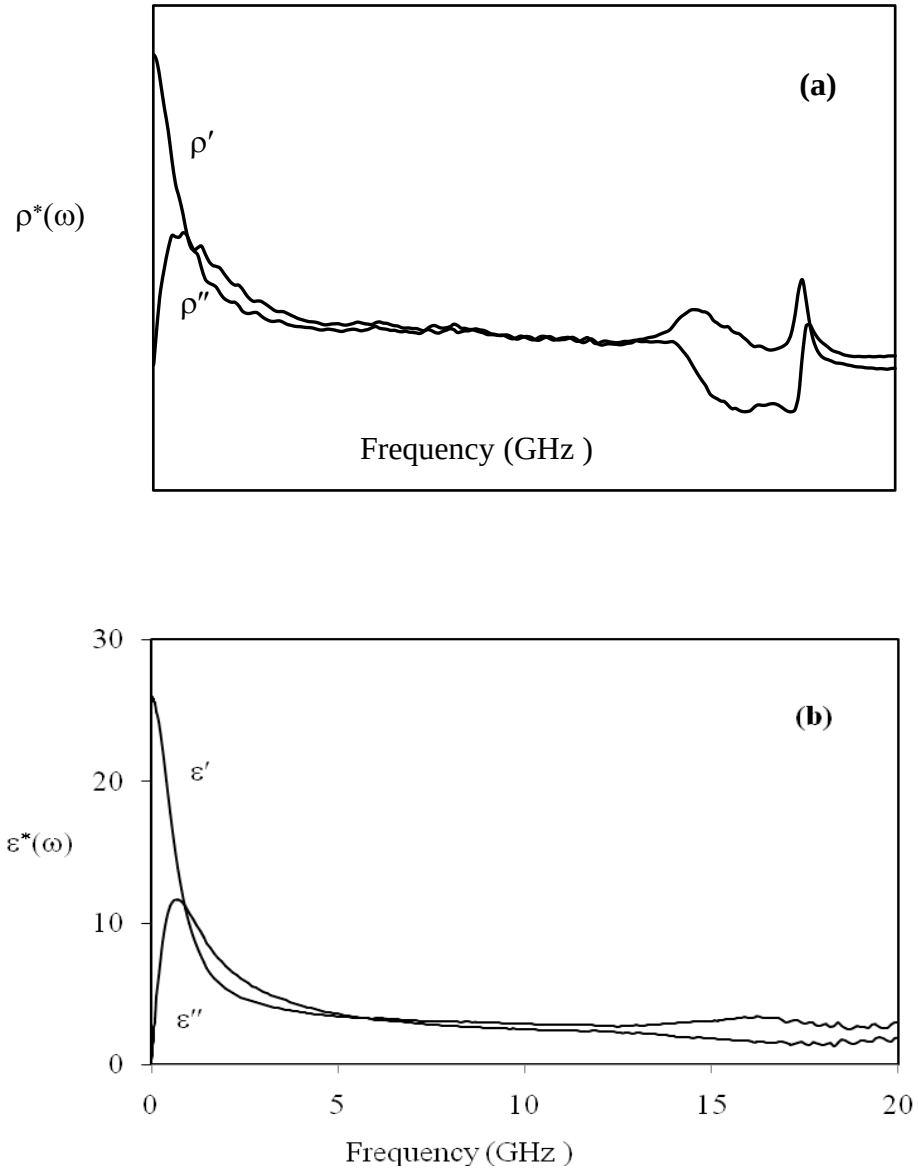

Figure 1.

a) $\rho^*(\omega)$ spectra of TB-EG for 80 % of TB at 25^{0}C.

b) $\varepsilon^*(\omega)$ spectra of TB-EG for 80 % of TB at 25^{0}C.

Transmission line system under test was placed at the end of coaxial line in the standard military applications (SMA) coaxial connector with 3.5 mm outer diameter and 1.35 mm effective pin length. All measurements were carried out under open load conditions. The change in the pulse after reflection from the sample placed in the cell was monitored by the sampling oscilloscope. In the experiment, time window of 5 ns was used. The reflected pulse without sample $R_l(t)$ and with sample $R_x(t)$ were digitized in 1024 points in the memory of the oscilloscope and transferred to a PC through 1.44 MB floppy diskette drive.

The temperature controller system with water bath and a thermostat has been used to maintain the constant temperature within the accuracy limit of ±1^{o}C. The sample cell is surrounded by a heat insulating container

through which the water of constant temperature using a temperature controller system is circulated. The temperature at the cell is checked using the electronic thermometer.

3. DATA ANALYSIS

The time dependent data were processed to obtain complex reflection coefficient spectra □*(□) over the frequency range from 10 MHz to 20 GHz using Fourier transformation [6 ,7] as

□*(□)=(c/j□d)[p(□)/q(□)] (1)

1. Comparison of data for the liquids used with literature values at 25^{0}c.

25^{0}C	TB		EG	
	Ref. values [a]	Reported values	Ref. values [b]	Reported values
ε_0	11.50	11.89	40.89	40.16
ε_∞	3.00	3.26	4.16	4.24
τ	276.9	289.15	104.6	109.181

[a]Ref. is [1] and [b]ref. is [2].

where p(ω) and q(ω) are Fourier transforms of [$R_1(t)$- $R_x(t)$]) and [$R_1(t)$ + $R_x(t)$] respectively, c is the velocity of light, ω is angular frequency, d is the effective pin length and j=$\sqrt{-1}$.

The complex permittivity spectra $\varepsilon^*(\omega)$ were obtained from reflection coefficient spectra $\rho^*(\omega)$ by applying bilinear calibration method [4].

The experimental values of $\varepsilon^*(\omega)$ are fitted with the Debye equation [8]

$$\varepsilon^*(\omega) = \varepsilon_\infty + \frac{\varepsilon_0 - \varepsilon_\infty}{1 + j\omega\tau} \quad (2)$$

with ε_0, ε_∞, and τ as fitting parameters. A nonlinear least-squares fit method [9] was used to determine the values of dielectric parameters. A sample of complex reflection coefficient $\rho^*(\omega)$ and complex permittivity spectra $\varepsilon^*(\omega)$ are shown in Figure 1 a,b. This corresponds to 60% of TB and 40% of EG mixture at 25^{0}C.

4. RESULTS AND DISCUSSION

The values of ε_0, ε_∞ and τ for the pure liquids used are given in Table 1. The static dielectric constant (ε_0), dielectric constant at infinite frequency (ε_∞) and relaxation time (τ) obtained by fitting experimental data with the Debye equation are listed in Table 2. The values of dielectric constant (ε_0) increases and relaxation time decreases with temperature as expected. Figure 2, shows the behavior of static dielectric constant and relaxation time for the system as a function of mole fraction of EG in TB at different temperatures.

The Kirkwood correlation factor g_f [10] is also a parameter for getting information regarding orientation of electric dipoles in polar liquids.

The g_f for pure liquid may be obtained by the expression

$$\frac{4\Pi N\mu^2\rho}{9kTM} g_f = \frac{(\varepsilon_0 - \varepsilon_\infty)(2\varepsilon_0 + \varepsilon_\infty)}{\varepsilon_0(\varepsilon_\infty + 2)^2} \quad (3)$$

where μ is dipole moment in gas phase, ρ is density at temperature T, M is molecular weight, k is Boltzmann constant, N is Avogadro's number. The dipole moments for TB and EG in gas phase are taken as 1.69 D and 2.2 D[11] respectively.

For the mixture of two polar liquids 1, 2 Eq. (3) is modified by [12] with the following assumptions:

Assume that g_f for the binary mixture is expressed by an effective averaged correlation factor g^{eff} such that the Kirkwood equation for the mixture can be expressed by

$$\frac{4\Pi N}{9kT}\left(\frac{\mu_1^2\rho_1}{M_1}\phi_1+\frac{\mu_2^2\rho_2}{M_2}\phi_2\right)g^{eff}=\frac{(\varepsilon_{0m}-\varepsilon_{\infty m})(2\varepsilon_{0m}+\varepsilon_{\infty m})}{\varepsilon_{0m}(\varepsilon_{\infty m}+2)^2} \quad (4)$$

with ϕ_1 and ϕ_2 as volume fractions of liquids 1 and 2 respectively.

Table 2. Temperature dependent dielectric relaxation parameters for TB+EG mixtures*

x_2	T= 25°C	T= 35°C	x_2	T= 25°C	35°C
ε_0					
0.0000	11.89(1)	11.31(0)	0.7121	31.18(7)	30.66(7)
0.1549	19.01(6)	18.31(4)	0.7937	34.09(8)	32.93(3)
0.2919	22.78(8)	21.66(7)	0.8684	36.59(4)	34.66(4)
0.4141	25.01(7)	24.54(6)	0.9369	38.65(2)	36.83(2)
0.5237	27.95(3)	27.27(5)	1.0000	40.76(0)	39.39(8)
0.6225	29.94(6)	28.52(8)			
ε_∞					
0.0000	3.26(1)	3.09(0)	0.7121	4.04(4)	3.76(5)
0.1549	3.51(3)	3.31(5)	0.7937	4.12(5)	3.89(6)
0.2919	3.68(6)	3.37(3)	0.8684	4.15(3)	4.08(1)
0.4141	3.75(5)	3.41(11)	0.9369	4.17(4)	4.16(3)
0.5237	3.84(11)	3.57(6)	1.0000	4.24(0)	4.31(1)
0.6225	3.92(7)	3.64(9)			
τ(ps)					
0.0000	289.15(0)	251.30(0)	0.7121	187.06(3)	138.64(13)
0.1549	258.19(4)	222.49(7)	0.7937	162.12(7)	119.69(6)
0.2919	241.99(8)	209.95(3)	0.8684	145.23(8)	101.40(3)
0.4141	233.97(7)	181.12(7)	0.9369	119.05(3)	97.96(4)
0.5237	215.90(11)	165.18(13)	1.0000	109.18(0)	79.29(0)
0.6225	205.62(6)	153.50(11)			

* x_2 is the mole fraction of EG in TB. Number in bracket represent error in the corresponding value, e.g., means 19.01(6) means 19.01 ± 0.6.

In equation (4), the values of g^{eff} will change from g_1 to g_2 as concentration of molecule 2 will decrease from 100% to 0%. The Kirkwood correlation factor, g_f, which gives angular correlation between the molecules of the system, are less than 1. The values of g^{eff} and g_f are calculated from equation (3) and (4) are shown in Figure 3 for the mixtures of the system. Errors are also estimated by assuming 2 % error in the values of the permittivity. The effective values of the correlation factor for EG are larger than the corresponding value in TB. Initially g_f value increases to its peak value at 100 % of TB then it decreases up to 40 %. Further from 50 % it increases linearly to the EG pure value. The g_f values are less than unity. The correlation factor g provides information about formation of multimers in the liquid as

i) g = 1 indicates, there is no interaction between the molecules in liquid. The system may be considered like nonpolar.

ii) g < 1 indicates that the intermolecular interaction is such that the total effective value of dipoles gets reduced. It suggests antiparallel alignment of dipoles.

iii) g > 1 indicates parallel alignment of dipoles in multimers.

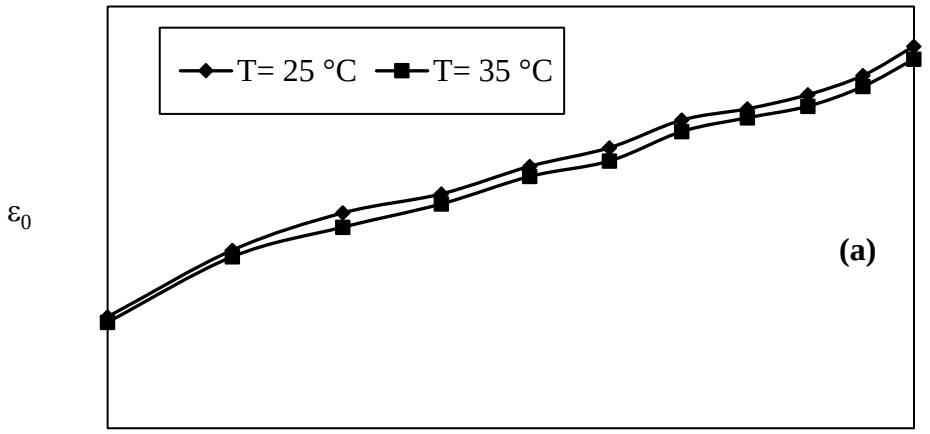

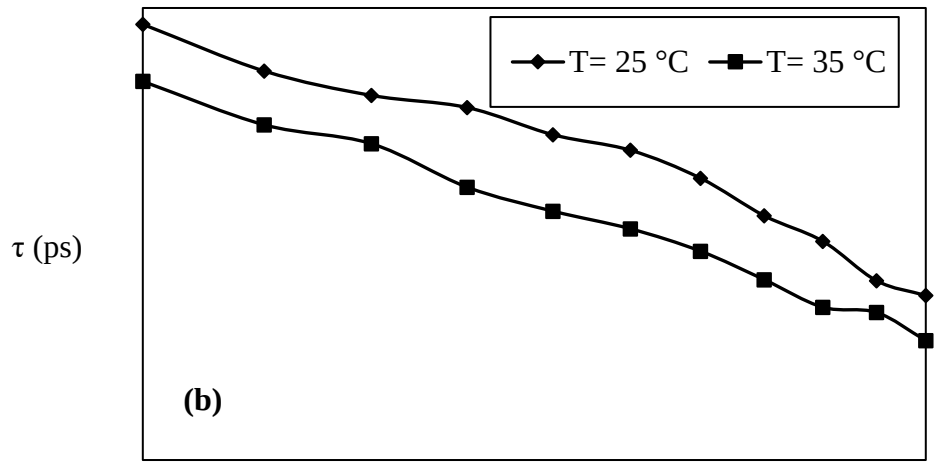

Figure 2. (a) Static dielectric constant (ε_0), (b) relaxation time (τ), versus mole fraction (x_2) of EG in TB at different temperatures.

The modified Bruggeman equation [13] is another parameter, which may be used an indicator of liquid 1 and 2 interaction. The Bruggeman factor f_B is given by,

$$f_B = \left(\frac{\varepsilon_{0m} - \varepsilon_{02}}{\varepsilon_{01} - \varepsilon_{02}}\right)\left(\frac{\varepsilon_{01}}{\varepsilon_{0m}}\right)^{1/3} = (1 - \phi_2) \qquad (5)$$

According to equation (5), a linear relationship is expected which will give a straight line when plotted f_B against ϕ_2. However, here the experimental values of f_B were found to deviate from the linear relationship. To fit the experimental data, Eq. (5) has been modified [14]

$f_B = 1-[a-(a-1)\phi_2]\phi_2$ (6)

where 'a' is numerical fitting parameter. The parameters 'a' has been determined by the least squares fit method and it is found to be 0.314, and -0.142 for temperature 25^{O}C, 35^{O}C respectively. The value of 'a' = 1 corresponds to the ideal Bruggeman mixture formula. The deviation from 1 relates to corresponding liquids 1 and 2 interaction.

Thermodynamic properties may be used to access the dipole under the influence of applied field. When two liquids are mixed together, there is change in energy of the system. This change in energy can be interpreted in terms of its activation energy.

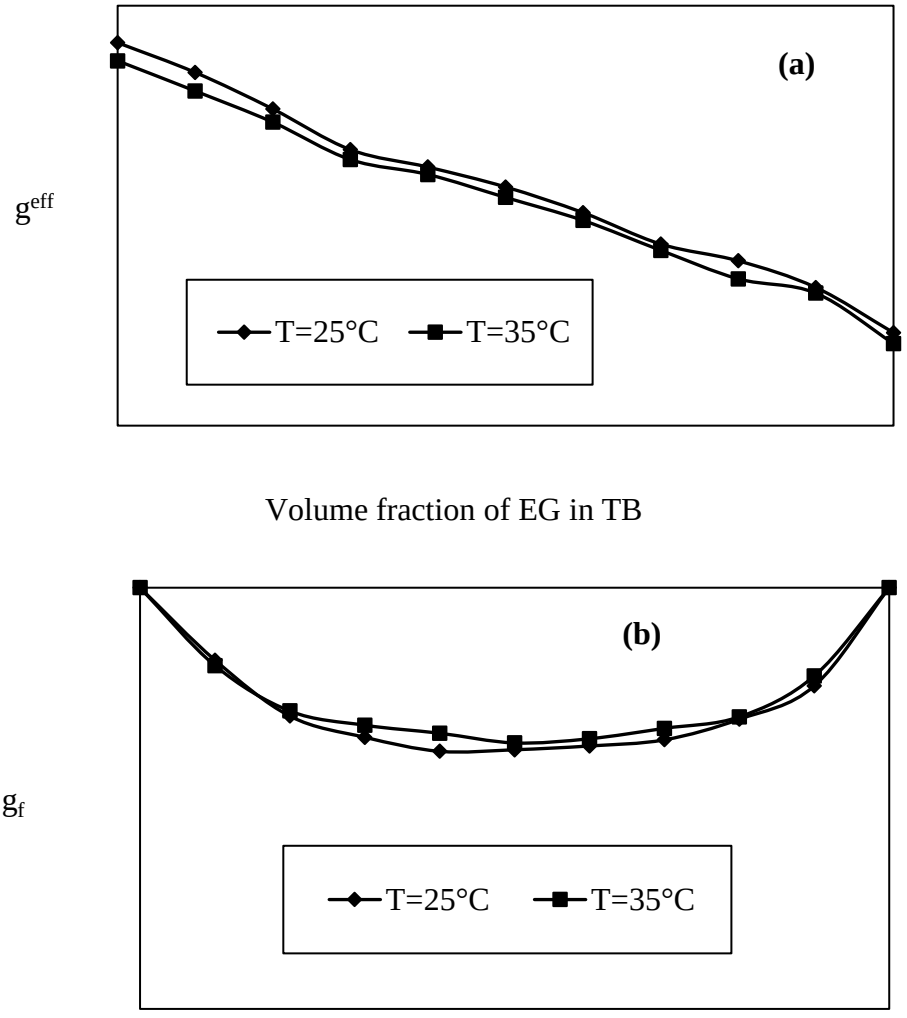

Figure 3. **(a)** Variation of g^{eff} versus Volume fraction of EG in TB at various temperatures.
(b) Variation of g_f versus Volume fraction of EG in TB at various temperatures.

The thermodynamic parameters like molar enthalpy of activation ΔH and molar entropy of activation ΔS are determined from the Eyring rate equation [15] by least square fit method as

$$\tau = \frac{h}{KT} \exp(\Delta H - T\Delta S)/RT \quad (7)$$

The values of enthalpy are positive and remain positive for all the concentrations studied. The positive values of enthalpy indicate endothermic interaction and strong hydrogen bonding between liquid 1 and liquid 2. The increase in enthalpy suggests that there is more hydrogen bonding. The thermodynamic parameters evaluated by considering dielectric relaxation and viscosity as rate process are independent of temperature within the experimental errors. The values reported are average values. The viscous flow involves translation and rotational motion of the molecules. Enthalpy refers to the total energy content of the system. It is basically the difference in heat of the product and reactants. Entropy is a term for disorder in a system and that the overall entropy in a system always increases. The molar energy of activation ΔH is greater for tert-Butyl alcohol than EG indicating that there is more hydrogen bonding for pure liquid state.

5. CONCLUSION

Dielectric relaxation data provide information regarding solute-solvent interaction in liquids. The dielectric behavior of this binary mixture is found to agree with the modified Bruggeman equation.

REFERENCES

[1] A. C. Kumbharkhane, S. M. Puranik , S.C. Mehrotra, j. of Chem. Soc., Faraday Trans.,1991,87(10),1569-1573.

[2] A. C. Kumbharkhane, S. M. Puranik , S.C. Mehrotra, j. of Soiution Chem.,vol-20,No.-12,1991.

[3] V. P. Pawar and S. C. Mehrotra, J. Mol. Liq., 95 (2002) 63-74.

[4] R. H. Cole, J. G. Berbarian, S. Mashimo, G. Chryssikos, A. Burns and E. Tombari, J. Appl. Phys., 66 (1989) 793.

[5] S. M. Puranik, A. C. Kumbharkhane and S. C. Mehrotra, J. Chem. Soc. Faraday Trans., 87 (1991) 1569.

[6] C. E. Shannon, Proc. IRE, 37 (1949) 10.

[7] H. A. Samulan, Proc. IRE, 39 (1951) 175.

[8] P. Debye, Polar molecules, Chemical Catalog, New York (1929).

[9] P. R. Bevington, Data reduction and error analysis for the physical sciences, Mc-Graw Hill, New York, (1969).

[10] H. Frolhich, Theory of dielectrics, Oxford University Press, London, (1949).

[11] R. C. Weast, Handbook of Chemistry and Physics, 64th ed. CRC Press Boca Raton, Florida (1983-84).

[12] A. C. Kumbharkhane, S. M. Puranik and S. C. Mehrotra, J. Sol. Chem., 22 (1993) 219.

[13] D. A. G. Bruggeman, Ann. Phys. (Leipzig), 5 (1935) 636.

[14] S. M. Puranik, A. C. Kumbharkhane and S. C. Mehrotra, J. Mol. Liq., 59 (1994) 173.

[15] Eyring H., *J. Chem. Phys.*,4,283 **(1936)**

ICRTMS-2024
International e-Conference on Recent Trends in Material Science
In Association with International Journal of Scientific Research in Science and Technology
Volume 11 | Issue 9 | Print ISSN: 2395-6011 | Online ISSN: 2395-602X (www.ijsrst.com)

Utilization of Biowaste Materials for Environmental Applications: A Comprehensive Review

Prashant P. Bharaswadkar
Nagnath Arts, Commerce & Science College, Aundha Nagnath Dist. Hingoli -431701, MS, India

ABSTRACT

Biowaste materials, generated from various organic sources, have garnered increasing attention in recent years for their potential in environmental applications. This paper presents a detailed review of the utilization of biowaste materials for various environmental purposes, including but not limited to waste management, soil remediation, water treatment, and renewable energy production. The paper discusses the diverse types of biowaste materials available, their characteristics, and their applications in mitigating environmental challenges. Furthermore, it examines the current state-of-the-art techniques and technologies employed for harnessing the potential of biowaste materials, along with the challenges and future prospects in this field.

Keywords : Biowaste, water treatment, pollution, waste management

I. INTRODUCTION

1.1 Background:

Biowaste materials, derived from organic sources such as agriculture, food production, and municipal activities, represent a significant portion of global waste streams. With increasing urbanization and population growth, the management of biowaste has become a pressing environmental issue. Biowaste not only occupies valuable landfill space but also contributes to greenhouse gas emissions and environmental pollution if not managed properly. Consequently, there is a growing need for sustainable strategies to utilize biowaste effectively while mitigating its environmental impact.

1.2 Objectives:

The primary objective of this research paper is to provide a comprehensive review of the utilization of biowaste materials for various environmental applications. By examining the types, characteristics, and potential applications of biowaste, this paper aims to elucidate the role of biowaste in waste management, soil remediation, water treatment, and renewable energy production. Additionally, the paper seeks to explore state-of-the-art techniques and technologies for harnessing the potential of biowaste, along with the challenges and opportunities associated with its utilization.

1.3 Scope of the Review:

This review will encompass a wide range of biowaste materials, including but not limited to agricultural residues, food waste, municipal solid waste, animal manure, sewage sludge, and other organic waste sources.

Furthermore, the environmental applications of biowaste materials will be examined in detail, with a focus on waste management practices, soil remediation techniques, water treatment methods, and renewable energy production processes.

2. Types and Sources of Biowaste Materials:

2.1 Agricultural Residues:

Agricultural residues refer to the biomass left behind after crop harvesting or processing activities. These include crop residues (e.g., stalks, leaves), straw, husks, and shells. Agricultural residues are abundant in agricultural regions and can be utilized for various purposes, such as biofuel production, soil amendment, and animal bedding.

2.2 Food Waste:

Food waste comprises organic materials discarded during food production, processing, distribution, and consumption. It includes both pre-consumer waste (e.g., trimmings, spoiled food from restaurants and supermarkets) and post-consumer waste (e.g., leftovers, expired food from households). Food waste is a significant contributor to global waste generation and environmental pollution. However, it also holds potential as a feedstock for composting, anaerobic digestion, and bioenergy production.

2.3 Municipal Solid Waste (MSW):

Municipal solid waste (MSW) consists of household waste, commercial waste, and institutional waste. It encompasses a wide range of materials, including biodegradable organics, plastics, paper, glass, and metals. Biowaste constitutes a substantial portion of MSW and can be diverted from landfill disposal through recycling, composting, and other waste management practices.

2.4 Animal Manure:

Animal manure refers to the organic waste produced by livestock farming operations. It includes feces, urine, and bedding materials such as straw or wood shavings. Animal manure is rich in nutrients and organic matter but can pose environmental risks if not managed properly. However, when used as fertilizer or processed through anaerobic digestion, animal manure can contribute to soil fertility and renewable energy production.

2.5 Sewage Sludge:

Sewage sludge, also known as biosolids, is the residual material generated during wastewater treatment processes. It contains organic matter, nutrients, and potentially harmful contaminants such as heavy metals and pathogens. Proper treatment and disposal of sewage sludge are essential to prevent environmental pollution and protect public health. However, sewage sludge can also be beneficially reused in agriculture, land reclamation, and soil improvement projects.

2.6 Other Biowaste Sources:

In addition to the aforementioned sources, biowaste materials can arise from various other activities and industries, including forestry, fisheries, and bioenergy production. These may include wood chips, sawdust, fish waste, and by-products from biofuel refineries. Each type of biowaste has its unique characteristics and potential applications, which warrant further exploration.

3. Characteristics of Biowaste Materials:

3.1 Physical Properties:

Biowaste materials exhibit diverse physical properties depending on their composition and origin. These properties include particle size, bulk density, porosity, moisture content, and surface area. Understanding the physical characteristics of biowaste is essential for determining suitable processing and utilization methods.

3.2 Chemical Composition:

The chemical composition of biowaste materials varies widely and can influence their suitability for different applications. Key chemical constituents of biowaste include organic matter, carbon, nitrogen, phosphorus, potassium, and trace elements. The nutrient content and organic carbon-to-nitrogen ratio are particularly important considerations for composting and soil amendment.

3.3 Biological Properties:

Biowaste materials harbor a diverse array of microorganisms, including bacteria, fungi, and actinomycetes. These microorganisms play crucial roles in biodegradation processes such as composting and anaerobic digestion. Understanding the microbial dynamics within biowaste is essential for optimizing waste treatment and conversion processes.

4. Environmental Applications of Biowaste Materials:

4.1 Waste Management:

4.1.1 Composting:

Composting is a biological decomposition process that converts organic waste into a stable, humus-like material known as compost. Biowaste materials such as food waste, yard waste, and agricultural residues can be composted to produce high-quality soil amendments for use in agriculture, landscaping, and horticulture. Composting not only diverts organic waste from landfills but also helps improve soil fertility, structure, and water retention capacity.

4.1.2 Anaerobic Digestion:

Anaerobic digestion is a biological process that breaks down organic matter in the absence of oxygen, producing biogas (a mixture of methane and carbon dioxide) and digestate. Biowaste materials such as food waste, animal manure, and sewage sludge can be anaerobically digested to produce renewable biogas for electricity generation, heat production, or vehicle fuel. Anaerobic digestion offers several environmental benefits, including greenhouse gas mitigation, odor reduction, and nutrient recovery.

4.1.3 Vermicomposting:

Vermicomposting is a composting process that utilizes earthworms to decompose organic waste materials. Biowaste materials such as food scraps, paper waste, and yard waste can be vermicomposted to produce nutrient-rich vermicompost and worm castings. Vermicomposting is an environmentally friendly waste management technique that can be implemented at various scales, from household composting bins to large-scale commercial facilities.

4.2 Soil Remediation:

4.2.1 Soil Amendment:

Biowaste materials can be used as soil amendments to improve soil quality, structure, and fertility. Compost, biochar, and other organic amendments can enhance soil organic matter content, nutrient levels, and microbial activity, leading to improved plant growth and productivity. Soil amendments derived from biowaste can also help remediate degraded soils, restore ecosystem health, and mitigate soil erosion and desertification.

4.2.2 Phytoremediation:

Phytoremediation is a plant-based remediation technique that utilizes the natural abilities of certain plant species to uptake, accumulate, and detoxify contaminants from soil and water. Biowaste materials such as compost and organic amendments can be applied to contaminated sites to enhance soil fertility and support the growth of phytoremediation plants. By combining biowaste utilization with phytoremediation, it is possible to achieve sustainable remediation of polluted environments while minimizing negative impacts on ecosystems and human health.

4.3 Water Treatment:

4.3.1 Adsorption:

Biowaste materials such as activated carbon, biochar, and agricultural residues can be used as adsorbents for removing pollutants from water and wastewater. The porous structure and high surface area of biowaste-derived adsorbents enable efficient adsorption of contaminants such as heavy metals, organic pollutants, and emerging contaminants. Adsorption-based water treatment using biowaste materials offers a cost-effective and environmentally friendly approach for purifying water resources and protecting aquatic ecosystems.

4.3.2 Coagulation/Flocculation:

Biowaste materials contain natural coagulants and flocculants that can be utilized for water and wastewater treatment. Substances such as tannins, polysaccharides, and proteins present in biowaste can promote the aggregation and removal of suspended solids, colloids, and microorganisms from water matrices. Coagulation/flocculation processes using biowaste-derived coagulants offer an alternative to conventional chemical treatment methods, with reduced chemical usage and lower environmental impact.

4.3.3 Biological Filtration:

Biowaste materials can serve as substrates for biological filtration systems used in water and wastewater treatment. Biofilters, constructed wetlands, and biochar filters utilize microbial communities present in biowaste to remove pollutants through biological degradation, sorption, and transformation processes. Biological filtration systems offer a sustainable and low-energy approach for treating various types of water pollution, including nutrient runoff, organic matter, and micropollutants.

4.4 Renewable Energy Production:

4.4.1 Biogas Production:

Biowaste materials are valuable feedstocks for biogas production through anaerobic digestion. Microbial fermentation of organic matter in biowaste generates biogas, which can be utilized as a renewable energy source for electricity generation, heat production, and vehicle fuel. Biogas production from biowaste offers

significant environmental benefits, including reduced greenhouse gas emissions, improved waste management, and energy diversification.

4.4.2 Biofuel Production:

Biowaste materials can be converted into liquid biofuels such as biodiesel and bioethanol through biochemical and thermochemical processes. Feedstocks such as food waste, crop residues, and algae biomass contain sugars, starches, and lipids that can be fermented or chemically converted into biofuels. Biofuel production from biowaste provides a sustainable alternative to fossil fuels, reduces dependence on imported energy sources, and contributes to climate change mitigation.

4.4.3 Bioelectricity Generation:

Biowaste materials can be utilized for bioelectricity generation through microbial fuel cells (MFCs) and anaerobic digestion coupled with microbial fuel cells (AD-MFCs). Microorganisms in biowaste degrade organic matter and produce electrons, which can be harvested to generate electricity in MFCs. Bioelectricity generation from biowaste offers a renewable and decentralized energy solution, suitable for off-grid applications, wastewater treatment plants, and organic waste recycling facilities.

5. State-of-the-Art Techniques and Technologies:

5.1 Advanced Composting Methods:

Advanced composting methods, such as thermophilic composting, vermicomposting, and aerobic digestion, enhance the efficiency and quality of compost production from biowaste. These methods optimize process parameters such as temperature, moisture, aeration, and microbial inoculation to accelerate decomposition and produce stable, pathogen-free compost.

5.2 Biorefinery Approaches:

Biorefinery approaches integrate various conversion technologies to valorize biowaste materials into a range of high-value products, including biofuels, biochemicals, biomaterials, and bioenergy. Biorefineries utilize biochemical, thermochemical, and microbial processes to fractionate biowaste components and convert them into valuable intermediates and end products.

5.3 Biochar Production and Applications:

Biochar production from biowaste involves pyrolysis or hydrothermal carbonization of organic materials to produce a stable, carbon-rich material with high porosity and surface area. Biochar has diverse applications in agriculture, environmental remediation, water treatment, and carbon sequestration. Advanced biochar production techniques optimize process conditions and feedstock selection to enhance biochar quality and performance.

5.4 Nanotechnology for Biowaste Utilization:

Nanotechnology-based approaches enhance the efficiency and effectiveness of biowaste utilization processes by leveraging nanomaterials and nanocomposites. Nanomaterials derived from biowaste exhibit unique physicochemical properties that can be exploited for catalysis, adsorption, sensing, and environmental remediation applications.

5.5 Genetic Engineering for Enhanced Biowaste Conversion:

Genetic engineering techniques enable the optimization of microbial strains and metabolic pathways for enhanced biowaste conversion and bioproduct synthesis. Synthetic biology approaches allow the design and construction of microbial platforms capable of efficiently utilizing complex biowaste substrates and producing target molecules of interest.

6. Challenges and Limitations:

6.1 Contaminant Presence:

Biowaste materials may contain contaminants such as heavy metals, pathogens, and organic pollutants, which can pose risks to human health and the environment. Managing and mitigating contaminant presence in biowaste requires careful monitoring, testing, and treatment to ensure safe utilization and disposal.

6.2 Technological Constraints:

The adoption of biowaste utilization technologies may be hindered by technical challenges such as process efficiency, scalability, and cost-effectiveness. Overcoming technological constraints often requires research and development efforts to optimize process parameters, develop novel materials, and improve process integration and automation.

6.3 Economic Viability:

The economic viability of biowaste utilization depends on factors such as feedstock availability, processing costs, market demand, and policy incentives. Despite the environmental benefits of biowaste utilization, competing with conventional waste management and energy production methods can be challenging, especially in regions with low waste management fees and limited market opportunities.

6.4 Regulatory Frameworks:

Regulatory frameworks governing the management and utilization of biowaste vary across jurisdictions and can impact the feasibility and implementation of biowaste utilization projects. Compliance with environmental regulations, waste management standards, and safety guidelines is essential to ensure the responsible and sustainable utilization of biowaste materials.

7. Future Perspectives and Opportunities:

7.1 Integration of Biowaste Valorization:

The integration of biowaste valorization into circular economy models offers opportunities to maximize resource efficiency, minimize waste generation, and create value-added products from biowaste streams. Closing the loop on biowaste utilization requires collaborative efforts across sectors, including waste management, agriculture, energy, and manufacturing.

7.2 Technological Innovations:

Technological innovations in biowaste utilization, such as advanced conversion processes, biorefinery concepts, and nanotechnology applications, hold promise for enhancing the efficiency, sustainability, and versatility of biowaste valorization. Research and development initiatives aimed at developing novel technologies and improving existing processes will drive progress in the field.

7.3 Policy and Regulatory Support:

Policy and regulatory support for biowaste utilization can create favorable conditions for investment, innovation, and market development. Governments can incentivize biowaste valorization through financial incentives, regulatory mandates, tax credits, and public procurement policies that promote sustainable waste management and renewable energy production.

7.4 Public Awareness and Education:

Raising public awareness and education about the environmental benefits of biowaste utilization is essential for fostering behavior change and promoting sustainable lifestyles. Outreach initiatives, educational programs, and community engagement efforts can empower individuals and organizations to adopt waste reduction practices, support recycling initiatives, and participate in biowaste utilization projects.

8. Conclusions:

In conclusion, biowaste materials represent valuable resources that can be harnessed for various environmental applications, including waste management, soil remediation, water treatment, and renewable energy production. By utilizing biowaste effectively, we can mitigate environmental pollution, conserve natural resources, and promote sustainable development. However, realizing the full potential of biowaste requires overcoming technical, economic, and regulatory challenges while embracing technological innovations and fostering collaboration among stakeholders.

9. References:

1. Agyeman, F. O., Tao, W., & Yang, X. (2020). Recent advances in biowaste utilization for sustainable bioenergy and bioproducts production. Bioresource Technology, 297, 122499. doi:10.1016/j.biortech.2019.122499
2. Bernal, M. P., Alburquerque, J. A., & Moral, R. (2009). Composting of animal manures and chemical criteria for compost maturity assessment. A review. Bioresource Technology, 100(22), 5444-5453. doi:10.1016/j.biortech.2008.11.027
3. Chowdhury, S., Kumar, S., & Mukherjee, S. (2020). Harnessing biowaste resources for sustainable bioenergy production: A review. Bioresource Technology Reports, 10, 100413. doi:10.1016/j.biteb.2020.100413
4. Ciavatta, C., Govi, M., & Vittori Antisari, L. (2016). Compost stability and maturity evaluation: Integrating chemical and biological assays. Advances in Agronomy, 139, 97-151. doi:10.1016/bs.agron.2016.04.001
5. Demirbas, A. (2009). Biorefineries for biofuel upgrading: A critical review. Applied Energy, 86(Suppl. 1), S151-S161. doi:10.1016/j.apenergy.2009.04.043
6. Gaurav, K., & Verma, S. L. (2019). Valorization of biowaste for sustainable development: A review. Environmental Technology & Innovation, 15, 100374. doi:10.1016/j.eti.2019.100374
7. Kadam, A. A., Panicker, L., Paul, S., & Prasad, B. (2021). Recent advances in biowaste utilization for sustainable environmental applications: A review. Journal of Environmental Management, 283, 111956. doi:10.1016/j.jenvman.2021.111956
8. Lim, S. Y., & Lee, Y. K. (2020). Advanced biorefinery approaches for biomass waste utilization. Bioresource Technology, 306, 123182. doi:10.1016/j.biortech.2020.123182

9. Lu, Q., & Chen, Y. (2020). Biowaste-to-bioenergy and biofuel production: Clean conversion technologies and environmental assessment. Renewable Energy, 155, 754-769. doi:10.1016/j.renene.2020.03.015
10. Pandey, A., Negi, Y. S., & Singh, V. K. (2020). Recent advances in biowaste conversion to biofuel. Biofuel Research Journal, 7(4), 1375-1386. doi:10.18331/BRJ2020.7.4.1
11. Singh, A., Kalamdhad, A. S., & Kazmi, A. A. (2018). Bioremediation of wastewater using biowaste materials: A review. Environmental Technology & Innovation, 9, 209-230. doi:10.1016/j.eti.2017.12.003
12. Srinivasan, A., & Viraraghavan, T. (2010). Decolourization of dye wastewaters by biosorbents: A review. Journal of Environmental Management, 91(10), 1915-1929. doi:10.1016/j.jenvman.2010.05.013
13. Taiwo, A. M., Kovo, A. S., Olayinka, A., Ademiluyi, J., Olubiyi, I. O., & Oyekunle, D. T. (2019). Comprehensive review on utilization of biowaste for biogas production in Nigeria. Renewable Energy, 134, 689-705. doi:10.1016/j.renene.2018.10.011
14. Wang, L., Li, H., & Li, Z. (2021). Advances in the utilization of biowaste for biochar production: A review. Bioresource Technology Reports, 14, 100646. doi:10.1016/j.biteb.2021.100646
15. Xie, L., Lu, W., Chen, C., Wang, C., & Wang, H. (2018). Utilization of biowaste for sustainable agricultural development: A review. Resources, Conservation and Recycling, 139, 109-120. doi:10.1016/j.resconrec.2018.08.016

ICRTMS-2024
International e-Conference on Recent Trends in Material Science
In Association with International Journal of Scientific Research in Science and Technology
Volume 11 | Issue 9 | Print ISSN: 2395-6011 | Online ISSN: 2395-602X (www.ijsrst.com)

Silver Doped Hydroxyapatite Bioceramic for Enhanced Anti Microbial And Antioxidant Applications

Manoj Junnarkar[1], Mukund Kale[1], Prateek Sawant[1], Mahadev Parekar[1], Meghmala Waghmode[2], Neha N. Patil[2], Ramakant P. Joshi[1], Ravindra U. Mene*[1],

[1] Department of Physics, PDEA's Annasaheb Magar Mahavidyalaya, Pune, Maharashtra, India
[2]Department of Microbiology, PDEA's Annasaheb Magar Mahavidyalaya, Pune, Maharashtra, India
Corresponding Author Email:-*ravimenepdea@gmail.com,

ABSTRACT

In the present investigation, nanostructured bio-ceramic hydroxyapatite (HAp) and silver-doped hydroxyapatite (Ag-HAp) were synthesized by a simple wet chemical precipitation method to explore their antimicrobial activity. The synthesized Ag-HAp was examined for structural, functional, morphological and elemental analysis through XRD, FTIR, SEM and EDS respectively. Pure and Ag modified HAp were used to examine the antimicrobial activity for E. coli, S. aureus, and Pseudomonas. The effect of silver doping concentration was studied on the microbial activity of HAp. Moreover, antioxidant activity was also studied by the DPPH and FRAP assay methods. It is remarkable to note that Ag-HAp (0.15 M) exhibits prominent results for antimicrobial and antioxidant activity.

Keywords: Antimicrobial, Antioxidant, Bioceramic, Hydroxyapatite (HAp), Silver doped Hydroxyapatite

I. INTRODUCTION

In recent years, there has been a growing interest in the utilization of bio-ceramics, particularly synthetic hydroxyapatite [$Ca_{10}(PO_4)_6(OH)_2$] (HAp), as prominent biomaterials for the restoration of damaged tissues and bones [1-2]. The outstanding biocompatibility of hydroxyapatite renders it an ideal choice for applications such as body implants, implant coatings, and prostheses in the field of biomedical engineering [3]. Moreover, hydroxyapatite has found versatile utility as a photocatalyst [4], drug delivery vehicle [5], antibacterial material [6], and in diverse applications such as electronic devices [7] and fertilizers [8]. The synthesis of hydroxyapatite employs various methodologies, including hydrothermal, wet chemical precipitation, microwave-assisted processes & many more [9-11]. Among these, the wet chemical precipitation method stands out as a simple and facile approach, consistently yielding high-quality HAp. This method not only ensures ease of fabrication but also offers an advantageous combination of properties desirable for multifaceted applications in the realm of biomaterials and beyond. However, it lacks inherent antibacterial properties, thereby posing a risk of microbial infection [12]. To address this limitation, various metal ions, including Zn, Mn, Fe, Co, Ag, Cu, Ni, and

Ce, have been doped into HAp to enhance its antibacterial efficacy [13-15]. Among these, silver ions exhibit broad-spectrum antimicrobial properties, demonstrating exceptional antibacterial capabilities [16-17]. Ciobanu et al. studied Ag-HAp with silver doping content of 0,4,5 wt % of Ag for Gram-positive and Gram-negative bacterial strains, irrespective of silver concentration found very good antimicrobial activity [18]. In another study, Predoi et al. identified that if HAp and Ag HAp were mixed with a few popular antibiotics, then their antimicrobial activity would improve tremendously [19]. Stanić et al. demonstrated silver-doped hydroxyapatite has excellent antimicrobial activity for *E. coli, S. aureus,* and *C. albicans*, it also does not show haemolytic activity with less silver ion content [20]. While in another study, Popa et al. studied Ag-HAp (50% silver nitrate and 50% calcium nitrate) with thermal treatment at 600 °C and 1000°C, which provided improved antimicrobial properties for Gram-positive, Gram-negative and fungal microorganisms [21]. Koizhaiganova et al. demonstrated Ag-HAp MIC values against gram-negative bacteria to be 2.09–12.25 μg/ml and against gram-positive bacteria 4.18 – 12.25 μg/ml [22]. While Jadalannagari et al. demonstrated that Ag-HAp(3 wt %) demonstrated excellent antimicrobial activity and hemocompatibility [23]. Moreover, Costescu et al. showed that Ag HAp with a high concentration of 5 mg/mL gives excellent antimicrobial activity against Gram-positive bacteria. [24]. Elbasuney et al. found Ag-HAp antibiofilm at 10.0 μg/mL, which demonstrated the highest percentage antimicrobial activity for *S. aureus* and *C. albicans* of 96.09% and 77.77%, respectively [25]. Wilcock et al. showed that 10 mol% Ag-HAp pastes exhibit excellent antibacterial activity against S. aureus and P. aeruginosa [26]. Iqbal et al. verified that 0.3 Ag HAp demonstrates excellent antimicrobial activity against S. aureus, B. subtilis, P. aeruginosa, and E. coli bacteria [27]. Zhou et al. demonstrated excellent antibacterial activity in *E. coli* and *S. aureus* for Ag-HAp [28]. In summary, the surveyed literature highlights the significant advancements in supplementing hydroxyapatite's antimicrobial attributes through silver ion incorporation. The reviewed studies consistently demonstrate the potential effectiveness of silver-doped hydroxyapatite against various bacterial strains and fungi, emphasizing its broad-spectrum antimicrobial activity. Hence, in the present work, we have synthesized pure and Ag-doped HAp via the wet chemical route. The effect of silver ion concentration in the HAp matrix for antimicrobial activity for *E. coli, S. aureus,* and *Pseudomonas* and antioxidant activity is studied in detail.

II. METHODS AND MATERIAL

A. Chemicals and Reagents

Calcium nitrate tetrahydrate ($Ca(NO_3)_2.4H_2O$), and di-ammonium hydrogen orthophosphate ($(NH_4)_2.HPO_4$) are used as starting precursors as a source of calcium and phosphate (>98% pure, Loba Chemicals), Silver Nitrate ($AgNo_3$) & Ammonia solution (NH_4OH), All the reagents were analytical grade and used as received without any further purifications.

B. Characterization Techniques

The structural, surface morphological and functional group identification of pure and doped HAp are carried out using XRD, SEM, and FTIR. X-ray diffraction pattern is recorded with a Bruker AXS Germany (Model D8 Advanced) having Cu Kα (l = 1.5405 A˚) incident radiation. The XRD peaks are recorded in the 2θ range of 20–60°. The surface morphology and elemental analysis are visualized by means of scanning electron microscope (FE-SEM Hitachi S-4800). The functional group determination is carried out using Shimadzu make FTIR spectroscopy in the frequency range 400–4000 cm^{-1}.

Antimicrobial activity is studied using well-diffusion method and antioxidant activity by the DPPH and FRAP assay methods.

C. Synthesis of Pure hydroxyapatite (HAp)

Wet chemical precipitation method was used to synthesize pure hydroxyapatite as mention earlier literature [2]. Calcium nitrate tetrahydrate ($Ca(NO_3).4H_2O$) and di-ammonium hydrogen orthophosphate ($(NH_4)_2.HPO_4$) were used as starting precursors. The molar concentrations of calcium and phosphorus was adjusted to have a theoretical Ca/P ratio of 1.67. The precipitation process was carried out by drop-wise addition of 0.6 M of di-ammonium hydrogen orthophosphate to 1 M of calcium nitrate tetrahydrate solution. The liquor ammonia was used to adjust the pH-10 of the reaction mixture. The process was carried out under continuous stirring at 100 ^oC for 3 hours, followed by aging for about 24 hours. The white precipitate was washed 3-4 times with double distilled water and dried in an air oven at 100 ^oC for overnight & crushed in agar mortar. Furthermore, synthesized hydroxyapatite powder was sintered in a muffle furnace at 800^oC for two hours.

D. Synthesis of Silver Doped Hydroxyapatite

For Silver-Doped hydroxyapatite, 0.05M, 0.1M and 0.15M solution of silver nitrate ($AgNo_3$) was made in 50 ml double distilled water & 1gm of hydroxyapatite (HAp) dissolved in it. These three conical flasks were kept for the ionization process for 6 hours at room temperature. This solution was filtered and dried at 100^0C in oven for 3 hours.

E. Antimicrobial Activity

The antimicrobial activity of the silver-Doped hydroxyapatite was tested against pathogenic microorganisms viz., *Escherichia coli* (NCIM 2256), *Staphylococcus aureus* (NCIM 2901) and *Pseudomonas aeruginosa* (NCIM 2200) the well-diffusion method [29]. In this assay, the Mueller Hinton Agar medium plates were spread evenly with 100 µL of an overnight log culture of test organisms (10^9cells/ ml). Wells were made on the MHA plates by using a gel puncture. Nano mixtures were dissolved in sterile deionized water to get the concentrations of 10, 100 and 1000 µg/ml. Next, 100 µL of the biosynthesized silver nanoparticle reaction mixture was added into each of the four wells, and the plates were kept at 4 ^oC for 2 hours to allow perfusion of the nanoparticles. Then plates were incubated at 37 °C for 24 h. After incubation, the susceptibility pattern of the test organisms was determined by measuring the diameter of the zone of inhibition of each well.

F. Antioxidant Activity

Ferric reducing ability assay (FRAP) and DPPH (1, 1-Diphenyl-2-picrylhydrazyl) radical scavenging activity assay

Antioxidant activity of pure HAp and Ag-HAp was tested using ferric reducing ability FRAP and DPPH assay [30,31]. To 0.2 mL of sample, 3.8 mL of FRAP reagent was added. The mixture was incubated for 30 minute at room temperature in the dark and the absorbance was measured at 593 nm.

The scavenging effect of the samples were determined using DPPH radical scavenging activity assay. To 0.5 mL of nanoparticle solution, 5mL of freshly prepared DPPH solution (0.2 mM) was added. The mixture was vigorously shaken and kept for 30 minute in the dark at room temperature. The control tubes contained deionized water. The DPPH scavenging activity was monitored by determining the absorbance at 517 nm [30].

The percent inhibition of activity was calculated as [(Ab Ctr- Ab Sam)/ Ab Ctr] * 100

(Ab Ctr = Absorbance of control;

Ab Sam = Absorbance of sample).

III.RESULTS AND DISCUSSION

A. X-Ray Diffraction Studies

Fig. 1 shows the XRD plots of Pure HAp and variation of intensity of diffracted X-rays as a function of 2θ value in the range of 20°-60° for pure HAp.

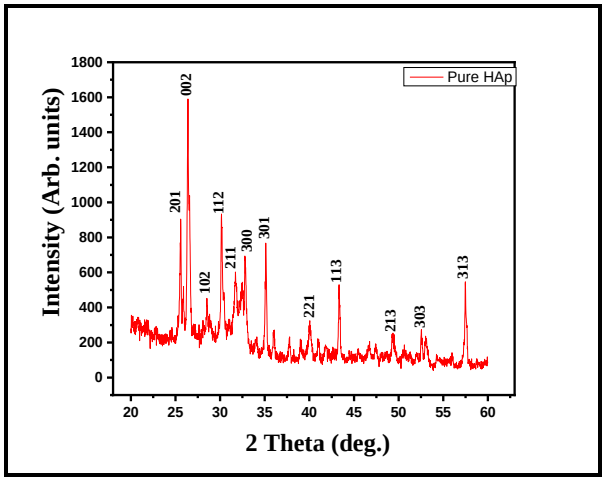

Fig.1: X-Ray diffraction patterns of Pure HAp

The XRD phase identification is performed by using JCPDS standard XRD card (09-432) for hydroxyapatite. The presence of all characteristics HAp peaks at 2θ value 25.6°, 26.4°, 28.5°, 30.1°, 31.7°, 32.7°, 35.1°, 36.1°, 40.1°, 43.3°, 49.3°, 52.5°, 57.5 °, confirm the crystalline hexagonal phase of HAp. The average crystallite size for pure HAp is calculated by using Debye–Scherrer formula [1] and it is found to be 32 nm.

B. Scanning Electron Microscopy

Fig. 2 (a-b) shows the FE-SEM image of Pure and Ag-Hap (0.15M) samples. It exhibits the spherical grain morphology with agglomeration of smaller particles. The presence of smaller grains with a uniform size (30-60 nm) covering whole surface along with microporous structure is observed. Fig 2 (c) illustrates the Elemental analysis of silver doped hydroxyapatite to confirm the occurrence of any impurity which may get incorporated while synthesis of material. EDS Spectra mainly constitute Calcium and phosphate groups. Moreover, the silver existence (1.56%) shows the replacing of calcium ions.

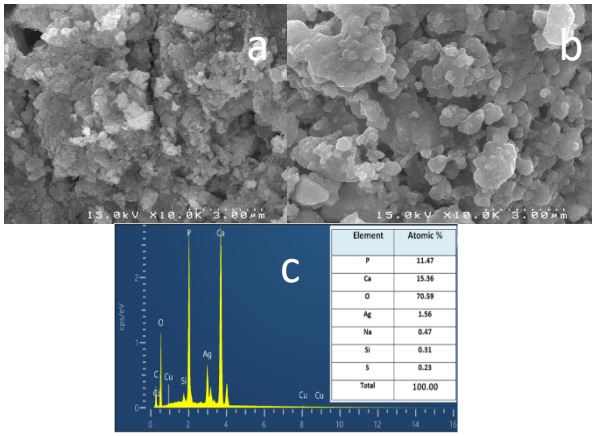

Fig 2: FE-SEM image of the synthesized (a) Pure HAp (b) doped Ag-HAp (0.15M) and (c) EDS of Ag-HAp (0.15M)

C. Fourier-transform infrared spectroscopy (FTIR)

Fig. 3 shows the FTIR spectrum of pure and Ag doped HAp carried out in the wave number range 4000 and 400 cm^{-1}. The FTIR spectra of all samples showed bands corresponding to HAp structure. The HAp spectrum confirms the characteristic bands of absorbed water, hydroxyl and phosphate species. The absorption peaks attributed to hydroxyl liberation mode are found at 721 cm^{-1}. The bands appearing at 963 cm^{-1} and 926 cm^{-1} correspond to anti symmetric bending motion of the PO_4^{3-} groups and the peaks in the range 1090–1030 cm^{-1} are ascribed to v_3 stretching modes in PO_4^{3-} group [3-4]. The study reveals that the FTIR spectra showed all bands corresponding to pure HAp structure also shows 0.05M, 0.1M and 0.15M Silver Doped HAp.

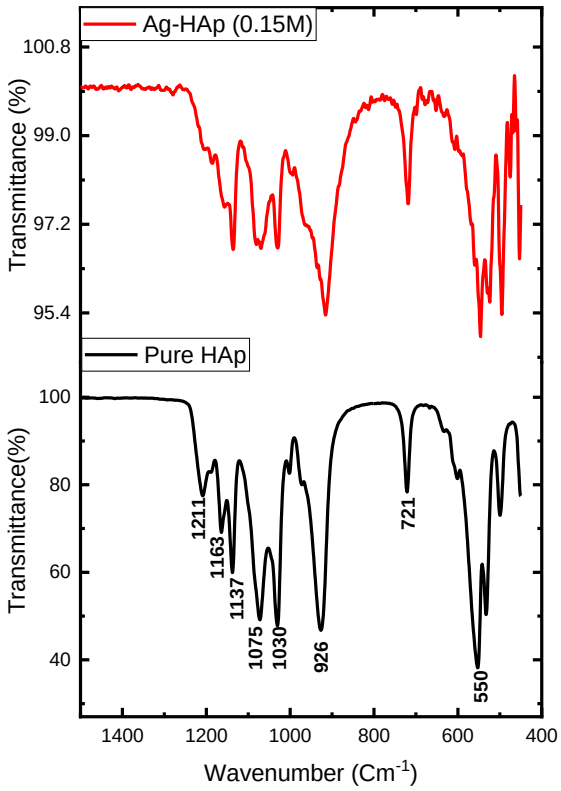

Fig.3: Fourier-transform infrared spectroscopy (FTIR) of Pure HAp, and Ag-HAp (0.15M)

D.Antimicrobial Activity

The antimicrobial activity of the silver doped HAp against pathogenic microorganisms such as *E. coli, S. aureus,* and *Pseudomonas aeruginosa* was measured on Muller- Hinton agar (MHA) plates using the well-diffusion method. The observed results are given in table 1 and graphical presentation in Fig. 4

Pathogens	Pure HAp (100 µg/ml)	Pure HAp (1000 µg/ml)	0.05 Ag-Hap (100 µg/ml)	0.05 Ag-Hap (1000 µg/ml)	0.10 Ag-Hap (100 µg/ml)	0.10 Ag-Hap (1000 µg/ml)	0.15 Ag-Hap (100 µg/ml)	0.15 Ag-Hap (1000 µg/ml)
E.coli (NCIM 2256)	ND	ND	4mm	6 mm	ND	4mm	20 mm	21 mm
S.aureus (NCIM 2901)	ND	ND	ND	ND	ND	ND	ND	ND
P.aeruginosa (NCIM 2200)	ND	ND	6 mm	8 mm	6 mm	8 mm	7 mm	9 mm

(ND: Not detected)

Table 1 Antimicrobial activity using well diffusion method

Silver doped hydroxyapatite found to have moderate inhibitory activity against Gram negative bacterial pathogens as compared to Gram positive bacteria *Staphylococcus aureus*. The data suggested that the antimicrobial activity is attributed to the silver metal content.

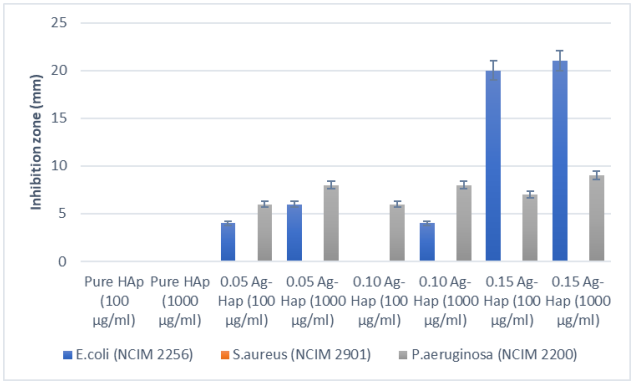

Fig 4 Antimicrobial Activity (in mm) of HAp and Ag HAp

E. Antioxidant Activity

Fig. 5 Shows the antioxidant activity using DPPH and FRAP assay. It was found that the antioxidant activity of nano-bioceramic hydroxyapatite get reduced with an increase in the silver concentration. As compared to the free radical scavenging potential, these nano mixtures have lower Fe reducing ability.

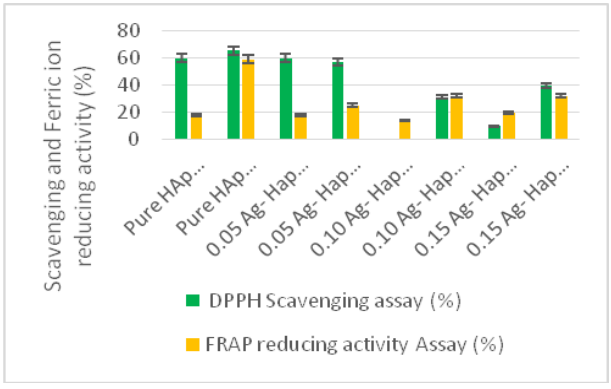

Fig.5 Antioxidant activity using DPPH and FRAP assay

As per the published literature, antioxidant potential of the nanocomposites depends upon the organic or inorganic contents [32].

IV. CONCLUSION

In the present work, nano-bioceramic hydroxyapatite was synthesized by using a simple wet chemical precipitation method. Moreover, the ion exchange process is successfully utilized to prepare silver-doped hydroxyapatite material. The formation of the hexagonal HAp phase is identified by XRD analysis, and the average crystallite size is calculated using the Debye–Scherrer method and is found to be 32 nm. Also, EDS analysis confirms the existence of silver ions in Ag-HAp. As silver doping percentage increases in hydroxyapatite, it exhibits better antimicrobial activities and provides good antioxidant activities, which is verified by the DPPH assay and the FRAP assay. For *E.coli* 20-21 mm and for *P.aeruginosa* 7-9 mm, antimicrobial activity inhibition was observed. However, Antimicrobial activity of *S. aureus* is null.

V. REFERENCES

[1] Kalaiselvi, V., Mathammal, R., & Anitha, P. (2017). Sol-gel mediated synthesis of pure hydroxyapatite at different temperatures and silver substituted hydroxyapatite for biomedical applications. J. Biotechnol. Biomater, 7(4), 275.

[2] Riaz, M., Zia, R., Ijaz, A., Hussain, T., Mohsin, M., & Malik, A. (2018). Synthesis of monophasic Ag doped hydroxyapatite and evaluation of antibacterial activity. Materials Science and Engineering: C, 90, 308-313.

[3] Iconaru, S. L., Chapon, P., Le Coustumer, P., & Predoi, D. (2014). Antimicrobial activity of thin solid films of silver doped hydroxyapatite prepared by sol-gel method. The Scientific World Journal, 2014.

[4] Jejurikar, S. M., Dadge, J. W., Bogle, K. A., Narwade, V. N., Halge, D. I., MUDULI, S., ... & Mahabole, M. P. (2020). Remarkable photocatalytic degradation of Remazol Brilliant Blue R dye using bio-photocatalyst'nano-hydroxyapatite'.

[5] Safi, S., Karimzadeh, F., & Labbaf, S. (2018). Mesoporous and hollow hydroxyapatite nanostructured particles as a drug delivery vehicle for the local release of ibuprofen. Materials Science and Engineering: C, 92, 712-719.

[6] Andrade, F. A. C., de Oliveira Vercik, L. C., Monteiro, F. J., & da Silva Rigo, E. C. (2016). Preparation, characterization and antibacterial properties of silver nanoparticles–hydroxyapatite composites by a simple and eco-friendly method. Ceramics international, 42(2), 2271-2280.

[7] Adamiano, A., Sangiorgi, N., Sprio, S., Ruffini, A., Sandri, M., Sanson, A., ... & Tampieri, A. (2017). Biomineralization of a titanium-modified hydroxyapatite semiconductor on conductive wool fibers. Journal of Materials Chemistry B, 5(36), 7608-7621.

[8] Azima, A., Siti Habibah, M. W., Nur Sabrina, W., Salmah, A. A., & Zamri, I. (2016). Synthesis of hydroxyapatite (HA) for the development of slow release fertilizer. Role of Plant Physiology, 144.

[9] Sivaperumal, V. R., Mani, R., Nachiappan, M. S., & Arumugam, K. (2017). Direct hydrothermal synthesis of hydroxyapatite/alumina nanocomposite. Materials characterization, 134, 416-421.

[10] Cahyaningrum, S. E., Herdyastuty, N., Devina, B., & Supangat, D. (2018, January). Synthesis and characterization of hydroxyapatite powder by wet precipitation method. In IOP Conference Series: Materials Science and Engineering (Vol. 299, p. 012039). IOP Publishing.

[11] Hassan, M. N., Mahmoud, M. M., Abd El-Fattah, A., & Kandil, S. (2016). Microwave-assisted preparation of Nano-hydroxyapatite for bone substitutes. Ceramics International, 42(3), 3725-3744.

[12] Baskar, K., Anusuya, T., & Venkatasubbu, G. D. (2017). Mechanistic investigation on microbial toxicity of nano hydroxyapatite on implant associated pathogens. Materials Science and Engineering: C, 73, 8-14.

[13] Robles-Águila, M. J., Reyes-Avendaño, J. A., & Mendoza, M. E. (2017). Structural analysis of metal-doped (Mn, Fe, Co, Ni, Cu, Zn) calcium hydroxyapatite synthetized by a sol-gel microwave-assisted method. Ceramics International, 43(15), 12705-12709.

[14] Bostancioglu, R. B., Gurbuz, M., Akyurekli, A. G., Dogan, A., Koparal, A. S., & Koparal, A. T. (2017). Adhesion profile and differentiation capacity of human adipose tissue derived mesenchymal stem cells grown on metal ion (Zn, Ag and Cu) doped hydroxyapatite nano-coated surfaces. Colloids and Surfaces B: Biointerfaces, 155, 415-428.

[15] Yuan, Q., Qin, C., Wu, J., Xu, A., Zhang, Z., Liao, J., ... & Zhang, P. (2016). Synthesis and characterization of Cerium-doped hydroxyapatite/polylactic acid composite coatings on metal substrates. Materials Chemistry and Physics, 182, 365-371.

[16] Tang, S., & Zheng, J. (2018). Antibacterial activity of silver nanoparticles: structural effects. Advanced healthcare materials, 7(13), 1701503.

[17] Li, W. R., Sun, T. L., Zhou, S. L., Ma, Y. K., Shi, Q. S., Xie, X. B., & Huang, X. M. (2017). A comparative analysis of antibacterial activity, dynamics, and effects of silver ions and silver nanoparticles against four bacterial strains. International Biodeterioration & Biodegradation, 123, 304-310.

[18] Ciobanu, C. S., Iconaru, S. L., Le Coustumer, P., & Predoi, D. (2013). Vibrational investigations of silver-doped hydroxyapatite with antibacterial properties. Journal of Spectroscopy, 2013.

[19] Predoi, D., Popa, C. L., Chapon, P., Groza, A., & Iconaru, S. L. (2016). Evaluation of the antimicrobial activity of different antibiotics enhanced with silver-doped hydroxyapatite thin films. Materials, 9(9), 778.

[20] Stanić, V., Janaćković, D., Dimitrijević, S., Tanasković, S. B., Mitrić, M., Pavlović, M. S., ... & Raičević, S. (2011). Synthesis of antimicrobial monophase silver-doped hydroxyapatite nanopowders for bone tissue engineering. Applied Surface Science, 257(9), 4510-4518.

[21] Popa, C. L., Ciobanu, C. S., Voicu, G., Vasile, E., Chifiriuc, M. C., Iconaru, S. L., & Predoi, D. (2015). Influence of thermal treatment on the antimicrobial activity of silver-doped biological apatite. Nanoscale Research Letters, 10, 1-10.

[22] Koizhaiganova, M., Yaşa, I., & Gülümser, G. (2016). Characterization and antimicrobial activity of silver doped hydroxyapatite obtained by the microwave method. Medziagotyra.

[23] Jadalannagari, S., Deshmukh, K., Ramanan, S. R., & Kowshik, M. (2014). Antimicrobial activity of hemocompatible silver doped hydroxyapatite nanoparticles synthesized by modified sol–gel technique. Applied Nanoscience, 4, 133-141.

[24] Costescu, A., Ciobanu, C. S., Iconaru, S. L., Ghita, R. V., Chifiriuc, C. M., Marutescu, L. G., & Predoi, D. (2013). Fabrication, characterization, and antimicrobial activity, evaluation of low silver concentrations in silver-doped hydroxyapatite nanoparticles. Journal of Nanomaterials, 2013, 5-5.

[25] Elbasuney, S., El-Sayyad, G. S., Radwan, S. M., & Correa-Duarte, M. A. (2022). Antimicrobial, and antibiofilm activities of silver doped hydroxyapatite: a novel bioceramic material for dental filling. Journal of Inorganic and Organometallic Polymers and Materials, 32(12), 4559-4575.

[26] Wilcock, C. J., Stafford, G. P., Miller, C. A., Ryabenkova, Y., Fatima, M., Gentile, P., ... & Hatton, P. V. (2017). Preparation and antibacterial properties of silver-doped nanoscale hydroxyapatite pastes for bone repair and augmentation. Journal of Biomedical Nanotechnology, 13(9), 1168-1176.

[27] Iqbal, N., Kadir, M. R. A., Malek, N. A. N. N., Mahmood, N. H., Murali, M. R., & Kamarul, T. (2012). Rapid microwave assisted synthesis and characterization of nanosized silver-doped hydroxyapatite with antibacterial properties. Materials letters, 89, 118-122.

[28] Zhou, Q., Wang, T., Wang, C., Wang, Z., Yang, Y., Li, P., ... & Nie, L. (2020). Synthesis and characterization of silver nanoparticles-doped hydroxyapatite/alginate microparticles with promising cytocompatibility and antibacterial properties. Colloids and Surfaces A: Physicochemical and Engineering Aspects, 585, 124081.

[29] Narayanan, P. M., Wilson, W. S., Abraham, A. T., & Sevanan, M. (2012). Synthesis, characterization, and antimicrobial activity of zinc oxide nanoparticles against human pathogens. BioNanoScience, 2, 329-335.

[30] Salari, S., Bahabadi, S. E., Samzadeh-Kermani, A., & Yosefzaei, F. (2019). In-vitro evaluation of antioxidant and antibacterial potential of greensynthesized silver nanoparticles using Prosopis farcta fruit extract. Iranian journal of pharmaceutical research: IJPR, 18(1), 430.

[31] Gecer, E. N. (2021). Green synthesis of silver nanoparticles from Salvia aethiopis L. and their antioxidant activity. Journal of Inorganic and Organometallic Polymers and Materials, 31(11), 4402-4409.

[32] Zare, E. N., &Lakouraj, M. M. (2014). Biodegradable polyaniline/dextrin conductive nanocomposites: synthesis, characterization, and study of antioxidant activity and sorption of heavy metal ions. Iranian Polymer Journal, 23, 257-266.

ICRTMS-2024
International e-Conference on Recent Trends in Material Science
In Association with International Journal of Scientific Research in Science and Technology
Volume 11 | Issue 9 | Print ISSN: 2395-6011 | Online ISSN: 2395-602X (www.ijsrst.com)

Impact of Solvent on Cobalt Ferrite: Structural, Morphological, Optical and Electrical Properties

Nandkumar D.Veer[1], Sopan M.Rathod[2], Ramesh B. Bhise[3]
[1]Research Scholar, Department of Physics, PDEA's Annasaheb Magar Mahavidyalay Hadapsar, Pune-411028, MS, India
[2]Department of Physics, MES Abasaheb Garware College Pune-411004, MS, India.
[3]Department of Physics, Hon. Balasaheb Jadhav Arts, Commerce and Science College Ale, Pune-412411, MS, India

ABSTRACT

Synthesis and characterization of Cobalt ferrite powders by a sol-gel combustion process is focused in the present work. The prepared precursors were calcined at 560 °C for 5 hours in order to get cobalt ferrite powder. The effect of solvents (Aloevera extract, Distilled water, Egg white solution, Neem extract) on $CoFe_2O_4$ and its structural, morphological, optical and electrical, properties was investigated. XRD is used to determine the crystalline size and it calculated by Debye Scherer formula which is varies from 29.94 nm to 72.7 nm with different solvent (Aloevera, Distilled water, Egg white, Neem extract) of lattice parameter ranging from 8.31 to 8.38 A^0 respectively confirmed the formation of single phase cubic spinel structure $CoFe_2O_4$. EDX measurements for $CoFe_2O_4$ NPs which indicate, the grown NPs are homogeneous and uniform. The morphology of prepared $CoFe_2O_4$ ferrite samples with various solvents (Aloevera extract, Distilled water, Egg white solution, Neem extract) was studied using a scanning electron microscopy. The band gap energy is varies from 1.5 to 1.7 eV. The band gap energy was studied using UV-Visible Spectroscopy. The optical characterization on $CoFe_2O_4$ ferrite samples were carried out using the Fourier Transform Infrared Spectroscopy (FT-IR) techniques. The formation of the ferrite is confirmed by FT-IR results. Dielectric Properties were studied for various samples, the dielectrics and AC conductivity of samples is decreases with increasing frequency of LCR-Q meter of samples with various solvents.

Keywords: Cobalt ferrite, XRD, EDX, SEM, FT-IR, UV-VISIBLE, Dielectric Properties

I. INTRODUCTION

Ferrites are electrically insulating material and have good electrical, magnetic and mechanical properties. Among the different types of ferrites, the $CoFe_2O_4$ spinel ferrite is one of the most versatile from the view point of their large number of potential applications. $CoFe_2O_4$ ferrite possesses large crystalline anisotropy and reasonable magnetization, as potential predominant magnetic and electrical resistive material, which has been applied in high density magnetic recording media, high performance electromagnetic and spintronic devices [1, 2]. Spinel $CoFe_2O_4$ has Face Centered Cubic (FCC) structure with a large unit cell. There are two kinds of lattice for cation occupancy.

Mainly two sites A (tetrahedral) and B (octahedral). In a normal spinel structure Co^{2+} occupying tetrahedral A sites, while Fe^{3+} is sitting on the octahedral B sites. In inverse spinel structure A site being Fe^{3+} ions while B sites populated by Co^{2+} and Fe^{3+} ions.

Ferrite can be prepared by using various experimental techniques like ceramic, hot spraying, evaporation condensation, matrix isolation, laser-induced vapour phase reactions and aerosols but most types of Nano-particles prepared by these methods gives broad particle size distribution and coarse particles so additional milling is required. Other chemical methods are co-precipitation, sol-gel, ball milling, citrate precursor, hydrothermal, micro emulsion [3-11]. Among above mentioned methods, a sol-gel process is less complicated and inexpensive method than the others.

In present work we focused on the synthesis and properties of cobalt ferrite powders prepared by a sol-gel autocombustion technique. This is unique combination of the chemical sol-gel process and the combustion process based on the gelling and subsequent combustion of an aqueous solution containing salts of desired metals and some organic fuel giving rise to porous fluffy product with large surface area. The effect of different solvents on structural, electrical, optical, morphological properties of prepared cobalt ferrite particles has been investigated.

1. Materials and Methods

2.1 Experimental Procedure:

A sol-gel autocombustion method is used to prepare $CoFe_2O_4$ particles with different solvents (Aloevera extract, Distilled water, Egg white solution, Neem extract).Starting materials are Cobalt (II) nitrate ($Co(No_3)_2$. $6H_2O$, Mw = 291.04 g/mol.), Iron nitrate ($Fe(No_3)_3$. $9H_2O$, Mw = 404.00 g/mol.) and Citric acid ($C_6H_8O_7{\cdot}H_2O$, Mw = 210.14 g/mol.). An aqueous solution of citric acid was mixed with metal nitrates and different solvents under vigorous stirring. To adjust pH of 7.0, the ammonia solution was slowly added in mixture. The solution was heated on hot plate at 80 °C to evaporate the water. During evaporation, the solution become viscous and finally formed a gel and by continuous heating the gel is ignited, the combustion rapidly propagated forward until all the gel burnt out completely to form ash and porous product was obtained. The ash-burnt obtained powder was calcined at 560 °C for 5 hours to get final product of cobalt ferrite powder.

2.2 Characterization:

The structural characterization on $CoFe_2O_4$ ferrite samples with different solvents (Aloevera extract, Distilled water, Egg white solution, Neem extract) were carried out using XRD to determine the crystalline size and it calculated by Debye Scherer formula which is varies from 29.94 nm to 72.7 nm with different solvent, The Fourier Transform Infrared Spectroscopy (FT-IR). Morphology of prepared $CoFe_2O_4$ powder samples were studied using a scanning electron microscopy. Band gap energy was studied using UV-Visible spectroscopy; Electrical properties were studied using Dielectric characterization.

2. Results and Discussion

3.1 Structural Properties:

(i) X- Ray diffraction study (XRD):

The structural property of samples is studied by taking X-ray diffraction (XRD) shown in figure 1. XRD pattern of the samples is recorded with Cu-kα radiation at room temperature at λ=1.54182 A^0. The crystallite size is calculated using formula of Debye-Scherrer [12].

$$t = \frac{0.9\lambda}{\beta\cos\theta} \text{---------- (1)}$$

Where,

β = Full width half maxima

λ = Wavelength of X-ray

θ = Angle of diffraction

t = Crystallite size

The crystallite size was increasing from 29.94 nm to 72.11 nm calculated using equation 1.

The values of lattice constant 'a' of $CoFe_2O_4$ samples were obtained from the analysis of X-ray data by formula, shown in table 4.

$a = d\sqrt{h^2 + k^2 + l^2}$ ---------- (2)

Where,

h k l = Miller indices

d = Interplaner distance.

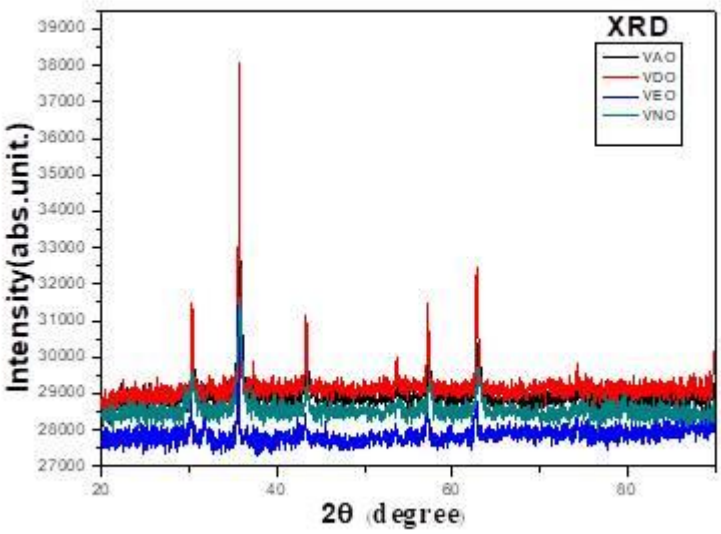

Figure1. XRD of samples of $CoFe_2O_4$ Samples a) Alovera extract, b) Distilled water c) Egg white solution d) Neem extract

			X -ray density d_x			Bulk density d_b		
Sample		M	8M	a	dx	V	db	%Porosity
VAO	8	234.619	1876.952	**8.3329**	**5.39198**	0.373163	3.188957	40.85741
VDO	8	234.619	1876.952	**8.3500**	**5.352798**	0.266659	4.875136	8.923604
VEO	8	234.619	1876.952	**8.3800**	**5.295516**	0.388378	3.707732	29.98355
VNO	8	234.619	1876.952	**8.3100**	**5.430468**	0.4116	3.012633	44.52352

Table1. Crystallite size and Lattice constant of Samples $CoFe_2O_4$ a) Alovera extract, b) Distilled water c) Egg white solution d) Neem extract

(ii) EDX properties and elemental mapping images:

The EDX measurements for $CoFe_2O_4$ NPs which indicate, the grown NPs are stoichiometric and homogeneous with a uniform distribution. For CFO NPs, the EDX micrographs confirmed the existence of Fe, Co and O without the presence of any signature of substituted metals. The EDX analysis for $CoFe_2O_4$ NPs confirmed that impurity elements were found in the some solution of synthesized samples [13].

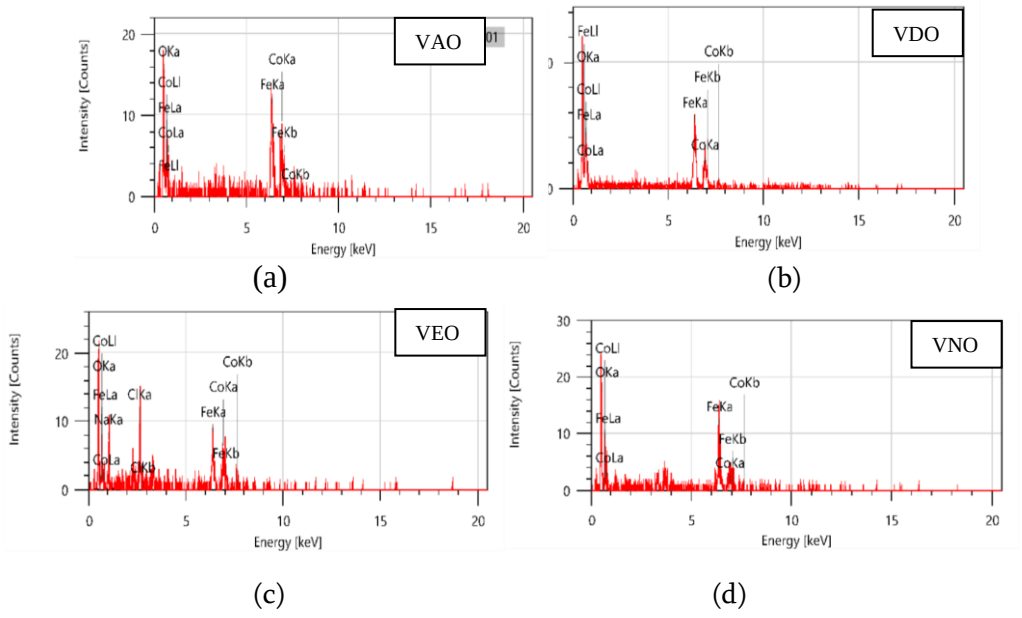

Figure 2. EDX measurement graphs of $CoFe_2O_4$ powders for different solvents (a) Aloevera extract, (b) Distilled water, (c) Egg white solution and (d) Neem extract.

(iii) Morphological Properties:

Micrographs were recorded on a LEO SEM model no. S - 440i. The SEM images of all $CoFe_2O_4$ ferrite samples are shown in figure 3 (a-d). It is clear from Fig. 3 (a-d) that grown $CoFe_2O_4$ particles are well developed; having non-uniform morphology with the individual particles are typically in nanometer size but there is agglomeration of particles. It is well known that the magnetic inter-particle interaction is

dominant between larger magnetic particles due to the magnetic attractive force. There is the magnetic attractive force among non-uniform coarse crystals lead to the formation of agglomeration. We conclude from SEM analysis that non-uniform morphology and grown $CoFe_2O_4$ particles have agglomeration due to magnetic force.

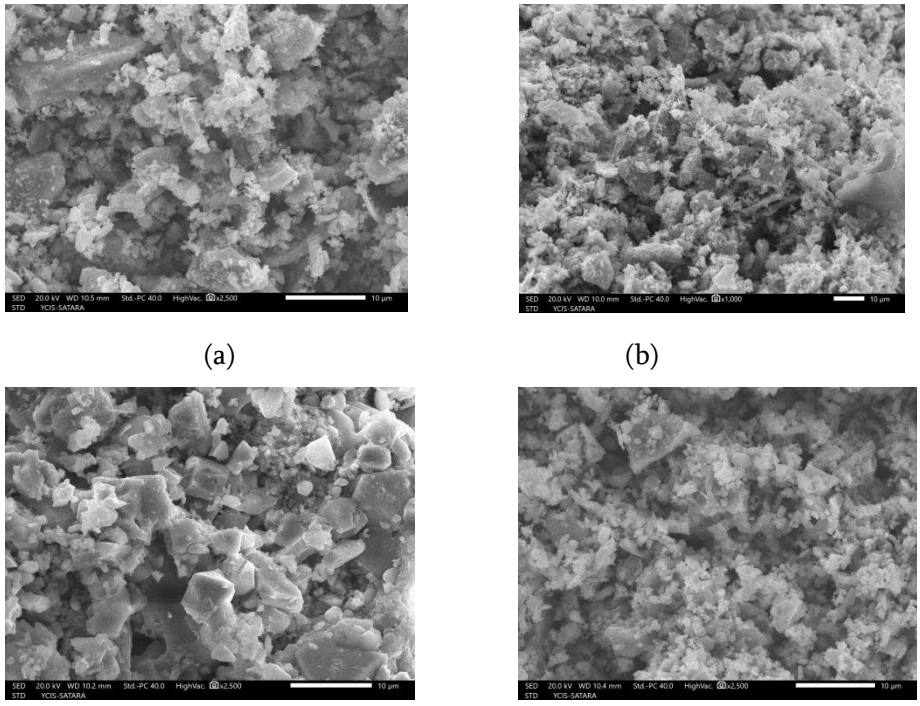

(a) (b)

(c) (d)

Figure 3. SEM micrographs of $CoFe_2O_4$ powders sintered at 560 °C for 5 hrs for different solvents (a) Aloevera extract, (b) Distilled water, (c) Egg white solution and (d) Neem extract.

3.2 Optical Properties

(i) FT-IR Characteristics:

Infrared absorption spectra (FT-IR) of calcined $CoFe_2O_4$ powders with different solvents (Aloevera extract, Distilled water, Egg white solution, Neem extract) were recorded on a Bruker Tensor 27 spectrometer in wave number range of 400-4500 cm^{-1}. FT-IR spectra of all samples are shown in figure 4

The existence of strong absorption bands around 528 cm^{-1} and 560 cm^{-1} are due to stretching of metal oxygen (M-O), which attributed to the formation of the ferrite phase [14].

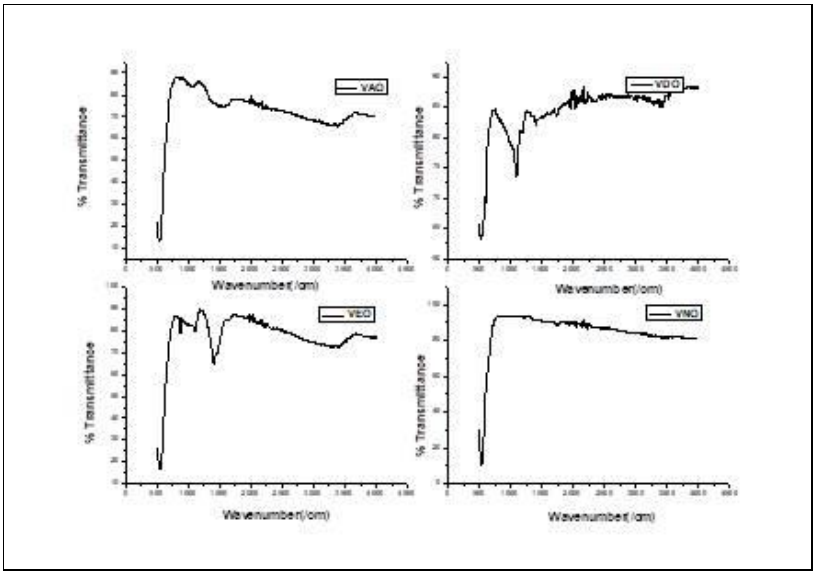

Figure 4- FT-IR spectra of $CoFe_2O_4$ powders calcined at 560 ºC

for 5 hours in air atmosphere.

(ii) UV-Visible Spectroscopy:

The optical property of the $CoFe_2O_4$ with different solvents was observed by taking UV-Vis absorption spectroscopy shown in figure 5 and figure 6 The values of λ_{max} vary from 746.55 to 850.50 nm with variation in solvents. On the basis of absorption peaks, the band gap of samples were calculated from formula [15],

$$E = \frac{hc}{\lambda} \text{ ---------- (3)}$$

Where,

λ = maximum value of wavelength or Absorption peak value

h = 6.6261×10^{-34} m^2 kg / s or 6.626×10^{-34} Joule sec.

c = velocity of light = 3×10^8 m/s,

And E = absorbed energy in an electronic transition

The impurity bands created due to the formation of level of impurity inside

an energy gap.

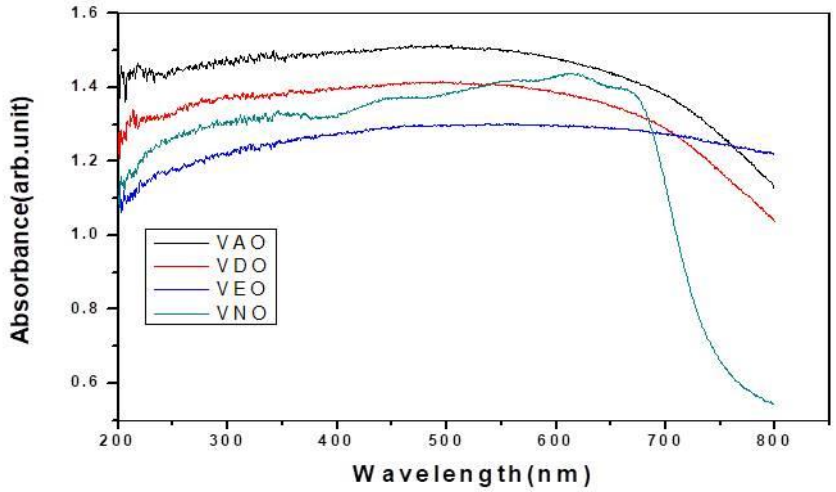

Figure 5-UV-Visible Spectra of $CoFe_2O_4$ for different solvents

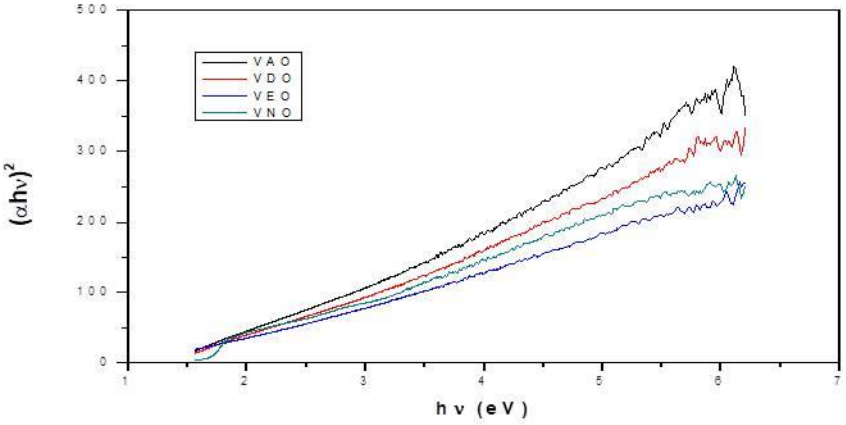

Figure 6- Tauc plot of $CoFe_2O_4$ for different solvents

3.3 Electrical Properties:

The study of the dielectric constant was studied using Maxwell-Wagner type of interfacial of polarization and Koop's theory [16].The electron displacement in direction of applied field causes interaction in between ions i.e. Fe^{2+} and Fe^{3+}. Variation in thickness of pellet is done due to exchange in electron $Fe^{2+} \leftrightarrow Fe^{3+}$ with alternating variation in electric field with variation in polarization, oxygen vacancies, defects in grain boundary, interfacial dislocation. The dispersion relation observed using dielectric constant with frequency variation shown in figure 2, exhibits inverse relation between in dielectric constant and frequency. The decreasing of dielectric constant and dielectric loss with increasing frequency is shown from figure 7 and figure 8 figure 9 gives the information of AC conductivity of $CoFe_2O_4$ that increasing with frequency linearly due to conduction by electron exchange between ions of same element with different valencies.

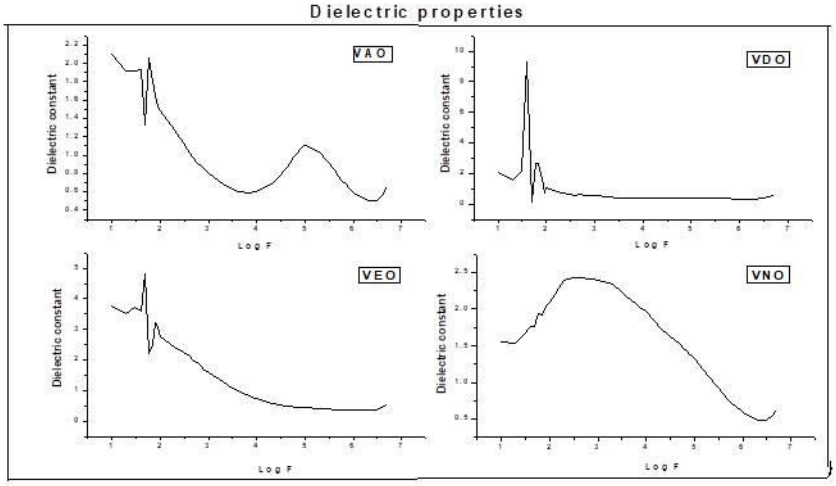

Figure 7-Dielectric constant variance with frequency for $CoFe_2O_4$ with different solvents

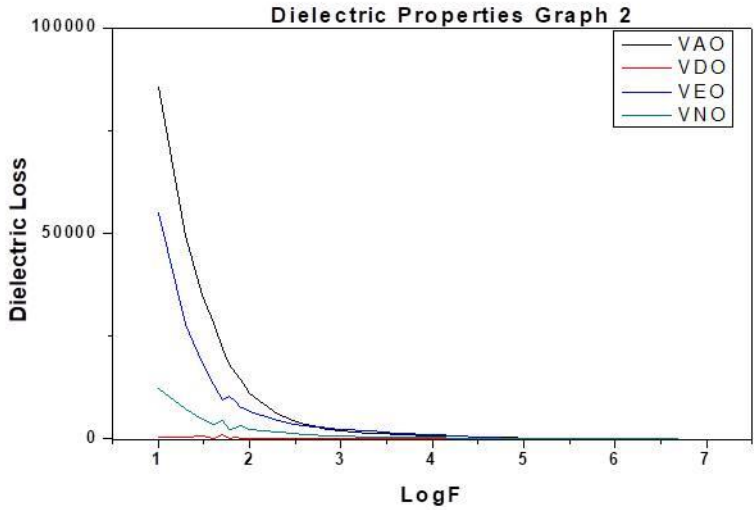

Figure 8- Dielectric loss variance with frequency for $CoFe_2O_4$ with different solvents

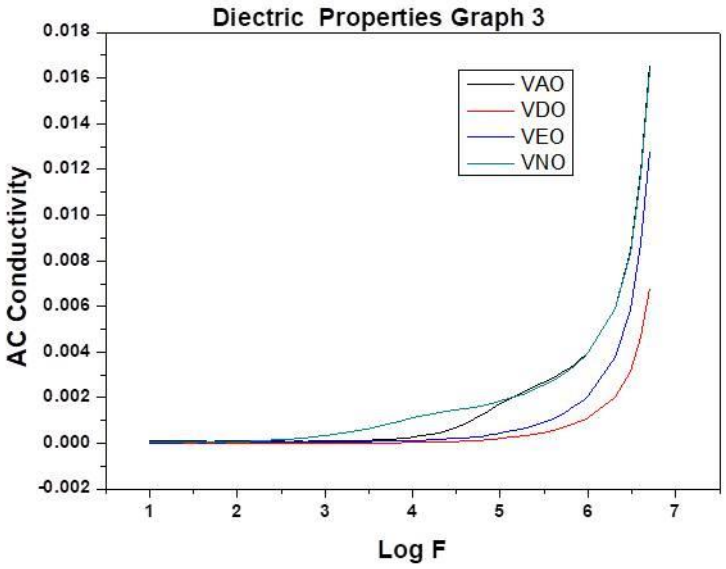

Figure 9- AC conductivity variance with frequency for $CoFe_2O_4$ with different solvents.

3. Conclusions

Spinel ferrite $CoFe_2O_4$ powders with different solvents (Aloevera extract, Distilled water, Egg white solution, Neem extract) were successfully synthesized using a sol-gel auto combustion method. Experiments results of XRD, EDX,SEM, FTIR, UV-Visible Spectroscopy and Dielectric Properties summarized as follows:

(i) XRD to determine the crystalline size and it calculated by Debye Scherer formula which is varies from 29.94 nm to 72.7 nm with different solvent.

(ii) EDX measurements for $CoFe_2O_4$ NPs which indicate, the grown NPs are stoichiometric and homogeneous with a uniform distribution.

(iii) SEM micrographs show non-uniform morphology and grown $CoFe_2O_4$ particles have agglomeration due to magnetic force.

(iv) FT-IR results confirm the formation of the ferrite.

(v) The band gap energy of the cobalt ferrite for different samples obtained from UV-Vis spectra varies for different solvents.

(vi) The dielectric constant and loss tangent decreases with frequency value and increasing conductivity, measured as a function of frequency by using L.C.R.-Q meter in frequency range 100 Hz to 5 MHz with accuracy 0.001 Hz.

Acknowledgments

1) The XRD characterisation was done in C.T. Bora college Shirur, Pune.
2) The SEM and EDX characterisation was done in Yashvantrao Chavan Institute of Science Satara.
3) The FT-IR and UV-Visible spectroscopy characterization was done in B.R. Gholap college Sangavi,Pune.
4) The Dielectric characterization was done in Swami Ramanand Teerth Marathwada University,Nanded.
5) The Synthesis of cobalt ferrite was done from Anantrao Thopte college Bhor, Pune.

References

1) Whitney, T. M. Searson, P. C. Jiang, J. S. Chien, C. L. "Fabrication and Magnetic Properties of Arrays of Metallic Nanowires".261(1993) P.1316–1319.
2) Versluijs J. J. Bari, M. A. Coey, "Magneto resistance of Half-Metallic Oxide Nano contacts". Physical Review Letters, 87(2001),P.026601.
3) Albuquerque, Adriana S. Ardisson, José D. Macedo, Waldemar A. A.; Alves, Maria C. M. "Nanosized powders of NiZn ferrite: Synthesis, structure, and magnetism". Journal of Applied Physics, 87(2000), P.4352.
4) Rajesh Iyer, Rucha Desai, R. V. Upadhyay "Low temperature synthesis of nanosized Mn1–xZnxFe2O4ferrites and their characterizations". 32(2009), P.141–147.
5) Mozaffari, M., Amighian, J. and Magn, J. "Preparation of Al-Substituted Ni Ferrite Powders via Mechanochemical Processing". Journal of Magnetism and Magnetic Materials,(2003)260,P. 244-249.
6) J.C. Upadhyay; H. C. Verma "Anomalous change in electron density at nuclear sites in nanosize zinc ferrite". *Appl. Phys. Lett.* 85, 2074 (2004).
7) RAVAL, ANAND; PANCHAL, NITAL; JOTANIA, RAJSHREE, "STRUCTURAL PROPERTIES AND MICROSTRUCTURE OF COBALT FERRITE PARTICLES SYNTHESIZED BY A SOL-GEL AUTO COMBUSTION METHOD". International Journal of Modern Physics: Conference Series, 22(2013), P.558–563.
8) R.S. de Biasi; A.B.S. Figueiredo; A.A.R. Fernandes; C. Larica. "Synthesis of cobalt ferrite nanoparticles using combustion waves". 144(2007), P. 15–17.
9) Moumen, N.; Pileni, M. P. "New Syntheses of Cobalt Ferrite Particles in the Range 2–5 nm: Comparison of the Magnetic Properties of the Nanosized Particles in Dispersed Fluid or in Powder Form". Chemistry of Materials, 8(2016), P.1128–1134.
10) Daliya S. Mathew; Ruey-Shin Juang. "An overview of the structure and magnetism of spinel ferrite nanoparticles and their synthesis in microemulsions". 129(2007), P. 51–65.
11) B.D. Cullity, *Elements of X-ray Diffraction*, Addison-Wesley, Reading, MA, 102 (1978).
12) Mohamed S. A. Darwish, Hohyeon Kim, Hwangjae Lee, Chiseon Ryu, Jae Young Lee and Jungwon Yoon, "Synthesis of Magnetic Ferrite Nanoparticles with High Hyperthermia Performance via a Controlled Co-Precipitation Method", Nanomaterials,9 (2019), p.1176

13) *Abdel Maksoud , Gharieb S. El-Sayyad, A.H. Ashour, Ahmed I. El-Batal, Mahmmoud S. Abd-lmonem, HassanA.M. Hendawy , E.K. Abdel Khalek, Sh. Labib , E. Abdeltwab "Synthesis and characterization of metals-substituted cobalt ferrite [$M_x Co_{(1-x)} Fe_2O_4$; (M = Zn, Cu and Mn; x = 0 and 0.5)] nanoparticles as antimicrobial agents and sensors for Anagrelide determination in biological samples". Materials Science and Engineering: Volume 92(2018), P.644-656*

14) V. Rathod, Anupama A.V., R. Vijaya Kumar, V. M. Jali and B. Sahoo,"Correlated vibrations of the tetrahedral and octahedral complexes and splitting of the absorption bands in FTIR spectra of Li-Zn ferrite"s, Vibrational Spectroscopy 92 (2017),p. 267-273

15) Patrycja Makula, Michal Pacia and Wojciech Macyk, "How To Correctly Determine the Band Gap Energy of Modified Semiconductor Photocatalysts Based on UV–Vis Spectra", J. Phys. Chem. Lett.9 (2018),P.6814–6817

16) Adrian Radon, Dariusz Łukowiec, Marek Kremzer, Jarosław Mikuła and Patryk Włodarczyk, "Electrical Conduction Mechanism and Dielectric Properties of Spherical Shaped Fe3O4 Nanoparticles Synthesized by Co-Precipitation Method", Materials. 11 (2018),P. 735

ICRTMS-2024
International e-Conference on Recent Trends in Material Science
In Association with International Journal of Scientific Research in Science and Technology
Volume 11 | Issue 9 | Print ISSN: 2395-6011 | Online ISSN: 2395-602X (www.ijsrst.com)

Exploring Various Experimental Conditions for Enhanced Textile Dye Degradation using TiO_2 as a Photocatalyst

Prateek Sawant[1], Mahadev Parekar[1], Avadhut Kardile[1], Yogesh Khollam[2], Ravindra Mene[1*]

[1]Department of Physics, PDEA's Annasaheb Magar Mahavidyalaya, Hadapsar, Pune, Maharashtra, India

[2]Department of Physics, PDEA's Baburaoji Gholap College, Sangavi, Pune, Maharashtra, India

ABSTRACT

This study focuses on the hydrothermal synthesis of Titanium dioxide (TiO_2) nanoparticles for the photocatalytic degradation of textile dyes. As-synthesized TiO_2 nanoparticles are examined for structural, morphological and optical analysis using XRD, FE-SEM and UV-Visible spectroscopy. The effect of various radiation conditions along with variations in dye concentration and types are studied for photocatalytic degradation. The as-synthesized TiO_2 shows the highest degradation rate of 0.043 min^{-1} under combined UV-A and UV-C radiation. Moreover, the impact of dye concentration on efficiency showcases the intricate balance between active sites and light absorption. Among the various dyes used in the degradation study, Methylene Blue showed the highest degradation of 94% after 100 minutes of radiation.

Keywords: Titanium-dioxide, Photocatalysis, Hydrothermal, Methylene Blue

I. INTRODUCTION

Textile dyeing processes have long been vital to the vibrant and diverse world of fashion and textiles, but they often come at a significant environmental cost [1]. Every year, the textile industries worldwide use about 10 million kilograms of these dyes and the unused dyes along with industrial wastewater is released into various water bodies [2]. The discharge of effluents containing synthetic dyes into water bodies poses a severe threat to ecosystems and human health [3]. For instance, in recent studies on pollution of river Ganga, it was revealed that the river receives about 250 million litres of industrial wastewaters on a daily basis [4,5]. Most of the textile dyes are highly water soluble and inhibit the penetration of sunlight into water bodies thereby affecting the photosynthesis processes in aquatic plants [6]. Such dyes are also known to form carcinogenic compounds leading to serious health conditions in humans such as cancer, asthma, diarrhoea and other allergic reactions [2,7]. In response to this environmental challenge, the exploration of advanced and sustainable technologies for the degradation of textile dyes has gained prominence [8]. Among these technologies, titanium dioxide (TiO_2) photocatalysis emerges as a promising solution, offering a pathway towards efficient and eco-friendly degradation of dye pollutants [9].

The unique photocatalytic properties of TiO_2, coupled with its inherent stability, compatibility and band position makes it an ideal candidate for addressing the complexities associated with textile dye effluent treatment [10]. When irradiated with ultraviolet or visible light, TiO_2 initiates a cascade of redox reactions, generating reactive oxygen species (ROS) that efficiently break down organic dye molecules into non-toxic byproducts [11,12]. This fundamental mechanism forms the basis of a sustainable and effective approach to combat the challenges posed by textile dye pollution. Various synthesis methods such as sol-gel [13,14], Hydrothermal/Solvothermal [15,16], Precipitation [17], Spray Pyrolysis [18], Chemical Vapour Deposition [19] etc. have been employed to produce TiO_2. Among these, the hydrothermal synthesis method offers advantages such as controlled growth of TiO_2 crystals, improved crystallinity, low agglomeration and the ability to achieve high specific surface areas [20] Cano-Casanova L. et al. demonstrated that efficient photocatalytic oxidation of propene can be achieved with highly crystalline TiO_2 having a surface area of approximately 135 m^2/g by varying the HCl concentration in the hydrothermal reaction mixture [21]. Chen K et. al. demonstrated the control over TiO_2 phase structure by variation of HNO_3 concentration. It showed 89% degradation of gaseous toluene in 100 minutes, which was much better than commercial P25 degradation efficiency (44%) [22]. Using the template assisted hydrothermal technique, Liu J. et. al. synthesized TiO_2 with uniform mesoporous structure having pore size of 9 nm which has substantial effect on the photocatalytic activity of TiO_2 [23]. Enesca A. and Isac L. demonstrated the effect of radiation source wherein, the highest photocatalytic degradation of tartrazine was achieved using a mixture three UV-A sources and one visible source [24]. The impact of UV-source and the distance between source and solution on the photocatalytic degradation of Methyl Orange was examined by Sativa S. et al. Power and distance were determined to be optimal at 20 watts and 20 centimetres, respectively [25]. Motivated by the foregoing notable studies, we attempt to examine the impact of various experimental parameters on the photocatalytic performance of TiO_2.

In this study, TiO_2 photocatalyst is synthesized via hydrothermal route. Structural, optical and morphological properties of the TiO_2 sample are examined by XRD, UV-Vis spectroscopy and FE-SEM respectively. Photocatalytic degradation of various textile dyes is carried out to study the effects of different experimental conditions such as radiation, dye concentration and dye type on the photocatalytic efficiency of the synthesized TiO_2 sample.

II. METHODS AND MATERIAL

A. Chemicals and Reagents

Titanium tetra-isopropoxide (>98% pure, Sigma Aldrich), Hydrochloric Acid (35-38%, Thomas Baker), Ethanol. Various organic dyes such as Methylene Blue, Rhodamine B, Congo Red and Malachite Green were used as model pollutants for photodegradation experiments. All the reagents were analytical grade and used as received without any further purifications.

B. Characterization Techniques

X-ray diffraction studies (Rigaku MiniFlex 600, Japan) were used to identify the crystalline structure of the catalyst. Scanning electron microscopy (FEI Nova NanoSEM 450) was used to study the morphology and size of the catalyst. In addition, UV-Visible spectroscopy (Shimadzu, Model UV-2600, Kyoto, Japan) was employed to monitor the light absorption and band gap of the synthesized compounds.

C. Synthesis of TiO2 Nanoparticles

TiO_2 nanoparticles were synthesized using a hybrid sol–gel/hydrothermal method. Briefly, 4 mL of titanium tetra-isopropoxide (TTIP) was mixed with 20 mL of ethanol and stirred for 1 hour. A solution of 4 mL of 0.3 M hydrochloric acid in 10 mL of ethanol was then added dropwise to the TTIP/ethanol mixture, which was then stirred continuously for 1 hour. The resulting solution was transferred to a Teflon-coated stainless-steel autoclave and subjected to hydrothermal conditions at 180°C for 24 hours. After cooling to room temperature, the sample was filtered and dried at 100°C for 12 hours. Finally, the sample was calcinated at 350°C for 2 hours in a muffle furnace to obtain pale white crystalline TiO_2 powder.

D. Photocatalytic Experiments

Photocatalytic degradation of the organic dyes was carried out under radiation from a combination of different light sources, which included UV-A (Philips, F18W/T8, λmax=365 nm), UV-C (Philips, F18/T8, λmax=295 nm) and visible (Philips, F18W/T8, 400-700 nm). The reflectors installed above the tube-lights ensured uniform distribution of light throughout the chamber.

Firstly, a stock solution with a concentration of 0.1 g/L of the desired dye was prepared by dissolving a required amount of dye in DI water. Subsequently, 100 mL of the reaction solution with the desired dye concentration (5, 10, or 15 ppm) was prepared using the stock solution. An appropriate amount of the catalyst was added to this dye solution. This reaction mixture was then kept in the dark for 30 minutes under stirring to attain adsorption equilibrium. The reaction mixture was subsequently irradiated using the light sources, with the light positioned at a fixed distance from the beaker containing the reaction mixture to ensure consistent illumination.

Throughout the experiment, the reaction mixture was continuously stirred to promote uniform contact between the catalyst and the dye molecules. The degradation process was monitored by sampling the solution every 20 minutes and analyzing the concentration of the dye using UV-vis spectra (Perkin Elemer Lambda 265, USA). The proportion of dye degradation and the photocatalytic efficiency of the catalyst with respect to irradiation time were assessed using the reduction in absorbance value at a specific wavelength, which corresponds to the typical peak for the absorption spectra of the selected dye.

III. RESULTS AND DISCUSSION

A. X-Ray Diffraction Studies

Figure 1 shows the XRD plot of the TiO_2 sample prepared at 0.3M concentration of HCl. Sharp peaks were observed at 2θ=25.2°, 37.8°, 47.9° and 54.9° corresponding to (101), (004), (200), (211) and (204) crystal planes respectively. The XRD pattern of the prepared sample matched closely with the reference XRD pattern of Anatase TiO_2 (JCPDS: 00-004-0477) confirming the formation of pure Anatase TiO_2 [26,27]. No peaks corresponding to rutile or brookite phases were observed. The average crystallite size was found to be approximately 7 nm calculated using Scherrer's equation [28].

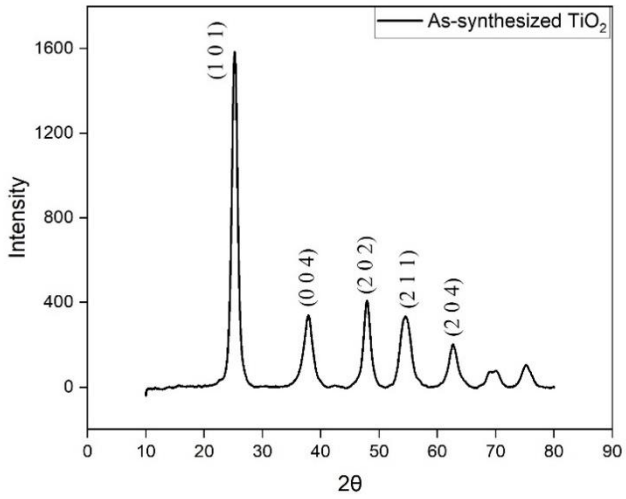

Fig. 1: X-Ray diffraction patterns of the sample synthesized with HCl concentration of 0.3 M, reacted for 24 hours.

B. UV-Visible Absorption Spectroscopy

The as-synthesized anatase TiO_2 nanoparticles show absorption edge in 350-400 nm range which can be attributed to the electron transition from valence band to conduction band of Titania [29]. Thus, it can be deduced that the prepared TiO_2 nanoparticles are UV–light active compounds [30]. The band gap of the sample was estimated using the Tauc-plot method and found to be ~ 3.22 eV, a result consistent with previous literature [31–34].

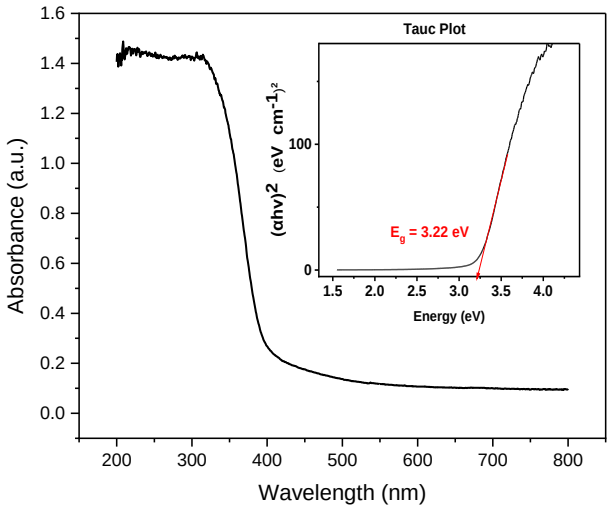

Fig. 2: UV-Visible absorption for the synthesized TiO_2 sample with Tauc Plot in the inset.

C. Scanning Electron Microscopy

The FE-SEM images of the TiO_2 samples prepared in HCl solution show a microporous structure having spherical smaller grain morphology on whole surface. The particle sizes observed were in the range of 13-19 nm which is in good agreement with the X-ray analysis.

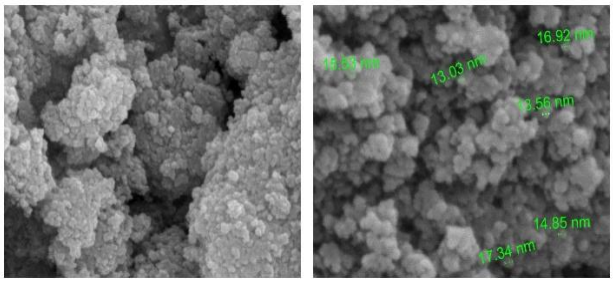

Fig 3: FE-SEM images of the synthesized TiO_2 sample

D. Effects of various Experimental Parameters on Photocatalytic Efficiency of TiO_2

1) Effect of Radiation

The effect of radiation on the photocatalytic activity of TiO_2 was explored using Methylene Blue (10 ppm conc.) as the target dye. The catalyst concentration was fixed at 1g/L and the photocatalytic degradation experiments were conducted under various combinations of UV-A, UV-C, and visible light sources to investigate their influence on the efficiency of the photocatalytic process. The photocatalytic degradation efficiency was calculated as:

$$\eta = \frac{C_0 - C}{C_0} \times 100$$

Where, C_0 is the initial dye concentration at 0 minutes and C is the concentration of the dye at time t [35]. The relative decrement in Methylene Blue concentration, C/C_0, for different radiation sources is shown in figure 4. Clearly, the type of radiation had a considerable effect on the amount of degradation of Methylene Blue.

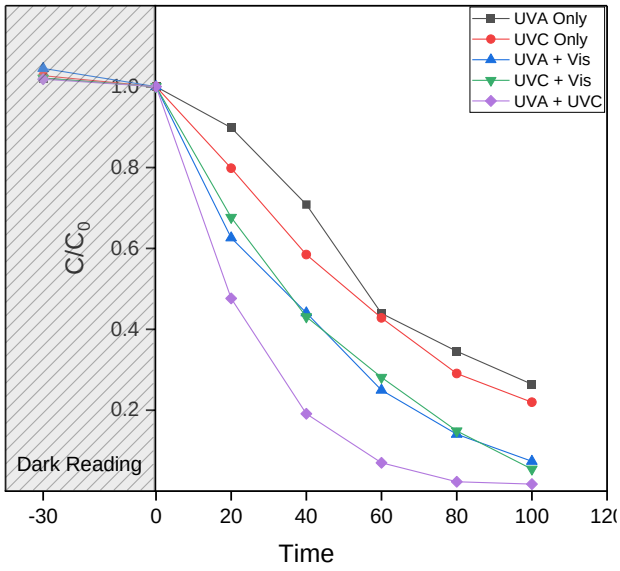

Fig. 4: Degradation of Methylene Blue under different radiation sources.

The photocatalytic efficiency of TiO_2 after 100 minutes of irradiation under different radiation conditions is shown in figure 5. The addition of visible light source to both UV-A and UV-C sources had a positive effect of the photocatalytic efficiency. When the degradation was carried out using UV-A and UV-C sources individually, the photocatalytic efficiency of TiO_2 was found to be 73.5% and 78.04% respectively. However, with the addition of the visible source, the efficiency drastically goes up to 92.6% and 94.5% respectively. The increased photocatalytic efficiency of TiO_2 can be attributed to its sensitization with organic dyes such as Methylene Blue [36]. Organic dyes like Methylene Blue efficiently absorb visible light, leading to the excitation of electrons to higher energy levels [37]. These photoexcited electrons are then transferred to the conduction band of the TiO_2 photocatalyst, effectively utilizing the visible light energy. Additionally, some energy is transferred to the lattice of the photocatalyst, resulting in lattice vibrations [38]. These lattice vibrations, in turn, promote the excitation of more electrons from the valence band to the conduction band, leading to the generation of additional electron-hole pairs. The increased number of electron-hole pairs contributes to the higher photocatalytic efficiency observed in the presence of visible light sensitization compared to using UV light alone [39]. The highest photocatalytic efficiency of 98.25% was achieved under radiation with UV-A and UV-C together.

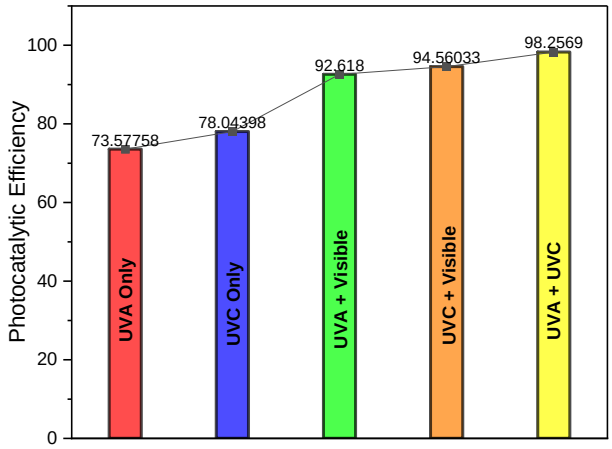

Fig. 5: Photocatalytic efficiency of TiO_2 after 100 minutes of irradiation under different radiation conditions.

The photocatalytic degradation of dyes adheres to the Langmuir-Hinshelwood kinetic model [40] where, the degradation rate depends on the amount of dye molecules present in the solution. The equation that governs the photocatalytic dye degradation is represented as:

$$\ln\left(\frac{C}{C_0}\right) = -kt$$

Where, k is the reaction rate constant. Thus, the slope of $ln(C/C_0)$ vs t graph gives the rate constant for the reaction. The reaction kinetic using the Langmuir-Hinshelwood reaction kinetics model is represent in figure 6 and the reaction rate constants for different radiation conditions are tabulated in table 1.

In our experiments, we found that degradation enforced using UV-A and UV-C radiations together gave the highest degradation rate of 0.043 min^{-1}.

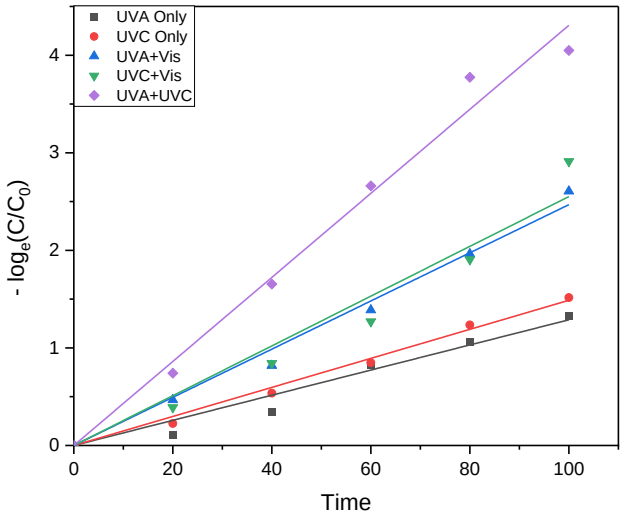

Fig. 6: Photocatalytic degradation kinetics of Methylene Blue using Langmuir-Hinshelwood model under various radiation conditions.

Table 1

Reaction rate constants for photocatalytic degradation of Methylene Blue under different radiation conditions.

Radiation Condition	Rate Constant (min^{-1})	Standard Deviation
UV-A Only	0.01288	7.21219×10^{-4}
UV-C Only	0.01488	3.50472×10^{-4}
UVA + Vis	0.02468	7.18084×10^{-4}
UVC + Visible	0.02551	0.00155
UVA + UVC	0.04307	0.00135

2) Effect of Dye Concentration

To study the effect of initial dye concentration on the photocatalytic efficiency of TiO_2, degradation of various concentration of Methylene Blue was carried out under UV-A+Visible radiation at catalyst concentration of 1g/L. The degradation of Methylene blue at different concentrations is shown in figure 7. The photocatalytic efficiency as a function of initial dye concentration is represented in figure 8.

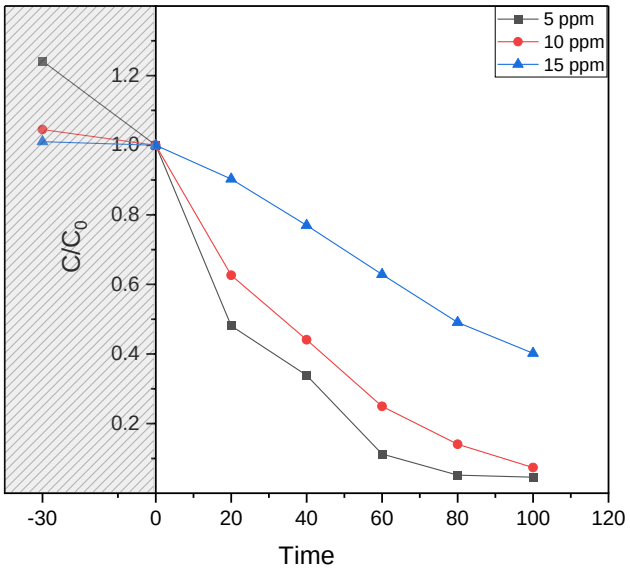

Fig. 7: Degradation of Methylene Blue at different concentrations under UVA+Visible radiation

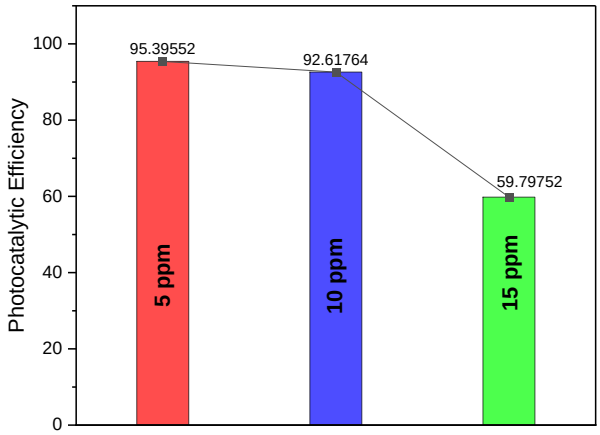

Fig. 8: Photocatalytic efficiency of after 100 minutes of irradiation under UVA+Visible radiation for different concentrations of Methylene Blue.

As seen from the figures 7 and 8, the initial dye concentration is a crucial parameter that impacts the photocatalytic efficiency of TiO_2. Although the efficiency for 5 ppm and 10 ppm dye concentrations is relatively same (95.3% and 92.6% respectively), the efficiency drastically falls to 59.79% at 15 ppm dye concentration. This could be because at lower dye concentrations, there are more active sites for the dye molecules to be adsorbed on the surface of the TiO_2 photocatalyst. Increasing the dye concentration increases the adsorption of MB on the surface of TiO_2 reducing the availability of active sites for more adsorption [41]. Increase in the number of dye molecules present in the reaction solution also leads to an increase in the light absorption and/or scattering by dye molecules. Thus, a smaller number of photons actually reach the photocatalyst leading to reduction in the degradation efficiency.

The reaction kinetics are shown in figure 9. The reaction rates are also affected by the initial dye concentration. As expected, the reaction rate is the lowest for 15 ppm dye concentration. The reaction rates for different dye concentrations are given in table 2.

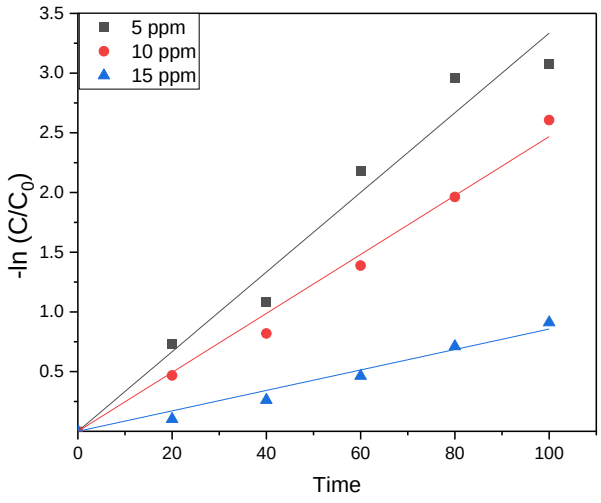

Fig. 9: Photocatalytic degradation kinetics of various concentrations of Methylene Blue on P25 under UVA+Visible radiation conditions.

Table 2

Reaction rate constants for photocatalytic degradation of different concentrations of Methylene Blue on P25 under UVA+Visible radiation

Initial Dye Concentration	Rate Constant (min^{-1})	Standard Deviation
5 ppm	0.03335	1.521×10^{-4}
10 ppm	0.02468	7.180×10^{-4}
15 ppm	0.00856	3.980×10^{-4}

3) Effect of Dye Type

The photocatalytic degradation experiment was carried out using four different dyes namely, Methylene Blue, Congo Red, Malachite Green and Rhodamine B. The catalyst concentration was kept constant at 1g/L in the reaction mixture. The light source used for irradiation was UVC + visible. The relative decrement and the percentage degradation of the various dyes is shown in figures 10 and 11 respectively.

It is observed that the TiO_2 sample showed highest degradation efficiency for Methylene Blue. About 94% of initial Methylene Blue concentration was degraded after 100 minutes of irradiation. However, it showed much lower efficiency for Malachite Green (~67%).

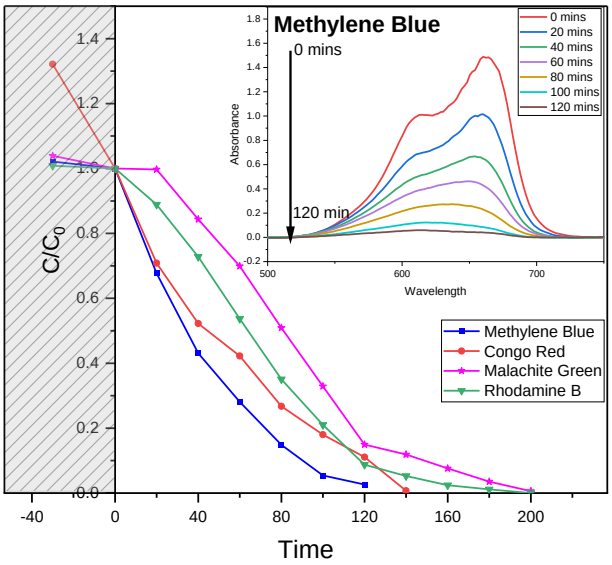

Fig. 10: Degradation of various dyes with time

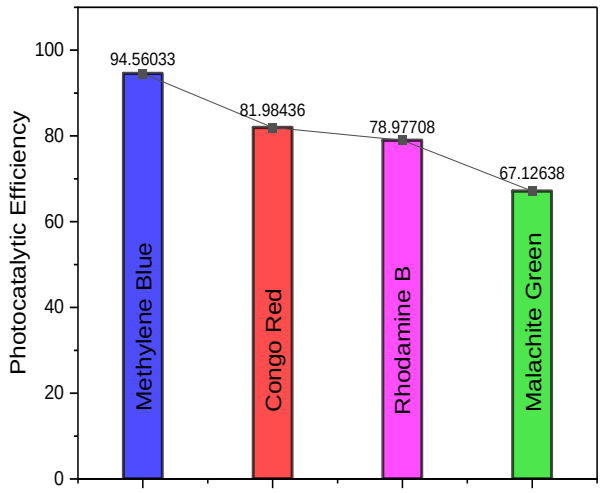

Fig. 11: Percentage degradation after 100 mins of radiation

IV. CONCLUSION

In conclusion, hydrothermally synthesized TiO_2 nanoparticles are utilized for photocatalytic degradation of textile dyes, emphasizing the optimization of key parameters. TiO_2 nanoparticles were characterized through X-ray diffraction, UV-Visible absorbance spectroscopy, and Field-emission Scanning Electron Microscopy. The formation of pure anatase TiO_2 nanoparticles are confirmed by XRD analysis. The optical characteristics and band gap (3.2 eV) are verified using UV-vis spectroscopy. SEM analysis showed microporous structure with average particles size of 13-19 nm. Photocatalytic degradation of Methylene Blue under various radiation conditions revealed that simultaneous UV-A and UV-C application achieved the highest efficiency (0.043 min-1). Investigation into initial dye concentration demonstrated that lower concentrations (5 ppm and 10 ppm) exhibited higher efficiency. While exploring the degradation efficiency of TiO_2 towards different dyes, we found that Methylene Blue exhibited the highest degradation efficiency of approximately 94%.

V. REFERENCES

1 H. tu Rauf, N. Yasmin, G. Ali, M. N. Ashiq, M. Safdar, M. Mirza New insight in photocatalytic degradation of textile dyes over CeO2/Ce2S3 composite. (2022) *Physica B Condens Matter*. **632**, 413760.

2 R. Al-Tohamy, S. S. Ali, F. Li, K. M. Okasha, Y. A-G Mahmoud, T. Elsamahy, et al. A critical review on the treatment of dye-containing wastewater: Ecotoxicological and health concerns of textile dyes and possible remediation approaches for environmental safety. (2022) .

3 H. A. Elbadawy, A. F. Elhusseiny, S. M. Hussein, W. A. Sadik Sustainable and energy-efficient photocatalytic degradation of textile dye assisted by ecofriendly synthesized silver nanoparticles. (2023) *Scientific Reports 2023 13:1*. **13**, 1–13.

4 S. Dwivedi, S. Mishra, R. D. Tripathi Ganga water pollution: A potential health threat to inhabitants of Ganga basin. (2018) *Environ Int*. **117**, 327–338.

5 D. Paul Research on heavy metal pollution of river Ganga: A review. (2017) .

6 M. M. Hassan, C. M. Carr A critical review on recent advancements of the removal of reactive dyes from dyehouse effluent by ion-exchange adsorbents. (2018) *Chemosphere*. **209**, 201–219.

7 P. Dutta, M. Razaya Rabbi, M. A. Sufian, S. Mahjebin Effects of textile dyeing effluent on the environment and its treatment: A review. (n.d.) .

8 S. Ganesan, T. Kokulnathan, S. Sumathi, A. Palaniappan Efficient photocatalytic degradation of textile dye pollutants using thermally exfoliated graphitic carbon nitride (TE–g–C3N4). (2024) *Scientific Reports 2024 14:1*. **14**, 1–13.

9 J. Schneider, M. Matsuoka, M. Takeuchi, J. Zhang, Y. Horiuchi, M. Anpo, et al. Understanding TiO2photocatalysis: Mechanisms and materials. (2014) *Chem Rev*. **114**, 9919–9986.

10 Z. Zeitoun, N. Y. Selem A comprehensive review on textile wastewater treatment by coupling TiO2 with PVDF membrane. (2023) *Bulletin of the National Research Centre 2023 47:1*. **47**, 1–16.

11 S. Banerjee, S. C. Pillai, P. Falaras, K. E. O'shea, J. A. Byrne, D. D. Dionysiou New insights into the mechanism of visible light photocatalysis. (2014) *Journal of Physical Chemistry Letters*. **5**, 2543–2554.

12 M. Zou, Y. Kong, J. Wang, Q. Wang, Z. Wang, B. Wang, et al. Spectroscopic analyses on ROS generation catalyzed by TiO2, CeO2/TiO2 and Fe2O3/TiO2 under ultrasonic and visible-light irradiation. (2013) *Spectrochim Acta A Mol Biomol Spectrosc*. **101**, 82–90.

13 N. Venkatachalam, M. Palanichamy, V. Murugesan Sol–gel preparation and characterization of nanosize TiO2: Its photocatalytic performance. (2007) *Mater Chem Phys*. **104**, 454–459.

14 A. Karami Synthesis of TiO2 nano powder by the sol-gel method and its use as a photocatalyst. (2010) *Journal of the Iranian Chemical Society*. **7**, S154–S160.

15 Z. Bian, J. Zhu, H. Li Solvothermal alcoholysis synthesis of hierarchical TiO2 with enhanced activity in environmental and energy photocatalysis. (2016) *Journal of Photochemistry and Photobiology C: Photochemistry Reviews*. **28**, 72–86.

16 H. Yin, Y. Wada, T. Kitamura, S. Kambe, S. Murasawa, H. Mori, et al. Hydrothermal synthesis of nanosized anatase and rutile TiO2 using amorphous phase TiO2. (2001) *J Mater Chem*. **11**, 1694–1703.

17 S. J. Kim, S. D. Park, Y. H. Jeong, S. Park Homogeneous Precipitation of TiO2 Ultrafine Powders from Aqueous TiOCl2 Solution. (1999) *Journal of the American Ceramic Society*. **82**, 927–932.

18 M. O. Abou-Helal, W. T. Seeber Preparation of TiO2 thin films by spray pyrolysis to be used as a photocatalyst. (2002) *Appl Surf Sci*. **195**, 53–62.

19 A. Mills, N. Elliott, I. P. Parkin, S. A. O'Neill, R. J. Clark Novel TiO2 CVD films for semiconductor photocatalysis. (2002) *J Photochem Photobiol A Chem*. **151**, 171–179.

20 A. H. Mamaghani, F. Haghighat, C. S. Lee Hydrothermal/solvothermal synthesis and treatment of TiO2 for photocatalytic degradation of air pollutants: Preparation, characterization, properties, and performance. (2019) *Chemosphere*. **219**, 804–825.

21 L. Cano-Casanova, A. Amorós-Pérez, M. Ouzzine, M. A. Lillo-Ródenas, M. C. Román-Martínez One step hydrothermal synthesis of TiO2 with variable HCl concentration: Detailed characterization and photocatalytic activity in propene oxidation. (2018) *Appl Catal B*. **220**, 645–653.

22 K. Chen, L. Zhu, K. Yang Tricrystalline TiO2 with enhanced photocatalytic activity and durability for removing volatile organic compounds from indoor air. (2015) *J Environ Sci (China)*. **32**, 189–195.

23 J. Liu, T. An, G. Li, N. Bao, G. Sheng, J. Fu Preparation and characterization of highly active mesoporous TiO2 photocatalysts by hydrothermal synthesis under weak acid conditions. (2009) *Microporous and Mesoporous Materials*. **124**, 197–203.

24 A. Enesca, L. Isac The influence of light irradiation on the photocatalytic degradation of organic pollutants. (2020) *Materials*. **13**,.

25 S. O. Sativa, M. A. Zulfikar, A. Alni Optimization of UV light source conditions for photocatalytic activity of methyl orange using TiO 2 . (2021) *IOP Conf Ser Mater Sci Eng*. **1143**, 012074.

26 E. Jalali, S. Maghsoudi, E. Noroozian A novel method for biosynthesis of different polymorphs of TiO2 nanoparticles as a protector for Bacillus thuringiensis from Ultra Violet. (2020) *Sci Rep*. **10**,.

27 N. Krishnarao Eswar, P. Chandrashekarapura, R. Ab, G. Madras High photoconductive combustion synthesized TiO2 derived nanobelts for photocatalytic water purification under solar irradiation. (2015) *New J. Chem*. **39**, 6040.

28 M. Sahadat Hossain, S. Ahmed Easy and green synthesis of TiO2 (Anatase and Rutile): Estimation of crystallite size using Scherrer equation, Williamson-Hall plot, Monshi-Scherrer Model, size-strain plot, Halder- Wagner Model. (2023) *Results in Materials*. **20**, 100492.

29 J. Ma, W. Li, N. T. Le, J. A. Díaz-Real, M. Body, C. Legein, et al. Red-Shifted Absorptions of Cation-Defective and Surface-Functionalized Anatase with Enhanced Photoelectrochemical Properties. (2019) *ACS Omega*. **4**, 10929–10938.

30 R. Abazari, A. R. Mahjoub, S. Sanati A facile and efficient preparation of anatase titania nanoparticles in micelle nanoreactors: Morphology, structure, and their high photocatalytic activity under UV light illumination. (2014) *RSC Adv*. **4**, 56406–56414.

31 H. N. C. Dharma, J. Jaafar, N. Widiastuti, H. Matsuyama, S. Rajabsadeh, M. H. D. Othman, et al. A Review of Titanium Dioxide (TiO2)-Based Photocatalyst for Oilfield-Produced Water Treatment. (2022) *Membranes (Basel)*. **12**,.

32 H. M. El Sharkawy, A. M. Shawky, R. Elshypany, H. Selim Efficient photocatalytic degradation of organic pollutants over TiO 2 nanoparticles modified with nitrogen and MoS 2 under visible light irradiation. (123AD) .

33 F. Abu Bakar, N. S. I. Mohd Foad Synthesis of Tio2 photocatalyst with tunable optical properties and exposed facet for textile wastewater treatment. (2023) *Results in Optics*. **13**, 100545.

34 S. Landi, I. R. Segundo, C. Afonso, O. Lima, M. F. M. Costa, E. Freitas, et al. Evaluation of band gap energy of TiO2 precipitated from titanium sulphate. (2022) *Physica B Condens Matter*. **639**, 414008.

35 M. Söyleyici Cergel, E. Demir, F. Atay The effect of the structural, optical, and surface properties of anatase-TiO2 film on photocatalytic degradation of methylene blue organic contaminant. (2019) *Ionics (Kiel)*. **25**, 4481–4492.

36 Y. C. Hsiao, T. F. Wu, Y. S. Wang, C. C. Hu, C. Huang Evaluating the sensitizing effect on the photocatalytic decoloration of dyes using anatase-TiO2. (2014) *Appl Catal B*. **148–149**, 250–257.

37 S. Y. Lee, D. Kang, S. Jeong, H. T. Do, J. H. Kim Photocatalytic Degradation of Rhodamine B Dye by TiO2 and Gold Nanoparticles Supported on a Floating Porous Polydimethylsiloxane Sponge under Ultraviolet and Visible Light Irradiation. (2020) *ACS Omega*. **5**, 4233–4241.

38 H. S. Hilal, L. Z. Majjad, N. Zaatar, A. El-Hamouz Dye-effect in TiO2 catalyzed contaminant photo-degradation: Sensitization vs. charge-transfer formalism. (2007) *Solid State Sci*. **9**, 9–15.

39 M. A. Hamza, S. A. Rizk, E.-E. M. Ezz-Elregal, S. A. Abd El-Rahman, S. K. Ramadan, Z. M. Abou-Gamra Photosensitization of TiO 2 microspheres by novel Quinazoline-derivative as visible-light-harvesting antenna for enhanced Rhodamine B photodegradation. (123AD) *Scientific Reports /*. **13**, 12929.

40 A. Enesca, L. Isac The influence of light irradiation on the photocatalytic degradation of organic pollutants. (2020) *Materials*. **13**,.

41 Z. Z. Vasiljevic, M. P. Dojcinovic, J. D. Vujancevic, I. Jankovic-Castvan, M. Ognjanovic, N. B. Tadic, et al. royalsocietypublishing.org/journal/rsos Research Photocatalytic degradation of methylene blue under natural sunlight using iron titanate nanoparticles prepared by a modified sol-gel method. (2020) .

ICRTMS-2024
International e-Conference on Recent Trends in Material Science
In Association with International Journal of Scientific Research in Science and Technology
Volume 11 | Issue 9 | Print ISSN: 2395-6011 | Online ISSN: 2395-602X (www.ijsrst.com)

Structural Study of Synthesiszed CMO and AC-CMO By Co-Precipitation Method

Digambar M. Sapkal *1, Harshal M. Bachhav 2

*1 Department of Physics, S.I.C.E.S. Degree College, Ambarnath(W), Maharashtra, India

2 Department of Chemistry, S.I.C.E.S. Degree College, Ambarnath(W), Maharashtra, India

ABSTRACT

The synthesis of hybrid materials has emerged as a pivotal avenue for enhancing the performance of energy storage devices and catalytic systems. In this chapter, we delve into the synthesis methods employed to create the activated carbon-$CoMoO_4$ hybrid material, a promising candidate for advanced supercapacitor applications. The precursor materials and their significance in influencing the final characteristics of the hybrid material. We elucidate the rationale behind the choice of activated carbon and $CoMoO_4$ as fundamental constituents, highlighting their individual attributes that contribute to the synergistic performance of the hybrid material. The subsequent sections delve into the stepwise synthesis processes, including precursor preparation, mixing techniques, and reaction kinetics. co-precipitation method, a top-down approach renowned for its precision. Within this methodology, we craft two distinct nanomaterials, beginning with the creation of $CoMoO_4$ (CMO) as the foundation. Subsequently, we elevate this synthesis by infusing activated carbon, culminating in the birth of the activated carbon- $CoMoO_4$ hybrid (AC-CMO). The XRD patterns of CMO and AC-CMO shows that both materials contain polycrystalline cobalt molybdenum oxide with monoclinic crystal structure.

Keywords: activated carbon, $CoMoO_4$, Hybrid material, monoclinic etc.

I. INTRODUCTION

Since the late 19th century, energy demand from the world is increasing rapidly. Industrialization being one of the major factors behind this tremendous energy consumption. To withstand this tremendous demand for energy generation, it is important to have capable energy storage devices and infrastructure. Supercapacitors are one of the most promising candidates of large-scale energy storage and they provide high energy and power density with wide range use from satellites to daily life electronic devices.

On the contrary, while single phase nanomaterials can be used for above mentioned applications, they often come with certain drawbacks. To address these limitations, scientists have turned to hybrid materials, which are composed of two or more nanoscale materials, such as combinations of metals with semiconductors or

organic with inorganic components. These hybrid materials have been employed for the same applications, not only overcoming the drawbacks of single nanomaterials but also significantly enhancing overall application efficiency. As a result, there is a significant focus on developing energy conversion and storage devices based on hybrid nanomaterials.

We embarked on the synthesis of $CoMoO_4$ (CMO) and activated carbon-$CoMoO_4$ (AC-CMO) employing a straightforward co-precipitation technique at ambient temperature. This method led to the creation of monoclinic-phase Cobalt Molybdate, a fact ratified through thorough examination via XRD, Raman studies.

II.TYPES OF SYNTHESIS METHODS

Within the realm of material synthesis, a diverse array of methodologies exists, each offering distinct avenues to engineer and tailor materials with targeted properties. In this chapter, we embark on a comprehensive exploration of the various synthesis methods employed in the creation of $CoMoO_4$ and related hybrid materials. This section serves as a crucial foundation to navigate the intricacies of material preparation.

Synthesis methods can be broadly categorized into two principal classifications: physical methods and chemical methods. These categories represent fundamental approaches that harness distinct mechanisms to assemble and structure materials at the nanoscale. The ensuring section will delve into each category, presenting an array of some synthesis methods under their respective umbrellas.

1.1 Physical methods

Physical synthesis methods encompass a range of techniques that manipulate and engineer materials through physical processes, without involving chemical reaction [1] These methods

leverage physical properties such as vapor phase, template-assisted growth, and mechanical forces to create materials with specific structures and properties.

Vapor Deposition: Vapor deposition techniques involve the condensation of vaporized precursor materials onto a substrate, forming thin films or coatings. Techniques like chemical vapor deposition (CVD) and physical vapor deposition (PVD) enable precise control over film thickness, composition, and crystallinity, making them suitable for producing uniform and high-quality materials [2].

Template-Assisted Synthesis: This method employs porous templates or scaffolds as substrates, guiding the growth of materials into desired structures. It offers a versatile approach to create materials with well-defined shapes and sizes. An example is the use of nano-porous templates to synthesize nanowires or nanotubes [3].

1.2 Chemical methods

Chemical synthesis methods encompass a diverse array of techniques that rely on chemical reactions to create materials with tailored properties and structures. These methods offer precise control over composition, morphology, and crystallinity, making them indispensable for engineering materials for specific applications [4].

Hydrothermal synthesis: Hydrothermal methods involve the reaction of precursor materials in a high temperature, high pressure aqueous environment. This controlled reaction environment allows the formation of crystalline materials with controlled particle sizes and shapes. Hydrothermal synthesis is particularly advantageous for producing nanoparticles and nanocrystalline materials. Di Guo et al. synthesized $CoMoO_4$

nanoplate arrays via hydrothermal route and observed electrochemical performance with a specific capacitance of 1.26 F/cm^2 [5].

Co-precipitation: Co-precipitation involves the simultaneous precipitation of multiple precursor ions from a solution, resulting in the formation of solid particles. This method enables the controlled formation of homogeneous mixtures and the production of materials with well-defined compositions. Co-precipitation is widely used for creating metal oxides, hydroxides and composite materials [6].

As we bid adieu to this overview of synthesis methods, our focus now shifts toward the unfolding chapters, where we will unveil our own experimental journey. We tread the path of co-precipitation, a chemical synthesis technique that empowers us to create the activated carbon- $CoMoO_4$ hybrid material. This method, operating at room temperature, brings forth its distinct advantages as we unravel its nuances and uncover its potential.

Our experimental approach stands poised to offer a novel perspective on the synthesis process, yielding insights into the interplay of variables, the intricate dance of precursor interactions, and the birth of a hybrid material with promising prospects. The following section is dedicated to delving into this process, elucidating the experimental conditions, and unveiling the key factors that drive the successful synthesis of this remarkable hybrid material.

III.EXPERIMENTAL

In the pursuit of tailored nanomaterials with advanced energy storage capabilities, our experimental journey commences with the co-precipitation method, a top-down approach renowned for its precision. Within this methodology, we craft two distinct nanomaterials, beginning with the creation of $CoMoO_4$ (CMO) as the foundation. Subsequently, we elevate this synthesis by infusing activated carbon, culminating in the birth of the activated carbon- $CoMoO_4$ hybrid (AC-CMO), a potent union poised to unlock new energy storage horizons.

The co-precipitation method was judiciously chosen as our synthesis approach due to its exceptional versatility, allowing precise control over material composition and properties. Its capacity for homogeneous integration of activated carbon within the $CoMoO_4$ matrix ensures a harmonious synergy of components. Moreover, the method's scalability, practicality, and room temperature operation align seamlessly with our goal of crafting an efficient and feasible energy storage solution. This method stands as the ideal conduit to engineer the activated carbon-$CoMoO_4$ hybrid, empowering us to unlock its full potential for enhanced supercapacitor performance.

Chemicals used for the synthesis of both CMO and AC-CMO are as follows Ammonium Molybdate $(NH_4)_2MoO_4$, Cobalt Chloride $CoCl_2$, Sodium Boro-hydrate $NaBH_4$, NMP/ N- Methyl-2-Pyrrolidone (C_5H_9NO), PVDF/Polyvinylidene Fluoride ($C_2H_2F_2$).

The synthesis of $CoMoO_4$ (CMO) and the activated carbon- $CoMoO_4$ hybrid (AC-CMO) was achieved through a facile co-precipitation method, meticulously executed to ensure the precise creation of these materials. Beginning with CMO, the synthesis involved a sequential process. Initially, 1mmol of ammonium molybdate $(NH_4)_2MoO_4$, was introduced into 50 ml of distilled water, followed by continuous stirring at room temperature for 30 minutes using a magnetic stirrer. Subsequently, 1mmol of Cobalt Chloride $CoCl_2$,

was introduced into the same solution, with consistent stirring maintained under identical conditions. Finally, the addition of 30mmol of $NaBH_4$ into a 50 ml mixture of ammonium molybdate and cobalt chloride completed the chemical reaction. This resultant aqueous solution was further subjected to continuous stirring for an additional 30 minutes. The synthesis process for AC-CMO mirrored that of CMO, with the inclusion of 200 mg of activated carbon into 50 ml of distilled water as the initial step.

After each variant's three-step synthesis process, the reaction solutions were left undisturbed for 12 hours, facilitating the formation of precipitates. Following this, the separation of supernatant and precipitate was achieved through a decanting process, meticulously repeated six times for both material variants.

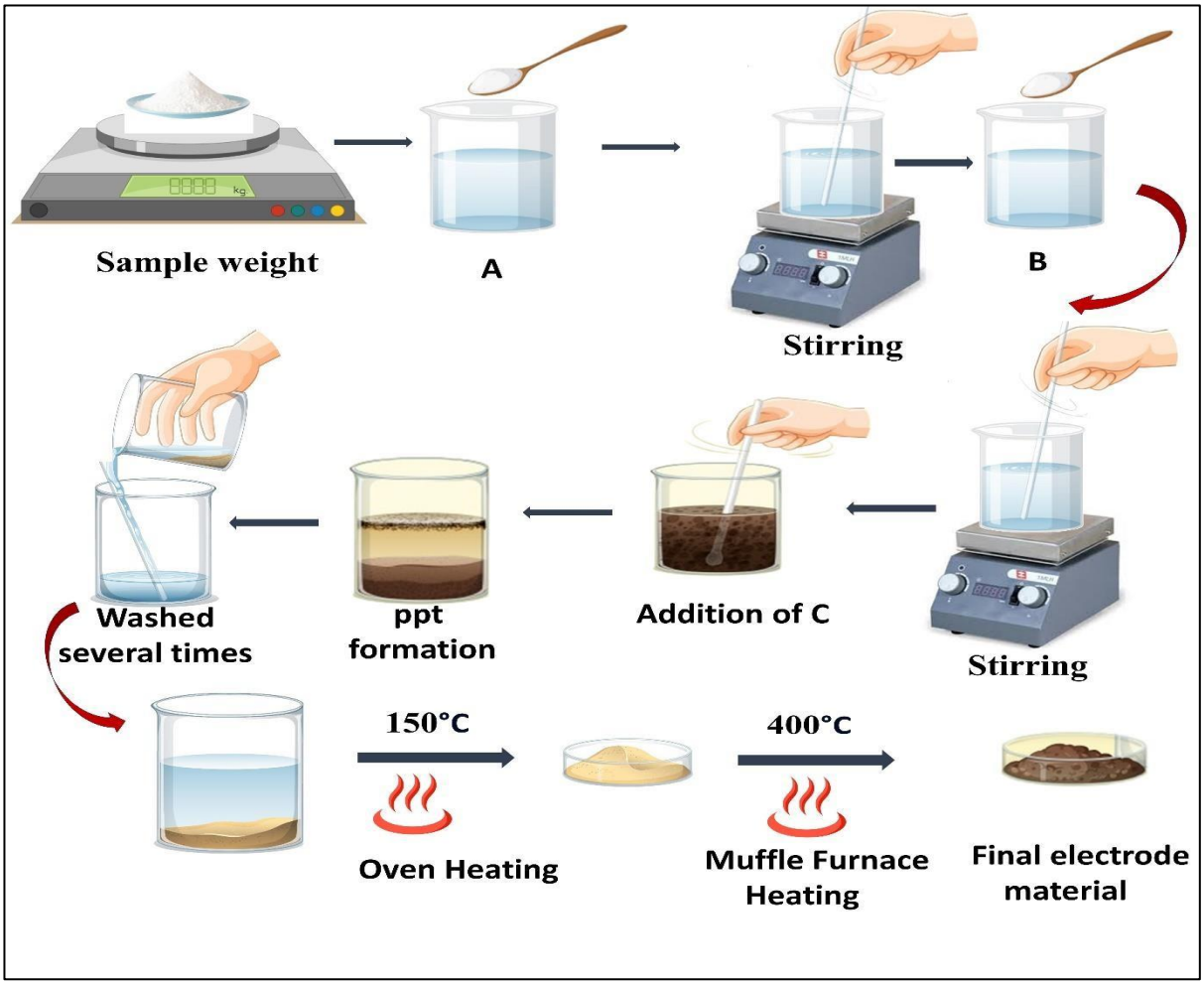

Figure 3.1 *Schematic representation of Co-precipitation experimental method for CMO* ***(A)****-addition of* $(NH_4)_2MoO_4$, ***(B)****-addition of* $CoCl_2$, ***(C)****-addition of* $NaBH_4$

Once excess water-soluble byproducts were eliminated, the resulting precipitate was isolated by draining excess supernatant. This precipitate was then subjected to heating in a hot air oven at 150°C for a duration of 12 hours, effectively eliminating any residual moisture content. The material was subsequently cooled and further crushed using mortar and pestle, refining the particle size into the nanoscale range.

IV.MATERIAL CHARACTERIZATION TECHNIQUES

1. X-Ray Diffraction (XRD)

XRD is a widely used and most famous technique to obtain information about the crystal structure of solid materials, such as the lattice parameter, orientation of single crystals, phase, and composition [7]. The XRD pattern of a material is like its fingerprint which can identify the material under observation. The XRD pattern from a material can be used for determining lattice stress, strain and structural and phase confirmation [8, 9]. It is also important to note that this technique more useful for crystalline solid phase materials.

The XRD technique is based on scattering of monochromatic X-ray reflection from the crystallographic phase of lattice [10]. The interplanar distance (d) can be determined using the Bragg's diffraction equation [11].

$$2d \sin\theta = n\lambda$$

Where, λ = wavelength of monochromatic x-rays, n = order of diffraction and θ = diffraction angle

Using this relation, the 'd' values are computed for known values of λ, Θ and n. This data is then compared with a standard data set either from Joint Committee Powder Diffraction Standards (JCPDS). The crystallite size for the sample can also be calculated using the XRD data and using Scherrer formula [12]. By determining the full width at half maxima (FWHM) of the most intense peak from the data, we can employ it in the following formula and obtain the crystallite size.

$$D = \frac{k\lambda}{\beta\cos\theta}$$

Where, D = crystallite size, β = FWHM in radians and k = constant (0.89-1.39, mostly 1)

X-Ray Diffraction (XRD)

XRD unveils the concealed structural nuances of our synthesized materials, providing insights into their crystalline arrangements at the atomic scale. Through XRD, we decode distinctive fingerprint patterns that shed light on the crystallographic essence and phase composition, enriching our understanding and seamlessly aligning with our comprehensive analysis [13].

Fig. .2 depicts the XRD patterns of CMO and AC-CMO. It is clear from the XRD pattern that both materials contain polycrystalline cobalt molybdenum oxide with monoclinic crystal structure. The sharp diffraction peak at 26.58° corresponds to the reflection of (012) plane. The

other diffraction peaks at 23.45°, 28.58°, 36.49°, 38.58°, 45.04°, 47.04°, 53.8°can be assigned to (0 2 1), (0 1 2), $(\bar{2}\ 2\ 0)$, $(\bar{1}\ 1\ 3)$, (2 0 2), (1 4 1), $(\bar{1}\ 4\ 2)$, (1 1 3) planes respectively.

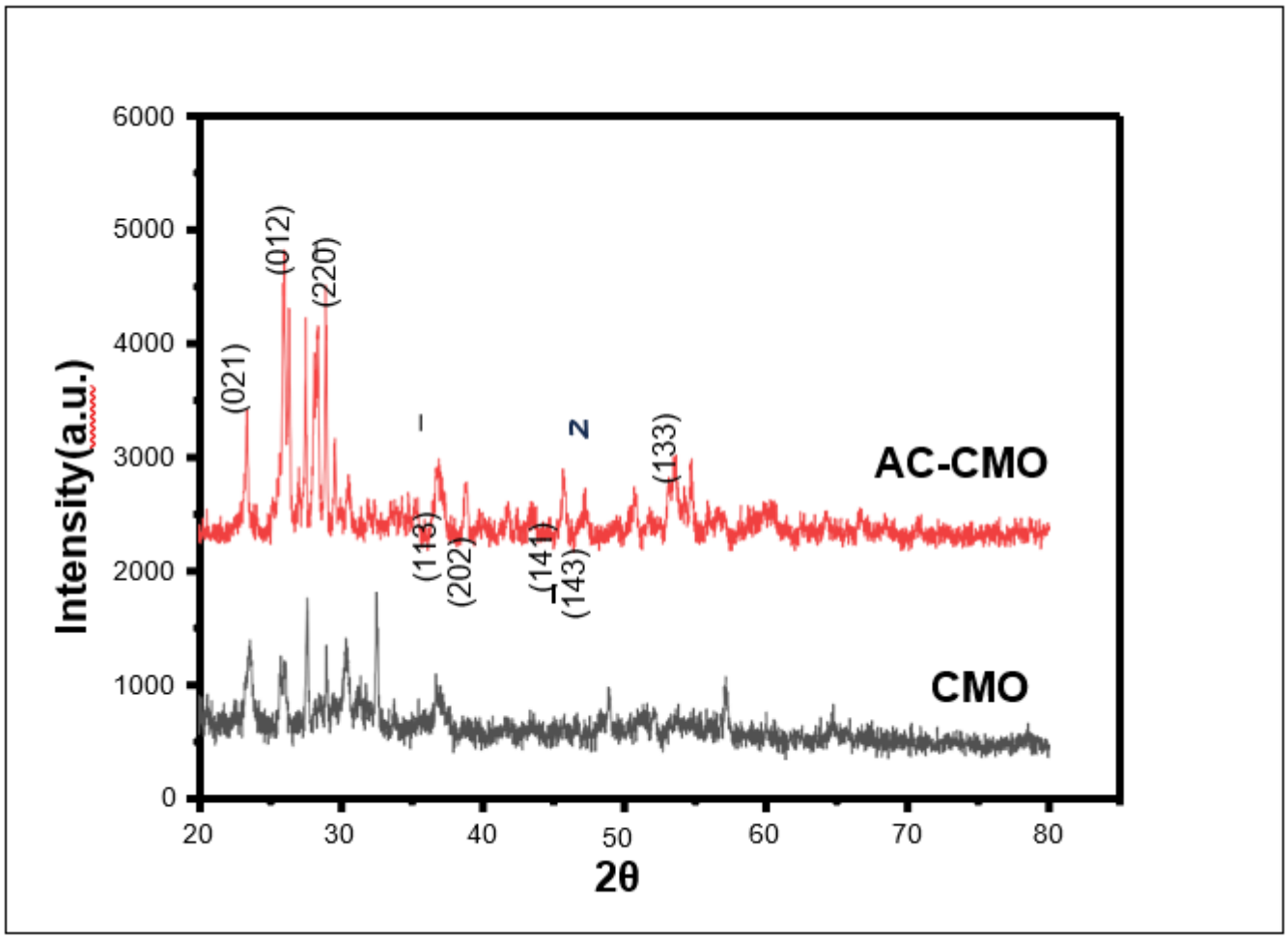

Figure 2 XRD graph of CMO and AC-CMO

The diffraction peaks of the samples can be ascribed to cobalt molybdate and are well matched in concordance with the standard JCPDS (card no. 26-0477). No peaks due to impurities or other residuals was observed for CMO, indicating hight purity of synthesized nanostructure. Further, the crystallinity of the hybrid material (AC-CMO) was comparatively higher than the CMO. The broad and weak diffraction peaks pattern evidenced small crystallite size and poor crystallization nature of the samples.

In present work, the crystal structures of thin films were analysed by using X-ray diffraction (XRD) patterns recorded with the Bruker D8 X-ray diffractometer in the 2□ = 20° – 80° range. X-ray tube with Cu anode (□ = 1.5406 Å) was operated at 30 kV and 20 mA.

Raman Spectroscopy

Raman spectroscopy is an amazing platform to discuss and learn about the vibrational modes and molecular chemistry such as chemical bonding and intramolecular bonds of molecule [14]. Raman measurement was carried out from 300 to 1800 cm^{-1} as shown in figure 3 , peaks present till 1000 cm^{-1} assigns to $CoMoO_4$ whereas peaks after 1000 cm^{-1} shows the presence of activated carbon. The peak position of $CoMoO_4$ nanostructure and activated carbon at 331, 359, 517, 878 and 935 cm^{-1}. Pasquan et al. the strong peak of pure $CoMoO_4$ at 935 cm^{-1} and the weaker band range is seen between 700-880 cm^{-1} [15]. Peak aroused at 1321 and 1585 cm^{-1} correlates with E2g mode of activated carbon which is directly linked to the vibration of Sp^2- bonded carbon atoms in 2D

hexagonal lattice. Raman bands present at 359, 874 and 940 cm^{-1} suggest Mo-O-Co stretching vibrations in Cobalt Molybdate. These main bands of pure $CoMoO_4$ and $CoMoO_4$/activated carbon suggest the thriving synthesis of $CoMoO_4$ is confirmed.

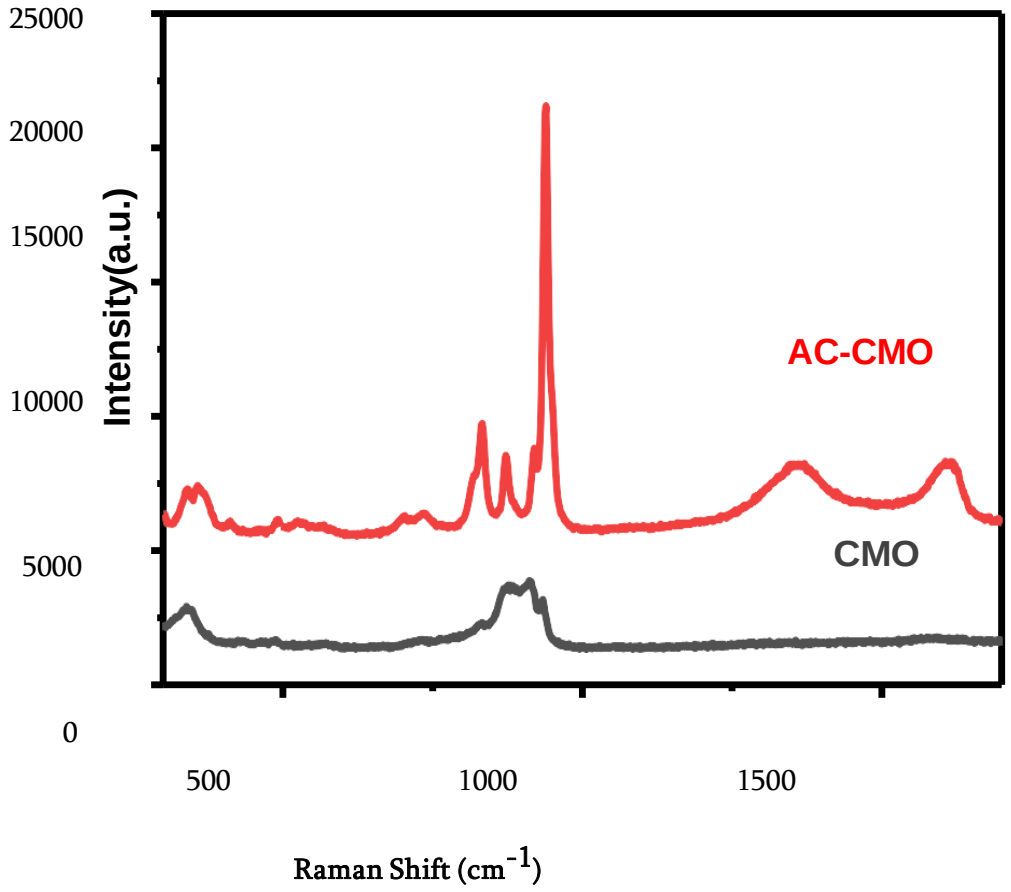

Figure 3 Raman Spectroscopy graph of CMO and AC-CMO

In the present work, Raman measurements were carried out micro-Raman microscope Renishaw (invia). The laser of wavelength of 532 nm with the power of 6 mW is operated from wave number range 200 to 3200 cm^{-1} (with resolution of 1 cm^{-1}) to obtain the Raman spectra of the thin films.

V. CONCLUSION

The synthesis of $CoMoO_4$ (CMO) and the activated carbon- $CoMoO_4$ was achieved through a facile co-precipitation method Material characterization such as XRD and Raman spectroscopy have provided invaluable insights into the structural nuances of the synthesized materials, The XRD pattern revels that both materials contain polycrystalline cobalt molybdenum oxide with monoclinic crystal structure The broad and weak diffraction peaks pattern evidenced small crystallite size and poor crystallization nature of the samples. Raman Spectroscopy identifies vibrational modes, CMO exhibits a uniform and well-defined nanostructure with an average particle size of around 20 nanometers.

VI.REFERENCES

1. Monshi, A., et al., *Modified Scherrer equation to estimate more accurately nano- crystallite size using XRD.* 2012. **2**(3): p. 154-160.
2. Lyon, L.A., et al., *Raman spectroscopy.* 1998. **70**(12): p. 341-362.

3. Villa, P., et al., *Study of the interaction between CoMoO4 and 341-1341-1341-1-Al2O3 by Raman spectroscopy.* 1974. **1**(3): p. 341-344.
4. Pawley, J.J.S.-N.Y. and B.B.T. MAHWAH-, *The development of field-emission scanning electron microscopy for imaging biological surfaces.* 1997. **19**: p. 324-336.
5. Veerasubramani, G.K., et al., *Synthesis, characterization, and electrochemical properties of CoMoO4 nanostructures.* 2014. **39**(10): p. 5186-5193.
6. Kissinger, P.T. and W.R.J.J.o.c.e. Heineman, *Cyclic voltammetry.* 1983. **60**(9): p. 702.
7. Cullity, B.D., *Elements of X-ray Diffraction*. 1956: Addison-Wesley Publishing.
8. Zak, A.K., et al., *X-ray analysis of ZnO nanoparticles by Williamson–Hall and size– strain plot methods.* 2011. **13**(1): p. 251-256.
9. Mote, V., et al., *Williamson-Hall analysis in estimation of lattice strain in nanometer- sized ZnO particles.* 2012. **6**: p. 1-8.
10. Li, J. and J.J.A.o.c.r. Sun, *Application of X-ray diffraction and electron crystallography for solving complex structure problems.* 2017. **50**(11): p. 2737-2745.
11. Nath, D., et al., *X-ray diffraction analysis by Williamson-Hall, Halder-Wagner and size- strain plot methods of CdSe nanoparticles-a comparative study.* 2020. **239**: p. 122021.
12. Vorokh, A.S.J.H.ф., химия, математика, *Scherrer formula: estimation of error in determining small nanoparticle size.* 2018. **9**(3): p. 364-369.
13. Monshi, A., et al., *Modified Scherrer equation to estimate more accurately nano- crystallite size using XRD.* 2012. **2**(3): p. 154-160.
14. Lyon, L.A., et al., *Raman spectroscopy.* 1998. **70**(12): p. 341-362.
15. Villa, P., et al., *Study of the interaction between CoMoO4 and 341-1341-1341-1-Al2O3 by Raman spectroscopy.* 1974. **1**(3): p. 341-344.

ICRTMS-2024
International e-Conference on Recent Trends in Material Science
In Association with International Journal of Scientific Research in Science and Technology
Volume 11 | Issue 9 | Print ISSN: 2395-6011 | Online ISSN: 2395-602X (www.ijsrst.com)

Review on Copper Oxide (CuO) Based H_2S Gas Sensors

Suyog Surendra Mankar
Department of Physics, Shivramji Moghe Arts, Commerce and Science College, Kelapur, Pandharkawada , Dist. Yavatmal, M.S., India

ABSTRACT

Hydrogen sulfide (H_2S) is an extremely toxic and hazardous gas. It is produced naturally or by human activities. H_2S have adverse effects on humans and the environment. Therefore it is necessary to develop rapid, sensitive, and accurate H_2S gas sensor for ensuring human, industrial and environmental safety. Various methods have been studied to detect H_2S which have some drawbacks. Metal oxide semiconductor (MOS) gas sensors have many advantages including high sensitivity, low cost, low power consumption, tunable performance, fast response speed. This paper gives review on CuO based gas sensor for detection of H_2S.

Keywords- Gas Sensors, Metal oxide semiconductor sensors, sensitivity, tunable performance , response speed

I. INTRODUCTION

With rapidly increasing industrialization and modernization there arises some environmental problems including various types of pollutions such as air pollution, water pollution , soil pollution etc. Among all these air pollution is one of the leading causes of various diseases. Carbon monoxide , nitrogen oxides, sulfur oxides, volatile organic compounds and other toxic gases are the main cause of air pollution. Hydrogen sulfide (H_2S) mainly comes from human activities, industry , paper manufacturing, oil refining, metal smelting,, rubber, dyes, pharmaceuticals and other industrial production processes and volcanic eruptions, biological decay. Hydrogen sulfide (H_2S) is a colorless, flammable, acidic, and toxic gas that smells like rotten eggs. H_2S have adverse effects on humans and the environment. Therefore it is necessary to develop rapid, sensitive, and accurate H_2S gas sensor for ensuring human, industrial and environmental safety.

Various methods have been studied to detect H_2S, including surface acoustic wave method, electrochemical method, optical analysis method and gas chromatography . Slow detection speed, complex equipments or high cost are the various limitations of these methods which restrict them to limited use in for industrial or environmental monitoring. Metal oxide semiconductor (MOS) gas sensors have many advantages including high sensitivity, low cost, low power consumption, tunable performance, fast response speed. These advantages of Metal oxide semiconductor (MOS) gas sensors attracts the attention of researchers to develop gas sensors based on metal oxides.Many n-type semiconductors and p-type semiconductors materials like ZnO,

In_2O_3, WO_3, TiO_2, Fe_2O_3, MoO_3, SnO_2, NiO, Co_3O_4, Mn_3O_4, CuO etc are used for making gas sensors. Due to its unique properties like low cost, non toxic nature and abundant availability copper oxide nanomaterials have attracted more attention in various applications. CuO (Cupric Oxide) is important oxide compound of copper. CuO is p-type semiconducting material with a narrow bandgap of 1.2 eV. High chemical stability and chemical sensitivity to gases, CuO attracted much attention as gas sensors. Nanoparticles CuO and its composite oxides have potential applications as gas sensor. The gas-sensing behavior of CuO has been studied under exposure to various gases such as NO_2, CO_2, H_2S, NH_3 CO and different volatile organic compounds. The CuO-based gas sensors are use in various fields, including the automotive industry, in exhaled breath analyzer environmental pollution detectors etc.Microwave assisted co-precipitation method, chemical precipitation method , sol gel combustion route , simple precipitation method, sonochemical method etc. are used for preparation of nanostructures of CuO like nanowire, nanorod, nanoneedle, nano-flower and nanoparticles.

Review of work on CuO based H_2S sensors.

Iqbal S Naji [1] prepared CuO-doped SnO_2 thin films prepared by pulsed-laser deposition. Findings shows that CuO ratio in the SnO_2 films and operation temperature affects the H_2S sensing properties of samples. It was found that 10% and 15% doped CuO is extremely sensitive to H_2S and the best operation temperature is 50^0C. Fang Peng et.al. [2] worked on CuO/WO_3 composites for H_2S sensing. The response of CuO/WO_3 composites changes from p-type to n-type as the CuO content decreases. In case of CuO/WO_3 composites gas sensors different working mechanisms like CuS formation mechanism, weakening mode of n-p type , the H_2S oxidation mechanism, barrier modulation shows their combine effect on response phenomena to H_2S gas. Yempati Nagarjuna and Yu-Jen Hsiao [3] prepared CuO/ZnO Heterojunction Nanostructured Sensor Prepared on MEMS Device for Enhanced H_2S. ZnO nanostructure was prepared using hydrothermal process and CuO films were deposited on the ZnO nanostructure using RF sputtering process. CuO coated ZnO MEMS device is tested for H_2S gas at 200 °C temperature. The sensor exhibited good sensitivity towards H_2S gas than other gases (SO_2, CO, NH_3 and ethanol) at the operating temperature of 200 °C. A surface acoustic wave (SAW) H_2S gas sensor based on CuO-TiO_2 p-n heterojunction film was designed and fabricated by Wei Wu et al [4] The sensor exhibits high sensitivity to H_2S due to the significant current response of CuO-TiO_2 film to H_2S gas. This SAW sensor also shows good selectivity and stability to H_2S with stable frequency shift under different humidity levels. Jianghao Wang et al [5] prepared copper oxide nanoflower/cobalt tetroxide nanofiber (CuO/Co_3O_4) composites by hydrothermal method and electrospinning technology for H_2S gas sensor. According to their study, the improvement of H_2S gas sensing properties of CuO/Co_3O_4 sensor was mainly due to the larger specific surface area brings more active sites, which promotes the adsorption of gas on the material surface. Jesse Nii Okai Amu Darko et al [6] Synthesize unique double-shelled hollow MOF based TiN–CuO nanoparticles by using a two-step technique involving co-precipitating and calcination. to fabricated sensor that exhibits high selectivity and response towards H_2S gas. The related sensor had high selectivity and stability towards H_2S, and the response of TiN/CuO-2 is still 2.5–5 ppm H_2S.

Feng et al [7] synthesized gas sensing materials of mesoporous MoO_3/CuO/g-C_3N_4 by a facile hydrothermal strategy which possessed high response and ultra-low LOD to H_2S at room temperature. They found that the excellent gas sensing properties were due to the larger specific surface area that can enable more gases to be adsorbed on the material surface. The oxygen vacancy reduces the energy required to adsorb the target gas and the formed heterojunctions by MoO_3/CuO/g-C_3N_4 expedite carrier migration. Zhenhua Li et al [8] prepared

CuO composite ZnO nanoparticles by a novel liquid phase synthesis method.The gas sensing test conducted show that the synthesized CuO/ZnO has significantly enhanced sensing performance to H_2S which is mainly due to the formation of p-n heterojunction and the strong chemical affinity and catalytic performance of CuO for H_2S. The highest response to 10 ppm H_2S is 941 at a relatively low working temperature of 175 °C. Lili Sui et al [9] Prepared novel hierarchical CuO/NiO nanowall arrays film sensor by one-step hydrothermal route without any surfactant or template. he 2.84 at % CuO decorated NiO sensor exhibits excellent sensing properties at 133 °C. The response to 5 ppm H_2S attains 36.9, which increases as high as 5.6 times compared to the NiO one. The CuO/NiO sensor shows a wide linear range from 50 to 1000 ppb, good repeatability, selectivity and long-term stability, Sihan Li et al [10] synthesized a bamboo-like CuO/In2O3 heterostucture by using novel MOF-derived method for H2S detection. It was found that The CuO/In_2O_3 (3.5 wt%) based sensor exhibits outstanding gas sensing performances toward H_2S. They also found excellent H_2S response (R_{air}/R_{gas} = 229.3–5 ppm), which are 8.5 times higher than that of with pristine In_2O_3. It also discloses low detection limits (200 ppb), low operating temperature (70 °C) and superior selectivity against other interfering gases. Caixuan Sun et al [11] prepared hollow-rounded cubes composed of copper oxide (CuO)-sensitized amorphous zinc stannate (zinc tin oxide (ZTO)) by a coprecipitation method combined with an impregnation treatment. They found that compared with the ZTO- and CuO-based sensors, the CuO/ZTO-based sensor exhibited excellent gas-sensing performance toward H2S, with a maximum response value of 574–10 ppm H_2S and a low operating temperature of 160 °C. Their findings indicate that the CuO/ZTO composite is promising as an H_2S-sensing material with potential applications in the field of environmental air monitoring.

Conclusion

From the review of different papers it can be concluded that CuO nanomaterials exhibited good response to various gases, large active surface area and semiconducting nature makes it promising material to be developed for an efficient H_2S gas sensor. With the help of different chemical synthesis procedures the structural and physical properties of CuO can be modified. Particle size of the material determines the sensitivity and response time of CuO based sensors. It is also found that sensitivity of sensor enhances by using various dopants and composite materials.

References

[1] Characterization of CuO-doped tin dioxide thin films prepared by pulsed-laser deposition for gas-sensing applications, Iqbal S Naji, Proc IMechE Part N: J Nanoengineering and Nanosystems 233(1), 2019.

[2] Gas Sensing Performance and Mechanism of CuO(p)-WO3(n) Composites to H2S Gas, Fang Peng , Yan Sun , Weiwei Yu , Yue Lu , Jiaming Hao , Rui Cong , Jichao Shi , Meiying Ge and Ning Dai, Nanomaterials 2020,

[3] CuO/ZnO Heterojunction Nanostructured Sensor Prepared on MEMS Device for Enhanced H_2S Gas Detection, Yempati Nagarjuna and Yu-Jen Hsiao, Journal of The Electrochemical Society, 2021

[4] P-CuO/n-TiO_2 heterojunction nanostructure-based surface acoustic wave sensor with strong electric loading effect for highly sensitive H_2S gas sensing, Wei Wu , Jingyu Long , Yuanjun Guo , Xiaotao Zu , Sean Li , Xia Xiang, Sensors and Actuators B: Chemical Volume 394, 2023,

[5] Fast-response hydrogen sulfide gas sensor based on electrospinning Co_3O_4 nanofibers-modified CuO nanoflowers: Experimental and DFT calculation,

Jianghao Wang , Dongzhi Zhang , Yonghai Gao , Fengjiao Chen , Tian Wang , Hao Xia , Xiaoxiao Sui , Zihu Wang, Sensors and Actuators B: Chemical Volume 396, 2023

[6] Exploring the gas-sensing properties of MOF-derived TiN@CuO as a hydrogen sulfide sensor, Jesse Nii Okai Amu Darko, Shahid Hussain, Xiangzhao Zhang, Mohamed Ouladsmane, Eliasu Issaka , Salman Ali , Mingsong Wang , Guanjun Qiao, Chemosphere, Volume 337, October 2023

[7] A room-temperature ppb-level H_2S sensor based on MoO_3/CuO/g-C_3N_4 via a simple synthesis , Feng, Congting Zhang ,Chang Xu ,Shuang Lin , Baohua

Zhang, Huanxing Wu , Zheng Zhang , Xinming Guo , Haineng Bai , Fuqiang Guo, Sensors and Actuators B: Chemical, Volume 374, 2023,

[8] Metal-organic framework-derived ZnO decorated with CuO for ultra-high response and selectivity H_2S gas sensor, Zhenhua **Li** , Lanlan **Guo** , Zeyao **Feng** ,

Siyuan **Gao** , Hao **Zhang** , Xueli **Yang** , Hongyan **Liu** , Junkai **Shao** , Caixuan **Sun** , Yehong **Cheng** , Guofeng **Pan, Sensors and Actuators B: Chemical, Volume 366, 1 September 2022, 131995**

[9] In situ deposited hierarchical CuO/NiO nanowall arrays film sensor with enhanced gas sensing performance to H_2S, Lili Sui , Tingting Yu , Dan Zhao , Xiaoli Cheng , Xianfa Zhang , Ping Wang , Yingming Xu , Shan Gao , Hui Zhao , Yuan Gao , Lihua Huo, Journal of Hazardous Materials,Volume 385, 2020

[10] Metal-Organic frameworks-derived bamboo-like CuO/In_2O_3 Heterostructure for high-performance H_2S gas sensor with Low operating temperature, Sihan Li , Lili Xie , Meng He , Xiaobing Hu , Guifang Luo , Cheng Chen , Zhigang Zhu, Sensors and Actuators B: Chemical, Volume 310, 2020

[11] CuO-sensitized amorphous $ZnSnO_3$ hollow-rounded cubes for highly sensitive and selective H_2S gas sensors, Caixuan Sun , Junkai Shao , Ziyan Wang , Hongyan Liu , Zhenhua Li , Hao Zhang , Tianyu Bai , Yawei Sun , Lanlan Guo , Guofeng Pan , Xueli Yang, Sensors and Actuators B: Chemical, Volume 362, 2022

ICRTMS-2024
International e-Conference on Recent Trends in Material Science
In Association with International Journal of Scientific Research in Science and Technology
Volume 11 | Issue 9 | Print ISSN: 2395-6011 | Online ISSN: 2395-602X (www.ijsrst.com)

Electrical Conductivity of Polymer Blend Dopped with Ammonium Bromide

S. R. Jadhao[1*], S. P. Bakde[2]

[*1]Department of Physics, Nehru Mahavidyalaya , Arts, Commerce &Science, Nerpersopant, Dist. Yavatmal, Maharashtra, India.

[2]Department of Physics, Shri R. R. Lahoti Science College Morshi, Dist. Amravati, Maharashtra, India.

ABSTRACT

Solid polymer blend electrolytes of polyvinyl alcohol (PVA) and Polyethylene glycol (PEG) complex with ammonium nitrate (NH_4Br) salt in different compositions have been prepared by solution cast technique using distilled water as a solvent. Prepared sample are subjected to investigate by XRD and electrical properties. Polymeric film AC electrical conductivity was measured using 4284 LCR meter in frequency range of 20Hz to 1MHz and at different temperature range. XRD shows the amorphous nature of the polymer PVA+PEG+NH_4Br. The dielectric constant, dielectric loss and ac conductivity of PVA: PEG has been observed to enhance along with the addition of ammonium bromide at the different frequency and temperature range.

Keywords: Polymer blends, Ammonium salts, Electrical conductivity.

I. INTRODUCTION

Poly (Vinyl Alcohol) (PVA) was widely used owing to its biodegradability, good film formation, non-toxicity, water-solubility, good chemical and thermal stability [1]. Polyethylene glycol (PEG) has low toxicity, flexibility, good chemical and physical characteristics [2]. The blending between PVA and PEG polymers was examined widely to be used in various applications [3-5]. Some modifications of the existing polymers, products with low cost and light weight may be developed for a wide range of applications with desirable properties such as mechanical, thermal, and optical properties. This makes them suitable as replacements for other traditional engineering materials such as metals. Blending is a simple and effective method to develop new materials with tailored properties. In the present work, the polymer blend electrolytes were subjected to XRD and electrical conductivity investigation.

II. METHODS AND MATERIAL

The solid polymer electrolyte of pure (PVA + PEG) with Ammonium Bromide were prepared in different concentration (95:05), (85:15), (75:25) by solution casting technique. In this technique, PVA and PEG were dissolving in water separately. After dissolving same concentration of PAV + PEG mix with ammonium bromide salt then stirred well by using magnetic stirred for 10-12 hr to obtained homogenous mixture. The obtained mixture is casted in petri dish. The whole assembly was placed in dust free chamber. The solvent was allowed to evaporate slowly at room temperature for 3-4 days. The dried blend solid polymer electrolyte films were formed. The AC conductivity were measured using 4284 LCR meter in frequency range of 20Hz to 1MHz and at different temperature.

III.RESULTS AND DISCUSSION

XRD (X-ray Diffraction Pattern)

The x-ray diffraction analysis is a powerful tool to determine the structure and crystallization of the polymer matrices. In order to investigate the effect of blending, XRD analysis has been performed and their respective diffraction patterns of polymer blend and complex ammonium bromide system are compared.

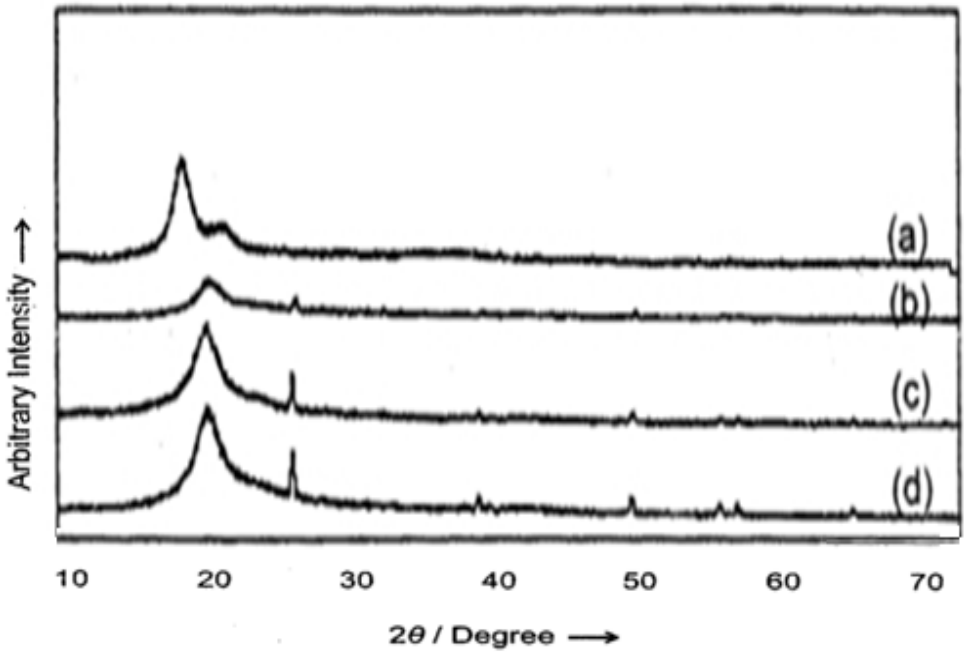

Fig 1: XRD spectra of (a) PVA-PEG (b) 5 mole %, (c) 15 mole %, (d) 25 mole % of NH_4Br.

Fig1. shows the XRD patterns of pure PVA+PEG and complex with ammonium bromide. The patterns revealed that all samples have the characteristics diffraction peak at about 2θ covering the 2θ range 16-25 get slightly shifted in the complex PVA+PEG+NH_4Br. Fig 1. shows the broad peak at 2θ =20° which shows the amorphous nature of the polymer PVA+PEG+NH_4Br [6].

Electrical Properties

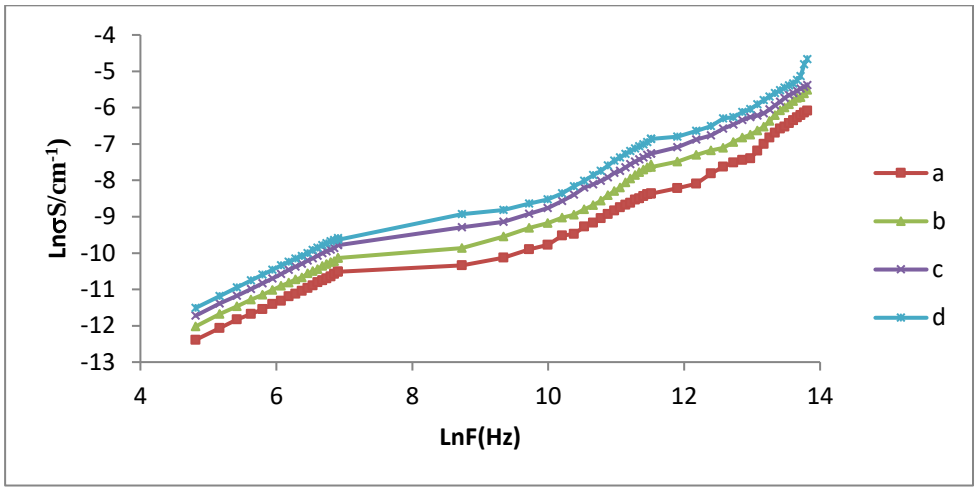

Fig 2: Variation of AC conductivity with frequency (a) PVA-PEG (b) 5 mole %, (c) 15 mole %, (d) 25 mole % of NH_4Br.

The fig. 2 shows that the variation between AC conductivity with frequency for (a) PVA:PEG, (b) PVA:PEG:NH_4Br (95:05) and (c) PVA:PEG:NH_4Br (85:15), PVA:PEG:NH_4Br (75:25). It is observed that the conductivity increases with an increase of frequency in all composition due to more number of free ions. This will increase mobile of charge carrier. [7-8]. It found that conductivity of PVA:PEG blend increases with increase in salt concentration upto 25 mol% due to enhancement of ionic mobility and the large number of carrier ions being introduced into the complex [10-11].

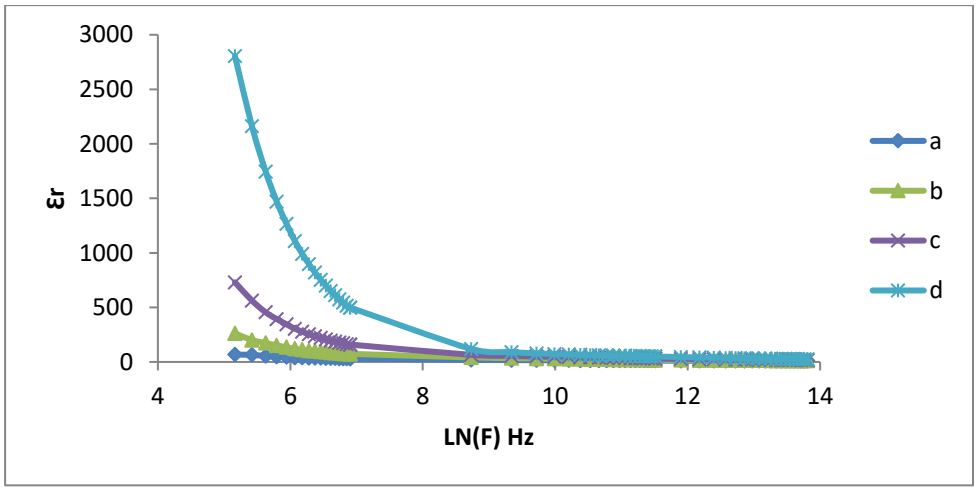

Fig 3: Variation of Dielectric constant with frequency (a) PVA-PEG (b) 5 mole %, (c) 15 mole %, (d) 25 mole % of NH_4Br.

The frequency dependent dielectric constant of PVA-PEG-NH_4Br mole % as shown in (figure 3) . It is observed that dielectric constant is high at low frequency. Due to contribution of charge accumulation at electrode-

electrolyte interface. But in high frequency dielectric constant decreases and nearly constant value with increases in frequency. This is due to the dipole not being able to follow apposite of electric field variation at higher frequency [12-13].

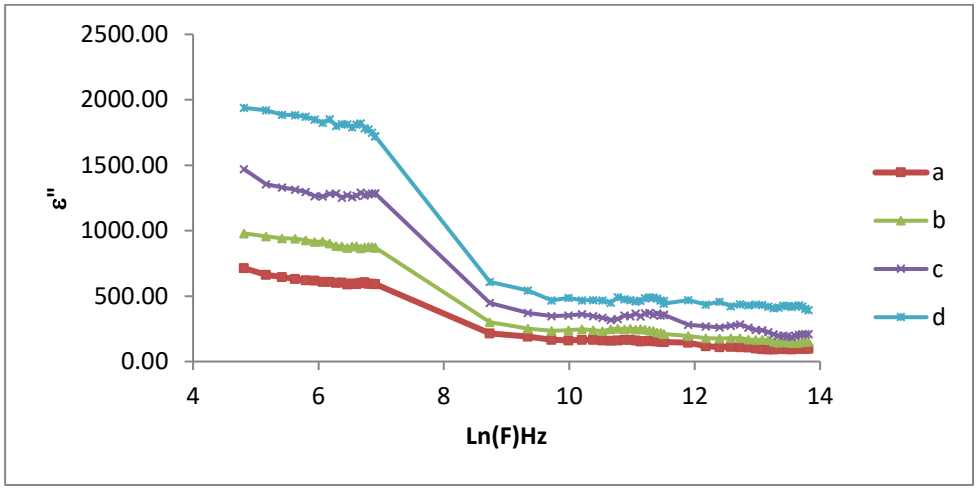

Fig 4: Variation of Dielectric loss with frequency (a) PVA-PEG (b) 5 mole %, (c) 15 mole %, (d) 25 mole % of NH_4Br.

The dielectric loss as a function of frequency is shown in fig 4 shows the dependence of (□") on the frequency at room temperature. It is found that the dielectric loss is high at low frequencies and decreases with increase in the frequency. The origins of the dielectric losses are the conduction of losses [14-15].

IV. CONCLUSION

Solid polymer blend electrolytes of polyvinyl alcohol (PVA) and Polyethylene glycol (PEG) complex with ammonium nitrate (NH_4Br) salt in different compositions have been prepared by solution cast technique. . XRD shows the broad peak at 2θ =20° which shows the amorphous nature of the polymer PVA+PEG+NH_4Br. The conductivity of PVA:PEG complexes with ammonium bromide (NH_4Br) increase with increasing frequency and concentration of ammonium salt. The frequency dependant dielectric constant and dielectric loss decreases with increase in frequency. It is reveal that electrical conductivity of PVA-PEG doped with NH_4Br increases with increasing salt concentration as well as temperature, which is attributed to the formation of charge transfer complexes.

V. REFERENCES

1. Heiba Z. K. et al., (2022), Alexandria Engineering Journal Volume 61, Issue 5, Pages 3375-3383.
2. Mohamed Bakr Mohamed , Abdel-Kader M. H., (2020), Materials Chemistry and Physics Volume 241, 122-285.
3. Swift G., (1994), Polymer Degradation and Stability, 45 (2), 215–231.
4. Braun D. B. & Delong D. J., (1982), Kirk-Othmer Encyclopedia of Chemical Technology, 3rd edn, 18, 616-32.

5. Gowrikar Y. R., Yishwanathan N. Y. & Sreedhar Jayadev, (1986), Polymer Science (Wiley Eastern Limited, New Delhi).
6. Zein K. Heiba, Mohamed Bakr Mohame, Sameh I. Ahmed, (2022), Elsevier, 61, 3375-3385.
7. Billmeyer Jr. F., (1984) Text book of polymer Science , Eiley Singapor.
8. Kumar M., Sekhon S. S., (2002), Eur polymer J 38, 1297-1304.
9. Ramesh S., Arof A. K., (2001), Mater Sci Eng B, 85, 11-15.
10. Pradhan D. K., Chaudhary R. N. P., Samantaray B. K., (2009), Mater Chem. Phys., 11, 557-561.
11. Vijaya N., Selvasekarapandian S., Hirankumar G., Karthikeyan S., Nithya H., Ramya C. S., Prabhu M., (2011),Ionics, 18, 91-99.
12. Palaa S. L., Varmaa S. N., Krishna Jyothib N. and KumarcJ K. V., (2019), Indian Chem. Soc., 96, 182-184,.
13. Ibrahim S., Yasin S. M. M., Nee N. M., Ahamad R., (2012), Johan M. R, solid state commun, 426-434.
14. Ramesh S., Yahana A. H., Arof A. K., (2002), solid state Ionics, 291-294.
15. Zareh E. H., P. N. Moghadam, E. Azarian, I. Sharifia, (2011), Iranian polymer Journal, 20 (4), 319-328.

ICRTMS-2024
International e-Conference on Recent Trends in Material Science
In Association with International Journal of Scientific Research in Science and Technology
Volume 11 | Issue 9 | Print ISSN: 2395-6011 | Online ISSN: 2395-602X (www.ijsrst.com)

Mini Review on Artificial Intelligence and Smart Sensors in Modern Farming

Ranjeet R. Mistry
Department of physics, Deogiri College, Chhatrapati Sambhajinagar, Maharashtra, India

ABSTRACT

Artificial Intelligence (AI) is one of the fastest growing technologies in this modern world. AI technology has undeniable scopes in health care devices, self driving vehicles, satellite imaging, landscape mapping, climate change monitoring, and health care systems. AI employs a variety of smart sensors that process data in real time with higher accuracy. Agriculture is an essential sector needed for survival of the human community. Several measures have been taken to enhance the crop production. However harsh environmental conditions and frequent pest infestation lead to the agricultural loss. In such scenario, integration of advanced technologies such as advanced sensors coupled with artificial Intelligence could escalate the agricultural production and minimize the economic loss. AI-smart sensors in monitoring environmental factors such as moisture, humidity, temperature, and soil composition that are critical for crop growth. Smart farming also enables measurement of nitrogen contents in soil that helps farmers to determine the amount of fertilizers to be used in farm lands. Some AI-enabled equipments and unmanned aerial vehicles are useful in accurate surveillance of pest attack and associated diseases in farm vegetation. Though the smart farming has great scopes in future, it faces certain limitations related to high implementation cost, data security, and lack of sufficient AI knowledge in farmers. Special economic policies, data encryption, and digital literacy could ease AI-enabled smart farming in future.
Keywords: Smart Sensor, AI, Agriculture, advanced technologies.

I. INTRODUCTION

Artificial Intelligence (AI) stands as one of the most rapidly advancing technologies in today's world. Its application spans across numerous industries [1], including healthcare devices, autonomous vehicles, satellite imaging, landscape mapping, climate change monitoring, and healthcare systems [2]. The proliferation of AI has led to significant advancements in robotics worldwide, substantially improving quality of life and well-being. The integration of AI-driven automation, particularly in sectors like agriculture, promises the production of high-quality goods with minimal environmental impact [3]. Utilizing a diverse array of smart sensors, AI processes data in real-time with unparalleled accuracy, paving the way for the development of advanced wireless systems. This technology has permeated nearly every domain of science and research, fostering innovation and the creation of novel models for consumer product development, including agricultural products [4].

Agriculture remains a fundamental pillar of human society, continuously evolving to bolster agricultural yields. Incorporating modern technologies in agriculture, horticulture, and forestry has enabled more

effective monitoring of plant growth, diseases, and pest populations. AI-enabled equipment in agriculture addresses various challenges, such as soil conditions, weather monitoring, pest detection, and optimal harvest timing [5]. By leveraging AI-enabled equipment and a variety of smart sensors, farmers can better manage crops and vegetables across large areas in shorter timeframes [6-11]. The implementation of AI-enabled equipment technology holds the potential to reduce resource wastage and enhance farmers' revenues significantly. Additionally, the integration of the Internet of Things (IoT) and smart sensors with existing devices can further improve agricultural production by facilitating accurate diagnosis of crop diseases [12]. Precision farming utilizes AI-enabled equipment technology to monitor agricultural factors, providing real-time data on crop, soil, water, and air conditions to protect the environment and sustain agricultural production [13]. Transforming irrigation into a smart irrigation system can expedite the irrigation process, while unmanned aerial vehicles (UAVs) collect crucial data on factors like pest infestations, soil quality, and water availability across vast areas in minimal time [13]. Smart greenhouse technology presents promising opportunities for cultivation with minimal human intervention. Continuous sensor-based monitoring of temperature, humidity, luminance, and soil moisture optimizes yield while minimizing agricultural damage [14]. Automated sensors enable informed decision-making to implement corrective measures efficiently. The Farm Management System (FMS), AI-enabled equipment technology offers a comprehensive tracing system to analyze various agricultural factors, enhancing both quality and quantity of agricultural production with minimal manpower and real-time data processing [14]. AI-enabled equipment technology, supported by intelligent decision-making systems, reduces human intervention in agricultural management, ensuring greater efficiency and accuracy in automated agricultural operations. Furthermore, AI-enabled equipment technology generates vast amounts of data, necessitating fast and efficient data analysis. AI algorithms, such as the optimal mobile network-based convolution neural network model (OMNCNN), excel in detecting plant diseases through stages like preprocessing, segmentation, feature extraction, and classification [15]. To predict soil properties like moisture and organic matter content, proximal soil sensors coupled with computer vision and machine learning algorithms offer quick, accurate, and non-destructive predictions. Various models, such as Exponential Gaussian Process Regression and Cubist models, demonstrate excellent performance in predicting soil properties [16]. Deep learning frameworks like convolution neural networks (CNNs), Recurrent Neural Networks (RNNs), Random Forests (RF), Deep Fully Connected Neural Networks (DFNN), and LASSO are extensively utilized to predict crop yields. For instance, a CNN-RNN model achieved remarkable accuracy in predicting average corn and soybean yields in the United States [17]. In summary, AI holds significant promise in enhancing the efficacy and accuracy of AI-enabled equipment technology deployed in agriculture. This article aims to explore the potential implications of AI-enabled equipment technology and smart sensors in monitoring various physicochemical factors like humidity, temperature, moisture content, nitrogen levels, soil quality, and greenhouse gases in agricultural lands.

AI-ENABLED EQUIPMENT-BASED TECHNOLOGY AND AGRICULTURE

AI-enabled equipment-based technology and smart sensors offer significant potential for acquiring real-time data and interpreting them to monitor soil health, water content, crop quality, and production on agricultural sites [18]. By replacing conventional agricultural methods, smart farming, characterized by enhanced yield, is becoming increasingly prevalent. These technologies facilitate the assessment of soil

health, erosion, fertilizer requirements, soil fertility, and crop quality [19]. They also support seed quality assessment, optical irrigation, and surveillance of crop growth at various stages. Real data obtained from remote sensing and AI-enabled equipment-based technology can be processed for precision agriculture and forestry. Innovative approaches such as infrared thermography coupled with smart sensors enable the sensing of topological data in agricultural land. Furthermore, AI-enabled equipment-based technology and smart soil moisture sensors are employed for pre-harvesting and post-harvesting assessments in agricultural lands. Microbial presence in agricultural products poses challenges to global populations [20–22], and microfluidics-based on-chip artificial pores enable the onsite detection of pathogens [23]. Deep learning approaches aid in interpreting data acquired from multiple sensors. Utilizing technologies like ZigBee and Arduino sensors, AI-enabled equipment-based technology allows for precise assessment of temperature, moisture, soil status, and crop types in specified areas [25]. Consequently, data analysis by AI-enabled equipment-based technology can facilitate planned increases in agricultural and crop yields. UAVs, combined with AI-enabled equipment, are key components of smart farming, requiring minimal manpower while enhancing yield. Sensors deployed in fields gather information on environmental parameters such as temperature, humidity, soil moisture, and nutrient levels, forming the basis of AI-enabled equipment-based smart crop monitoring systems. These networked sensors transmit real-time data to centralized cloud-based platforms, enabling farmers to make informed decisions on crop management, including irrigation, pest control, and harvesting. Wireless sensor technologies alert administrators and farmers to equipment faults, initiating troubleshooting. Additionally, automated repair tools contribute to energy conservation, streamlined data processing, and improved actuation [26]. AI-enabled equipment-based smart sensors accurately monitor environmental factors such as temperature, moisture, and humidity. Some sensors assess soil quality by determining nitrate levels and water content. High-resolution cameras coupled with GPRS systems detect plant diseases and insect pests, while UAV-based surveillance monitors crop growth and farm land topology. Automated mass flow sensors estimate crop production.

SENSORS FOR SMART FARMING

Various sensors are emerging with implications for smart farming, aiding in automated harvesting, environmental monitoring, and crop measurement. AI-enabled equipment-based technology-based sensors in farm lands sense critical factors like temperature, humidity, and nutrient contents, transmitting data to communication gateways such as cloud servers, satellites, and computing systems for analysis, decision-making, and necessary actions.

Smart sensors, when coupled with components like amplifiers, transducers, analog-to-digital converters, and analog filters, enhance their performance. Acoustic-based sensors detect changes in sound frequencies, enabling the detection of sounds generated by various insects during movement, feeding, and mating events [27]. Data collected by acoustic devices are transferred to global databases for analysis by researchers, facilitating the development of automated acoustic sensors for accurate pest detection at the species level [28]. Electromagnetic sensors detect agricultural soil and contamination, mapping topological features of agricultural lands by detecting electromagnetic waves from various objects. Techniques such as electromagnetic induction, ground-penetrating radar, and gamma radiometric devices, deployed through unmanned flying vehicles, provide high-resolution insights into surface processes and vegetation types. Ground-penetrating radar and electromagnetic induction estimate soil-water content [29]. Electrochemical sensors, lightweight, eco-friendly, monitor plant growth, diseases, and environmental pollution accurately in real-time. These sensors have

minimal environmental impact and have been tested for critical biochemical parameters affecting agricultural yields. For instance, humidity sensors containing graphene oxide sense plant leaf water, while NO_2 sensors detect toxic gases in agricultural fields. Optical sensors, based on their ability to detect light of various wavelengths, gather information on weed distribution in agricultural fields [30]. Optical sensors coupled with spectroscopy accurately detect cells infected with green weeds, providing valuable data for weed management [31].

CHALLENGES AND FUTURE POSSIBILITIES

Global studies on internet and smart sensor-based modern farming have yielded satisfactory results. However, significant challenges remain, including the financial costs associated with installing internet-tagged sensors and accessories over large agricultural areas. Outdoor installation exposes internet-based devices to harsh environmental conditions, potentially leading to mechanical failure. Moreover, a global drive to enhance technology literacy among farmers is necessary for the widespread adoption of internet technology in farming. Government policymakers must formulate economic policies to support the successful implementation of internet-based farming.

CONCLUSION

AI-enabled equipment-based smart farming holds great promise for the future, with smart sensors employed to monitor environmental factors for maximum agricultural yield. AI-enabled devices aid in measuring moisture and nitrogen content in soil, as well as monitoring CO_2 levels to ensure better crop health. Despite these advantages, challenges such as the high purchase and maintenance costs of sophisticated hardware and software, along with limited technology literacy among rural farmers, hinder the widespread adoption of AI-enabled equipment-based smart sensors in agriculture.

REFERENCES

[1] Q. Guo, M. Ren, S. Wu, Y. Sun, J. Wang, Q. Wang, Y. Ma, X. Song, Y. Chen, Applications of artificial intelligence in the field of air pollution: a bibliometric analysis, Front. Public Health 10 (2022),933665.

[2] T. Davenport, R. Kolkata,The potential for artificial intelligence in healthcare, Future Health J 6 (2019), 94–98.

[3] M.Shepherd, J.A. Turner, B. Small, D. Wheeler, Priorities for science to overcomehurdles thwarting the full promise of the 'digital agriculture'revolution, J. Sci. Food Agric. 100 (2020) 5083– 5092.

[4] L. O'Malley, A. Bronson, K. van der Burg, S.L. Klerkx, The future (s) of digital agriculture and sustainable food systems: an analysis of high-level policy documents, Ecosyst. Serv. 45 (2020), 101183, https://doi.org/10.1016/j. ecoser.2020.101183.

[5] A. Kaloxylos, J. Wolfert, T. Verwaart, C.M. Terol, C. Brewster, R. Robbemond, H. Sundmaker, The use of future internet technologies in the agriculture and food sectors: integrating the supply chain, Proc. Technol 8 (2013), 51–60.

[6] S. Sarkar, P. Rajak, S. Roy, Toxicological evaluation of a new lepidopteran insecticide, flubendiamide, in non-target drosophila melanogaster Meigen (Diptera: drosophilidae), Iran J. Toxicol 12 (3) (2018) 45–50.

[7] M.Dutta, P. Rajak, S. Roy, Determination of chronic median lethal concentration of sodium fluoride in Drosophila melanogaster and exploring effect of sub-lethal concentrations on differential hemocyte count, Proc. Zool. Soc. 72 (2019) 111–117.

[10] P. Rajak, S. Roy, S. Podder, M. Dutta, S. Sarkar, A. Ganguly, M. Mandi, A. Dutta, S. Nanda, S. Khatun, Synergistic action of organophosphates and COVID-19 on inflammation, oxidative stress, and renin-angiotensin system can amplify the risk of cardiovascular maladies, Toxicol. Appl. Pharmacol. 456 (2022), 116267.

[11] P.Rajak, S. Roy, A. Ganguly, M. Mandi, A. Dutta, K. Das, S. Nanda, S. Ghanty, G.Biswas, Agricultural pesticides–Friends or foes to biosphere? J. Hazard. Mater. Adv 10 (2023),100264.

[12] E. Navarro, N. Costa, A. Pereira, A systematic review of IoT solutions for smart farming, Sensors 20 (2020) 4231, https://doi.org/10.3390/s20154231.

[13] D. Gao, Q. Sun, B. Hu, S. Zhang, A framework for agricultural pest and disease monitoring based on internet-of-things and unmanned aerial vehicles, Sensors 20 (2020) 148.

[14] L. Lan, X. Le, H. Dong, J. Xie, Y. Ying, J. Ping, One-step and large-scale fabrication of flexible and wearable humidity sensor based on laser-induced graphene for real-time tracking of plant transpiration at bio-interface, Biosens. Bioelectron. 165 (2020), 112360.

[15] S. Ashwinkumar, S. Rajagopal, V. Manimaran, B. Jegajothi, Automated plant leaf disease detection and classification using optimal MobileNet based convolutional neural networks, Mater. Today Proc. 51 (2022) 480–487.

[16] P. Taneja, H.K. Vasava, P. Daggupati, A. Biswas, Multi-algorithm comparison to predict soil organic matter and soil moisture content from cell phone images, Geoderma 385 (2021), 114863.

[17] S. Khaki, L. Wang, S.V. Archontoulis, A CNN-RNN framework for crop yield prediction, Front. Plant Sci. 10 (2020) 1750.

[18] M. Ayaz, M. Ammad-Uddin, Z. Sharif, A. Mansour, E.-H.M. Aggoune, Internet-of- Things (IoT)-based smart agriculture: toward making the fields talk, IEEE Access 7 (2019) 129551–129583.

[19] R.P. Sishodia, R.L. Ray, S.K. Singh, Applications of remote sensing in precision agriculture: a review, Rem. Sens. 12 (2020) 3136.

[20] P. Rajak, A. Ganguly, Computational study unravels inhibitory potential of epicatechin gallate against inflammatory and pyroptosis-associated mediators in COVID-19, MedComm–Future Medicine 2 (2023).

[21] A. Ganguly, M. Mandi, A. Dutta, P. Rajak, In silico analysis reveals the inhibitory potential of madecassic acid against entry factors of SARS-CoV-2, ACS Appl. Bio Mater. 6 (2023) 652–662.

[22] P. Rajak, A. Ganguly, Silico study unfolds inhibitory potential of epicatechin gallate against SARS-CoV-2 entry and replication within the host cell, Mechanobiology in Medicine (2023), 100015.

[23] W. Su, D. Liang, M. Tan, Microfluidic strategies for sample separation and rapid detection of food allergens, Trends Food Sci. Technol. 110 (2021) 213–225.

[24] S. Roy, F. Arshad, S. Eissa, M. Safavieh, S.G. Alattas, M.U. Ahmed, M. Zourob, Recent developments towards portable point-of-care diagnostic devices for pathogen detection, Sens. Diagn 1 (2022) 87–105.

[25] J.R. Robles, A´. Martin, S. Martin, J. Ruip´erez-Valiente, M. Castro, Autonomous sensor network for rural agriculture environments, low cost, and energy self- charge, Sustainability 12 (2020) 5913.

[26] L. Ruiz-Garcia, L. Lunadei, P. Barreiro, I. Robla, A review of wireless sensor technologies and applications in agriculture and food industry: state of the art and current trends, Sensors 9 (6) (2009) 4728–4750.

[27] R. Mankin, D. Hagstrum, M. Guo, P. Eliopoulos, A. Njoroge, Automated applications of acoustics for stored product insect detection, Monitoring, and Management, Insects 12 (2021) 259.

[28] T.T. Høye, J. A¨rje, K. Bjerge, O.L.P. Hansen, A. Iosifidis, F. Leese, H.M.R. Mann, K. Meissner, C. Melvad, J. Raitoharju, Deep learning and computer vision will transform entomology, Proc. Natl. Acad. Sci. USA 118(2021).

[29] D. De Benedetto, F. Montemurro, M. Diacono, Mapping an agricultural field experiment by electromagnetic Induction and ground penetrating radar to improve soil water content estimation, J. Agron. 9(10)(2019) 638.

[30] A. Freidenreich, G. Barraza, K. Jayachandran, A.A. Khoddamzadeh, Precision agriculture application for sustainable nitrogen management of Justicia brandegeana using optical sensor technology, Agriculture 9 (5) (2019) 98.

[31] J. Barroso, J. McCallum, D. Long, Optical sensing of weed infestations at harvest, Sensors 17 (10) (2017) 2381.

ICRTMS-2024
International e-Conference on Recent Trends in Material Science
In Association with International Journal of Scientific Research in Science and Technology
Volume 11 | Issue 9 | Print ISSN: 2395-6011 | Online ISSN: 2395-602X (www.ijsrst.com)

Agreement of experimental and theoretical values of dielectric parameters of powder turmeric at X-band microwave

S. M. Delmade*[1], A. S. Mule[2], P. G. Gawali[3]
*[1]Asst. Professor, Dept. of Physics, Yeshwant Mahavidyalaya, Nanded, Maharashtra, India
[2]Research scholar, P.G. Dept. of Physics, B.S. College, Basmath, Maharashtra, India
[3]Professor, P.G. Dept. of Physics, B.S. College, Basmath, Maharashtra, India

ABSTRACT

The dielectric parameters of powder turmeric were measured by using X band at 9.85 GHz. The observations are taken with different densities and temperatures. These values are then compared with theoretical formulas of Landau-lifshiz-Looyenga and Bottcher. The fair agreement is found between experimental and theoretical values under consideration that smallest size of turmeric powder is to be 100% solid bulk under specific force.

Keywords: Dielectric Parameters, Microwave X-band, Turmeric.

I. INTRODUCTION

As non-availability of the waveguides for solid materials used in X-band microwave to determine the dielectric wavelength (λ_d) the pulverized form of solid of lowest particle size in micron (50) with compact is considered as solid bulk. Many researchers [1,2] have tried to co-relate the dielectric behaviour of bulk materials with their powders.

The interactions of agriproducts dielectric with microwave energy which depends on the frequency, temperature, compactness of material, moisture content, particle size have been studied [3, 4, 5, 6]

In the paper the dielectric properties of turmeric were determine at various relative packing fraction (δ_r), and temperatures (20^0C, 30^0C, 40^0C, 50^0C). Dielectric constant (ϵ'), Dielectric loss (ϵ''), Relaxation time (τ), conductivity (σ), of turmeric powder were calculated by accurate measurement of dielectric wavelength (λ_d). Then the values of dielectric constant and dielectric loss are co-related with formulae of Landau-Lifshitz-looyenga and Bottcher [7,8]. The turmeric sample variety is procured from Marathwada Agricultural University, Parbhani.

II. METHODS AND MATERIAL

The dielectric constant (ϵ') and dielectric loss (ϵ'') were calculated by accurate measurement of dielectric wavelength (λ_d) by using reflectometric technique of measuring the reflection coefficient from the air dielectric boundary of turmeric sample in the microwave X-band at 9.85 GHz frequency [9].

The Following formulae are used to calculate dielectric constant (ϵ') and dielectric loss (ϵ'')

$$\epsilon' = \left(\frac{\lambda_0}{\lambda_c}\right)^2 + \left(\frac{\lambda_0}{\lambda_d}\right)^2 \quad \text{------(1)}$$

$$\epsilon^{"} = \frac{1}{\Pi}\left(\frac{\lambda_0}{\lambda_c}\right)^2 (\alpha_d \lambda_d) \quad \text{------(2)}$$

λ_0 is the free space wavelength
λ_d is the dielectric wavelength
λ_c is cutoff wavelength of waveguide
α_d is the attenuation introduced per unit length of dielectric material.

For low loss material ϵ' and ϵ'' for bulk materials can be co-related with their powder form by relations derived independently by landau, Lifshitz and Looyenga.

$$\epsilon_s{}' = \frac{[(3\delta+2\epsilon_p{}'-2)\epsilon_p{}']}{(3\delta-1)\epsilon_p{}'+1} \quad \text{------(3)}$$

$$\epsilon_s{}'' = \left(\frac{\epsilon_p{}''}{\Pi}\right)\left(\frac{\epsilon_s{}'}{\epsilon_p{}'}\right)^{2/3} \quad \text{------(4)}$$

For $\frac{\epsilon''}{\epsilon'} \ll 1$

The experimental Values have been verified by using Bottcher's equation [8]

The values of conductivity (σ_p), Loss Tangent (Tanδ) and Relaxation time (τ_p) are obtained by using following relations [3]

$$\sigma_p = \omega\epsilon_0\epsilon^{"} \quad \text{------(5)}$$

$$\text{Tan}\delta = \frac{\epsilon''}{\epsilon'} \quad \text{------(6)}$$

$$\tau_p = \frac{\text{Tan}\delta}{\omega} \quad \text{------(7)}$$

ϵ_0 is the permittivity of free space and ω is the angular frequency of measured 9.85 GHz ($\omega = 2\Pi f$)

III.RESULTS AND DISCUSSION

The turmeric were prepared in powder form by crushing and grinding. Then by using sieves it prepared into four particle size as 2000 μm, 500 μm, 125 μm and 50 μm. Then these are transferred into separate glass bottles so as to avoid any moisture intake. These bottles are labelled according to their particle sizes. For each sample densities are measured to calculate relative packing fraction (δ_r) i.e., ratio of density of different size powder to the density of finest crushed smallest size, 50 μm particle size is assumed as solid bulk for the comparison of co-relation formula between powder and bulk.

Figure 1 : Microwave X Band Setup

Table 1: Values of ϵ_p', ϵ_p'', τ_p and σ_p for turmeric powder at temp 20°C to 50°C and various relative packing factor (δ_r)

Temp °C	δ_r	ϵ_p'	ϵ_p''	τ_p (P.S.)	σ_p (10^{-2})
20 °C	0.85	2.55	0.17	1.08	9.3
	0.90	2.82	0.23	1.35	12.9
	0.95	2.91	0.28	1.53	15.1
	1.00	3.02	0.45	2.39	24.4
30 °C	0.85	2.46	0.154	1.02	8.5
	0.90	2.62	0.21	1.26	11.2
	0.95	2.69	0.24	1.41	12.9
	1.00	2.77	0.26	1.50	14.1
40 °C	0.85	2.42	0.150	1.00	8.2
	0.90	2.51	0.19	1.21	10.3
	0.95	2.53	0.20	1.30	11.1
	1.00	2.55	0.22	1.40	12.1
50 °C	0.85	2.40	0.146	0.984	8.0
	0.90	2.44	0.14	1.15	9.5
	0.95	2.47	0.19	1.25	10.4
	1.00	2.50	0.213	1.37	11.6

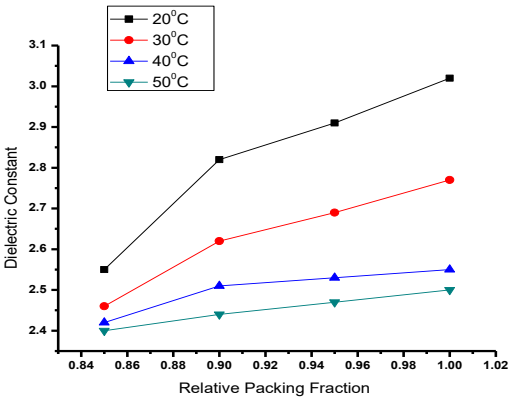

Figure 2

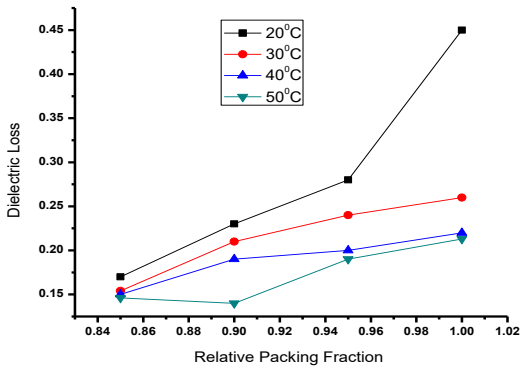

Figure 3

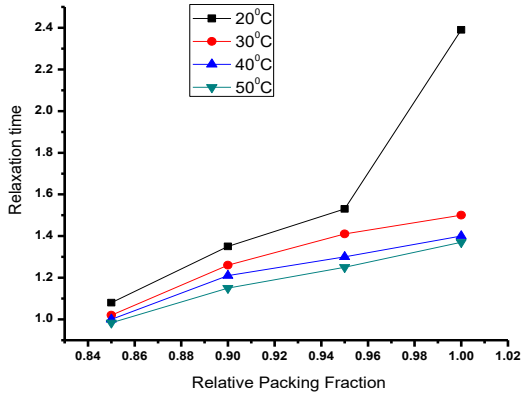

Figure 4

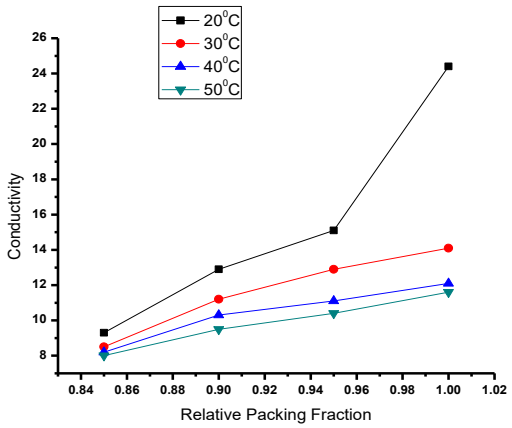

Figure 5

From Table 1. The Values of ϵ' and ϵ'' are increases by increasing value of δ_r. This is expected because the interparticle hindrance offered to the dipolar motion of material in electromagnetic field at microwave frequency for compact medium. Such observations are already found by other researcher for higher values of packing fraction [2, 3, 10].

By increasing δ_r there is increase in σ and τ and there is decrease in σ, τ with increasing the temperature it is due to increase hindrance to the process of polarization and number of collisions increases causes increase in energy loss.

Table 2: The values of ϵ_s' and ϵ_s'' for solid bulk from powder measured and computed at different temp. 20°C to 50°C and at $\delta_r = 1.00$

Temp °C	ϵ_s'			ϵ_s''		
	Measured	By L-L-L	By Bottcher's	Measured	By L-L-L	By Bottcher's
20 °C	3.02	3.0	2.97	0.45	0.44	0.43
30	2.77	2.76	2.74	0.26	0.25	0.24
40	2.55	2.54	2.53	0.22	0.22	0.20
50	1.00	2.50	2.52	0.248	0.213	0.198

Table 2. suggests the values of ϵ_s' and ϵ_s'' for solid bulk measured and compared with theoretical values given by L-L-L and Bottcher. It is found these measured and computed values are nearly same.

IV. CONCLUSION

- The reflectometer technique can be used for powdered sample for determination of dielectric parameters.
- The co-relation formulae can be used to provide accurate estimate of ϵ' and ϵ'' for turmeric powder.
- There is fair agreement between experiments and theoretical values of Dielectric parameters of powder of turmeric at X-band microwave bench.

V. REFERENCES

[1] R. A. Jangid etal, Indian journal of pure and applied physics 34, 1996, PP 316-318.
[2] J. S. Yadav etal, Indian journal of pure and applied physics 30, 1992, 427.
[3] A. K. Bansal etal, Indian journal of pure and applied physics 39, 2001, PP 799-803.
[4] G. Ghodmalle etal, Indian journal of scientific research Vol.9, Issue 10, 10 Oct 2020.
[5] A. Kraszenswki etal, Journal of Agricultural engineering research 58, 1994, PP 37-46.
[6] S. O. Nelson, IEEE trans. On Instrumentation and measurement 41(1), 1992, PP 116-122.
[7] L. D. Landau etal, "Electrodynamics of continuous media", Peogamon press, London, 1960, P-44.
[8] C. J. F. Bottcher. "The theory of dielectric polarization", Elsevier, Amsterdam, 1952, PP 415.
[9] M. L. Sisodia and G. S. Raghuvanshi, " Basic microwave techniques and laboratory manual", Willey Eastern Ltd, 1990.
[10] P. G. Gawali etal, Indian journal of applied research, Vol 3, Issue 10, Oct 2013.

ICRTMS-2024
International e-Conference on Recent Trends in Material Science
In Association with International Journal of Scientific Research in Science and Technology
Volume 11 | Issue 9 | Print ISSN: 2395-6011 | Online ISSN: 2395-602X (www.ijsrst.com)

Metal Catalyst Mediated Synthesis of Some Heterocyclic Compounds : A Brief Review

Mr. Achut R. Shinde
Department of Analytical Chemistry, Sanjeevanee Mahavidyalaya, Chapoli,Tq. Chakur, Dist. Latur. (Maharashtra)

ABSTRACT
Heterocyclic compounds play a vital role in the various metabolism as well as in the pharmaceutics. Heterocyclic compounds show various biological and pharmacological activities which results attraction of researchers towards the world of heterocycles. Recently various methodologies were invented and adapted for the synthesis of heterocyclic motif. From last decade number of researchers brought huge revolution in the field of metal mediated efficient synthesis of heterocyclic compounds. In the present review we have mentioned some efficient, ecofriendly Calcium, magnesium and Copper metal catalyst mediated synthesis of heterocyclic compounds.

Keywords : Heterocyclic compounds, Pharmacological, Biological Activity, Metal catalyst mediated, Magnesium, Calcium, Copper.

I. INTRODUCTION

Heterocyclic compounds are the class of organic compounds containing one or more than one same or different hetero atoms other than carbon as a part of cyclic ring. Variety of heterocyclic compounds are known some are found in nature but number of similar heterocyclic compounds are artificially synthesized in laboratories. The word heterocycles denotes a class of cyclic organic compounds that mostly contain N, S, or O as a heteroatom. The ring may be from three to eight members and carbon being the most common ring atom, almost all the heterocycles behave as aromatic compounds[1]. Literature survey reveals that there are wide verities of condensed heterocyclic compounds are known for their biologically potent and exhibits pharmacological activities, such as anti-fungal activity [2-5], anti-inflammatory activity[6-13], antibacterial activity[14-21], anticonvulsant activity [22-25], anti-allergic activity[26-34], herbicidal activity[35-42], and anticancer activity[43-46].

Heterocyclic compounds have been crucial in the development of cellular metabolism, comprising five and six-membered rings with one to three heteroatoms. Examples include pyrimidine and purine bases essential for DNA function. Isolation or combination with other heterocyclic systems facilitates diverse applications in biological and chemical research. Studies of heterocycles with heteroatoms like Sulphur and Nitrogen are crucial in heterocyclic chemistry. The 1,4-Thiazine ring systems are particularly important due to their presence in various natural products and pharmaceutical agents [47-49]. They serve as a cornerstone in the

synthesis of compounds with diverse biological activities. The presence of heterocycles with a 1, 4-thiazine ring is also recognized as important in the formation of pigments and dyestuffs [50-51]. Furthermore, 4H-1,4-benzothiazines and their derivatives have been found to exhibit a variety of biological activities [52-53], including anticancer [54-55], antifungal [56-57], antagonistic[58], antioxidant[59], antihypertensive[60], analgesic[61], cardiovascular activity[62], antibacterial[63], antimalarial[64], antimicrobial[65], and more. Amino acids like proline and histidine, along with heterocyclic compounds like tryptophan, are common in medicines. Essential precursors for vitamins and coenzymes, such as thiamine, riboflavin, pyridoxine, and folic acid, also play key roles. Heterocyclic compounds in vitamin families like biotin, B_{12}, and E are pharmacologically active and widely used in clinical settings, with pyrimidines and derivatives being crucial for living organisms. Sulphanilamidopyrimidines like Sulphadiazine are well-known antibacterial agents.

Heterocycles are significant structures found in a wide variety of natural products and biologically active compounds, as well as in organic and "plastic" electronics materials. Thus, the creation of effective techniques for producing heterocyclic compounds is consistently a top priority in the field of organic synthesis. Over the last few decades[76], numerous methods focused on creating heterocycles have been established, with many relying on the cyclization of appropriate substances using metal-catalyzed or organocatalyzed techniques. Still, there are numerous unresolved issues in this field: such as the need for overall advancements in terms of chemo-, regio-, and stereoselectivity, which can frequently be accomplished through precise adjustments to the catalytic system, as well as the creation of eco-friendly and sustainable methods, made possible in part by the utilization of heterogeneous and/or recoverable catalysts.

In the recent there numerous methods were available for the synthesis of heterocyclic compounds and their derivatives for the various purposes such as their biological, pharmacological and other important uses. Some methods such as metal catalyzed cyclization, Michel addition, Robinson's annulation, photochemical reaction, base catalyzed reaction, thermal cyclization, condensation reactions, Ugi reaction, Heck reaction, Ulmann coupling, Goldberg reaction and use of homogeneous and heterogeneous catalyst etc.

The C–N and C–O bonds are widely present and significant in organic substances, natural products, drugs, and agricultural chemicals[66]. Nearly 80% of drugs available in the market include a C–N or C–O bond. Heterocyclic compounds containing nitrogen and oxygen are notable for their diverse nature among the many different types of heterocycles. In addition, these heterocycles are especially crucial in the pharmaceutical field because of their exceptional solubility and ability to form salts. The synthesis of nitrogen and oxygen containing heterocycles involves an important step in forming C-N or C-O bonds, for which various synthetic strategies using transition metal catalysts have been developed[67,68]. The Ullmann group[69] and the Goldberg group[70] were the first to discover Cu-catalyzed C-N and C-O bond forming reactions. Subsequently, the Buchwald[71] and Hartwig groups[72] showed the Pd-catalyzed reaction that forms C-N bonds. Recently, the Chan and Lam group made a significant advancement in Cu-catalyzed formation of C–N bonds [73, 74]. Other than palladium or copper, various transition metals like nickel, zinc, iron, cobalt, and manganese have been observed to participate in C–N and C–O bond formation reactions[75]. However, these methods have inherent drawbacks including high reaction temperature, costly ligands, limited substrate scope, and excessive waste generation. As a result, it is beneficial for a variety of organic synthesis applications to have environmentally friendly, uncomplicated, and direct methods for forming C-N or C-O bonds.

Palladium is a widely used metal catalyst in heterocyclic chemistry for creating C–N and C–O bonds. These catalysts are expensive and not very stable, and they do not work well with a variety of functional groups. Copper has become an appealing and diverse choice for catalytic systems due to the need for them to be versatile, affordable, multipurpose, and eco-friendly. Cu-catalyzed reactions are extensively utilized in organic synthesis due to their ease of access, safety, and cost-effectiveness. Copper has been proven to be an effective replacement for expensive noble metals such as palladium in catalysis. Over the past ten years, the reports of several new processes have demonstrated the importance of copper in transition metal catalysis. Copper is considered the most versatile and efficient catalyst among transition metals and is known for its effectiveness as a redox catalyst. Both Cu (I) and Cu (II) species effectively undergo reactions with chemicals to produce a variety of heterocycles. Copper salts and complexes, in addition to their traditional role as metals, are now extensively utilized for their remarkable catalytic properties in various chemical processes. Additionally, it is extremely urgent to advance the development of organic synthesis in ways that are sustainable. The field of microwave chemistry has been established and has various well-established applications, along with several benefits in terms of reaction rate and yield. Due to this, microwave-assisted organic synthesis has become a useful method for sustainable organic synthesis due to its dependability and effectiveness. Thanks to microwave aided chemistry, researchers now have the freedom to make significant advances in the design and development of cutting-edge heterocyclic molecules. The use of microwaves in the industrial preparation of aromatic compounds, metal-mediated chemistry, and heterocyclic synthesis has now been expanded to include continuous-flow organic synthesis. Finally, the extensive use of microwaves in organic synthesis can increase its usefulness for creating valuable organic compounds, polymers, and nanomaterial's in a shorter time compared to traditional heating methods [76-79]. In a recent review, Szostak and his team also discussed the potential for microwave irradiation in synthesizing privileged heterocyclic moieties [80, 81].

In this review we have covered some examples of synthesis heterocyclic compounds using various metal catalyst mediated synthesis as well as microwave assisted synthesis of some five and six membered heterocyclic Compounds. This review specially focused on the copper and palladium catalyzed microwave assisted green synthesis of five and six membered heterocyclic compounds.

Synthesis of heterocyclic compounds by using Calcium catalyst:

Safaei et al.[82] discussed the synthesis aryl substituted pyridines by condensation of aldehyde **1**, thiol **3** and malononitrile **2** in the presence of calcium oxide nanoparticle **4**.(Scheme.1). Calcium oxide nanoparticle have more advantageous than the homogeneous base catalyst because it is inexpensive, have high basicity, non-corrosive, cheap, and easy to handle. When it comes to high yields and quick reaction times, this method offers reusability and requires minimal catalyst loading. Improved technique for syntheis 2-amino-4-aryl-3,5-dicyano6-sulfanylpyridines **5**. When the reaction is carried out under the 'ideal circumstances with a selection of aldehydes and thiols, at the start of the reaction, electron-withdrawing groups such as NO_2, Cl, and Br readily reacted with malononitrile to yield 2-amino-3,5-dicarbonitrile-6-thio-pyridines **4**. The time required for this conversion is very less. Furthermore, in comparison to unhindered aldehydes, sterically hindered aldehydes exhibited a slower reaction rate. When we react malononitrile, thiophenol and benzaldehyde obtain good result.

Gao et al.[83] and coworkers given a cascade synthesis of bicyclic sulphonamide by using nonhazardous cheap calcium catalyst. They took advantage of the high Lewis acidity of the calcium catalyst which effectively convert starting material into carbocations for the cascade synthesis of bicyclic sulphonamides. Calcium catalyst is inexpensive as compare to the high-cost hazardous Nobel metal catalyst. The reaction begins with the ionization of hexanol **6** in presence of Bu_4NPF_6 **10** and calcium (II) bis(trifluromethanesulphonamide) **9**. The conclude that there is no effect of changing the substituent on sulphonamide but the obtain high yield of the desired product **11** with full diastereoselectivity when one can substitute bulkier group on alkyne. (Scheme2)

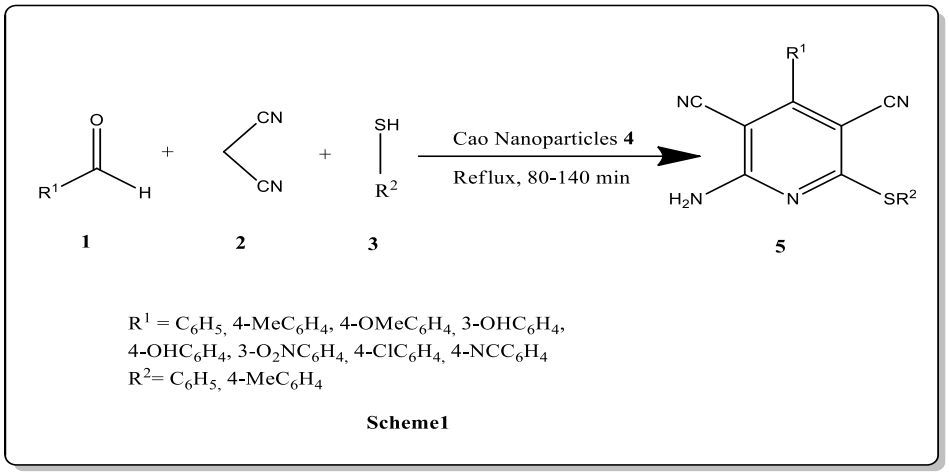

Scheme1

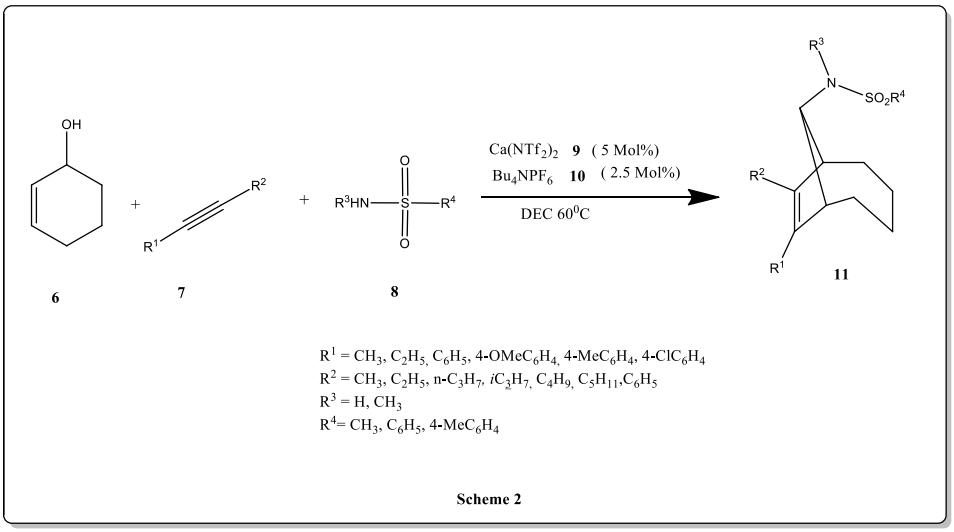

Scheme 2

In 2007 Kobayashi et al[84]. invented a novel calcium complex**12** catalyzed asymmetric [3+2] Cycloaddition of the α- amino acid derivatives **14** with α, β unsaturated carbonyl compound**13** which results 99% yield of chiral pyrrolidine derivative. catalyst carryout the reaction efficiently no need of additional base or nucleophile and stereocenter is also generated. (Scheme 3).

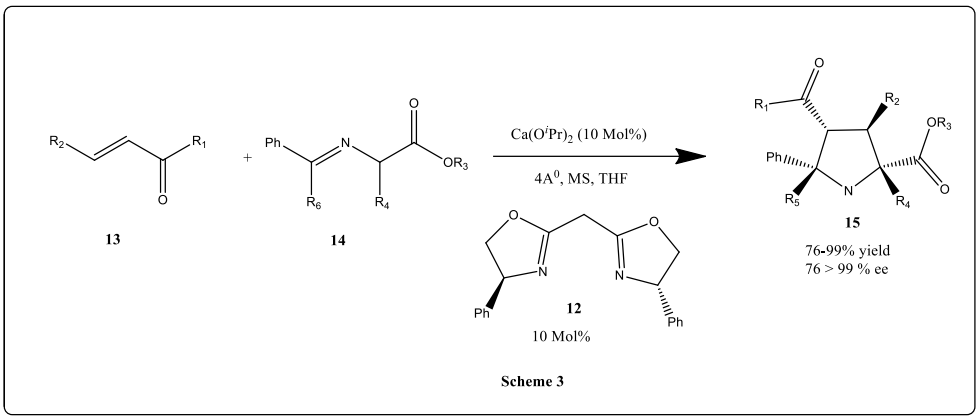

Scheme 3

A unique calcium hexafluoroisopropoxide complex was reported by Stambuli's and coworker in 2008. This complex catalyzed the Pictet-Spengler reaction between m-tyramine **16** and aldehydes **17** to install 1,2,3,4-tetrahydro isoquinoline**18** (scheme 4). Notably, in certain transformations with little regioselectivity, this mild condition could replace strong Bronsted acid[85]. Numerous aryls, heteroaryl, and alkyl aldehydes can be tolerated by this approach, which results in excellent yield and regioselectivity of the related products.

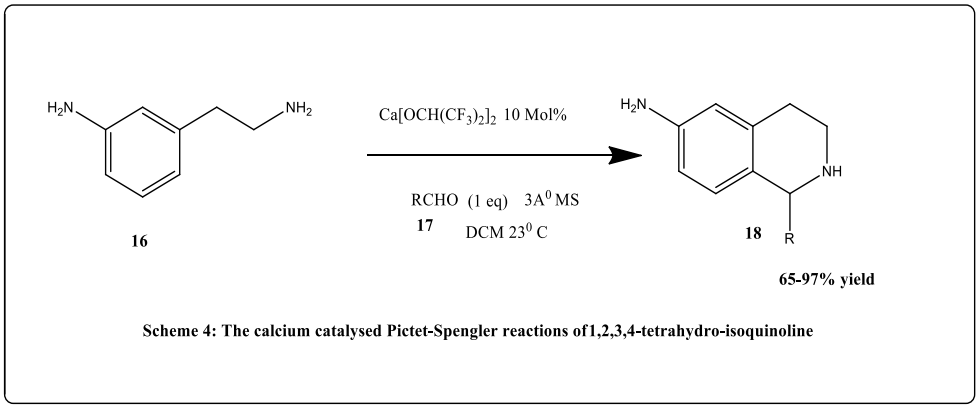

Scheme 4: The calcium catalysed Pictet-Spengler reactions of1,2,3,4-tetrahydro-isoquinoline

Yaragorla et al[86]. described an effective one-pot, four-component synthesis of benzyl pyrazolyl coumarins in water, catalyzed by calcium (Scheme 5a). This reaction can tolerate a wide range of aromatic aldehydes with electron-donating and electron-withdrawing groups, as well as aliphatic aldehydes and hydrazine, depending on the substrate scope. In accordance with their suggested process (Scheme 5b), pyrazolone A was produced by treating ethylacetoacetate **21** and phenylhydrazine **22**. This adduct B was then produced via a Knoevenagel condensation reaction with an aldehyde. A second Michael addition reaction with 4-hydroxycoumarin **19** took place to get the final product **23** when Ca ions were present in the reaction.

Alternatively, Path may be used by the reaction to continue. Adduct C was produced by the Knoevenagel condensation of 4-hydroxycoumarin **19** with benzaldehyde **20**. Pyrazones A were then added using a Ca-catalyzed Michael to results final product **23.**

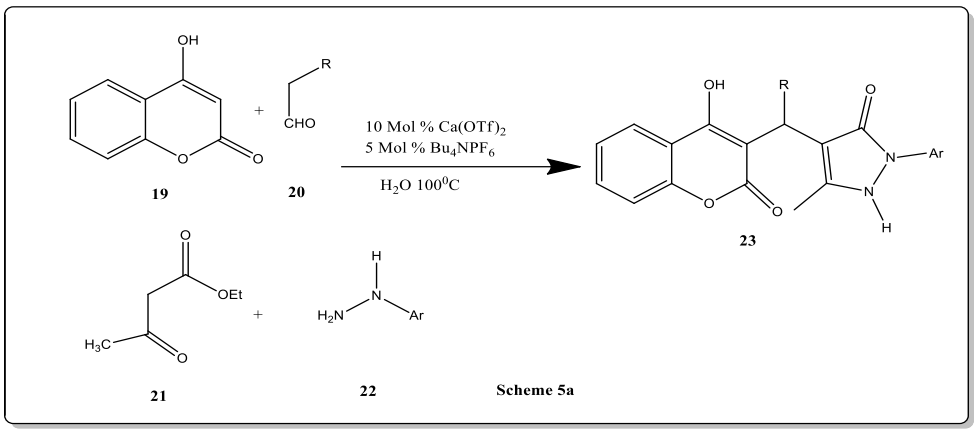

Synthesis of heterocyclic compounds by using Magnesium catalyst:

Magnesium is the most extensively studied alkaline earth element. Apart from their frequent application as Grignard reagents, other magnesium chiral compounds or reagents have been effectively intended for use in the synthesis of organic materials. Many changes, such as the creation of heterocyclic compounds, have been applied to magnesium catalysts or reagents. In this section, the use of magnesium as a catalyst or reagent in heterocyclic synthesis will be discussed.

Antilla and co-workers[87] described the chiral magnesium phosphate catalyzed enantioselective Aza-Darzens reaction. (Scheme 6) This reaction results enantioselective trisubstituted aziridine **26** when α-chloro-1,3-diketone **24** treated with N-benzoyl imine **25** in the presence of catalyst $Mg[P_3]_2$.

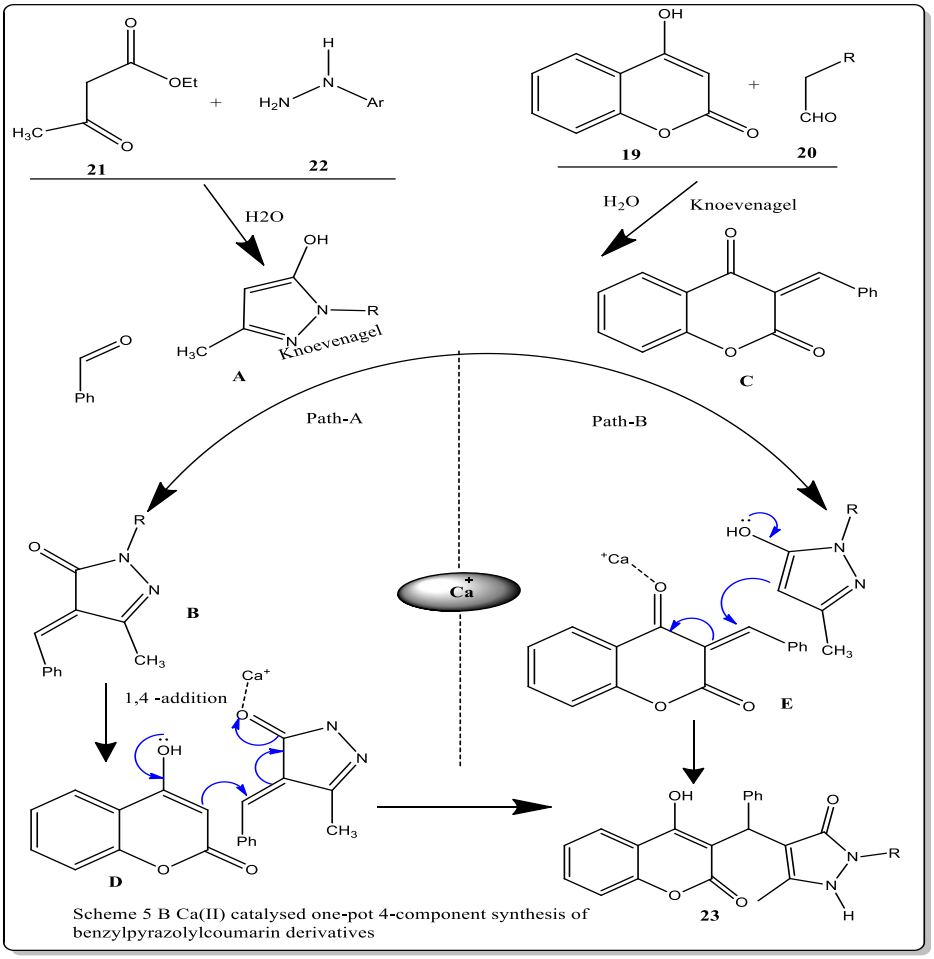

Banerjee and co-workers also described the MgI_2 catalyzed N- transferring electrophilic synthesis of ternary heterocyclic ring by exposing functionalized aziridine(oxaziridine) molecule **27** with activated olefines **28** and MgI_2 results final product aziridine in cis configuration.**29**(Scheme 7).

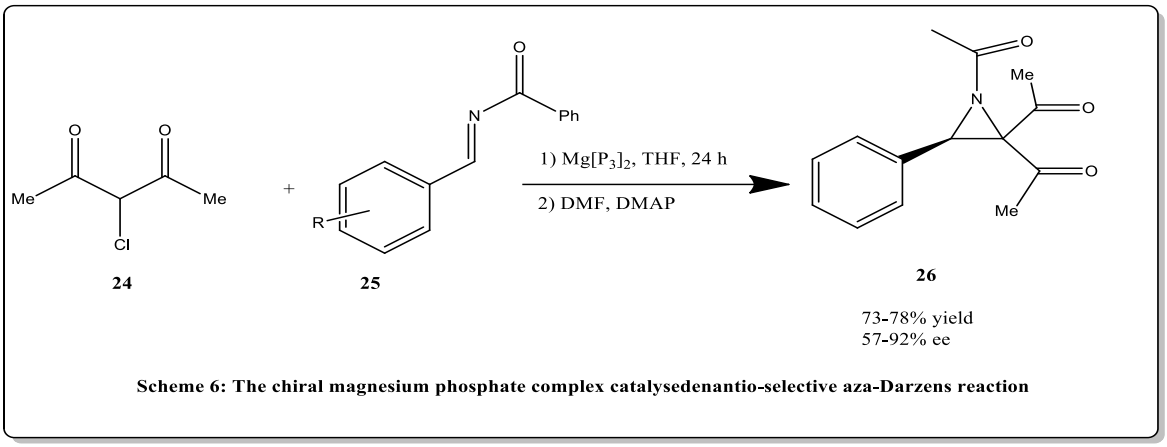

Scheme 6: The chiral magnesium phosphate complex catalysedenantio-selective aza-Darzens reaction

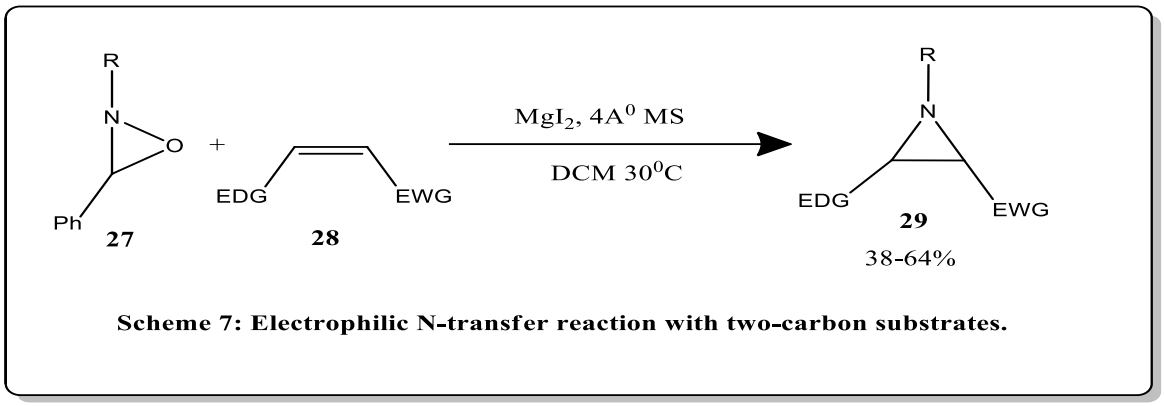

Scheme 7: Electrophilic N-transfer reaction with two-carbon substrates.

Banerjee and coworkers[87] reported synthesis Nitrogen containing cyclobutene **32** (Scheme 8). This transformation is carried out by MgI_2 mediated electron N- transfer of phenyl substituted N-tosyl oxaziridines **30** with cyclopropane **31**.

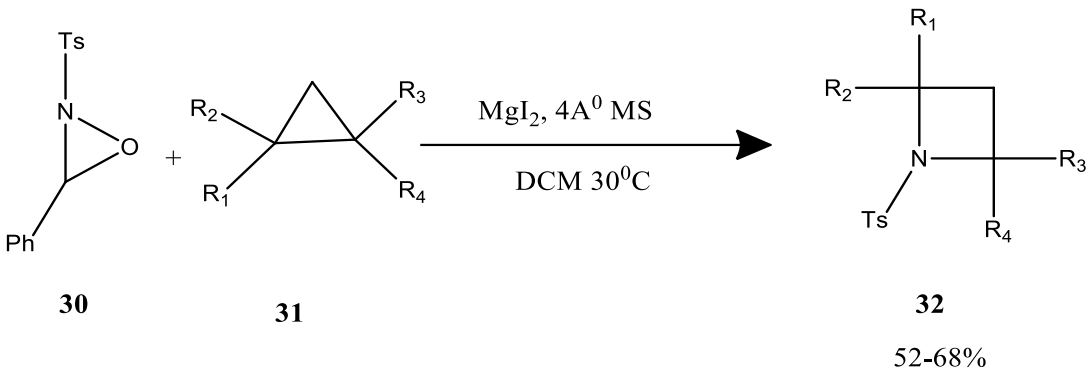

Scheme 7: Electrophilic N-transfer reaction with three-carbon substrates.

DiMauro's and coworkers[88] reported microwave assisted one pot synthesis of various 2,6-disubstituted 3-amino-imidazopyridines 35 by Suzuki coupling using MgCl2 as a catalyst (Scheme 8). The transformation is carried out by using paraformaldehyde as the aldehyde precursor in this Ugi-type cyclization.

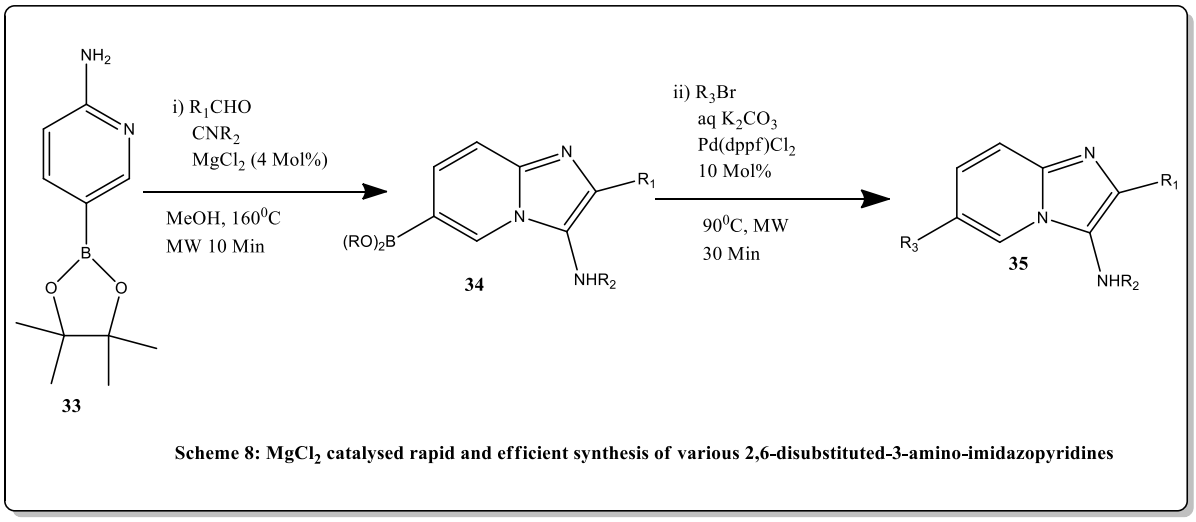

Scheme 8: $MgCl_2$ catalysed rapid and efficient synthesis of various 2,6-disubstituted-3-amino-imidazopyridines

Synthesis of Heterocyclic compounds by using Copper Catalyst:

There are various methods known for the copper catalyzed reactions for the synthesis of various heterocyclic compounds by means of C-H functionalization such as amination, alkynylation, hydroxylation, and arylation. Daugulis and co-workers described the copper catalyzed synthesis and compatibility of five and six membered heterocyclic compounds by C-H functionalization through amidation and amination reaction. This transformation is carried out by using Cu (OAc)2 in presence of Na2CO3. (Scheme 9).

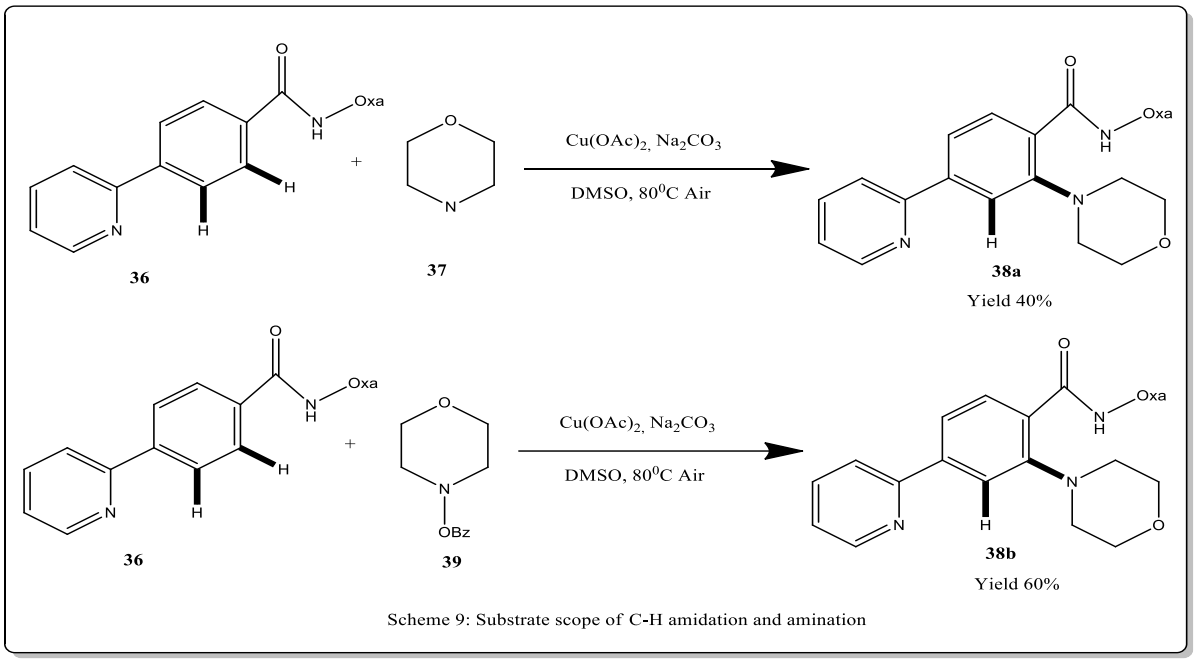

Scheme 9: Substrate scope of C-H amidation and amination

Hammond and group[89] describe ecofriendly copper metal mediated one pot tandem synthesis of heterocyclic compounds by hydroamination alkylation using microware heating (Scheme 10). This is environmentally sustainable and cheap copper catalyst results a good yield of the final product. This transformation is carried out by the intermolecular cyclization of aminoalkyne which results into enamine intermediate that finally undergoes intermolecular addition with terminal alkyne. By application of this method one can able to synthesize six and seven membered heterocyclic compounds.

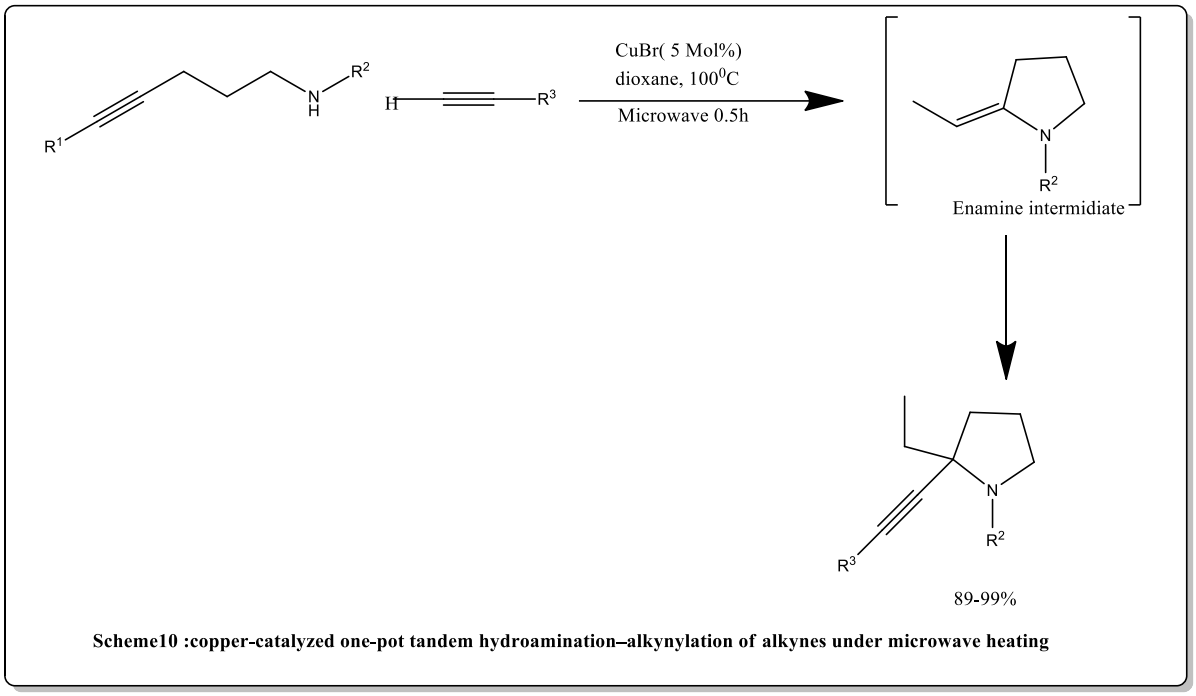

Scheme10 :copper-catalyzed one-pot tandem hydroamination–alkynylation of alkynes under microwave heating

Fokin and Raushel described copper(I) thiophene 2- carboxylate (CuTC) catalyzed synthesis of 1-sulfonyl-1,2,3 triazole under non basic anhydrous and aqueous conditions. To carry out this transformation in situ generation of Cu(I) acetylides and sulfonyl azides at room temperature. Scheme11.

In resent there are numerous methods are metal mediated methods are available for the synthesis of heterocyclic compounds such as Gold catalyzed, platinum catalyzed, palladium catalyzed zinc catalyzed, ruthenium catalyzed synthesis was known. but in the current review we have mentioned only calcium, magnesium and copper catalyzed synthesis of heterocyclic compounds.

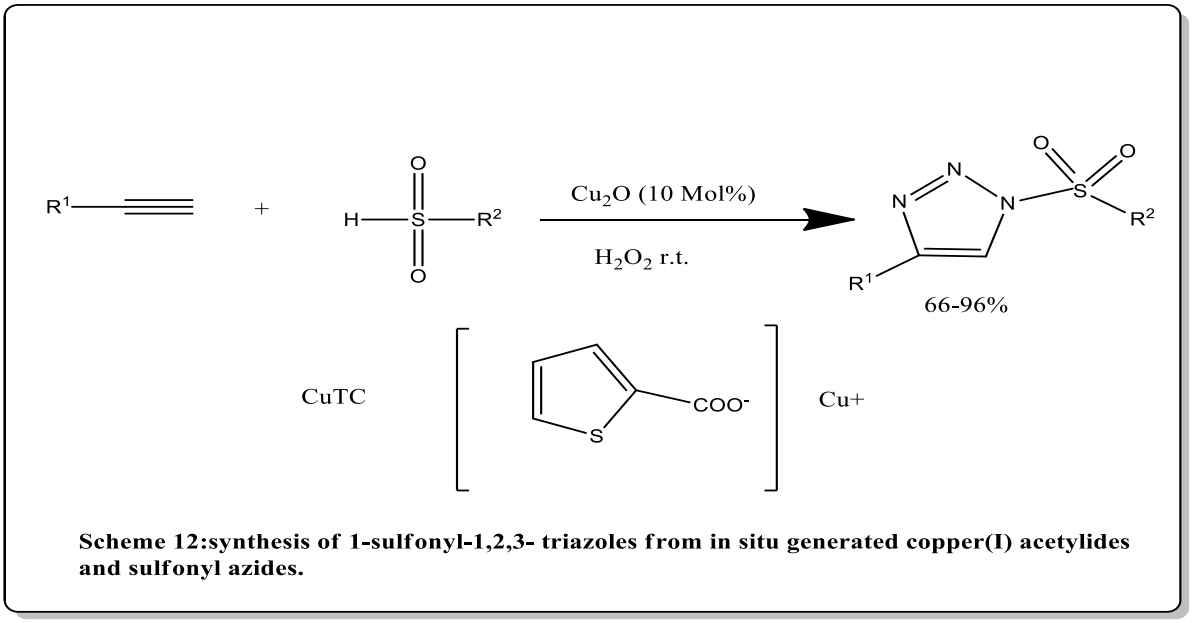

Scheme 12:synthesis of 1-sulfonyl-1,2,3- triazoles from in situ generated copper(I) acetylides and sulfonyl azides.

Conclusion: Since from last decade there are numerous metals catalyzed synthetic methods was devised which are used in the pharmaceutically, biologically potent heterocyclic compounds. From these transition metal catalyzed synthetic methods are more efficient and environmental beings.

References:

1. Jin T. – S. , L. - Liu B., Zhao Y. and Li T. -S., 2005, *Synth. Communi.*, 35, 1859–1863.
2. Chen jun-cai, Song An-Bao, et al., 2007 "Synthesis and antifungal activities of 5-(3,4,5-trimethoxyphenyl)-2-sulfonyl-1,3,4-thiadiazole and5-(3,4,5-trimethoxyphenyl)-2-sulfonyl-1,3,4-oxadiazole derivativees.",3981-3989.
3. Andotra C.S., Langer T.C.,Sumita Dham (1993)Synthesis of some 2,6-disubstituted imidazo[2,1-b]-1,3,4-thiadiazoles and their biological activities. *PROC.NAT. ACAD. SCI. INDIA*,63(A), iv
4. Arora D. S., Singh, J. and Aneja, K. R (1999) Some Indian spices and their antimicrobial properties. Pp. 33-40. In:(Eds.). From Ethnomycology to Fungal Biotechnology: Exploiting Fungi from Natural Resources for Novel Products. Kluwer Academic/Plenum Publishers, New York
5. Qiong Chen, Xiao-Lei Zhu, Li-Li, Zu-Ming Liu, Guang-Fu Yang (2008) Synthesis, antifungal activity and CoMFA analysis of novel 1,2,4-triazolo[1,5-a]pyrimidine derivatives. *European Journal of Medicinal Chemistry* 43(3):595-603.
6. Amir Mohd., Javed SA, kumar Harish, 2007*, Indian journal of chemistry*, "synthesis of some 1, 3, 4-oxadiazole derivatives as potential anti-inflammatory agents.", vol.46B, june, pp-1014-1019.
7. Burbuliene Milda Malvina, Jakubkiene Virginija, Mekuskiene Giedrute, 2004, "Synthesis and anti-inflammatory activity of derivatives of 5-[(2-disubstitutedamino-6-methyl-pyrimidin-4-yl)-sulfanylmethyl]-3H-1,3,4-oxadiazole-2-thiones, 767–774.
8. Erhan Palaska, Gu S¸ahinay, Pelin Kelicen, 2001,"Synthesis and anti-inflammatory activity of 1-acylthiosemicarbazides, 1,3,4- oxadiazoles, 1,3,4-thiadiazoles and 1,2,4-triazole-3-thiones.", 101-107.
9. Chandra Trilok, Garg neha, Lata Suman, Saxena S S, (2010), *European Journal of Medicinal Chemistry* "Synthesis of substituted acridinyl pyrazoline derivatives and their evaluation for anti-inflammatory activity."45,1772-1776.
10. Husain Asif, Ajmal Mohammed, Acta Pharm. 59 (2009), "Synthesis of novel 1,3,4-oxadiazole derivatives and their biological properties." 3898 -3902.
11. Akhter mymoona, Husain Asif, Azad Bismillah, *European Journal of Medicinal Chemistry* (2009), "Aroylpropionic acid based 2,5-disubstituted-1,3,4-oxadiazoles: Synthesis and their anti-inflammatory and analgesic activities." 2372-2378
12. Dewangan Dhansay, Pandey Alok, *international journal of chemistry,* "Synthesis of some Novel 2, 5-Disubstituted 1, 3, 4-Oxadiazole and its Analgesic, Anti-Inflammatory, Anti-Bacterial and Anti-Tubercular Activity." vol.2, page no.1397-1412.
13. Jayashankar.B, Rai lokanath KM, Baskaran N, European *Journal of Medicinal Chemistry 44* (2009)," Synthesis and pharmacological evaluation of 1,3,4-oxadiazole bearing bis(heterocycle) derivatives as anti-inflammatory and analgesic agents."
14. Chao jun-shu, Huia ping-xin, Lia shuo, 2005, "Synthesis and Antibacterial Activities of Novel Biphenyltetrazole Derivatives Bearing 1,3,4-Oxadiazole." *Journal of the Chinese Chemical Society*, 52, 539-544 539.
15. Srinivas K, Srinivas U, Bhanuprakash K, Harakishore K. 2006; Synthesis and antibacterial activity of various substituted s-triazines. *Eur J Med Chem* 41: 1240-1246

16. Banday R Mudasir, Matto H Rayees, Rauf Abdul, 2010*, J. Chem. Sci,* "Synthesis, characterization and anti-bacterial activity of 5-(alkenyl) 2-amino- and 2-(alkenyl)-5-phenyl-1,3,4-oxadiazoles. 122, No. 2, pp. 177–182.
17. AateshOÈznur, Kocabalkanli AysËe, Cesur Nesrin, (1998), "Synthesis and antimicrobial activity of some 5-aryl-2-[(N,N-disubstituted thiocarbamoylthio)acylamino]-1,3,4-oxadiazoles" *, Il Farmaco* 53, 541-544.
18. SAAD H (1996). Design synthesis, characterization and antibacterial activity of 1,3,4-Oxadiazolederivatives*. Indian Journal.of Chemistry* 35B: 980.2.
19. Nanjunda S, Swamy S, Basppa, Priya Bs, Prabhuswamy B, Doreswamy BH (2006). Crystal Structure of Novel2-butyl-4-chloro-1HImidazolyl- 5-Carboxaldehyde. *European Journal. of Medicinal Chemistry* 41: 531-538.3.
20. Hui xp, Chu ch, Zangzu, Wang Q and Zhang Q (2002). Synthesis and antibacterial activity of 1,3,4-Thiadiazole derivatives of 5-amino,2-hydroxybenzoic acid. *Indian Journal of. Chemistry*.,41B: 2176.
21. Yar Shahar mohammad, Akhter Wasim Mohd., Acta Poloniae Pharmaceutica Synthesis and anticonvulsant activity of substituted oxadiazole and thiadiazole derivatives Vol. 66 No. 4 pp. 393-397.
22. Zarghi Afshin, Hamedi Samaneh, Tootooni fatemeh, "Synthesis and Pharmacological Evaluation of New 2-Substituted-5-{2-[(2- halobenzyl)thio)phenyl}- 1,3,4-oxadiazoles as Anticonvulsant Agents.", 185-201.
23. Zarghi A, Tabatabai SA, faizi, ahadian A. (2005).
24. "synthesis anticonvulsant activity of new 2-substituted benzyloxyphenyl -1,3,4-oxadiazoles, *bioorg lett*. 15: 1863-1865,
25. Almasirad A, tabatabai SA, faizi M, " synthesis & anticonvulsant activity of new 2-substituted-5-[2-(2-fluorophenoxy)phenyl]-1,3,4-oxadiazole & 1,2,4-triazoles, Bioorg med. *Chem. Lett.* 14 : 6057-6059.
26. C. Landreau, D. Deniaud, M. Evain and A. Reliquet, "Efficient Regioselective Synthesis of Triheterocyclic Com- pounds: Imidazo[2,1-b]benzothiazoles, Pyrimido[2,1-b]- benzothiazolones and Pyrimido[2,1-b]benzothiazoles," *Journal of the Chemical Society, Perkin Transactions* 1, No. 6, , pp. 741-745.
27. Roy P. J., Landry K. and Leblanc Y, (1997), "Condensation of 2-Amino-5-chlorobenzoxazole with α-Bromoketones: A Mechanistic Study," Heterocycles, Vol. 45, No. 11, pp. 2239-2246.
28. Tanabe Y., Kawai A., Yoshida Y., Ogure M. and Okumura H., (1997), "Preparation of Fused Thiadiazolo- and Imi-dazobenzothiazoles from 2-Aminobenzothiazoles. Their Fungicidal Activity," *Heterocycles,* Vol. 45, No. 8, pp. 1579-1588. doi:10.3987/COM-97-7839
29. Trapani G., Frang A. Latrofa G. and. Genchi G, (1992), "Synthesis and Benzodiazepine Receptor Binding of Some 4H- Pyrimido[2,1-b]benzothiazol-4-ones," *European Journal of Medicinal Chemistry*, Vol. 27, No. 1, pp. 39-44. doi:10.1016/0223- 5234(92)90058-9
30. Chan C. K., Ma J. C. N. and Mak T. C. W., (1977), "Synthesis and X-Ray Structure of Methyl 2-Oxopyrimido [2,1- b] benzothiazole-4- carboxylate from Condensation of 2- Aminobenzothiazole and Dimethyl But-2-ynedioate," *Journal of the Chemical Society, Perkin Transactions* 2, No. 8, pp. 1070-1074.
31. Wade J. J., Hegel R. F. and C. B. Toso, (1979) "Reaction of 2-Aminobenzazoles with Dimethyl 2-Aminofumarate. Synthesis and Nuclear Magnetic Resonance Spectroscopy of 4-Oxopyrimido [2,1-b] benzazoles," *The Journal of Or- ganic Chemistry*, Vol. 44, No. 11, pp. 1811-1816. doi:10.1021/jo01325a013.
32. Gupta A. and Rawat S, (2010) "Synthesis and Cyclization of Benzothiazole: Review," *Journal of Current Pharmaceutical Research*, Vol. 3, No. 1, pp. 13-23.
33. Bartovic A., Ilavski D., Simo O., Zalibera L., Belicová A. and Seman,M. (1995), "Synthesis of Nitro-Substituted 4-Oxo- 4H-pyrimido[2,1-b] benzothiazole-3-carboxylic Acids and Their Spectral

Characteristics," Collection of Czechoslo- vak *Chemical Communications*, Vol.60, No. 4, pp. 583-593. doi:10.1135/cccc19950583

34. El-Sherbeny M. A., (2000), "Synthesis of Certain Pyrimido[2,1- b]benzothiazole and Benzothiazolo[2,3-b]quinazoline Derivatives for invitro Antitumor and Antiviral Activities," Arzneimittel Forschung/Drug Research, Vol. 50, No. 9, pp. 848-853.
35. Kettles MK, Browning SR, Horstman SW. (2000), "Triazine herbicide exposure and breast cancer incidence: an ecologic study of Kentucky counties". Environ Health Perspect 1977; 105: 1222–1227.
36. Du, X.H. (1997).Amide Thiourea and 1,2,4-Triazoles Synthesis and Plant Growth Regulating Activity. Ph.D. Dissertation, China Agricultural University, Beijing, China,
37. Wong, R.; Dolman, S.J. 2007, Isothiocyanates from Tosyl Chloride Mediated Decomposition of in situ Generated Dithiocarbamic Acid Salts. *J. Org. Chem.* 72, 3969–3971.
38. Chen, H.S.; Li, Z.M.; Li, J.F. (2000), Synthesis of 2-Pyrazoyl-5-substituted-1,3,4-oxadiazoles and Their Biological Activities. *Chem. J. Chin. Univ*. 21, 1520–1523
39. Zhang, K.S.; Mu, L.J.; Long, W.X. Synthesis and Preliminary Bio activity Studies of α-Pyrazyl-N-phenyl-α-aminophosphonates. Chem. J. Chin. Univ. 1999, 20, 741–743.
40. Zhao, W.G.; Chen, H.S.; Li, Z.M.; Han, Y.F.; Yan, H.; Lai, J.Y.; Wang, S.H. 2001, "Synthesis of Pyrazolyl-heterocycles and Their Fungicidal Activities". *Chin. J. Chem*. 22, 939–942.
41. Zhao, W.G.; Cao, Y.B.; Li, Z.M.; Gao, F.W.; Wang, S.H.; Wang, J.G. (2001), Synthesis and Biological Activity of 1-Sulfonyl-3,5-diamino-1H-Pyrazole Derivatives. *Chin. J. Appl. Chem.* 18, 423–427.
42. Hatton, L.R.; Buntain, I.G.; Hawkins, D.W.; Parnell, E.W.; Pearson, C.J.; Roberts, D.A. Derivatives of N-phenylpyrazoles. EP Patent 0967206, 29 June 1999.
43. Hatton, L.R.; Buntain, I.G.; Hawkins, D.W.; Parnell, E.W.; Pearson, C.J.; Roberts, D.A. Derivatives of N-phenylpyrazoles. EP Patent 295117, 20 August 1996.
44. Stanton HLK, R Gambari, Chung HC, Johny COT, Filly C, Albert SCC(2008);. Synthesis and anti-cancer activity of benzothiazole containing phthalimide on human carcinoma cell lines. *Bioorg Med Chem*. 16:3626-3631.
45. Wang M, Gao M, Mock B, Miller K, Sledge G, Hutchins G, Zheng Q.(2006); Synthesis of C-11 labelled fluorinated 2-arylbenzothiazoles as novel potential PET cancer imaging agent. *Bioorg Med Chem.* (14):8599-8607.
46. Jin, Jiang Chen, Baoan Song,* Zhuo Chen, Song Yang, (2006) "Synthesis, structure, and bioactivity of N0-substituted benzylidene-3,4,5- trimethoxy benzohydrazide and 3-acetyl-2-substituted phenyl-5-(3,4,5-trimethoxyphenyl)-2,3-dihydro-1,3,4-oxadiazole derivatives.", *Bioorganic & Medicinal Chemistry Letters* 16 ,5036–504.
47. Aboraia S. Ahmed, Rahman-abdel.M hamdy, Mahouz M. nadia, (2006) "Novel 5-(2 hydroxyphenyl)-3-substituted-2,3-dihydro-1,3,4- oxadiazole-2-thione derivatives: Promising anticancer agents."*Bioorganic & Medicinal Chemistry* 14, 1236–1246.
48. Schreiber, S.L. (2000), Target-oriented and diversity-oriented organic synthesis in drug discovery. *Science,* 287(5460), 1964-1969.
49. Teague, S.J.; Davis, A.M.; Leeson, P.D.; Oprea, T. (1999), The Design of Leadlike Combinatorial Libraries. Angew. *Chem. Int. Ed. Engl.,* 38(24), 3743-3748.
50. Armstrong, R.W.; Combs, A.P.; Tempest, P.A.; Brown, S.D.; Keating, T.A. 1996, Multiple-Component Condensation Strategies for Combinatorial Library Synthesis. *Acc. Chem. Res.*, 29, 123-131.

51. Stoodley, R.J.; Katritzky, A.R. Boulton, *A.J.* (1979); *Advances in Heterocyclic Chemistry;* Eds, , 24, 293-361.
52. Cook, M.J.; Boulton, A.J.; McKillop, A., Eds. 1984; Comprehensive Heterocyclic Chemistry; *Eds*, 3, 1037-1038.
53. Ashok, D. Pallavi, K. (2006), Synthesis of 6-(6'-arylpyridin-2'-yl) and 6-(4\6'-diarylpyridin-2'-yl)- 3(4h)-oxo-l, 4-benzothiazines under microwave. *Heterocycl. Commun.*, 12(3-4), 197-200.
54. Galarreta, B.C.; Sifuentes, R. Amado, M.I.; Maruenda, H. 2008, The use of natural product scaffolds as leads in the search for trypanothionereductase inhibitors. *Bioorg. Med. Chem.,* 16, 6689-6695.
55. Hashimoto, T.; Amano, K.O.; Nakamura, Y.; Kanda, Y.; Kunii, S.; Motohashi, N.; Sakagami, H. 2008, Tumor-specific cytotoxicity andtype of cell death induced by benzocycloheptoxazines in humantumor cell lines. *Anticancer,* 28, 1069-1078.
56. Morak-Mlodawska, B.; Pluta, K. 2007, Synthesis of Novel Dipyrido-1,4-thiazines. *Heterocycles*, 71, 1347-1361.
57. Kamila, S.; Koh, B.; Zhang, H.; Biehl, E.R. Synthesis of (Z)-hetarylmethylene and (Z)-substituted benzylidene derivatives of 4H-benzo[1,4]thiazine-3-thiones and their subsequent conversion to benzothiopyrano-[3,2-b][1,4]benzothiazines. ARKIVOC, 2006, 2, 1-14.
58. Jagath, R.G. SrinivasaRao, K; Khalilullah, Md.; Latha, D.; Thirupathaiah, C2005,. synthesis of 9-arylthieno [3',2': 4,3]pyrimido[2,1-c][1,4] benzoxa/thiazines under microwave irradiation conditions. *Heterocycl. Commun.*, 11, 195-198.
59. Corelli, F.; Manetti, F.; Tafi, A.; Campiani, G.; Nacci, V.; Botta, (1997). Diltiazem-like calcium entry blockers: a hypothesis of the receptor-binding site based on a comparative molecular field analysis model. *J. Med. Chem.*, , 40(1), 125-131.
60. Bakavoli, M.; Sadeghian, H.; Tabatabaei, Z.; Rezaei, E.; Rahimizadeh, M.; Nikpour, M. (2008), SAR comparative studies on pyrimido[4,5-b][1,4] benzothiazine derivatives as 15-lipoxygenase inhibitors, using ab initio calculations. *J. Mol. Model.*, 14(6), 471-478.
61. Fringuelli, R.; Milanese, L.; Schiaffella, F. (2005), Role of 1,4-benzothiazine derivatives in medicinal chemistry. *Mini Rev. Med. Chem.,* 5(12), 1061-1073.
62. Bhavani, N.; Perumal, S.; Banureka, R. (2003) Ethyl cis-3-(2-methoxyphenyl)-1-4-thiazine-2-carboxylate 1,1-dioxide at 150 K. *Acta Cristallographica section* E, , 59(9), 1400-1402.
63. Cecchetti, V.; Calderone, V.; Tabarrini, O.; Sabatini, S.; Filipponi, E.; Testai, L.; Spogli, R.; Martinotti, E.; Fravolini, A. (2003), Highly potent 1,4-benzothiazine derivatives as K(ATP)-channel openers. *J. Med. Chem.,* 46(17), 3670-3679.
64. Sabatini, S.; Kaatz, G.W.; Rossolini, G.M.; Brandini, D.; Fravolini, A. (2008), From phenothiazine to 3-phenyl-1,4-benzothiazine derivatives as inhibitors of the Staphylococcus aureus NorA multidrug efflux pump. *J. Med. Chem.,* 51(14), 4321-4330.
65. Barazarte, A.; Camacho, J.; Domínguez, J.; Lobo, G.; Gamboa, N.; Rodrigues, J.; Capparelli, M.V.; Alvarez-Larena, A.; Andujar, S.; Enriz, D.; Charris, J. (2008), Synthesis, antimalarial activity, structure-activity relationship analysis of thieno-[3,2-b]benzothiazine S,S-dioxide analogs. *Bioorg. Med. Chem.*, 16(7), 3661-3674.
66. Mandour, A.H.; El-Sawy, E.R.; Ebid, M.S.; El-Sayed, Z.G. (2007), *Egypt. J. Chem.,* 50, 555-568.
67. Huang J.; Ding F.; Rojsitthisak P.; He F. S.; Wu J. (2020), Recent Advances in Nitro-Involved Radical Reactions. *Org. Chem. Front.* 7 (18), 2873–2898.

68. Louillat M. L.; Patureau F. W. (2014), Oxidative C-H Amination Reactions. *Chem. Soc. Rev*. 43 (3), 901–910.
69. Zhou K.; Yu Y.; Lin Y. M.; Li Y.; Gong L. (2020), Copper-Catalyzed Aerobic Asymmetric Cross-Dehydrogenative Coupling of C(Sp3)-H Bonds Driven by Visible Light. *Green Chem.* 22 (14), 4597–4603.
70. Ullmann F. Ueber Eine Neue Bildungsweise von(1903), Diphenylaminderivaten. Berichte der *Dtsch. Chem. Gesellschaft* 36 (2), 2382–2384.
71. Goldberg I. Über (1907), Phenylierung von primären aromatischen Amine. *Dtsch. Chem. Ges*. 40, 4541–4546.
72. Guram A. S.; Rennels R. A.; Buchwald S. L. A (1995), Simple Catalytic Method for the Conversion of Aryl Bromides to Arylamines. *Angew. Chem., Int. Ed. Engl*. 34 (12), 1348–1350.
73. Hartwig J. F. (1998), Transition Metal Catalyzed Synthesis of Arylamines and Aryl Ethers from Aryl Halides and Triflates: Scope and Mechanism. *Angew. Chemie Int. Ed.* 37 (15), 2046–2067.
74. Chan D. M. T.; Monaco K. L.; Wang R.-P.; (1998), Winters M. P. New N- and O-Arylations with Phenylboronic Acids and Cupric Acetate. *Tetrahedron Lett.* 39 (19), 2933–2936.
75. Lam P. Y. S.; Clark C. G.; Saubern S.; Adams J.; Winters M. P.; Chan D. M. T.; Combs A. (1998), New Aryl/Heteroaryl C-N Bond Cross-Coupling Reactions via Arylboronic Acid/Cupric Acetate Arylation. *Tetrahedron Lett.* 39 (19), 2941–2944.
76. Shilpa T.; Neetha M.; Anilkumar G. (2021) Recent Trends and Prospects in the Copper-Catalysed “on Water” Reactions. Adv. Synth. *Catal.*, 363 (6), 1559–1582.
77. Gu Q.-S.; Li Z.-L.; Liu X.-Y. (2020), Copper (I)-Catalyzed Asymmetric Reactions Involving Radicals. *Acc. Chem. Res*. 53 (1), 170–181.
78. Nishanth Rao R.; Jena S.; Mukherjee M.; Maiti B.; Chanda K. (2021), Green Synthesis of Biologically Active Heterocycles of Medicinal Importance: A Review. Environ. *Chem. Lett.* 19 (4), 3315–3358.
79. Martina K.; Cravotto G.; Varma R. S. (2021), Impact of Microwaves on Organic Synthesis and Strategies toward Flow Processes and Scaling Up. *J. Org. Chem.* 86, 13857–13872.
80. Shalaby M. A.; Fahim A. M.; Rizk S. A. (2023), Microwave-assisted synthesis, antioxidant activity, docking simulation, and DFT analysis of different heterocyclic compounds. *Sci. Rep.* 13, 4999.
81. Urbina K.; Tresp D.; Sipps K.; Szostak M. (2021), Recent Advances in Metal-Catalyzed Functionalization of Indoles. *Adv. Synth. Catal*. 363, 2723–2739.
82. Liu F.; Anand L.; Szostak M. (2023), Diversification of Indoles and Pyrroles by Molecular Editing: New Frontiers in Heterocycle-to-Heterocycle Transmutation. *Chem.Eur. J.* 29, e202300096.
83. Safaei, G. J., Ghasemzadeh, M. A., and Mehrabi, M. (2013). Calcium oxide nanoparticles catalyzed one-step multicomponent synthesis of highly substituted pyridines in aqueous ethanol media. *Sci. Iran.* 20, 549–554.
84. Gao, S., Stopka, T., and Niggemann, M. (2015). Calcium-catalyzed dynamic multicomponent reaction. *Org. Lett.* 17, 5080–5083.
85. Saito S., Tsubogo,T. and Kobayashi S., (2007), *J. Am. Chem. Soc* 129, 5364-5365.
86. Vanden Eynden M. J., and Stambuli J. P., (2008), *Org. Lett.*, 10, 5289-5291.
87. Yaragorla, Pareek S. A., and Dada, R. (2015), *Tetrahedron Lett.,* 56, 4770-4774.
88. Ghosh A., Chawla V., and Banerjee P., (2019), *Eur. J. Org. Chem.*, 3806-3814.
89. DiMauro E. F., and J. Kennedy M., (2007), *J. Org. Chem.*, 72, 1013-1016.
90. Han, J.; Xu, B.; Hammond, G. B. J. (2010), *Am. Chem. Soc*. 132, 916.

ICRTMS-2024
International e-Conference on Recent Trends in Material Science
In Association with International Journal of Scientific Research in Science and Technology
Volume 11 | Issue 9 | Print ISSN: 2395-6011 | Online ISSN: 2395-602X (www.ijsrst.com)

Models and Variations in The Thermal Conductivity of Nanofluids

Vijay S. Raykar

Department of Physics, G. M. Vedak College of Science, Tala 402111, (Affiliated to University of Mumbai) Maharashtra, India

ABSTRACT

The representations or equations of effective thermal conductivity in the current work were discussed and are applied to data. The proposed revised model with the latest empirical findings has been reported, which explains the anomalous behavior in the thermal conductivity of Nanofluid samples
Keywords: Effective medium theory, Brownian motion, Carbon nanotubes, Nanofluids, Thermal Conductivity

1) INTRODUCTION

Recent work suggests that Nanofluids, a mixture of nanometer-sized particles and carbon Nanotubes (CNTs) in fluid, can increase the amount of thermal transport beyond what most conventional coolants can see today [1-3]. Since carbon nanotubes exhibit the highest ability to transfer the heat of any material known to us, the addition of them to conventional heat transfer liquids should, in turn, increase the liquid's thermal conductivity and Effusivity [3-6]. Results indicate that through the uses of hydrophilic entities, functional groups, and the use of sound energy stable dispersions, on the order of months, were obtained in water and ethylene glycol with the addition of carbon nanotubes as low as 0.001 wt%. [7]. 85-90% increase was observed in the estimated thermal conductivity and Effusivity of the prepared samples [8]. Further tests on the viscosity and electrical conductivity of the added nanoparticles/CNTs reveal that charge interactions implemented by surfactants play an important role in the stability and subsequent increase in transport properties of the fluids [9]. The large thermal conductivity enhancements reported by the experiment led to excitement but also to controversy [10]. The origin of the enthusiasm was that the measured thermal conductivity was often much larger than that predicted by well- established effective medium theories under the assumption of well-dispersed particles. [11].

Nanofluids fall naturally into two classes: those Nanofluids in which one element is a metal/metal oxide Nanoparticle and surface-active agent and those in which the former is replaced with CNTs. Many Nanofluids in both classes have been studied, but, because the macroscopic scale for suspensions and composites description has now changed to the nanoscale with different physics, the Effective Medium Theory (EMT) of Maxwell and Brugemann is not appropriate to predict their transport properties [12]. Instead, the differential EMT developed by Gao and his coworkers for rod-like inclusions and modified by us for Carbon Nanotube (CNT) based Nanofluids has been applied in conjunction with the Brownian motion theory developed by Choi

et al [13-18]. Unfortunately, despite its wide application to Nanofluids, the validity of this approach is still open to some questions.

2) METHODS OF SYNTHESIS

Synthesis of Nanofluids:

The existing methods of Nanofluid synthesis are divided into the single-step and two-step processes. In the single step, Nanofluid can be produced using one process cycle. The process is favorable as exhibited by the fact that produced nanoparticles are usually small (2-30 nm), agglomeration is minimized and the prepared Nanofluids are the stable ones.

3) THEORETICAL APPROACH

Stationary or static mode:

The static thermal conductivity of Nanofluid obeys the classical Maxwell model from Effective Medium Theory [19]. The Maxwell model of effective thermal conductivity of solid–liquid mixtures is given for micro or millimeter-sized particles suspended in base fluids.

$$\lambda_{eff} = \frac{\lambda_p + 2\lambda_{bf} + 2(\lambda_p - \lambda_{bf})\phi}{\lambda_p + 2\lambda_{bf} - (\lambda_p - \lambda_{bf})\phi}\lambda_{bf} \qquad (1)$$

where λ_{eff} is the thermal conductivities of the solid–liquid mixture. Maxwell's model is good for spherical-shaped particles with low particle volume concentrations. Hamilton and Crosser modified Maxwell's model by incorporating shape factors to account for the effect of the shape of particles [20]. The ETC of the Nanofluid is given as

$$\lambda_{eff} = \frac{\lambda_p + (n-1)\lambda_{bf} - (n-1)\phi(\lambda_{bf} - \lambda_p)}{\lambda_p + (n-1)\lambda_{bf} + \phi(\lambda_{bf} - \lambda_p)}\lambda_{bf} \qquad (2)$$

Where n is the empirical shape factor given by 3/ψ, and ψ is the particle Sphericity, defined as the surface area of a sphere (with the same volume as the given particle) to the surface area of the particle. For spherical particles, the value of n is 3. In the above model, if the particles in fluid are cylindrical, just like CNTs, λ_{eff} can be calculated by taking n=6, $\lambda_P = \lambda_{CNT,}$ and ϕ is the volume fraction of CNTs in fluid [21].

Brownian motion-induced Nano-convection mode

A theoretical model has been proposed by Jang and Choi [22] that involves four modes contributing to the energy transfer resulting in the enhancement of thermal conductivity of Nanofluids [22]. The first mode is a collision between base fluid molecules, the second mode is the thermal diffusion in nanoparticles, the third mode is the collision of nanoparticles with each other due to the Brownian motion, and the fourth mode is a collision between base fluid molecules and nanoparticles by thermally induced fluctuations. Considering all the above four modes, the ETC of Nanofluid is given as

$$\lambda_{nf} = \lambda_{bf}(1-\phi) + \beta_1 \lambda_p \phi + C_1 \frac{d_{bf}}{d_p} \lambda_{bf} \, \mathrm{Re}_{dp}^2 \, \mathrm{Pr} \, \phi \qquad (3)$$

where $\beta_1 = 0.01$ is a constant for considering the Kapitza resistance per unit area; $C_1 = 18 \times 10^6$ is a proportionality constant; Pr is the Prandtl number defined by $\mathrm{Pr} = \frac{\mu_{bf}}{p_{bf}\alpha_{bf}}$ of the base fluid, and the Reynolds number is defined by $\mathrm{Re}_{d_p} = \frac{\left(\overline{C}_{R.M.} d_p\right)}{\nu}$ where $\overline{C}_{R.M.} = \frac{\kappa T}{3\pi\mu_{bf} d_p l_{bf}}$ is the random motion velocity of a nanoparticle and ν is the kinematic viscosity of base fluid. They recommend, for water-based Nanofluids the equivalent diameter $d_{bf} = 0.384$ nm and mean-free path of water $l_{bf} = 0.738$ nm at a temperature of 300 K. The overall thermal conductivity of Nanofluids could be found by adding equations consisting of static and dynamic parts.

$$\lambda_{eff} = \lambda_{static} + \lambda_{dynamic} \qquad (4)$$

The model proposed by Koo and Kleinstreuer is one among the existing models that predict the thermal conductivity of Nanofluids based on Brownian motion [23]. This model was composed of two parts. One is referred to as the static part (λ_{static}) evaluated by mixture models, i.e. the Maxwell model and the other part ($\lambda_{dynamic}$) is attributed to the Brownian motion. According to this model the ETC of NFs given as

$$\lambda_{eff} = \frac{\lambda_p + 2\lambda_{bf} - 2(\lambda_{bf} - \lambda_p)\phi}{\lambda_p + 2\lambda_{bf} + (\lambda_{bf} - \lambda_p)\phi} \lambda_{bf} + 5\times10^4 \beta\phi\rho_{bf} C_{pbf} \sqrt{\frac{\kappa T}{\rho_p d_p}} f(T,\phi) \qquad (5)$$

Where β shows the fraction of the liquid volume that travels with a particle and decreases with the particle concentration because of the viscous effect of moving particles. β is a function of the volume fraction ϕ of nanoparticles, which is given by

$$\beta = 0.0137(100\phi)^{-0.8229} \quad \text{for } \phi<0.01 \qquad (6)$$

$$\text{And} \quad \beta = 0.0011(100\phi)^{-0.7272} \quad \text{for } \phi>0.01 \qquad (7)$$

The function f (T, ϕ) is given by

$$f(T,\phi) = (-6.04\phi + 0.4705)T + (1722.3\phi - 134.63) \qquad (8)$$

Which is valid for $0.01<\Phi<0.04$ and $300\ \mathrm{K}<T<325\ \mathrm{K}$.

New empirical correlations were derived by Das et al [24] from a broader set of experimental data derived from three Nanofluids.

Where,

$$f(T,\varphi) = (2.8217\times10^{-2}\phi + 3.917\times10^{3})\left(\frac{T}{T_0}\right) + (-3.0669\times10^{-2}\phi - 3.91123\times10^{-3}) \quad (9)$$

And $$\beta = 8.4407 \times (100\phi)^{-1.07304} \quad (10)$$

$$\beta = 9.881 \times (100\phi)^{-0.9446} \quad (11)$$

for ZnO and CuO-based Nanofluids respectively.

Chon et al. [25] proposed an empirical correlation based on experimental data for the thermal conductivity of Al_2O_3 Nanofluid using the Buckingham-Pi theorem with a linear regression scheme. They showed that the Brownian motion of the suspended nanoparticle is the most important factor in the enhancement of the thermal conductivity of Nanofluids. The correlation is given as

$$\frac{\lambda_{eff}}{\lambda_{bf}} = 1 + 64.7\,\mathrm{Re}^{1.2321}\left(\mathrm{Pr}\right)^{0.9955}\left(\frac{d_{bf}}{d_p}\right)^{0.3690}\left(\frac{\lambda_p}{\lambda_{bf}}\right)^{0.7476}\left(\phi\right)^{0.7460} \quad (12)$$

where d_{bf} is the molecular diameter of the base fluid; $\mathrm{Pr} = \dfrac{\mu_{bf}}{p_{bf}\alpha_{bf}}$ is the Prandtl number of the base fluid and $\mathrm{Re} = \dfrac{\left(\rho_{bf}\kappa T\right)}{\left(3\pi\mu_{bf}^2 l_{bf}\right)}$ is the Reynolds number; l_{bf} is the mean-free path for the base fluid.

Prasher et al. [26] proposed the Multi-Sphere Brownian model (MSBM) to predict the enhancement in the thermal conductivity of Nanofluid is primarily due to the convection caused by the Brownian motion of the nanoparticles. They introduced a convective–conductive model, which is a combination of the Maxwell–Garnett conduction model and the convection caused by the Brownian motion of suspended nanoparticles.

$$\frac{\lambda_{nf}}{\lambda_{bf}} = 1 + A\mathrm{Re}^m\left(\mathrm{Pr}\right)^{0.333}\phi\left(\frac{\left[\lambda_p\left(1+2\alpha\right)+2\lambda_m\right]+2\phi\left[\lambda_p\left(1-2\alpha\right)-\lambda_m\right]}{\left[\lambda_p\left(1+2\alpha\right)+2\lambda_m\right]-\phi\left[\lambda_p\left(1-\alpha\right)-\lambda_m\right]}\right) \quad (13)$$

where the coefficient $A = 4\times10^4$; m = 2.5 ± (15% of 2.5) for water-based Nanofluids, m = 1.6 ± (15% of 1.6) for EG-based Nanofluids, and m = 1.05 ± (15% of 1.05) for oil-based Nanofluids; $\lambda_m = \lambda_{bf}\left[1+\left(\frac{1}{4}\right)\mathrm{Re}.\mathrm{Pr}\right]$ is the matrix conductivity; $\mathrm{Re} = \dfrac{1}{\nu}\sqrt{\dfrac{18\kappa T}{\pi\rho_p d_p}}$ is the Brownian–Reynolds number; $\alpha = 2R_b\lambda_m/d_p$ is the nanoparticle Biot number; R_b is the interfacial thermal resistance between nanoparticles and different fluids; ν is the kinematic viscosity and Pr is the Prandtl number of the base fluid.

Another model based on regression analysis is used to predict temperature-dependent ETC enhancement in Nanofluids [27]

$$\frac{\lambda_{eff}}{\lambda_f} = 1 + 4.4\,\mathrm{Re}^{0.4}\left(\mathrm{Pr}\right)^{0.66}\left(\frac{T}{T_{fr}}\right)^{10}\left(\frac{\lambda_s}{\lambda_f}\right)^{0.03}\left(f_{eff}\right)^{0.66} \quad (14)$$

Following the work of Corcione [27], he developed an ETC enhancement model based on regression analysis. The correlation proposed is based upon 11-12 data sets of thermal conductivity of Nanofluids mainly containing TiO_2, Al_2O_3, and CuO nanoparticles. The nanoparticle volume fractions are in the range from 0.002 to 0.09 whereas temperature lies from 294 K to 324 K. The effective thermal conductivity enhancement of Nanofluid is given by equation as a function of Reynolds number, Prandlts number, and effective volume fraction.

Conclusion

The classical models are inadequate to explain the anomalous increase in the effective thermal conductivity of Nanofluids. Therefore, there is a need to further develop the effective thermal conductivity model, which encompasses all the prepared Nanofluids with different variety of nanoparticles of different shapes.

Acknowledgment

The V.S.R. is thankful to Mr. J. V. Deore, Incharge Principal, G. M. Vedak College of Science, Tala for his valuable guidance during this research work.

5) REFERENCES

[1] Eastman, J., Choi, S., Li, S., Yu, W., and Thompson, L., 'Anomalously increased effective thermal conductivities of ethylene glycol-based nanofluids containing copper nanoparticles,' Applied Physics Letters, Vol. 78, No. 6, 2001, pp. 718–720.

[2] Das, S., 'Nanofluids - The cooling medium of the future,' Heat Transfer Engineering, Vol. 27, No. 10, 2006, pp. 1–2.

[3] Hosseini, M. and Ghader, S., 'A model for temperature and particle volume fraction effect on nanofluid viscosity,' Journal of Molecular Liquids, Vol. 153, No. 2-3, 2010, pp. 139–145.

[4] Li, C.H., P. G., 'Experimental investigation of temperature and volume fraction variations on the effective thermal conductivity of nanoparticle suspensions (nanofluids),' Journal of Applied Physics, Vol. 99, No. 8, 2006,

[5] Jang, S., Lee, J. H., Hwang, K., and Choi, S., 'Particle concentration and tube size dependence of viscosities of Al_2O_3 water nanofluids flowing through micro- and minitubes,' Applied Physics Letters, Vol. 91, No. 24, 2007,

[6] Zhang, X., Gu, H., and Fujii, M., 'Effective thermal conductivity and thermal diffusivity of nanofluids containing spherical and cylindrical nanoparticles,' Journal of Applied Physics,

Vol. 100, No. 4, 2006,

[7] Gharagozloo, P., Eaton, J., and Goodson, K., 'Diffusion, aggregation, and the thermal conductivity of nanofluids,' Applied Physics Letters, Vol. 93, No. 10, 2008.

[8] V.S. Raykar, A. K. Singh, Photoacoustic method for measurement of thermal effusivity of Fe_3O_4 nanofluid,J. of Thermodynamics, 464368, (2011).

[9] Cherkasova, A. and Shan, J., 'Thermal conductivity enhancement of nanofluids,' Carbon Nanotubes, Vol. 222, 2006, pp. 235–237

[10] Xie, H., Lee, H., Youn, W., and Choi, M., 'Nanofluids containing multiwalled carbon nanotubes and their enhanced thermal conductivities,' Journal of Applied Physics, Vol. 94, No. 8, 2003, pp. 4967–4971

[11] Murshed, S., Leong, K., and Yang, C., 'A combined model for the effective thermal conductivity of nanofluids,' Applied Thermal Engineering, Vol. 29, No. 11-12, 2009, pp. 2477–2483.

[12] Hasselman, D. P. H. and Johnson, L. F., 'Effective Thermal Conductivity of Composites with Interfacial Thermal Barrier Resistance,' Journal of Composite Materials, Vol. 21, 1987,
pp. 508–515.

[13] Gao, L. and Zhou, X., 'Differential effective medium theory for thermal conductivity in nanofluids,'Physics Letters, Section A: General, Atomic and Solid State Physics, Vol. 348, No. 3-6,2006, pp. 355–360.

[14] Bandyopadhyaya, R., Nativ Roth, E., Regev, O., and Yerushalmi Rozen, R.,Stabilization of Individual Carbon Nanotubes in Aqueous Solutions,' Nano Letters, Vol. 2, No. 1, 2002, pp. 25–28.

[15] Ding, Y., Alias, H., Wen, D., and Williams, R., 'Heat transfer of aqueous suspensions of carbon nanotubes (CNT nanofluids),' International Journal of Heat and Mass Transfer, Vol. 49, No. 1-2, 2006, pp. 240–250.

[16] A. K. Singh, V. S. Raykar, Microwave synthesis of silver nanofluids with polyvinylpyrrolidone (PVP) and their transport properties, Colloid Polym. Sci., 286, no. 14-15 (2008), p. 1167.

[17] V.S. Raykar, A. K. Singh, Thermal and rheological behavior of acetylacetone stabilized ZnO nanofluids, Thermochim. Acta., 502, no. 6 (2010), p. 60.

[18] V.S. Raykar, A. K. Singh, Dispersibility dependence of thermal conductivity of carbon nanotube based nanofluids, Phys. Lett. A, 374, no. 45 (2010), p. 4618.

[19] Maxwell, J. C., Treatise on Electricity and Magnetism, Vol. Claredon Press, 1873, pp. Oxford, U. K.

[20] Hamilton, R. and Crosser, O., 'Thermal conductivity of heterogeneous two component systems,' I and EC Fundamentals, Vol. 125, 1962, pp. 187.

[21] Jiang, W., D. G. P. H., 'Measurement and model on thermal conductivities of carbon nanotube nanorefrigerants,' International Journal of Thermal Sciences, Vol. 48, No. 6, 2009, pp. 1108– 1115.

[22] Jang, S. and Choi, S., 'Role of Brownian motion in the enhanced thermal conductivity of nanofluids,'Applied Physics Letters, Vol. 84, No. 21, 2004, pp. 4316–4318.

[23] Koo, J., K. C., 'A new thermal conductivity model for nanofluids,' Journal of Nanoparticle Research, Vol. 6, No. 6, 2004, pp. 577–588.

[24] Vajjha, R.S.and Das, D., 'Experimental determination of thermal conductivity of three nanofluids and development of new correlations,' International Journal of Heat and Mass Transfer, Vol. 52, No. 21-22, 2009, pp. 4675–4682.

[25] Chon, C., Kihm, K., Lee, S., and Choi, S., 'Empirical correlation finding the role of temperature and particle size for nanofluid (Al2O3) thermal conductivity enhancement,' Applied Physics Letters, Vol. 87, No. 15, 2005, pp. 1–3.

[26] Bhattacharya, P., Saha, S., Yadav, A., Phelan, P., and Prasher, R., 'Brownian dynamics simulation to determine the effective thermal conductivity of nanofluids,' Journal of Applied Physics, Vol. 95, No. 11 I, 2004, pp. 6492–6494.

[27] Corcione, M., 'Heat transfer features of buoyancy-driven nanofluids inside rectangular enclosures differentially heated at the sidewalls,' International Journal of Thermal Sciences, Vol. 49, No. 9, 2010, pp. 1536–1546.

ICRTMS-2024
International e-Conference on Recent Trends in Material Science
In Association with International Journal of Scientific Research in Science and Technology
Volume 11 | Issue 9 | Print ISSN: 2395-6011 | Online ISSN: 2395-602X (www.ijsrst.com)

Global Environmental Sustainablity Through Green Technology

Janardhan H. Shendkar and Suresh D. Dhage*
Department of Physics, SSJES's, Arts, Commerce and Science College, Gangakhed.
Dist. Parbhani (M.S.)
*Department of Chemistry, SSJES's, Arts, Commerce and Science College, Gangakhed.
Dist. Parbhani (M.S.)

ABSTRACT

Green technology is the technology which is environment friendly, developed and used in such a way so that it doesn't disturb or harm our environment and conserves natural resources. Green Technology is a part of renewable technology. Importance of this technology cannot be ignored. Green Technology is also called as "Environmental technology" or "Clean technology". There are many more application of Green Technology. Its applications includes environmental science, green chemistry, monitoring of environment and also the electronic devices and equipment which are used to monitor, control, protect and conserve the environment and natural resources. It is related to sustainable technologies.
Keywords: Green technology, Sustainable Development, Environment etc.

I. INTRODUCTION

Green technology is a term which has been recently introduced and the main idea is to create new technologies which are environment friendly. Energy efficiency, recycling, health and safety concerns, renewable resources are the factors that contribute to green technology. The aim of adopting green technology is reduce damage to the environment, birds and animals and plants as well as damage to the world in general. It is also referred as clean technology. It is safe for use and promotes a safety and healthy environment. The purpose of this technology is to reduce global warming and greenhouse effect.

Green technology is an environmental technology that is mainly adopted to protect the environment and conserve resources. As it is the part of the renewable energy branch of the environmental technology movement, the importance of green technology cannot be ignored. By developing green technology we can reduce the damage caused by the pollution and other factors that affect the environment and animals. Its aim is to reduce the degradation of the environment. As the environment is full of pollution and hazardous there is an urgent need for to adopt the green environment before the things get worsen.

1. Goals of Green Technology

The main goals of green technology are

- Sustainability- Meeting the needs of the future without damaging or depleting the natural resources.
- Source reduction – The wastes and pollution to be reduced by changing the production and consumption patterns.
- Innovation – Developing alternative to technologies to prevent further damage to the health and environment.
- Viability- Economic viability of technologies and products that benefit the environment and truly protect the planet.

2. Objectives of Green Technology

Green technology is mostly focused on developing new technologies which has no or little impact on environment and which is harmless to society. Some of the objectives of green technology are as follows:

- To achieve the good quality of life.
- To reduce increasing the rate of growth of energy consumption.
- To enhance the economic development.
- To reduce the level of pollution and waste generation thus protecting or improving the environmental quality.
- To motivate for new innovations in Green Technology development.
- To increase the awareness and education among the public about Green Technology.
- To increase the use raw materials and to promote the utilization of residues, recyclable waste, local materials as raw materials for conversion process.
- To encourage for sustainable development and preserve the environment for future generations.

3. Importance of Green Technology

Green technology, an environmentally friendly technology is developed and used in a way that protects the environment and also conserves natural resources. A part of the renewable energy branch of the environmental technology, the importance of green technology cannot be ignored. We have come to a point, where we need to pause and reflect on the growing green technology importance and why it is going to be important for humanity. With many reasons behind green technology importance, perhaps volumes can be written and spoken on the subject. Whether it is the growing importance of green technology in the industry or at homes, it is certain that things need to be done fast. It does not take a rocket scientist to state that mankind has to do something about clean environment and save energy resources. Going green can only help us come out of the present tough situation. Before things turn for the worst, we should realize the green technology importance to solve this problem [1-2].

The main four pillars of green technology policy are

- Energy – Seek to attain energy independent and promote efficient utilization;
- Environment - Conserve and minimize the impact on the environment;
- Economy - Enhance the national economic development through the use of technology; and
- Social - Improve the quality of life for all [3].

DISCUSSION

Solar energy, wind energy, ocean energy, energy conservation, Bioremediation are some of the green technologies which are intended to protect environment and conserve natural resources.

Solar Energy

Solar power is quickly becoming a major contender in the race for renewable energy. About 89 petawatts of power are available at any given point in time, 6,000 times the power consumed by all human civilization. In 14.5 seconds, the earth absorbs as much solar energy as humanity consumes in 24 hours. There are various application of solar energy. For example solar energy can be harnessed for water distillation through evaporation. After placing translucent material over a moist patch of ground, in a manner that does not allow air to escape, the evaporated water which becomes a liquid on the surface of the material. This water can then be gathered into a cup or another container of some sort. The water produced is pure, and can be safely drunk.

India's solar power generation capacity stood at over 9 GW as on December 31, 2016 with Tamil Nadu having the largest output capability followed by Rajasthan and Gujarat. "As on December 31, 2016, Gujarat (1.16 GW), Rajasthan (1.32 GW), and Tamil Nadu (1.6 GW) have crossed 1 GW solar installations…, while Andhra Pradesh (0.98 GW), Telangana (0.97 GW) and Madhya Pradesh (0.84 GW) are close to these states. Solar power development varies from state to state depending on solar irradiance, availability of conducive state policy for the sector, availability of land, cost of financing and business environment such as willingness of DISCOMS to purchase the solar power, power evacuation infrastructure, etc.

The government is promoting solar energy through fiscal and promotional incentives such as capital and/or interest subsidy, tax holiday on the earnings for 10 years, generation-based incentive, accelerated depreciation, viability gap funding (VGF), financing solar rooftop systems as part of home loan, concessional excise and custom duties, preferential tariff for power generation from renewables, and foreign investment up to 100 per cent under the automatic route, etc. This apart, the government has been supporting solar manufacturing by way of various mechanisms such as Modified Special Incentive Package Scheme (M-SIPS) of the Ministry of Electronics & Information Technology [7].

Wind Energy

Wind energy is a capable source for renewable energy, but the uncontrollable nature of the wind presents concerns. Unsteady winds do not provide the best aerodynamic performance for wind turbines and sudden, uneven gusts can lower the productivity of the blades. Under National Wind Resource Assessment programme, Ministry through National Institute of Wind Energy, Chennai (erstwhile Centre for Wind Energy Technology (C-WET)) and State Nodal Agencies had installed and monitored 794 dedicated Wind Monitoring Stations (WMS) of height ranging from 20 m to 120 m (20m, 25m, 50m, 80m, 100m & 120m) throughout the country as on 31.12.2014. Initially the wind monitoring was carried out only in known windy areas. Now it is extended to new/ uncovered areas which are not explored in earlier projects to complete the Indian Wind resource mapping. Further hundreds of private winds monitoring stations are also operational in the country. Based on the analysis on the data collected from these 700 plus WMS, it is found that 237 stations have economically preferable wind power potential greater than 200 W/m2 [8].

Ocean Energy

At present, the possibility of globally-dominant, large-scale, ocean energy plants is just that: an attractive possibility. As with any new technology, existing marine energy devices possess limitations. Their construction and maintenance may currently prove financially demanding, and not all sites are suitable for their effective implementation. However, these problems will likely soon see solutions, and ocean energy conversion may

soon produce as much as, if not more electricity than other forms of green energy, such as traditional wind power systems.

Energy Conservation

Energy Conservation can be achieved by the use of equipment which requires lesser amount of energy, following low consumption of electricity; thereby reducing the use of fossil fuels to generate the same. Energy conservation and efficiency are both energy reduction techniques.

Water Treatment

It is a step by step processes used to make the water more suitable for the end users. The use of such water categorized broadly among drinking water, industrial use, and medical use and also for other uses. The main objective of water treatment is the removal of pollutants in the water, so as to make it suitable for further use. From the viewpoint of environment water treatment is used to reduce the adverse impact of the water returning to the environment after its use. Settling, filtration, disinfection, coagulation are some of the basic physical and chemical processes employed for water treatment. Also aerated lagoons, activated sludge or slow sand filter are some prominent process.

Environmental Remediation

Environmental Remediation deals with the removal of pollutants from the natural resources such as ground water, water reserves on earth surface, soil for the protection of environment and human health.

Attaining Environmental Sustainability via Green Technologies

By using various green technologies in a systematic way with strategic plan there is a probability of attaining environmental sustainability which helps in conservation of natural resources and protection of environment. The technologies like fuel cell and renewable energies are getting much exposure as green technologies as they can be easily adapted in the existing infrastructure. Green Transport is an application of fuel cell and renewable energies, so the adaptability of this depends on how well fuel cell and renewable energies are implemented.

The risk associated with "dirty" technologies such as the petroleum products are alarmingly raising. The "clean" technologies as a result, are expected to provide lower risk alternatives. Most of the governing bodies in developing and developed countries are investing large amount of money into clean energy market and pursuing businesses facilitating renewable energy technologies that are energy efficient. One of United Nations Environmental Program's report states, in 2006, $2.9 billion was invested in clean technologies (mostly in wind, solar and other low-carbon energy technologies), which was 80% higher over 2005. As climate change threat has spurred green investing, UNEP coins this trend as the "world's newest gold rush" [4, 5].

Green Technology (GT) covers a broad group of methods and materials for generating energy to non-toxic cleaning products. The main reason, this area has been significantly important is because most of the people expect a dramatic innovation and changes in their livelihood. The development of alternative technology should attempt to benefit the planet truly protecting the environment and mother earth. This technology meets the needs of society in ways that can continue indefinitely into the future without damaging or depleting natural resources. In terms of the technology that can create products, which can be fully reclaimed or re-used,

such cradle to grave cycle of manufacturing has successfully reduced waste and pollution by changing patterns of production and consumption. The innovations in technology have aroused interest in developing alternative fuels as a new means of generating energy and energy efficiency. Furthermore, GT is the application of green chemistry and green engineering, one of the most exciting fields of technology, which is supposed to transform the way that everything in the world is manufactured. The world relies on large amounts of energy. The level of dependency has increased on fossil fuels such as oil, gas and coal. Energy is important for sustaining the planet and therefore the task before us is to assess and utilize various sources of energy that occur naturally in the environment. Green technologies definitely shows prominent results in utilizing various alternative energy resources to overcome the present energy demands and also promotes sustainable development.

CONCLUSION

From the above discussion we can conclude that green technology is a must in today's scenario to achieve environmental sustainability and also to lead sustainable life. Because the conventional technology is challenging the sustainability of today's environment. Although some problems are coming in the way of its implementation but if we see its long term implication it's for sure we and our future generation will be benefitted. Also using green technology we can conserve our limited energy sources to some extent. In India, the demand for private transportation is alarmingly increasing because of the inadequacy of public transportation system. The development of eco-friendly and affordable public transportation solution is not therefore, a question of choice, but the need of hour. This can be solved by green technologies with proper research and development. There is a huge construction work going on in India. The concept of environment-friendly or green building needs to be adopted by developing locally relevant all-weather building technologies and construction methodologies to reduce increasing dependency on air-conditioning. Almost 70 per cent of Indian population depends on agriculture, which is one of the energy intensive sectors. Agriculture consumes about 35 per cent of the total power generated through electrically operated pump sets. It is expected that about 30 per cent of savings is possible through appropriate technology [6]. For example, larger valve can save fuel and power to draw water from the well. It has been shown that the farmers can save 15 litres of diesel every month by simply reducing the pipe height by 2m. The use of good quality PVC suction pipe can save electricity up to 20 per cent. Finally, Green technologies would definitely help in attaining environmental sustainability if utilized systematically.

REFERENCES

1. www.ajcebeats.com/the-importance-of-greentechnology/
2. Menu Bhardwaj and Neel am (2015), the Advantages and Disadvantages of Green Technology, Journal of Basic and Applied Engineering Research, 2 (22); pp. 1957-1960.
3. http://www.gpnm.org/e/articles/Definition-of-Green-Technology-by-Kettha-Ministry-of-Energy-Green-Technology-and-Water-a5.html
4. Sustainability and Green Technology, An e-book on strategies for sustainability authored by the Class of 2012 Massachusetts Academy of Mathematics and Science.
5. http://www.unapcaem.org/publication/greentech.pdf
6. http://www.nedcap.org/index_files/ Page2210.htm.
7. http://indianexpress.com/article/india/indias-solarpower-capacity-crosses-9-gw 4510799/
8. http://mnre.gov.in/schemes/grid-connected/solarthermal-

ICRTMS-2024
International e-Conference on Recent Trends in Material Science
In Association with International Journal of Scientific Research in Science and Technology
Volume 11 | Issue 9 | Print ISSN: 2395-6011 | Online ISSN: 2395-602X (www.ijsrst.com)

Current Advancements in Bismuth Vanadate Materials for Supercapacitor: A Review

Mr. Vilas S. Jadhav[1], Dr. Kunal D. Gaikwad[2]

[1]Dept. Of Electronics Assistant Professor K. K. Wagh Arts science & commerce College Pimpalgaon (B), Nasik

[2]Dept. Of Electronics Associate Professor Dadasaheb Dr. Suresh G. Patil College chopda Dist. Jalgoan

ABSTRACT

Human life has been seriously threatened by the rising energy usage of nonrenewable fossil fuels in recent decades. Consequently, there is a pressing need to create inexpensive, environmentally safe, and dependable energy storage technologies. Supercapacitors are a potential energy technology because of their high power density, superior cycle stability, and quick charge/discharge times. Studies on metal-based compounds and their composites abound; bismuth-based materials and their composites stand out due to their charge storage capacity, redox behavior, environmental friendliness, and growing interest in their potential applications in supercapacitor and battery technologies. Firstly describe the development of supercapacitor and working principle and mechanism of supercapacitor and we summarize bismuth vanadate based electrode material supercapacitor parameter like cyclic stability, specific capacitance, electrolyte and method of preparation of nanoparticle. Furthermore, the difficulties and prospects for bismuth-based composites for energy storage are explored in the concluding section.

Keywords- Energy density, Power density, Specific Capacitance, energy storage, supercapacitor

I. INTRODUCTION

Scientists and researchers have been looking into electrode materials that can combine batteries' high energy density with supercapacitors quick charging times in recent years [48]. Fossil fuel use and consumption are the primary causes of the recent massive increase in energy demand because they have a persistently negative impact on ecosystems and the environment [1]. Supercapacitors, batteries, and capacitors are examples of larger energy storage devices with high power and energy densities that are required due to the recent technological breakthroughs and the rapid rise of energy consumption [2]. The availability of drinking water is decreasing in comparison to sea water, electricity, fuel, and air. For the biosphere and all living beings, this lack is detrimental [3, 4]. There are many choices for renewable energy solutions that have been investigated because using renewable energy sources is essential for improving the environment and human health. For both developed and developing countries, RuO2, MnO2, Co3O4, NiO, SnO2, and NiFe2O3 must be constructed with efficiency. This applies to supercapacitors, fuel cells, and batteries. Nanoelectrodes made using a range of chemical and physical deposition techniques have been researched for utilization in supercapacitors for commercialization [5-7]. These electrode materials include compounds based on bismuth (Bi), such as oxides,

chalcogenides, and halides. These compounds have a variety of uses, such as supercapacitors, batteries, solar cells, gas sensors, and photocatalysis [8-9]. Supercapacitors based on vanadium oxide outperform other materials because of their high level capacitance, good rate capability, low cost, and superior store capacity [10]. Among the previously available techniques for generating m-BiVO4 are the microwave-assisted approach, flame spray pyrolysis, solid-state reaction, co-precipitation, hydrothermal, solvothermal, and solution combustion procedures. The produced items included uniform sizes, unique morphologies, well defined self-assembled structures, and high phase purity. The hydrothermal process may offer simple and environmentally friendly testing conditions [12].

Classification of supercapacitors

Supercapacitors come in three different varieties: EDLC, Psudocapacitive, and hybrid. Because the capacitance is proportional to the surface area of the electrode material and electrosorption and redox reaction mechanisms take place on the electrode surface, super capacitive supercapacitors are utilized. Their energy density and specific capacitance are higher than those of an electrostatic double-layer capacitor because of their faradic redox reaction and broad operating potential window [32].

Electrostatic double-layer capacitor

The electrostatic double-layer capacitors store energy through the accumulation of electrostatic charges, or the physical adsorption-desorption of ions in the electrode-electrolyte interfacial double layers. This process is known as the Helmholtz electrical double-layer and leads to the electrostatic separation of charges. One electrode, one electrolyte, and one separator make up the capacitor's three main parts. A double-layer of electrostatic material forms at both electrodes of the capacitor when an external voltage is applied. One layer of charges, known as the electronic layer, is created when electrons build up on the electrode surface lattice, while the other layer is created when solvated ions of opposing charges from the electrolyte accumulate. Together, these layers comprise the electrostatic double-layer. The solvent molecule's monolayer, which physically sticks to the electrode's surface and helps with charge separation, divides these layers [49]. As a result, the electrodes form an electrostatic double-layer, as seen in Figure 1.

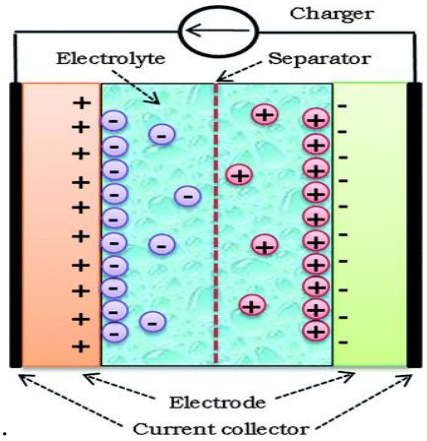

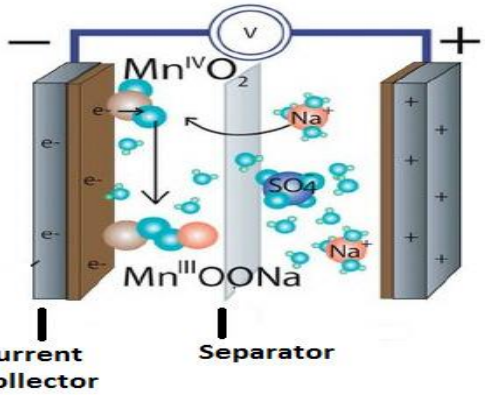

Fig. 1. Schematic representation of electrostatic Double-layer at the electrodes of EDLCs [50]

Fig. 2. Schematic representation of pseudo capacitor [54]

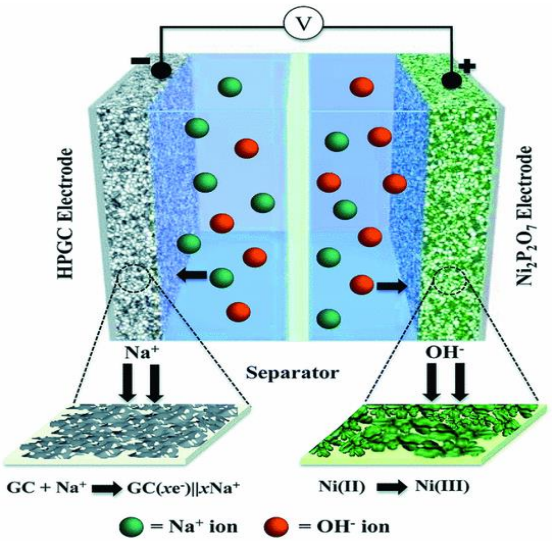

Fig. 3. Schematic representation of the working principle of the hybrid supercapacitor [55]

Carbon-based electrode materials, such as activated carbon, carbon aerosol, graphene, and others, are utilized in electrostatic double-layer capacitors. Because of the ions' physical adsorption at the electrode surface, the materials have a large surface area but a low specific capacitance [52].

Pseudocapacitor

It is the reversible faradic reaction at the electrode-electrolyte interface that drives the charge storage mechanism in the pseudocapacitor. During the procedure, the reversible redox interaction between the electrode and the electrolyte facilitates the charge transfer, or electron transfer. Only electron transport happens during the procedure; there is no chemical reaction at the electrode surface. The electrode material consists of conducting polymers including polyaniline, polypyrrole, and polythiophene as well as transition metal oxides like RuO_2, MnO_2, Co_3O_4, Fe_2O_3, and binary metal oxide. Throughout the redox process, the transition metal's valence electron participates in electron transfer. In the pseudocapacitor, there are three distinct methods by which electron charge transfer takes place [53].

1. Electrosorption of ions at the electrode
2. Reversible redox reaction at the electrode
3. Intercalation process i.e. doping and de-doping of electrolyte ions.

Figure 2 displays the schematic representation of a pseudocapacitor. The capacitance is proportional to the surface area of the electrode material, where the redox reaction and electrosorption processes take place. Due to their wide working potential window and faradic redox reaction, they have a larger specific capacitance and energy density than an electrostatic double-layer capacitor [54].

Hybrid supercapacitor

The battery and capacitor electrodes that work with a wider voltage window are combined to form the electrodes of hybrid supercapacitors. These electrodes operate via faradic and non-faradic response mechanisms, respectively. The hybrid capacitor's cathode is composed of lithiated compounds for the lithium-ion capacitor and transition metal oxides for the asymmetric supercapacitor. Through the reversible redox process, these materials store energy. The carbon-based materials activated carbon, carbon nanotubes, and graphene, which make up the hybrid capacitor's anode, store charge electrostatically that is, through the physical adsorption and desorption of electrolyte ions at the electrode [55].

Figure 3 displays the schematic diagram illustrating the hybrid capacitor's operation. The energy density of the hybrid supercapacitor can be increased by using faradic materials as the cathode, and the power density and cycle life of the finished product can be increased by using EDLC materials as the anode.
[56].

Bismuth-based materials

Since they are inexpensive, non-toxic, have a high oxygen conductivity, and exhibit dielectric behavior, bismuth materials have found extensive application in a variety of fields, including gas sensors, photocatalysis, catalysts, energy storage devices, and many more. Due to the fact that their redox reactions take place over a large potential range, compounds based on bismuth can also act as negative electrodes while using a symmetric supercapacitor. [57]

Properties of bismuth

Group 15, period 6, p-block element bismuth has the atomic symbol Bi, atomic mass 208.98 g, and atomic number 83. It has an electronic structure of [Xe] 4f145d106s26p3 with electron distributions in the following shells: 2, 8, 18, 32, 18, and 5. At 156 pm for the radius and 207 pm for the van der Waals radius, the bismuth atom is an element that is brittle and silvery-white in colour. Because of its low melting point, lowest thermal conductivity, and volume expansion upon freezing, it finds unique uses in the printing and electronics industries. The only heavy metal that is not poisonous is bismuth [58].

Materials and composites based on bismuth for use as supercapacitor electrode materials

Bismuth oxides and hydroxides have been reported by many researchers as pseudocapacitors for supercapacitor applications (Table 1)

M. Isacfranklin et al reported that the best approach for creating vanadium oxide electrode materials is hydrothermal synthesis. In terms of electrochemical performance, cobalt vanadium oxide electrode material outperformed nickel and bismuth vanadium oxide electrodes in this investigation. In Cyclic Voltammetry, the potential window at 10 mV/s provided the SC of 426.11 F/g, while 0.5 mA/g current density yielded 285.65 F/g in GCD. Additionally, the produced anode electrode material demonstrated excellent capacitance after 5000 cycles, at 83.64%. EIS spectra verified the cobalt vanadium oxide material's superior conductivity. It said that cobalt vanadium oxide material is best electrode materials for supercapacitor applications [24]. Patil SS et al reported Energy density of 2.63mWh/cm^3 in per kg it is 38.43 Wh/Kg and power density of 558mW/cm^3 in per kg it is 8.1 kW/kg are reached in 1.6 V voltage windows utilizing the hydrothermally manufactured Ag:$BiVO_4$ dendritic architecture [19]. Lakshmana Kumar Bommineedi et al reported as an active electrode for a supercapacitor, nanostructured bismuth vanadate ($BiVO_4$) was grown utilizing the SILAR process. $BiVO_4$ has developed into an orthorhombic structure, according to structural studies, with a surface structure resembling spongy nano-pebbles. At a scan rate of 3 mV/s, and SC is 707 F/g. The capacitive and faradic contributions have been thoroughly investigated. Electrochemical impedance spectroscopy (EIS) studies show that the electrode has series and charge transfer resistance values of 5.723 and 0.89 ohm cm^2, and achieve of cyclic stability 102% even at 3500 cycles [23]. Guangtao Zan et al reported a new monoclinic $BiVO_4$ nanocoral-assembled superstructure at low temperature archived a narrow band gap and good conductivity using the solid-hydrothermal approach. When used as the negative electrode of a supercapacitor, its highest specific capacitance can reach 788 F/g, outperforming all previous $BiVO_4$ based electrode materials and exceeding 97% of its theoretical value. It has a high capacitance while also having a high rate capability of 537 F/g at 30 A/g and cycling stability of 75% retention ratio after 1500 charge discharge cycles. [25]. S.A. Pawar et al reported at

the expense of this article, metal sulfide-based electrochemical supercapacitors are created on nickel foam using the SILAR technique in a common sulphur source beaker for both copper and silver. The electrodes outperform pure Cu2S and Ag2S in terms of cycling stability, with a capacity 89% after 2000 CV cycles and a SC of 772 C/g at a scan rate of 10 mV/s [26]. Bin He et al. reported to manufacture porous 1D Cu-BVO nanotubes, the solvothermal method and electro spinning are used. When 5.0% Cu is doped into BVO nanotubes, the BET surface area increases from 10.2 m2/g to 26.5 m2/g, suggesting that Cu doping boosts specific surface area while decreasing average pore size. The increased surface area of BVO may be attributed to the reduction in pore size caused by Cu doping. The increased surface area is projected to result in more active sites and faster transfer of photo generated carriers to the photo catalyst's surface [27]. Rajkumar Srinivasan et al. report In-situ polymerization was used to generate a composite comprising $BiVO_4$ and PANI. According to GCD experiments, the $BiVO_4$/PANI composite had a specific capacitance of 701 F/g at 1 A/g current density, and it retained 95.4% of that capacitance even after 5000 GCD cycles at this current density [22]. Deng L et al. reported by using the HD approach, polycrystalline monoclinic $BiVO_4$ and rGO nanocomposite electrodes were created. The as-obtained $BiVO_4$/rGO, using aqueous Na_2SO_4 solution as the electrolyte, showed a SC value of 479 F/g at 5 A/g [29]. Arora Y et al. reported on the solvothermal method's application to the construction of an electrode made of a composite of monoclinic scheelite $BiVO_4$ and MoS_2. A SC value of 610 F/g, whereas bare $BiVO_4$ displayed a SC of just 108 F/g and around 80% stability over 200 cycles [30]. Zhang Z et al. reported the 2-D monoclinic the room-temperature precipitation method was used to create $BiVO_4$ and its $BiVO_4$: Ag nano composite. According to the CV and GCD investigations, adding Ag enabled improved electrochemical performance SC is 109 F/g and stability over 5000 cycles is 85.4% [31].

Table 1: Survey data of $BiVO_4$ literatures on supercapacitor applications.

Electrode material	Deposition method	Electrolyte	ED (Wh /Kg)	PD Kw/ Kg	SC (F/g)	CD/Scan rate	CR (%)	References
$BiVO_4$/RGO	Hydrothermal	6MKOH	33.7	8	151	0.15mA/cm^2	80@2000	[16]
SWCNT/$BiVO_4$	Solvothermal	2MNaOH	--	--	395	2.5A/g	88@200	[17]
$BiVO_4$/RGO	Hydrothermal	1MNa_2So_4	35.37	2.05	400	5mV/s	70@1000	[18]
Ag:$BiVO_4$	hydrothermal	6MKOH	38.43	8.1	7.39F/Cm^3	10 A/g	82@4000	[19]
$BiVO_4$/RGO	hydrothermal	2MKOH	--	--	484	5mV/s	87@2000	[20]
$BiVO_4$/MoS_2	Solvothermal	2M NaOH	--	--	610	1A/g	80@200	[21]
$BiVO_4$/PANI	Hydrothermal	1MKOH	--	--	701	1A/g	95.4@5000	[22]
$BiVO_4$	SILAR	1MKCL	--	--	707	3mV/s	102@3500	[23]
Ni,Bi,$CoVO_4$	Hydrothermal	-	--	--	426.11	10mV/s	83.64@5000	[24]
$BiVO_4$	Hydrothermal	6MKOH	--	--	537	30A/g	75@1500	[25]
Cu_2S-Ag_2S	SILAR	--	--	--	772	10mV/s	89@2000	[26]

$BiVO_4$/rGO	Hydrothermal	2MNaOH	10.75	40	400	5A/g	84@1000	[29]
$BiVO_4$, MoS_2	Solvothermal	2MNaOH	--	--	108	3A/g	80@200	[30]
$BiVO_4$: Ag	Room temperature precipitation	--	15.2	0.500w/kg	109	1A/g	85.4@5000	[31]
$BiFe1_xCr_xO3$	sol–gel	2MKOH	--	--	421	10mV/s	78@2000	[33]
$BiVO_4$	Hydrothermal	2MKOH	--	--	1203	2 A/g	2000	[34]
$BiVO_4$	Sol -gel	$1MNa_2So_4$	435	1.69	494.1	5mV/s	88.67	[35]
g-C3N4/ $BiVO_4$	Hydrothermal	3.5MKOH	61	16.2	2171	2A/g	130@20000	[36]
Bi_2O_3 NT-graphene	Wet-spinning	PVA/$H3PO_4$	--	--	69.3m Fcm^{-2}	0.1mAcm^{-2}	1000	[37]
BVO-V_2O_5	electrodeposition	--	40	0.24	288 mF/cm2	0.12 mA/cm2	99.7@4000	[38]
$CuBi_2O_4$	Electrochemical deposition	6MKOH	--	--	647	1 A/g	80@500	[39]
T-NT/ Bi_2O_3	electrodeposition	1 M NaOH	--	--	430 mF cm–2	5 mA/cm^2	75@500	[40]
Sub-micron $BiVO_4$	co-precipitation & sonochemical	3M KOH	30.6	1.983	153	0.3A/g	98@5000	[41]
V2O5/graphene	Hydrothermal	1 M Na2SO4	--	--	288	1 A/g	82@5000	[42]
V2O5/graphene hybrid aerogels	Sol- gel method	1 M Na2 SO4	68	--	486	0.5 A/g	90@20000	[43]
V2O5nano sheets	Hydrothermal	1 M Na2SO4	107	9.4	451	0.5 A/g	90@4000	[44]
3D V2O5/PPy	Hydrothermal	1 M Na2SO4	21	21.5	502	0.25 A/g	74@10000	[45]
V2O5+ MPC	Liquid phase route	5 M LiNO3	--	--	257	0.5 A/g	80@5000	[46]
$BiVO_4$	simple sol–gel auto-combustion method	1 M Na2SO4	--	--	1160.05	5 mV/s	--	[47]

Conclusion:

Chemical processes, like as the hydrothermal process, can be used to create materials for bi-based supercapacitor electrodes. Bismuth-based nanostructured electrode materials have successfully been envisioned for electrochemical supercapacitor applications due to their topologies, morphologies, surface areas, pore sizes, and electrochemical properties. Bismuth vanadate is regarded as one of the best n-type semiconducting materials due to its strong absorption capabilities, high reduction potential, and generation of the band gap energy in the range of 2.4 to 2.5 eV, among other qualities [11].We methodically outlined and emphasized the most recent information regarding Bi-based materials used in energy storage applications in this research. Bi-based materials can be combined with other metal oxide materials, that perform several redox processes, or have their conductivities increased.

Bismuth-based materials and their nanocomposites may resist a substantial number of charge-discharge cycles, according to a literature analysis that indicated a remarkable specific capacitance value. It is interesting that the majority of the research studies that are now available exclusively report on the alkaline electrolyte with different molarity KOH, Na_2So_4 and other electrolyte is used. To increase the operating potential window, more investigation into other electrolytes is necessary. Additionally, there is a dearth of information regarding how temperature variation affects the system, a vital factor for real-world applications.

Acknowledgements

The authors sincerely thank the Electronics Department Dadasaheb Dr. Suresh G. Patil College Chopda, Jalgoan. K.K.Wagh Arts science & Commerce college pimpalgoan (B), Nasik providing technical support.

Research Data Policy and Data Availability Statements

This review article does not present any new research data. All data and figures presented in the article have been cited from published sources.

Author Contribution

VSJ: Conceptualization, Investigation, Writing original draft, Review and editing

KDG: Supervision, Investigation, Validation, Methodology.

Conflict of interest: All authors read and approved the final manuscript. The authors declare that they have no conflict of interest.

References

1. G. Wang, L. Zhang, J. Zhang, Chem. Soc. Rev., 41 (2012) 797-828.
2. P. Simon, Y. Gogotsi, Nat. Mater., 7 (2008) 845-854.
3. Dunn B, Kamath H, Tarascon JM. Electrical energy storage for the grid: a battery of choices. Science 2011;334:928–35.
4. Zhang Q, Uchaker E, Candelaria SL, Cao G. Nanomaterials for energy conversion and storage. Chem Soc Rev 2013;42:3127–71.
5. Wang G, Zhang L, Zhang J. A review of electrode materials for electrochemical supercapacitors. Chem Soc Rev 2012;41:797–828.
6. Noori A, El-Kady MF, Rahmanifar MS, Kaner RB, Mousavi MF. Towards establishing standard performance metrics for batteries, supercapacitors and beyond. Chem Soc Rev 2019;48:1272–341.
7. Huang M, Li F, Dong F, Zhang Y, Zhang L. MnO2-based nanostructures for high-performance supercapacitors. J Mater Chem A 2015;3:21380–423.
8. Zhao H, Tian F, Wang R, Chen R. A review on bismuth-related nanomaterials for photocatalysis. Rev. Adv. Sci. Eng. 2014;3:3–27.
9. Ling C, Withers Ray L, SiegbertSchmid, Thompson John G. A review of bismuth-rich binary oxides in the systems Bi2O3–Nb2O5, Bi2O3–Ta2O5, Bi2O3–MoO3, and Bi2O3–WO3. J Solid State Chem 1998;137:42–61.

10. S. Boukhalfa, K. Evanoff, G. Yushin, Atomic layer deposition of vanadium oxide on carbon nanotubes for high-power supercapacitor electrodes, Energy Environ. Sci. 5 (2012) 6872–6879, https://doi.org/10.1039/c2ee21110f.
11. Q. Wang, J. He, Y. Shi, S. Zhang, T. Niu, H. She, Y. Bi, Designing non-noble/ semiconductor Bi/BiVO 4 photoelectrode for the enhanced photoelectrochemical performance, Chem. Eng. J. 326 (2017) 411–418, https://doi.org/10.1016/j. cej.2017.05.171 .
12. Y. Jiang, Y. Wu, B. Xie, S. Yuan, X. Liu, Y. Qian, Hydrothermal preparation of uniform cubic-shaped PbS nanocrystals, J. Cryst. Growth 231 (2001) 248–251, https://doi.org/10.1016/S0022-0248(01)01510-X.
13. Nanasaheb M. Shinde et al.” Solution-method processed Bi-type nanoelectrode materials for supercapacitor applications: A review” Renewable and Sustainable Energy Reviews 1364-0321/© 2020 Elsevier Ltd.
14. T. K. Van, H. G. Cha, C. K. Nguyen, S. W. Kim, M. H Jung, Y.S. Kang, Cryst. Growth Des., 12 (2012) 862–868.
15. W. Shi, S. Song, H. Zhang, Chem. Soc. Rev. 42 (2013) 5714–5743.
16. Santosh S patil, Deepak Prakash dubal et al. Fern-like rGO/$BiVO_4$ hybrid nanostructures for high-energy symmetric supercapacitor. ACS Applied Material & Interfaces 2016 DOI: 10.1021/acsami.6b08165.
17. Khan Ziyauddin, Shateesh Bhattu SH, DK. SWCNT/BiVO4 composites as anode materials for supercapacitor application. RSC Adv 2014;4:17378e81.
18. Dutta S, Pal S, De S. Hydrothermally synthesized $BiVO_4$- reduced graphene oxide nanocomposite as a high performance supercapacitor electrode with excellent cycle stability. New J Chem 2018;42:10161e6.
19. Patil SS, Dubal DP, Tamboli MS, Ambekar JD, Kolekar SS, Gomez-Romero P, et al. Ag:BiVO4 dendritic hybridarchitecture for high energy density symmetric supercapacitors. J Mater Chem 2016;4:7580e4.
20. Sengottaiyan C, Kalam NA, Jayavel R, Shrestha RG, Subramani T, Sankar S, et al. BiVO4/RGO hybrid nanostructure for high performance electrochemical supercapacitor. J Solid State Chem 2019;269:409e18.
21. Arora Y, Shah AP, Battu S, Maliakkal CB, Haram S,Bhattacharya A, et al. Nanostructured MoS_2/$BiVO_4$composites for energy storage applications. Sci Rep 2016;6:1e7.
22. Srinivasan R, Elaiyappillai E, Anandaraj S, kumar Duvaragan B, Johnson PM. Study on the electrochemical behavior of $BiVO_4$/PANI composite as a high performance supercapacitor material with excellent cyclic stability. J Electroanal Chem 2020;861:113972.
23. Lakshmana Kumar Bommineedi et al.” Spongy nano surface architecture of chemically grown $BiVO_4$: High-capacitance retentive electrochemical supercapacitor”0360-3199/© 2021 Hydrogen Energy Publications LLC. Published by Elsevier Ltd.
24. M. Isacfranklin et al.” Nickel, bismuth, and cobalt vanadium oxides for supercapacitor applications” Ceramics International (2020), Published by Elsevier Ltd.
25. Guangtao Zan et al.” $BiVO_4$ nanocoral superstructures and their excellent electrical/optical dual-functions.” Journal of Alloys and Compounds 852 (2021) 157035© Elsevier
26. S.A. Pawar, D.S. Patil, J.C. Shin et al. “ Electrochemical battery-type supercapacitor based on chemosynthesized Cu_2SAg_2S composite electrode, Electrochimica Acta (2017), doi: 10.1016/ j.electacta.2017.11.006.
27. Bin He Zhipeng Li, Dian Zhao, Huanhuan Liu, Yijun Zhong et al.” Fabrication of porous Cu-doped $BiVO_4$ nanotubes as efficient oxygen-evolving photocatalystsACS Appl. Nano Mater DOI: 10.1021/acsanm.8b00281.
28. Devi N, Ray SS, Performance of bismuth-based materials for supercapacitor applications: A review, Materials Today Communications (2020), doi:http://doi.org/10.1016/j.mtcomm.2020.1016
29. Deng L, Liu J, Ma Z, Fana G, Liu Z. Free-standing graphene/bismuth vanadate monolith composite as a binder-free electrode for symmetrical supercapacitors. RSC Adv 2018;8:24796–804.
30. Arora Y, Shah A, Battu S, Maliakkal C, Haram S, Bhattacharya A, Khushalani D. Nanostructured MoS_2/$BiVO_4$ composites for energy storage applications. Sci Rep 2016;6:36294–300.
31. Zhang Z, Zheng Q, Sun L. Synthesis of 2-D nanostructured $BiVO_4$: Ag hybrid as an efficient electrode material for supercapacitors. Cer. Int. 2017;43:16217–24.
32. F. Yi, H. Ren, J. Shan, X. Sun, D. Wei, Z Liu, Chem. Soc. Rev., 47 (2018) 3152-3188.
33. Kumar, S.; Ahmed, F.;Ahmad, N.; Shaalan, N.M.; Kumar,R.; Alshoaibi, A.; Arshi, N.; Dalela,S.;Albossed, M.; Chae, K.H.; et al. Role of Cr Doping on the Structure, Electronic Structure, and Electrochemical Properties of BiFeO3Nanoparticles. Materials 2022, 15, 4118. https://doi.org/10.3390/ma15124118.
34. Subramanian Balachandran, Rajan Karthikeyan, de Kumaravel Jeeva Jothi,Veerappan Manimuthu, Natarajan Prakash,h Zheming Chen,a Tongxiang Liang, Chengzhi Hu, Feng Wang and Mingshu Yang,”Fabrication of flower-like bismuth vanadate hierarchical spheres for an improved supercapacitor efficiency”, Mater. Adv., 2022, 3, 254–264 DOI: 10.1039/d1ma00810b.
35. Shankar G. Randive, Rohan M. Kore, Balkrishna J. Lokhande,” Sol-gel Synthesis and Supercapacitive Characterization of Bismuth Vanadate”, JOURNAL OF NANO- AND ELECTRONIC PHYSICS Vol. 12 No 2, 02027(4pp) (2020) DOI: 10.21272/jnep.12 (2).02027.

36. C. Murugan, K. Subramani, R. Subash, M. Sathish, and A. Pandikumar," High-Performance High-Voltage Symmetric Supercapattery Based on a Graphitic Carbon Nitride/Bismuth Vanadate Nanocomposite" https://dx.doi.org/10.1021/acs.energyfuels.0c03261.
37. K. Gopalsamy, Z. Xu, B. Zheng, T. Huang, X. Zhao, L. Kou and C. Gao," Bismuth Oxide Nanotubes/Graphene Fiber-Based Flexible Supercapacitors Nanoscale, 2014, DOI:10.1039/C4NR02615B.
38. Atefeh SharifiRenani , Mohamad Mohsen Momeni , Hossein Mohammadzadeh Aydisheh ,Byeong-Kyu Lee,"New photoelectrodes based on bismuth vanadate-VO@TiNT for photo-rechargeable supercapacitors,Journal of Energy Storage,Volume 62, June 2023, 106866, https://doi.org/10.1016/j.est.2023.106866.
39. Ali A. Ensafi, N. Ahmadi, B. Rezaei," Electrochemical preparation of CuBi2O4 nanoparticles on nanoporous stainless steel as a binder-free supercapacitor electrode", Journal of Alloys and Compounds 652 (2015) 39e47 http://dx.doi.org/10.1016/j.jallcom.2015.08.226.
40. Biplab Sarma, Abraham L. Jurovitzki, York R. Smith, Swomitra K. Mohanty, and Mano Misra," Redox-Induced Enhancement in Interfacial Capacitance of the Titania Nanotube/Bismuth Oxide Composite Electrode", dx.doi.org/10.1021/am302738r | ACS Appl. Mater. Interfaces 2013, 5, 1688−1697.
41. Subbiah, M, Ansalin Gnana Sowndarya, A, Sundaramurthy, A, Venkatachalam, S, Saravanan, N, Pitchaimuthu, S & Srinivasan, N 2023, 'Tailoring hierarchical BiVO4 sub-micron particles for enhanced cyclability in asymmetric supercapacitor', Journal of Energy Storage, vol. 71, 108137. https://doi.org/10.1016/j.est.2023.108137.
42. Minoh Lee, Suresh Kannan Balasingam, Hu Young Jeong, Won G. Hong4, Han-Bo-Ram Lee, Byung Hoon Kim & Yongseok Jun," One-step hydrothermal synthesis of graphene decorated V2O5 nanobelts for enhanced electrochemical energy storage", SCIENTIFIC REPORTS | 5: 8151 | DOI: 10.1038/srep08151.
43. Y.Wu, G. Gao and G. Wu, Self-assembled three-dimensional hierarchical porous V2O5/graphene hybrid aerogels for supercapacitors with high energy density and long cycle life J. Mater. Chem. A, 2014, DOI: 10.1039/C4TA05537C.
44. Jixin Zhu, Liujun Cao,Yingsi Wu, Yongji Gong, Zheng Liu, Harry E. Hoster, Yunhuai Zhang, Shengtao Zhang, Shubin Yang, Qingyu Yan, Pulickel M. Ajayan, and Robert Vajtai,"Building 3D Structures of Vanadium Pentoxide Nanosheets and Application as Electrodes in Supercapacitors," 2013 American Chemical Society dx.doi.org/10.1021/nl402969r Nano Lett. 2013, 13, 5408−5413.
45. Liujun Cao, Jixin Zhu, Yanhong Li, Peng Xiao, Yunhuai Zhang, Shengtao Zhang and Shubin Yang," Ultrathin single-crystalline vanadium pentoxide nanoribbon constructed 3D networks for superior energy storage", J. Mater. Chem. A, 2014, 2, 13136–13142 DOI: 10.1039/c4ta02229g.
46. Liang Hao, Jie Wang, Laifa Shen, Jiajia Zhu, Bing Ding and Xiaogang Zhang," Synthesis and electrochemical performances of mixed-valence vanadium oxide/ordered mesoporous carbon composites for supercapacitors", RSC Adv., 2016, 6, 25056–25061DOI: 10.1039/c5ra22520e.
47. Pardeshi, O.M., Gite, A.B., Jain, G.H. et al. Sol gel auto-combustion synthesis of bismuth vanadate (BiVO4) nanoparticles and its supercapacitor applications. J Mater Sci: Mater Electron 34, 1817 (2023). https://doi.org/10.1007/s10854-023-11229-5.
48. Zhou R, Wei S, Liu Y, Gao N, Wang G, Lian J, et al. Charge Storage by Electrochemical Reaction of Water Bilayers Absorbed on MoS 2 Monolayers. Sci Rep 2019:1– 11.https://doi.org/10.1038/s41598-019-40672-w.
49. H. Gu, W. Fan, T. Liu, Nanoscale Horiz., 2 (2017) 277– 283.
50. S. Bose, T. Kuila, A. K. Mishra, R. Rajasekar, N. H. Kim, J. H. Lee, J. Mater. Chem., 22 (2012) 767-784.
51. G. Wang, L. Zhang, J. Zhang, Chem. Soc. Rev., 41 (2012) 797-828.
52. K. K. Purusothaman, G. Muralidharan, Solar Energy Materials & Solar cells, 93 (2009) 1195–1201.
53. Y. Zhang, H. Feng, X. Wu, L. Wang, A. Zhang, T. Xia, H. Dong, X. Li, L. Zhang. Int.J Hydrogen Energy, 34 (2009) 4889 – 4899.
54. F. Yi, H. Ren, J. Shan, X. Sun, D. Wei, Z Liu, Chem. Soc. Rev., 47 (2018) 3152-3188.
55. B. Senthilkumar, Z. Khan, S. Park, K. Kim, H. Ko, Y. Kim, J. Mater. Chem. A, 3 (2015) 21553-21561.
56. M. Nagui, V. N. Mochalin, M. W. Barsoum, Y. Gogotsi, Adv. Mater., 26 (2014) 992–1005.
57. Deka BK, Hazarika A, Kwon Ob, Kim DY, Park Y Bin, Park HW. Multifunctional enhancement of woven carbon fiber/ZnO nanotube-based structural supercapacitor and polyester resin-domain solid-polymer electrolytes. Chem Eng J 2017;325:672–80. https://doi.org/10.1016/j.cej.2017.05.093.
58. Raut SS, Sankapal BR. Comparative studies on MWCNTs, Fe2O3and Fe2O3/MWCNTs thin films towards supercapacitor application. New J Chem 2016;40:2619–27. https://doi.org/10.1039/c5nj03628c.

.

ICRTMS-2024
International e-Conference on Recent Trends in Material Science
In Association with International Journal of Scientific Research in Science and Technology
Volume 11 | Issue 9 | Print ISSN: 2395-6011 | Online ISSN: 2395-602X (www.ijsrst.com)

Dielectric Relaxation Study of Acetate Using Time Domain Reflectometry Technique (TDR)

P. D. Hambarde *[1], N. P. Garad [2], A. C. Kumbharkhane[3]
*[1] *School of Physical Sciences, Swami Ramanand Teerth Marathwada University, Nanded 431606, India.*
[2] *School of Physical Sciences, Swami Ramanand Teerth Marathwada University, Nanded 431606, India.*
[3] *School of Physical Sciences, Swami Ramanand Teerth Marathwada University, Nanded 431606, India.*

ABSTRACT

The complex permittivity spectra of acetate have been measured in the frequency range from 10MHz to 30GHz using the Time Domain Reflectometry Technique at 250 C and fitted to the Debye Model. Acetate is an ester of carboxylic acid. To impart favorable thermoplastic behavior, esters are used in the polymer processing industry as plasticizers. Dielectric relaxation parameters such as static dielectric constant and relaxation time are determined using the least squares fit method.
Keywords: Complex Permittivity Spectra, Time Domain Reflectometer, static dielectric constant, relaxation time.

I. INTRODUCTION

Dielectric relaxation spectroscopy (DRS) is a highly sensitive and practical technique for studying various phenomena in binary liquid mixtures. The main advantage of DRS, as compared to other similar techniques for studying molecular dynamics, is the broad frequency range, which can be relatively easily covered [1-2]. R.M. Shirke et.al. Studied the temperature dependent dielectric relaxation study of acetate-Alcohol mixtures using the time domain technique in the frequency range of 10 MHz to 20 GHz to understand the intermolecular interaction in the mixture. S.S. Birajdar et.al. Investigated the structural and molecular dynamics of methyl acetate-xylene solutions using dielectric relaxation spectroscopy [3-4].

Acetate is an ester of a carboxylic acid in which a -O-alkyl (alkoxy) group substitutes for at least one -OH (hydroxyl) group. Because of their inoffensive nature, esters are significant organic liquids that are least associative, low poisonous, and reasonably priced. They are categorized based on the molecular shape and quantity of carbon atoms [5-6].

In the present study, we report the dielectric behaviour of esters using the Time Domain Reflectometry (TDR) technique at 25o C temperature over the frequency range from 10MHz to 30GHz. To determine the dielectric parameters such as complex dielectric permittivity spectra, dielectric constant, and relaxation time.

II. METHODS AND MATERIAL

The source and purity of Methyl Acetate (MA), Ethyl Acetate (EA), Isopropyl Acetate (IPA), n-butyl Acetate(n-BA), and Isoamyl Acetate (IAA) are tabulated in Table 1.

Table 1. Source and purity of pure ester components

Chemicals	Supplier	Purity in mass Fraction
Methyl Acetate	Loba Cheme. Pvt. Ltd.	99.5%
Ethyl Acetate	Merk life science Pvt. Ltd.	99.5%
Iso Propyl Acetate	Loba Cheme. Pvt. Ltd.	99.5%
n- Butyl Acetate	Thermo-fisher Scientific India Pvt. Ltd.	99.0%
Amyl Acetate	Qualigens Fine Chemicals, Mumbai	99.0%

The experimental setup and block diagram of the TDR technique is shown in fig.1. The Tektronix DSA8300 sampling main frame oscilloscope sampling with the dual channel sampling module 80E10B has been used for time domain reflectometry. 12 ps incident and 15 ps reflected rising time pulses are provided by the sampling module. At a time, window of 5 ns, the reflected pulses without sample R1(t) and with sample R2(t) were collected and digitally digitised in 2000 points. The addition [q(t) = R1(t) + R2(t)] and subtraction [q(t) = R1(t) - R2(t)] of these pulses are done in oscilloscope memory. These subtracted and added pulses are transferred to PC for further analysis. The Fourier transformation of the pulse and data analysis were done earlier to determine complex permittivity spectra $\varepsilon^*(\omega)$ using non-linear lesquares fit method [7-8].

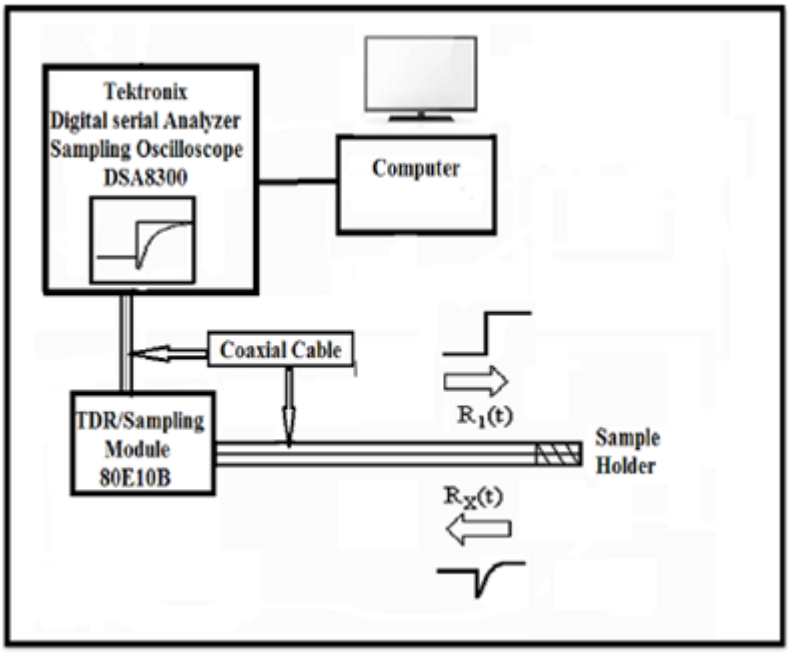

Fig. 1: Block Diagram of Time Domain Reflectometry (TDR).

II. RESULT AND DISCUSSION

Frequency dependent complex permittivity spectra of esters like primary and secondary acetate such as Methyl Acetate (MA), Ethyl Acetate (EA), Isopropyl Acetate (IPA), n-butyl Acetate(n-BA) and Isoamyl Acetate (IAA) at 25° C shown in fig.2. It is observed that as the number of carbon atom increase, the values of dielectric permittivity (ε') drop and the peak of the dielectric loss (ε'') shifts to the lower frequency side. As the frequency increases and the length of the molecular chain increases, the value of ε' lowers as well. Dielectric permittivity is impacted by a decrease in total polarization brought on by an increase in frequency [9-11].

Experimentally obtained CPS is fitted using non-linear least squares fit method to Harvrilik-Negami equation,

$$\varepsilon^*(\omega) = \varepsilon_\infty + \frac{\varepsilon_0 - \varepsilon_\infty}{[1 + (j\omega\tau)^{1-\alpha}]^\beta}$$

where ε_s is static dielectric constant, ε_∞ is permittivity at high frequency, ω is angular frequency, τ is relaxation time, j is imaginary number and α, β are distribution parameter. Debye (α=0 & β=1) is used for present system to fit the raw data [12].

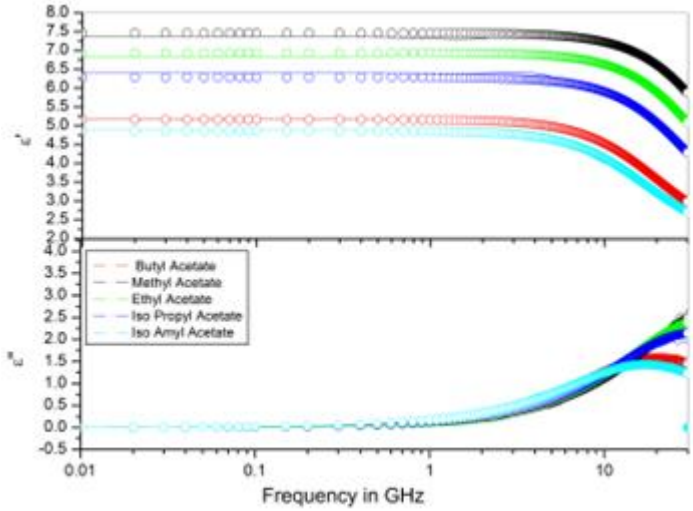

Fig 2. Complex permittivity Spectra of MA, EA, IPA, n-BA and IAA at 25° C using TDR

Compound	ε_s	τ
1. Methyl Acetate	7.46(1)	3.40(1)
2. Ethyl acetate	6.93(1)	4.12(1)
3. Isopropyl Acetate	6.28(1)	4.97(1)
4. n-Butyl Acetate	5.16(1)	7.96(1)
5. Isoamyl Acetate	4.85(1)	9.25(1)

Table 2. Dielectric Relaxation Parameter of Esters

The number in the bracket indicates errors obtained by the least squares fit method e.g., 7.46(1) means 7.46± 0.01.

The dielectric constant of liquids is dependent on a number of variables, including temperature, the number of carbon atoms in the molecule, the intermolecular interactions present, the dipole moment and the angle at which dipoles correlate with one another. The molecular interaction reduces as chain length rises, as shown by the drop in ε_s as the chain length and number of carbon atoms increase from MA to IAA as shown in Table 2.

The length of the relaxation period is determined by the molecules' functional group, size, and viscosity. The observation shows that in primary acetate, relaxation time increases. This could be because acetate's longer chains impede molecules' ability to rotate, causing the molecules to relax more slowly [13].

III. CONCLUSION

Frequency dependent complex permittivity spectra of Acetate were studied by using the Time Domain Reflectometry Technique in the frequency range 10MHz to 30GHz at 25^0 C. The number of carbon atoms increases, with the dielectric constant decreasing whereas relaxation time increases due to the polymeric structure in the Acetate.

Acknowledgment

We acknowledge the financial support given by the School of Physical Sciences at S. R. T. M. U. Nanded, Maharashtra and DST, New Delhi (Project Number DST PROJECT SB/S2/LOP-032/2013) for the use of the instrumental facility

IV. REFERENCES

[1] Birajdar, S.S., Deshmukh, A.R., Kumbharkhane, A.C. and Suryawanshi, D.B., 2023. Study of co-operative dynamics and thermo-dielectric parameters of n-butyl acetate-xylene solutions using dielectric spectroscopy https://doi.org/10.56042/ijc.v62i8.4794 .

[2] Kremer, F. and Schönhals, A. eds., 2002. *Broadband dielectric spectroscopy*. Springer Science & Business Media.

[3] Shirke, R.M., Chaudhari, A., More, N.M. and Patil, P.B., 2001. Temperature dependent dielectric relaxation study of ethyl acetate—Alcohol mixtures using time domain technique. *Journal of molecular liquids*, *94*(1), pp.27-36 https://doi.org/10.1016/S0167-7322(01)00239-2 .

[4] Birajdar, S.S., Deshmukh, A.R., Kumbharkhane, A.C. and Suryawanshi, D.B., 2022. Structural and molecular dynamics of methyl acetate-xylene solutions using dielectric relaxation spectroscopy. *Journal of the Indian Chemical Society*, *99*(10), p.100733 https://doi.org/10.1016/j.jics.2022.100733.

[5] Sen, D.J., 2015. Esters, terpenes, and flavors: Make the mood Cheer by three musketeers. *World Journal of Pharmaceutical Research*, *4*(8), pp.01-40.

[6] Birajdar, S.S., Deshmukh, A.R., Kumbharkhane, A.C. and Suryawanshi, D.B., 2023. Dielectric Relaxation Spectroscopy of Esters Using Time Domain Reflectometry. *Russian Journal of Physical Chemistry B*, *17*(4), pp.990-995. https://doi.org/10.1134/S1990793123040036

[7] Kumbharkhane, A.C., Puranik, S.M. and Mehrotra, S.C., 1991. Dielectric relaxation of tert-butyl alcohol–water mixtures using a time-domain technique. Journal of the Chemical Society, Faraday Transactions, 87(10), pp.1569-1573. https://doi.org/10.1039/FT9918701569

[8] Cole, R.H., Berberian, J.G., Mashimo, S., Chryssikos, G., Burns, A. and Tombari, E., 1989. Time domain reflection methods for dielectric measurements to 10 GHz. Journal of Applied Physics, 66(2), pp.793-802. https://doi.org/10.1063/1.343499

[9] Guerra, J.D.L.S. and Eiras, J.A., 2007. Mechanical and electrical driving field induced high-frequency dielectric anomalies in ferroelectric systems. *Journal of Physics: Condensed Matter*, *19*(38), p.386217. https://doi.org/10.1088/0953-8984/19/38/386217

[10] Bibi, F., Villain, M., Guillaume, C., Sorli, B. and Gontard, N., 2016. A review: Origins of the dielectric properties of proteins and potential development as bio-sensors. *Sensors*, *16*(8), p.1232. https://doi.org/10.3390/s16081232

[11] Mehrotra, S.C., Kumbharkhane, A. and Chaudhari, A., 2017. *Binary polar liquids: structural and dynamic characterization using spectroscopic methods*. Elsevier.

[12] Debye, P., 1929. Polar molecules. By P. Debye, Ph. D., Pp. 172. New York: Chemical Catalog Co., Inc., 1929. $3.50. *Journal of the Society of Chemical Industry*, *48*(43), pp.1036-1037. https://doi.org/10.1002/jctb.5000484320

[13] Deshmukh, A.R. and Kumbharkhane, A.C., 2020. Dielectric relaxation study of aqueous diethylamine using a time domain reflectometry. *Journal of Molecular Liquids*, *314*, p.113648 https://doi.org/10.1016/j.molliq.2020.113648.

ICRTMS-2024
International e-Conference on Recent Trends in Material Science
In Association with International Journal of Scientific Research in Science and Technology
Volume 11 | Issue 9 | Print ISSN: 2395-6011 | Online ISSN: 2395-602X (www.ijsrst.com)

Dielectric Studies of Acetonitrile with non-Polar Solvent

Daiwashala G. Dongre*[1] and Ashok C. Kumbharkhane[2]
*[1]*School of Physical Sciences ,S.R.T.M.U.Nanded, Maharashtra, India*
[2]*School of Physical Sciences ,S.R.T.M.U.Nanded, Maharashtra, India*

ABSTRACT

The Time Domain Reflecometry (TDR) method has been used to study dielectric relaxation in a binary solution of acetonitrile (ACN) and 1,4-dioxane(DX) in the frequency range of 10 MHz to 30 GHz. The complex permittivity spectrum of the acetonitrile-1,4-dioxane mixture reveals Debye-type relaxation processes. The dielectric relaxation time (τ) in picoseconds and the static dielectric constant (ε0) have been calculated using the least squares fit method. The interaction between ACN-1,4DX systems has been studied using the Bruggeman factor.
Keywords: complex permittivity spectra, Least squares fit method, Time domain reflectometry, relaxation time, static dielectric constant.

1. INTRODUCTION

The different spectroscopic techniques are used to study the structural information of liquid molecules [1-4].Short-range molecular organisation that changes quickly over time is a characteristic of liquids. Dielectric spectroscopy has been employed to observe this arrangement and its thermal changes. The Broadband dielectric spectroscopy is a powerful technique for the electrical characterizations, charge distributions as naturally present in liquid and to understand intermolecular interaction between the binary mixtures of liquids. The intermolecular interaction of microscopic heterogeneous structure gives the information about relaxation process. In pharmaceutical and analytical sciences, the dielectric constant of mixed solvents is required to predict the solubility and chemical stability of the drug. TDR techniques are used to determine the various dielectric relaxation parameters such as dielectric permittivity, dielectric loss, static dielectric constant, and dielectric relaxation time. Understanding the non-hydrogen-bonded aprotic solute in a non-polar solvent is the primary goal of the study since it sheds light on how the systems' molecular multimer configurations disintegrate. Acetonitrile (CH_3CN) is the simplest organic nitrile. It is mostly produced as a by-product of acrylonitrile. Acetonitrile is used as a polar aprotic solvent in organic synthesis and purification of butadiene. It is widely used in battery applications due to its relatively high dielectric constant. The various literature surveys show the dielectric properties of acetonitrile with the polar and non-polar solvent [5-10].1,4-Dioxane($C_4H_8O_2$) is a heterocyclic organic compound, classified as an ether. It is a colorless liquid with a faint sweet odor similar to that of diethyl ether. There are number of research article in literature dealing with the dielectric study of dioxane as a solvent [11-15]. In present work, the complex dielectric spectra (CPS) were measured, and the least squares fit technique was used to get the static dielectric constant (ε_0) and relaxation time (τ). The Bruggeman factor has been also computed in order to study intermolecular interactions between ACN-DX molecules.

2. METHODS AND MATERIAL

S.D. Fine Chem. Ltd. supplied ACN and 1,4 DX in 99% purity. Ltd. The solutions were produced at various volume fractions of ACN in 1,4DX. To obtain the Complex permittivity spectra, the TDR technique was utilized [16, 17]. The experimental setup and block diagram of TDR technique is shown in Fig. 1(a,b). It shows the experimental setup and block diagram for the TDR method. Time domain reflectometry has been studied using the Tektronix DSA8300 sampling main frame oscilloscope sampling with the dual channel sampling module 80E10B. The sampling module outputs an incident time pulse of 12 ps and a reflected rising time pulse of 15 ps. The coaxial wire that feeds the pulse has an outer diameter of 1.19 mm, an inner diameter of 0.28 mm, and an impedance of 50 ohms. Following reflection from the end of the line, changes in pulse are monitored by sampling oscilloscopes. The reflected pulse was digitized into 2000 points and recorded within a 5 ns time window, both with and without sample R1(t) and Rx(t). Oscilloscope memory is used to add [q (t) = R1 (t) + Rx (t)] and subtract [p (t) = R1 (t) - Rx (t)] these pulses. The pulses that have been added and deleted are moved to a PC for further study. In order to find the complex permittivity spectra ε*(ω) using the nonlinear least square fit method, the Fourier transforms of the pulse and data analysis were completed earlier.

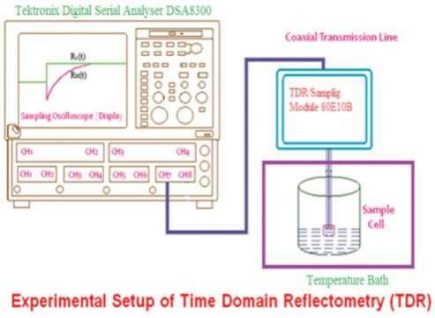

(a)

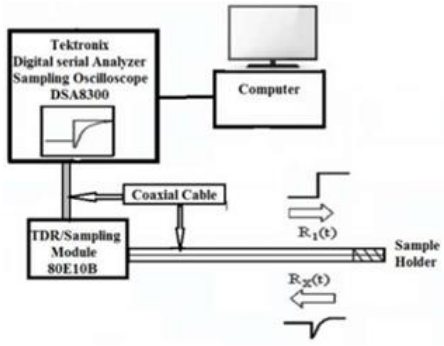

(b)

Fig. 1 (a) Experimental setup and (b) block diagram of TDR.

3. RESULTS AND DISCUSSION

3.1 *Complex permittivity spectra*

The experimental CPS has been fitted to a Debye-relaxation model, which describes the dielectric relaxation parameters; using the nonlinear Least squares fit (LSF) method [18].

$$\varepsilon * (\omega) = \varepsilon_{\infty} + \frac{\varepsilon_o - \varepsilon_{\infty}}{[1+(j\omega\tau)^{1-\alpha}]^{\beta}} \quad (1)$$

where, ε∞, ε_0, τ, α and β as fitting parameters. The relaxation models for Debye (α = 0, β = 1), Cole-Cole (β = 1), and Davidson-Cole (α = 0) are shows in equation (1).The complex permittivity spectra (CSP) for the ACN-1,4,DX mixture in the 10MHz–30GHz frequency range are displayed in Fig. 2. The systematic

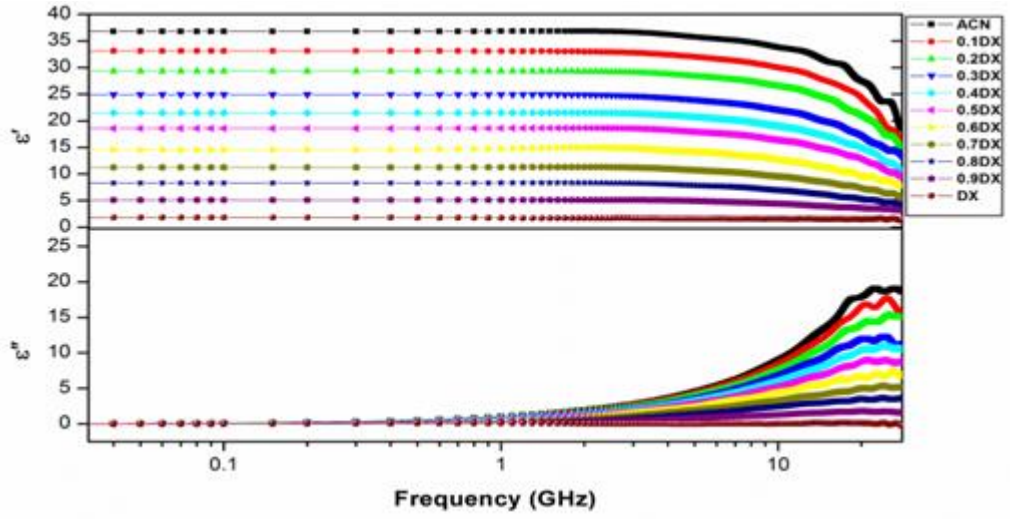

Fig. 2 Complex permittivity spectra for ACN-1, 4DX binary mixture at 25ºC

variations in dielectric permittivity (ε') and dielectric loss (ε") are displayed in this spectrum. Dielectric permittivity decreases with frequency at all concentrations of DX. From pure ACN to pure 1,4DX, the dielectric permittivity value changes linearly. When the DX in ACN solutions increases, the loss peak in the dielectric loss spectrum moves towards the lower frequency range.

3.2 *Static dielectric constant and relaxation time*:

Static dielectric constant values are depends on various factors such as temperature, the number of carbon atoms, the dipole moment, and intermolecular force [19]. The values of dielectric parameters static dielectric constant (ε_0) and relaxation time (τ) in picoseconds are obtained from equation (1) . The molecular size and functional group determine the relaxation time. The current study's calculated relaxation times at 25°C for DX and ACN are 3.95 and 4.33 ps, respectively. The non-linear relaxation behavior of the ACN-DX system is depicted in Table1. The maximum value is observed at 0.9 volume fraction of Dioxane which indicates that at these concentration molecular increases due stronger bonding in molecule's. This nonlinear change in relaxation time and dielectric constant indicates that intermolecular interaction is occurring in the system.

Table 1. Static dielectric constant (ε_0)and relaxation time (τ) of ACN-1,4DX mixture at 25ºC

Vol. frac.	ε_0	(τ)
0.0	36.62(2)	4.33(1)
0.1	32.82(2)	4.66(1)
0.2	29.17(2)	4.86(1)
0.3	25.46(2)	5.33(1)
0.4	22.05(2)	5.65(1)
0.5	18.63(1)	5.91(1)
0.6	14.77(1)	6.25(1)
0.7	11.24(1)	6.97(1)
0.8	8.32(1)	7.68(1)
0.9	5.21(1)	8.05(1)
1.0	2.21(1)	3.95(1)

3.*3 Bruggeman Factor*

The static dielectric constant of binary mixes can be determined using the Bruggeman factor, which can be computed as follows: [20]

$$f_B = \left(\frac{\varepsilon_m - \varepsilon_{DX}}{\varepsilon_{ACN} - \varepsilon_{DX}}\right)\left(\frac{\varepsilon_{ACN}}{\varepsilon_m}\right)^{1/3} = 1 - V_{DX} \qquad (2)$$

where, $f_B, \varepsilon_m, \varepsilon_{DX}, \varepsilon_{ACN}$ denotes Bruggeman factor, static dielectric constants of the mixture,1,4 DX and ACN respectively. V_{DX} is the volume fraction of 1,4-DX, respectively. Bruggeman's equation indicates a linear relationship (green line) between fB and $V_{DX,}$ however an experimental value (black point) deviates from this expectation, as seen in Figure 3. However, the following equation [21] describes the non-linear behavior of different kinds of molecules.

$$f_B = \left(\frac{\varepsilon_m - \varepsilon_{DX}}{\varepsilon_{ACRN} - \varepsilon_{DX}}\right)\left(\frac{\varepsilon_N}{\varepsilon_m}\right)^{1/3} = 1 - [a - (a-1)V_{DX}]V_{DX} \qquad (3)$$

where 'a' is a parameter that can be arbitrary and is always equal to 1 for the ideal mixture which indicates that there is no solute-solvent interaction. The green line in Figure 3 depicts the mixes' ideal behavior as determined by Equation (2), but the black point on the experimental values indicates the non-linear nature of the data. This shows a deviation from the mixture's ideal behavior and indicates the molecular interaction in ACN-1.4DX mixes.

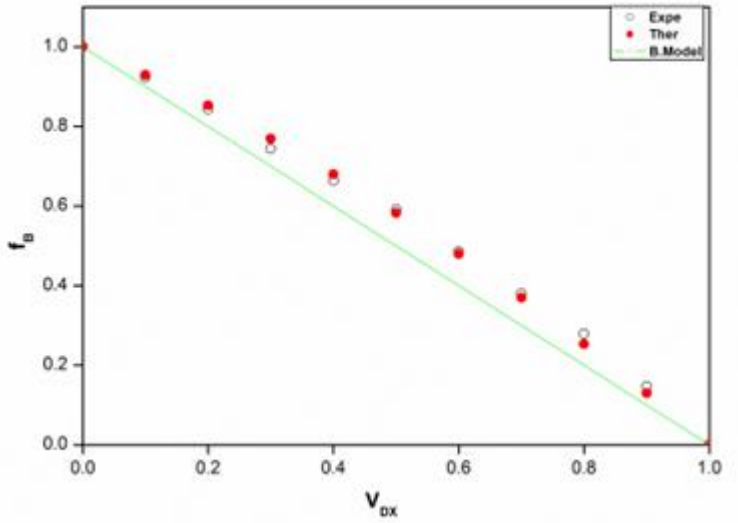

Fig.3 Bruggeman Factor for ACN-DX at 25ºC

4. Conclusion

The Frequency dependent complex permittivity spectra for ACN-1,4DX mixture have been obtained in the frequency region 10 MHz -30 GHz. The nonlinear change in relaxation time and dielectric constant indicates that intermolecular interaction is occurring in the system. A modification of the Bruggeman Equation was used to provide a more accurate description of the dielectric behaviour of theACN-1,4DX mixture.

Acknowledgment

We acknowledge the financial support given by the School of Physical Sciences at S. R. T. M. U. Nanded, Maharashtra and DST, New Delhi (Project Number DST PROJECT SB/S2/LOP-032/2013) for the use of the instrumental facility

REFERENCES

[1]Bakker, H. J., and J. L. Skinner. "Vibrational spectroscopy as a probe of structure and dynamics in liquid water." Chemical reviews 110.3 (2010): 1498-1517. https://doi.org/10.1021/cr9001879

[2] Czarnecki, Mirosław Antoni, et al. "Advances in molecular structure and interaction studies using near-infrared spectroscopy." Chemical reviews 115.18 (2015): 9707-9744. https://doi.org/10.1021/cr500013u

[3] Neilson, G. W., and J. E. Enderby. "Aqueous solutions and neutron scattering." *The Journal of Physical Chemistry* 100.4 (1996): 1317-1322. https://doi.org/10.1021/jp951490y

4] Otting, Gottfried, Edvards Liepinsh, and Kurt Wüthrich. "Protein hydration in aqueous solution." *Science* 254.5034 (1991): 974-980. https://doi.org/10.1126/science.1948083

[5] Sastry, S. Sreehari, et al. "Dielectric relaxation studies of acetonitrile/propylene glycol and their binary mixtures." Indian Journal of Pure & Applied Physics (IJPAP) 55.6 (2017): 403-412. http://op.niscpr.res.in/index.php/IJPAP/article/view/15357

[6] Orhan, Mehmet. "Dielectric and transport properties of acetonitrile at varying temperatures: a molecular dynamics study." Bulletin of the Korean Chemical Society (2014). https://doi.org/10.5012/bkcs.2014.35.5.1469

[7] Helambe, S. N., M. P. Lokhande, A. C. Kumbharkhane, S. C. Mehrotra, and S. Doraiswamy. "Dielectric study of aqueous solution of acetonitrile." Pramana 44 (1995): 405-410. https://doi.org/10.1007/BF02848492

[8] Choudhary, Shobhna, and R. J. Sengwa. "Characterization of dielectric dispersion and ionic conduction behaviour of acetonitrile at low frequencies." (2012).

[9] Thakur, Nagesh, and D. R. Sharma. "Dielectric relaxation of acetonitrile in benzene solution from microwave absorption studies." (2003). http://nopr.niscpr.res.in/handle/123456789/14184

[10] Shere, I. G., V. P. Pawar, and S. C. Mehrotra. "Temperature dependent dielectric relaxation study of acetonitrile with chlorobenzene at microwave frequency using time domain reflectometry." Journal of molecular liquids 133.1-3 (2007): 116-119. https://doi.org/10.1016/j.molliq.2006.07.002

[11] Ahn-Ercan, Gudrun, Hartmut Krienke, and Georg Schmeer. "Structural and dielectric properties of 1, 4-dioxane–water mixtures." Journal of molecular liquids 129.1-2 (2006): 75-79. https://doi.org/10.1016/j.molliq.2006.08.004

[12] Garad, Nitin P., and Ashok C. Kumbharkhane. "Structural and dielectric relaxation studies of 1, 4, and 1, 3-butanediol–1, 4-dioxane mixtures using TDR technique." Ferroelectrics 616.1 (2023): 70-79. https://doi.org/10.1080/00150193.2023.2269162

[13] Gubre, A. G., and A. C. Kumbharkhane. "Dielectric relaxation and hydrogen bonding studies of chlorobutane-dioxane mixtures using a time domain technique." Journal of the Indian Chemical Society 100.6 (2023): 101016. https://doi.org/10.1016/j.jics.2023.101016

[14]Sudo, Seiichi, et al. "Dielectric properties of ethyleneglycol− 1, 4-dioxane mixtures using TDR method." *The Journal of Physical Chemistry A* 111.16 (2007): 2993-2998. https://doi.org/10.1021/jp068222s

[15] Kumar, S., P. Periyasamy, and P. Jeevanandham. "Dielectric relaxation studies of binary liquid mixtures of a few glycols with 1, 4-dioxane." *Int J ChemTech Res* 3.1 (2011): 369-375.11

[16] Deshmukh, A. R., et al. "Dielectric relaxation and hydrogen bonding interaction of solvents using time domain reflectometry technique from 10 MHz to 50 GHz." (2018). http://nopr.niscpr.res.in/handle/123456789/44193

[17] Saknure, S. H., et al. "Dielectric Relaxation Studies of Cellulose-Water Mixtures Using Time and Frequency Domain Technique." Indian Journal of Pure & Applied Physics (IJPAP) 61.1 (2023): 27-32. http://nopr.niscpr.res.in/handle/123456789/44193

[18] Havriliak, S., and S. Negami. "A complex plane analysis of α-dispersions in some polymer systems." Journal of Polymer Science Part C: Polymer Symposia. Vol. 14. No. 1. New York: Wiley Subscription Services, Inc., A Wiley Company, 1966. https://doi.org/10.1002/polc.5070140111

[19]Kaatze, Udo. "Microwave dielectric properties of liquids." Radiation Physics and Chemistry 45.4 (1995): 549-566. https://doi.org/10.1016/0969-806X(94)00070-Z

[20] Bruggeman, D.A.G., Ann. Phys. (Leipzig).24,636(1935).

[21] Puranik, S.M, Kumbharkhane, A.C & Mehrotra, S.C: *J. Mol. Liq.*, 59,173(1994). https://doi.org/10.1016/0167-7322

ICRTMS-2024
International e-Conference on Recent Trends in Material Science
In Association with International Journal of Scientific Research in Science and Technology
Volume 11 | Issue 9 | Print ISSN: 2395-6011 | Online ISSN: 2395-602X (www.ijsrst.com)

A Comprehensive Assessment of Sensor-Based Healthcare Monitoring and IoT-Enabled Smart Ventilator Systems: A Dual Review

K. Y. Rokde*[1], S. S. Shende[2]
[1*]Assistant Professor, Department of Electronics, Dr. Ambedkar College, Nagpur, India
[2]Assistant Professor, Department of Electronics, Sharadchandra Pawar College, Lonand, India

ABSTRACT

This paper provides a comprehensive Assessment of sensor-Based Healthcare Monitoring and IOT-Enabled smart ventilator System addressing the current paramount health concerns. Despite various available solutions, leveraging sensors for health monitoring offers real-time precautionary parameters. The integration of healthcare wireless sensor networks (HWSNs) facilitates continuous patient monitoring, allowing immediate detection and alerts concerning their medical state. This continuous access to patient sensors significantly enhances patient health monitoring. The paper introduces a simplified approach to healthcare monitoring using MATLAB software, enabling prompt disease diagnosis and precautionary measures for patients, especially in critical conditions, with minimal effort.
Furthermore, the paper delves into the realm of Internet of Things (IoT)-based smart health monitoring systems. This patient monitoring system operates 24/7, revolutionizing technological infrastructures. IoT, as a transformative force, enables seamless interaction between various modules, paving the way for complex systems like smart home appliances, traffic control, office systems, environment monitoring, vehicles, and temperature control. Health monitoring systems stand out as notable applications of IoT, showcasing diverse designs and patterns. The review explores the latest innovative technologies in IoT-based smart health monitoring systems, discussing their merits and demerits.

Keywords - Sensors, Healthcare, HWSNs, MATLAB, Intelligent smart health monitoring, internet of things, temperature sensor, pulse sensor, humidity sensor

I. INTRODUCTION

1.1 HEALTHCARE WIRELESS SENSOR NETWORK (HWSNS)

This paper delves into the specialized domain of sensor networks applied to healthcare solutions, an intersection characterized by the integration of electronics devices, computers, and the internet. The system efficiently collects and wirelessly transmits data globally, finding applications in diverse fields such as forests, traffic monitoring, and environmental surveillance. However, its most crucial application lies in the realm of medical science, profoundly impacting human life. Traditionally, hospital staff engages in periodic monitoring tasks, receiving parameter information at specific intervals. The introduction of Healthcare Wireless Sensor Networks (HWSNs) transforms this approach, enabling continuous information access without frequent physical visits to patients. Sensors embedded in HWSNs play a pivotal role, transmitting collected data to

remote locations through the internet. The use of sensor nodes within hospital environments presents unique challenges, particularly in maintaining patient mobility to enhance their quality of life. HWSNs must support mobility of sensor nodes to align with patient movements. Network coverage becomes a critical concern with sensor node mobility, necessitating the expansion of multiple access ports and support for route variations to ensure connectivity with each sensor node.

A crucial aspect is handover mechanisms, facilitating seamless transition and power optimization during network attachment changes. The paper emphasizes recent advancements in handover mechanisms, specifically addressing sensor nodes' intra-mobility to maintain continuous connections in HWSNs. The principles governing HWSNs focus on real-time monitoring, accommodating random and continuous motion of sensor nodes, and ensuring desirable long battery life [1].

1.2 IoT SYSTEM

The Internet of Things (IoT) has evolved into a ubiquitous technological standard, permeating various aspects of daily life and becoming a focal point of extensive research. Sensors, integral to this technological landscape, find applications ranging from everyday products to industrial monitoring systems. The integration of IoT and sensor-based healthcare systems is burgeoning, revolutionizing health monitoring with increased efficiency and accessibility. Utilizing smart phones as data computing platforms, prototype models offer user-friendly voice recognition and alert functionalities, enhancing the overall user experience.

This paper explores the pivotal role of IoT-based systems in monitoring life-threatening diseases, with a focus on Cardiovascular Disease (CVD), a leading cause of global mortality. The convergence of information technology and smart phones has propelled the popularity of Smartphone-based health monitoring systems. These systems enable real-time health data collection and feedback, empowering individuals to proactively manage their health and seek immediate treatment during emergencies, potentially saving lives and reducing overall healthcare costs. The seamless integration of mobile internet with health service systems, leveraging Android open-source design, has become easily achievable in today's era of widespread mobile internet access.

In the context of recent advancements, Electrocardiography (ECG) has emerged as an accessible service for monitoring heart functionality. Smart devices facilitate continuous observation of heart rate, providing crucial data for doctors and patients to take preventive measures against severe damages. Emphasizing the significance of heart rate and body temperature, crucial indicators of a patient's health, this paper sheds light on their role in determining overall health conditions [2].

1.3 WIRELESS BODY AREA NETWORK

Wireless Body Area Network (WBAN) stands as a specialized category within biomedical sensor networks, where the biomedical sensor nodes are strategically placed on, near, or within the human body. Primarily utilized in medical healthcare systems, WBAN plays a pivotal role in continuously monitoring the health of elderly or ill individuals, delivering timely insights wherever required. The biomedical nodes embedded in WBAN are designed to sense and process vital signs, including heart rate, blood pressure, body temperature, and respiratory metrics, originating from the human body.

Subsequently, the collected data is transmitted to a medical center through a base station, establishing a seamless connection for healthcare professionals to monitor human health. In the medical center, doctors and caregivers rely on monitoring systems/interfaces to process, analyze, and visualize the data received from WBAN-based systems. This integrated approach ensures efficient and real-time healthcare monitoring, contributing to the well-being of individuals in need.

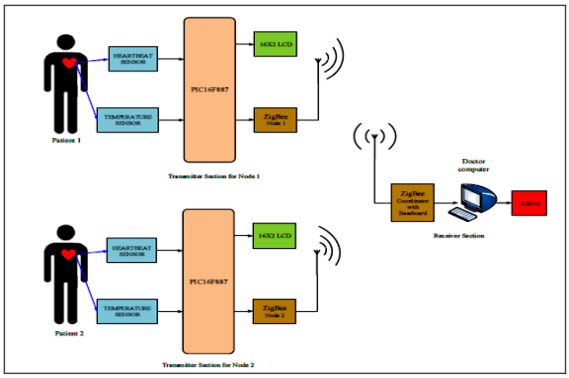

Figure 1: Block diagram of Functional System

These systems leverage wireless technologies to transmit vital signs, facilitating medical evaluation and primarily serving as a means of conveying diverse monitoring information about patients within hospital settings. Wireless sensor networks encompass a range of technologies, including Infrared, Bluetooth, ZigBee, and Touch screen. Notably, the choice of technology is influenced by specific considerations [3].

Infrared, despite its limitations in physiological signal transmission due to angle constraints, is one of the technologies considered. Bluetooth, offering higher transmission rates than ZigBee, competes in this domain. However, ZigBee stands out for its markedly lower power consumption, making it the preferred choice for continuous 24-hour monitoring in communication transmission systems. In comparison to Bluetooth, ZigBee offers enhanced network flexibility, a greater number of nodes connectivity, and an extended transmission range, all while maintaining low power consumption.

The scalability of ZigBee-enabled systems is emphasized, enabling the incorporation of a large number of nodes, thereby facilitating system expansion. Recent experiments with ZigBee-based wireless networks have demonstrated their efficacy in diverse applications, showcasing their potential for widespread implementation in healthcare monitoring systems.

It is also referred to as the pulse rate of the body. The normal pulse rate of a healthy adult is 60 to 100 beats per minute. The average human pulse rate is 70 beats per minute for males and 75 beats per minute are for females. Females aged 12 and older has faster heart rates than males. The rate changes with illness, due to damage to body, heart, and exercise. Hence heart rate is essential in determining one's health condition. Diabetes is a very common disease throughout the world. According to the World Health Organization (WHO), there are about 422 million people in the world suffering from diabetes and the amount is increasing day by day. Smart health monitoring devices determine the health condition i.e. rate of the pulse, body temperature, respiratory rate, blood glucose rate, the position of the body, ECG, EEG, and other things by using sensors. The sensors are connected and controlled through various microcontroller-based systems such as Arduino, raspberry pi, etc [4].

II. METHODOLOGY

This research aims to simulate an intra-mobility solution with a specific focus on Healthcare Wireless Sensor Networks (HWSNs). In hospital settings, patients often experience prolonged waiting times to meet with doctors, posing challenges, especially in critical conditions where immediate attention is vital. The primary goal of this study is to streamline the process by delivering diagnostic information and instant precautions to patients through software, eliminating the need for additional effort or intermediaries.

The study addresses the critical issue of patients facing challenges in accessing timely medical attention, especially in emergency situations. Through the implementation of software solutions, patients can communicate their symptoms and receive instant disease diagnosis along with precautionary measures. This approach not only facilitates efficient communication but also provides a prompt and direct means for patients to seek solutions to their health concerns. The research emphasizes leveraging technology to bridge the gap between patients and healthcare, ensuring timely interventions and improved healthcare outcomes [5].

This paper introduces an automated system designed for comprehensive patient monitoring, encompassing body temperature, heart rate, body movements, and blood pressure. The system is extended to predict potential chronic disorders or diseases by analyzing various health parameters and symptoms obtained through the system. Unlike conventional ventilators that primarily control oxygen levels, our proposed system monitors additional vital signs such as oxygen levels, heartbeats, temperature, and humidity. The collected data is transmitted to the cloud, enabling remote patient monitoring by healthcare professionals.

The system employs a variety of sensors to measure diverse patient parameters, including ECG, temperature, heart rate, and pulse. Biometric information gathered by these sensors is relayed to a Raspberry Pi, acting as an intermediary before transferring the data to a central server. The collected data is stored in a secure database and can be accessed through a dedicated website, restricted to authorized personnel only. Authorization is granted to doctors, resident medical officers (RMOs), patients, or their family members. The system also facilitates retrospective analysis, allowing doctors to review the patient's previous medical history stored in the system's memory. This integrated approach enhances patient monitoring, diagnosis, and overall healthcare management [6].

III. SYSTEM CONFIGURATION

This study utilizes MATLAB as the simulation model for implementing an intra-mobility solution within Healthcare Wireless Sensor Networks (HWSNs). MATLAB is chosen for its high-performance computation and

visualization capabilities, offering an intuitive and user-friendly interface. The ease of learning and utilization is a significant advantage of MATLAB, making it a suitable tool for this purpose.

The proposed model enables users to transmit their health symptoms, including temperature, blood pressure, ECG, and heart rate, via sensors. Using these input parameters, the system generates predictions and provides insights into the user's health condition. The user-friendly interface allows individuals to conveniently share their symptoms and obtain accurate predictions, contributing to an efficient and accessible healthcare monitoring system. The integration of MATLAB into the simulation model enhances the performance, usability, and predictive capabilities of the proposed intra-mobility solution within HWSNs [7].

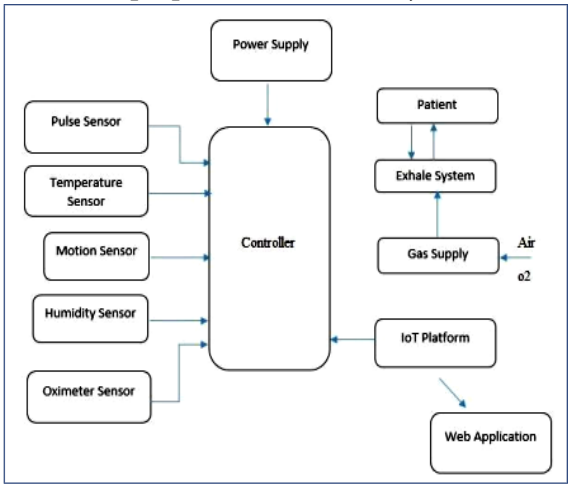

Figure 2: System Architecture diagram

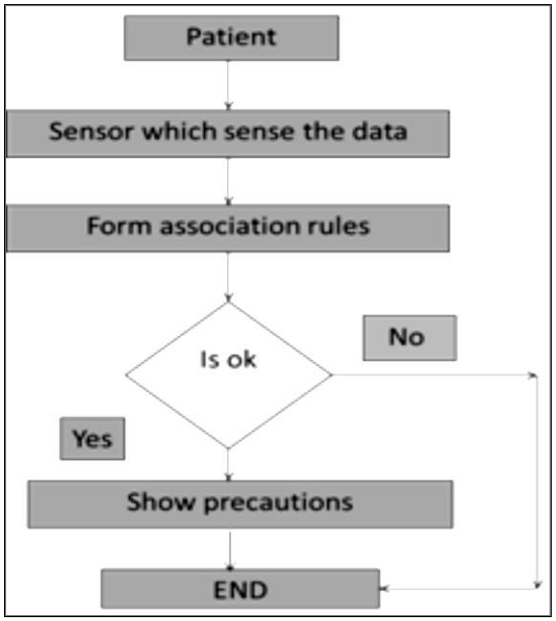

Figure 3: Flowchart of System

3.1 System overview

This automatic health monitoring system comprises a Raspberry Pi controller and an array of sensors including pulse sensor, temperature sensor, motion sensor, humidity sensor, and Oximeter sensor. The system architecture, detailed in Figure 2, elucidates the interconnection between these components. Notably, this project proves invaluable as it allows doctors to monitor patient health parameters remotely through a website or URL. With the advent of IoT applications, health tracking becomes even more accessible, enabling healthcare oversight via Android applications by doctors or family members [8].

The system employs a diverse range of sensors for monitoring various vital signs such as heart rate, body temperature, ECG, respiration, non-invasive blood pressure, and oxygen saturation. Wireless health monitoring eliminates geographical barriers, facilitating access to specialist care. The primary objective of this project is to design and implement a smart patient health tracking system, with Figure 1 providing an overview of the proposed system. Sensors embedded on the patient's body capture temperature and heartbeat data, contributing to a comprehensive health monitoring solution [9].

These systems have four main parts,

1. **Sensing Module:** It provides ability to collect certain parameters.
2. **Processing Module:** It includes the microcontroller which detects the capacity of Sensor node to run Program and process data.
3. **Communication Module:** It sends the data wirelessly to a network typically compliant with IEEE802.15.
4. **Power Supply:** It is an important part, work as energy source for keeping node alive [10].

IV. CONCLUSION

This paper introduces a wireless health monitoring system designed to receive real-time patient data, enabling immediate actions based on the obtained results. The proposed system offers an effective solution for enhancing existing health systems through the integration of various sensors into a single platform. Leveraging Healthcare Wireless Sensor Networks (HWSNs), this system enables a detailed and comprehensive analysis of a patient's disease, optimizing time efficiency in healthcare diagnostics [11].

The system communicates textual information directly to the patient, providing accessibility and convenience for patients to review their health data anywhere and take necessary actions. This approach fosters increased interaction between patients and doctors, mitigating unforeseen health crises. The incorporation of this technology for patient monitoring serves as a crucial aspect for healthcare precaution, ultimately contributing to the improvement of healthcare services. The implementation of such a wireless health monitoring system

has the potential to revolutionize healthcare delivery, emphasizing proactive and timely interventions for patient well-being. [12].

This paper presents a comprehensive exploration of the construction of a functional, low-cost, and open-source mechanical ventilator. The authors' primary objective is to address the critical shortage of ventilators worldwide, particularly impacting deprived areas. The paper introduces a numerical method capable of real-time monitoring to assess the pulmonary condition of patients, providing a valuable tool for both theory and practice in the context of mechanical ventilators.

The numerical method outlined in the paper serves as a means to distinguish between healthy and unhealthy pulmonary conditions, offering broader applications beyond the specific ventilator design presented. The contribution of this paper is twofold, addressing both the theoretical aspects and the practical implementation of a cost-effective mechanical ventilator. Additionally, the potential incorporation of alarms into the project is discussed, allowing for timely alerts to clinicians through either an alarm screen or speakers when pressure thresholds are reached. This multi-faceted approach significantly enhances the versatility and impact of the proposed ventilator system [13].

V. APPLICATION OF WSN IN HEALTHCARE

Healthcare is always a big concern, since it involves the quality of life a given individual can have. It is always better to prevent an illness than to treat it, so individual monitoring is required as a periodic activity. The aging population of developed countries present a growing slice of government's budget, and presents new challenges to healthcare systems, namely with elderly people living on independent senior housing. Traditionally, health monitoring is performed on a periodic check basis, where the patient must remember its symptoms; the doctor performs some check and formulates a diagnostic, then monitors patient progress along the treatment, if possible.

However, some symptoms only manifest themselves in daily activities, where an individual may feel some pain or discomfort. Healthcare applications of wireless sensor networks allow in-home assistance, smart nursing homes, clinical trial and research augmentation [14].

In-home healthcare becomes mandatory for diseases like Parkinson or Alzheimer, providing memory enhancement through medicine reminders, mental stimulation through sounds or images of object's location control over home appliances, medical data lookup, and emergency situations. Such approach may lead to a multi-tiered architecture, with lightweight mobile computers and smart sensors in conjunction with more powerful computational devices [15].

5.1 Healthcare Application

1. Glucose level monitoring
2. Asthma.
3. Preventing medical accidents.
4. Cardiovascular diseases
5. Alzheimer, depression, and elderly people monitoring.
6. Stroke and post-stroke.
7. Artificial retina.
8. Home monitoring
9. Heart rate monitoring
10. Artificial retina.
11. Mobihealth
12. Multi-electrophysiological system [16].

REFERENCES

[1] Jung, J.Y., Lee, J.W.: Improved WBAN Communication at *Mental Healthcare System with the Personalized Bio Signal Devices.* In: The Proceedings of 8th International Conference Advanced Communication Technology, Korea, pp. 812–816 (2006). 8. Vaudenay, S.: On the need for Multipermutations: Cryptanalysis of MD4 and SAFER. In: Preneel, B. (ed.) FSE 1994. LNCS, vol. 1008, pp. 286–297. Springer, Heidelberg (1995).

[2] U. Anliker, J. A. Ward, P. Lukowicz, G. Tröster, F. Dolveck, M. Baer, F.Keita, E. Schenker, F. Catarasi, and R. Schmid, *"AMON: A Wearable multiparameter medical monitoring and alerts system"*, IEEE Trans. On Inf.Technol., Biomed., vol. 8, no. 4, pp. 415-427, 2004.

[3] Istepanian, R.S.H., Jovanov, E., Zhang, Y.T.: M-Health: *Beyond Seamless Mobility and Global Wireless Health-Care Connectivity.* The Proceedings of the IEEE Transactions on Information Technology in Biomedicine, 405–414 (2004).

[4] Hairong Yan, Hongwei Huo, *"Wireless Sensor Network Based E-Health System- Implementation and Experimental Results", Member*, IEEE Trans. On Consumer Electronics, vol. 56, no. 4, November 2010.

[5] Aung Soe Phyo, Zaw Myo Tunand, Hla Myo Tun, *"Wireless Patient Monitoring System using point to multipoint Zigbee Technology",* ISSN:2277-8616, Vol. 4, Issue(6), June 2015, pp 267-274.

[6] ZiyuLv, Feng Xia, Guowei Wu, Lin Yao, Zhikui Chen, *"iCare: A MobileHealth Monitoring System for the Elderly"*, Member, IEEE/ACMInternational Conference, November 2010

[7] S. M. Ghatole, K.Y. Rokde, S. S. Shende, P.B. Dahikar, *"Role of Wireless Body Area Network in Remote Healthcare Monitoring"* published in International Journal of Researches in Biosciences, Agriculture and Technology (IJRBAT), ISSN: 2347-517X, Volume II, issue (7), Nov 2015, pp 154-157.

[8] Chin-Teng Lin, Fellow, Kuan-Cheng Chang, Chun-Ling Lin, Chia-ChengChiang, Shao-Wei Lu, Shih-Sheng Chang, Bor-Shyh Lin, Hsin-Yueh Liang,Ray-Jade Chen, Yuan-Teh Lee, and Li-Wei Ko, *"An IntelligentTelecardiology System Using a Wearable and Wireless ECG to Detect AtrialFibrillation"* Member, IEEE Transaction on Information technology inbiomedicine, Vol. 14, No. 3, May 2010

[9] K. Y. Rokde, P. B. Dahikar, M. J. Hedau, S. M. Ghatole, S. S. Shende *"Study of Biosensors using nanotechnology"* published in International Journal of Advances in Science, Engineering and Technology (IJASEAT), ISSN: 2321-9009, Special Issue-1, June- 2015, pp 155-157.

[10] K. Y. Rokde, S. M. Ghatole, A. G Kshirsagar, N. D. Meshram, S. S. Shende *"Design and Implementation of Speed Control Motor Using Fuzzy Logic Technique"* International Journal of Industrial Electronics and Electrical Engineering (IJIEEE), Volume 4, Special Issue 2, June 2015, ISSN: 2347-6982, pp 120-124.

[11] S. M. Ghatole, K. Y. Rokde, S. S. Shende, P.B. Dahikar *"Healthcare System with Interactive Biosensors"* published in International Journal of Electronics, Communication & Soft Computing Science and Engineering (IJECSCSE), ISSN: 2277-9477, Volume 4, Issue 4, July 2015, pp 1-4.

[12] Chandani Suryawanshi, Bhakti Kurhade, *"A WSN based System for Enhancing Intra Mobility Solution for Healthcare"*, International Journal of Emerging Trends in Engineering and Development(IJETED), Issue 5, Vol. 4 (June.-July. 2015), ISSN 2249-6149.

[13] M. Alwan, S. Kell, B. Turner, S. Dalal, D. Mack, and R. Felder, *"Psychosocial Impact of Passive Health Status Monitoring on Informal Caregivers and Older Adults Living in Independent Senior Housing,"* in 2nd Information and Communication Technologies, Surabaya, Indonesia, 2006, pp. 808-813.

[14] J. A. Stankovic, Q. Cao, T. Doan, L. Fang, Z. He, R. Kiran, S. Lin, S. Son, R. Stoleru, and A. Wood, *"Wireless Sensor Networks for In-Home Healthcare: Potential and Challenges,"* in High Confidence Medical Device Software and Systems Workshop, Pennsylvania, USA, 2005.

[15] Paulo Neves, Michal Stachyra, Joel Rodrigues, *"Application of Wireless Sensor Networks to Healthcare Promotion"*, Journal Of Communications Software And Systems, Vol. 4, No. 3, September 2008.

[16] Prof. Punam Chabukswar, Gadge Sayali Sanjay, Belote sonali Dayanand, Kadam Rutuja Sanjay, *"Review paper on automated health monitoring and smart ventilator system using IOT"*, International Journal of Creative research thought, Vol.9, Issue 11, November 2021, ISSN No: 2320-2882, pp. 38-43.

ICRTMS-2024
International e-Conference on Recent Trends in Material Science
In Association with International Journal of Scientific Research in Science and Technology
Volume 11 | Issue 9 | Print ISSN: 2395-6011 | Online ISSN: 2395-602X (www.ijsrst.com)

Study of Sensing Mechanism of PPy and CuO Metal Oxide for CO_2 Gas

M.N.Pawar[a], A.V.Rajgure[a], G.T.Lamdhale*[b]

[a] Department of Physics, G. S. Tompe Arts, Commerce & Science College, Chandur Bazar, Dist.- Amravati (M.S.), 444704 (India)

*[b]Department of Physics,Vidyabharti Mahavidylaya Amravati, Dist.- Amravati (M.S.), 444704 (India)

ABSTRACT

The sensing mechanism of polymer and metal oxide based material depends upon its chemical, physical characteristics and amount of mixing of PPy and CuO, which are strongly keen in to the preparation conditions, dopant and grain size. A Polypyrrole (PPy) has been a subject of many studies because it exhibits relatively high electrical conductivity, good environmental stability and versatility of synthesis. Pyrrole(Py) the monomer of PPy has been polymerized via chemically oxidative polymerization in the presence of an oxidant ($Fecl_3$). CuO has been Prepared by sol-gel method. PPy and CuO powder of different weight % ratio were prepared by screen printing technique on a glass substrate. This praises that the development of the sensor thick film is a important step for the preparation of good mixed metal oxide semiconductor gas sensor. Sensing properties of thick film studied by at different concentration of carbon dioxide gas and also study surface morphology of sample by using SEM and X-ray diffraction (XRD). It has also been studied the Sensitivity, Resistivity and Conductivity, Dynamic response of sensors against sensing gas. The Sensitivity of sensors at different concentration of CO_2 gas was measured by a voltage drop method at room temperature 300K and different temperature.

Keywords :-Polypyrrole, CuO nanocomposite, Chemical polymerization, Screen-printing technique, Gas Sensor, CO_2, XRD, SEM

1. INTRODUCTION

Now, a days There is great interest in using sensing devices to improve the environmental and safety control, monitoring of CO_2 gas because of a green house gas contributing to global warning. It has been observed that CuO is a promising material for various types of gas sensing including CO_2. Much work has been reported on CO_2 gas sensing using CuO and along with dopant material also.

There potential application includes sensors for chemicals and biomolecule [1-3]. Field –effect transistor [4], light emitting diode [5] and capacitor [6].Manny conducting polymer have shown changes in resistivity on expose to different gases and humidity. Polypyrrole (PPy) composite films are highly sensitivity to gases but they show a saturation effect at higher concentration of gases [7-9]. Komilla Suri et al [10] reported that iron

oxide-polypyrrole nanocomposite sensors showed the maximum response to CO_2 gas as compared to N_2 and CH_4 gases. Waghuley et al. [11] reported the increased sensitivity of a PPy composite sensor in the presence of CO_2 gas. A conducting polymer, Polypyrrole (PPy) can be prepared by various methods such as chemical, electrochemical, and vapor phase route.

'A sensor is a device that receives a signal or stimulus and responds with an electrical signal.' 'A Sensor is a device which converts the physical parameters like temperature, presence of gas , blood pressure, humidity, speed, etc into a signal which can be measured electrically.' Based on different parameters sensors are classified in several ways. The parameter to be measured, Conversion phenomenon, Contact-noncontact type, Power requirement, Analog and Digital Sensors, Absolute and Relative Sensors are some ways used to classify sensors.

The chemical sensor is well defined by IUPAC in 1991. 'A chemical sensor is a device that transforms chemical information, ranging from the concentration of a specific sample component to total composition analysis, into an analytically useful signal.' Some examples of chemical sensors are Gas sensor, Humidity sensor, Biochemical sensor etc. 'The gas sensor is a device used to monitor the presence or concentration of gas in the environment.' A gas sensor detects a specific gas and measures

In the present work, The CuO and PPy powder of different weight % ratio of were prepared by screen-printing technique on a glass substrate. Sensors parameter such as response magnitude and dynamic response were studied at room temperature and for different temperature for different concentration of CO_2 gas with an aim to know the behavior of electrical and conductivity properties of CuO and PPy under CO_2 gas. The characteristic was done through XRD, SEM to know about the material structure and thermal stability, variation of resistance, morphology, which may related to its detection properties.

The main purpose of this work is to study new material for gas sensing elements starting from the knowledge in thick film production using screen-printing technique.

2. Experimental Work

2.1 Material

The list of chemical and material along with the sources and grades used for the preparation of sensors are given in the table 1.

Table 1. Chemical and materials with sources and grade

Chemicals	Acronym	Grade	Source
Magnesium oxide	MgO	AR	SD Fine India
Polypyrrole	PPy	AR	SD Fine India
Ammonium persulphate	APS	AR	SD Fine India
Sodium hydroxide	NAOH	AR	SD Fine India
Alumina	Al_2O_3	GR	LOBA Chemi,India
Methanol	CH_3OH	AR	SD Fine India
Acetone	CH_3COCH_3	AR	SD Fine India
Ethyl Cellulose	$[C_6H_7O_2(OC_2H_5)_3]n$	AR	SD Fine India
Butyl Carbitol	$C_8H_8O_3$	AR	Merck,India

2.2 Synthesis of CuO

CuO nano particles are synthesized by Sol-Gel method using copper (II) acetate [Cu(CH3COO)2·H2O)] and Ammonia (NH_3). In short, 0.2 M copper (II) acetate solutions (100 ml) and Ammonia was added drop wise to maintained pH in a round-bottom flask and under magnetic stirrer. The colour of the solution revolve from blue to black instantaneously and a black suspension formed simultaneously. The reaction was carried out under stirring and boiling for 3 hr. The mixture was cooled to room temperature CuO precipitate was obtained. The precipitate was filtered and washed with distilled water for several times. The resulting product was dried at 60˚C for 2 hr to obtain the dry powder of CuO Nano Composite.

2.3 Synthesis of PPy

Polypyrrole (PPy) was synthesized by chemical oxidative polymerization technique using monomer pyrrole. Analytical grade ammonium per sulphate APS, was used as oxidizing agent. The chemical polymerization was carried out in a beaker by mixing 0.1 M aqueous solution of pyrrole and 0.1 Mol APS in 1:1 ratio by volume. The polymerization was carried out for a period of three hours. After termination of polymerization process, the precipitate obtained was filtered. The product was washed successively by methanol followed by distilled water.

2.4 Synthesis and Sensor Preparation

In the present work, the work concentrates on thick film sensors of CuO-PPy. The experimental method for the preparation of materials, fabrication of sensors, effect of dopant, screen –printing method and fabrication of gas chamber and gas flow meter is discussed. The powder of MgO, PPy and Al_2O_3 were calcinated at 820^{o}C in an automatically temperature controlled muffle furnace for 5 to 6 hrs. The powder of theses samples were crushed in pestle before after the calcination to get the homogeneity in the powders. The series of the sample were prepared. The different combination is shown in table 2.

Table 2: Sample codes and mole percent for series CuO and PPy

Sr.No.	Sample Code	Composition of CuO (mole %)	Composition of PPy (mole %)
1	B1	90	10
2	B3	70	30
3	B5	50	50
4	B7	30	70
5	B9	10	90

Table 3: Sample codes of Pure CuO and PPy

Sr.No.	Sample Code	Pure
1	PC	Pure CuO
2	PP	Pure PPy

The paste of the sample was prepared by using screen-printing (Thick film technology) [12-13] technique. The standard basic materials: ethyl cellulose (EC), Butyl Carbitol acetate (BCA) was used for the screen-printing process [14-15]. The ethyl cellulose and Butyl Carbitol acetate were used as binders. The active

powder and Ethyl cellulose were mixed thoroughly.During this mixing process, the BCA was added drop by drop to obtain the proper viscosity of the paste. Paste for screen-printing was prepared by taking 60 wt. % CuO, PPy powder with 40 wt.% binder in an agate mortal and thoroughly mixing it. The paste thus prepared was screen printing onto a chemically cleaned glass substrate of size 75mm ×25mm used. The substrate is an important part of any thick film process. It must also be proper shaped. For normal electronic purpose, the substrate structure should be rectangle. Then dried at room temperature for 24 h. The prepared film was heated at 373-403 K for 3h. During this stage, the volatile organic solvent was removed via decomposition and the prints adhered to the substrate. Therefore the ink solvent does not diffuse in samples. For surface resistance measurements the electrodes of conducting silver paint were formed on adjacent sides of the film and then the films were subjected to heating at 600° C for 50 min for drying the silver paint. The electrical resistance of the film was measured by using a voltage drop method adapted by Yawale et al. [16].The measurements were carried out in the laboratory of Department of physics of Vidyabharti Mahavidyalaya Amravati. The gas chamber having dimensions 30cm × 30cm × 30cm with an attached CO_2 gas flow meter (Flowtron make, India having range 1-10ml/min) was used for keeping the sensors for testing. The gas flow was adjusted to 1ml/min. The reading was carried out in a CO_2 gas environment at different ppm levels and various temperatures. The experiment was carried out 4-5 times for reproducibility of the sensors. The thickness of the sensors films was measured by Digital Micrometer having a resolution of 0.001mm.

3. Result and Discussion

3.1 Gas sensing properties of CuO:PPy composites-

The variation of sensitivity of sensors of pure and CuO:PPy composite materials with concentration of CO_2 gas at room temperature and different temperature as shown in following figure1.

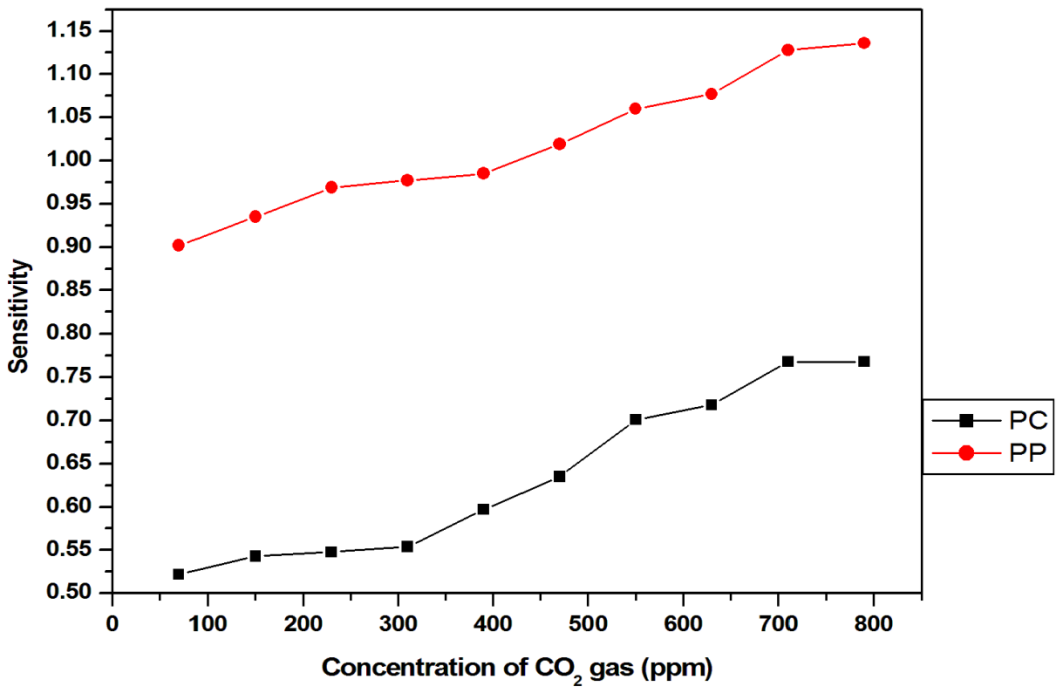

Fig. 1(a): Variation of Sensitivity of Pure CuO, PPy with CO_2 gas concentration (ppm) at room temperature (300K)

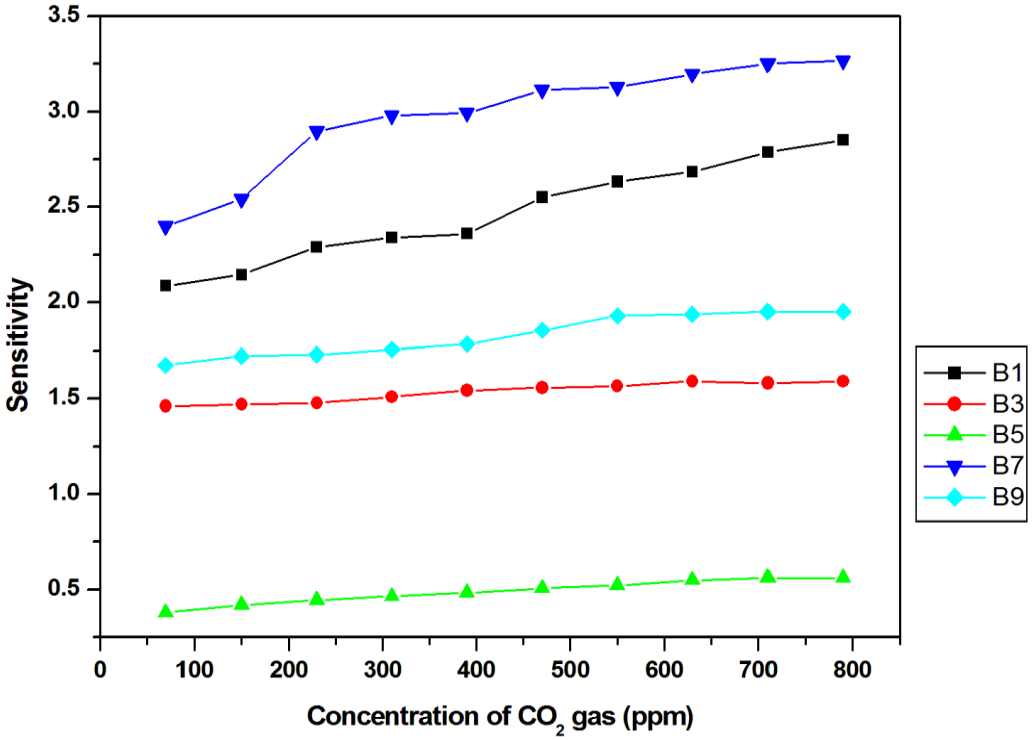

Fig. 1(b): Variation of Sensitivity of CuO:PPy composites with CO_2 gas concentration (ppm) at room temperature (300K)

The above Figure show that the variation of Sensitivity of CuO and PPy of composites sample B7 (30 Cuo:70PPy) are high Sensitivity of other composites.

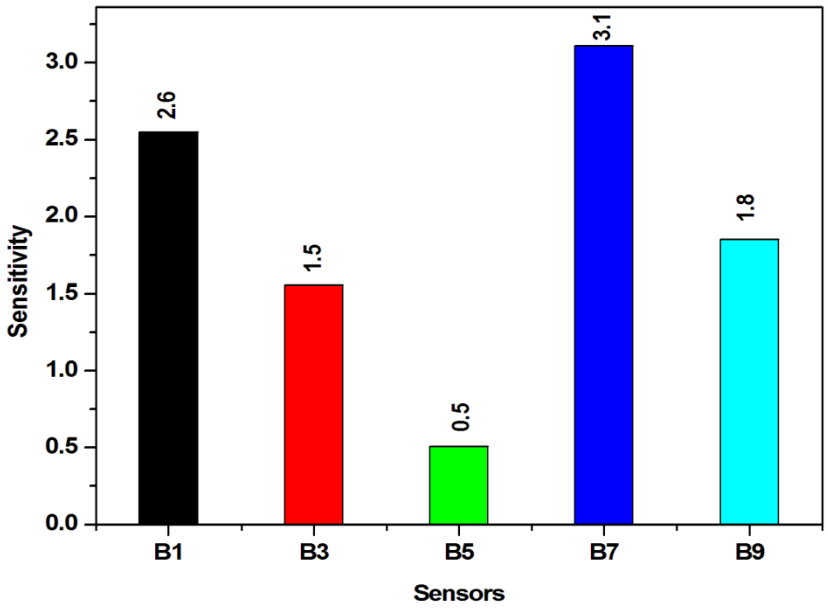

Fig. 1(c): Variation of Sensitivity of CuO:PPy composites at 470 ppm of CO_2 gas concentration

The above fig 1(c) shows that Sample B7 of sensitivity 3.1 is high other than composites. The B7 sample is optimize sample.

3.2 Dynamics response

The dynamics response of CuO and PPy composites for 100 ppm, 300 ppm,500 ppm are shown in the figure

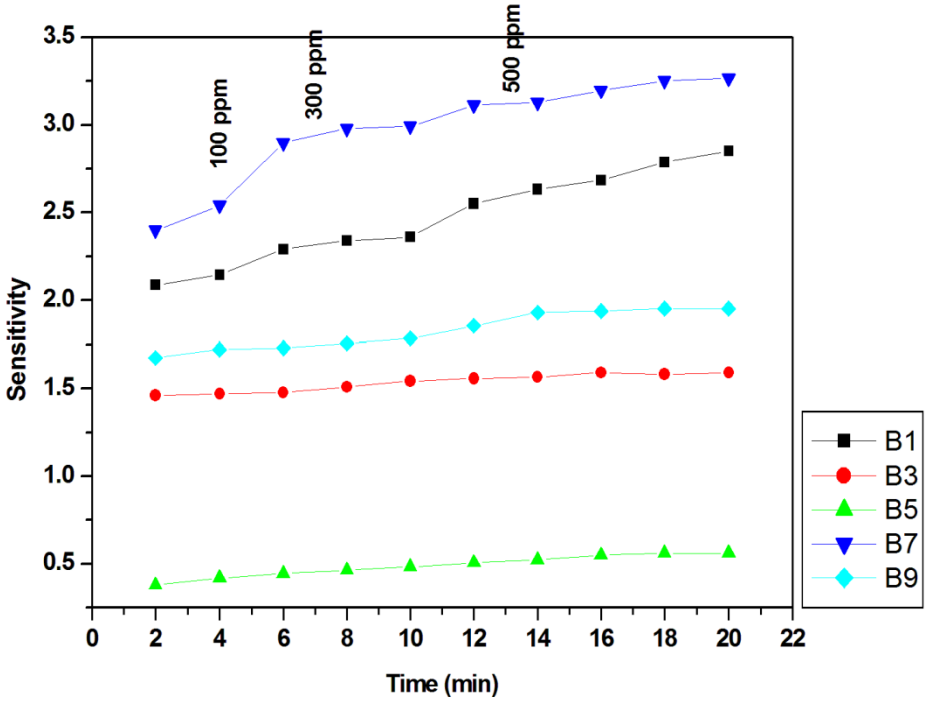

Fig.2: Dynamics response of composite sensors at 100 ppm,300 ppm and 500 ppm of CO_2 gas concentration at room temperature (300K)

From above figure, It is show that B7 sensors, this sensor shows that the fast recovery as compared to other composition sensors. Therefore B7sensors is the best sensors among the various reported sensors.

3.3 XRD analysis

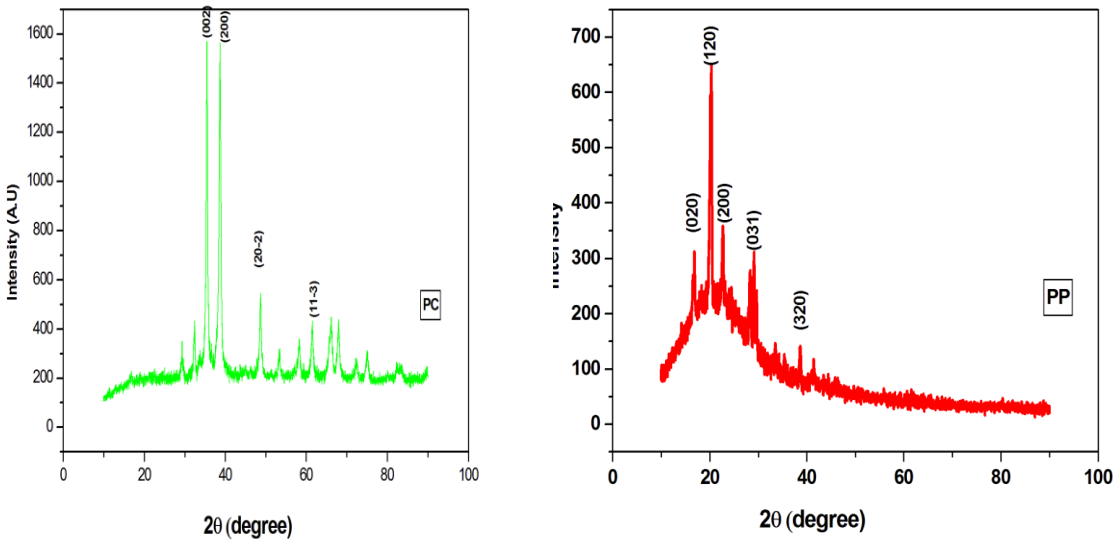

Fig 3(a):XRD of Pure CuO and PPy

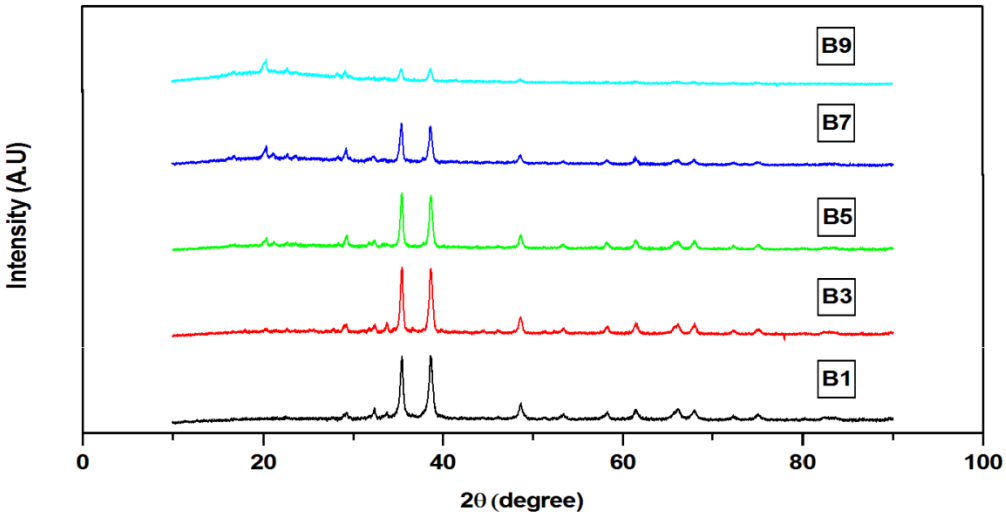

Fig 3(b):XRD of Composites CuO and PPy

From the X-ray diffraction spectra all samples show matching well with the monoclinic structure The B3 sample (70 CuO- 30 PPy) has smallest (63.47 nm) crystalline size.

3.4 Scanning Electron Microscopy (SEM) Analysis

Figure 4(a),(b) show that SEM Image of Pure CuO and PPy and Composite sample

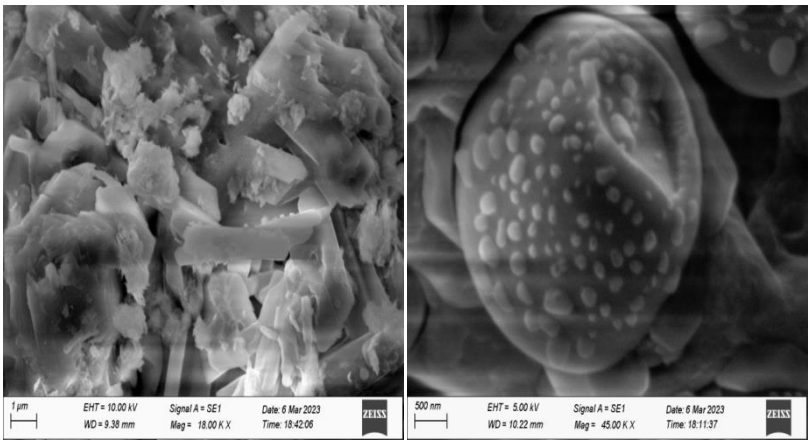

Fig.4:SEM Pure CuO and PPy

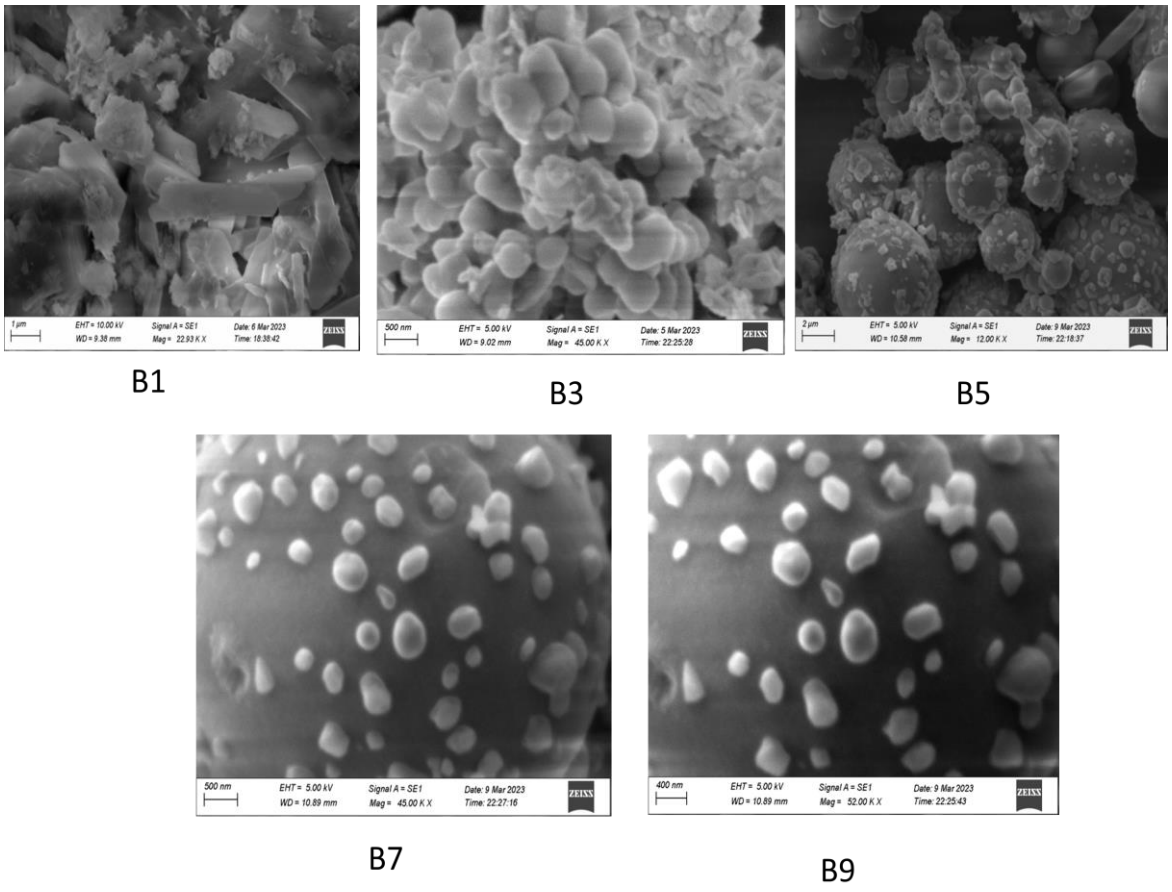

Fig4(b):SEM of Composites Sample

From the SEM pictures it is observed that sample **B7: 30CuO-70PPy** have more pores per inch (calculated for x 2,000 magnification for each composition) than other sensors of Composites. Thus, these sensors have more active surface areas and exhibit moresensing nature.

Refrences

[1] F.Selampinar,L.Toppare,U.Akbulut,T.Yalcin,S.Suzer,A conducting composite of Polypyrrole,II as a gas sensor,Synth.Met.68,pp.109-116,(1995)

[2] M.Onoda,T.Moritake,T.Matsuda,H.Nakayama, "Physical properties and application of conducting polypyrrole-silica glass composite films prepared by electrochemical polymerization",Synth.Met.Volume 71, pp.2255-2256, (1995).

[3] S.Brahim,D.Narinesingh,A.Guiseppi-Elie, "Polypyrrole-hydrogel composites for the construction of clinically important biosensors",Biosens.Bioelectron,Volume 17,pp.53-59, (2002).

[4] H.Koezuka,A.Tsumura, "Field effect transistor utilizing conducting polymers",Synth.Met.Volume 28, pp.753-760, (1989).

[5] J.Geo,H.Heegar,J.Y.Lee,C.Y.Kim,Soluble, "polypyrrole as the transparent anode in polymer light emitting diodes",Synth.Met.Volume 82, pp.221-223, (1996).

[6] Y.Liu,T.Cui,K.Varahramyan, "Fabrication and characterization of polymeric thin film capacitor",Solid-State Electron.Volume 47, pp.811-814, (2003).

[7] M.Penza, E.Milella, V.I.Anisimkin, "Monitoring of NH_3 gas by LB polypyrrole-based SAW Sensor",Sens.Actuators B,Chem. Volume 47, pp.218-224,(1998).

[8] J.J Miasik, A.Hooper,B.C.Tofield, "Conducting polymer gas sensors",J.Chem.Soc.,Faraday Trans. Volume 82, pp.1117-1126, (1986).

[9] G.Bidan, "Electroconducting conjugated polymers": New sensitive matrices to build up chemical or electrochemical sensors: a review, Sens, Actuators B,Chem. Volume 6, pp.45-56,(1992).

[10] K.Suri,S.Annapoorni,A.K.Sarkar,R.P.Tondon, "Gas and humidity sensors based on iron oxide-polypyrrole nanocomposite",Sens. Actuators B,Chem. Volume 81, pp.277-282,(2002)

[11] S.A.Waghuley,S.M.Yenorkar,G.T.Lamdhade,V.R.Bhonde,S.S.Yawale,S.P.Yawale, "Conducting polymer-polypyrrole as a CO_2 gas sensors", Proc.Solid-State phys.(India) Volume 46, pp.277-278, (2003)

[12] T.Ishihara,Kazuhirokometani,yukakomizuhara,andYusaku Takita.J.Am.Ceram.Soc.,Volume 75, 3, (1992)

[13] G.K.Mani,&Rayappan,J.B.B, "A highly selective room temperature ammonia sensor using spray deposited zinc oxide thin film", Sensors and Actutors B:Chemical, Volume 183, pp.459-466, (2013).

[14] Y.Shimizu,&M.Egashira,Basic aspects and challenges of semiconductors gas sensors.Mrs Bulletin,24(6),pp.18-24,(1999).

[15] S.K.Joshi,T.Tsurata,Rao C.M.R.,nagakura S. ,New Materials, Narosa Publishing House,(1992).

[16] S.P.Yawale, S.V.Pakade, "D.C.conductivity and hopping mechanism in Bi_2O_3-B_2O_3 glasses", J.Mater.Sci. Volume 28, pp.5451-5455, (1993).

ICRTMS-2024
International e-Conference on Recent Trends in Material Science
In Association with International Journal of Scientific Research in Science and Technology
Volume 11 | Issue 9 | Print ISSN: 2395-6011 | Online ISSN: 2395-602X (www.ijsrst.com)

Recent Advances in Green Technology towards Sustainable Development

Ishwar Baburao Ghorude* & Kirti Sadhurao Niralwad**
*Department of Environmental Science, Kohinoor Arts, Commerce & Science College, Khultabad, Chhatrapati Sambhajinager
**Department of Chemistry, Nutan Mahavidhyalaya, Selu, Parbhani

ABSTRACT

Green technology, driven by the urgent need for sustainable development, has witnessed remarkable advancements in recent years. This research article provides an overview of key innovations and developments in green technology across various sectors contributing to sustainable development. It explores advancements in renewable energy, waste management, green materials, pollution control, and sustainable agriculture. The article discusses the potential of green technology to address environmental challenges while promoting economic growth and social well-being. By highlighting recent breakthroughs and ongoing research efforts, this article aims to inspire further exploration and adoption of green technologies for a more sustainable future.
Keywords: Green technology, Sustainable development, Renewable energy, Waste management, Green materials.

I. INTRODUCTION

The global pursuit of sustainable development has become increasingly urgent in the face of mounting environmental challenges, including climate change, biodiversity loss, and pollution. Central to this pursuit is the advancement and adoption of green technology, which offers innovative solutions to mitigate environmental degradation while promoting economic prosperity and social equity. In recent years, significant strides have been made in various sectors, driven by technological innovation, policy support, and societal demand for more sustainable practices.

Green technology encompasses a wide array of technologies, processes, and materials designed to minimize environmental impact throughout their lifecycle. From renewable energy sources to waste management systems, green technology spans diverse fields and industries, offering promising avenues for sustainable development. This research article aims to provide a comprehensive overview of recent advances in green technology and their contributions towards achieving sustainable development goals.

Renewable energy stands at the forefront of the green technology revolution, offering a clean and sustainable alternative to fossil fuels. The rapid advancement of solar photovoltaic, wind, hydroelectric, and biomass technologies has transformed the energy landscape, driving down costs and increasing efficiency. These renewable energy sources not only reduce greenhouse gas emissions but also enhance energy security and foster local economic development.

In parallel, innovations in waste management technologies have revolutionized how societies handle and dispose of waste. From traditional landfilling to sophisticated waste-to-energy processes, advancements in recycling, composting, and anaerobic digestion have turned waste streams into valuable resources. Circular economy principles, which emphasize resource recovery and material reuse, have gained traction, offering a holistic approach to waste management and resource conservation.

Green materials play a crucial role in reducing the environmental footprint of various industries, including construction, manufacturing, and consumer goods. The development of biodegradable polymers, recycled aggregates, and eco-friendly packaging materials reflects a growing commitment to sustainability and circularity. Nanotechnology-based materials offer novel properties and functionalities, paving the way for greener and more efficient products and processes.

Pollution control technologies have also undergone significant innovation, addressing air, water, and soil pollution through advanced filtration, treatment, and remediation techniques. From electrochemical water purification to phytoremediation of contaminated sites, these technologies offer scalable and cost-effective solutions to environmental pollution. Green infrastructure interventions, such as green roofs and urban forests, contribute to climate resilience and ecosystem services, enhancing the quality of life in urban environments.

In agriculture, sustainable practices are revolutionizing food production systems, prioritizing soil health, biodiversity, and resource efficiency. Precision agriculture technologies enable data-driven decision-making, optimizing inputs and minimizing environmental impacts. Agroecological approaches promote biodiversity conservation and ecosystem resilience, while vertical farming and urban agriculture address food security and resource constraints in densely populated areas.

Despite these advancements, challenges remain in scaling up and mainstreaming green technologies across sectors and regions. Regulatory barriers, economic constraints, and technological limitations may hinder the widespread adoption of green solutions. Moreover, equity considerations, including access to technology and capacity building, are essential for ensuring inclusive and sustainable development.

Advancements in Renewable Energy: Renewable energy, encompassing solar, wind, hydroelectric, biomass, and geothermal sources, has experienced significant advancements in recent years. These innovations have propelled renewable energy technologies into the mainstream, transforming the global energy landscape. Key advancements include:

1. **Solar Photovoltaic (PV) Technology**: Advances in solar PV technology have led to increased efficiency and reduced manufacturing costs. Innovations such as PERC (Passivated Emitter Rear Cell) and bifacial solar panels have improved energy conversion rates and performance under varying light conditions. Additionally, research in next-generation materials like perovskite solar cells shows promise for further enhancing efficiency and lowering costs.
2. **Wind Turbine Design and Offshore Wind Farms**: The development of larger and more efficient wind turbines has driven down the cost of wind energy production. Offshore wind farms, harnessing stronger and more consistent winds, have emerged as a significant contributor to renewable energy generation. Floating offshore wind turbines represent a cutting-edge technology with the potential to unlock vast wind resources in deep waters.
3. **Energy Storage Solutions**: Advancements in energy storage technologies, particularly batteries, are essential for integrating intermittent renewable energy sources into the grid. Lithium-ion batteries, with improvements in energy density and cycle life, are widely used for grid-scale and residential

energy storage applications. Emerging technologies such as flow batteries, solid-state batteries, and hydrogen storage offer further opportunities for enhancing grid flexibility and reliability.

4. **Grid Integration and Smart Grid Technologies**: The integration of renewable energy into existing grids requires advanced grid management and control systems. Smart grid technologies enable real-time monitoring, optimization, and demand response, facilitating the efficient integration of renewable energy resources. Grid-scale energy management solutions, including virtual power plants and energy trading platforms, enhance grid stability and resilience.
5. **Emerging Renewable Energy Sources**: Beyond solar and wind, emerging renewable energy sources such as marine energy, including tidal and wave power, hold potential for sustainable electricity generation. Bioenergy technologies, including advanced biofuels and biomass co-firing, offer renewable alternatives to conventional fossil fuels in transportation and industrial sectors. Geothermal energy, tapping into the Earth's heat reservoirs, provides a reliable and baseload renewable energy source.

Innovations in Waste Management: Effective waste management is essential for minimizing environmental pollution and conserving resources. Recent developments in waste-to-energy technologies, such as anaerobic digestion and thermal conversion processes, have enabled the generation of renewable energy from organic waste streams. Additionally, advancements in recycling technologies and circular economy models have facilitated the recovery of valuable materials from waste streams, reducing the need for raw material extraction and landfill disposal.

Progress in Green Materials: The development of sustainable and environmentally friendly materials is crucial for reducing the environmental footprint of various industries. Recent advancements in green materials include the use of biodegradable polymers, recycled aggregates, and eco-friendly construction materials. Nanotechnology-based coatings and composites offer new possibilities for enhancing the durability and performance of materials while minimizing environmental impact.

Innovative Pollution Control Technologies: Pollution control technologies play a vital role in mitigating air, water, and soil pollution. Recent innovations in pollution control include the development of advanced air filtration systems, electrochemical water treatment technologies, and phytoremediation techniques. Green infrastructure solutions, such as green roofs and permeable pavements, help mitigate urban heat island effects and reduce stormwater runoff, thereby enhancing environmental quality.

Advancements in Sustainable Agriculture: Agriculture is undergoing a transformation towards more sustainable and environmentally friendly practices. Recent advances in precision agriculture, agroecology, and vertical farming have improved resource efficiency and productivity while minimizing environmental impacts. Sustainable farming practices, such as organic farming, integrated pest management, and conservation agriculture, promote soil health, biodiversity, and ecosystem resilience.

Conclusion:

The recent advancements in green technology hold immense promise for addressing global sustainability challenges. From renewable energy and waste management to green materials and pollution control, innovative technologies are driving the transition towards a more sustainable future. However, widespread adoption and implementation of green technologies require concerted efforts from governments, industries, academia, and civil society. By fostering collaboration, investment, and policy support, we can accelerate the transition towards a greener and more sustainable world.

References:

1. A. Y. Saber, "Smart grid: An overview and recent advancements," IEEE Transactions on Industrial Informatics, vol. 7, no. 4, pp. 589-597, 2011.
2. B. Polajžer, M. Hadžiselimović, and A. Švarc, "Advancements in marine energy: A review," Renewable and Sustainable Energy Reviews, vol. 82, pp. 1253-1265, 2018.
3. Ellen MacArthur Foundation. (2020). The New Plastics Economy: Rethinking the future of plastics.
4. International Energy Agency. (2021). Renewables 2021: Analysis and forecasts to 2026.
5. J. C. Parra et al., "Bioenergy technologies: A review," Renewable and Sustainable Energy Reviews, vol. 82, pp. 1122-1138, 2018.
6. J. L. Suárez et al., "Geothermal energy: An overview on resources and potential," Renewable and Sustainable Energy Reviews, vol. 107, pp. 76-86, 2019.
7. Klemes, J. J., Fan, Y. V., & Jiang, P. (2020). Advances in Eco-Efficient Materials.
8. L. F. O. Lopes, E. M. R. Oliveira, and M. A. M. Alves, "Recent advances in energy storage systems: A review," Renewable and Sustainable Energy Reviews, vol. 107, pp. 484-499, 2019.
9. N. Jenkins, D. Milborrow, J. Richard, and K. Strbac, "Advances in wind turbine technology," IET Renewable Power Generation, vol. 3, no. 4, pp. 403-430, 2009.
10. S. M. Islam, S. Ayoub, N. Uddin, and S. A. Akand, "Advancements in solar photovoltaic technology: A review," Renewable and Sustainable Energy Reviews, vol. 135, p. 110037, 2020.
11. United Nations Environment Programme. (2019). Global Waste Management Outlook.
12. Zhang, Y., Chen, X., & Li, H. (Eds.). (2021). Green Materials for Sustainable Water Remediation and Treatment.

ICRTMS-2024
International e-Conference on Recent Trends in Material Science
In Association with International Journal of Scientific Research in Science and Technology
Volume 11 | Issue 9 | Print ISSN: 2395-6011 | Online ISSN: 2395-602X (www.ijsrst.com)

Nano Catalyst for Facial Synthesis of Potentially Active Heterocyclic Compounds

Fuse S A[1], Madje B R[*]
[1]Department of Chemistry, ASC College, Badnapur, Jalna, India
[*]Department of Chemistry, Vasantrao Naik College, Chatrapati Sambhajinagar, India

ABSTRACT

Synthesis of various potentially active heterocyclic compounds is done with the help of catalyst. Catalyst helps to convert reactant to product but not consumed. Heterocyclic compounds with N, O and S has heteroatoms are mostly potentially active heterocyclic compounds. Due to applications synthesis of this potentially active heterocyclic compounds is done on industrial scale. Synthesis is done with routine methods that is use of various reagent, use of various heating methods, and use of multistep synthesis. All this methods result in production of nature pollution which affects human begin. We can reduce this pollutions by using various catalyst which helps to speedup reaction not consuming in reaction. This used catalyst is again used for another batch of heterocyclic compounds synthesis. Now a day's Nano catalyst as heterocyclic catalyst plays important role. Nano catalyst having particle size is between 1 to 100 nm so there is increase in surface so it gives good results. 1, 4-Dihydropyridine, 4-H Pyran, Quinolines so many heterocyclic compounds are synthesized using various Nano catalyst.

Keywords: Nano catalyst, Heterocyclic Compounds, synthesis

ICRTMS-2024
International e-Conference on Recent Trends in Material Science
In Association with International Journal of Scientific Research in Science and Technology
Volume 11 | Issue 9 | Print ISSN: 2395-6011 | Online ISSN: 2395-602X (www.ijsrst.com)

An Overview of Nanotechnology

Bhagvat K Kumthekar
Department of Physics, Nutan mahavidyalaya, Sailu Dist Parbhani (MS) – 431503, Maharashtra, India

ABSTRACT

I this paper, I would like to discuss about Nanotechnology and its developments. There are so many applications of nanotechnology some of them are discussed in this paper like information technology medicine, transportation, energy, food safety, and environmental science.

I. INTRODUCTION

Nanotechnology is the science and engineering of functional systems at the molecular scale. This covers both current work and concepts that are more advanced. It is defined as the breach of science and engineering devoted to designing producing and using structures devices and systems by manipulating atoms and molecules at nanocale[1] i.e. having one or more dimensions of the order of 100 nanometres. The concepts that seeded nanotechnology were first discussed in 1959 by physicist Richard Feynman. The emergence of nanotechnology as a field in the 1980s occurred through convergence of Drexler's theoretical and public work, which developed and popularized a conceptual framework for nanotechnology, and high-visibility experimental advances that drew additional wide-scale attention to the prospects of atomic control of matter.

In its original sense, nanotechnology refers to the projected ability to construct items from the bottom up, using techniques and tools being developed today to make complete, high-performance products. One nanometer (nm) is one billionth part of the 1 meter. 1nm = 10^{-9}m. For example our DNA double-helix has a diameter around 2 nm. Typical carbon–carbon bond lengths, or the spacing between these atoms in a molecule, are in the range 0.12–0.15 nm. Development of applications incorporating semiconductor nanoparticles to be used in the next generation of products, such as display technology, lighting, solar cells and biological imaging. Nanomaterials can be classified in 0D, 1D, 2D and 3D nanomaterials. The dimensionality play a major role in determining the characteristic of nanomaterials including physical, chemical and biological characteristics. With the decrease in dimensionality, an increase in surface-to-volume ratio is observed. This indicate that smaller dimensional nanomaterials have higher surface area compared to 3D nanomaterials. Recently, two dimensional (2D) nanomaterials are extensively investigated for electronic, biomedical, drug delivery and biosensor applications.

II. TECHNIQUES OF NANOTECHNOLOGY

There are two early versions of techniques lauched by nanotechnology namely the atomic force microscope (AFM) and the Scanning Tunneling Microscope (STM) [3] are two early versions of scanning probes that launched nanotechnology. The tip of a scanning probe can also be used to manipulate nanostructures (a process called positional assembly).[2] There are various techniques of nanolithography such as optical lithography, X-ray lithography, dip pen nanolithography, electron beam lithography or nanoimprint lithography were also developed[3].

It also include those used for fabrication of nanotubes and nanowires, those used in semiconductor fabrication such as deep ultraviolet lithography, electron beam lithography, focused ion beam machining, nanoimprint lithography, atomic layer deposition, and molecular vapor deposition, and further including molecular self-assembly techniques such as those employing di-block copolymers. The sole purpose of creating nanotechnology and which were results of nanotechnology research [4].

III.APPLICATIONS OF NANOTECHNOLOGY

Nanotechnology is helping to considerably improve many technology and industry sectors such as information technology, homeland security, medicine, transportation, energy, food safety, and environmental science.

Using nanotechnology, materials can effectively be made stronger, lighter, more durable, more reactive, more sieve-like, or better electrical conductors, among many other traits. Many everyday commercial products are currently on the market and in daily use that rely on nanoscale materials and processes. Nanoscale additives to or surface treatments of fabrics can provide lightweight ballistic energy deflection in personal body armor, or can help them resist wrinkling, staining, and bacterial growth. Nanoscale materials are beginning to enable washable, durable “smart fabrics” equipped with flexible nanoscale sensors and electronics with capabilities for health monitoring, solar energy capture, and energy harvesting through movement.

Lightweighting of cars, trucks, airplanes, boats, and space craft could lead to significant fuel savings. Nanoscale additives in polymer composite materials are being used in baseball bats, tennis rackets, bicycles, motorcycle helmets, automobile parts, luggage, and power tool housings, making them lightweight, stiff, durable[5]

It has greatly contributed to major advances in computing and electronics, leading to faster, smaller, and more portable systems that can manage and store larger and larger amounts of information. Transistors, the basic switches that enable all modern computing, have gotten smaller and smaller through nanotechnology. Other computing and electronic products include Flash memory chips for smart phones and thumb drives; ultra-responsive hearing aids; antimicrobial/antibacterial coatings on keyboards and cell phone casings.

The most important application of nanotechnology in medicine, draws on the natural scale of biological phenomena to produce precise solutions for disease prevention, diagnosis, and treatment. Gold nanoparticles as probes for the detection of targeted sequences of nucleic acids, and gold nanoparticles are also being clinically investigated as potential treatments for cancer and other diseases.[6]

Better imaging and diagnostic tools enabled by nanotechnology are paving the way for earlier diagnosis, more individualized treatment options, and better therapeutic success rates.

The use of nanotechnology-enabled gas lift valves in offshore operations or the use of nanoparticles to detect microscopic down-well oil pipeline fractures. It is improving the efficiency of fuel production from raw

petroleum materials through better catalysis. It is also enabling reduced fuel consumption in vehicles and power plants through higher-efficiency combustion and decreased friction.

Researchers are investigating carbon nanotube “scrubbers” and membranes to separate carbon dioxide from power plant exhaust. Scienstists are developing wires containing carbon nanotubes that will have much lower resistance than the high-tension wires currently used in the electric grid, thus reducing transmission power loss.[6]

Nanotechnology also has a prominent role in the fast developing field of Tissue Engineering. When designing scaffolds, researchers attempt to mimic the nanoscale features of a cell's microenvironment to direct its differentiation down a suitable lineage [7]

IV. REFERENCES

[1]. https://en.wikipedia.org/wiki/Nanotechnology

[2]. Lapshin, R. V. (2004). "Feature-oriented scanning methodology for probe microscopy and nanotechnology" (PDF). Nanotechnology. 15 (9)

[3]. Binnig, G.; Rohrer, H. (1986). "Scanning tunneling microscopy". IBM Journal of Research and Development. 30 (4): 355–69.

[4]. Lapshin, R. V. (2011). "Feature-oriented scanning probe microscopy". In H. S. Nalwa (ed.). Encyclopedia of Nanoscience and Nanotechnology (PDF). Vol. 14. US: American Scientific Publishers. pp. 105–115

[5]. Kafshgari, M. H.; Voelcker, N. H.; Harding, F. J. (2015). "Applications of zero-valent silicon nanostructures in biomedicine". Nanomedicine (London). 10 (16): 2553–71

[6]. https://www.nano.gov/about-nanotechnology/applications-nanotechnology

[7]. Cassidy, John W. (2014). "Nanotechnology in the Regeneration of Complex Tissues". Bone and Tissue Regeneration Insights. 5: 25–35

ICRTMS-2024
International e-Conference on Recent Trends in Material Science
In Association with International Journal of Scientific Research in Science and Technology
Volume 11 | Issue 9 | Print ISSN: 2395-6011 | Online ISSN: 2395-602X (www.ijsrst.com)

Dielectric Study and FTIR Characterization of Polar-Polar Ternary Liquid Mixtures

Kanchan L. Pattebahadur*[1], Snehal D. Deshmukh[2], Ajay J. Mohod[2], P.W. Khirade[2]

*[1]Department of Engineering Science, Hi-Tech Institute of Technology, Chh. Sambhajinagar 431136, Maharashtra, India

[2]Dielectric Research Lab, Department of Physics, Dr. Babasaheb Ambedkar Marathwada University Aurangabad - 431001, Maharashtra, India

ABSTRACT

Many chemical foods, pharmacological and other industries need to know dielectric properties and physical properties of non-ideal mixtures which could be involved in process design. The study of properties like static dielectric constant, density, refractive index are essential to understand the intermolecular interactions and inherent properties of liquids and may directly be used in various industrial requirements viz. pharmaceuticals, polymer industry, agriculture etc. To confirm the nature of interactions within the liquid mixture excess properties were used. The intermolecular interaction in ternary mixtures of 2-Ethoxy Ethanol (2-EE) + Ethyl Methyl Ketone (EMK) with (10%) of Dimethyl Sulfoxide (DMSO) have been investigated at 11 different concentrations at room temperature using Pulse Width Measurement Technique. The Static Dielectric constant, density and refractive index of ternary mixture were measured. The concentration-dependent values of excess static dielectric constant and excess molar volume were determined using the measured values of the Static dielectric constant and Density. A distinct antiparallel arrangement of dipoles is obtained for a studied ternary system according to the Kirkwood correlation factor (geff), calculated from the static dielectric constant. The Fourier transform infrared (FTIR) spectra of the ternary system under study have been characterized for studying the intermolecular interaction. The results of FTIR are in good agreement with the obtained excess parameters of the systems.

Keywords: Static Dielectric Constant, Pulse Width Measurement Technique, Kirkwood Correlation Factor, FTIR, Excess Parameters.

I. INTRODUCTION

Dielectric study of polar liquid mixtures provides valuable information regarding the complex formation in the solution. The composition of liquid mixtures is an important parameter for chemical and pharmaceutical applications [1, 2], biochemical engineering [3], optical applications [4, 5] etc. In liquid mixtures, the interactions occur between the like molecules and unlike molecules. Alkoxyethanols (2-Ethoxyethanol) have wide range of applications. These are used as industrial solvents, surfactants, detergents and wetting agents. The ketones (Ethyl Methyl Ketone) are among the most important organic compounds because they are central importance to organic chemistry and biochemistry. Dimethyl sulfoxide (DMSO) is aprotic solvent. A sulfoxide is a chemical compound containing S=O functional group attached to two carbon atoms. In liquid mixtures

using dielectric study it is possible to predict interactions between the constituents such as molecular association's viz. hydrogen bonding, dipole–dipole and dipole-induced dipole interactions [6-14].

A literature survey shows that a few researchers have tried to investigate some binary systems taking ethyl methyl ketone [15-16] and dimethyl sulfoxide [17-18] as one of the constituent components in the binary mixtures. Dielectric study of H-bonded interactions in amyl alcohols with ketones and dimethyl sulfoxide at temperature 298.15 K by Gilani et al. [19]. The FTIR spectroscopy is used to characterise the polar liquids and for the reorganisation of the functional groups. FTIR spectroscopy gives the absorption spectra of compounds that are a unique reflection of their molecular structure. It also used to confirm the presence of intermolecular interaction between the unlike molecules in the solution.

In the present work, the dielectric parameter i.e. static dielectric constant (ε_0) of the system 2-EE + EMK + DMSO ternary mixture have been carried out using Pulse Width measurement technique. The physical parameters like density (ρ), refractive index (n_D) of these ternary systems were obtained. Using these parameters, excess parameters such as excess static dielectric constant (ε_0^E), excess molar volume (V_m^E) and Effective Kirkwood correlation factor (g^{eff}) have been determined related to molecular interactions. Also, The FTIR spectra of the same ternary system have been recorded for 11 different concentrations at room temperature using Fourier Transform Infrared Spectroscopy (FTIR).

II. METHODS AND MATERIAL

AR grade chemicals 2-Ethoxyethanol, Ethyl Methyl Ketone and Dimethyl Sulfoxide were obtained commercially and used without further purification. The solutions were prepared for ternary mixture 2-EE+ EMK as one component and DMSO as a second component were prepared at 11 different volume percentages over the entire concentration range for their dielectric and FTIR measurements. The detailed explanation of the apparatus and procedures is the same as described elsewhere [20-22]. The conformational analysis of the formation of hydrogen bonding interaction in ternary system was studied using FT-IR spectra in the 500-4000cm^{-1} region with a Bruker spectrometer.

III.RESULTS AND DISCUSSION

The Static dielectric constant, densities, refractive index and effective Kirkwood correlation factor (g^{eff}) of ternary liquid mixture containing namely (2-EE + EMK + DMSO) respectively at room temperature over entire composition range are presented in Table 1. For ternary system it can be seen that variation of Static dielectric constant, densities and refractive index with composition of the mixture is non-linear which indicates the presence of molecular interactions.

TABLE I

I. The variation of Static Dielectric Constant (ε_0), Density (ρ), Refractive Index (n_D) and Effective Kirkwood Correlation Factor (g^{eff}) at room temperature of (2-EE + EMK + 10%DMSO) ternary mixture				
Volume fraction of 2-EE	**Static Dielectric Constant (ε_0)**	**Density (ρ)**	**Refractive Index (n_D)**	**Effective Kirkwood Correlation Factor (g^{eff})**
0.00	20.11	0.8352	1.389	0.1318

0.09	22.08	0.8586	1.392	0.1521
0.18	22.26	0.8682	1.395	0.1607
0.27	21.64	0.8746	1.398	0.1639
0.36	20.88	0.8862	1.400	0.1665
0.45	20.76	0.8944	1.403	0.1750
0.54	20.93	0.9094	1.406	0.1874
0.63	19.60	0.9206	1.409	0.1863
0.72	19.25	0.9212	1.411	0.1961
0.81	18.64	0.9340	1.414	0.2042
0.90	18.49	0.9399	1.416	0.2200

A. Excess Static dielectric constant (ε_o^E):

Excess Static dielectric constant (ε_o^E) is a dielectric parameter, which gives information about the interaction between the components of mixture (13). They had pointed out that the change in value of (ε_o^E) with concentration is due to the interaction between dissimilar molecules which may produce structural changes. Binary and ternary mixtures can also be investigated by observing the shapes of the excess mixing property.

The excess static dielectric constant of the binary mixture were calculated using the following equation [23],

$$\varepsilon_0^E = (\varepsilon_0)_{mix} - [\ (\varepsilon_0)_A X_A + (\varepsilon_0)_B X_B\ ] \qquad (1)$$

Where X is Volume Fraction and subscript mix, A and B represents mixture, pure liquids 1 and 2 respectively.

The excess static dielectric of the ternary mixture were calculated using the following equation [24],

$$\varepsilon_0^E = (\varepsilon_0)_{mix} - [(\varepsilon_0)_A X_A + (\varepsilon_0)_B X_B + (\varepsilon_0)_C X_C] \qquad (2)$$

Where X is Volume Fraction and subscript mix, A, B and C represents mixture, pure liquids 1, 2 and 3 respectively.

The information extracted from the (ε_0^E) values for the liquid mixtures [25-27] are as follows:

i) $\varepsilon_0^E = 0$ indicates that the mixture constituents do not interact at all.

ii) $\varepsilon_0^E < 0$ indicates that mixture constituents interact so as to reduce the total number of effective dipoles.

iii) $\varepsilon_0^E > 0$ indicates that the constituents of the mixture interact in such a way that the effective number of dipoles increases.

The ε_0^E values for volume fraction 0.1 (10%) of DMSO in (2-EE + EMK) were changes from negative to positive as shown in fig 1(a). The negative values of ε_0^E indicates the total effective number of dipoles gets reduced in ternary mixture. The positive values of ε_0^E indicates the total effective number of dipoles gets increased in ternary mixture. The positive deviation with increasing volume fraction of DMSO in 2-EE + EMK indicates, the complex formation after the intermolecular interaction, with total number of dipoles gets increased.

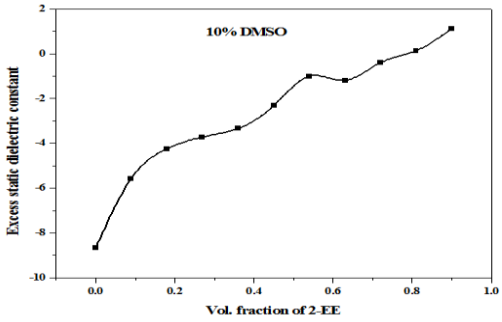

Figure 1(a): Variation of excess static dielectric constant (ε_0^E) with change in concentration of 2-EE in (EMK+10%DMSO)

B. Excess molar volume (VmE):

Excess molar volume can be expressed as a function of volume fraction of the component 1 and 2 in the case of binary and ternary systems. It has been expressed that the sign and magnitude of excess function give a good estimate of the strength of the unlike interaction in a liquid mixture.

The excess molar volume of the binary mixture were calculated using the following equation,

$$V_m^E = V_{mix} - (V_1X_1 + V_2X_2) \quad (3)$$

Where, V_m^E represents excess molar volume. V_1, V_2, and V_{mix} represent molar volume of pure liquids 1, 2 and mixture respectively. The X_1 and X_2 represents the volume fraction of component 1 and 2 of the mixtures.

The excess molar volume of the ternary mixture were calculated using the following equation,

$$V_m^E = V_{mix} - (V_1X_1 + V_2X_2 + V_3X_3) \quad (4)$$

Where, V_m^E represents excess molar volume. V_1, V_2, V_3 and V_{mix} represent molar volume of pure liquids 1, 2, 3 and mixture respectively. The X_1, X_2 and X_3 represents the volume fraction of component 1, 2 and 3 of the mixtures.

The excess molar volume function can be expressed as follows:

1) $V_m^E = 0$: indicates the liquid A and B do not interact at all.
2) $V_m^E \leq 0$: suggesting the contraction of volume and the presence of specific interactions.
3) $V_m^E \geq 0$: exhibiting the expansion of volume and the dispersion forces become increasingly predominant over the specific interactions which explain a non-ideal behaviour of the solvent system.

Patil et al. (28) observed that V_m^E may be discussed in terms of several effects which may be arbitrarily divided into physical, chemical and geometrical contributions. The Physical interaction involved mainly dispersion forces giving a positive contribution. The chemical or specific interactions result in a volume contraction and these include charge-transfer type forces, forming or breaking of H-bonds and other complex forming interactions such as donor-acceptor, dipole-dipole and dipole-induced dipole.

The excess molar volume (V_m^E) values for volume fraction 0.1 (10%) of DMSO in (2-EE + EMK) were found to be negative as shown in fig 1(b). The negative values of excess molar volume (V_m^E) indicates the molecules are come closer to each other, it gives the confirmation about contraction of volume in the liquid system.

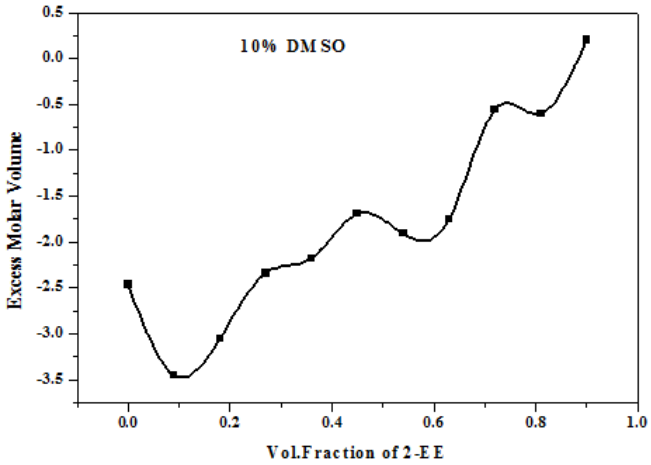

Figure 1(b): Variation of excess molar volume (V_m^E) with change in concentration of 2-EE in (EMK+10%DMSO)

C. Effective Kirkwood correlation factor (geff):

The Kirkwood correlation factor g is a parameter for obtaining information regarding the orientation of electric dipoles in polar liquids. The Kirkwood correlation factor g is a measure for preferential local ordering of molecular dipole moments and thus a hint at the formation of self–aggregates. For perfectly random dipole orientation, there is g = 1(29).

The g for pure liquid can be obtained by the expression (29)

$$\frac{4\pi N\mu^2\rho}{9KTM}g = \frac{(\varepsilon_0-\varepsilon_\infty)(2\varepsilon_0+\varepsilon_\infty)}{\varepsilon_0(\varepsilon_\infty+2)^2} \qquad (5)$$

Where μ is the dipole moment in gas phase, ρ is density at temperature T, M is molecular weight, K is Boltzman constant and N is Avogadro's number.

The effective angular correlation (g^{eff}) between molecules is calculated using modified form of equation (6). g^{eff} has been used to study the orientation of electric dipoles in binary mixtures.

The Kirkwood equation for the binary mixture may be expressed as (29);

$$\frac{4\pi N}{9KT}\left(\frac{\mu_A^2\rho_A}{M_A}X_A + \frac{\mu_B^2\rho_B}{M_B}X_B\right)g^{eff} = \frac{(\varepsilon_{0_m}-\varepsilon_{\infty_m})(2\varepsilon_{0_m}+\varepsilon_{\infty_m})}{\varepsilon_{0_m}(\varepsilon_{\infty_m}+2)^2} \qquad (6)$$

Where (g^{eff}) is the effective Kirkwood correlation factor for a binary mixture, and X_A, X_B are volume fraction of liquids A and B.

The modified equation of effective Kirkwood correlation factor (g^{eff}) for ternary mixture is as follow (24),

$$\frac{4\pi N}{9KT}\left(\frac{\mu_A^2\rho_A}{M_A}X_A + \frac{\mu_B^2\rho_B}{M_B}X_B + \frac{\mu_C^2\rho_C}{M_C}X_C\right)g^{eff} = \frac{(\varepsilon_{0_m}-\varepsilon_{\infty_m})(2\varepsilon_{0_m}+\varepsilon_{\infty_m})}{\varepsilon_{0_m}(\varepsilon_{\infty_m}+2)^2} \qquad (7)$$

(i) If g^{eff} = 1 is a measure of the extent of intermolecular interaction.

(ii) If g^{eff}>1 the molecules with parallel dipole moments or orientation.

(iii) If g^{eff}<1for anti-parallel dipole orientation (24)

To confirm the effect intermolecular interactions on the orientation of the dipoles, the values of the effective Kirkwood correlation factor g^{eff} were evaluated over the entire concentration range of the mixtures.

The g^{eff} values increases with increase in volume fraction of 2-EE in (EMK- 10% DMSO) mixture. The values of g^{eff} are diverged from unity which indicates the formation of structures and approves the change in dipolar orientation due to hydrogen bonding interaction. The g^{eff} values greater than unity indicates parallel alignment of the dipoles.

D. FTIR Studies

The variation of FTIR spectral data at room temperature of ternary mixture (2-EE + EMK + 10% DMSO) is reported in table II. The recorded FTIR spectra with change in concentration of 2-EE in EMK with 0.1 volume fraction (10%) of DMSO at room temperature are shown in fig 2(a) -2(c). From recorded spectra, When 0.1 volume fraction (10%) of DMSO is mixed with 2-EE and EMK mixture, the shift of O–H bond stretching frequency from 3408 cm^{-1} to 3414 cm^{-1}, C=O stretching frequency from 1713 cm^{-1} to 1712 cm^{-1} and S=O stretching frequency from 1061 cm^{-1} to 1064 cm^{-1} respectively.

FTIR studies predict that the frequency shifts are observed for the ternary mixture, indicating existence of intermolecular interaction. Due to the presence of carbonyl group and sulfonic group, the oxygen atom of EMK and DMSO molecules becomes more electronegative than oxygen atom of 2-EE molecule. Therefore, the hydrogen bonding occurs between the hydrogen atom of hydroxyl (O–H) group of 2-EE molecule and the oxygen atom of carbonyl (C=O) group of EMK or Sulfonic (S=O) group of DMSO molecules.

Table II

II. The variation of FTIR spectral data at room temperature of (2-EE + EMK + 10% DMSO) Ternary mixture			
Volume fraction of 2-EE	**O-H**	**C=O**	**S=O**
0.00	---	1713	1061
0.09	3408	1713	1059
0.18	3413	1713	1059
0.27	3415	1713	1060
0.36	3413	1713	1061
0.45	3418	1712	1062
0.54	3415	1712	1063
0.63	3415	1712	1063
0.72	3416	1712	1063
0.81	3415	1712	1063
0.90	3414	1712	1064

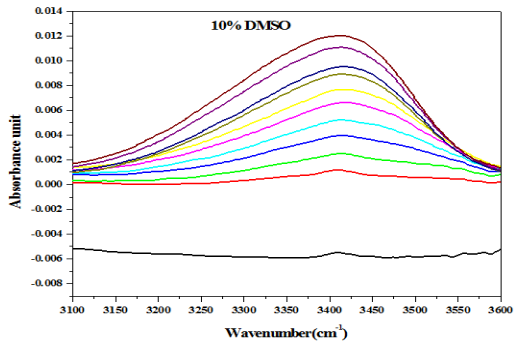

Figure 2(a): FTIR spectra for O-H of 2-EE + EMK + 10% DMSO ternary mixture

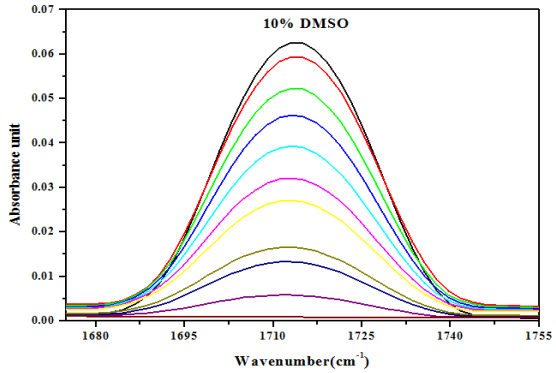

Figure 2(b): FTIR spectra for C=O of 2-EE + EMK + 10% DMSO ternary mixture

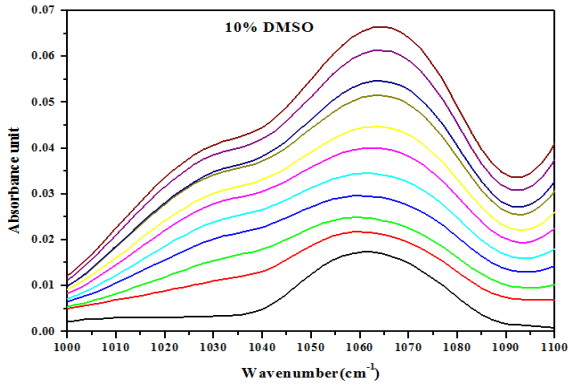

Figure 2(c): FTIR spectra for S=O of 2-EE + EMK + 10% DMSO ternary mixture

IV. CONCLUSION

As from the above results it can be concluded that

- The parameter static dielectric constant (ε_0), density (ρ) and refractive index (η_D) shows the systematic change with the concentration.
- The excess static dielectric constant (ε_0^E) values are changes from negative to positive for all concentrations of ternary mixture which attributes the hydrogen bonding intermolecular interaction.
- The excess molar volume (V_m^E) values are negative for all concentrations at room temperature which point out the contraction of volume and the occurrence of the strong complex formation in the ternary system.
- The g^{eff} values for ternary system are deviated from unity indicates the formation of structures which approves the change in dipolar orientation due to hydrogen bonding.
- FTIR spectroscopy study supports to the dielectric characterization and confirms the intermolecular association in (2-EE+ EMK) with 10% of DMSO.

V. REFERENCES

[1]. S Sharma, P.B. Patel, R.S. Patel and J.J. Vora, 2007 "Eur. J.Chem., Vol. 4, 343-349, (2007). ISSN: 0973-4945

[2]. M.P. Pena, V. Martinez-Soria and J.B. Monton, 1999 Fluid. Phase Equilibria, vol. 166, pp. 53-65, (1999). doi.org/10.1016/S0378-3812(99)00284-8

[3]. H. Watanabe, Y. Tanji, H. Unno and K. Hori, 2008 J. Biosci. Bioeng., vol. 106, pp. 226-230, (2008). DOI: 10.1263/jbb.106.226

[4]. F. Dai, Y. Xu and X. Chen, 2010 Chin. Opt. Lett. Vol. 8, pp. 14-17, (2010). DOI: 10.3788/COL20100801.0014

[5]. Y. Xu, X. Chen and Y. Zhu, 2008 Sensors, vol. 8, pp. 1872-1878, (2008). https://doi.org/10.3390/s8031872

[6]. K Pattebahadur, S D Deshmukh, AG Mohod, PB Undre, SS Patil, 2018 AIP Conference Proceedings 1953 (1) 050038 (2018). https:// doi.org/ 10.1063/1.5032693

[7]. K. L. Pattebahadur, P. B. Undre, A. G. Mohod, S.D. Deshmukh, S. S. Patil and P. W. Khirade, 2018 Ferroelect., 519, 33-42 (2018). https://doi.org/10.1080/00150193.2017.1362282

[8]. A. G. Mohod, S. D. Deshmukh, K. L.Pattebahadur, P. B. Undre, S. S. Patil and P. W.Khirade, 2018 AIP Conf. Proc., 1953 050069 (2018) https://doi.org/10.1063/1.5032724

[9]. S. D. Deshmukh, K. L. Pattebahadur, A. G.Mohod, P. B. Undre, S. S. Patil and P. W. Khirade, 2018 AIP Conf. Proc., 1953, 050039 (2018). https://doi.org/10.1063/1.5032694

[10]. S. D. Deshmukh, K. L. Pattebahadur, A. G. Mohod, S. S. Patil and P. W. Khirade, 2018 AIP Conf. Proc., 1942, 040016 (2018). https://doi.org/10.1063/1.5028625

[11]. S. D. Deshmukh, P. B. Undre, K. L.Pattebahadur, A. G. Mohod, S. S. Patil and P. W.Khirade, 2018 Ferroelect., 519, 23, (2018). https://doi.org/10.1080/00150193.2017.1362280

[12]. SD Deshmukh, KL Pattebahadur, AG Mohod, SS Patil, PW Khirade, 2020 J. Mol. Liq. 297, 111819 (2020) https://doi.org/10.1016/j.molliq.2019.111819

[13]. A. G. Mohod, S. D. Deshmukh, K. L. Pattebahadur, P. B. Undre, S. S. Patil and P. W. Khirade, 2019 IJRAR 06(1) (2019) www.ijrar.org (E-ISSN 2348-1269, P- ISSN 2349-5138)

[14]. S Deshmukh, A Mohod, K Pattebahadur, S Patil, A Kumbharkhane, P. W. Khirade 2021 Physics and Chemistry of Liquids60(1),(2021)141-163 https://doi.org/10.1080/00319104.2021.1916931

[15]. V.A.Rana, K.N.Shah, H.P.Vankar, C.M.Trivedi, 2018 J.of Mol. Liq., 271, 686-695 (2018). https://doi.org/10.1016/j.molliq.2018.09.041

[16]. T. Ganesh, M. Maria Sylvester, S. Bhuvaneswari, P. Jeevanantham, S. Kumar 2014 J.of App. Phys. 6, 59-63, (2014). https://doi.org/10.9790/4861-06225963

[17]. Z. Lua, E. Manias, M. Lanagan, D. D. Macdonald,ECS Transactions 2010 28(18), 11-21, (2010). https://doi.org/10.1149/1.3491274

[18]. Xiao-Qing Yang, Li-Jun Yang, Ka-Ma Huang, 2010 J. of Sol. Chem., 39(6), 849–856, (2010). https://doi.org/10.1007/s10953-010-9543-8

[19]. A. Ghanadzadeh Gilani, M. Moghadam, T. Ghorbanpour 2017 J. Chem. thermodynamics 113, 263-275, (2017). https://doi.org/10.1016/j.jct.2017.06.020

[20]. K. L. Pattebahadur, S. D. Deshmukh, P. B. Undre, S. S. Patil, P.W. Khirade, 2015 Bio. Fro. 8 (3), 230 (2015). ISSN 0974-0678

[21]. A. Tidar, S. P. Kamble, S. S. Patil, B. R. Sharma, P. W. Khirade and S. C. Mehrotra, 2010 J. Sens.& Transducers 123, 52-59 (2010).

[22]. S.D.Deshmukh, K.L.Pattebahadur, P.B.Undre, S.S. Patil and P.W. Khirade, 2015 Bio. Frontier 8, 223-226 (2015). ISSN 0974-0678

[23]. S. C. Mehrotra, A.C. Kumbharkhane and A.S.Chaudhari, 2017 Binary Polar Liquids, Elsevier,788, Netherlands,(2017). https://doi.org/10.1016/b978-0-12-813253-1.05001-1

[24]. K. L. Pattebahadur, S. D. Deshmukh, A.G.Mohod, S. S. Patil, P.W. Khirade, 2021 Int. J. of Res. and Ana. Rev. (IJRAR) 8 (2), 240-253 (2021). E-ISSN 2348-1269, P- ISSN 2349-5138

[25]. Hasted, J.B. 1973. Aqueous Dielectrics, Chapman and Hall, London.(1973)

[26]. Ahire, S. Chaudhari, A. Lokhande, M. Mehrotra, S C. 1998. J. of Sol. Chem., 27: 993–1008 (1998) https://doi.org/10.1023/a:1022648204099

[27]. Chaudhari, A. More, N M. Mehrotra, S C. 2001. Bull. Kor. Chem. Soc., 22: 357–361.(2001)

[28]. Patil P P, Patil S R, Borse A U and Hundiwale D G 2011, Rasayan J.Chem, 4:599. (2011) ISSN: 0974-1496

[29]. Arti Deo Tripathi; 1994 J.Sol.Chem.23, 7, (1994). https://doi.org/10.1007/bf00972671

ICRTMS-2024
International e-Conference on Recent Trends in Material Science
In Association with International Journal of Scientific Research in Science and Technology
Volume 11 | Issue 9 | Print ISSN: 2395-6011 | Online ISSN: 2395-602X (www.ijsrst.com)

Optical, Structural and Morphological Study of Chemical Bath Deposited CdS Thin Film

G. P. Urkude, G. A. Karhale
Department of Physics, Madhavrao Patil Arts, Commerce & Science College, Palam, Dist. Parbhani - 431720, Maharashtra, India

ABSTRACT

CdS thin film was deposited onto glass substrates by chemical bath deposition method at 700C for 60 minutes of deposition time. Thickness of the deposited film was measured 5.35 μm. Prepared films were characterized for optical, structural, and morphological studies. XRD analysis shows broad peaks indicating the crystalline structure with cubic phase. From the UV visible Spectra Energy band gap is found to be 2.37 eV.

I. INTRODUCTION

CdS is II-VI group important semiconductor with the direct band gap of 2.42 eV. Wide energy band gap and low absorption loss makes it suitable for variety of applications. It is widely used in gas sensors [1], optoelectronic and solar devices [2, 3]. Particle size has great importance in the technological applications of CdS thin films which depends on the preparation techniques. In recent years, efforts have been made to synthesize thin films by different techniques such as dc- sputtering [4], chemical bath deposition Method [5], pulsed chemical vapor deposition (CVD) [6], spray pyrolysis [7]. Each technique has some advantages over the other and is used depending upon the applicability of devices. Deposition technique plays an important role in the film parameters. In CBD technique reaction takes place at low temperature between the precursors dissolved in aqueous solution [8]. In the present work chemical bath deposition (CBD) method has been employed to synthesize thin films. Synthesized film was characterized by the UV visible, SEM, XRD and EDX characterization.

II. MATERIAL AND METHODS

To prepare CdS thin film, the chemicals cadmium sulfate hydrate ($3CdSO_4.8H_2O$) and thiourea (NH_2CSNH_2) of AR grade were used as source of Cd^{+2} and S^{-2} ions, respectively. pH of solution was adjusted to 10 using aqueous NH_3. Initially 50 ml of 0.05 M of cadmium sulfate was taken in a beaker. Liquid ammonia was added to it drop by drop till the pH was adjusted to 10. The precipitate disappeared on addition of liquid ammonia. 50 ml of 0.08 M thiourea was added to the prepared solution and stirred well. Commercial glass slide (75 mm x 25 mm x 1 mm) was vertically dipped in the solution. The solution was placed at constant temperature 70^0 C for 60

minutes and stirred slowly using magnetic stirrer. After 60 minutes the slide was taken out from the bath and rinsed with distilled water and dried in the air. The film appears compact, adhesive with yellowish color.

III.RESULTS AND DISCUSSION

3.1. Thickness of thin film:

Synthesized film thickness was calculated using weight and difference method by formula $t = \frac{m}{\rho A}$, where m is the mass of deposited film in gm, ρ the density of the CdS (4.84 gm/cm^3) and A the area of the deposited film in cm^2. Thickness of the film was observed 5.35 μm.

3.2. Optical analysis of CdS thin film:

Optical analysis of deposited film was performed using UV visible spectra from 300 to 900 nm range. From the spectra the band gap of deposited film was obtained by extrapolating the linear portion of the graph plotted for the $(\alpha h\upsilon)^2$ verses $h\upsilon$ as shown in fig 1. The energy band gap was found to be 2.37 eV.

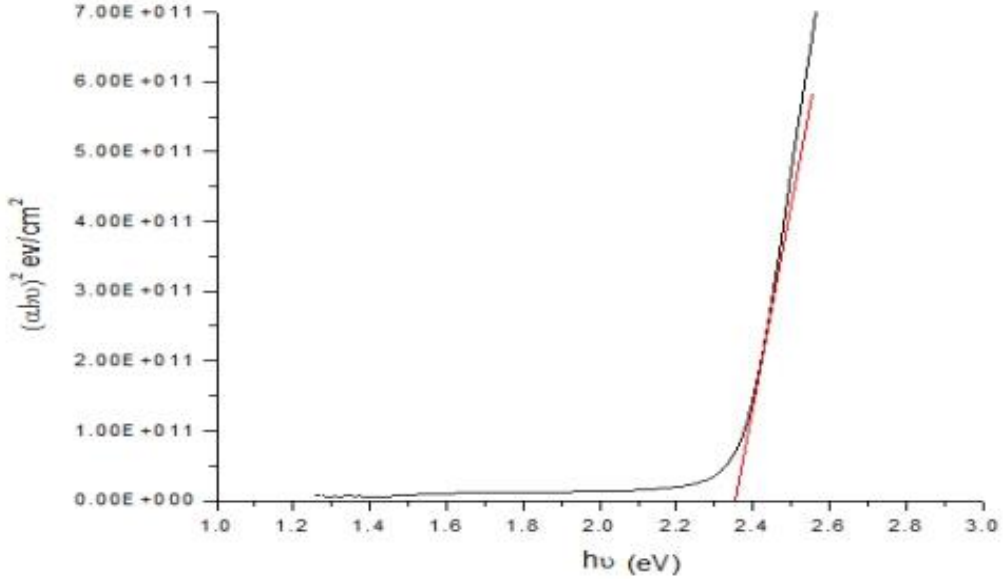

Fig. 1 Plot of $(\alpha h\upsilon)^2$ Vs. $h\upsilon$ of UV vis. spectra

3.3. XRD analysis of CdS thin film:

X-ray diffraction pattern of thin film is shown in fig 2. XRD pattern of the synthesize sample is compared with the standard ICDD data (card No. 96-101-1252) which belongs to the cubic crystal system. XRD pattern exhibits prominent peaks at 2θ values of 26.91^0, 44.49^0 and 52.42^0 which are assigned to (111), (202) and (311) reflections of cubic CdS structure. These are in good agreement with data reported in [8]. The XRD peaks are broad indicating that fine size of sample grains. The observed and standard data is given in the table 1.

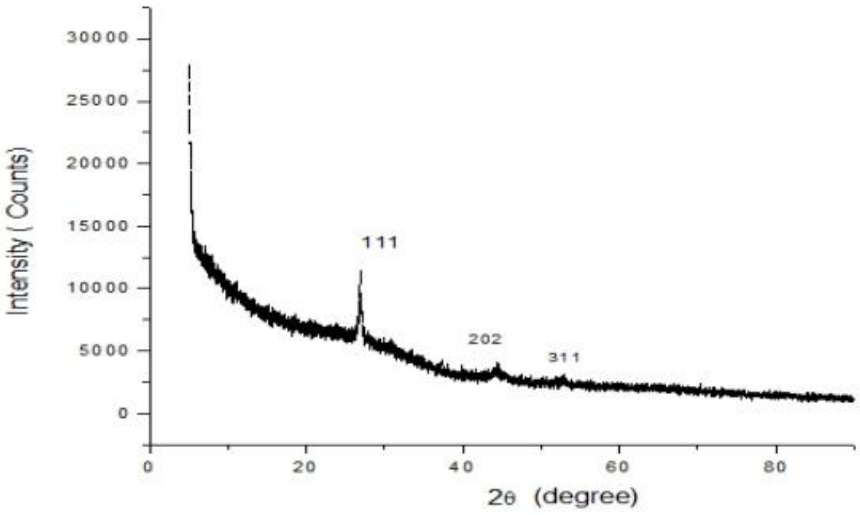

Fig. 2 XRD pattern of Cds thin film

Table 1 Observed and ICDD data for d spacing and 2 θ values of some peaks.

Sr. No.	2θ (0)		hkl	d spacing (Å)	
	ICDD	Observed		ICDD	Observed
1.	26.61	26.91	111	3.3544	3.3105
2.	44.14	44.49	202	2.0554	2.0518
3.	52.31	52.42	311	1.7518	1.7883

3.4. Surface morphology of CdS thin film:

Fig. 3 shows the SEM image of the thin film. SEM image shows that sample is well covered with the spherical particles. The average crystallites size was calculated 116 nm.

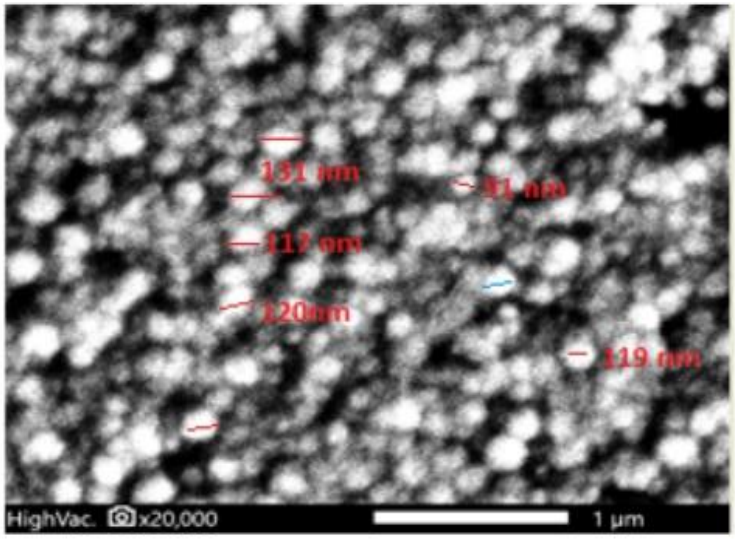

Fig. 3 The plot of $(\alpha h\upsilon)^2$ Vs. $h\upsilon$ of UV vis. spectra

3.5. EDX analysis:

Fig. 4 shows the EDX spectrum of the CdS thin film. From the spectra formation of CdS film is confirmed and the film is Cd rich. However, some additional peaks are observed in the spectra that arises from the film coating and elements of commercial glass substrate.

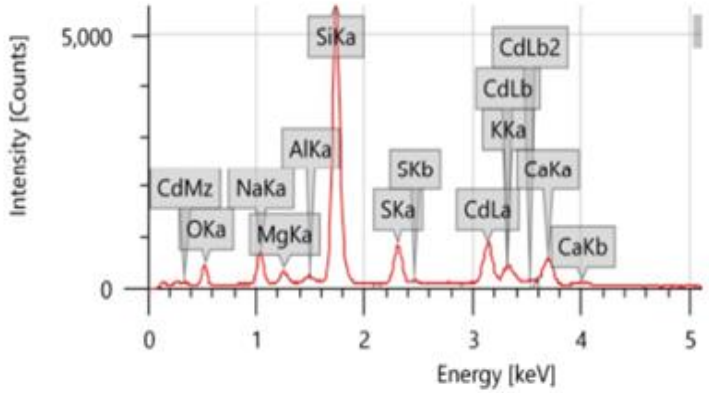

Fig. 4 EDX spectra of CdS thin film

IV. CONCLUSION

CdS thin film was synthesized with low cost CBD method. XRD data reveals that the particles have cubic structure. From UV visible spectra the band gap is found 2.37 eV. SEM image shows the average particle size of 116 nm. EDX analysis confirm the presence of CdS nanoparticles. Parameters obtained from the synthesize thin film indicates that the CdS nanoparticles are suitable for various optoelectronic and technological applications.

V. REFERENCES

[1]. Y. Kanemitsu, T. Nagai, T. Kushida (2002) Appl. Phys. Lett., 80, 267–269.
[2]. Barman, J., Borah, J. P., & Sarma, K. C. (2008) Chalcogenide Letters, 5(11), 265-271.
[3]. Narayana Swamy, T. N., Shelke, A. R., Lokhande, A. C., Pushpalatha, H. L., Lokhande, C. D., & Ganesha, R. (2017) Optik-International Journal for Light and Electron Optics, 138, 192-199.
[4]. Ghosh, P.K., Maiti, U.N., Chattopadhyay (2006) Mater. Lett., 60, 2881–2885.
[5]. Zhou J., Wu X., Teeter G. et al (2004) Phy. Stat. Sol., 24 (13), 775-778.
[6]. Maruyama T(1998) Jpn. J. Appl. Phys, 37,4099.
[7]. S. Martinuzzi (1982) Sol. Cells, 5, 243.
[8]. Abdullah M.A. Al-Hussam a, Salah Abdul-Jabbar Jassim b (2012) Journal of the Association of Arab Universities for Basic and Applied Sciences , 11, 27-31.

ICRTMS-2024
International e-Conference on Recent Trends in Material Science
In Association with International Journal of Scientific Research in Science and Technology
Volume 11 | Issue 9 | Print ISSN: 2395-6011 | Online ISSN: 2395-602X (www.ijsrst.com)

Structural Investigation of Nano-Solid Polymer Composite Electrolyte System Doped with ZnO

R. Risodkar*
Department of Physics, R.A. College, Washim, Maharashtra, India

ABSTRACT

The polyvinyl alcohol (PVA) thin film added with different concentrations of nano Zink Oxide (ZnO) powder with 20 & 25 weight% were prepared by solution cast technique investigated for Structural Properties. The structural properties of polymer electrolyte films has been confirmed by XRD. The complex formation of salt with the polymer was confirmed by Fourier transform infrared (FTIR) Spectroscopy.When PVA doped with ZnO, we found that (C= O) and (-C–O-C) stretch the bond which shows that there is structural change that increases with dopant salt concentration.

Keywords: PVA, XRD, FTIR, Polymer composite

I. INTRODUCTION

In recent years polymers have been a subject of considerable interest because of both Natural and synthetic Polymers are remarkably involved in comfort and fascillation of human life. Solid Polymer electrolyte are defined as solvent free salt solution in Polymer host material that conducts ions though the Polymer Chain. Solid Polymer are formed of entagled linear macromolecules which interact with their neighbors by physical and weak physicochemical forces (Hydrogen bonds) and are more or less free to move. The mobability of Polymer segments (chain Fragment of 10-20 atoms) very much depends on the physical state of the polymer. Globally, there has been a tremendous interest in the preparationof polymer electrolytes with high ionic conductivity, good mechanical strength and thermal stabilities. Solid polymer electrolytes (SPEs) have been studied for application in many electrochemical devices such as rechargeable batteries, fuel cell, sensors, super capacitors[1].

Solid polymer electrolytes (SPEs) fulfill the requirements and overcomethe limitations of conventional liquid electrolytes by addressing drawbacks suchas electrolyte leakage, flammable organic solvent, and electrolytic degradationof electrolytes. Nanocomposites are materials that have a solid structure in which the distance between the phases is leastwise formed of a dimension with nanoscale size and general form of an inorganic matrix set in organic phase, or vice versa, from an organic matrix set in the inorganic phase. Nanocomposites can be formed by blending inorganic nanoclusters, fullerence, clays, metals, oxides or semiconductors with numerous organic polymers or organic and organometallic compounds, biological molecules, enzymes. A range of polymeric nanocomposites are used for biomedical applications such as tissue

engineering, drug delivery, cellular therapies. Due to unique interactions between polymer and nanoparticles, a range of property combinations can be engineered to imitating native structure and properties.[2-5]

In this work, We prepared Solid polymer electrolytes based on polyvinyl alcohol (PVA) complexed with Zink oxide nano powder at different weight percent ratios and characterized by using XRD and FTIR spectroscopic analysis. The structural properties of the polymer electrolyte films was confirmed by XRD. The complex formation of the salt with the polymer was confirmed by Fourier transform infrared (FTIR) spectroscopy.

II. MATERIALS AND METHOD

Poly(vinyl alcohol) (PVA), with a degree of hydrolysis more than 99% and averagemolecular weight of 146000, was procured from Aldrich, USA with dopant zink oxide(Zno)nano powder. PVA is a potential material having high dielectric strength, goodcharge storage capacity and dopant dependentelectrical and optical properties. It has carbonchain backbone with hydroxyl groups attached to methanecarbons/these OH groups can be a source of hydrogen bonding and hence assistthe formation of polymer complexes [13]. Polyvinyl alcohol which is a semicrystalline and biodegradable polymer has very important applications due to the role of OH group and hydrogen bonds[14].

First of all, PVA was dissolved in Deionized water to which ZnO was added in different wt% along with continue stirring (4 hours) to obtain homogeneous viscous solution. These homogenous viscous solutions were casted in a glass Petri dish and left to dry for a week to remove any residual solvent. These polymer films were cut into circular pieces for further characterization.

III.RESULTS AND DISCUSSION

1. X-ray Diffraction

The XRD pattern of PVA doped with ZnO nanoparticles typically shows characteristic diffraction peaks that correspond to the l structure of ZnO nanoparticles. The most intense diffraction peak is usually observed at 2θ = 15.52 and wavelength 79.78 , which corresponds to the of Monoclinic structurein fig.1.1.

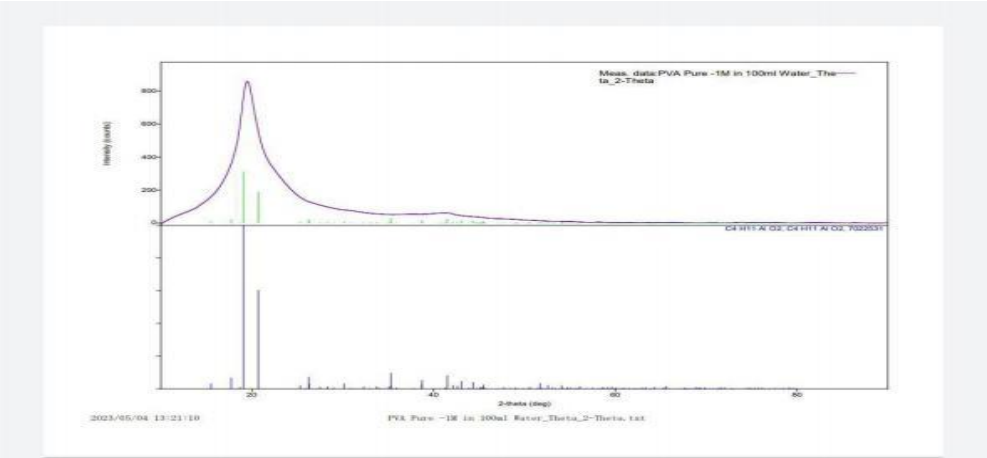

Fig. 1.1 X-ray Diffraction of pure PVA

From fig.1.2 The values of lattice parameter a=26.9702 b=11.4912 c=24.9646 and lattice parameter α=90.000 β=90.000 γ=90.000 and Volume is 3737.028 having range 2Theta is 6.55 and wavelength is 35.90 from this values we say that structure is orthorhombic.

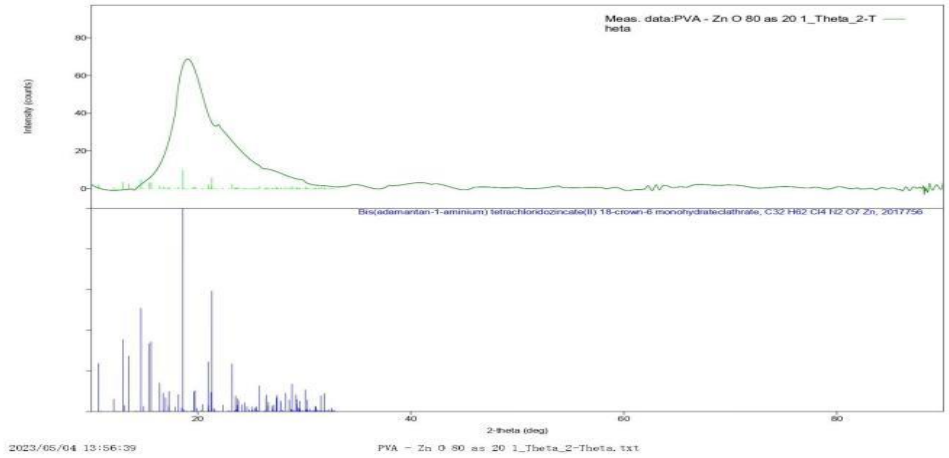

Fig. 1.2 X-ray Diffraction of PVA doped with Zno 20 wt%

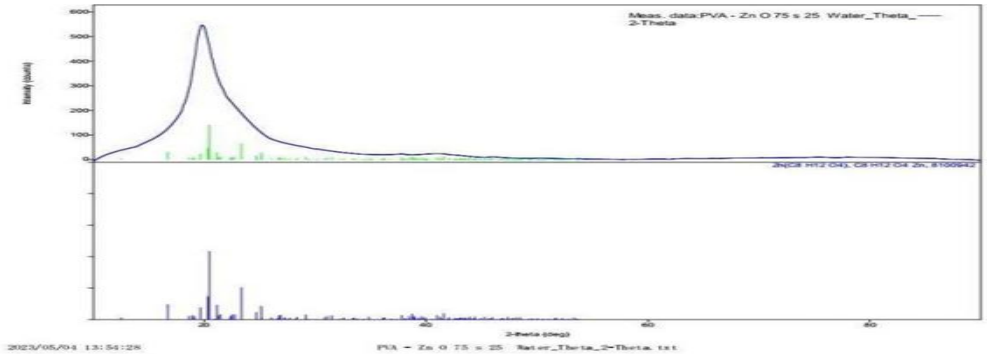

Fig. 1.3 X-ray Diffraction of PVA doped with Zno 25 wt%

From fig. 1.3 a=21.2420 b= 4.7550 c= 9.3660 and lattice parameter α=90.000 β=93.132 γ=90.000 and lattice parameter Volume is 944. 606 and having range 2θ(Theta) is 20 to 80 and intensity 0 to 600. From these values it is clear that structure of lattice parameter is Monoclinic.

2. FTIR Spectroscopy

Generally, the infrared spectroscopy includes the region of electromagnetic spectrum of approximately from 0.78 to 1000 μm. The most useful segment of the infrared region of the spectrum is from 2 to 16 μm. The absorption bands, which occur in this region, are due to the fundamental molecular vibrations. Consequently, they lend themselves for identification, qualitative analysis and band assignment. In fact, the matter absorbs infrared radiations selectively with respect to the wavelength. The presence of broad absorption peaks in FTIR spectra for all the samples is evident. The broadening of absorption peaks in each spectrum is attributed to semicrystalline/partial amorphousness of complexes. The broadening of absorption peaks increases with increase in increase in dopant concentration. Obviously such broadening of absorption peak(s) indicates increased amorphous nature owing to doping.

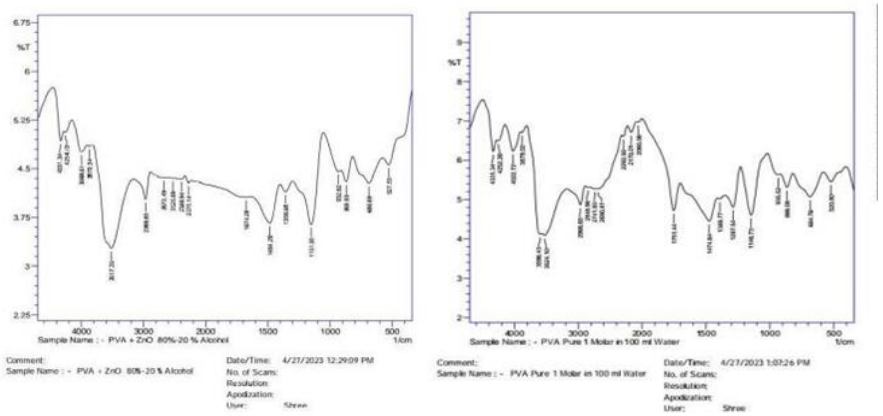

Fig.2.1 FTIR Spectra of pure PVA Fig. 2.2 FTIR Spectra of PVA : Zno 20wt%

PVA typically exhibitspeaks in the FTIR spectrum at around 3200- 4000 cm^- 1 (O-H stretching), 2900 cm^-1 (C-H stretching), 1400- 1450 cm^- 1 (C-H bending), and 1100- 1300 cm^- 1 (C-O stretching). The presence of ZnO may cause shifts or changes in the intensity of these peaks, indicating chemical interactions between PVA and ZnO. Appearance of new peaks or bands: ZnO has characteristic peaks in the FTIR spectrum at around 430-460 cm^- 1 (Zn-O stretching) and 550-580 cm^- 1 (Zn-O bending). These peaks may become more pronounced or shift in position when ZnO is added to PVA, indicating the formation of new chemical bonds or interactions.

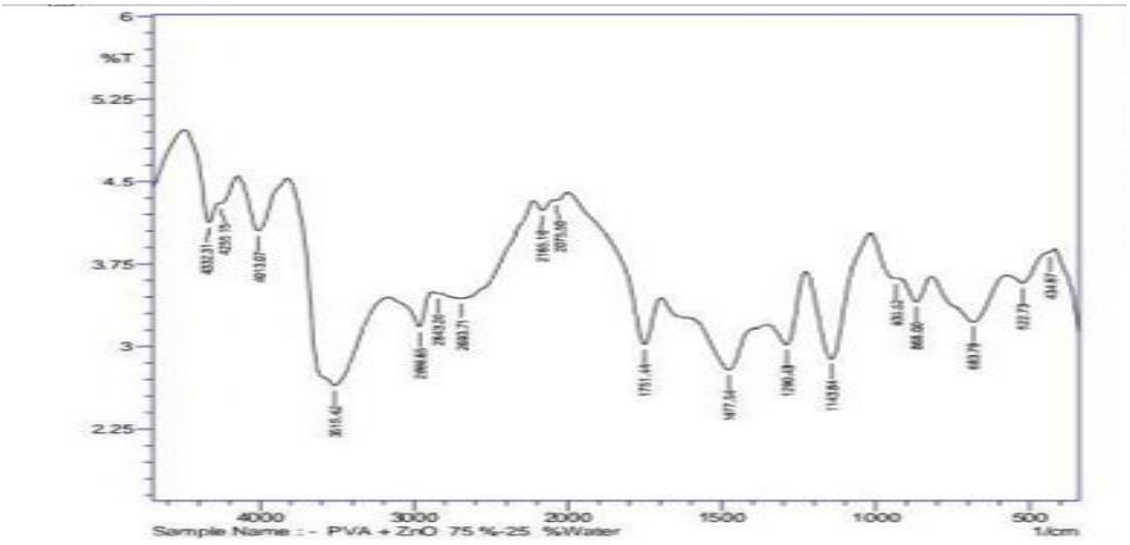

Fig. 2.3 FTIR Spectra of PVA : Zno 25wt%

Form Fig. 2.3 FTIR spectra of PVA typically exhibit absorption bands associated with the O-H stretching vibrations of the hydroxyl groups (around 3200-3500 cm- 1), the C-H stretching vibrations of the methylene groups (around 2800-3000 cm- 1), and the C=O stretching vibrations of the carbonyl groups (around 1600- 1750 cm- 1). ZnO may contribute additional vibrational modesto the spectrum, such as Zn-O stretching vibrations (around 400-500 cm-1).

IV. CONCLUSION

In this study the polymer thin films of pure PVA and doped with ZnO are synthesized using Solution Casting technique. From x-ray diffraction it confirms polymerizationof ploymer complex. FTIR study it has been found that, the concentrations of ZnO(25%) increases the structural disorder. PVA before doping acts as an insulator and after doping it became semiconductor.

The synthesis and characterization of PVA/ZnO nanocomposites can lead to the development of new materials with improved properties for various applications. The physical and chemical properties of the nanocomposites can be tailored by adjusting the concentration of ZnO nanoparticles. The biocompatibility of the nanocomposites can make them suitable for use in biomedical applications such as drug delivery and tissue engineering.

V. REFERENCES

[1]. ABDOLLAHI, M., REZAEI, M. and FARZI, G. 2012. A novel active bio nanocomposite film incorporating rosemary essential oil and nanoclay into chitosan. J. Food Eng. 111,343– 350.

[2]. ABDOLLAHI, M., ALBOOFETILEH, M., BEHROOZ, R.,REZAEI, M. and MIRAKI, R. 2013. Reducing water sensitivity of alginate bio-nanocomposite film using cellulose nanoparticles. Int. J. Biol. Macromol. 54, 166– 173. M., REZAEI, M., HOSSEINI, H. and ABDOLLAHI, M. 2013. Effect of montmorillonite clay and biopolymer concentration on the physical and mechanical properties of alginate nanocomposite film. J. Food Eng. 117,26–33.

[3]. ARORA, A. and PADUA, G.W. 2010. Review: Nanocomposite in food 4. packaging. J.FoodSci.75,43–49.ASTM2002. http://www.astm.org/DATABASE.CART/HISTORICAL/D882-02.htm(accessed December 21, 2002.)4.

[4]. AZAM, A., AHMED, F., ARSHI, N., CHAMAN, M. and NAQVI,A.H. 2010. Formation and characterization of ZnO nanopowder synthesized by sol-gel method. J. Alloys Compd.496, 399–402.

[5]. CAO, X., CHEN, Y., CHANG, P.R., STUMBORG, M. and HUNEAULT, M.A. 2008.

[6]. CHANDRAKALA, H.N., RAMARAJ, B., MADHU, G.M., SHIVAKUMARAIAH 2012 The influence of zinc oxide cerium oxide nanoparticles on the structural characteristics and electrical properties of polyvinyl alcohol films. J. Mater. Sci. 42, 8076-8084.CHAUDHRY, Q., SCOTTER, M., BLACKBURN, J., ROSS, B.,

[7]. BOXALL, A. and CASTLE, L. 2008. Applications and LI, J.H., HONG, R.Y., LI, M.Y., LI, H.Z., ZHENG, Y. and DING,J. 2009a. Effects of ZnO nanoparticles on the mechanical and antibacterial properties of polyurethane coatings. J. Pro. Org. Coat 64, 504–509.

[8]. LI,Q.,ZHOU, J. and ZHANG, L. 2009b. Structure and properties of the nanocomposite films of chitosan reinforced with cellulose whiskers. J. Polym. Sci. 47,1069- 10

[9]. LIVAGE, J., HENRY, M. and SACHEZ, C. 1988. Sol-gel-chemistry transition metaloxide. Prog. Solid State Chem. 18, 258– 341.

[10]. NAFCHI, A.M., ALIAS, A.K., MAHMUD, S. and ROBAL, M.2012. Antimicrobial, rheological, and physicochemical properties of sago starch films filled with nanorod- rich zinc oxide. J. Food Eng. 113, 511– 519.

[11]. NAIR, M.G., NIRMALA, M., REKHA, K. and ANUKALIANI, A.2011. Structural, optical, photo catalytic and antibacterial activity of ZnO and Co doped ZnO nanoparticle. Matter. Lett. 65, 1797–1800.

[12]. PEREDA, M., AMICA, G., RACZ, I. and MARCOVICN, N.E.2011. Structure and properties of nanocomposite films based on sodium caseinate and nanocellulose fibers. J. Food Eng. 103, 76–83.

[13]. RAJAMANICKAM,N.,RAJASHABALA,S. and RAMACHANDRAN, K. 2013. Theoretical and experimental investigation on enhance thermal behavior in chunk-shaped nano ZnO. Mol. Phys. 112, 142– 150.

[14]. RAO, M.S., KANATT, S.R., CHAWLA, S.P. and SHARMA, A.2010. Chitosan and guar gum composite films preparation: physical, mechanical and antibacterial properties. Carbohydrate. Polym. 82, 1243–1247.

[15]. ROY, A.S., GUPTA, S., SINDHU, S., PARVEEN, A. and RAMAMURTHY, P.C. 2013. Dielectric properties of novel PVA/ZnO hybrid nanocomposite films. Compos. Part B Eng.47, 314– 319.

ICRTMS-2024
International e-Conference on Recent Trends in Material Science
In Association with International Journal of Scientific Research in Science and Technology
Volume 11 | Issue 9 | Print ISSN: 2395-6011 | Online ISSN: 2395-602X (www.ijsrst.com)

Exploring the Frontier : A Comprehensive Review of Cadmium Oxide Nanoparticles - Synthesis, Properties, and Diverse Applications in Cancer Treatment and Beyond

Bharat K Kajale*[1], Raju S Shaikh[2], Mangesh D Kadam[3]

*[1]Department of Physics, D.S.M. College Parbhani, Maharashtra, India

[2]Department of Physics, S.G.B. College, Purna, Maharashtra, India

[3]Department of Physics, A.C.S. College, Gangakhed, Maharashtra, India

ABSTRACT

This comprehensive review paper explores the multifaceted landscape of Cadmium Oxide (CdO) nanoparticles, providing a thorough synthesis and analysis of the current state of knowledge in the fields of material science and nanotechnology. The review encompasses a wide spectrum of topics, including synthesis methods, properties, and applications, with a significant emphasis on the potential of CdO nanoparticles in cancer treatment.The paper begins by acknowledging the rapid advancements in material science and nanotechnology, necessitating a consolidated understanding of CdO nanoparticles. The review systematically examines existing literature, key developments, emerging trends,unresolved challenges,gaps in research and future scope. It seeks to establish a cohesive overview of the current landscape in CdO, offering valuable insights into its applications and future research directions.

A substantial portion of the review is dedicated to the exploration of CdO nanoparticles in cancer treatment. Various studies are surveyed, revealing promising findings that suggest the potential of CdO nanoparticles to selectively target and eliminate cancer cells. The discussion spans topics such as composition, morphology, and the impact of CdO nanoparticles on human cancer cells. Notably, CdO nanoparticles are considered for applications in early cancer diagnosis and present new possibilities for cancer prevention and treatment.

Beyond cancer treatment, the review delves into the applications of CdO nanoparticles in semiconductor films, highlighting their versatility in gas sensors, solar cells, lasers, and Spintronics. Synthesis methods, including cost-effective techniques like the Spray Pyrolysis Technique, are explored, emphasizing their relevance in industrial applications.The distinctive characteristics of CdO, combining semiconductor and piezoelectric properties, are discussed, with a focus on laser ablation as a precise and cost-efficient method for shaping CdO nanoparticles. The optical and biomedical characteristics of CdO nanoparticles are elucidated, showcasing their lower toxicity compared to other semiconductors and their applications in various products.

The review concludes by emphasizing the multifunctional potential of CdO nanoparticles in cancer treatment, including drug delivery, targeted attacks on cancer cells, and enhanced sensitivity to imaging. Recent applications in early pancreatic cancer diagnosis further highlight the diverse and promising nature of CdO nanoparticles in the biomedical field. This review paper serves as a comprehensive resource for researchers, practitioners, and scholars in the field of material science and nanotechnology. It not only consolidates the existing knowledge base but also identifies gaps and suggests potential avenues for future research, contributing to the ongoing dialogue within the scientific community.

Keywords: Cadmium Oxide Nanoparticles, Cancer Treatment, Synthesis Methods, Laser Ablation, Biomedical Applications, Cancer Diagnosis, Semiconductor Properties, Exciton Binding Energy, Nanoparticle Size Control, Industrial Applications.

I. INTRODUCTION

The field of material science and nanotechnology has witnessed significant advancements in recent years, prompting a comprehensive review to synthesize and analyze the current state of knowledge. This review paper aims to provide a thorough examination of the existing literature in cadmium oxide nanoparticles, offering a comprehensive overview of key developments, emerging trends, and unresolved challenges. By surveying a wide range of research studies, methodologies, and findings, this review seeks to establish a cohesive understanding of the current landscape in cadmium oxide and its applications. As research in material science and nanotechnology continues to evolve rapidly, this review paper not only consolidates the existing knowledge base but also identifies gaps in current understanding and suggests potential avenues for future research. Through a systematic exploration of key themes, methodologies, and findings, this review aims to contribute to the ongoing dialogue within the scientific community, fostering a deeper comprehension of the critical issues at the forefront of material science and nanotechnology. Ultimately, this review paper aspires to be a valuable resource for researchers, practitioners, and scholars seeking to navigate and contribute to the ever-expanding body of knowledge in the field of material science and nanotechnology.

Cadmium oxide (CdO) nanoparticles have gained significant attention in cancer treatment research due to their potential ability to selectively target and eliminate cancer cells. Several studies have explored the use of CdO nanoparticles in cancer treatment, with promising findings suggesting their potential as an effective treatment modality. One study hypothesized that CdO nanoparticles may selectively kill cancerous cells more than normal cells, indicating their potential for targeted cancer therapy. Furthermore, the study of the composition and morphology of CdO nanoparticles has shown promising results in eliminating cancer cells, thus supporting a new avenue for cancer treatment research. Additionally, research has indicated that CdO nanoparticles may have a role in early cancer diagnosis and present new hope for finding a cure for cancer. Moreover, the potential of CdO nanoparticles as an anti-cancer drug has been investigated through various synthesis methods and properties, aiming to understand their impact on human cancer cells. This research has shed light on the possible application of CdO nanoparticles as a viable option for cancer treatment. Another study proposed the use of CdO nanoparticles-based drug delivery in cancer prevention, prognosis, diagnosis, and imaging, further highlighting the multifaceted potential of CdO nanoparticles in cancer treatment.

Cadmium Oxide (CdO) is a distinctive chemical, demonstrating both semiconductor and piezoelectric characteristics, with a higher Exciton binding energy and a gap energy of approximately 4.05 eV[1-9] compared to other semiconductors. While various methods exist for synthesizing CdO nanostructures, laser ablation is emerging as a cost-efficient alternative, providing precise control over particle size through parameter adjustments. This study explores the laser ablation method for shaping CdO nanoparticles, investigating the impact of laser pulse energy and wavelength on nanoparticle size, and examining the optical

and medical characteristics of CdO at room temperature. Its unique properties, including sharp exciton transitions, make it suitable for applications such as LEDs with short wavelengths and semiconductor lasers, as well as transparent electrodes in photovoltaic cells[10],detectors[11], catalysts[12], and solar cells[13]. Semiconductor films composed of nanostructured Cadmium Oxide (CdO) exhibit a direct and wide band gap[14], making them versatile for applications in various fields such as gas sensors, solar cells, lasers, and Spintronics. CdO, classified as a polycrystalline n-type semiconductor with a wurtzite structure, can be synthesized using diverse techniques like magnetron sputtering, Pulsed Laser Deposition (PLD), Spray Pyrolysis Technique, and sol–gel[15-17]. Notably, the cost-effective Spray Pyrolysis Technique is widely adopted in industrial applications.

Compared to nanoparticles of other toxic semiconductors, CdO nanoparticles demonstrate lower toxicity and find applications in various products, including multivitamin pills, dietary supplements, cosmetics, and anti-solar creams. The optical characteristics of CdO nanoparticles, such as fluorescence and high-resolution second harmonic generation, enhance their suitability for various bioapplications. Cadmium Oxide (CdO) nanoparticles exhibit notable anti-cancer properties, capable of eliminating cancer cells in low concentrations. Their mechanism of action involves DNA and protein damage, along with the destruction of cell walls. Importantly, these nanoparticles show no harmful effects on human and mammalian cells, contributing to their widespread use in industrial contexts.

Beyond their anti-cancer properties, CdO nanoparticles hold promise for cancer prevention and treatment. The study of CdO nanoparticles-based therapy has emerged as a new dimension in nano-based treatments, including applications in drug delivery to tumor cells, cancer cell extraction, targeted attacks on cancer cells, enhanced sensitivity of cancer cells to imaging, and precise observation. Recent applications include the use of multifunctional CdO nanoparticles for early pancreatic cancer diagnosis, leveraging their ability to adhere to cancer cells and facilitate detection through MRI. Additionally, CdO nanoparticles find application in drug delivery to cancer cells, addressing the challenge of targeted drug delivery without adversely affecting healthy cells. This study explores, for the first time, the linear and non-linear optical characteristics, as well as medicinal and pharmaceutical applications of CdO nanoparticles in the context of eliminating cancer cells. The investigation encompasses the effects of CdO nanoparticles on the DNA of human cancer cells, emphasizing their potential role in advancing cancer treatment methodologies.

II. METHOD OF SYNTHESIS AND CHARACTERIZATION

A) Synthesis of CdO nanoparticles:

Laser Ablation Method in the Synthesis of Cadmium Oxide Nanoparticles:

Laser ablation, a versatile and precise technique, has gained prominence as an effective method for the synthesis of nanoparticles, including Cadmium Oxide (CdO). This method involves the use of a laser beam to ablate a target material, generating a plume of vaporized particles that subsequently condenses into nanoparticles. The laser ablation method offers several advantages, including control over particle size, minimal contamination, and the ability to synthesize a variety of materials. This section provides an overview of the laser ablation method and its application in CdO nanoparticle synthesis.

The fundamental principle of laser ablation involves the interaction of a high-intensity laser beam with a target material. In the case of CdO nanoparticle synthesis, a cadmium target is often utilized. The intense energy from the laser induces rapid heating of the target, causing material ablation and generating a plume of vaporized

cadmium particles. The vaporized material undergoes rapid cooling and condensation in the surrounding environment, leading to the formation of CdO nanoparticles.

Advantages of Laser Ablation Method:

1. **Controlled Particle Size:** One of the key advantages of the laser ablation method is the ability to control the size of the synthesized nanoparticles. By adjusting laser parameters such as wavelength, pulse duration, and energy, researchers can precisely influence the size distribution of the resulting CdO nanoparticles.
2. **Minimal Contamination:** Laser ablation is a "green" synthesis method as it typically involves minimal or no additional chemicals. This reduces the risk of contamination, making the method particularly attractive for applications where purity is crucial, such as in biomedical and electronic devices.
3. **Material Diversity:** The laser ablation method is versatile and can be applied to various target materials, allowing for the synthesis of CdO nanoparticles with different characteristics. This flexibility opens avenues for tailoring CdO nanoparticles for specific applications.

Challenges and Considerations:

While laser ablation offers numerous advantages, certain challenges and considerations need to be addressed. Uniformity in the size and distribution of nanoparticles can be influenced by factors such as laser fluence, repetition rate, and ambient conditions.Additionally,optimizing these parameters requires careful experimentation and characterization.

Applications of CdO Nanoparticles Synthesized via Laser Ablation:

CdO nanoparticles produced through the laser ablation method find applications in diverse fields. Their unique properties, influenced by the synthesis conditions, make them suitable for applications in sensors, catalysis, and optoelectronic devices. Furthermore, the precise control over particle size makes them valuable for studies exploring size-dependent phenomena in CdO.

Conclusion: The laser ablation method stands as a powerful tool in the synthesis of CdO nanoparticles, offering precise control over particle size and purity. Its versatility and minimal contamination make it an attractive choice for various applications. As advancements in laser technology continue, the laser ablation method is likely to play an increasingly significant role in the synthesis of tailored CdO nanoparticles for emerging technological and biomedical applications.

B) Characterization of CdO Nanoparticles by X-ray Diffraction (XRD):

X-ray Diffraction (XRD) is a powerful analytical technique widely employed for the characterization of crystalline materials, including nanoparticles. This section provides an overview of the XRD method and its application in elucidating the structural properties of Cadmium Oxide (CdO) nanoparticles.XRD relies on the principle of X-ray diffraction, which occurs when X-rays interact with a crystalline material. When X-rays strike a crystal lattice, they undergo constructive interference, resulting in diffraction patterns that contain information about the crystal structure. By analyzing the angles and intensities of these diffraction peaks, one can deduce valuable information about the crystallographic properties of the material.

Sample Preparation: To characterize CdO nanoparticles using XRD, the sample must first be appropriately prepared. Typically, CdO nanoparticles are synthesized using a specific method, such as laser ablation or sol-gel, and the resulting powder is then mounted onto a sample holder. It is crucial to ensure a homogenous and well-packed sample to obtain accurate XRD results.

XRD Analysis of CdO Nanoparticles: XRD analysis involves exposing the CdO nanoparticle sample to X-rays, and the resulting diffracted X-rays are detected and recorded. The XRD pattern manifests as a series of diffraction peaks, each corresponding to a specific set of crystallographic planes within the CdO nanoparticles. The positions and intensities of these peaks provide valuable information about the crystalline structure, crystal size, and orientation of the CdO nanoparticles.

Information Extracted from XRD Patterns:

1. **Crystal Structure:** The positions and shapes of the diffraction peaks in the XRD pattern are indicative of the crystal structure of CdO nanoparticles. For CdO, which commonly adopts a cubic structure, the positions of the peaks can be matched with known crystallographic databases for confirmation.
2. **Crystal Size:** The broadening of XRD peaks is related to the size of the crystalline domains in the material. Applying the Scherrer equation to the peak broadening allows for the estimation of the average crystallite size of the CdO nanoparticles.
3. **Orientation and Texture:** The relative intensities of XRD peaks provide information about the orientation and texture of the CdO nanoparticles. A more textured material will exhibit preferential orientation of crystalline planes.

Interpretation of XRD Results: The XRD pattern obtained from CdO nanoparticles is analyzed using dedicated software, and the diffraction peaks are compared with reference patterns to confirm the crystal structure. The calculated crystallite size and information on orientation contribute to a comprehensive understanding of the CdO nanoparticle's structural characteristics.

Conclusion: XRD analysis plays a crucial role in the characterization of CdO nanoparticles, offering insights into their crystal structure, size, and orientation. This information is fundamental for researchers and scientists in tailoring the synthesis processes and optimizing CdO nanoparticles for specific applications in areas such as catalysis, sensors, and electronic devices.

III.APPLICATIONS

Cadmium Oxide (CdO) nanoparticles have demonstrated promising applications in cancer treatment, leveraging their unique properties for therapeutic interventions. The multifaceted characteristics of CdO nanoparticles contribute to their effectiveness in various aspects of cancer treatment. Here are some notable applications of CdO in cancer therapy:

1. **Photothermal Therapy (PTT):** CdO nanoparticles exhibit strong absorbance in the near-infrared (NIR) region, making them suitable candidates for photothermal therapy. When exposed to NIR light, CdO nanoparticles generate heat, leading to localized hyperthermia in the cancerous tissue. This hyperthermia can induce selective cancer cell destruction while minimizing damage to surrounding healthy tissues.

2. **Drug Delivery Systems:** CdO nanoparticles can be employed as carriers for drug delivery in cancer treatment. Surface modifications and functionalizations enable the attachment of therapeutic agents onto the CdO surface. The controlled release of drugs at the targeted cancer site enhances the therapeutic efficacy while minimizing systemic side effects associated with conventional chemotherapy.
3. **Imaging Agents:** Due to their unique optical properties, CdO nanoparticles can serve as imaging agents for diagnostic purposes. These nanoparticles can be utilized in various imaging modalities, including magnetic resonance imaging (MRI) and fluorescence imaging. Their ability to selectively accumulate in tumor tissues enhances the precision of cancer diagnosis and allows for real-time monitoring of treatment response.
4. **Reactive Oxygen Species (ROS) Generation:** CdO nanoparticles have been reported to induce the generation of reactive oxygen species within cancer cells. Elevated levels of ROS can lead to oxidative stress, causing damage to cellular components and triggering apoptosis in cancer cells. This property is particularly advantageous for targeted cancer cell elimination.
5. **Synergistic Therapy:** CdO nanoparticles can be integrated into synergistic therapy approaches, combining multiple treatment modalities for enhanced efficacy. For example, combining photothermal therapy with drug delivery systems or utilizing CdO nanoparticles in conjunction with other therapeutic agents can create a synergistic effect, leading to improved cancer treatment outcomes.
6. **Radiotherapy Sensitization:** Studies suggest that CdO nanoparticles may enhance the sensitivity of cancer cells to radiotherapy. Their radiosensitizing effect can potentiate the damage inflicted by ionizing radiation on cancer cells, potentially allowing for lower radiation doses and minimizing damage to surrounding healthy tissues.
7. **Anti-Angiogenic Effects:** CdO nanoparticles have demonstrated anti-angiogenic properties, inhibiting the formation of new blood vessels in tumors. By disrupting the tumor's blood supply, CdO nanoparticles can impede tumor growth and metastasis, offering a potential avenue for cancer treatment.
8. **Immunotherapy Enhancement:** CdO nanoparticles may play a role in enhancing the effectiveness of immunotherapy in cancer treatment. Their ability to modulate the tumor microenvironment and stimulate immune responses could synergize with immunotherapeutic approaches, such as checkpoint inhibitors, for more robust antitumor effects.

While these applications show promise, it's essential to note that the field of using CdO nanoparticles in cancer treatment is still in the early stages of research, and further studies are needed to establish their safety and efficacy in clinical settings.

IV. FUTURE SCOPE, CHALLENGES AND GAPS

A) Future scope and challenges:

The future scope of research in the synthesis of cadmium oxide nanoparticles for cancer treatment is promising yet challenging. Here are some potential areas of focus and associated challenges:

Enhanced Biocompatibility: Future research may aim to improve the biocompatibility of cadmium oxide nanoparticles to minimize potential toxicity concerns in cancer treatment.

Targeted Drug Delivery: Developing methods to target cancer cells specifically using cadmium oxide nanoparticles can enhance treatment efficacy while reducing side effects. Challenges include ensuring precise targeting and minimizing off-target effects.

Combination Therapy: Investigating the synergistic effects of cadmium oxide nanoparticles with other treatment modalities such as chemotherapy or immunotherapy can lead to more effective cancer treatment regimens. However, finding the optimal combination and understanding their interactions pose challenges.

Safety and Regulatory Hurdles: Addressing safety concerns associated with the use of cadmium-based nanoparticles and navigating regulatory hurdles for clinical translation are essential for advancing research in this area.

Mechanistic Understanding: Further elucidating the mechanisms of action underlying the anticancer properties of cadmium oxide nanoparticles can provide insights for refining treatment strategies. However, deciphering complex cellular interactions and pathways remains a challenge.

Sustainability and Environmental Impact: Exploring green synthesis methods and assessing the environmental impact of large-scale production and usage of cadmium oxide nanoparticles are crucial for sustainable development in this field.

Resistance and Relapse: Investigating mechanisms of resistance to cadmium oxide nanoparticle treatment and developing strategies to overcome it can improve long-term treatment outcomes. However, resistance mechanisms may vary among cancer types and individuals, posing challenges for personalized medicine approaches.

Overall, while the synthesis of cadmium oxide nanoparticles holds promise for advancing cancer treatment, addressing these challenges will be essential for realizing their full potential in clinical practice. Collaboration among multidisciplinary research teams and integration of advanced technologies will be key to overcoming these hurdles and driving progress in this field.

B) Gaps in research:

Some gaps in the methods for synthesizing cadmium oxide nanoparticles and their applications in cancer treatment include:

Standardization of Synthesis Techniques: There is a lack of standardized protocols for synthesizing cadmium oxide nanoparticles, leading to variations in particle size, shape, and surface properties. Standardization efforts are needed to ensure reproducibility and reliability of synthesized nanoparticles for biomedical applications.

Controlled Size and Shape: Achieving precise control over the size and shape of cadmium oxide nanoparticles is essential for optimizing their anti-cancer properties. Current synthesis methods may lack the ability to precisely control these parameters, limiting their effectiveness in targeted cancer therapy.

Surface Modification and Functionalization: Surface modification and functionalization of cadmium oxide nanoparticles can improve their stability, biocompatibility, and targeting specificity. However, there is a need for more research to develop efficient and scalable methods for modifying the surface of nanoparticles with biocompatible coatings or targeting ligands.

Biological Compatibility and Toxicity: Understanding the biological interactions and potential toxicity of cadmium oxide nanoparticles is crucial for their safe use in cancer treatment. More comprehensive studies are needed to evaluate their biocompatibility, biodistribution, and long-term effects in vivo.

Optimization of Drug Delivery Systems: Cadmium oxide nanoparticles can serve as carriers for anti-cancer drugs or therapeutic agents. However, there is a need for optimization of drug loading and release kinetics to enhance their efficacy while minimizing off-target effects and systemic toxicity.

In vivo Efficacy and Clinical Translation: Despite promising results in vitro, the efficacy of cadmium oxide nanoparticles in vivo and their clinical translation for cancer treatment remain relatively unexplored. More preclinical studies and translational research are needed to evaluate their therapeutic potential and safety in animal models and eventually in human clinical trials.

Addressing these gaps will be crucial for advancing the field of cadmium oxide nanoparticle synthesis and their applications in cancer treatment, ultimately leading to the development of more effective and targeted therapies for cancer patients.

V. REFERENCES

[1]. Nadtinan Promphet, Poomrat Rattanarat, Ratthapol Rangkupan,Orawon Chailapakul, Nadnudda Rodthongkum (2015) An electrochemical sensor based on graphene/polyaniline/polystyrene nanoporous fibers modified electrode for simultaneous determination of lead and cadmium. Sensors and Actuators B:Chemical 207: 526-534.

[2]. Gunnar F Nordberg, Koji Nogawa, Monica Nordberg (2015) In Handbook on the Toxicology of Metals. In: Gunnar F Nordberg et al. (Ed.), Chapter 32, (4th edn), Academic Press, San Diego, USA, pp.667-716.

[3]. Mukesh K Sharma, Narayanan J, Sanjay Upadhyay, Ajay K Goel(2015).Electrochemical immunosensor based on bismuth nanocomposite film and cadmium ions functionalized titanium phosphates for the detection of anthrax protective antigen toxin.Biosensors and Bioelectronics 74: 299-304.

[4]. Vinod Gupta K, Deepak Pathania, Mohammad Asif, Gaurav Sharma (2014) Liquid phase synthesis of pectin– cadmium sulfide nanocomposite and its photocatalytic and antibacterial activity.Journal of Molecular Liquids 196: 107-112.

[5]. Wang WS, Zhen L, Shao WZ, Chen ZL (2014) Sodium chloride induced formation of square-shaped cadmium molybdate nanoplates. Materials Letters 131: 292-294.

[6]. Sharma RK, Aditi Puri, Yukti Monga, Alok Adholeya (2014) Newly modified silica-based magnetically driven nanoadsorbent: A sustainable and versatile platform for efficient and selective recovery of cadmium from water and fly-ash ameliorated soil.Separation and Purification Technology 127: 121-130.

[7]. Ayman M Darwish, Wael H Eisa, Ali A Shabaka, Mohamed H Talaat (2016) Investigation of factors affecting the synthesis of nano cadmium sulfide by pulsed laser ablation in liquid environment.Spectrochimica Acta Part A: Molecular and Biomolecular Spectroscopy 153: 315-320.

[8]. Qu R, Wang X, Wang Z, Wei Z, Wang L (2014) Metal accumulation and antioxidant defenses in the freshwater fish Carassius auratus in response to single and combined exposure to cadmium and hydroxylated multi-walled carbon nanotubes. J Hazard Mater 275:89-98.

[9]. Taher AS, Ahmad M Mohammad, Hassan MA, Bahgat E El-Anadouli (2014) Development of nano-hydroxyapatite/chitosan composite for cadmium ions removal in wastewater treatment. Journal of the Taiwan Institute of Chemical Engineers 45(4): 1571-1577.

[10]. Kumari, R.; Kumar, V. Impact of zinc doping on structural, optical, and electrical properties of CdO film prepared by sol–gel screen printing mechanism. Journal of Sol-Gel Science and Technology 2020, 94, 648- 657, https://doi.org/10.1007/s10971-019-05202-0.

[11]. Ye, C.; Xu, F.; Wu, Z.; Gao, Z.F.; Wang, M. Ultra-sensitive photo electrochemical platform with microemulsion-based p-type hollow silver iodide enabled by low solubility product (Ksp) for H2S sensing. Nanotechnology 2021, 32, https://doi.org/10.1088/1361-6528/ac1094.

[12]. Shashanka,R.; Jayaprakash,G.K.; Kumar,M.; Kumara Swamy, B.E. Electro catalytic determination of ascorbic acid using a green synthesised magnetite nano-flake modified carbonpaste electrode by cyclic voltametric method. Materials Research Innovations 2021, 1-11, https://doi.org/10.1080/14328917.2021.1945795..

[13]. Shashanka, R. Investigation of optical and thermal properties of CuO and ZnO nanoparticles prepared by Crocus Sativus (Saffron) flower extract. Journal of the Iranian Chemical Society 2021, 18, 415-427, https://doi.org/10.1007/s13738-020-02037-3.

[14]. Jefferson,P.H.; Hatfield,S.A.; Veal,T.D.; King,P.D.C.; McConville,C.F.; Zúñiga–Pérez,J.; Muñoz–Sanjosé, V. Band gap and effective mass of epitaxial cadmium oxide. Applied Physics Letters 2008, 92, https://doi.org/10.1063/1.2833269

[15]. Rajendrachari, S.; Yilmaz, V.M.; Karaoglanli, A.C.; Uzun, O. Investigation of activation energy and antibacterial activity of CuO nano-rods prepared by Tilia Tomentosa (Ihlamur) leaves. Moroccan Journal of Chemistry 2020, 8, https://doi.org/10.48317/IMIST.PRSM/morjchem-v8i2.17765

[16]. Mthethwa, T.; Pullabhotla, V.R.; Mdluli, P.S.; Wesley-Smith, J.; Revaprasadu, N. Synthesis of hexa decylamine capped CdS nanoparticles using heterocyclic cadmium dithio carbamates as single source precursors. Polyhedron. 2009, 28, 2977-2982, https://doi.org/10.1016/j.poly.2009.07.019 .

[17]. Rajendrachari, S.; Kumara swamy, B.E. Biosynthesis of silver nanoparticles using leaves of Acacia melanoxylon and their application as dopamine and hydrogen peroxide sensors. Physical Chemistry Research 2020, 8, 1-18, https://doi.org/10.22036/pcr.2019.205211.1688.

ICRTMS-2024
International e-Conference on Recent Trends in Material Science
In Association with International Journal of Scientific Research in Science and Technology
Volume 11 | Issue 9 | Print ISSN: 2395-6011 | Online ISSN: 2395-602X (www.ijsrst.com)

Study of Optoelectronic Properties of ZnO Thin Film Grown by Facile Solution Growth Technique

Parag R. Patil[1], Harshal P. Borse[2], Neha P. Chaware[1], Nanasaheb P. Huse[1]*

[1]Advanced Nanomaterials & Interfaces Laboratory, Department of Physics, G. T. Patil Arts, Commerce and Science College, Nandurbar, Maharashtra, India

[2]Department of Physics, C. T. Bora College of Arts, Commerce and Science, Shirur, District - Pune, Maharashtra, India

ABSTRACT

Zinc oxide thin films have been deposited by economic and facile solution growth technique at low temperature and short deposition time with equimolar concentration. Silica glass substrates have been used as a substrate for the deposition with optimized parameters with AR grade reagents zinc sulfate, thiourea, triethanolamine, and ammonia. The as-grown thin films were characterized by X-ray Diffractometer, UV-Visible spectrophotometer and I-V source meter of Keithley interfaced to class AAA solar simulator for structural, optical and electrical properties respectively. From the XRD pattern, formation of Hexagonal Wurtzite crystalline structure of as-grown ZnO thin film has been confirmed when compared with standard JCPDS card (79-0207). The estimated average crystallite size was ~20.6 nm. Along with the characteristics peak of ZnO, a big hump at ~25° has been observed which may be attributed to the silica which is present in the glass substrate. The optical properties revealed higher absorbance in the UV region and a sharp absorption edge at ~400 nm which resulted in a wide band gap of ~3.18 eV. Such a wide band gap shows its promising candidature for the window layer in solar cells and other optoelectronic devices. The electrical properties have been investigated by I-V characteristics in dark and under light illumination which shows linear nature passing through origin confirming the ohmic contact of the film. The sudden increase in current after light illumination reveals the Photosensing nature of the film. The photosensitivity has been calculated at the 2 V bias and was found to be ~66.9 %.

Keywords: ZnO, Thin Film, CBD, Hexagonal Wurtzite, and Photosensitivity.

I. INTRODUCTION

The increasing need for integrated electronic devices and their applications have received the immense interest of researchers in the finding of economic and efficient materials. Recently nanostructured semiconductors received incredible consideration due to their facile synthesis and potential applications in nano-scale functional devices [1, 2]. One such material is zinc oxide (ZnO), which has exceptional optoelectronic properties like large surface to volume ratio and long stability[3]. ZnO is an n-type crystalline compound having hexagonal wurtzite structure which is optically transparent in the visible range and belongs to II-VI group with wide energy band gap of ~3.37 eV at room temperature and high binding energy of ~60 meV[4-6]. However, ZnO nanoparticles have been under the scanner for a couple of decades but still, there is plenty of a

scope to use ZnO in different applications. ZnO thin films are widely used for different applications such as optoelectronic and sensor applications, light emitting diode (LED), laser diodes(LDs), touchscreen, transistors, antireflection coating, optical filter, photo conductor's, solar cells etc.[7-13]. The literature review shows the good electronic stability of ZnO thin films maximizes the quality, stability, and processing time of the devices[6].

The ZnO Thin-films have been synthesized by various methods such as pulsed laser deposition technique[14], RF magnetron sputtering[15], spin coating[16], successive ionic layer adsorption and reaction (SILAR) method[17], laser molecular beam epitaxy[18], electrodeposition[19], chemical vapour deposition (CVD)[20], spray pyrolysis[21] and solution growth technique [22]. In comparison with all other methods, the solution growth method is facile, economic, and effective to deposit the thin film of ZnO. Solution growth method has its own advantage over other methods like large area deposition which is the key aspect for idustrial production [23, 24]. Along with this, its growth can be controlled by various preparative parameters like molecular concentration of the precursor solutions, the temperature of the bath, pH of the final solution and, deposition time[25].

In view of this, in present paper, we report the photosensing properties of ZnO thin-film synthesized by solution growth technique at low temperature and camparatively short deposition time, which reduces the fabrication time of devices. Apart from photosensing properties structural and optical properties of as-grown ZnO thin film have been studied and the results are reported.

II. EXPERIMENTAL

Silica glass substrates have been used to deposit the ZnO thin film which was cleaned by using chromic acid, laboline soluti,on and distilled water. Glass slides were dipped in chromic acid and maintained at ~70°C for 5-6 hours which were then rinsed rigorously with distilled water. These glass slides were then washed with laboline solution followed by distilled water and dried in air atmosphere subsequently. An equimolar precursor solution of zinc and oxygen source has been prepared by using AR grade reagents Zinc Sulphate ($ZnSO_4$) and Thiourea ($CS(NH_2)_2$) respectively in 100 ml deionized water in separate beakers. A few drops of Triethanolamine (TEA) have been added as a complexing agent in a Zinc precursor solution with constant stirring followed by the drop-by-drop addition of ammonia (NH_3) till the solution becomes transparent from milky white. Finally, Thiourea solution was added to a zinc precursor solution with constant stirring, and pre-cleaned glass substrates were immersed vertically in the final solution which was kept at ~50°C for 60 min. The obtained thin films were rinsed with distilled water once and dried subsequently.

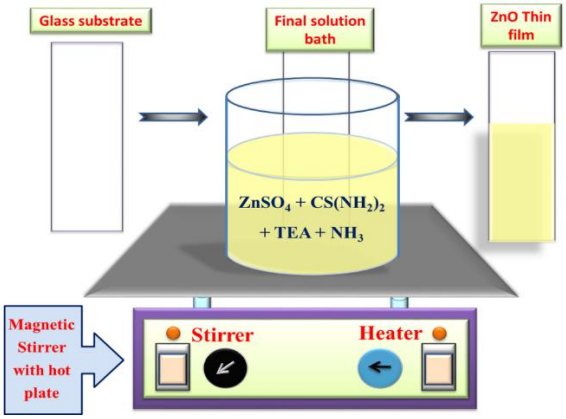

Fig 1. Schematic representation of solution growth technique for synthesis of ZnO thin film

III.CHARACTERIZATION

The structural, optical and electrical properties investigation of as-grown thin films has been performed by various characterization techniques. The structural investigation was performed by X-ray Diffractometer (Bruker, AXS-D8 Advaate) in the scanning angle of 10°-70° with using CuKα_1 radiation with wavelength 1.5406 Å. The optical properties were investigated by UV-Vis spectrophotometer (Perkin-Elmer Lambda-25) with a spectral range extending from wavelength range of 300 to 900 nm. The electrical measurements were performed by the I-V source meter of Keithley model 2400 interfaced to class AAA solar simulator by applying silver contacts over a unit cm^2 area of the thin film in dark and under the illumination of light.

IV.RESULTS AND DISCUSSION

A) Structural Analysis:

The structural analysis was confirmed the rom X-ray diffraction (XRD) pattern obtained from the X-ray Diffractometer shown in Fig. 2. The typical XRD pattern shows the presence of two distinct prominent peaks along with two minor peaks at 2θ values of 14°, 16.28°, 21.53°, 24.56° and 29.25° which all are attributed to the orientation diffracted from (100), (002), (102), (103), (004) planes respectively. Along with these distinct peaks a big hump i.e. a broad peak in xrd pattern is observed which may be attributed to the silica glass substrate used for the deposition of ZnO thin film.

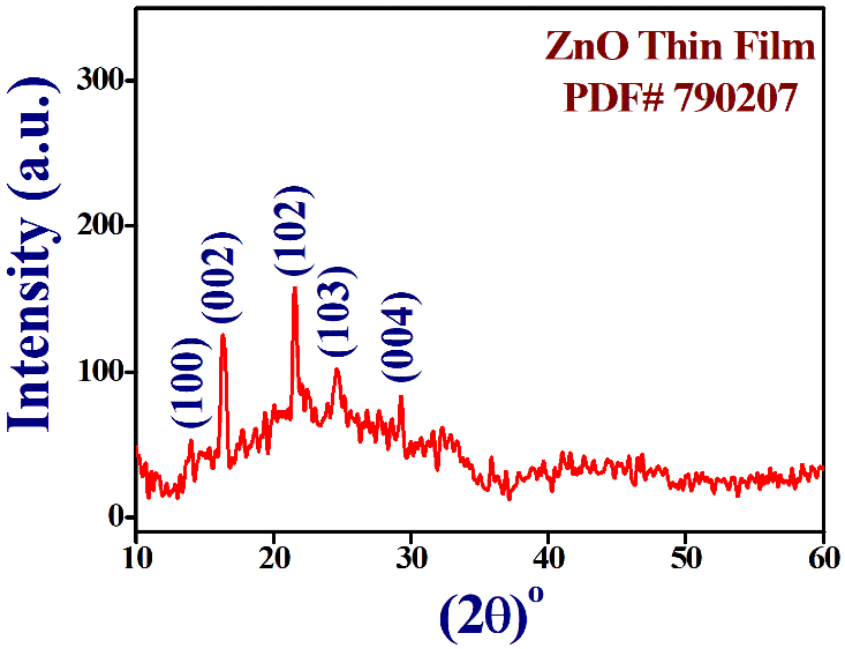

Fig 2. XRD pattern obtained of as-grown ZnO thin film

$$\mathbf{D(hkl)} = \frac{\mathbf{K\lambda}}{\mathbf{\beta cos\theta}} \quad (1)$$

$$\boldsymbol{\delta} = \frac{\mathbf{1}}{\mathbf{D^2}} \quad (2)$$

$$\boldsymbol{\varepsilon} = \frac{\mathbf{\beta cos\theta}}{\mathbf{4}} \quad (3)$$

Where, D is crystallite size, δ is dislocation density, ε is micro-strain, K is shape constant, λ is the wavelength of the x-rays used and β represents full width at half maxima and θ represents angle of diffraction.

The obtained XRD pattern was compared with the standard JCPDS data cards and it shows hexagonal wurtzite crystal structure of as-grown ZnO thin film (PDF #79-0207)[26, 27]. The average crystallite size has been

calculated from the XRD data by using Scherer formula given in Eq. 1 and it was found to be ~20.6 nm[28]. The XRD data was further used to calculate the dislocation density, micro-strain by using Eq. 2 and 3 respectively. From the XRD pattern broadening of the diffraction peaks have been observed which may be attributed to the dislocation density and strain present in the thin film. The calculated structural parameters of the as-grown ZnO thin film is shown in Table 1. The average values were calculated by adding all the values and by dividing the sum with number of values, which represents the overall information of the entire sample studied.

Table 1. The calculated structural parameters of the as-grown ZnO thin Film

(2θ)°	Interplanar spacing (Å)	FWHM β (10^{-3}rad)	Crystallite size D (nm)	Dislocation Density (10^{15}) (lines/m^2)	Strain ε (10^{-3})
14	6.31	11.75	11.88	7.08	2.917
16.28	5.43	8.189	17.10	3.41	2.027
21.53	4.12	5.759	24.50	1.66	1.414
24.56	3.62	10.787	13.15	5.77	2.635
29.25	3.04	3.924	36.51	7.50	0.949
Average values			20.6	3.738	1.988

B) Optical Study:

The optical properties of the as-grown ZnO thin film have been performed by recording the absorption spectra with the help of UV-Vis. spectrophotometer in the wavelength range of 300-800 nm at room temperature shown in Fig. 3. The absorption spectra show minimum absorbance in the visible region with increase in absorbance towards UV region with an absorption edge at ~400 nm. The less absorbance in visible region makes ZnO a good option for window layer in solar cells. The absorbance data were further utilized to estimate the optical band gap by plotting absorption coefficient [$(\alpha h\upsilon)^2$] as a function of photon energy ($h\upsilon$) and Tauc's formula given in Eq. 4. The band gap value was obtained by extrapolating the straight curve to energy axis in Tauc's plot and was found to be ~3.18 eV, which is in good agreement with the earlier reports[2, 29]. Due to such wide band gap, ZnO becomes the potential candidate for window layer in solar cells and for other optoelectronic devices.

$$\boldsymbol{\alpha = \frac{\alpha_0(h\nu - E_g)^n}{h\nu}} \qquad (4)$$

Where, α stands for absorption coefficient which is a function of bandgap and hence varies with the wavelength, h is the Plank constant, ν is the frequency of incident light $h\nu$ is the photon energy and n takes the values of ½ & 2 for an indirect and direct band gap respectively. Since ZnO is direct band gap semiconductor, we have taken value of n=2.

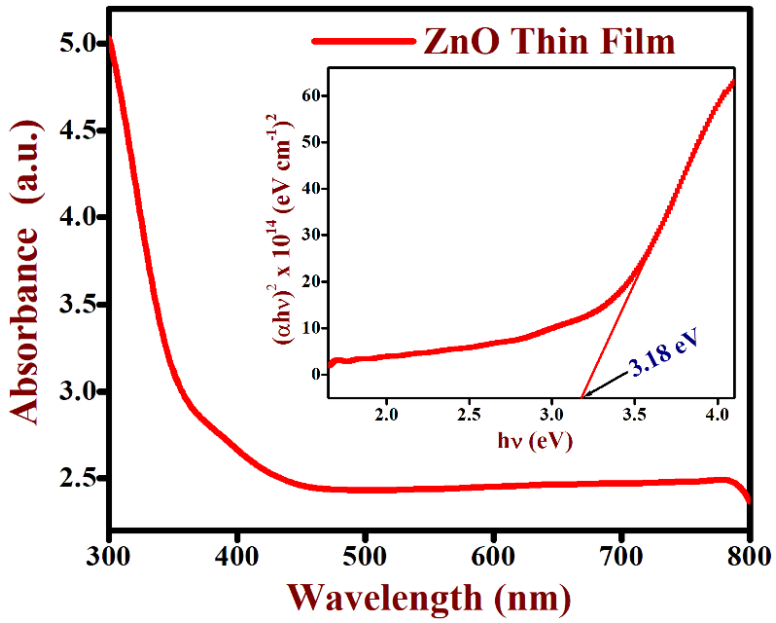

Fig.3: UV-Vis. Absorption spectra whereas inset image show Tauc's plot of ZnO thin film

C) Photosensing study:

The electrical properties have been investigated by I-V characteristics in dark environment and under light illumination (100 Watt) in the applied voltage range of ± 2 V depicted in Fig. 4. The electrical properties shows high current both in dark environment and under light illumination passing through origin exhibits the ohmic metal-semiconductor contact. The dark current is due to the free charge carriers present. The drastic increase in current after light illumination has been the evidence of photosensing nature of the as-grown ZnO thin film. This enhancement in photocurrent after light iis llumination attributed to the free charge carrier generation due to the incident photons which breaks electron-hole pairs and make them free for conduction[30]. The photosensing properties like photosensor efficiency/photocurrent gain (P), photoresponsivity (R) and photosensitivity (S) have been calculated by the Eqs. (5), (6) and (7) and found to be 2.973 %, 0.5 μA/W-cm^2 and 66.4 % respectively [30-38]. The obtained photosensing properties are the evidence of promising candidature of the ZnO thin film for various optoelectronic device applications.

$$\boldsymbol{P} = \frac{\boldsymbol{I_p}}{\boldsymbol{I_d}} \quad (6)$$

$$\boldsymbol{R} = \frac{\boldsymbol{I_p - I_d}}{\boldsymbol{SP_i}} \quad (7)$$

$$\boldsymbol{S}\ (\%) = \frac{\boldsymbol{R_d - R_l}}{\boldsymbol{R_d}} \times \mathbf{100} \quad (8)$$

where, R_d is the resistance in dark, R_l is the resistance in light, I_p stands for photonic current, I_d stands for dark current and P_i the stands for power of the incident light per unit area.

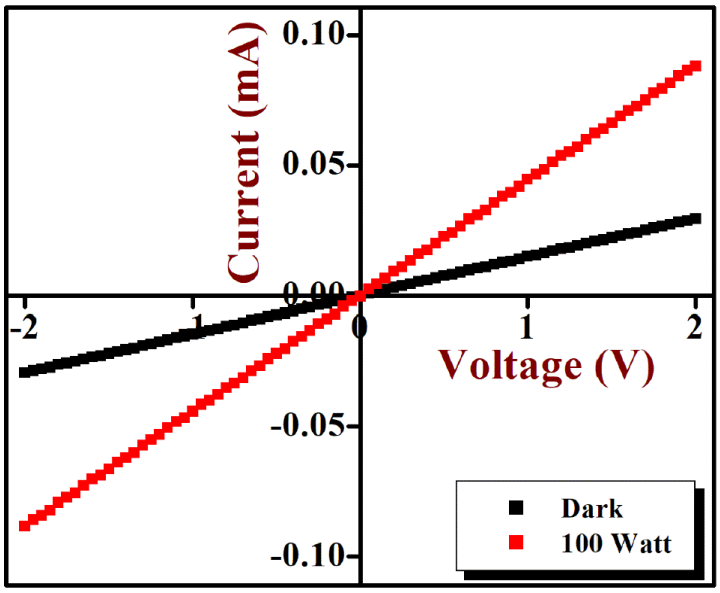

Fig.4: I-V characteristics of as grown ZnO thin film in dark and under light illumination

V. CONCLUSIONS

The ZnO thin films have been successfully synthesized by economic and simple solution growth technique at low temperature. The structural properties of the as-grown ZnO thin film have been confirmed by X-ray diffraction which shows hexagonal wurtzite crystal structure of as-grown ZnO thin film with average crystallite size of ~20.6 nm. The as-grown ZnO thin film were further investigated for optical properties which revealed minimum absorption in visible region with wide band gap of ~3.24 eV. The I-V characteristics revealed drastic enhancement in current after light illumination which is the evidence of photosensing nature of the as-grown ZnO thin film that proves its promising candidature for optoelectronic devices.

VI. ACKNOWLEDGEMENTS

Authors are thankful to the Principal, NTVS's G. T. Patil College, and Nandurbar forthe providing necessary lab facilities to carry out the research work. Wgratefulso thankful to the Head, Department of Physics and Department of Nanotechnology, Dr. Babasaheb Ambedkar Marathwada University, Aurangabad for the support and characterization facilities. We are also thankful to the Director, School of Physical science, K. B. C. North Maharashtra University, Jalgaon for XRD characterization facilities.

VII. REFERENCES

[1]. Djurišić, A.B., et al., ZnO nanostructures: growth, prop,erties and applications. Journal of Materials Chemistry, 2012. 22(14): p. 6526-6535.

[2]. Mahajan, S.V., et al., Enhancement of photo sensor properties of nanocrystalline ZnO thin film by swift heavy ion irradiation. AIP Conference Proceedings, 2015. 1665(1): p. 080063.

[3]. Lu, H., et al., High Surface-to-Volume Ratio ZnO Microberets: Low Temperature Synthesis, Characterization, and Photoluminescence. The journal of physical chemistry. B, 2006. 110: p. 23211-4.

[4]. Kaupužs, J., et al., Origin of n-type conductivity in ZnO crystal and formation of Zn and ZnO nanoparticles by laser radiation. Optics & Laser Technology, 2019. 111: p. 121-128.

[5]. Chen, K.J., et al., Optoelectronic characteristics of UV photodetector based on ZnO nanowire thin films. Journal of Alloys and Compounds, 2009. 479(1): p. 674-677.

[6]. Wang, Z., et al., Light-induced pyroelectric effect as an effective approach for ultrafast ultraviolet nanosensing. Nature Communications, 2015. 6(1): p. 8401.

[7]. Roy, S., et al., Development of an ethanol sensor based on CBD grown ZnO nanorods. Solid-State Electronics, 2013. 87: p. 43-50.

[8]. Singh, O., N. Kohli, and R.C. Singh, Precursor controlled morphology of zinc oxide and its sensing behaviour. Sensors and Actuators B: Chemical, 2013. 178: p. 149-154.

[9]. Chu, J.B., et al., Nanostructured ZnO thin films by chemical bath deposition in basic aqueous ammonia solutions for photovoltaic applications. Applied Physics A, 2009. 95(3): p. 849-855.

[10]. Hara, K., Molecular Design of Sensitizers for Dye-Sensitized Solar Cells, in Molecular Catalysts for Energy Conversion, T. Okada and M. Kaneko, Editors. 2009, Springer Berlin Heidelberg: Berlin, Heidelberg. p. 217-250.

[11]. Service, R.F., Will UV Lasers Beat the Blues? Science, 1997. 276(5314): p. 895-895.

[12]. Hoffman, R.L., B.J. Norris, and J.F. Wager, ZnO-based transparent thin-film transistors. Applied Physics Letters, 2003. 82(5): p. 733-735.

[13]. Huse, N., D. Upadhye, and R. Sharma, An economic approach to fabricate photo sensor based on nanostructured ZnO thin films. AIP Conference Proceedings, 2016. 1728(1): p. 020410.

[14]. Franklin, J.B., et al., Optimised pulsed laser deposition of ZnO thin films on transparent conducting substrates. Journal of Materials Chemistry, 2011. 21(22): p. 8178-8182.

[15]. Alfaro Cruz, M.R., et al., ZnO thin films deposited by RF magnetron sputtering: Effects of the annealing and atmosphere conditions on the photocatalytic hydrogen production. International Journal of Hydrogen Energy, 2018. 43(22): p. 10301-10310.

[16]. Patil, N.B., A.R. Nimbalkar, and M.G. Patil, ZnO thin film prepared by a sol-gel spin coating technique for NO2 detection. Materials Science and Engineering: B, 2018. 227: p. 53-60.

[17]. Santhamoorthy, A., et al., SILAR-deposited nanostructured ZnO thin films: effect of deposition cycles on surface properties. Bulletin of Materials Science, 2021. 44(3): p. 188.

[18]. Opel, M., et al., Laser molecular beam epitaxy of ZnO thin films and heterostructures. Journal of Physics D: Applied Physics, 2013. 47(3): p. 034002.

[19]. George, L., et al., Electrodeposition of ZnO nanostructures on graphene for optoelectronic applications. AIP Conference Proceedings, 2019. 2162(1): p. 020014.

[20]. Müller, R., et al., Chemical Vapor Deposition Growth of Zinc Oxide on Sapphire with Methane: Initial Crystal Formation Process. Crystal Growth & Design, 2019. 19(9): p. 4964-4969.

[21]. Lehraki, N., et al., ZnO thin films deposition by spray pyrolysis: Influence of precursor solution properties. Current Applied Physics, 2012. 12(5): p. 1283-1287.

[22]. Wang, M., et al., Low-Temperature Solution Growth of High-Quality ZnO Thin Films and Solvent-Dependent Film Texture. The Journal of Physical Chemistry C, 2008. 112(6): p. 1920-1924.

[23]. Huse, D.-N., et al., Study of Opto-Electronic Properties of Copper Sulphide Thin Film Grown by Chemical Bath Deposition Technique for Electronic Device Application. Invertis Journal of Renewable Energy, 2016. 6: p. 74.

[24]. Dive, A.S., et al., Single step chemical growth of ZnMgS nanorod thin film and its DFT study. Materials Science and Engineering: B, 2018. 228: p. 91-95.

[25]. Ortega-López, M., et al., Improved efficiency of the chemical bath deposition method during growth of ZnO thin films. Materials Research Bulletin, 2003. 38(7): p. 1241-1248.

[26]. Kim, C.-Y., et al., ZnO nanorod growth by plasma-enhanced vapor phase transport with different growth durations. Journal of Vacuum Science & Technology A, 2014. 32(5): p. 051505.

[27]. Zhao, Z., et al., Pt/Ni0.17Zn0.83O hybrids with enhanced photocatalytic performance: Effect of reduction treatments. Results in Physics, 2019. 14: p. 102434.

[28]. Huse, N.P., et al., Facile, one step synthesis of non-toxic kesterite Cu2ZnSnS4 nanoflakes thin film by chemical bath deposition for solar cell application. Journal of Materials Science: Materials in Electronics, 2018. 29(7): p. 5649-5658.

[29]. Muchuweni, E., T.S. Sathiaraj, and H. Nyakotyo, Synthesis and characterization of zinc oxide thin films for optoelectronic applications. Heliyon, 2017. 3(4).

[30]. Huse, N.P., et al., An experimental and theoretical study on soft chemically grown CuS thin film for photosensor application. Materials Science in Semiconductor Processing, 2017. 67: p. 62-68.

[31]. Dive, A.S., et al., A high visible light ZnMgS nanorod thin film photosensor by solution growth technique. AIP Conference Proceedings, 2017. 1832(1): p. 120007.

[32]. Dive, A.S., et al., Theoretical and experimental investigations of intermediate bands in ZnS–Mg nanocrystalline thin film photosensor. Journal of Materials Science: Materials in Electronics, 2017. 28(20): p. 15161-15167.

[33]. Huse, N.P., et al., Effect of quantum confinement on photosensitivity in ZnS thin film grown by facile chemical bath deposition. Ferroelectrics, 2017. 519(1): p. 170-177.

[34]. Dive, A.S., et al., Soft chemical growth of Zn0.8Mg0.2S one dimensional nanorod thin films for efficient visible light photosensor. Sensors and Actuators A: Physical, 2017. 266: p. 36-45.

[35]. Mohammed, I.M.S., et al., Effect of Cd/S ratio on growth and physical properties of CdS thin films for photosensor application. Journal of Materials Science: Materials in Electronics, 2020. 31(13): p. 9989-9996.

[36]. Gubari, G.M.M., et al., Synthesis and photosensor study of as-grown CuZnO thin film by facile chemical bath deposition. AIP Conference Proceedings, 2018. 1953(1): p. 100072.

[37]. Gubari, G.M.M., et al., Synthesis and characterization of structural, morphological and photosensor properties of Cu0.1Zn0.9S thin film prepared by a facile chemical method. AIP Conference Proceedings, 2018. 1953(1): p. 100014.

[38]. Gubari, G.M.M., et al., An Experimental and Theoretical Study of Cu0.2Zn0.8S Thin Film Grown by Facile Chemical Bath Deposition As an Efficient Photosensor. Journal of Electronic Materials, 2018. 47(10): p. 6128-6135.

ICRTMS-2024
International e-Conference on Recent Trends in Material Science
In Association with International Journal of Scientific Research in Science and Technology
Volume 11 | Issue 9 | Print ISSN: 2395-6011 | Online ISSN: 2395-602X (www.ijsrst.com)

Graphical Study of Chandarapur and Sangali Saline Soil at C-Band Microwave Frequency

Santosh S. Deshpande[1], Ashish B. Ietolikar[2]
[1]Rashtramata Indria Gandhi College, Jalna-431203, Maharashtra, India
[2]Assistant Professor, Physics MIT Alandi Pune, Maharashtra, India

ABSTRACT

The dielectric properties, both ε', (real part) and ε" (imaginary part) of complex dielectric constant are measured for Chandarapur And Sangali in Maharashtra state saline soil at 5 GHz. The study also includes measurement of dielectric properties for various percentages of moisture contents, The Shorted waveguide technique is used for dielectric measurements using automated C-Band microwave bench set up. The least square fitting technique is used to calculate dielectric constant, ε', and dielectric loss, ε", and errors in their measurements. The laboratory data obtained are useful for the interpretation of data in remote sensing applications, particularly in agriculture.
Keywords: Saline soil, Dielectric properties, 5 GHz microwave frequency, Alkalinity; Videography; Remote sensing; Hyper spectral; Microwave; Image classification; Modeling; Monitoring remote sensing, ERDAS, arid region, Landsat satellite.

I. INTRODUCTION

Soil salinity caused by natural or human-induced processes is a major environmental hazard. Nearly about 40% of all irrigated land is salt-affected due to heavy water supply and same crop in same land and this proportion tends to increase in spite of considerable efforts dedicated to land reclamation. This requires careful monitoring of the soil salinity status and variation to curb degradation trends, and secure sustainable land use and management. Multi temporal optical and microwave remote sensing can significantly contribute to detecting temporal changes of salt-related surface features. Airborne geophysics and ground-based electromagnetic induction meters, combined with ground data, have shown potential for mapping depth of salinity occurrence. Constraints on the use of remote sensing data for mapping salt-affected areas. Results of various remote sensing image techniques of (TM) data were used to show the spectral classes and the corresponding areas of the different land uses covering the region, and to delineate and map those areas that are salt-affected, and finally to monitor the temporal changes in salinity in terms of its severity and real extent for the period under investigation. Results of the study have indicated that a serious salinity problem exists and it is getting worse. Moreover, it calls for an urgent salinity management program to control the spread of salinity and to reclaim the damaged areas to be used for economic agriculture in Maharashtra state in India. Agriculture productivity is affected badly due to salinity in soil. The agriculture pattern of cash crops is day-by-day becoming popular for obvious reasons. More and more irrigation facilities are used to increase yield of cash crops. However many

agriculture land, it is found that excessive of water for cash crop like sugarcane, cotton, etc is resulting into production of water logging areas ultimately causing the increase in salinity of soil. Inappropriate cropping systems, reduction in crop diversity, inadequate post-harvest infrastructure are other major areas of concern. Hence, mapping and monitoring of soil are highly important and usually done by microwave Remote Sensing. Remote sensing (Eugene A. Sharkov, 2003; Ulaby et al., 1986) usually refers to the technology of acquiring information about the earth's surface (atmosphere, land, vegetation, forest and ocean) using sensors onboard airborne (aircraft, balloons) or space-borne (satellites, space shuttles) platforms. The electromagnetic radiation is used as an information carrier in Remote Sensing. Remote sensing employs passive and/or active sensors. Passive sensors are those, which sense natural radiations, either reflected or emitted from the earth. On the other hand, the sensors, which produce their own electromagnetic radiation, are called active sensors (e.g. LIDAR, RADAR). In passive microwave, remote sensing the radiometer measures the emissivity of soil, whereas in active remote sensing the radar measures the back-scattering coefficient of the soil, both factors depend on dielectric properties of soil. The complex dielectric constant is a measure of the electric properties of the surface. It consists of two parts: the real part, known as the dielectric constant (ε') and is a measure of the ability of a material to be polarized and store energy. The imaginary part (ε'') is a measure of the ability of the material to dissipate stored energy into heat. The two are related by the expression: $\varepsilon^* = \varepsilon' - j\varepsilon''$ Where ε^* is complex dielectric constant. The measurement of these parameters is significant for remote sensing applications.

II. MATERIAL AND METHOD

The soil samples is collected from location latitude 190 96' 18 '' N longitude,790 29' 63'' E, Chandrapur which is , in this area so soil having water holding capacity due to Coal area soil is become saline the pH of the collected soil sample is 9.7 hence it is saline in nature. another Saline soil Sample collected from Sangali District latitude 160 98' 48 '' N longitude, 740 12'84'' E, in this area farmers are taking cash crop like Sugarcane so due to maximum use of water soil water holding capacity increased and soil become saline, the pH of collected soil sample is 9.8 so it is saline in nature. Both locations are in Maharashtra

The saline soil samples dry and different percentage of moisture contain 5% - 30% are prepared. Dielectric measurements of all these samples are done at 5.2 GHz at room temperature.

Experimental set-up

The C-Band microwave bench setup (Von Hipple A.R., 1954) consisting of a low power microwave source VTO, isolator, coaxial-waveguide adapter, attenuator, SS tuner, slotted section and solid dielectric cell. The Block diagram of the setup is shown in figure 1.

Microwave generated by VTO are propagated through passive components of rectangular wavelength to the dielectric cell with perfect reflector at closed end. The source is tuned to give 5.2 GHz frequency by applying tuning voltage of 7 volts. The attenuator is used to keep the desired power in waveguide assembly of the bench. A slotted section with a tunable probe containing 1N23 detector with the square law characteristics has been used to measure power (current) along the slotted line. The detector is connected to a micro ammeter and to the PC to read and record the measured power. The probe sits on slot line such that the tip of the tunable probe is penetrated and it can be moved forwarded and backward along the slot line section. The depth of the tip is adjusted for its critical position to get a symmetrical standing wave pattern. The empty dielectric cell is connected to the other end of the microwave bench. The bench is tuned for symmetrical standing wave pattern

in the slot line. The dielectric sample under consideration (soil sample) is inserted in the dielectric cell with a constant compaction. The probe is transverse along the slot line at equal intervals and the probe positions are recorded with corresponding power (current). This data is acquired and store in file using microcontroller interface system. This data makes use of α and β as fitting parameters, where α = attenuation factor, β=phase shift constant.

The data is stored for soil samples of different thickness. The dielectric properties of the solid material can be calculated for best fit of parameters. The guided wavelength, λ_g is measured from the minima of the standing wave pattern

$$\beta = \frac{2\pi}{\lambda_g}$$

The free space wavelength in determined using the relation

$$\frac{1}{\lambda_0^2} = \frac{1}{\lambda_g^2} + \frac{1}{\lambda_c^2}$$

Whereλ_c^2=2a=2*4.73 cm=9.46 cm, 'a' being the broader side of the C-band rectangular wave-guide.

The real and imaginary parts of the complex dielectric constant are calculated using the relations

$$\varepsilon' = \lambda_0^2\left(\frac{1}{\lambda_c^2} + \frac{(\alpha^2 - \beta^2)}{4\pi^2}\right)$$

$$\varepsilon'' = \frac{\lambda_0^2 \alpha\beta}{2\pi^2}$$

A source code for computing dielectric constant has been developed. The numbers of data files, for different thickness of samples are combined to get single input data, which can be used, in the source code for calculating dielectric constant and loss. Experimentally calculated dielectric constant ε' and loss ε'' with error in measurement in both Δε', Δε'' are tabulated.

Figure 1 Block diagram of a C-band microwave bench

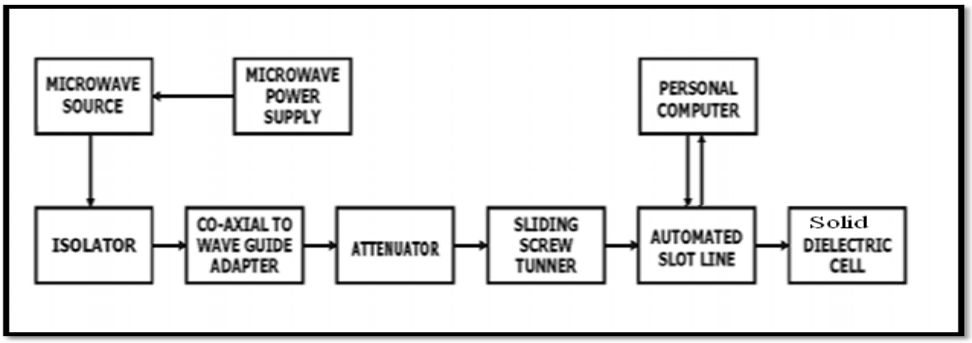

III.RESULT AND CONCULSION

The dielectric properties of dry Chandrapur saline soil and Sangali saline soil are studied at 5.2 GHz at room temperature. Table 1 shows Chandrapur saline soil details of dielectric constant ε' and loss ε'' and error in measurement in both Δε', Δε''.

Table 2 shows Sangali saline soil details of dielectric constant ε' and loss ε'' and error in measurement in both Δε', Δε''.

Dielectric properties of dry Chandrapur and Sangali saline soil are measured as a function of moisture contents shown in table 1 for Chandrapur and table2 for Sangali.

The samples were oven dried and considered at a level of 0% moisture. Then a desired weight of distilled water is added to achieve different moisture content levels. The variations of moisture content up 5% to 30% are studied at 5 GHz.

The response to the dielectric constant ε' is sensitive to moisture for saline soil , as soon as 5% moisture is added significant increase in dielectric constant is found, which remain increasing with addition of more moisture content in figure 2 for Chandrapur and figure 3 for Sangali.

Higher is the magnitude of humidity, the stronger the effect of salinity on the imaginary part. Since ε'' is proportional to the conductivity, increase in soil moisture content increases conductivity.

Thus, behavior of the increase in ε'' with increase in moisture content is seen in table. (Wang. Jet al., 1978, 1980; Y. Lasne et al., 2008).and (Yueru Wu, Weizhen Wang, Shaojie Zhao, and Suhua Liu in IEEE TRANSACTIONS ON GEOSCIENCE AND REMOTE SENSING, VOL. 53, NO. 1)

Table 1 Dielectric constant ε', dielectric loss ε'', error in dielectric constant Δε' and loss Δε'' for Different moisture content Chandrapur saline soil samples at 5.2 GHz.

Sr No.	Moisture Percentage %	Dielectric Constant ε'	Error In Dielectric constant Δε'	Dielectric loss ε''	Error in Dielectric loss Δε''
1	0	7.4132	2.3894 E002	3.9958 E002	6.8096 E002
2	5	10.3782	4.4943 E002	4.2799 E002	2.3585 E002
3	10	14.8628	5.5958 E002	8.8145 E002	5.5232 E002
4	15	20.7164	3.9877 E002	4.6948 E002	1.8746 E002
5	20	24.8701	3.2444 E002	5.7789 E002	2.2871 E002
6	25	29.3318	5.4234 E002	6.2495 E002	5.1574 E002
7	30	33.5640	6.2801 E002	7.2321 E002	6.97 E002

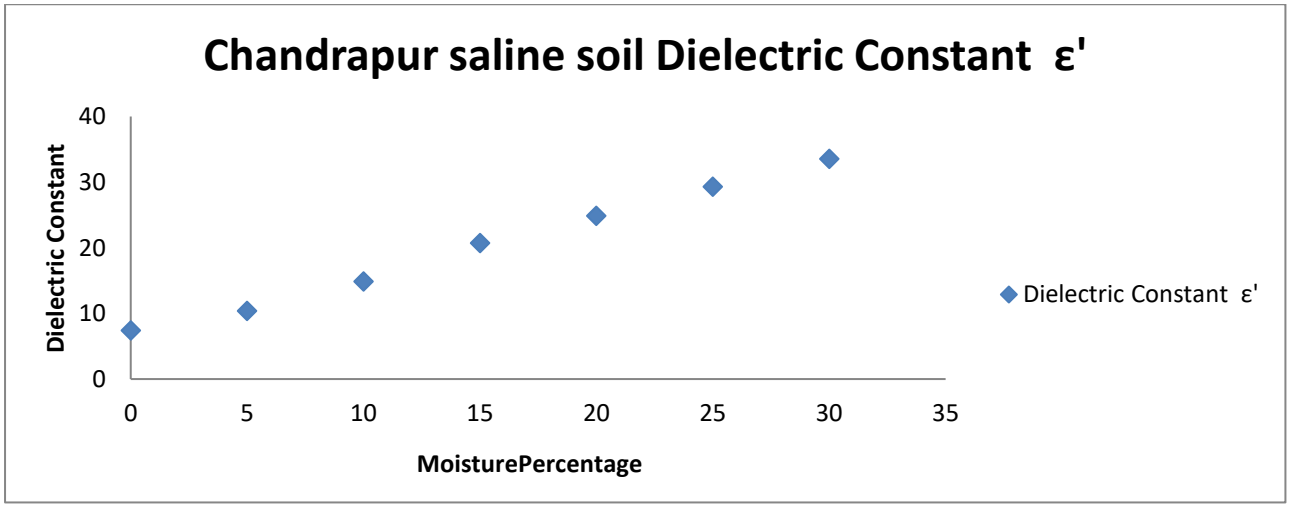

Figure 2 Variations of dielectric constant Versus Moisture% contain of Chandrapur saline soil.

Table 2 Dielectric constant ε', dielectric loss ε'', error in dielectric constant Δε' and loss Δε'' for Different moisture content Sangali saline soil samples at 5.2 GHz.

Sr No.	Moisture Percentage %	Dielectric Constant ε'	Error In Dielectric constant Δε'	Dielectric loss ε''	Error in Dielectric loss Δε''
1	0	8.5132	6.4494 E002	5.7738 E002	9.6123 E002
2	5	13.6682	7.8643 E002	6.9869 E002	4.9585 E002
3	10	16.2828	8.9858 E002	8.5575 E002	7.7832 E002
4	15	21.9064	6.8477 E002	9.9445 E002	6.8846 E002
5	20	23.9901	5.6944 E002	4.6789 E002	8.9871 E002
6	25	29.5918	8.8934 E002	7.6797 E002	9.7874 E002
7	30	34.8940	7.5701 E002	8.3824 E002	8.64 E002

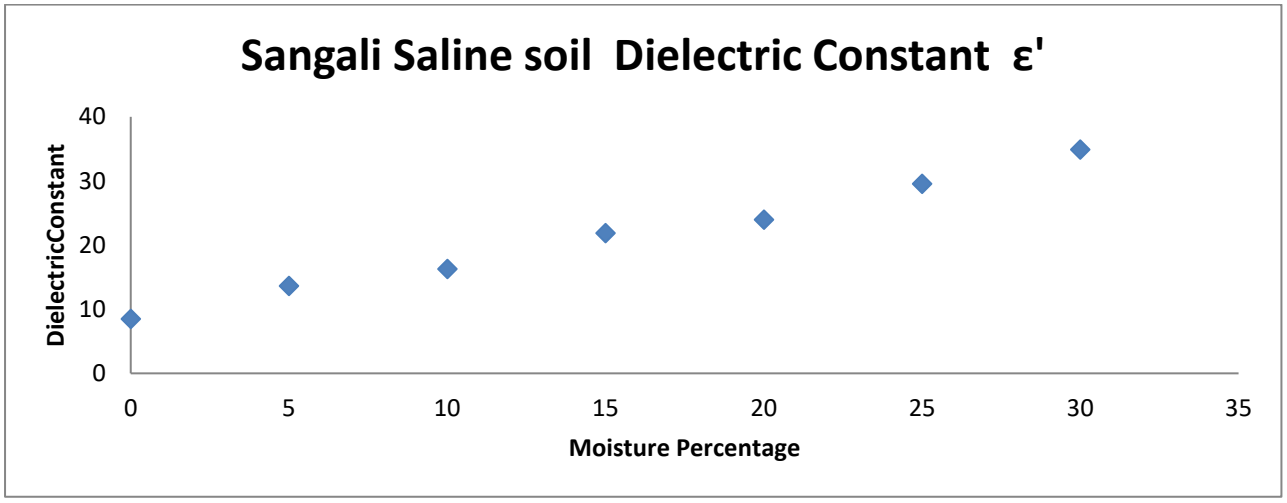

Figure 3 Variations of dielectric constant Versus Moisture% contain of Sangali saline soil.

IV. ACKNOWLEDGEMENTS

I Hearty Thanks my Guide Dr. M.L. Kurtadikar, and Principal and H.O.D.Dept. Of Physics J.E.S. College, Jalna, And specially thanks my teacher who give mi knowledge of physics Principal Shri Shivaji college Parbhani Dr. B.U. Jadhav Sir And Head of Electronics Ravishankar Zingare sir,& KShetty Sir. The Authors are thankful to Indian Space Research Organization (ISRO) for providing the C-Band Microwave Bench facilities under RESPOND..

V. REFERENCES

[1]. Yaduvanshi, N.P.S., P.Dey and Singh, Gurbachan, Analysis of Soil and Water for Salt Affected Areas (Practical Manual). CSSRI, Karnal, India, 2008, pp 10-15.

[2]. Ulaby, F. T., R. K. Moore and A. K. Fung, 1986. Microwave remote sensing: active and passive, Vol. 3, Artech House, Norwood, Mass.

[3]. Von Hipple A.R., (1954) Dielectric Materials and Applications, New York, Wiley.

[4]. Wang. J., Schmugge T. and Williams (1978), Dielectric constants of soils at microwave frequencies-II, NASA Technical paper, 1238.

[5]. Wang J.R., and Schmugge T., (1980), An empirical model for the complex dielectric Permittivity of soils as a function of water content. IEEE Transactions on Geoscience and Remote Sensing, 18, pp. 288-295

[6]. Y. Lasne, Ph. Paillou, G. Ruffié, C. Serradilla, F., A. Freeman, T. Farr, K. McDonald, B. Chapman (2008) Effect of Salinity on The Dielectric Properties of Geological Material: Implication for Soil Moisture Detection by Means of Remote Sensing, Author manuscript, published in "IEEE Transactions on Geoscience and Remote Sensing 46, 6, 1674-1688.

[7]. K. Sreenibvas, L Venkataraknam, and P.V. Narasimha Rao, “Dielectric properties of salt-affected soil,” Int. J Remote Sens., vol. 16,pp. 641-649, 1994

[8]. Agrawal R.S., Kurtadikar M.L. and Murugkar A.G. Dielectric Properties of Soil at 5 GHz, “Microwaves and Optoelectronics”, Anamaya Publishers, New Delhi, 2004, pp. 261-265.

[9]. Kulkarni P.G. “Study of dielectric properties of different soil texture at C. Band microwave frequency,” Ph.D. Thesis Dr. Babasaheb Ambedkar Marathwada University Aurangabad October – 2006Kulkarni P.G. “Study of dielectric properties of different soil texture at C.

[10]. Soil Series of Maharashtra NBSS Publ. 79, Technical Bulletin, Nov. 1999. National Bureau of Soil Survey and Land use Planning, Nagpur – 440010. In Co-operation with Department of Agriculture Govt. of Maharashtra, Pune – 411001.

[11]. The Chemical composition of soils – Philip A Helmke, University of Wisconsin Madison.

ICRTMS-2024
International e-Conference on Recent Trends in Material Science
In Association with International Journal of Scientific Research in Science and Technology
Volume 11 | Issue 9 | Print ISSN: 2395-6011 | Online ISSN: 2395-602X (www.ijsrst.com)

Effect of Al-doping on Structural Properties of CDS Thin Film Prepared Via Chemical Bath Deposition Technique

A.D. Kanwate[1], L.H. Kathwate[2]
[1]Shri Vyankatesh Art's, Commerce and Science College, Deulgaon Raja, Maharashtra, India
[2]Department of Physics, Dayanand Science College, Latur, Maharashtra, India

ABSTRACT

Nano-sized semiconductors have gotten a lot of attention in both basic research and advanced technological uses because of their unique optical and electronic properties that depend on their size. One of these is CdS, which is widely used in many advanced technological fields, including photochemical catalysis, gas sensors and detectors, solar cells, nonlinear optical materials, and different luminescence, and optoelectronic devices. Undoped and Al-doped CdS thin films were prepared using chemical bath deposition method. Effect of Al doping concentration on thickness of the films and structural properties were studied using gravimetric wight by difference method and X-ray diffraction spectrum. X-ray diffraction spectra shows formation undoped and Al-doped CdS thin films with cubic crystal structure.

Keywords: Semiconductor, Al-doped CdS, chemical bath deposition, X-ray diffraction.

I. INTRODUCTION

Cadmium Sulphide (CdS) is an II-VI group semiconductor. It has received considerable attention because of its potential use in the fabrication of solar cells. CdS is a substance that is widely used in many advanced technological areas, including photochemical catalysis, gas sensors and detectors, solar cells, nonlinear optical materials, different luminescence, and optoelectronic devices [1]. Adding foreign elements like copper and aluminium to CdS film changes its optical, structural, and electrical qualities, which makes it work better. Al-doped CdS thin film has become a significant material owing to its practical uses in photovoltaic cells and optoelectronic devices [2]. The effects of heat treatment to photo anode and addition of salts like KCl and NaCl in an electrolyte on the stability of the PEC cells were indicated that though the PEC cells formed with CdS films were stable in NaOH-Na2S-S electrolyte and the stability of PEC cells formed with Al doped CdS films was achieved only after the addition of saturated salts in the electrolyte. Several methods have been used to study the formation of CdS films such as electrochemical deposition, electroplating, cathodic reduction, chemical vapour deposition, and pulsed laser deposition [3-5]. Chemical bath deposition (CBD) is one of the most appealing techniques because it has many benefits over other thin film deposition techniques, including low cost, simple low deposition temperature, low evaporation temperature, and easy coating of big surfaces.

Enriquez et at. [6] reported CdS films of different thicknesses by chemical bath deposition The XRD patterns show that the films were of hexagonal phase with preferred (002) orientation and the grain size were increased

with the thickness of the film. Atay et al. [7] deposited CdS and CdS: Al films onto glass substrates using ultrasonic spray pyrolysis. The study revealed that the electrical, structural, morphological, and elemental properties of CdS films significantly changed with doping, making CdS: Al films more desirable for window layer applications in photovoltaic solar cells than CdS. Bilgin et al. [8] prepared cadmium sulfide (CdS) films using ultrasonic spray pyrolysis (USP) at different temperatures. They found that 573 K substrate temperature is suitable for CdS film production, with good crystallinity and low resistivity, making it feasible for technological purposes, especially solar cell applications. Zouling Fu et al. [9] prepared a series of CdS nanoparticles by precipitating them from a mixture of cadmium salts and sulfur salts without any surface-termination agent. X-ray diffraction studies revealed three phases: cubic, hexagonal, and hybrid.

In this study, we prepared undoped and Al doped CdS thin films by simple and economical chemical bath deposition technique. The structural characteristics can be tailored by changing the amount of Al concentration in CdS films to see if they are practical for a possible technological use.

II. MATERIALS AND METHODOLOGY

2.1. Materials used

For the deposition of undoped and Al doped CdS thin films, cadmium chloride monohydrate ($CdCl_2.H_2O$), thiourea ($CS(NH_2)_2$), aqueous ammonia solution, triethanolamine, and aluminum chloride anhydrous ($AlCl_3$) were used without further purification. All the chemical used in the present study were analytical grade with 99.00% purity and purchased from Merc India. For the preparation of precursor solution double distilled water were used.

2.2. Substrate cleaning

Substrate cleaning plays an important role in the deposition of thin films. The contaminated substrate surface provides nucleation sites facilitating the growth, which results in non-uniform film growth. Therefore, the glass slides of dimensions $26 \times 76 \times 2$ mm^3 were boiled in chromic acid for 2 h and kept in it for 12 h. Then, they were washed with detergent, and again rinsed in acetone before the deposition of the films. The cleaned substrate was kept dipped in de-ionized water before use.

2.3. Deposition of thin films

A deposition bath was prepared by adding 0.1 M $CdCl_2.H_2O$, 4 ml of triethanolamine, and double distilled water to a 100 ml beaker. Al doping was done by adding $AlCl_3$ to the precursor solution. A 0.5 M $CS(NH_2)_2$ solution was prepared separately and added slowly to the deposition bath. The pH was adjusted to 13 by adding ammonia and sodium hydroxide. The total volume of the reaction mixture was then made 100 ml by adding double distilled water. A well-cleaned glass substrate was introduced into the bath vertically. The beaker was kept in an oil bath at 60 °C during the reaction. The deposition was carried out for 1 h, and the samples were removed from the reaction mixture and detached from the substrate holder. The films were cleaned with double distilled water and dried using a micro-oven at 50-80 °C for 30 minutes. The films were uniform and well-adherent to the substrate, resulting in transparent, homogenous yellowish, orange-coloured thin films.

2.3. Characterization Techniques

In the present study weight by difference method was used to measure thickness of the prepared films. The crystal structure of Al doped CdS thin films were determined by powder X-ray diffraction (XRD). XRD patterns are recorded on a Rigaku D/Max ULTIMA III diffractometer using CuKα radiation (λ = 1.5406 Å) at 40kV and 30 mA from $2\theta = 10^0$ to 80^0.

III.RESULT AND DISCUSSION

3.1. Growth mechanism

The film's growth should be heterogeneous to prevent powdery and non-adherence films. Heterogeneous growth can be accomplished by quick reactions by changing low reactant concentrations and high aqueous ammonia concentrations. The reaction mechanism for the formation of CdS films as follow [10]:

$$CdCl_2 + 4NH_3 \rightarrow [Cd(NH_3)_4]^{2+} + 2Cl^-$$

$$[Cd(NH_3)_4]^{2+} \rightarrow Cd^{2+} + 4NH_3 \quad (1)$$

$$CS(NH_2)_2 + OH^- \rightarrow CH_2N_2 + H_2O + HS^-$$

$$HS^-OH^- \rightarrow H_2O + S^{2-} \quad (2)$$

$$Cd^{2+} + S^{2-} \rightarrow CdS\ (Formation) \quad (3)$$

3.2. Thickness measurement

The thickness of the as-prepared CdS films with Al doped were estimated using the weight difference method. The relationship used to calculate thickness (t) was [11]:

$$t = \frac{\Delta m}{A \times \rho} \quad (4)$$

where 'Δm' is weight difference between before and after the deposition of substrate, 'A' area of the deposited substrate and 'ρ' is bulk density CdS = 4.826 g/cm^3 material. Fig. 1 shows variation in thickness with Al concentrations. It is observed that when Al concentration increases from 0 to 1% the films thickness decreased from 2.125 μm to 0.8420 μm. Several factors such as deposition time, the deposition rates, pH, and amount of material used in the process decided the growth of the films. The films thickness increases gradually increases from 1 to 3 % of Al then saturated at higher concentration of Al. The increase in thickness of the Al-doped CdS thin films may be due to the high rate of deposition of films between 1 to 5% [13].

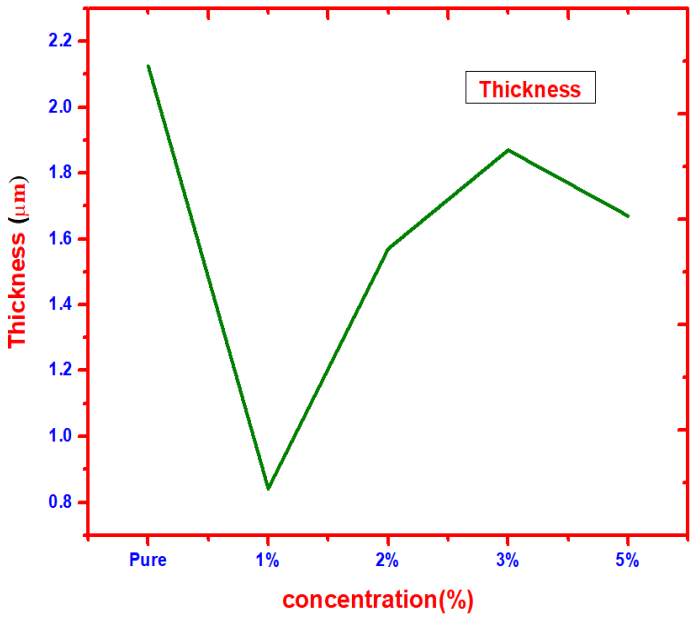

Fig.1: Variation in thickness of CdS thin films as function of Al concentration

3.3. Structural analysis

Fig. 2 (a-d) shows XRD patterns of undoped CdS and Al-doped CdS thin films. As shown in Fig. 2a represented a pure CdS having oriented peaks at (220), (400) & it has good agreement with the standard X-ray diffraction data

which has reported in JCPDS card no. :10-0454. The planes of the Al-doped CdS thin film are (220), (400), (311) for 1% is shown in Fig. 2b, (220), (400), (311) for 3% is shown in Fig. 2c and (111), (220), (400), (311) for 5% is shown in Fig. 2d. The pure and Al doped CdS thin film are crystalline nature with diffraction planes that corresponding to cubic structure JCPDS card no.10-0454. In our study we observed in all the patterns, indicating the successful dissolution of the Al atoms in CdS structure. Also, by increasing the dopant concentration of Al the intensity of the peaks increases. In 5% doping get (111) additional peaks of CdS thin film.

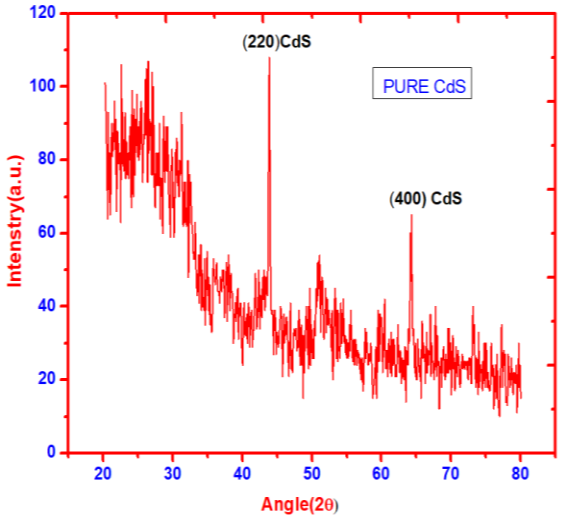

Fig. 2 (a)

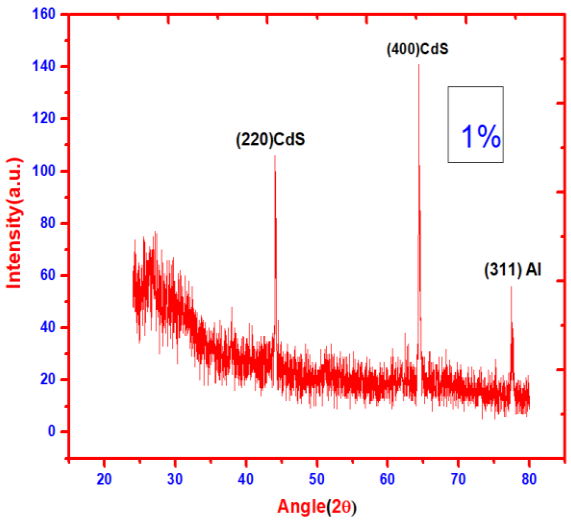

Fig. 2 (b)

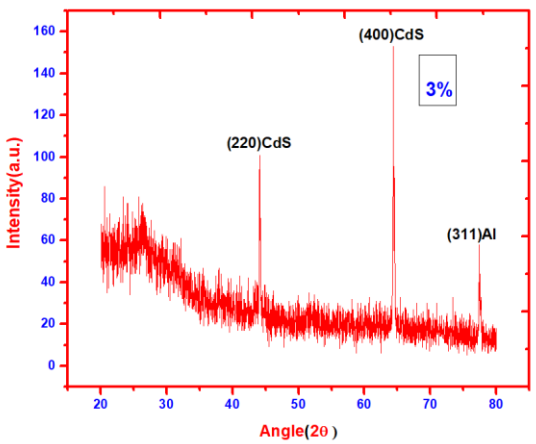

Fig. 2 (c)

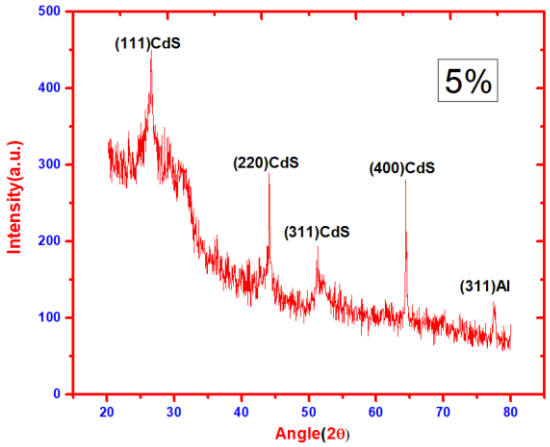

Fig. 2 (d)

Fig. 2: XRD pattern of (a) undoped CdS (b) 1% Al-doped CdS (c) 3% Al-doped CdS (d) 5% Al-doped CdS thin films deposited by CBD technique.

The average crystallite sizes of undoped CdS and Al-doped CdS thin film were measured using Debye-Scherer formula shown in below [14]:

$$D = \frac{K\lambda}{\beta cos\theta} \qquad (5)$$

where, D is average grain size of thin film, λ is the wavelength of radiation (1.5406 Å), β is full width at half of maxima, θ is the Braggs angle. The calculated average grain size was 72.60 nm for undoped and 55.26 nm for 1%, 87.12 nm for 3%, 29.50 nm for 5%. The peaks become sharper by increasing concentration of the Al & which indicates the grain size increases. The X-ray diffraction pattern of Al-doped CdS thin film deposited with different concentration (undoped, 1%, 3%, and 5% Al) in the starting solution are shown in Fig. 2 (a-d). If the intensity increases, grain size is small which is significantly enhanced because of Al-incorporation the spectrum

shows that the very sharp diffraction peaks that indicates high crystallinity [15-16]. The peak (111) intensity increased with concentration of Al is increased. A maximum Intensity of peak observed in 5 % Al doping CdS thin film as shown in Fig.2 (d). The observation Table-1 of planes, 2θ, d and D is given by below:

Table 1: XRD parameters of undoped and Al-doped CdS thin films.

Concentration	Planes	2θ(calculated)	2θ (Standard)	d (A˚)	D (nm)
Undoped	220	43.10	43.99	2.0639	72.60
	400	64.2	64.08	1.4452	
1% Al	220	44.62	43.98	2.0127	55.26
	400	64.28	64.28	1.4452	
	311	77.89	77.86	1.2480	
3% Al	220	43.86	43.98	2.1366	87.12
	400	64.28	64.28	1.4452	
	311	77.89	77.86	1.3068	
5% Al	111	26.47	64.08	3.3314	29.50
	220	43.62	43.98	2.0127	
	311	51.42	52.13	1.8160	
	400	64.28	64.28	1.4452	
	311	77.14	77.86	1.2261	

IV. CONCLUSION

In the present study, undoped and Al-doped CdS thin films have been successfully deposited on a glass substrates using chemical bath deposition method. Thickness of the films initially decreases and the increase at higher Al concentration. Structural parameters of the films studied using X-ray diffractometer. X-ray analysis shows formation of undoped and Al-doped CdS thin films has cubic crystal structure. The average crystal size of the films was found in the range of 87.12 to 29.50 nm.

V. REFERENCES

[1]. X.C. Liu, E.W. Shi, Z.Z. Chen, H.W. Zhang, B. Xiao, L.X. Song, Appl. Phys. Lett. 88, 252503 (2006)
[2]. D. Chakraborti, S. Ramachandran, Trichy G. Narayan and JT. Prater. J. Appl. Phys. 101, 053918 (2007)
[3]. M. Elango, K. Gopalakrishnan, S. Vairam, M. Tamilselvam, J. Alloys Compd. 538, 48 (2012)
[4]. I.O. Oladeji, L. Chow, Thin Solid Films 474, 77 (2005)
[5]. N.V. Hullavarad, S.S. Hullavarad, P.C. Karulkar, J. Nano Sci. Nano Technol. 8, 3272 (2008).
[6]. C. D. Lokhande, S. H. Pawar Solid State Communications, 49 (1984) 765.
[7]. M. N. Mammadov, A. Sh. Aliyev and M. Elrouby, Int. J. Thin Film Sci. Tec. No. 2, 43-53 (2012).
[8]. Joel Pantoja Enriquez, Xavier Mathew, Sol. Energy Mater. & Sol. Cells 76 (2003) 313.
[9]. F. Atay, V. Bilgin, I. Akyuz, S. Kose, Mater. Sci. Semicond. Proce. 6 (2003) 197.
[10]. V. Bilgin, S. Kose, F. Atay, I. Akyuz, Mater. Chem. Phys. 94 (2005) 103.
[11]. Zuoling Fu, Shihong Zhou, Jinsheng Shi, Siyuan Zhang, Mater. Res. Bull. 40 (2005) 1591.
[12]. J. Hiieet, T. Dedova, V. Valdna, K. Muska, Thin Solid Films, 511 (2006) 443.

[13]. E. Çetinörgü, C. Gümüş, R. Esenss, Thin Solid Films 515 (2006)1688.
[14]. Hani Khallaf, Guangyu Chai, Oleg Lupan, Lee Chow, S Park and Alfons Schulte Published 29 Aug 2008.
[15]. A. Fernandez-Perez, Navarrete, H. Fernandez 1Feb 2017, Vol 623:127-134.
[16]. M. Altosaar, K. Ernits, J. KrustokThin Solid Films 480–481 (2005).

ICRTMS-2024
International e-Conference on Recent Trends in Material Science
In Association with International Journal of Scientific Research in Science and Technology
Volume 11 | Issue 9 | Print ISSN: 2395-6011 | Online ISSN: 2395-602X (www.ijsrst.com)

Structural, Magnetic and Electrochemical Properties of $Li_{0.2}Ni_{0.2}Cd_{0.4}Fe_{2.2}O_4$ Ferrites for Energy Storage Devices

Dhanraj Aepurwar*[1], Yogesh Kute[1], D. R. Shengule[2], B. H. Devmunde[2]

[1]Department of Physics, Deogiri College, Chatrapati Sambhajinagar 431005, Maharashtra, Bharat

[2]Department of Physics, Vivekanand Arts, Sardar Dalipsingh Science and Commerce College, Chatrapati Sambhajinagar431005, Maharashtra, Bharat

ABSTRACT

Nano structural Lithium Nickel Ferrite doped with Cadmium nanostructured with formula Li0.4-x/2Ni0.2CdxFe2.4-x/2O4, (x = 0.4) was synthesized by Sol-Gel auto-combustion method. The analysis of X-ray diffraction pattern confirms the formation of cubic spinel structure with phase group Fd-3m phase (227). By using X-ray the lattice parameters were calculated 8.32 Å. The saturation magnetization (Ms), magnetic retentivity (Mr), Coercivity (Hc) of Li0.4-x/2Ni0.2CdxFe2.4-x/2O4, (x = 0.4) is found which shows the material is suitable for fluidic applications. Specific capacitance calculated from cyclic voltammetry which is increase in increasing scan rate.

Keywords: Spinel Ferrite, Structural Properties, Magnetization, Cyclic Voltammetry, Impendance Spectoscopy

I. INTRODUCTION

Lithium ferrite stands out as a distinct category among spinel ferrites, garnering significant attention in technological research for many decades. This interest is primarily due to its magnetic characteristics, notable Curie temperature, and considerable saturation magnetization. In various technological applications, such as microwave technology, lithium ferrites have emerged as preferable alternatives to garnets and other ferrites due to their cost-effectiveness and superior performance[1]. Numerous investigations have explored the incorporation of different metal ions, such as Ni, Mg, and Co, into lithium ferrite structures[2-6].Among these explorations, the lithium-cadmium ferrite system has received considerable focus, owing to its utility in latched microwave components, sensors, switching devices, and similar applications . However, investigations into mixed spinel Li-Ni-Cd ferrites have been notably absent. In this study, we present findings on the structural and magnetic properties of mixed Li-Ni-Cd ferrites.

II. EXPERIMENTAL

Cd^{2+} Substituted Li-Ni ferrite powders were Synthesized by sol-gel auto combustion technique, with two different compositions of $Li_{0.4-x/2}Ni_{0.2}Cd_xFe_{2.4-x/2}O_4$ (where $x = 0.4$). The AR grade nitrates of SD fine chemicals and Merck Company (purity of 99%) are used in proposed research such as Lithium Nitrate ($LiNO_3$), Nickel

Nitrate ($Ni(NO_3).6H_2O$), Cadmium Nitrate ($Cd(NO_3).6H_2O$), Ferric Nitrate ($Fe(NO_3)_3.9H_2O$). These nitrates are in stoichiometric ratio with chelating agent citric acid ($C_6H_8O_{12}$) 1:3 proportion added in distilled water and were stirred on magnetic stirrer until homogeneous solutions formed. To maintain pH up to 7 ammonium hydroxide (NH_4OH) added dropwise to homogeneous solution. Then the solution was stirred and heated at 80°C for about 4-5 hours to obtained gel, after gel formation the gel was heated 200°C until gel goes for ignition after ignition gel converts into puffy ash and ash grounded in mortar pestle to get fine nanoparticles. Finally, the $Li_{0.4-x/2}Ni_{0.2}Cd_xFe_{2.4-x/2}O_4$ (where x=0.4) nanoparticles was sintered at 800°C for 2 hours. Structural and magnetic properties can be studied by X-ray diffraction (XRD). Magnetic properties were studied by using VSM.

III.RESULT AND DISCUSSION

X-ray analysis:

The X-ray diffraction patterns of the $Li_{0.4-x/2}Ni_{0.2}Cd_xFe_{2.4-x/2}O_4$ where (x = 0.4) ferrite after annealing at 800 °C temperatures are shown in Fig. 1.

From X-ray diffraction pattern crystallite size calculated by using Scherer Equation

$$D = \frac{0.9\,\lambda}{\beta Cos\theta} \quad (1)$$

Where, λ is wavelength of X-Ray used in Å, β is the full width half-maximum (FWHM) in radians for 2θ, θ is the Bragg angle, D is the Crystallite size in nm. A sharp, intense peak shows the crystallanity of prepared sample. The data is match with JCPDS card no. 00-039-1277 and Fd3m (227) space group [7]. The crystallite size varies from 40 nm for 311 peaks. The peaks observed from 20 to 70° with some impurities and planes (220), (311), (222), (400), (422), (511), (440) respectively. The lattice constant of prepared sample is found in the range of which is 8.32 **Å** tabulated in table 1. The lattice parameter were calculated from given equation [8].

$$a = d\sqrt{h^2 + k^2 + l^2} \quad (2)$$

Intarplaner spacing (d spacing) calculated from the XRD data by using equation 3 which is tabulated in table 1 [9] .

$$d = \frac{(n*\lambda)}{(2*Sin\theta)} \quad (3)$$

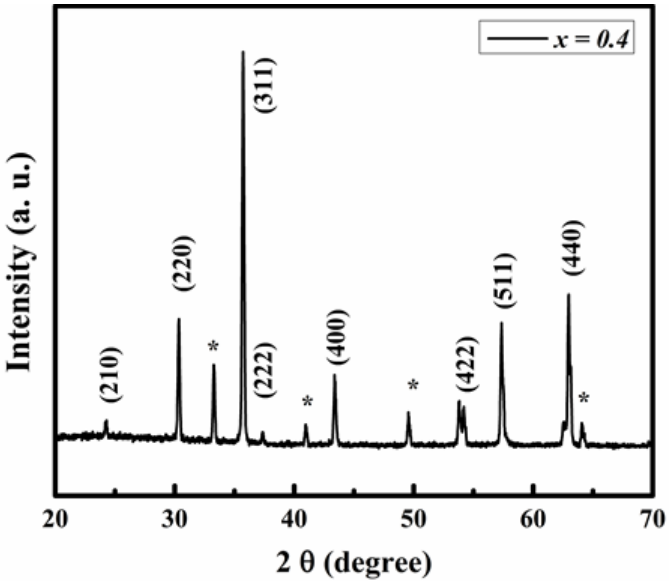

Fig. 1. XRD pattern of $Li_{0.4-x/2}Ni_{0.2}Cd_xFe_{2.4-x/2}O_4$ where x = 0.4

Table 1. shows crystallite size (D), Intarplaner spacing (d), lattice constant (a), Rententivity (Mr), Coercivity (Hc), Saturation magnetization (Ms),

Sample Code	D (nm)	d (interplaner spacing)	a (Å)	Mr	Hc	Ms	K (erg/Oe)	η_B	SQR (Mr/Ms)
x=0.4	40.44	2.51	8.32	9.43	130.15	40.19	5448.67	1.7626	0.2346

Magnetic Analysis

Magnetic hysteresis loops, at room temperature were recorded by VSM Lakeshore (7400) for the annealed sample. The loop were recorded within the applied magnetic field vary from – 15000 to 15000 Oe for prepared sample. The saturation magnetization (Ms), remanent magnetization (Mr) and coercivity (Hc) was calculated 40.19 emu/g, 9.43 emu/g, and 130.15 for $x = 0.4$ sample, which shows typical loops for the prepared sample. The anisotropy constant are calculated using the relation [10].

$$K = \frac{Ms*Hc}{0.96} \qquad (4)$$

Anisotropy constant shows the same behavior as of coercivity (Table 1). The magnetron number or sometimes also known as magnetic moment (η_B) is evaluated using following simple relation given by [11]

$$\eta B = \frac{Molecular\ wt.(Mw)*Saturation\ Magnetisation\ (Ms)}{5585} \qquad (5)$$

The anisotropy value and magnetic moment were observed to increase, indicating a proportional relationship with the saturation magnetization of the nanoparticles. Similar enhancements in saturation magnetization have been documented by other research groups. The squareness ratio (Mr/Ms) was calculated, as detailed in Table 1, indicating values less than 0.5, indicative of a multi-domain structure. This ratio assesses the squareness of the hysteresis loop, which is crucial for various applications. For instance, in memory devices, a larger squareness ratio is desirable, whereas in magnetic fluids, it should be minimized, ideally reaching zero[12]. However, structural formations sometimes prevent magnetization from reducing to zero immediately upon removal of the applied field, necessitating some relaxation time to reach a zero-field value.

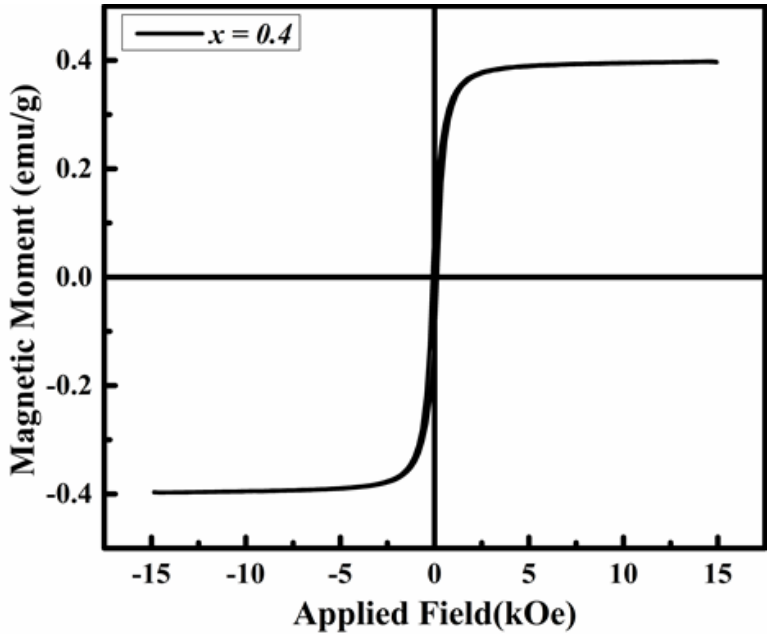

Fig. 2. Hystersis loop of $Li_{0.4-x/2}Ni_{0.2}Cd_xFe_{2.4-x/2}O_4$ where $x = 0.4$

CV Measurements

Figure 3, illustrate that the cyclic voltammetry curves of Li-Ni-Cd ferrite electrode measurements were carried out at different scan rate, as 5mV/s, 10mV/s, 20mV/s, 30mV/s, 50mV/s, 100mV/s between the range of 0.01v to 0.3v potential window in 1 Molar KOH electrolyte for fabricated electrode x=0.4. Further, that higher and lower region and peak to peak separation shows the faradic behavior, which verify electrochemical behavior of synthesized material [13]. Specific capacitance can be measured from CV curves by using following formula [14]. It is observed that with increase of scan rate, the peak current also increased.

$$Cs = -\frac{1}{\Delta V m v}\int idV \qquad (6)$$

Where, Cs is specific capacitance, $\int idV$ is integral area under curve, ΔV is potential window, m is the active mass of material, v is the scan rate in mV/s[15].

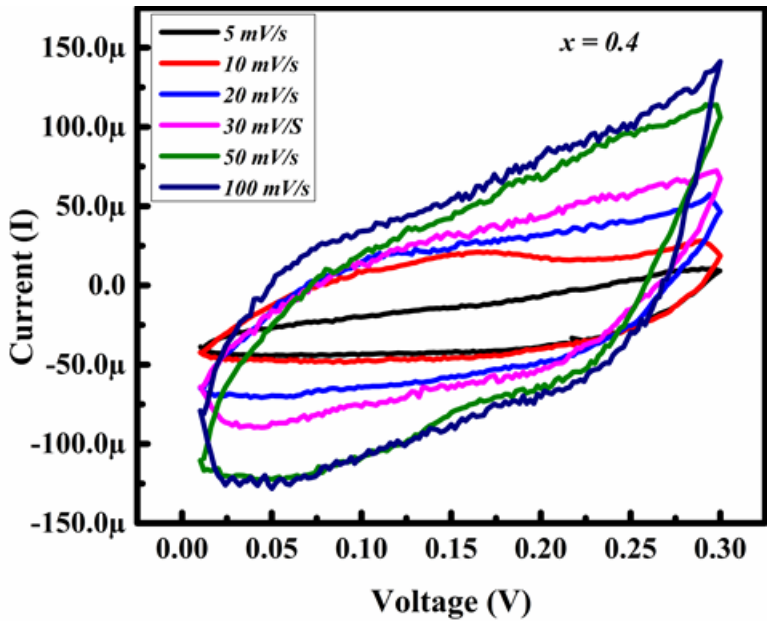

Fig. 3. Cyclic Voltammetry $Li_{0.4-x/2}Ni_{0.2}Cd_xFe_{2.4-x/2}O_4$ where $x = 0.4$

Table 2. Specific capacitance at different scan rate of $x = 0.4$

Scan Rate (mVs)	Area under curve(VA)	Potential Window (Vf -Vi)	Mass (g)	Specific Capacitance (F/g)
5	6.89E-06	0.3	0.056	0.0409
10	1.36E-05	0.3	0.056	0.0806
20	1.86E-05	0.3	0.056	0.1108
30	2.22E-05	0.3	0.056	0.1321
50	3.08E-05	0.3	0.056	0.1836
100	3.63E-05	0.3	0.056	0.2160

Electrochemical Impedance Spectroscopy (EIS)

Electrochemical impedance spectroscopy analysis of the samples was conducted in the frequency range of 0.1 Hz to 1 MHz with 10mV AC perturbation amplitude at open circuit potential. All electrochemical measurements were carried out in 1 M aqueous KOH electrolyte.

The electrochemical impedance spectroscopy (EIS) study was performed to investigate the fundamental characteristics of electrode samples such as ion transfer and electrical conductivity etc. The EIS spectrum

shown in fig. small semicircle is observed in EIS spectra this indicates that charge transfer resistance (Rct) between electrode and electrolyte is good for carbon foil. The straight line characteristics of EIS spectra in the low-frequency range depict a small Warburg impedance, which indicates the diffusion of solution and the adsorption of ions on the surface of the electrode occur very fast.[16]

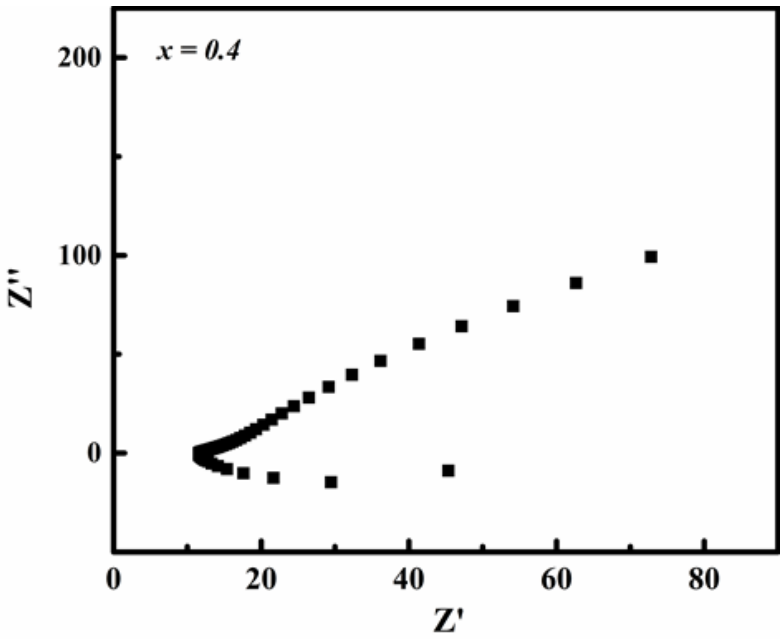

Fig. 3. Nyquiest Plot of $Li_{0.4-x/2}Ni_{0.2}Cd_xFe_{2.4-x/2}O_4$ where $x = 0.4$

IV. CONCLUSION

Cd-substituted lithium nickel ferrites with the chemical formula $Li_{0.4-x/2}Ni_{0.2}Cd_xFe_{2.4-x/2}O_4$, where x = 0.4, were effectively synthesized using the sol-gel auto-combustion method. Analysis of XRD patterns confirmed the crystalline formation of the ferrite, displaying a phase group characteristic of cubic spinel structure. Saturation magnetization (Ms), coercivity (Hc), squareness ratio, and Bohr magneton were determined for x = 0.4, indicating that the material is well-suited for fluidic applications. The cyclic voltammetry and EIS measurements taken in 1 M KOH solution which shows increase in specific capacitance with increase in scan rate, given material can be useful for small scale portable electronic energy storage devices. Nyquiest plot of Impedance spectroscopy shows diffusion of electrolyte.

Credit authorship contribution statement

Dhanraj Aepurwar: Methodology, Investigation, Validation, Writing review & editing, Software, Data curation, **B. H. Devmunde:** Conceptualization, Writing-review & editing, Supervision.

Declaration of competing interest

The authors declare that they have no known competing financial interests or personal relationships that could have appeared to influence the work reported in this paper.

Data availability

Data will be made available on request.

Acknowledgement

This author thanks to Vivekanand Arts, Sardar Dalipsingh Science and commerce college, Chhatrapti Sambhajinagar for providing synthesis facility, INUP Government of India for providing instrumental facilities

and also wants to thank CIF and the Department of Physics, Centre for Nanotechnology, IIT Guwahati, for providing a testing facility.

V. REFERENCES

[1]. Prof. Ahmad, M., et al., Lithium ferrite (Li0.5Fe2.5O4): synthesis, structural, morphological and magnetic evaluation for storage devices. Journal of Materials Research and Technology, 2022. 18: p. 3386-3395.

[2]. Devmunde, B.H., et al., Synthesis, cation distribution, morphology, and physicochemical properties of Ni1-xCdxFe2O4 NPs. Materials Today: Proceedings, 2022. 67: p. 254-258.

[3]. Anagha, A., et al., Structural, optical and magnetic properties of MgFe2O4 and Ni0.5Zn0.5Fe2O4. Materials Chemistry and Physics, 2024. 313: p. 128746.

[4]. Kumar Das, M., et al., Investigation of the structural, magnetic, and dielectric properties of Al-substituted Li-Ni-Mn ferrites. Results in Physics, 2024. 58: p. 107460.

[5]. Saini, S., et al., Enhanced Water Splitting by Strained Lithium-Substituted Nickel Ferrite Hydroelectric Cells. ACS Applied Energy Materials, 2022. 5(7): p. 8178-8188.

[6]. Xi, G., H. Xu, and L. Yao, Study on preparation of NiCo ferrite using spent lithium-ion and nickel–metal hydride batteries. Separation and Purification Technology, 2015. 145: p. 50-55.

[7]. Bellad, S.S., et al., Cadmium substituted high permeability lithium ferrite. Bulletin of Materials Science, 2000. 23(2): p. 83-85.

[8]. Watawe, S.C., et al., Preparation and magnetic properties of cadmium substituted lithium ferrite using microwave-induced combustion. Thin Solid Films, 2006. 505(1): p. 168-172.

[9]. Gupta, M., M. Gupta, and B.S. Randhawa, Influence of Mg concentration on physico-chemical properties of Cd ferrites (CdMg1.5xFe2–xO4) synthesized by sol–gel combustion method. Journal of Alloys and Compounds, 2015. 626: p. 421-427.

[10]. Abu-Elsaad, N.I., S.A. Mazen, and H.M. Salem, The effect of zinc substitution and heat treatment on microstructural and magnetic properties of Li ferrite nanoparticles. Journal of Alloys and Compounds, 2020. 835: p. 155227.

[11]. Namgyal, T., et al., δ-Phase evolution in Cd-doped lithium ferrites: Their thermal, electrical and magnetic properties. Journal of Molecular Structure, 2012. 1019: p. 103-109.

[12]. Ismail, M.M. and N.A. Jaber, Structural Analysis and Magnetic Properties of Lithium-Doped Ni-Zn Ferrite Nanoparticle. Journal of Superconductivity and Novel Magnetism, 2018. 31(6): p. 1917-1923.

[13]. Mordina, B., et al., Binder free high performance hybrid supercapacitor device based on nickel ferrite nanoparticles. Journal of Energy Storage, 2020. 31: p. 101677.

[14]. Lim, C.-S., et al., Electric double layer capacitor based on activated carbon electrode and biodegradable composite polymer electrolyte. Ionics, 2014. 20(2): p. 251-258.

[15]. Prakasha, K.R. and A.S. Prakash, A time and energy conserving solution combustion synthesis of nano Li1.2Ni0.13Mn0.54Co0.13O2 cathode material and its performance in Li-ion batteries. RSC Advances, 2015. 5(114): p. 94411-94417.

[16]. Li, N., D. Shan, and H. Xue, Electrochemical synthesis and characterization of poly(pyrrole-co-tetrahydrofuran) conducting copolymer. European Polymer Journal, 2007. 43(6): p. 2532-2539.

ICRTMS-2024
International e-Conference on Recent Trends in Material Science
In Association with International Journal of Scientific Research in Science and Technology
Volume 11 | Issue 9 | Print ISSN: 2395-6011 | Online ISSN: 2395-602X (www.ijsrst.com)

Physico-Chemical Assessment of Borewell Water across Beed District (MH) India

Jadhav R.L.[1], Dhond G.M.[2]

[1]Department of Chemistry, Swa. Sawrkar Mahavidyalaya, Beed, Dist.: Beed, Maharashtra, India

[2]Department of Zoology, Swa. Sawrkar Mahavidyalaya, Beed, Dist.: Beed, Maharashtra, India

ABSTRACT

In this current study, the work is carried out to assess the physico-chemical characteristics of bore well water near Beed city across (District Beed), Maharashtra, India. The investigation, conducted in January 2024, focuses on analyzing parameters such as pH, dissolved solids, chlorides, O2, and CO2. Our aim is to assess the borewell water quality by comparing these parameters with the standard desirable limits set for drinking water by different regulatory agencies. This study reveals that pH, dissolved solids, chlorides, O2, and CO2 levels exceed permissible limits.

Keywords: physico-chemical, bore well water, pH, dissolved solids, O2, CO2 etc.

I. INTRODUCTION

The word "Marathwada" has been used for a long time, dating back to the Nizam state. It's in the Aurangabad Division of Maharashtra. It borders attached to the state of Karnatka and Telangana and it lies to the south of the Vidarbha and east of Khandesh region of Maharashtra. This region is many time affected by drought condition. This region includes seven districts out of which Beed is one of them, located in the south-central part of Maharashtra. People and animals drink water from borewells in Beed.

Water is the essential requirement of human life, for health, sanitation as well as for manufacturing of essential commodities. It is provided by nature without cost and abundantly present, stands as a fundamental necessity for all forms of life, as aptly articulated by the Greek philosopher Pinder, who believed it “Water is the best of all things”. Human survival hinges greatly on this vital resource, as emphasized by Bhawankar A. S. et al. (2011), reflecting our unparalleled exploitation of water for sustenance. Poor water quality causes a lot of health problems. Every year, about 37.7 million people in India get sick from waterborne diseases spread through dirty water. Just from diarrhea, around 1.5 million kids die. Plus, people miss work a lot - about 73 million days a year - because they're sick from waterborne diseases. All this sickness costs the country about $600 million every year. Chemicals in the water also cause problems. In India, nearly 2 lakh (195,813) places where people live have bad water. Two big worries are fluoride and arsenic. Also, lots of places have too much iron in the water, which is becoming a big problem too.

II. METHODOLOGY

In this study, eight sampling stations were chosen from the nearby Beed city (District Beed). High-quality polythene bottles were employed to collect water samples in January 2024. No preservatives were used during the collection process; only rinsed bottles were used directly to prevent any potential contamination. Groundwater samples were taken from Wasanwadi(S1), Sumatinagar(S2) Ramnagar (S3), Anandwadi (S4), Jirewadi (S5), Sanskar Colony (S6), Sawarkarnagar (S7) and Gurukulnagar(S8). These samples were then analyzed for various physico-chemical parameters using standard methods outlined by APHA (1998), Trivedi and Golel (1981), and IAAB (1998).

Table: Physico-chemical parameters of Bore well waters samples

Samples site	TDS (mg/L.)	E.C. (µS/cm)	CO_2 mg/L	DO mg/L	pH	Chlorides ppm
Wasanwadi(S1)	**1.62**	**46.75**	**10.79**	**3.73**	**7.2**	**103**
Sumatinagar(S2)	**1.75**	**45.79**	**10.88**	**3.78**	**7.1**	**116**
Ramnagar (S3),	**1.74**	**46.67**	**10.87**	**3.81**	**7.0**	**113**
Anandwadi (S4),	**1.88**	**47.71**	**10.91**	**3.86**	**6.99**	**128**
Jirewadi (S5),	**1.95**	**47.75**	**10.21**	**3.79**	**6.96**	**133**
Sanskar Colony (S6),	**2.68**	**52.34**	**11.96**	**4.75**	**6.78**	**165**
Sawarkarnagar (S7)	**2.69**	**53.19**	**11.78**	**4.61**	**6.75**	**168**
Gurukulnagar(S8)	**2.74**	**54.41**	**11.98**	**4.76**	**6.80**	**178**

Figures: Graphical presentation of Physico-chemical parameters of Bore well waters samples

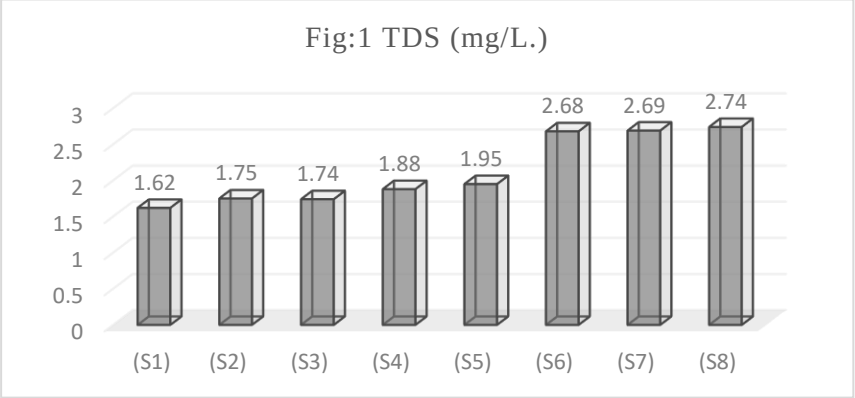

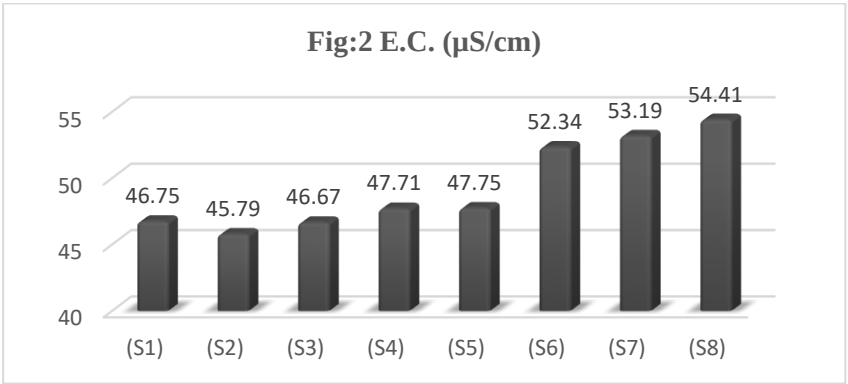

Fig:3 CO2 mg/L

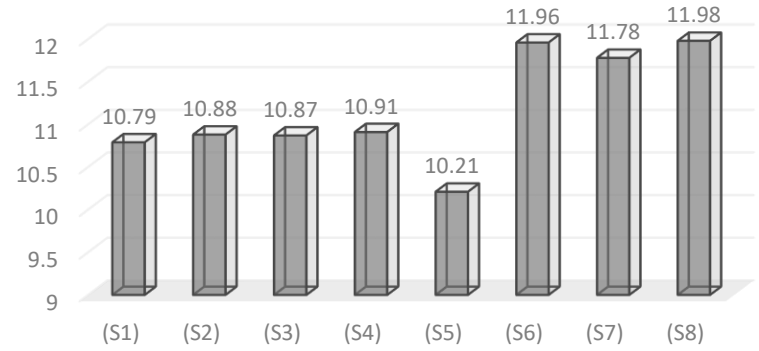

Fig:4 DO mg/L

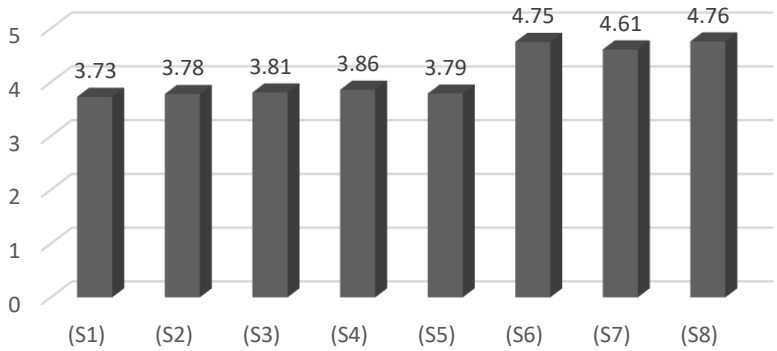

Fig: 5 pH

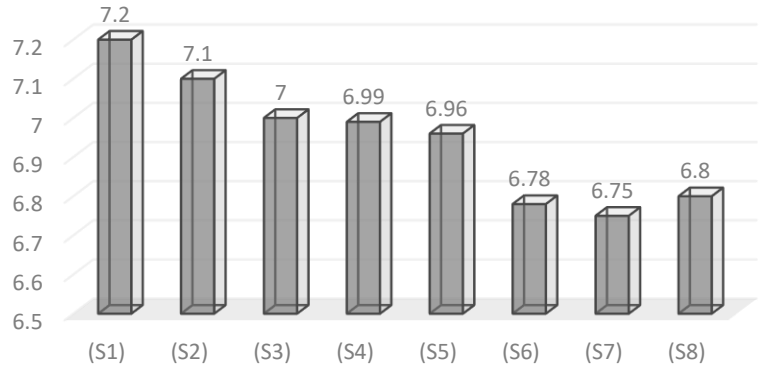

Fig:6 Chlorides ppm

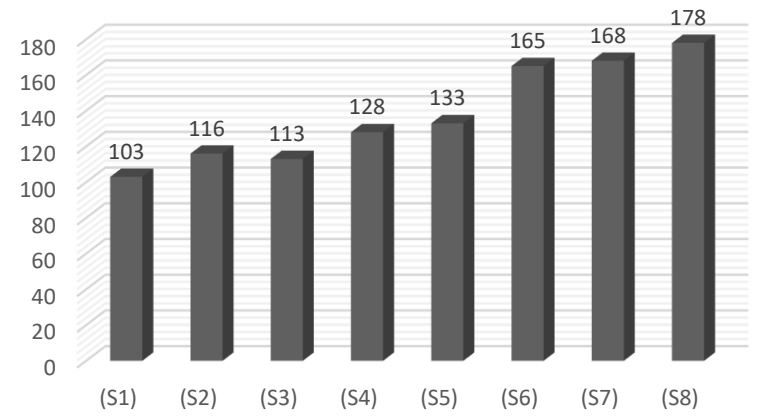

III.RESULT AND DISCUSSION

Total Dissolved Solids (TDS) levels varied across the eight samples, ranging from 1.62 mg to 2.74 gm. The concentrations were notably low in the Sumatinagar (S2) and Wasanwadi (S1) water samples, while they peaked in the Sanskar Colony (S6), Sawarkarnagar (S7), and Gurukulnagar (S8) samples (Delphine Rose et al., 2005).

Electrical conductivity (EC) levels range from 45.79 to 54.41 µS/cm. Among the borewells tested, Sumatinagar (S2) and Ramnagar (S3) exhibit lower electrical conductivity. Moderately lower levels are observed in Wasanwadi (S1), Anandwadi (S4), Jirewadi (S5), while higher levels are recorded in Sanskar Colony (S6), Sawarkarnagar (S7), and Gurukulnagar (S8) water samples (Pondhe, et. al., 2008).

Free CO_2 in water primarily originates from the diffusion of CO_2 from the atmosphere and inflow groundwater. Surface waters typically exhibit dissolved CO_2 levels below 10 ppm (mg/L), whereas deeper groundwater may contain several hundred ppm (mg/L), with certain sources surpassing this concentration. Karadkhele S.V. et al. (2008), In this study shows, that CO_2 concentrations ranged from 10.21 to 11.98. Notably, CO_2 levels significantly influence water pH, with carbon dioxide being a significant contributor to acidity in unpolluted water bodies.

Dissolved oxygen (DO) concentration in a water is important factor, it indicates ability to support to the life of organisms. Low levels of oxygen or no oxygen can happen when too much organic material like algal blooms decompose in water. This happens because microorganisms use up the dissolved oxygen during decomposition. The amount of dissolved oxygen in water is crucial because it shows how well it can support life. In present study, the dissolved oxygen levels ranged from 3.73 mg/L to 4.76 mg/L. Samples 1,2,3,4 and 5 had the lowest levels, while samples 8,6 and 7 had the highest (Madhuri Pejaver and Minakshi Gurav 2003). When DO levels drop too low, , aquatic organisms can't live, and water quality suffers. The primary reasons for low dissolved oxygen are rising temperatures, decaying organic matter from plants and algae, and changes in weather.

The pH level is a crucial ecological factor that offers valuable insights into various geochemical equilibrium and solubility calculations. It indicates the concentration of hydrogen ions in a solution, denoted as pH, and plays a significant role in environmental assessments and scientific analyses. In this investigation, the pH values range from 6.78 to 7.2, with the lowest recorded in sample S7. Samples S1 and S2 exhibited a slightly alkaline trend, while S3 and S4 demonstrated a neutral nature. These pH readings fall within the acceptable range for drinking water quality standards (Ingole et al., 2009).

Chloride concentrations of between 1 and 100 ppm (parts per million) are normal in freshwater. Water tastes salty when chloride levels exceed 250-400 milligrams per liter (mg/L). Detecting high chloride levels is crucial for identifying wastewater contamination. The safe limit for chloride in drinking water is 250 mg/L. Chloride ions dissolve in water found in underground aquifers and geological formations. This Cl- ion is one of the major inorganic anions in water. High chloride levels may indicate dehydration, kidney disease, or metabolic acidosis. Healthy chloride levels in blood serum range from 96 to 106 milliequivalents per liter (mg/L). Levels above 110 mg/L often signal kidney dysfunction. Chloride levels above 750 mg/L, as mentioned, are unusually high for well water. In potable water, the salty taste produced by chloride concentrations is variable and dependent on depending on water chemistry. In this investigation, chloride levels ranged from 103 mg/L to 178 mg/L. Sample S1 had the lowest chloride, while samples S6, S7, and S8 had the highest chloride levels (Jeyaseeli et al., 2007).

IV. CONCLUSION

During the study period of January 2024, the assessment of bore water quality parameters from eight different sites near Beed city (Beed District), Maharashtra, reveals that pH, dissolved solids, chlorides, O_2, and CO_2 levels exceed permissible limits.

V. REFERENCES

[1]. APHA Standared methods for examination of water and waste water 19thEd.APHA, AWWA Washington. (1998)

[2]. Delphine Rose, M.R., A. Jeyaseeli, A. Joice Mary and J. A. Rani, Study on charecteristics of ground water quality of selected areas of Dindugal District, Tamilnadu J. Aqua. Bio. Vol-23(2);40-43. (2005)

[3]. Gonjari G. R. and Hydrobiological studies on TirupatiReservior near Satara, J. Aqua, Bio. Vol-23(2) 73-76

[4]. Goel P.K. Trivedy and S, K. Bhave; Studies on limnology of fresh water in southern Maharashtra, India J. Env. Prot. 5-19-25. (1985)

[5]. Ingole S.B., Pawale R.G. and Wavde P. N.; Studies of water quality on MajalgaonDam,Beed district, Maharashtra. (2009)

[6]. Jadhav V.R., Ghorade I.B. and Patil S.S.; Studies on assessment of ground water quality in and around Nagothane Region Dist.Raigad,(MS),J.Aqua Bio.Vol.-25(2)-91-99. (2010)

[7]. Jaybhaye U.M., M.S.Pentewar and C.J.Hiware; Studies on physic chemical parameter of minor reservoir Swana Hingoli District Maharashtra. (2007)

[8]. karaddkhele S.V.et. al.Studies on physic chemical characteristic of recreational water body in Nana Nani Park, Latur , Maharashtra.

[9]. Kamble S. P. and D. V. Muley; Studies on Physico chemical parameters of Kalbadevi Estuary in Ratnagiri District. MH. J.Aqua. Biol. Vol -23(2):61-66-52. (2008)

[10]. Kamble S.M. Kamble A. H, Narke S. Y., Study of Physico chemical Paramter of Ruti Dam Tq. Ashti Dist. Beed, Maharashtra. (2009)

[11]. Lokhande M.V., Waghmare V. N. and Bais U.E.; Studies on Physical Parameters of Gharni Reservior at Shivpur. Dist. Latur. Aquatic Ecology &Toxicology pp :82-90. (2007)

[12]. Mete Y.T. and Kulkarni D.A.; Studies on Limnology of Babhalgaon Reservoir of Kaij Tahsil, District Beed, Aquatic Ecology & Toxicology pp: 146=150. (2006)

[13]. Manjappa S., Suresh B., Aravinda H. B. Puttaih E. T.Thirumala S.; Studies on Environmental Status of Tungbhadra River Near Harihar. Karnatka J.Aqua.Biol. Vol -19(1):107-110. (2004)

[14]. Nisar Shaikh and Yeargi S. G.; Study on Physicochemical asepects of Tansa River of Thane District. Maharashtra. J.Aqua. Biol. Vol -19(1):99-102. (2001)

[15]. N.Subhashchandra Meitei, P.M. Patil and |Bhosale A.B.; Studied on Physico chemical analysis of Purna River for potability. J.Aqua. Biol. Vol -19(1):103-105. (2001)

[16]. Pranita H. Wath, Smita V. Dhote; Studies on Evaluation of Ground Water quality in & around industrialized are of Nagpur city, Maharashtra J.Aqua.Biol. Vol -25(2):104-110. (2010)

[17]. Pondhe G. M., Hase P.C. Thitame S. N. and PatilS.S;. was studied on Characteristics and quality of ground water in Ghylewadi and maldad villages near sugar factory, Sangamner, District. Ahmednagar, (M.S.). (2008)

[18]. Quadri Naveed N, Seema Hashmi, Asef Iqbal andMohmmed Shaker; Studies on the Physicochemical Characteristics of river Bindusara, Beed, Maharashtra. J.Aqua. Biol. Vol -25(2):100-103. (2010)

[19]. R. S. Lendhe and S. G. Yeragi; Study on Physicochemical parameters of Phirange Kharbav lake Dist. Thane Maharashtra. J.Aqua. Biol. Vol -19(1):49-52. (2004)

[20]. Shashtri, Gaytri Neelam, N. K. Singh and UttaraTewari; Studies on Physico Chemical Analysis of Chingrajpara pond water in Bilaspur, Chattisgarh . J.Aqua. Biol. Vol -23(2):87-90. (2007)

[21]. Jadhav R.L., Dhond G. M.Dr. Ubale S. B.; Research Journey,Int. National Multidisiplinary e- Research Journal ISSN 2348-7143, Physico-Chemical studies of bore well undergroundwater samples in and around beed city district, Beed(MS), India. (2019)

ICRTMS-2024
International e-Conference on Recent Trends in Material Science
In Association with International Journal of Scientific Research in Science and Technology
Volume 11 | Issue 9 | Print ISSN: 2395-6011 | Online ISSN: 2395-602X (www.ijsrst.com)

Synthesis and Characterization of ZnS Nanoparticles by Chemical Co- Precipitation Method

Prashant P. Gedam, Ajit Jat
Shri Radhakisan Laxminarayan Toshniwal College of Science, Akola, Maharashtra, India

ABSTRACT

ZnS nanoparticles are prepared by simple chemical co-precipitation method. The structural and chemical properties of as synthesized nanoparticles are investigated by X-ray Diffraction and, Fourier transform infrared spectroscopy. FTIR confirms the chemical composition of synthesized nanoparticles. The x-ray diffraction pattern exhibits a zinc-blended crystal structure and average particle size is about 22.53 nm by the Debye- Scherrer formula.

Keywords: nanoparticles, Zinc sulfide, coprecipitation

I. INTRODUCTION

Nowadays due to wide variety of potential applications of nanomaterials due their high aspect ratio, lighter weight and higher strength, researchers find out number of new techniques to synthesises of nanomaterials [1]. Zinc sulphide nanoparticle used as optical devices[2-3] and optical sensors [4]. Zinc sulphide nanoparticles are synthesised by mechanochemical route required short reaction time without using diluents[5]. Zinc sulphide nanoparticles are synthesised by solgel method, The factors that influenced this method is reaction time for gel formation, PH conditions and chemical reagents [6]. Zinc Sulphide nanoparticles are synthesized by hydrothermal method, required high reaction time, consume more energy and expensive stainless steel autoclave and Teflon[7]. Pruthvi Raju et al. [8] the growth of nanoparticles by SH synthesis exhibits non-linear behaviour and higher current density than the HT method. Nanoparticles of ZnS can be synthesized by various methods while the chemical method is one of the most important method due to its simplicity. Dasari Ayodhya et al. [9] ZnS nanoparticles are prepared by coprecipitation method using various capping agents like PVP (polyvinylpyrrolidone), PVA (polyvinylalcohol) and PEG-4000 (polyethyleneglycol),UV-Visible absorption spectra are used to find the optical band gap and the values obtained have been found to be in the range of 3.80-4.00eV. Iranmanesh Parvaneh et.al [10] Synthesis ZnS nanoparticles are prepared by homogeneous chemical co-precipitation method using EDTA as a stabilizer and capping agent. The ultraviolet absorption spectrum shows the blue shift in the band gap due to the quantum confinement effect. Due to an ease of synthesis and low cost, comparable to different synthesis method, ZnS nanoparticles are synthesized by Chemical Co-Precipitation method in present work.

II. MATERIALS & METHOD

All the chemicals used in this work are Zinc Sulphate heptahydrate ZnSO4·7H2O and Sodium sulphide (Na2S) . All metal solutions were prepared from deionised water.

Synthesis of ZnS Nanoparticles:-

Preparing a clear stock solution of 0.1 M ZnSO4 and Na2S in different beaker with 100 ml deionised water separately. Take 100 ml DI water add 20 ml ZnSO4 stir continuously for 15 minutes, then add 20 ml of Na2S drop by drop with vigorous stirring for 20 minutes till the milky white precipitate obtained in the beaker. The reaction follows as

$ZnSO4 + Na2S \longrightarrow ZnS + SO4 + 2\,Na$

To remove the impurities of sodium Obtained precipitate were filter and washed several times with deionised water. After washing precipitate were dry at 3000 C in muffle furnace. Dry nanoparticles were milled in the motor paster to achieve fine power for characterization.

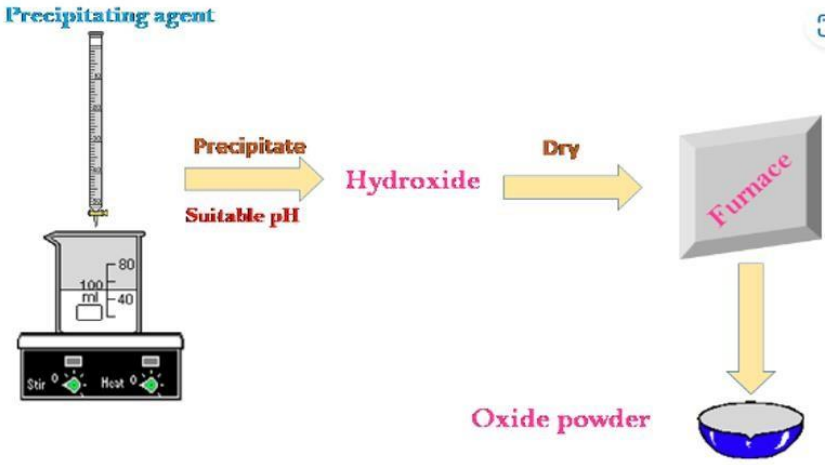

Fig.1: synthesis of ZnS nanoparticles

III.RESULTS & DISCUSSIONS

The X-Ray diffraction pattern of synthesized ZnS sample is show that cubic Zinc blende structure. The typical peak at 28.56, 47.50 and 56.11 in the XRD spectra corresponding to the plane(111) (220) and (311) are in good agreement with the cubic zinc blend structure of ZnS by comparing with JCPDS card (JCPDS-5-560). The broadening of peaks were observed which implies that the size of nano-particles is small. The size of NPs was calculated using Debye- Scherrer formula using peak (111) from XRD pattern. The Debye- Scherrer formula for particle size determination is given by,

$$D = \frac{0.9\,\lambda}{\beta \cos\theta}$$

Where, λ- wavelength of x-ray β- FWHM

θ – Angle of diffraction

D- Particle crystalline size

The calculated size of ZnS NPs was found to be 22.53 nm.

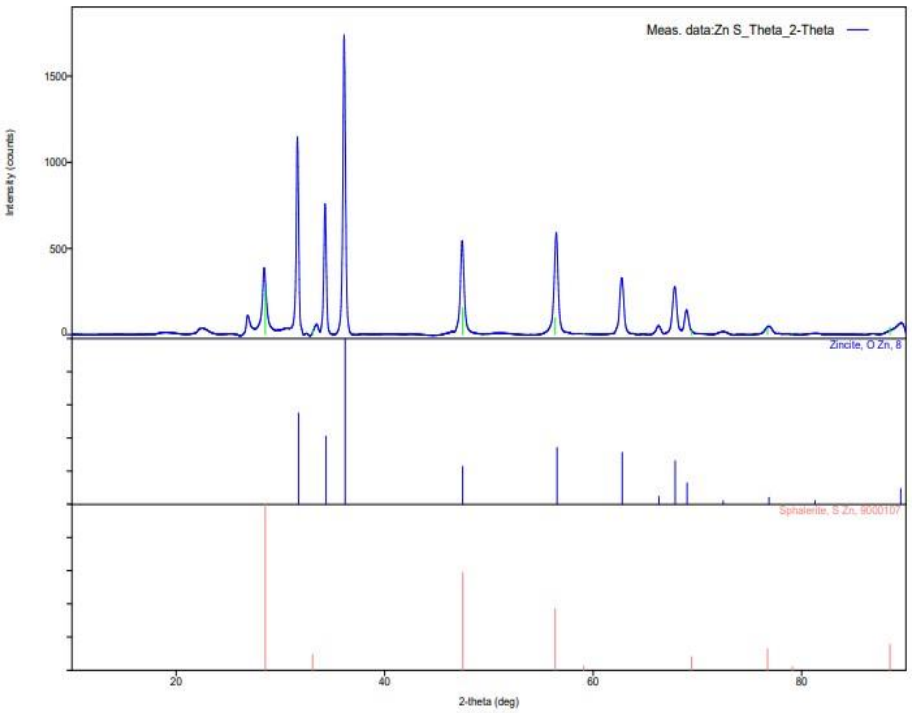

Fig. 2: The x-ray diffraction pattern of ZnS sample

The FTIR Spectrum of ZnS nanoparticles are shown in fig.3 spectrum shows IR absorptions due to various vibration modes. The characteristics major peaks of ZnS were observed at about 1141 cm-1, 983 cm-1 and 625 cm-1 which are in good agreement with the reported result in reference [9]. The observed peaks 1500 cm-1 – 1700 cm-1 are assigned to the C=O stretching modes and broad absorption peaks in the range of 3200 cm-1 – 3600 cm-1 corresponds to the O-H stretching mode shows absorption of water molecules on the surface of nanoparticles.

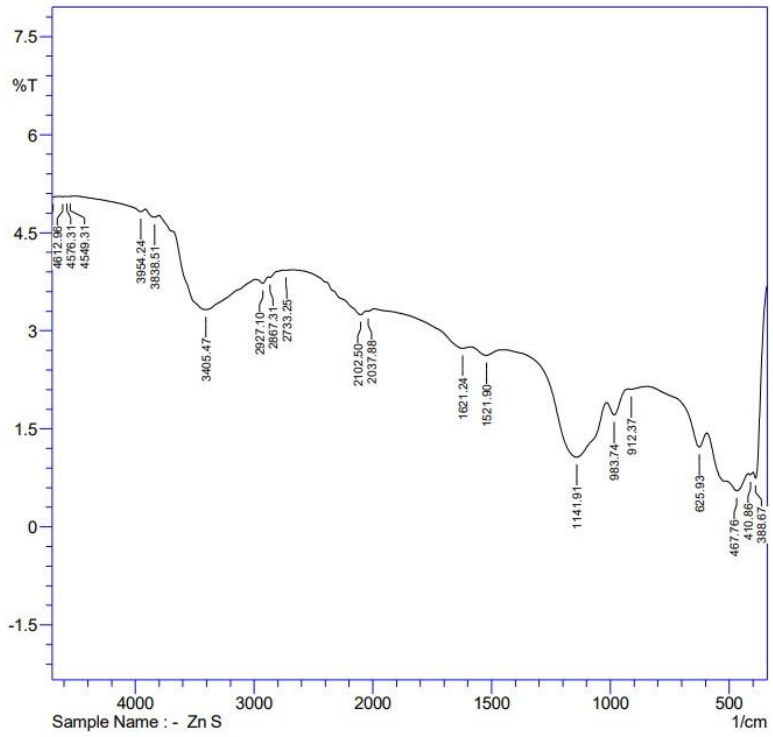

Fig 3: FTIR Spectrum of ZnS nanoparticles.

IV. CONCLUSIONS

ZnS nanoparticles are successfully synthesized by chemical co- precipitation method. The structural properties of samples are characterized by X- ray diffraction to identify crystal structure and chemical properties are characterized by FTIR to identify chemical bonding. The particle size are found to be 22.53 nm by The Debye-Scherrer formula.

V. ACKNOWLEDGEMENT

The Characterization facility of XRD and FTIR are provided by IIC of shri Shivaji Science College Amravati.

VI. REFERENCES

[1]. A. Claudia , C. Enrico (Eds), Inorganic nanoparticles: Synthesis, Applications and Perspectives, CRC Press, Taylor & Francis Group 2010.
[2]. Hong K J, Jeong T S, Yoon C J and Shin Y J 2000 J. Cryst. Growth 218 19
[3]. Yokogawa M and Chen N 2001 J. Crystal Growth 223 369
[4]. Sapsford K E, Pons T, Medntz I L and Mattoussi H 2006 Sensors 6 925
[5]. C. S. Pathak, M, K, Mandal and V. Agarwala "Synthesis and characterization of zinc sulphide nanoparticles prepared by mechanochemical route" Superlattices and Microstructures, volume 58, June 2013, Pages 135-143.
[6]. B. Bhattacharjee, et al., Synthesis and Characterization of Sol-Gel Derived ZnS: Mn2+ Nnocrystallites Embedded in Silica Matrix. Indian Academy of Science, 3: 170-180 (2002)
[7]. Z. H. Ibupoto, K. Khun, X. Liu, and M. Willander, Hydrothermal Synthesis of Nanoclusters of ZnS Comprised on Nanowired. Nanomaterials, 3(3): 564-571 (2013).
[8]. Prudhvi Raju, Saurav Lahir, Devesh Tripathi, Vipin Kumar Materials Science and Engineering: B Volume 286, December 2022, 115983.
[9]. DasariAyodhya, MaragoniVenkatesham, Amrutham Santoshi Kumari, Kotu Girija Mangatayaru, Guttena Veerabhadram IOSR Journal of Applied Chemistry (IOSR-JAC) e-ISSN: 2278-5736.Volume 6, Issue 1 (Nov. – Dec. 2013), PP 01-09
[10]. Iranmanesh Parvaneh, Saeednia Samira and Nourzpoor Mohsen1, Chinese Physics B, 2015, 24(4): 046104.

ICRTMS-2024
International e-Conference on Recent Trends in Material Science
In Association with International Journal of Scientific Research in Science and Technology
Volume 11 | Issue 9 | Print ISSN: 2395-6011 | Online ISSN: 2395-602X (www.ijsrst.com)

The Static Magnetic Field Effect on Crystal growth of Uric Acid

A. C. Bhagat*
*PG Department of Physics, Physics Research Centre, J. E. S. College, Jalna -431203, Maharashtra, India

ABSTRACT

In the present work, Uric Acid crystal one of the crystalline components of urinary stone were grown by single diffusion gel method in the presence of static magnetic field for different strengths such as 0, 0.1, 0.2 Tesla for constant pH, density and concentration of the solution at room temperature. Yields and morphology of grown crystals were studied. These crystals were characterized by using XRD and FTIR method.
Keywords: Uric Acid Crystal, Single Diffusion Gel Method, XRD, FTIR.

I. INTRODUCTION

The systematic study of growth of crystal is very significant to understand the process of stone formation in human body. Uric acid is one of the constituent of renal stone. It has formula ($C_5H_4N_4O_3$) is a heterocyclic compound of carbon, nitrogen, oxygen, and hydrogen. It has molecular mass 168.11gm. It appears white solid. It has melting point 300 °C (572 °F; 573 K). Uric Acid is one of the crystalline components of urinary stone which occurs in human. It is insoluble 0.0006g/100 mL (at 20 °C) in Water but easily soluble in HCl. The renal calculi; which are major health problem found in all habitats around the globe. Hence various crystals were grown by researchers using gel media [1]. Exposure of growth [2, 3]. The Struvite and Whewellite crystallization in gel media studied [4,5]. In in-vitro gel; the environment is similar to physiological environment of living human and animal body so in this present research paper In-Vitro gel method used. The origin of this research work is to explore findings on crystallization of Uric Acid by studying effects of time varying electro-magnetic field as promotes or inhibits; Also crystal size, morphology and yields with and without microwave exposure are studied. After that grown Uric Acid crystals were characterized by using XRD and FTIR method.

II. METHODS AND MATERIAL

AR grade chemicals used for study of Uric Acid crystal growth, Sodium Meta Silicate (SMS), Acetic Acid (glacial), Dilute Hydrochloric Acid, Na OH, Distilled water. Borosilicate Glass Test tubes of diameter (25x15) cm with stand, pH meter, Dropper, filter papers, graph papers, Mask, Hand Gloves.

Gel Setting for Uric Acid crystal

The Uric Acid crystals were grown in silica gel media using chemical reaction in gel method by two ways 1. Without Static Magnetic Field setup and 2. With Static Magnetic Field set up. Crystal growth parameters are shown in Table 1 and the steps 1 to 7 are same and step 9 used for step II.

Table 1. Uric Acid Crystal Growth Parameters.

Sr. No.	Uric Acid Crystal Growth	Parameters
1	Specific Gravity of stock solution	1.045 g/cc
2	Acid used for pH setting	Acetic acid
3	Stock solution at pH	6.5 Temp.
4	Concentration of Reactant I	Dilute Hydrochloric Acid
5	Concentration of Reactant II	1.0M
6	Uric Acid in Na OH	2.5M
7	Gel Aging	48hrs
8	Time variation of Static Magnetic Field	30-120mins.
9	Duration Growth Period 120hours	

Step I: The gel was prepared by dissolving Sodium Meta Silicate powder in double distilled water and shaking this solution well. This solution is filtered and kept in clean flask. This solution was mixed with glacial acetic acid at pH 6.5 and with specific gravity1.04 g/cc. This solution were mixed in 1M concentration of Dilute Hydrochloric Acid solution in the ratio 1:1 and allowed to set for 48 hours at room temperature. After setting the gel, concentrations 2.5M of Uric Acid in Na OH solution is poured slowly and gently around edges of test tubes over set gel. The test tubes were tighten using cork and kept in a quiet and vibration free condition. The following reaction takes place **$(C_5H_4N_4O_3+NaOH)+H\ Cl= C_5H_4N_4O_3+NaCl+H_2O$.** After 120 hours; Fine Uric Acid crystals were observed in test tube at the centre of gel region and some at surface of test tube. Then crystals were collected from test tubes on filter paper for weighing.

Study of Effect of Exposure of Static Magnetic Field on Uric Acid Crystal Growth:

An Electromagnets (EMU-50) of 7.5 kg placed at 10mm air gap with flat pole pieces (50 mm diameter) is used to apply magnetic field strength as shown in figure 1.The magnetic field strengths were varied by using appropriate current to the coils and it is measured by Gauss meter. The study of effect of static magnetic field on crystal growth of uric acid is carried out by applying static magnetic field at nucleation state in Silica Gel media. The experimental setup and various components and their arrangements are as in figure 1and 2.

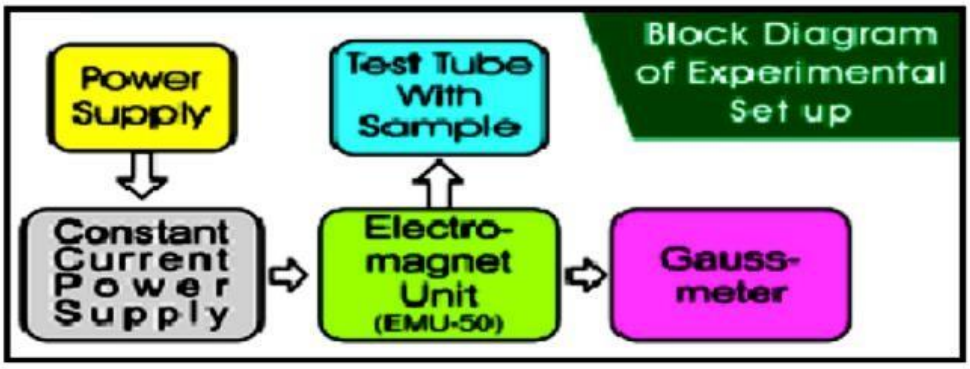

Figure1 Block diagram of Static Magnetic Field Experimental Set up.

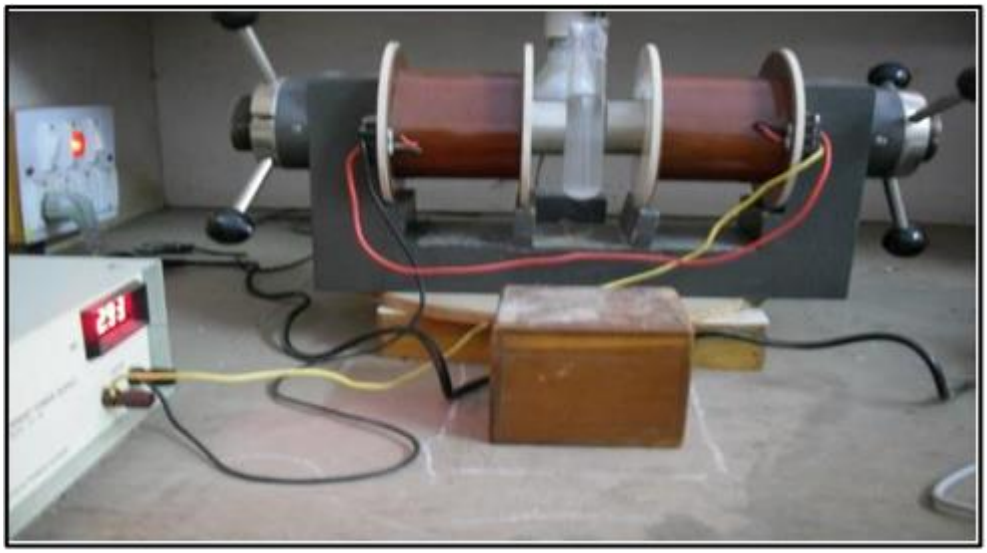

Figure.2. Experimental Set up for Uric Acid Crystal growth at 0.1 and 0.2 Tesla magnetic field strengths.

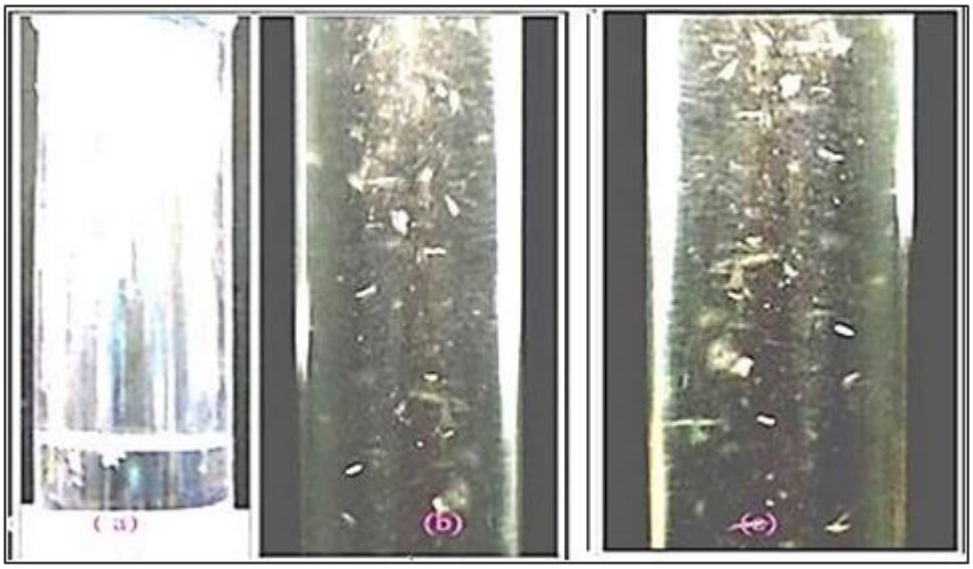

Figure.3. Crystallization of Uric acid (a) At Nucleation State (b) & (c) After 120 Hours for Static Magnetic fields 0,0.1 Tesla & 0.2 Tesla

The study of crystal growth of Uric Acid is carried out[6] by applying the growth process at nucleation state with static magnetic field strengths 0.1 T and 0.2 T for the periods of 30min., 60min., 90min. and 120min.as given in figure1.The crystal growth parameters used for Uric Acid are as in table 1. Using the procedure discussed in above; the gel for crystal growth is prepared in a set of eight test tubes using 2M concentration of reactant one. Then gently add the second reactant of 2.5 M concentration in the first test tube. Now the nucleation of crystals will start this state is called the nucleation state of crystal growth. At this state of nucleation the test tube is kept in between the poles of electromagnet for exposure of static magnetic field strength 0.1 Tesla (Core coil current 1.46 Ampere) for the period of 30 min. After addition of reactant two of 2 M concentration the second test tube is kept at the nucleation state for exposure of same magnetic field strength for the period of one hour (60 min.). Similarly the third and fourth test tubes after addition of second reactant of 2.5 M concentration are exposed for same magnetic field strength for the period of 90 min. and 120 min. respectively. And then allow to grow for the defined period (total 120 hours from the nucleation state) in vibration free steady environment.

Similar procedure is followed for exposing the test tube for magnetic field strength 0.2 Tesla for the period of 30 min, 60 min, 90 min and 120 min. at nucleation state. Then the exposed test tubes are kept in vibration free steady environment for the defined period of 120 hours from the nucleation state.

Crystal Yield Analysis:

Yield of Uric Acid crystals grown are given in table no.1 plotted in figure 3.

Table.2. Yields of Uric Acid Crystal after 120 hours in gm. at pH 6.5

Magnetic field in Tesla	Time in Minutes	Yield of Uric Acid Crystal
0	0	1.4
0.1	30	0.8
0.1	60	1.1
0.1	90	1.18
0.1	120	1.25
0.2	30	0.9
0.2	60	1.05
0.2	90	1.18
0.2	120	1.32

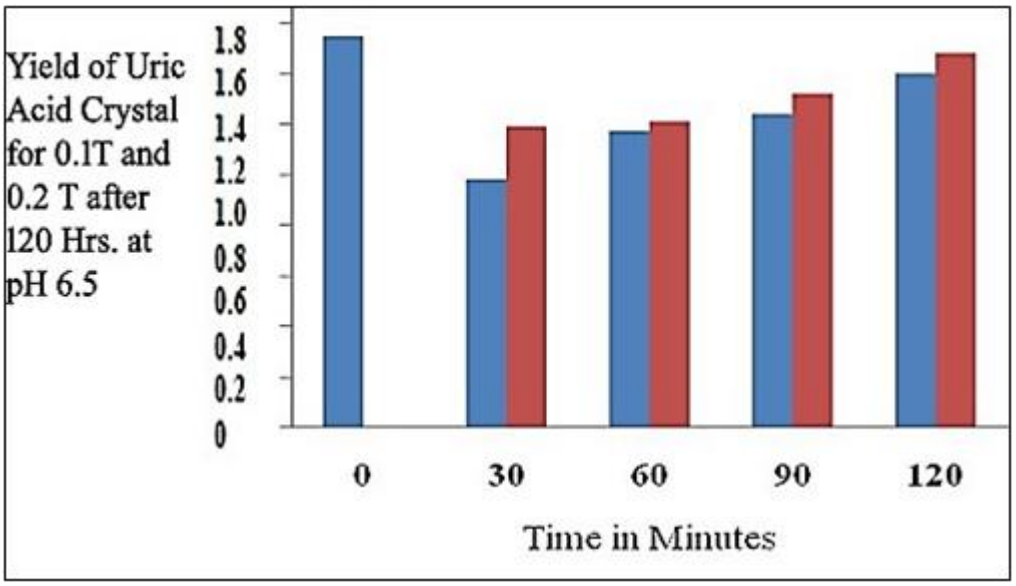

Figure.4. Plot of Yields of Uric Acid Crystals

Crystal Characterization Analysis:

XRD and FTIR Studies were conducted to characterize the crystals grown in silica gel media.

Powder X Ray Diffraction Analysis:

A Philips X-ray Diffract meter model PW/1840 with Ni filter, Cu-Kα radiation from Department of Physics, Savitribai Phule University Pune is used to identify the crystal structure of Uric Acid crystal as given in figure5.It is found that Uric Acid crystallized in the monoclinic with unit cell parameters [7,8] as P21/a space group with unit cell parameters as;

a =14.465Å, b =7.403Å, c=6.208Å and

β =65.20 Z =4, V= 602.9A03

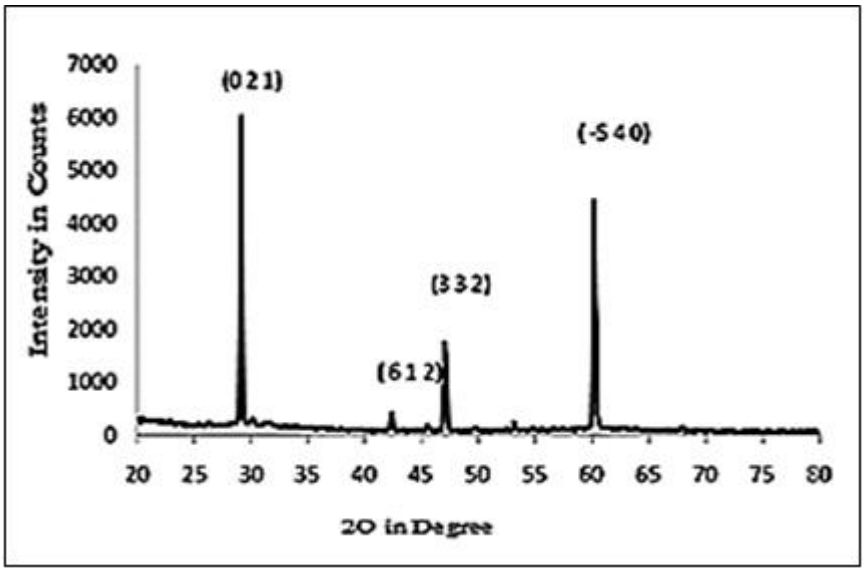

Figure.5.Powder XRD pattern of Uric Acid crystal

FTIR Analysis:

The FTIR spectrum of Uric acid Crystal is recorded using FTIR-BUSY-6100A JASCO spectrometer in a scan range (4000-400cm-1) from Department of Physics Savitribai Phule University of Pune. It is found that FTIR spectra revealed functional group for Uric acid crystal.

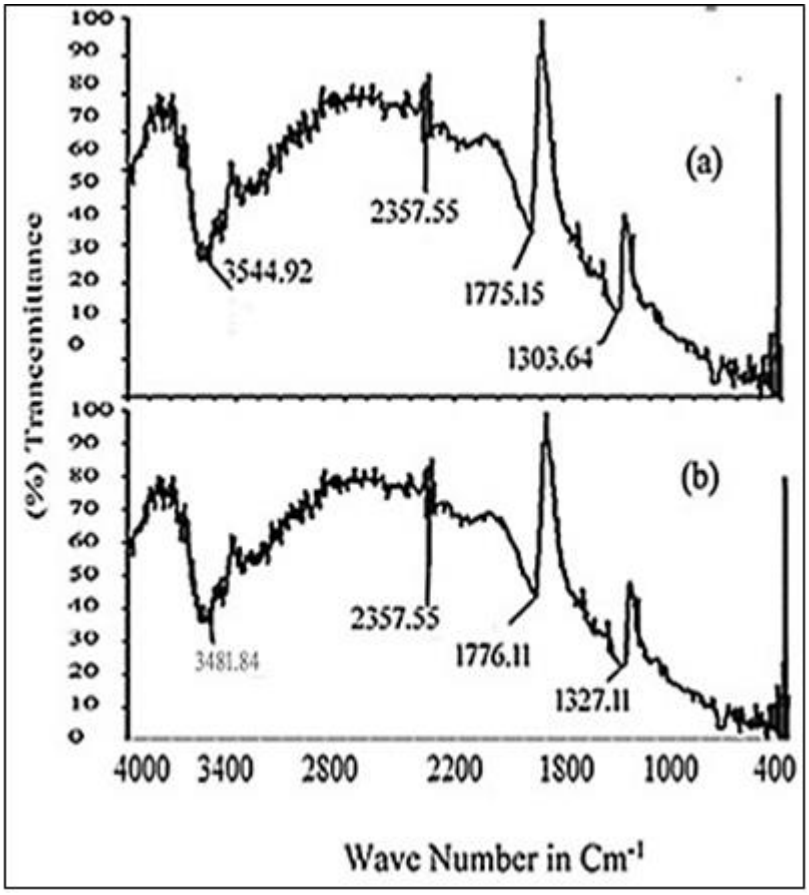

Figure.6. (A) FTIR of UN Exposed Uric Acid crystal (B) FTIR of Static Magnetic field Exposed Uric Acid crystal.

The compared FTIR spectra of Uric acid with and without exposure reveals the presence of water and O- H stretching absorbed at 3481.84 cm-1. C-C, C-O and C- N stretching absorbed at 2357.55cm-1. The C=O

stretching absorbed at 1776.11cm-1. O-H deformation absorbed at 1327.11cm-1. which varies and indicates as presence of water and O-H stretching absorbed at 3544.92 cm-1. C-C, C-O and C-N stretching absorbed at 2357.55cm-1. The C=O stretching absorbed at 1775.15cm-1. O-H deformation absorbed at 1306cm-1.

III.RESULTS AND DISCUSSION

The photographs of Uric Acid crystals grown are shown in figure3. The morphology of Uric Acid crystals observed as elongated rod like morphology and is in good agreement with result published. The powder XRD pattern shown in figure no. 4 of Uric Acid crystal confirmed and results are in good agreement with results reported in literatures.

Also FTIR analysis pattern shown in figure no.5 (A,B) of Uric Acid crystal confirmed and results are in good agreement with results reported in literatures.

FTIR pattern obtained for crystal for crystal grown under exposure of magnetic field at the nucleation time exhibits more % transmittance for magnetic field strength 0.1 T than 0.2 T. The difference of % transmittance found decreased and depth of %transmittance dip at frequency is found increased as exposure time is increased.

Rate of nucleation observed reduced and size of crystals decreased with increasing strength of magnetic field but number of crystals found increased.

Yields of Uric Acid crystals grown are given in table no.1 and plotted in figure 3 is found slightly increased as influence of increasing magnetic field. Overall yield found less as compared to without exposure of magnetic field.

IV.CONCLUSION

1. Platy Rectangular Type Morphology of Uric acid crystal remains same without and with increasing strength of magnetic field.
2. Yield of Uric acid crystals grown are found slightly increased as influence of increasing magnetic field. Overall yield found less as compared to without exposure of magnetic field.

V. REFERENCES

[1]. Patel A R, Rao A V, 1982. Bull. Mater. Sci.(1982)

[2]. A.C. Bhagat, S.K. Popalghat 2013 J. Sci. Res. Rept., (April2013) ISSN: 2249-2321 (Print).

[3]. Bhagat A.C.,Popalghat S.K.2015 International Journal of Recent Scientific Research, ISSN: 0976-3031 (Online).

[4]. Bhagat, A., C., & Popalghat, S. K.2013. Deccan Current Science Research (Dec2013) ISSN: 0975-0344.

[5]. A.C. Bhagat, S.K. Popalghat 2015, International Journal of Recent Scientific Research, (Feb2015) ISSN: 0976-3031.

[6]. A.C. Bhagat, S.B.Bjaj, AR Lathi 2022 Journal of Advances in applied Science and Technology, (Jan2022) ISSN: 2393-8196 (Online).

[7]. JCPDS Card No. (28-2016).

[8]. Hans Ringertz 1965 Acta Cryst., 1965

ICRTMS-2024
International e-Conference on Recent Trends in Material Science
In Association with International Journal of Scientific Research in Science and Technology
Volume 11 | Issue 9 | Print ISSN: 2395-6011 | Online ISSN: 2395-602X (www.ijsrst.com)

Ionization Rate Coefficients of Different Ionic Species in Copper Vapor Laser as a Function Electron Temperature

S N Keshetti[1], A G Chawhan[2]
[1]Shri Shivaji College, Parbhani, Maharashtra, India
[2]Department of Electronics, LBS College, Dharmabad, Dist Nanded, Maharashtra, India

ABSTRACT

In the present work Ionization rate Coefficients of different ionic species like helium, neon and copper have been obtained by using widely used formulae proposed by Lotz as a function of electron temperature. The knowledge of ionization potential of different ionic species is necessary for a given laser discharge. The discharge is generally characterized by the values of electron temperature, electron density, ion temperature, ion density and the types of particles which are ionized.
Keywords: collision, ionization, Ionization rate Coefficient, charge transfer, electron temperature

I. INTRODUCTION

The CVL discharge consists of electrons, ions of helium (neon) and copper having different densities depending upon the electron temperature. These atoms, ions and electron undergo collision among themselves and with walls of the discharge tube. The collision between these elements results in increase or decrease of their charge unity. When the ions of charge z are produce from the ions of charge z-1, the process is called as Ionization. When ions of charge z are produced from ions of charge z+1, the process is called as recombination. Many times collision between these particles changes the energy of the colliding particles. Such type of collision might causes excitation of the particles. At the operating conditions, the total density of inert gas atoms or ions is of the order of $10^{17}/cm^3$ [1, 2]. The electron density is of the order of $10^{13}/cm^3$ [3] and the density of copper is of the order of $10^{13}/cm^3$. Among all gas lasers the collision frequency [4] between the heavy particles is high in CVL as the operating temperature is about 1400 ^{0}C much more than other laser discharge.

Ionization processes

In CVL discharge tube the inert gas particles are ionized by electron impact ionization or by collision with metastable state and singly ionized helium or neon. The ionization may take place by the process of autoionization and photoionization. All these ionization process are discussed as below.

The ionization process of Helium

Electron Impact Ionization (EII)

$He\ I + e$ ------$He\ II^* + e + e$

He II + e -----He III* +e + e
Photo ionization
HeI + hv ------ He II + e
HeII + hv ------ He III + e
Autoionization
Since there only two electrons in the outer most orbit of helium atom and there is no electron in the inner orbit, thus autoionization process need not be considered.

The ionization process of Neon
Electron Impact Ionization
Ne I + e ------Ne II* + e + e
Ne II + e -----Ne III* + e + e
Photo ionization
NeI + hv ------ -Ne II + e
NeII + hv ------ Ne III + e
Autoionization
NeI** ------ -Ne II* + e
NeII **------ Ne III* + e

The ionization process of Copper
Electron Impact Ionization
Cu I + e ------Cu II* + e + e
Cu II + e -----Cu III* + e + e
Photo ionization
CuI + hv ------ -Cu II + e
CuII + hv ------ Cu III + e
Autoionization
CuI** ------ -Cu II* + e
CuII **------ Cu III* + e
The EII process may produce ions either in the ground or excited state. The stars on the species indicates the number of electrons in the excited state

The Penning reaction
There is an important class of inelastic collisions between heavy atoms or ions and helium atoms in excited states where potential energy of helium atom is transferred to atom and therefore the atom may get excited to upper state or may get ionized. Such a process is made more probable if the excited helium atom is in a metastable state and has longer lifetime within which it undergoes effective collision. The process is then known as penning effect. This process of transfer of energy is called as Penning transfer.
The inert gas atoms in the triplet metastable state like in case of He-Cd^{+} laser [1,2,3,6] may transfer their energy to the copper atoms in the ground state and ionize them as follow
He I* + Cu I --------- He I + Cu II* + e
Ne I* + Cu I --------- Ne I + Cu II* + e

The Duffenduck reaction (Charge transfer)

An ion in ground state collides with another ion or atom and transfers its energy to the colliding partner. In the process of collision energy as well as the charge is transferred from one ion to another ion or atom. This process is called as Duffenduck reaction. In this process the inert gas ions transfers their energy to copper atoms and ionize them. The copper ions produced may be either in the ground or excited state.

He II + Cu I ---------- Cu II* + He I

Ne II + Cu I ---------- Cu II* + He I

The process of penning reaction and charge transfer reaction do not produce ionization of any other species of copper.

Penning ionization rate and rate coefficient

The rate of production of Cu II ions by penning process depends upon the density of neutral copper, density of helium metastable states and penning transfer coefficient P. The ionization rate by penning process can be expressed as

$$\frac{dN_{CuII}}{dt} = N_{CuI} * N_{He} * P \quad (1)$$

where Penning reaction rate coefficient is dictated by gas temperature, gas density and reaction cross section. The gas temperature governs the effective number of collisions between helium and copper atoms. The velocity of helium may be treated as an effective velocity. The rate coefficient P, the reaction cross section σ_p and the thermal velocity vHe are related as

$$P = < vHe\ \sigma_p > \quad (2)$$

The ionization rate coefficient can be expressed in terms of energy of helium atoms, the gas temperature θ in eV and the reaction cross section σ_p as

$$P = \frac{6.7*10^7}{86(\theta)^{3/2}} \int_0^\infty \sigma_p\ E \exp(-E/\theta)\ dE\ cm^3/sec \quad (3)$$

where E is the energy helium atom expressed in eV.

The penning excitation cross section σ_p is independent of the velocity colliding helium atoms [5]. And thus can be taken out of integration and we write

$$P = \frac{7.79*10^5}{\theta^{3/2}}\ \sigma_p \int_0^\infty E\exp\left(-E/\theta\right)dE\ \ cm^3/sec \quad (4)$$

The above integral is a standard integral and substituting its value from standard integral table [14], the above equation reduces to

$$P = \frac{7.79*10^5}{\theta^{3/2}} \sigma_p \frac{1!}{(\frac{1}{\theta})^2} \quad (5)$$

$$P = 7.79 * 10^5 \sigma_p\ \theta^{1/2} cm^3 sec^{-1} \quad (6)$$

In the above equation gas temperature is expressed in eV. If it is to be expressed in degree Kelvin, then above equation becomes

$$P = 7.23 * 10^3 \sigma_p\ \theta^{1/2} cm^3 sec^{-1} \quad (7)$$

The Penning reaction cross section is assumed to be independent of velocity of helium atoms.

Duffenduck ionization rate and rate coefficient

The rate of production of copper ions (Cu II) by Duffenduck reaction depends upon the density of copper atoms, helium ion density and rate coefficient T of Duffenduck process. Rate of ionization of Duffenduck process is expressed as

$$\frac{dN_{CuII}}{dt} = N_{HeII} N_{CuI} T \quad 8$$

The rate coefficient of Duffenduck reaction is expressed as

$$T = < vHe\ \sigma_T > \quad 9$$

where vHe is thermal velocity of helium atoms relative to copper atoms and σ_T is charge transfer cross section. The Duffenduck ionization rate coefficient can be expressed in terms of energy of helium atoms, the gas temperature θ in eV and the reaction cross section σ_T as

$$T = \frac{6.7*10^7}{86(\theta)^{3/2}} \int_0^\infty \sigma_T\ E \exp(-E/\theta)\ dE\ cm^3/sec \quad 10$$

Charge transfer cross section also does not depend upon the velocity of colliding particles. Thus the Duffenduck reaction rate coefficient has the same form as the Penning reaction rate coefficient.

$$T = 7.23 * 10^3 \sigma_T\ \theta^{1/2} cm^3 sec^{-1} \quad 11$$

Where θ is temperature in degree Kelvin.

Electron Impact Ionization

An astrophysist Seaton [12, 13] developed theory for obtaining fractional abundance of ions in order to study the spectral emission of solar corona. He proposed the equation for ionizations and recombination rate coefficients and hence the fractional abundances of ionic species. The equation proposed by him for obtaining ionizations rate coefficient depends upon ionization potential I and the electron temperature T is written as

$$S = 2.0 * 10^{-8} \left(J/I^2\right) T^{1/2} 10^{-5040(\frac{I}{T})} cm^3 sec^{-1} \quad 12$$

where J is the number of electrons in the outer most shell from where ionization takes place, I is ionization potential in eV and T is the electron temperature in degrees Kelvin.

But it is believed that this formula gives spurious results and hence mat not be considered for calculations of ionizations rate coefficient. The electron impact ionization rate coefficient S_z is a function of electron velocity distribution, electron energies and electron impact ionization cross section σ_z. Mathematically it is expressed as

$$S_z = < v_e\ \sigma_z > \quad 13$$

It is clear that S_z can be computed if ionization cross-section σ_z and velocity distribution of the discharge electron v_e is known. Wilson and White proposed [8] an empirical equation for the calculation of ionization rate coefficient, which is expressed as

$$S = J\ \frac{0.9*10^{-5}}{X^{\frac{3}{2}}} * \frac{\left(kTe^{1/2}/\chi^{1/2}\right)}{\left(4.88+\frac{kTe}{\chi}\right)} \exp\left(\frac{-\chi}{kT_e}\right) cm^3/sec \quad 14$$

Where χ is ionization potential in eV, T_e is electron temperature in degree Kelvin and J is the number of electron in the outer most orbits with same quantum number.

Lotz [9,10,11] also proposed a semi empirical formula for the calculation of ionization rate coefficient which is expressed as

$$\sigma = \sum_i a_i \chi_i\ \frac{(\ln E/P_i)}{(Ep_i)} [1 - b_i] \exp\left\{-c_i \left(E/P_i\right) - 1\right\}]\ cm^2 \quad 15$$

Where E is the energy of the electron, P_i is the binding energy of the electron which is to be removed and χ_i is the number of the electrons in the i^{th} sub shell. The constants a_i, b_i and c_i can be determined using experimental results. When the energy E of the colliding electron is very near to Pi, the factor E/Pi≈1. Hence

$$\sigma = \sum_i a_i \chi_i \frac{\ln\left(E/P_i\right)}{EP_i}[1 - bi]cm^2 \qquad 16$$

For the electron energy very high compared to P_i, the factor $E/P_i << 1$ and thus above equation get modified to

$$\sigma = \sum_i a_i \chi_i \frac{\ln\left(E/P_i\right)}{EP_i} \qquad 17$$

This derivation of rate coefficient from cross section depends upon electron velocity distribution.

Kushner [3] is of the opinion that electron energy distribution in the CVL discharge is Maxwellian velocity distribution. The density of the electrons having energy range between E and E+dE which follow the Maxwellian distribution function is given by

$$\frac{dn}{n} = \left(2/kT\right)\left(E^{1/2}/\pi kT^{1/2}\right)\exp(-E/kT)dE \qquad 18$$

Where n is the electron density and is the electron temperature in eV.

Assuming Maxwellian velocity distribution the electron impact ionization rate coefficient using Lotz cross section is obtained by equation

$$S_z = 6.7 * 10^7 \sum_{i=1}^{N}\left(a_i\chi_i/T_e^{3/2}\right)\left\{\frac{1}{p_i/T_e}\int_{p_i/T_e}^{\chi}\frac{e^{-x}}{x}dx - \frac{b_i\exp(c_i)}{\left[\frac{p_i}{T_e}+c_i\right]}\int_{\left(\frac{p_i}{T_e}+c_i\right)}^{\chi}\frac{e^{-y}}{y}\right\}cm^3sec^{-1} \qquad 19$$

Where T_e is the electron temperature in eV, p_i is the ionization energy in eV of the electrons in the i^{th} sub shell of the ion charge z and χ is the number of electrons in the sub shell.

The lower limit of the integration goes on changing as the electron temperature and ionization potential changes. The contribution of the second term may be neglected in comparison with the first term as the values of the constants b_i and c_i are very small. Thus the expression for the electron impact ionization can be modified to

$$S_z = 6.7 * 10^7 \sum_{i=1}^{N}\left(a_i\chi_i/T_e^{3/2}\right)\left\{\frac{1}{p_i/T_e}\int_{p_i/T_e}^{\chi}\frac{e^{-x}}{x}dx\right\}cm^3sec^{-1} \qquad 20$$

II. RESULTS

We have calculated penning ionization rate coefficient P as a function of gas temperature θ. The maximum value of θ is taken as 2000 ^{0}K as the operating temperature of the CVL is 1400 ^{0}C [7]. For the calculations of penning reaction rate coefficient the metastable density is considered as $5x10^{12}$ cm^{-3}. The equation for penning reaction rate coefficient shows that as the gas temperature is increased the penning reaction rate coefficient increases. It also increases as the density of copper atoms in the ground state increases. The behavior is as shown in fig 1.

We have calculated charge transfer rate coefficient as a function of gas temperature. The behavior is as shown in fig 2. The behavior of charge transfer rate coefficient is same as that shown in fig 1 except dividing factor 2. The electron density in the discharge is of the order of 10^{13} cm^{-3} [2] for the optimum conditions of the laser

operation. Obviously the density of helium ions and copper atoms should not exceed 10^{13} cm^{-3}. The density of helium ions is less than 10^{13} cm^{-3}. This indicates that the Duffenduck rate is less than penning rate by a factor of 2.

We have calculated ionization rate coefficient for HeI and HeII as a function of electron temperature for the electron temperature ranging from 0 to 10 eV by using Lotz formula and the results are displayed in figure 3. The ionization of HeI starts from T = 1. 5 eV and goes on increasing up to T= 4 eV. Above this electron temperature the ionization rate gets saturated. The ionization of HeII starts at about T=4.5 eV and it increases as the electron temperature is increased up to 6 eV. For the electron temperature higher than 6 eV the ionization rate get saturated.

The ionization rate coefficient for CuI, CuII and CuIII are obtained using Lotz formula as a function of electron temperature. The results are displayed in figure 4. In computations of ionization of CuI, CuII and CuIII the removal of 3d electron is also considered in addition to the removal of 4s electron. The contribution of removal of 3p electron is not considered as they are tightly bounded and the probability of their removal is also very small. The ionization of CuI starts from electron temperature 0.5 eV and increases up to 2.5 eV. When the temperature is increased above 2.5 eV the increase in the rate of ionization decreases. The ionization of CuII starts at about 1.5 eV and go on increasing up to 5 eV. Above this temperature rate of increase of this coefficient becomes less and starts saturating for higher temperatures. The ionization of CuIII starts at about T= 3 eV and increases as electron temperature is increased. The rate coefficient gets saturated at temperatures more than 9 eV.

We have calculated ionization rate coefficient for NeI and NeII as a function of electron temperature and the results are displayed in figure 5. The behavior of rate coefficient as analogous to the behavior of He and Cu.

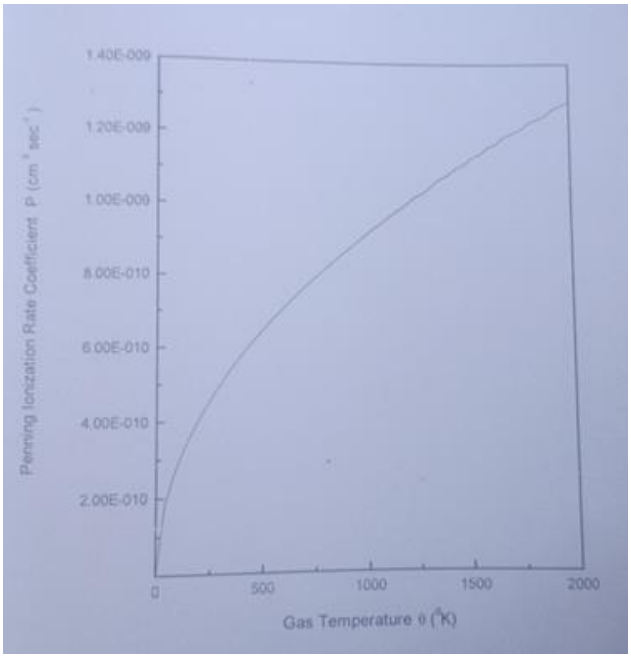

Fig.1: Penning Ionization rate coefficient P as a Function of Gas temperature

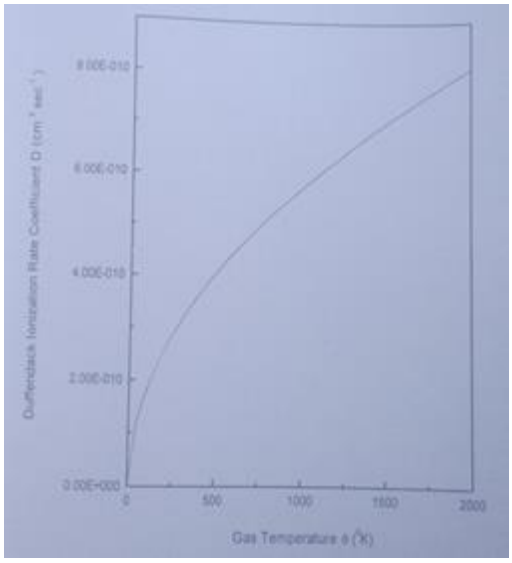

Fig.2: Duffenduck Ionization rate coefficient D as a Function of Gas temperature

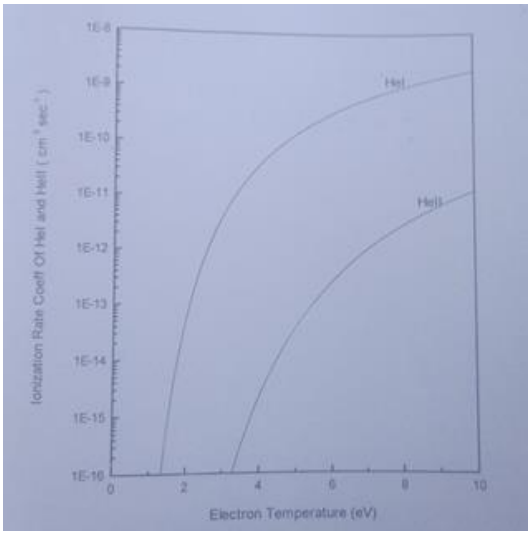

Fig 3. Electron Impact Ionization Rate Coefficient of He I and He II as a Function of Gas temperature

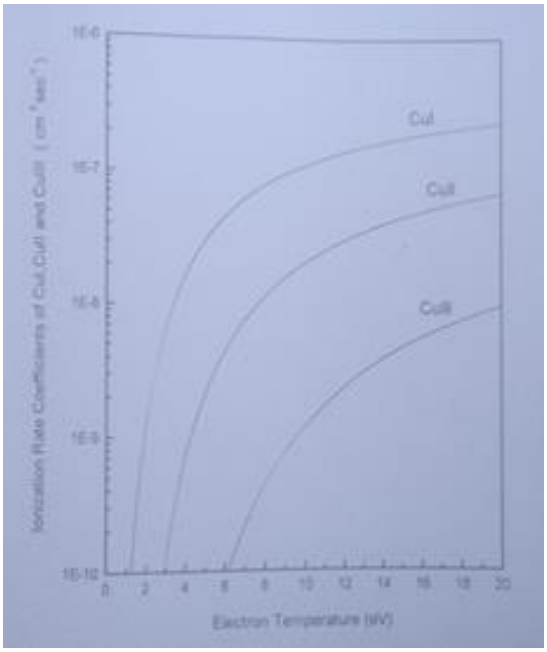

Fig 4. Electron Impact Ionization Rate Coefficient of Cu I, Cu II and Cu III as a Function Gas Temperature

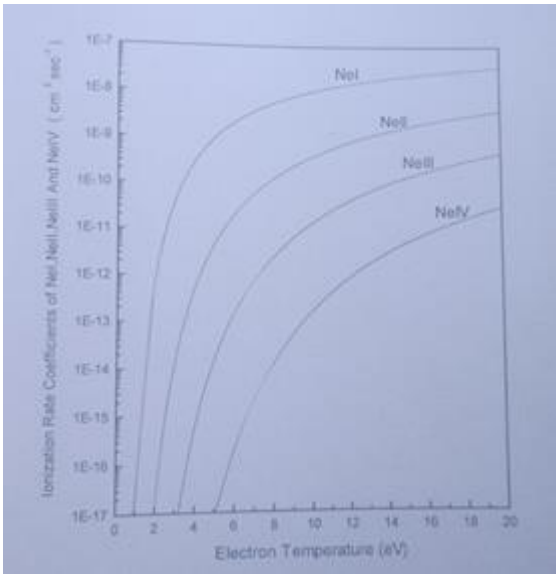

Fig 5. Electron Impact Ionization Rate Coefficient of Ne I, Ne II, Ne III and Ne IV as a Function of Gas temperature

III. REFERENCES

[1]. P G Browne and M H Dunn, J Phys B : At mol phys, Vol 6, pp 1103-17 (1973)
[2]. T Goto, Y Shimizu, S Hatttoti and T Sakurai, J phys D: Appl phys, Vol 16 pp 261-68 (1983)
[3]. M J Kushnar, J Quantumm Electronics, Vol QE-17, No 8, pp 1555-65 (1983)
[4]. W T Silfvast, Appl Phys. Lett 15, pp 23, (1979)
[5]. P Gill and C E Webb, J Phys D: Appl Phys, Vol II, pp 245-55 (1978)
[6]. A L Mckenzie, J phys B : Atom and Mol phys, Vol 10, No 10 pp 2023-33
[7]. T W Alger and W L Bennet, Rev Sci Instrum, vol 53, pp762 (1982)
[8]. Wilson and White, Unpublished
[9]. W Lotz, J Optical society of America, Vol 57, pp 873 (1967)
[10]. W Lotz, J Optical society of America, Vol 58, pp 915 (1968)
[11]. W Lotz, Z Physik, Vol 216, pp 241 (1968)
[12]. M J Seaton, Planet Space Sci, Vol 12, pp 55 (1964)
[13]. M J Seaton, Mon Not R Astro Soci, Vol 119 pp 81, (1959)
[14]. B O Pierce: Revised by Ronald M Foster, A short table on Integrals, fourth edition (1986)

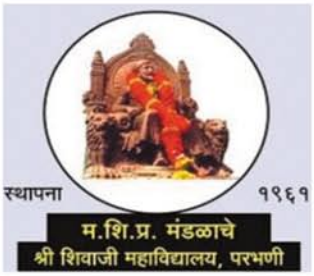

International e-Conference on Recent Trends in Material Science

[ICRTMS-2024]

Organized By

Department of Physics and And Electronics ,
Shri Shivaji College
Parbhani, Maharashtra, India

Publisher

Technoscience Academy

Website : www.technoscienceacademy.com

Email : editor@ijsrst.com Website : http://ijsrst.com